Low-velocity impact loading
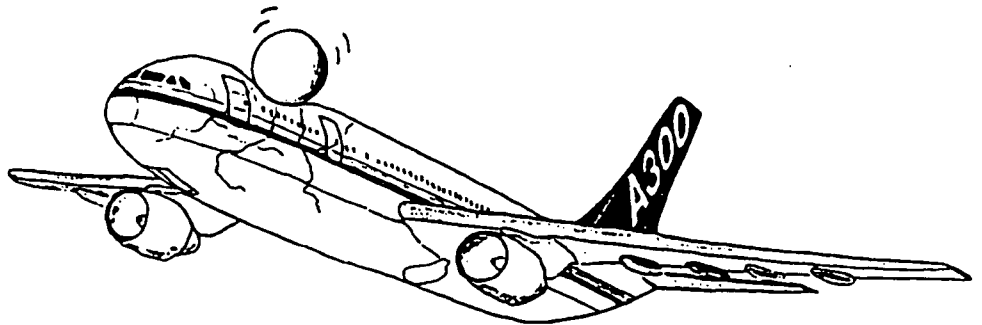
on fibre reinforced aluminium laminates (ARALL and GLARE)
and other aircraft sheet materials
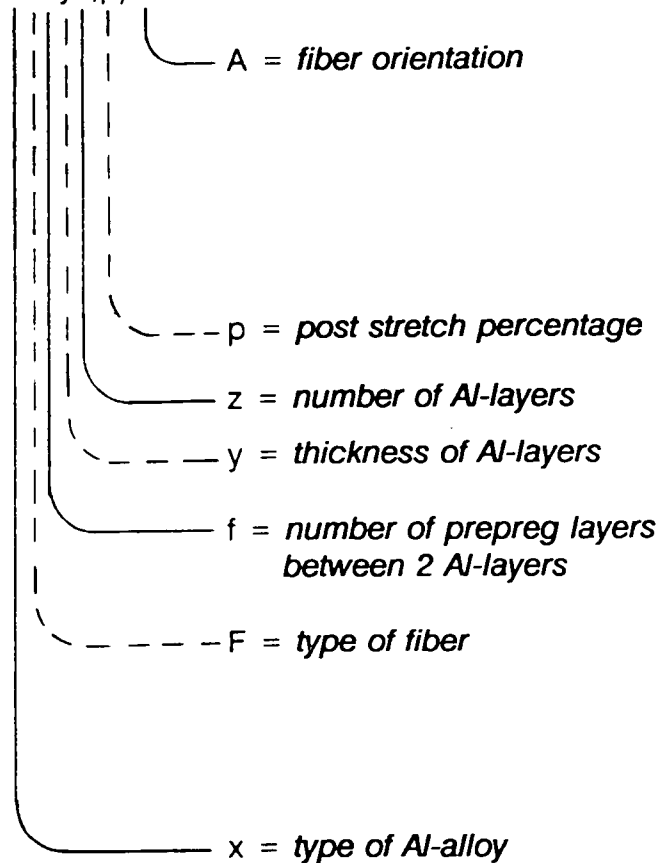
A. Vlot

TUDelft

Delft University of Technology

Faculty of Aerospace Engineering

ARALL-code

xF'yz,p/A

A = fiber orientation

if A is omitted then UD fibres.
A = 90-10 → 90 % of fibres in one direction,
10 % in the other direction.
A = w → square weave
A = Cxx → cross-ply variant,
C73 → 70 % of fibres in one direction,
30 % in the other direction.

p = post stretch percentage

p = 0.4 means 0.4 % post stretch.
If post stretch is not done, p is omitted (p=0).

z = number of Al-layers

y = thickness of Al-layers

y = 3 means t_{Al} = 0.3 mm

f = number of prepreg layers between 2 Al-layers

if f = 1 then f is omitted.

F = type of fiber

H → high modulus aramid fibre
S → S-glass fibre (S_2)
R → R-glass fibre (R_1,R_2,R_3,R_4,R_5 or R_6)
C → carbon fibre (C_1 or C_2)
AF → no fibres, only AF 163-2 adhesive

x = type of Al-alloy

x = 2 → 2024-T3
x = 7 → 7075-T6

Example : **2H33,.42/w**

→ 2024-T3 sheets,

→ high modulus aramid fibres,

→ 3 Al-alloy layers, of 0.3 mm thickness,

→ 0.42 post stretch applied,

→ square weave fibres.

'Alle daden des menschen staan in levend verband met zijn geloof'

(K.J. Popma)

'Laten dan de ingenieurs inzien dat het, om ingenieur te zijn, niet voldoende is ingenieur te zijn.'

(José Ortega y Gasset)

I

Abstract

The impact properties of new aircraft materials play an important role for the design and certification of aircraft structures. Low velocity impact tests were carried out on monolithic aluminium alloys, various types of ARALL laminates and thermoplastic composites. The damage resistance of aramid ARALL and carbon ARALL is comparable with that of the composite materials, it is poor relative to aluminium alloys. The damage resistance of GLARE (ARALL with R-glass fibres) is in general only slightly less than for monolithic material, and is it therefore satisfactory.

The damage tolerance (residual strength after impact damage) of aramid ARALL is also comparable to that of the thermoplastic composites. The residual strength of GLARE is superior to that of aramid ARALL.

In the literature only dynamic linear elastic models and a static non linear elastic model are available. A non linear elastic impact model (NOLEIM) was developed, which is able to calculate the force-time, velocity-time and deflection-time curves accurately. The calculations of this model were compared with experimental and finite element results. A static elasto plastic impact model (EPIM) was derived which is able to calculate deflection-energy and force-deflection curves.

survey of chapters

contents

part two Impact experiments

part three Impact modelling

part four   Residual strength after impact

list of symbols

A	length of rectangular plate
A_{ij}	stretching stiffness of laminate
a	acceleration (of impactor), semi crack length, axis of ellipse radius of circular plate
B	width of rectangular plate
b	axis of ellipse
c	stiffness, radius of the contact area
D_{ij}	bending stiffness of laminate
d	damage width
E	Young's modulus
e	restitution coefficient
e_v	velocity restitution coefficient
e_T	energy restitution coefficient
F	(contact) force
F_{max}	maximum force during impact
F_f	force at first failure
F_u	force at ultimate load
f	frequency
g	acceleration of gravity
G	energy release rate, shear modulus
H	transfer function
h	impact height
I	rotatory inertia
K	stress intensity factor
k	stiffness, Hertzian indentation stiffness, shear correction factor
l	length
M	mass on top of the load cells of the clamping
m	mass
m_p	impactor mass
m_{eq}	equivalent plate mass
$m_{tot} = m_p + m_{eq}$	
N	number of points, normal stress resultant
n_{ij}	non linear term in the derivative of the internal energy
p	pressure
Q	shear stress resultant
q	distributed pressure between impactor and plate

q_0 maximum pressure

R   radius (of impactor tip)

r   coordinate in radial direction

S   initial tensile stress

s   displacement of impactor

T   kinetic energy, temperature, period of vibration

t   time, sheet thickness

t_c contact time

U   internal energy

U_{el} elastic internal energy

U_f internal energy at (first) failure, strain energy in fibre layer

U_u internal energy at ultimate load

U_s extra internal energy due to initial loading

u   displacement (in x direction)

v   velocity (of impactor), displacement (in y direction), volume fraction

v_0 impact velocity

v_0^* initial velocity of impactor/plate combination

v_r velocity after impact

v_f fibre volume fraction

V   gravitational energy, potential energy

w   deflection (= displacement in z direction)

w_0 central deflection

$\bar{w}_0$ permanent central deflection

w_0' elastic part of the central deflection

$w_{0,f}$ central deflection at first failure

$w_{0,u}$ central deflection at ultimate load

$w_{0,s}$ central deflection due to shear only

x   coordinate (in the plane of the plate)

y   coordinate (in the plane of the plate)

z   coordinate (in thickness direction of the plate)

α top angle of conical tip of the impactor, indentation, linear work hardening parameter

Γ average shear strain

γ shear strain

δ material constant for Hertzian indentation

ε strain

    ε_r radial strain

    ε_θ tangential strain

    ε_u failure strain

    ε_m membrane strain

    $\dot{\varepsilon}$ strain rate

ϕ (loading direction relative to) fibre orientation

η normalized coordinate (= r/a)

θ polar coordinate

ν Poisson's ratio

ψ planar rotation of cross section

ρ density

    ρ_s surface density

σ stress, attenuation factor

    σ_{crit} critical (buckling) stress

    σ_y yield stress

    σ_u tensile strength

    $\sigma_{res,\ u}$ residual tensile strength after impact damage

    σ_n attenuation factor

    σ_e von Mises effective stress

τ shear stress

ξ shape of the dent (= w/w_0)

ω radial frequency

chapter 1 Introduction

Impact, the collision of two or more objects, occurs in our everyday life. When you bump your head, drop a plate on the floor, have a car accident, or when you are cracking an egg, you are experiencing impact problems.

Apparently two aspects of the phenomenon play an important role. First there is the motion of the striking object, and secondly this motion causes deformation in the target which may lead to failure and cracking. Often an impact loading is caused by an accident.

Impact is of technical relevance. For example: during a car accident the structure has to absorb energy in a controlled way, such that the occupants are subjected to decelerations which are as small as possible. Another example: damage inflicted by impact may reduce the strength of an aircraft structure and may lead to damage growth and catastrophic failure. It is also possible that impact loading occurs regularly in service, e.g. the landing of life boats and flying boats on water.

Impact is a phenomenon with a large variety of problems. Impact problems have to be divided in different categories depending on the velocity regime and the type of structure involved. For example: the impact of a bullet on armour is completely different from the collision between two ships.

The aim of this study is to describe the impact behaviour of ARALL laminates under realistic impact loading, and to compare the impact behaviour of this material with other aerospace materials, like composites and conventional aluminium alloys. The impact velocity in this study is limited to low velocities (max. 15 m/s) and the specimens are thin (max. 2 mm).

ARALL laminates belong to a new family of materials, developed by the Delft University of Technology. ARALL laminates sheet material is built up from very thin alloy sheets bonded to one laminate by intermediate fibre/adhesive layers, see figure 1.1. The fibre/adhesive layers are called the 'prepreg' layers. The prepregs are aramid, glass or carbon fibres in an epoxy adhesive. ARALL laminates were developed as a material with a high

fatigue resistance, achieved by fibre bridging of fatigue cracks and a favourable residual stress system in this hybrid material. 'If a crack has been initiated in the aluminium alloy layers, some limited delamination will occur at the interfaces between the epoxy and the fibres. That will accommodate stress redistribution from the metal to unbroken fibres in the wake of the crack. Crack bridging provided by the strong fibres, constrains crack opening, and thus reduces the driving force for crack growth in the metal layers (figure 6.2).'[6]

Various properties of this material are described by Vogelesang and Gunnink[1,2,3]. ARALL laminates combine the formability and machinability of aluminium alloys with the good fatigue resistance and high specific strength of composite materials ('The best of both worlds'[4]). The development of this family of fibre reinforced laminates started in the late seventies in the laboratory of Materials and Structures of the Faculty of Aerospace Engineering of the Delft University of Technology. Initially, aramid fibres were applied, therefore this material received the name 'ARALL', which stands for: Aramid Reinforced ALuminium Laminates. In the late eighties new variants of ARALL laminates were developed, in order to improve the blunt notch and residual strength of the material. For this new generation of ARALL laminates high strength glass fibres were used. The trade name of the AKZO company for this material with high strength glass fibres is: GLARE (GLAss REinforced). GLARE is a promising candidate for highly stressed aircraft components, like wing and fuselage structures. Also a carbon fibre variant (CARE) has been developed, with potentials for spacecraft applications[5]. In this study we will use the name 'ARALL laminates' or 'ARALL' (both as the generic name) to indicate the whole family of fibre reinforced aluminium laminates.

In this thesis report the variants with aramid, glass and carbon fibre will be designated with:

ARALL (laminates) ──┬── aramid ARALL (fibre: aramid)
                    ├── GLARE or R-glass ARALL (fibre: R-glass)
                    └── CARE or carbon ARALL (fibre: carbon)

The ARALL material has many variants; it is a family of materials. Variables are:

- type of aluminium alloy

- thickness of the prepreg layers

- thickness of aluminium layers

- type of fibre

- type of adhesive

- lay-up (e.g. fibres unidirectional, cross-ply or weave; number and order of the aluminium and prepreg layers).

Moreover, the material can be poststretched. Poststretching causes a reversal of the residual stress system from tensile stresses in the aluminium layers and compressive stresses in the prepreg layers after curing (due to the difference in thermal expansion coefficients) to compression in the aluminium and tension in the prepreg. The compressive stresses in the aluminium make the fatigue properties of the poststretched material even better than of the as cured material.

The code on the inside of the front cover was adopted in this report to identify an ARALL variant.

Composite material is another candidate to replace the conventional aluminium alloys in aircraft structures. Composite materials, which are a combination of relatively strong and brittle fibres embedded in a more tough and weak matrix, are known to be prone to impact damage. The damage reduces the strength significantly, and as a consequence the allowable design stress of a structure is decreased, thus reducing the possible weight and fuel savings. A new development of composites are based on thermoplastics: composites with a thermoplastic matrix. The increased toughness of this matrix relative to the brittle thermosetting matrices (like epoxies) and the 'simple' and fast manufacturing methods due to the formability under high temperatures, makes this material very attractive.

The impact related properties of aircraft structural materials have two different aspects:

1. the behaviour of the material during impact (caused by runway debris, falling tools during maintenance, hailstones, etc.), the extent and types of damage created during impact loading.
2. the residual (mechanical) properties of the materials after impact.

Both aspects will be treated in this study. Various impact tests were performed. Analytical tools were developed to study the effect of the material variables of ARALL laminates and composites on the behaviour during impact. Additionally, residual strength tests were performed, to study the effect of damage (cracking and a plastically deformed dent) on the tensile strength and fatigue properties of ARALL, and to determine the behaviour of a delamination under compressive loading.

This report is divided in four parts.

1. Introduction on impact and damage tolerance

The first part is a general introduction to impact, to set the scene and to give the background for the remainder of the report.

2. Impact tests on aircraft materials

Part two gives the results of the impact test series on aircraft materials. It starts with a literature survey (chapter 4), and it also includes a description of the impact tester developed for the present investigation (chapter 5), the impact on sheet material (chapters 6 and 7), and impact tests on specimens under load (chapter 8).

3. Theoretical analysis

Part three describes theoretical analyses proposed to model the impact phenomenon for sheet specimens, in order to obtain a better understanding of what happens during impact, and of the significance of the various parameters which are involved. Chapter 9 gives a literature survey on this topic. In chapter 10 the relation between the shape of the dent and the internal strains are given. Chapter 11 describes the effect of the strain rate on the input parameters of a model and gives results of high velocity tensile and puncture tests on ARALL laminates, composites and aluminium alloys. A non linear elastic impact model (NOLEIM) will be derived in

chapter 12. Results of this model will be compared with finite element calculations, the experimental results in part three of this study and with results of linear models described in the literature.

4. Residual properties after impact

The last part deals with the residual properties of materials after impact. The residual tensile strength will be treated in chapter 11. In this chapter results will be presented of measurements of the strain around a plastically deformed dent, fatigue tests under tension on ARALL laminates, and a comparison of the residual strength of ARALL, monolithic aluminium alloys and thermoplastic composites. Delamination, which may be induced by impact loading, especially affects the compressive strength. Chapter 12 deals with delamination buckling under compressive loading of ARALL laminates.

This thesis report ends with a summary of the results and conclusions of the study and with appendices.

references

1. Vogelesang, L.B.; Gunnink, J.W.; ARALL, a material for the next generation of aircraft, TU Delft report LR400, Delft, 1983.

2. Gunnink, J.W.; Vogelesang, L.B.; Aerospace ARALL, The advancement in aircraft materials, Proceedings 35th International SAMPE symposium, Anaheim, California, April 2-5, 1990.

3. Vogelesang, L.B.; Gunnink, J.W.; ARALL; a materials challenge for the next generation of aircraft, Materials and design, Vol.7, No.6, 1986.

4. Best of both worlds - AKZO metal/composite hybrids prepare for takeoff, Air and cosmos monthly, June 1990.

5. Vermeeren, C.A.J.R.; Vogelesang, L.B.; Gunnink, J.W.; New developments in fibre metal laminates (ARALL), Proceedings of international symposium, European Space Agency ESTEC, Noordwijk, The Netherlands, March 21-23, 1990.

6. Chen, D.; Bulging of fatigue cracks in a pressurized aircraft fuselage, PhD thesis, Delft Technical University, 1991.
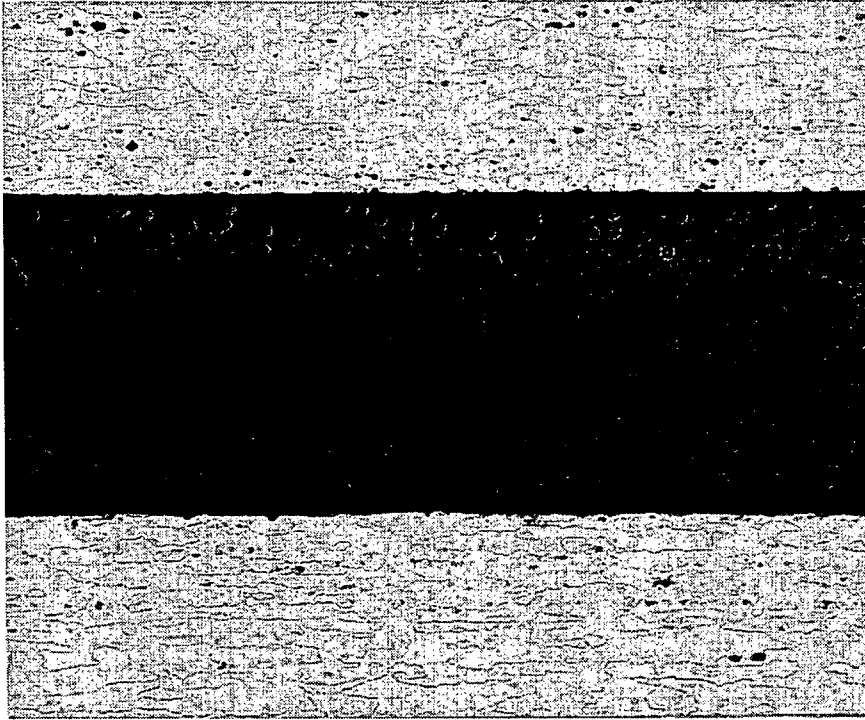
figure 1.1 Cross section of ARALL
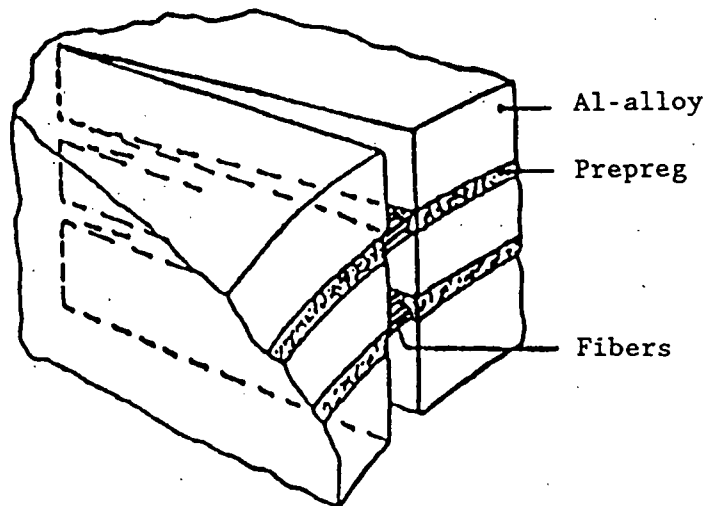
figure 1.2 Crack bridging of fatigue crack in ARALL

PART I: IMPACT DAMAGE AND DAMAGE TOLERANCE

chapter 2: Damage tolerance of composite aircraft structures

chapter 3: Impact, the process and its significance for aircraft structures

chapter 2 Damage tolerance of composite aircraft structures

2.1 Introduction

The present thesis deals with impact loading on aircraft materials. Impact is one of the types of damage which may occur in a structure. A damage tolerance concept has to deal with this type of damage for the design and certification of the structure. Impact loading is especially important for composite materials. This chapter gives an overview of the types of damage which may be found in composite structures and their influence on the residual strength, the design and certification. It is based on the literature given at the end of the chapter.

The literature on damage tolerance of composite materials is in general not very clear. The authors draw general conclusions on test results of composites with different fibres, matrices, lay-ups and specimen types. Results of coupon tests are projected to the behaviour of structures, which also offer problems.

2.2 Types and sources of damage

'Damage tolerance is defined as the ability of a structure to tolerate a reasonable level of damage or defects that might be encountered during manufacture or while in service'[1].

The literature refers to 'damage tolerance' as a property of the material or the structure related with damage. However, it is important to realize that there are four damage properties:
  - damage resistance (sensitivity for damage)
  - damage tolerance (residual mechanical properties in the presence of damage)
  - inspectability (ease of detection of damage)
  - repairability (ease of repair).

Damage of conventional metallic materials generally consists of well characterized cracks. A damage tolerance methodology is available which describes fatigue crack growth and residual strength.

Damage in composites is complex, because it is a combination of failure of the constituents: fibre breakage, fibre-matrix debonding, matrix cracking

and delamination. For example, impact damage in thick laminates is usually a combination of resin shear fracture and interlaminar delamination[1]. Impact damage in thin laminates will be dominated by fibre failure. No generally applicable strategy is available to prove the damage tolerance of a composite structure.

Damage tolerance of composites is a matter of concern because of the relatively brittle nature of these materials. The brittleness makes composites sensitive to damage, and less tolerant if of damage is present as compared with conventional aluminium alloys. It implies that much care has to be taken to avoid damage and defects. Accurate non-destructive testing (NDT) methods are needed to detect damage when it occurs. Damage and defects may be induced during the fabrication of the part and the material (e.g. voids and porosity), or may occur during the service life of the aircraft. Tables 2.1, 2.2 and 2.3 give a summary of manufacturing defects and in service mechanical and environmental damage.

Damage can be caused during the manufacturing process (e.g. delamination induced at the edge of a hole by drilling) or by handling. Quality control by ultrasonic inspection is needed to detect whether the area of defects exceeds a certain threshold level.

In service damage can be divided in four categories: fatigue damage, environmental degradation, accidental damage (impact) and wear and erosion (by rain, sand and dust). These causes of damage do not act independently: impact damage causes moisture ingress and fatigue damage accumulation.

2.3 Residual strength

2.3.1 Residual strength and impact damage

It is important to know the residual mechanical properties of a damaged structure. Figures 2.1 and 2.2 give an impression of the effect of damage and defects on the residual strength and fatigue properties, both under compressive loading. The figures show that impact damage is the most severe source of damage because it has a large effect on the residual mechanical properties. Moreover, the probability of occurrence is high[5].

Delaminations and fibre failure caused by impact are the most serious of

the various defects and damage types, especially because of the poor blunt notch behaviour under tensile loading and the reduction in compressive strength due to delamination buckling.

Barely visible impact damage (BVID) significantly reduces the strength of the material (reductions to a level of 40% of the original strength), while visible damage may reduce the strength to 30% of the original strength[13]. Impact damage becomes visible at the side of impact when the largest reduction in the (compressive) strength has occurred, see figure 2.3.

Impact damage in composites can cause fibre failure, matrix cracking, fibre/matrix debonding and delamination. Fibre failure is caused by bending and stretching of the laminate. Delamination is due the bending stiffness mismatch of the laminae (the largest delamination area will be present between the laminae with the largest difference in ply orientation)[21] and transverse shear. Matrix cracking is mainly due to shear, and fibre/matrix debonding is present in the form of fibre splitting. The delamination and shear failure will be present in a conical region in the thickness direction of the laminate under the impact point. This combination of damage types affects the tensile as well as the compressive strength. Moreover, this damage may grow under cyclic loading.

2.3.2 Residual tensile strength

If damage is present in composite material, the static residual tensile strength may be seriously reduced. The residual tensile strength is mainly influenced by fibre failure in the material and less by matrix failure, delamination and fibre/matrix debonding. The composites have a relatively poor notch behaviour relative to metals. Stress peaks are not relieved by plastic deformation which is characteristic for metals. A through crack in composites may cause approximately the same strength reduction as a hole with the same diameter, but there is little additional sharp notch effect[1]. If a sharp notch effect is present, higher impact energies may lead to a higher residual strength, because of a cleaner perforation. The residual tensile strength is mainly of importance for thin laminates (thickness smaller than 3 mm), because fibre failure prevails in these laminates under low energy impact loading. In metallic materials a crack due to impact loading always will be a through crack. Fibre failure in

composites due to impact starts at low impact energies at the non-impacted side; the crack is not necessarily a through crack. If the failure is not a through crack, the intact fibres act as a barrier against damage growth in the thickness direction. Damage growth thus tends to be interlaminar[1].

A straightforward fracture mechanics approach is not available at this moment, but there are ways to estimate the residual tensile strength of laminates with a given crack length due to fibre failure[2].

2.3.3 Compressive strength

The compressive strength of a delaminated composite due to impact is poor (figure 2.1), and this delamination can not always be easily found in a structure. Most of the work on damage tolerance of composites found in the literature concerns tests on coupons under compressive loading and on compression panels. In these tests the Euler buckling strain of the specimens has to be higher than the failure strain in the presence of the damage. Usually the lower boundary of the failure strain is between 3000 and 4000 micro strain, which limits the design strain for compression panels in a structure to this value. Compressive failure occurs by:

- delamination buckling
- transverse shear as a result of the degraded ability of the
  matrix to stabilize the fibres due to matrix cracking, and
- shear crippling (micro buckling of the fibres) caused by
  fibre/matrix debonding and matrix cracking[18].

Two parameters are used to calculate the residual (compressive) strength of delaminated laminates: the strain energy release rate approach and the strain energy density approach. The latter method assumes that growth occurs when the available energy density at a certain distance from the delamination front reaches a critical value[15]. Because a delaminated region acts as a low modulus zone, the reduction in compressive strength may be of the same order as for an unfilled hole[2], but for small zones (smaller than 0.3 of the width of the specimen) the reduction of the compressive strength is larger for impact damage[18].

Much theoretical work was done on delamination buckling under compressive loading and methods were derived to calculate energy release rates. More

about this subject will be discussed in chapter 14, including the delamination buckling of ARALL laminates.

2.3.4 Fatigue properties

Damage may grow under cyclic loading; however, composite materials have good fatigue properties in comparison with metals. Static strength requirements usually determine the design strain, and not damage growth due to fatigue, as is the case for many metallic structures. During the certification of a composite structure the aspect of fatigue is generally treated by a 'no-growth approach': it is shown that no growth of damage will occur under service load conditions.
Fatigue may become important if interlaminar stresses do occur, e.g. at the edges of holes, at free edges, in regions of section changes and in bonded joints.

If damage growth takes place, the in-plane fibres are barriers against the formation of a through crack, and the damage thus tends to grow interlaminarly. Sufficient experimental data and analytical tools are not available for the prediction of damage growth and residual strength.

The fatigue loading during tests on composite materials has to be chosen carefully. Typical aircraft load spectra for conventional (metallic) structures are relatively benign for composites, compared to constant-amplitude loading, because of the few peak load cycles encountered. This is in contrast to metals, for which the numerous low-stress cycles significantly contribute to crack growth, whereas the high-stress cycles may actually be beneficial because of their retardation effect[1]. For composites a severe design spectrum has to be used, because peak loads cause fracture in these materials. Low loads (smaller than 30% limit load stress) may be omitted from tests on composite materials to save testing time. Mixed structures (composites and metals) should be evaluated individually[4]. During fatigue tests a testing frequency of 5 Hz is commonly used, because tests have shown that it gives the same results as with a frequency of 0.3 Hz[1], which is a more realistic frequency in a spectrum.
The fatigue curves, as shown in figure 2.2, generally are relatively flat,

and a large scatter in fatigue lives is found compared with monolithic metals[1]. This is associated with the flat shape of the fatigue curves.

Tension-tension fatigue loading is considered to be less critical than compression-compression and tension-compression loading[15]. Delamination and splitting caused by tension fatigue loading of damaged laminates tends to remove stress concentrations from the damage. The removal of stress concentrations even may increase the tensile strength to net-section strength[2].

Compressive fatigue loading may cause delamination growth due to delamination buckling. In this case the delamination growth per cycle decreases with increasing delamination length, because the peel stresses are reduced[19].

2.4 Influence of fibres and matrix

Damage resistance and damage tolerance of composites can be improved by selecting higher strain-to-failure fibres and tougher resins. Fibre failure due to impact damage and the blunt notch strength are directly related to the fibre strain to failure and the ability to absorb energy. Delamination induced by impact is related to the adhesion between fibre and matrix and to the toughness of the matrix. Also delamination growth due to delamination buckling is related to the interlaminar fracture toughness. The residual compressive strength after impact is therefore a function of the interlaminar critical strain energy release rate G_{Ic}[1]. Tough resins tend to change the fracture mode under compression after impact from delamination growth caused by delamination buckling to transverse shear fracture[18].

Improving the toughness of the resin is not always beneficial. Materials with tougher resins may have the advantage of a smaller damaged area after impact, but it can also lead to a higher notch sensitivity under tensile loading because stress concentrations are not relieved by delaminations and splitting[10].

Elber[6] warns of unsafe impact failure modes for too tough or strong resin systems. To improve impact resistance, both fibre and matrix must be improved. If the matrix system is tough, while the fibres are brittle, the

failure mode tends to change from delamination to fibre failure and penetration. Elber shows that the effect of a tougher matrix will be beneficial only if the plate is thick (relative to the supported width of a sheet in the structure), because in this case the transverse shear stresses may become high, and the interlaminar strength (highly dependent on the resin) will become important. Otherwise the failure mode will be dominated by fibre failure instead of delamination.

The use of hybrid laminates (e.g. glass and carbon fibres) has proven to be an effective way to improve damage tolerance[1]. Glass fibres are able to absorb more energy before failure and will bridge a damaged zone after impact under tensile loading. Also through-the-thickness stitching of the laminate has shown the potential for improving interlaminar strength and damage tolerance[13].

2.5 Test methods

In the literature three ways are followed to study the damage resistance and the damage tolerance behaviour:
- residual strength tests
- delamination tests
- impact damage resistance tests

Residual strength tests
This method determines the compression behaviour of a specimen with artificial delamination damage (obtained by introducing a non-adhering thin film, e.g. teflon) or of specimens with damage induced by impact. Compression tests are done on stiffened panels, or on coupon level (small specimens) by experiments with plates supported in a fixture.
The stiffened panels are close to a realistic structural application. They are designed for a specific panel loading. These kinds of tests are therefore more like a test on a part of a specific aircraft structure than tests on simple plate specimens.
The latter type of test is generally done with a fixture to support the edges of the specimen as defined by NASA, i.e. the dimensions of the specimen are 250x150 mm, the loaded edges are clamped, and the unloaded edges are simply supported with knife edges. Damage is induced by impact or

by inserting an artificial delamination in the laminate. Artificial delaminations close to the surface tend to grow after popping-out[2].

In general, impact loading on specimens on coupon level gives more damage and a lower residual strength compared with results on stiffened panels[13], but it depends on the dimensions and the boundary conditions of the subpanels of the stiffened panel and of the coupon specimen. Tests on stiffened panels showed that a maximum damaged area is obtained if the impact occurs midway between the stiffeners or spars[13].

The coupon specimens as well as the stiffened panels can be impacted under an initial load. The results show that initially loaded specimens are more damaged by impact than unloaded specimens[5].

Delamination tests

The second approach is a more fundamental one, based on the determination of the fracture energy for the interlaminar fracture modes. The G_{Ic} and the G_{IIc} are important parameters. According to Horton and McCarthy[1] the compressive strength after impact will increase when G_{Ic} is increased (while the fibre type and the lay-up are kept constant). The G_{Ic} is generally measured in double cantilever beam experiments. The G_{IIc} is more difficult to determine because most specimens, which are nominally loaded in mode II do still exhibit some mixed mode I/II failure.

Impact damage resistance tests

To study the damage resistance and the behaviour of materials during impact, tests are done on small clamped or simply supported sheet specimens. These tests can be instrumented to obtain information about the impact process. More information on this type of testing and test results will be given in part II of this thesis report.

2.6 Design aspects

According to the damage tolerance requirements the design limit compressive strain should be 0.003 to 0.004[1) for classical composites with an epoxy matrix (see section 2.3.3). The limit design tensile strain may be somewhat

---

1)
It is interesting to note that the strain at yield of Al 2024-T3 is also approximately 0.004.

higher, because the influence of impact damage on the tensile strength will be smaller. A limit strain with approximately the same value may also be needed to reach a blunt notch strength which is high enough for dealing with stress raisers, such as fastener holes [2,16].

The design strain for compression members is based on compression tests after impact, with or without loading during impact. Such tests generally show a lower bound of approximately 0.003 to 0.004, see figure 2.4. This figure shows the so called 'threshold curve': the initial strain boundary between failure and no failure of the specimen at impact for different impact velocities under initial strain.

The limit strain restriction implies that the weight savings for wings of large transports are not high enough if compared to high strength aluminium alloy designs[5]. Therefore the use of composites until now is mainly limited to secondary and stiffness dominated structural parts. The introduction of new tougher resins (e.g. thermoplastics) may increase the possible weight savings[2).

Wiggenraad[5] has considered the possible effects of material and design improvements on the design limit strain. For current resin systems with unidirectional materials the limit design strain is limited to 0.004. The application of fabrics may improve this value to 0.0045. Stitching and the use of tougher resins (e.g. thermoplastics) means that the limit design strain can be increased to approximately 0.005. Further design improvements of composite structures are needed to reach a still higher limit design strain in the order of 0.006.

Damage tolerance is not an inherent property of a material. It is also dependent on the structural design. There are several ways in which a design of a stiffened panel in composites can have an improved damage tolerance. The first one is related to the ply orientation (lay-up) of the

---

2)
De Jong recently proposed in his inau g uration address [22] temporarily to give up the aim of saving weight by the introduction of composites in primary structures of civil aircraft. Other advantages of composites like a decrease of the number of parts and the possibility to manufacture smooth complex shapes should be stressed. When the possible weight savings are not used but translated into thicker laminates, it might be a solution for the damage tolerance problem of the composites. Weight savings can be reached in the future, as a result of an evolution of composites structures, and should not be aimed for at this moment.

skin. A skin of a damaged panel with a 'soft' orientation (with a low percentage of plies oriented parallel to the loading direction) will have a higher strain to failure than a skin with a stiff ply orientation. If a 'soft skin' is adopted, the stiffness and load-carrying capability of the panel in loading direction is provided for by thick, damage resistant stiffeners[1].

Demuts et al.[13] compare results of multirib (typical for a transport wing) and multispar (typical for fighter aircraft) designs of wings. The multispar design has a 'soft skin' (low modulus skin, predominance of $\pm 45^0$ plies) and a 19% higher compressive strength after impact than the multirib design with the worst type of damage for both designs.

The outer layer of a composite lay-up has to be $\pm 45^0$ or 90^0 to assure good damage tolerance. The application of weave as an outer layer showed to improve damage tolerance[24]. Also a protection layer of glass or aramid on the outer layer at the possible side of impact is suggested[25].

Wiggenraad[5] mentions a design solution for a structure type with inherent fail-safe properties because of the multiple load paths: a grid stiffened panel. This type of structure shows some similarity with a truss structure. It is striking that both the 'soft skin' approach and a grid stiffened panel in a certain way appear to be a step backwards in the evolution of an aircraft structure. The load carrying function of the skin is taken away, and given back to the frame of the aircraft (stiffeners, frames, ribs and spars).

It is evident that the thickness of the composite will have a large influence on the sensitivity for impact damage. Thin composite structures (e.g. the facings of a honeycomb structure) are very sensitive to low-level impacts, which implies high repair costs[4]. Also the concentration of material of stiffened panels in the stiffeners (e.g. 'soft skin' approach and grid stiffened panel) to improve damage tolerance will make the skin itself less damage resistant.

2.7 Environmental effects

It is well known that the properties of composites are degraded, especially by hot/wet conditions. Moisture absorption reduces the strength and stiffness of the material, although this effect is reversible[9]. The resin

swells due to moisture absorption and in this way internal stresses are introduced in the material. This reduces the failure stress. The internal stresses due to moisture absorption can be calculated, for example to estimate the knock-down factor needed to include environmental effects for the full scale test (as was done for the B737 carbon/epoxy horizontal stabilizer[26]). Moisture absorption may also have a negative effect on the glass transition temperature of the resin[26].

On the other hand, higher temperatures and moisture absorption tend to plasticize the resin. Laminates even may have improved impact resistance and residual strength under hot/wet conditions, because the peel toughness is improved[2]. Demuts et al.[13] state that cold/dry or hot/wet environments have no significant effect on the residual strength, but the environment may be important, e.g. for the strength of compression members[2].

It is currently assumed for the certification of civil aircraft that the environmental degradation is only caused by moisture absorption under service temperatures. Thermal cycling, solar radiation[9] and freeze/thaw thermal cycling of moistened laminates[2] for example, are assumed not to degrade the material. The maximum moisture content at the end of the aircraft life has to be estimated. The static strength has to be demonstrated for this moisture content[9].

2.8 Requirements and inspection

The safety of aircraft is regulated by airworthiness certification requirements as defined in FAR 25[7] and JAR 25. Advisory Circular AC 20-107A[8] gives guidelines for compliance of composite structures with FAR 25. For metals the requirements lead to an inspection interval such that uncontrolled crack growth will not occur. For composite structures it must be proven that they will be as safe as conventional aluminium alloy structures. The approach needed for composites is different from metallic structures, which is illustrated in figure 2.5. Impact damage in composite structures will lead to a sudden strength reduction. Generally the damage width will not grow during fatigue loading. The strength will be reduced until repair at the next inspection.

The structure should be able to sustain damage or defects that might be undetected (or not repaired) during the life of the aircraft, in a realistic environment. Generally a structure has to be able to carry ultimate load with barely visible impact damage. This can be achieved by designing the undamaged structure at reduced strain levels.

Detectable damage (e.g. by NDT methods) should be able to be sustained for a certain period before its detection. Detectable impacts should not reduce the strength below limit load[14], see figure 2.6. Also in the military specifications (U.S. Air Force) the detectability is very important[1]: in the absence of a comprehensive inspection program the flaws and damage of table 2.4 should be assumed[1,4]. Visible defects and damage to be detected by periodical inspections have to be repaired prior to next flight.

The structure should be able to sustain the loads which are expected during the completion of the flight if heavy (impact) damage occurs (i.e due to uncontained engine failure).

Some important guidelines of AC 20-107A amplify the above arguments:
- 'The effect of service environment...should be determined.'
- 'Impact damage is generally accommodated by limiting the design strain level.'
- 'The structure should be able to withstand static loads (considered as ultimate loads) which are reasonably expected during a completion of the flight on which damage resulting from obvious discrete sources occur (i.e., uncontained engine failures, etc.). The extent of damage should be based on a rational assessment of service mission and potential damage relating to each discrete source.'
- 'It should be shown that impact damage that can be realistically expected from manufacturing and service, but not more than the established threshold of detectability for the selected inspection procedure, will not reduce the structural strength below ultimate load capability.'

Advisory circular AC 20-107A allows a certification on a damage tolerance

or on a safe life approach. The two fundamental aspects of the damage tolerance approach: crack growth and residual strength analysis, and the associated inspection program, are not practical for composites for two reasons: fatigue damage in this material occurs in unpredictable areas with no well characterized cracks as in metals and secondly because NDT methods are problematic. As a consequence a safe life approach is required with a load/life factor to cover the (large) scatter[9]. The fatigue performance is usually covered by a no growth approach (see section 2.3.4).

Usually a building block approach is used for certification[4,9,23], as shown in figure 2.7. This approach starts with coupon and element testing, progresses through subcomponent and component testing, and ends with a full-scale test.

During the coupon tests the basic properties of the material are determined, which are necessary for the analysis of higher level tests.

The tests on coupon and element level reveal the sensitivity of the material to environmental conditions. In this way so-called 'knock-down factors' for the full scale test can be determined. An example of a test on element level is the test of a lap-joint. Typical defects or impact damage and holes can be applied to the elements. Also the sensitivity of the material for fatigue loading can be treated on this level.

On the structural level an interaction of different failure modes takes place. The full-scale test which is usually necessary for certification, can be supported by the test results of the lower levels, or by analysis based on the lower level results.

For example: the damage tolerance demonstration of the A310-300 CFRP (Carbon Fibre Reinforced Plastic) fin is extensively described in the literature[11]. The certification is done with various component tests (e.g. on lugs, skin panels, shear webs) and full scale tests on two fins. The component tests were also done to obtain design allowables with various types of damage, defects and environmental conditions. The life was proven by full scale fatigue tests on the two fins. The fin was designed for 40,000 flights; scatter was taken into account by a scatter factor of 3 on life and an enhancement factor of 1.15 on the load. The scatter factor on

the load is applied because of the flat shape of the fatigue curves. One of the fins was completely saturated with the maximum moisture content. Tolerable manufacturing defects, visible impacts and repair solutions were included. After the fatigue loading ultimate strength was demonstrated on ambient temperature and at 70 $^\circ$C.

A second certification example is the Fokker 100 rudder and flap (CFRP and some metal parts)[3]. Full scale fatigue testing is done with flaws and impact damage. A no-growth concept is applied for 180,000 flights (i.e. 4 times 'crack free life'). In this case it was proposed not to apply a scatter factor on the load because of the metal parts. The environmental effects are taken into account by a factor on the load, determined by the testing of components. The full scale fatigue test is performed at ambient temperature and humidity.

The inspections of the outside surfaces of a structure are mainly done by visual examination (e.g. during walk around), because NDT methods are very time consuming. NDT inspections are applied to the Airbus A 310-300 carbon/epoxy fin in the case of visibly detected impact marks or visible delamination to determine the real delamination size[11]. If damage is detected, a decision must be made whether the damage will be repaired. The inspection philosophy for the A 310-300 fin follows (see figure 2.8)[11]:

1. when the damage size is larger than the critical size D_c, which brings the strength below ultimate load, the damage should be repaired prior to next flight. The critical damage size is determined from component (panel) tests and finite element calculation of the strain at the position of the damage,

2. damage areas between 0.7 D_c and D_c must be repaired within the next 2500 flights,

3. damage areas smaller than 0.7 D_c may be repaired at the surface only.

A summary of critical sizes is given in the structural repair manual of the aircraft.

---

3) private information Fokker

2.9 Damage tolerance of ARALL laminates

It makes no sense to try to find an answer on the question whether ARALL is a composite or a modified metal. ARALL combines the properties of both. In some aspects (like formability and processing) it behaves like a metal, in other aspects (like blunt notch behaviour, fatigue resistance and damage tolerance) it resembles the behaviour of composites.

The static ultimate design strength of ARALL is restricted by the blunt notch strength[3]. The blunt notch strength takes into account the presence of (fastener) holes in the structure. ARALL shows excellent fatigue behaviour. The most critical type of damage seems to be accidental damage (with a through crack)[3]. According to the requirements the structure must be able to sustain limit load when this type of damage is present.

2.10 Conclusions

We may conclude that impact plays a dominant role in damage tolerance of composite materials, because these materials have good fatigue resistance but are sensitive to impact damage. The residual compressive and tensile strength may be seriously reduced due to a poor notch behaviour and delamination buckling.

Also ARALL laminates show a similar damage tolerance behaviour. They are almost fatigue insensitive under realistic service loading and have a good resistance to environmental effects (like corrosion and moisture absorption). Accidental damage due to uncontained engine failure, maintenance induced damage, etc. are possible types of damage which must be considered.

Demuts et al.[13] recommend that 'rigorous studies aimed at better understanding of the mechanism and process during impact damage infliction may help to find more effective impact resistant designs. The adequacy and appropriateness of the following parameters in characterizing impact damage must be examined: size, shape, weight, velocity and kinetic energy of the impactor, size and thickness of specimen, type and span of specimen support, planform projection of damage area or summation of all delaminated

areas through specimen thickness as a damage area measurement. Reducing the number of parameters to a few that adequately describe and measure impact damage should be the goal. Damage tolerant designs with improved capability to prevent or arrest damage growth and increase failure load must be developed.'

References

1. Horton, R.E; McCarty, J.E.; Damage tolerance of composites, Composites, pp.259-267, ASM, 1988.

2. Baker, A.A.; Jones, R.; Callinan, R.J.; Damage tolerance of graphite/epoxy composites, Composite structures, Vol.4, pp.15-44, 1985.

3. Gunnink, J.W.; Damage tolerance and supportability aspects of ARALL laminate aircraft structures, Composite structures, Vol.10, pp.83-104, 1988.

4. Whitehead, R.S.; Qualification of primary composite aircraft structures, 14th ICAF symposium Canada, 1987.

5. Wiggenraad, J.F.M.; Damage tolerance of thin-walled composite structures, experiments, failure characteristics and design implications, NLR Memorandum SC-86-021U, 1986.

6. Elber, W; The effect of matrix and fiber properties on impact resistance, in: Tough composite materials, NASA CP 2334, pp.99-120, 1983.

7. Federal Airworthiness Regulations Part 25, Federal Aviation Admimistration, USA.

8. Advisory circular AC 20-107A, Federal Aviation Administration, USA, 1984.

9. Rouchon, J.; Certification of civil aircraft composite structures, general aspects, Specialists conference on ARALL laminates in Delft, 1988.

10. Challenger K.D.; The damage tolerance of carbon fiber reinforced composites-a workshop summary, Composite structures, pp.295-307, 1986.

11. Gökgöl, O.; A310-300 CFRP fin damage tolerance demonstration, 7th international SAMPE conference Munich, 1986.

12. Kitchenside, A.W.; Prospects for the use of composites in civil

aircraft, 7th international SAMPE conference, Munich, 1986.

13. Demuts, E.; Whitehead, R.S.; Deo, R.B.; Assessment of damage tolerance in composites, Composite structures, Vol.4, pp.45-58, 1985.

14. Bristow, J.W.; Structural composites airworthiness in civil aircraft, 6th international SAMPE conference, Scheveningen, 1985.

15. Jones, R.; Paul, J.; Tay, T.E.; Williams, J.F.; Assessment of the effect of impact damage in composites: some problems and answers, Composite structures, Vol.10, pp.51-73, 1988.

16. Davis, G.W.; Sakata, I.F.; Design considerations for composite fuselage structure ofcommercial transport aircraft, NASA CR-159296, 1981.

17. Chaumette, D.; Certification problems for composite airplane structures, in: Progress in advanced material and process: durability, reliability and quality control, ed. G. Bartelds and R.J. Schliekelmann, pp.19-28, Elsevier, Amsterdam, 1985.

18. Williams, J.G.; Effect of impact damage and open holes on the compression strength of tough resin/high strain fiber laminates, in: Tough composite materials, NASA CP 2334, pp.61-79, 1983.

19. Mar, J.W.; Fracture, longevity, and damage tolerance of graphite/epoxy filamentary composite material, J.Aircraft, Vol.21, No.1, pp.77-83, 1984.

20. Jones, R.; Williams, J.F.; Tay, T.E.; Is fatigue testing of impact damaged laminates necessary?, Composite structures, Vol.8, No.1, pp.1-12, 1987.

21. Liu, D.; Impact-induced delamination- A view of bending stiffness mismatching, J. composite materials, Vol.22, pp.674-692, 1988.

22. Jong, Th. de; Flying with composites (in Dutch), inauguration adress, TU Delft, 1989.

23. McCarty, J.E.; Full-scale tests, in: Composites, Vol.1; pp.346-351, ASM, 1987.

24. Hart, W.G.J.; Impact/fatigue performance of a $(\pm45_2,0_4)_s$ type carbon/epoxy laminate, National Aerospace Laboratory NLR, NLR TR 85108 U, 1985.

25. Veggel, L.H. van; Impact and damage tolerance properties of CFRP sandwich panels - an experimental parameter study for the Fokker 100 CA-EP flap, 14th ICAF symposium, Ottawa, 8-12 June 1987, EMAS, pp.557-583, 1987.

26. Laméris, J.; The use of load enhancement factors in the certification of composite aircraft structures, National Aerospace laboratory, NLR TP 90068 L, 1990.

table 2.1   Typical manufacturing defects[2]

defects	typical causes
voids	poor process control
delaminations	inclusion of release film
	poor process control
	faulty hole formation procedure
disbonds (in bonded joints)	poor fit of parts
	inclusion of release film
	poor process control
surface damage	poor release procedure
	bad handling
misdrilled holes	faulty jigging

table 2.2   Typical in service mechanical damage[2]

defect	typical causes
cuts, scratches	mishandling
abrasion	rain/grit erosion
delaminations	impact damage
disbonds	impact damage
	overload
hole elongation	overload/bearing failure
dents (with delamination	impact damage
and crushed core)	walk in no-step regions
	runway stones
edge damage	mishandling of doors and
	removable parts
penetration	battle damage
	severe mishandling-e.g.fork lift

table 2.3   Typical in service environmental damage[2]

defect	typical causes
surface oxidation	lightning strike
	overheat
	battle damage (e.g. laser)
delamination	freeze/thaw stressing (due to moisture expansion)
	thermal spike (causing steam formation)
disbonds (in honeycomb panels)	as for delaminations
core erosion	moisture penetration into honeycomb
surface swelling	use of undesirable solvents, e.g. paint stripper

type	size
scratches	a surface scratch that is 100 mm (4.0 in.) long and 0.50 mm (0.02 in.) deep
delamination	an interply delamination that has an area equivalent to a 50 mm (2.0 in) diameter circle with dimensions most critical to its location
impact damage	damage caused by the impact of a 25 mm (1.0 in.) diameter hemispherical impactor with 135 J (100 ft lbf) of kinetic energy, or with that kinetic energy required to cause a dent 2.5 mm (0.10 in.) deep, whichever is least

table 2.4 Assumed nondetectable flaw/damage (U.S. Air Force)[1]
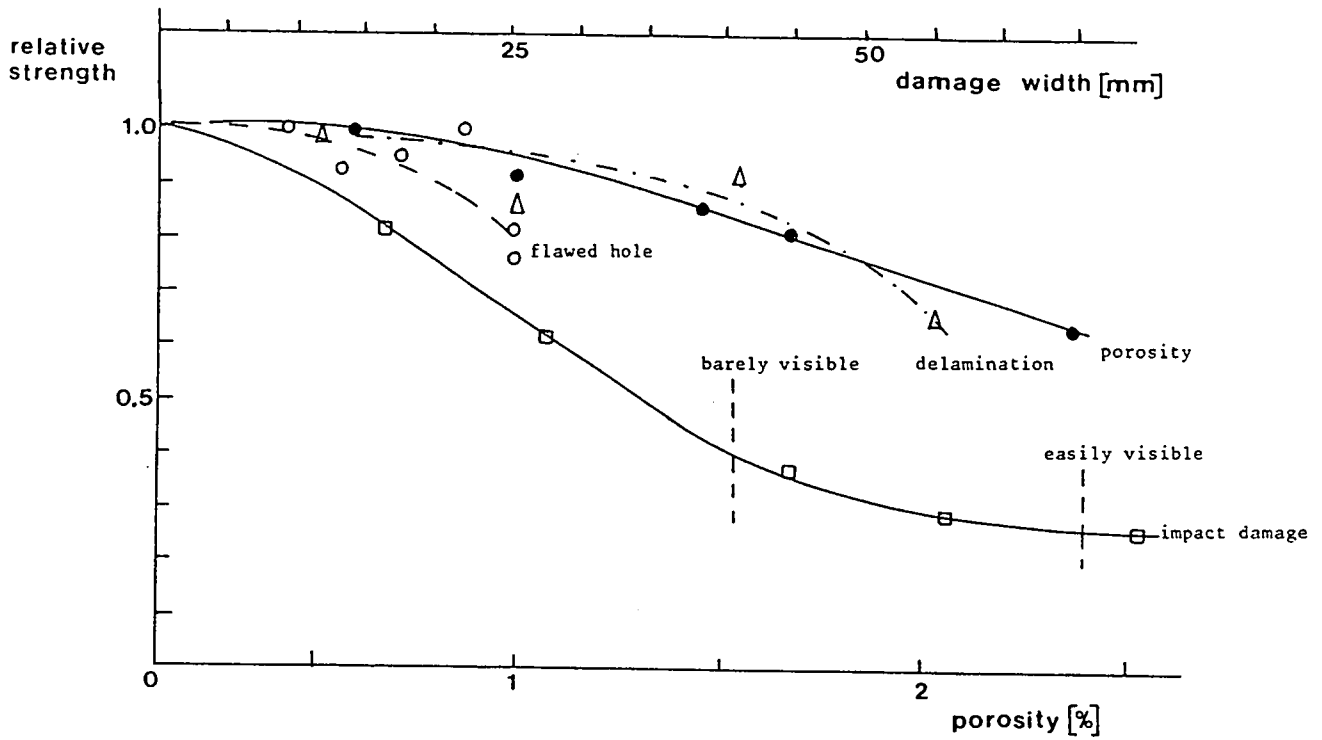
figure 2.1 The effect of various types of damage on the compressive
strength of carbon/epoxy specimens, room temperature, ambient (ref.4,13).
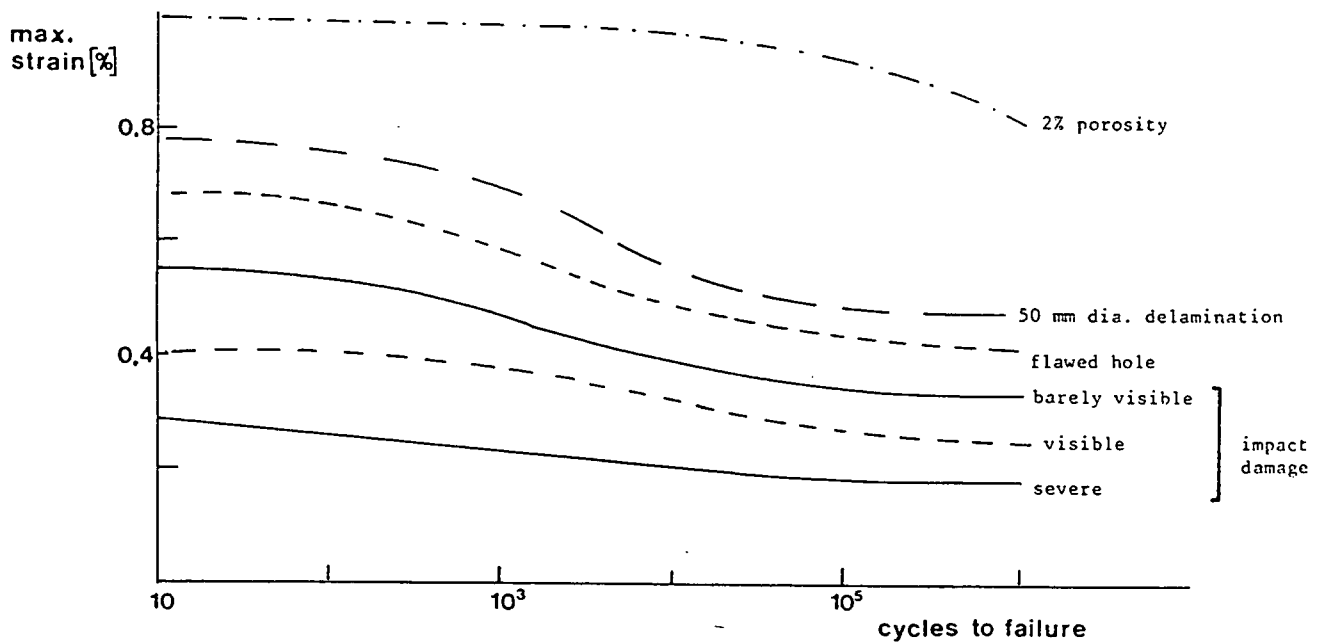
figure 2.2 The effect of various types of damage on the fatigue properties
of carbon/epoxy specimens, ambient, constant amplitude R = 10, compressive
loading (ref.4,13).
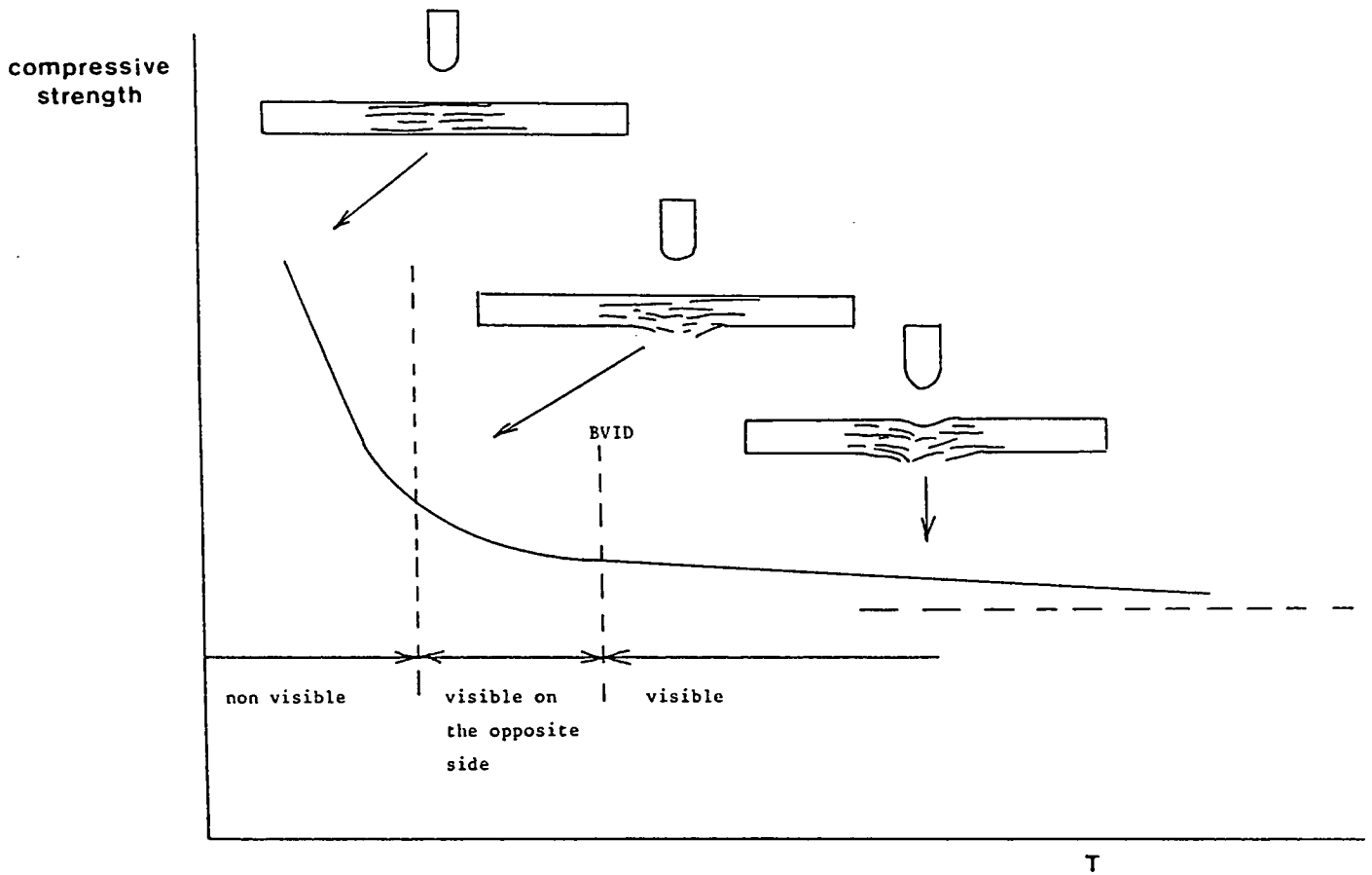
figure 2.3 The compressive strength as function of the impact energy T, BVID = barely visible impact damage (ref.9).

initial
strain
[%]

0.8

0.4

0

● did fail on impact

○ did not fail on impact

50   100   150

v_0 [m/s]

simply
supported

254

127
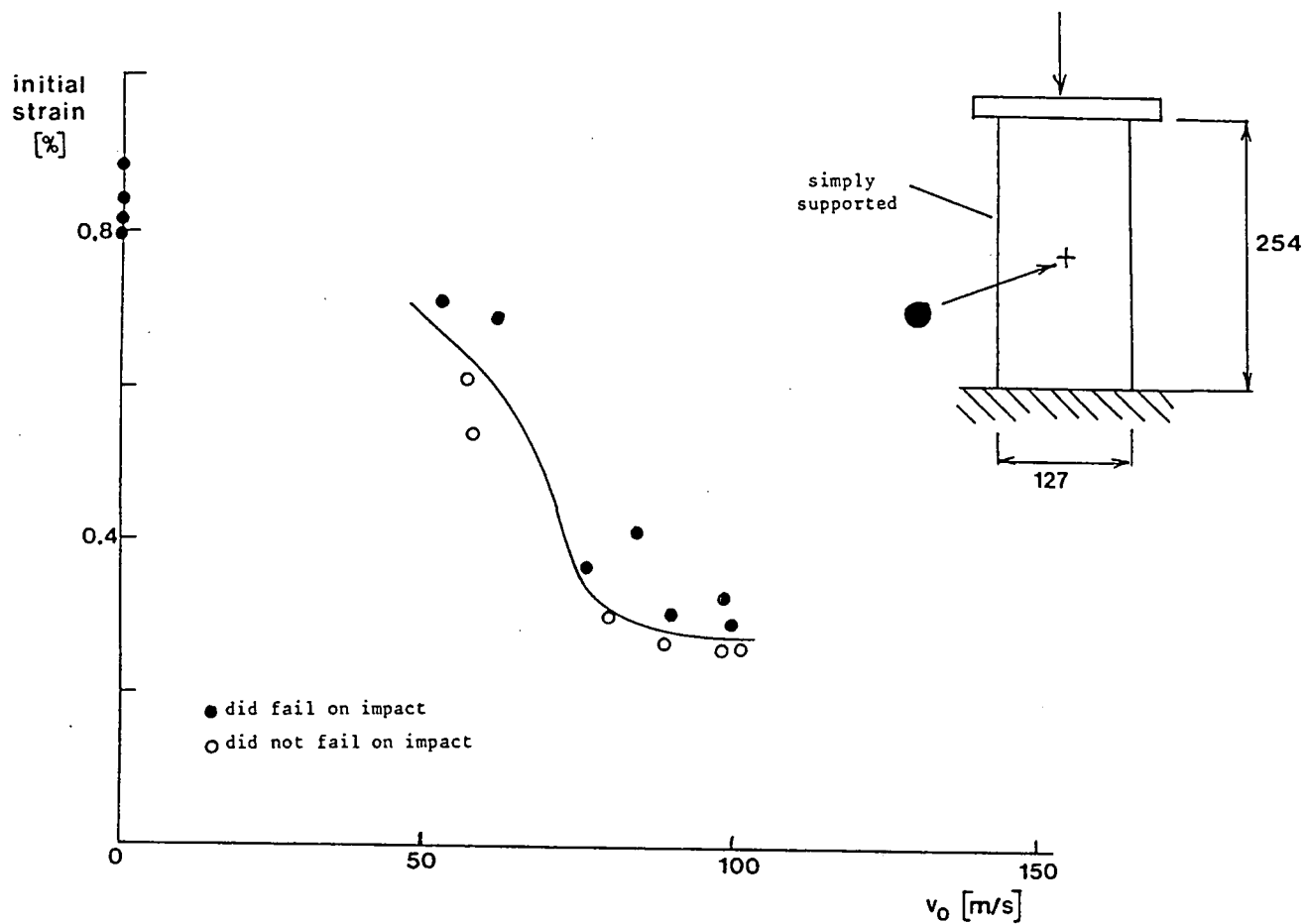
figure 2.4 The failure threshold of the initial strain: the boundary
between failure and no failure as a function of the impact velocity.
48 ply carbon/epoxy laminate, lay-up [±45/0_2/±45/0_2/±45/0/90]$_{2s}$
(ref.18).

metallic structure

composite structure

a

detectable
length

inspection interval

damage
width

impact

strength

ultimate

limit

strength

ultimate

limit

flights

flights
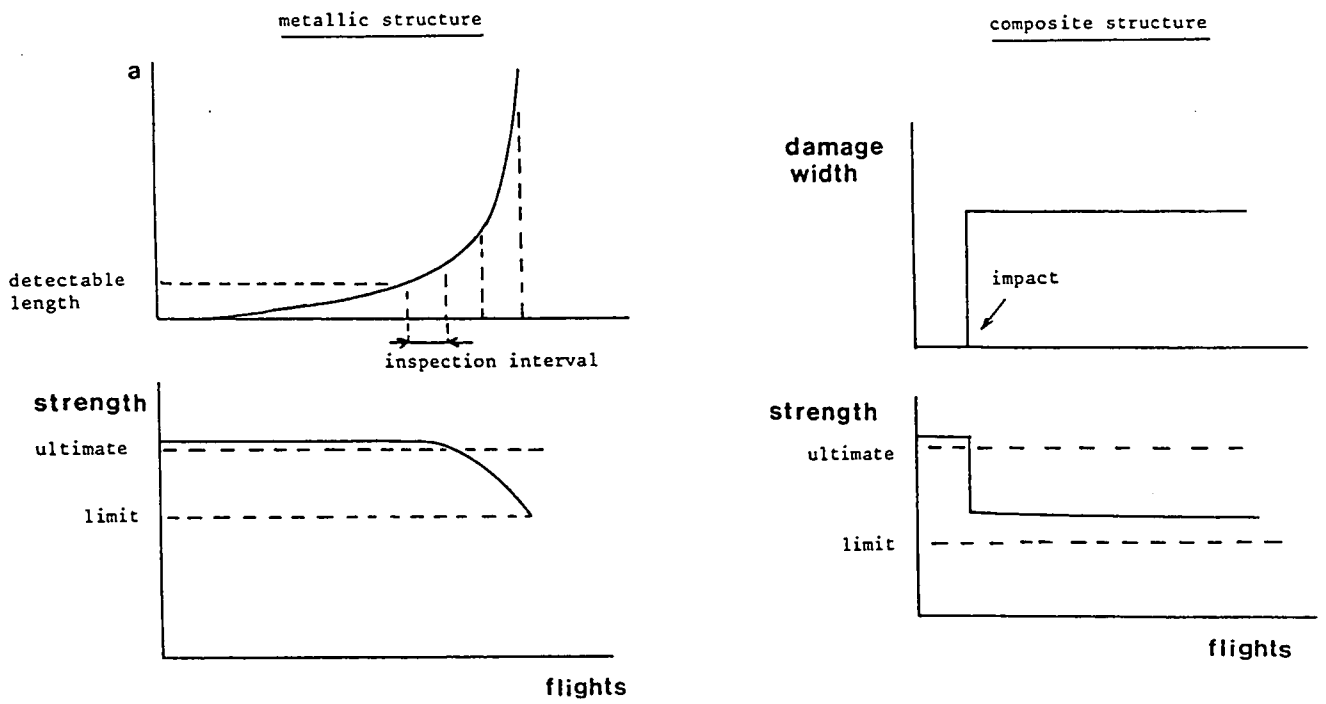
figure 2.5 The difference between conventional metals and composites
in possible damage size or crack length a and residual strength in
service (ref.17).

strength

ultimate

limit

component behaviour

requirement boundary

detectable

maximum expected impact damage

T

figure 2.6 The strength of a component as function of the impact
energy T, compared with its limit and ultimate values (ref.14).

31
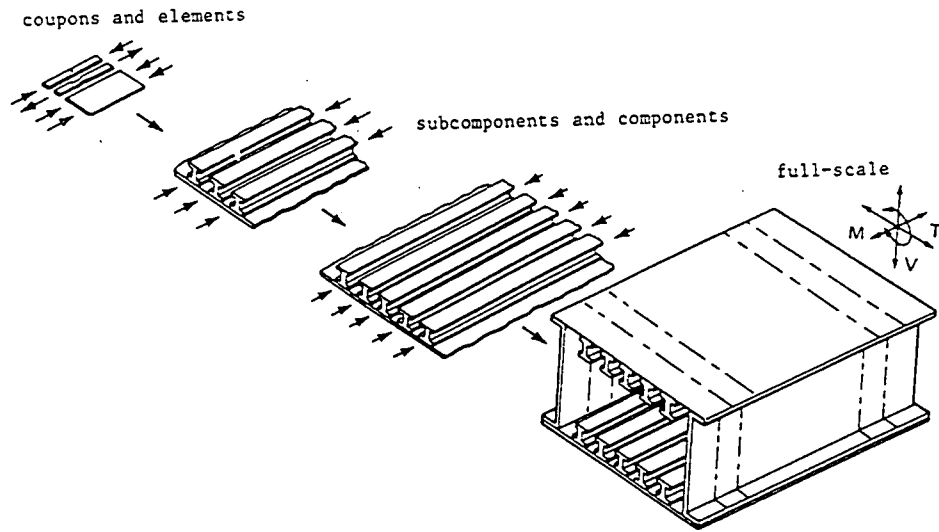
figure 2.7 An impression of the building block approach used for the
certification of a composite structure (ref.23).
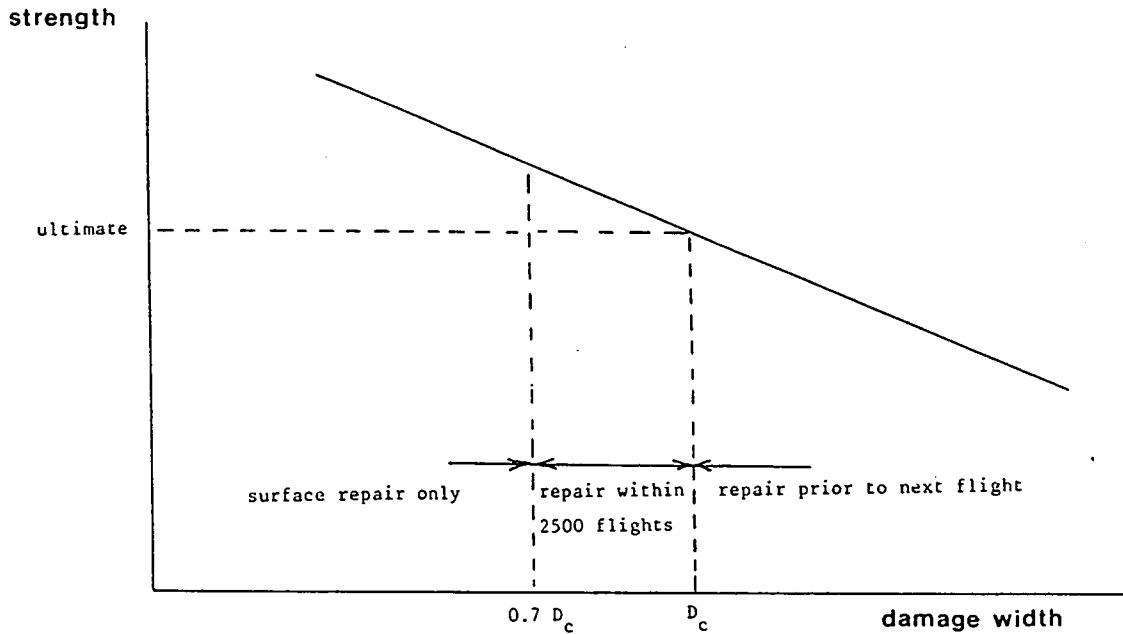
figure 2.8 The residual strength as function of the damage size for
the fin of the Airbus A310-300 (ref.11).

Chapter 3 Impact, the process and its significance for aircraft structures

In the previous chapter we concluded that the implications of damage are an important problem for the application of composite materials. This chapter gives more details on impact loading, impact damage and the variables involved.

3.1 Impact definition

Impact, in its physical context, is defined as the deformation and failure process during the collision of two or more objects[2]. Impact is of a dynamic nature: mass effects have to be taken into account, and forces and displacements are time dependent. Forces created by collisions are exerted and removed in a very short interval of time and initiate stress waves which travel away from the region of impact. A brief contact between two (solid) objects is typical for impact.

3.2 A brief history of the study of impact

It took mankind centuries to establish the current concepts which describe the impact process[1]. The study of impact is as old as mechanics. The oldest work on impact is written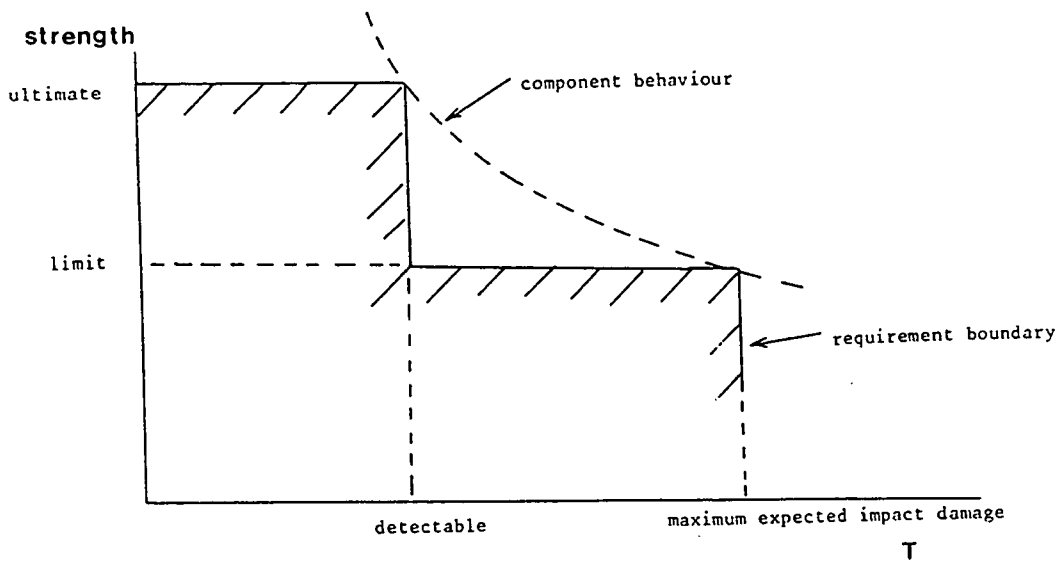 by Aristotle. One of the 35 problems treated by Aristotle in his 'Quaestiones Mechanicae' treats an impact problem. He wondered how it is possible that the strokes of an axe cleave wood, while a static loading by a heavy weight on the axe has to be very large to obtain the same result. Aristotle concluded that a moving axe will have a higher weight than an axe at rest. This confusion about impact loading and weight lasted for ages. It continued until 1667 when Borelli ended it by stating that an impact loading is not equal to a weight. In the Middle Ages Buridan (1300-1358) was the first one who described the elasticity of materials as a major phenomenon. A hard sphere retakes its shape after impression during the contact with the earth, by which the sphere is lifted. Leonardo da Vinci (1452-1519) studied the impact problem mainly experimentally. He impacted an object with a hammer and determined the relation between release height, weight, area of the hammer and the impression depth.

The phenomenon was studied because many investigators recognized its practical significance. Baldi (1553-1617) for example worked on the problem of impact of a sword on a helmet, and questioned at which point the sword could have the largest impact: at the tip, at the center of gravity or near the hilt. Obviously a solution for this problem was very useful at that time, and it also illustrates the very old link of the impact problem with military applications.

The damage in the target had to be described as a result of the impact loading. Cardanus (1501-1576) thought that it was the compressed air between the projectile and the target, which entered the voids of the target and induced fracture. Mydorge (1630) pointed out the importance of the boundary conditions of the target: a blow on a brick causes more damage when this brick is not supported by a foundation.

Descartes (1596-1650) reduced reality to physics, physics to mechanics and mechanics to mathematics. Descartes proposed in his 'Principia Philosphia' (1644) that an object will stay in motion, unless impact occurs with another object. He also stated 7 rules about impact of which the first one is the most obvious (and the only one which is correct): two central colliding equal masses return with equal velocity in an opposite direction, they exchange their motions.

Many problems had to become clear by establishing a correct concept of impact. A proper distinction had to be made between elastic and (partly) plastic impact. A few universal laws had to be found to cover the numerous different rules (e.g. the first rule of Descartes) which described the direction and velocity after impact as function of masses and velocities before impact. A proper distinction had to be made between weight (later: mass) and velocity. And finally the concepts of the relativity of motion and the resolution of the velocities into components in the case of oblique impact had to be found.

Finally with Huygens (1629-1695), Wallis (1671) and Mariotte (1620-1684) it became possible to give a mathematical treatise of the impact problem, which describes the collision of two masses. Classical mechanics does not describe what happens during impact. Thee laws of conservation of momentum and kinetic energy are used to calculate the velocities after impact as a

function of the masses and the velocities before impact. For the case of a central elastic impact of two masses, figure 3.1 can be derived. With this classical mechanical formulation numerous mechanical problems concerning impulsive loading of bodies can be solved.

Newton (1686) introduced the notion of the coefficient of restitution[2], taking into account the loss of kinetic energy due to plasticity, vibration, friction and fracture. Bernoulli (1751), Navier (1823) and Poisson (1833) studied vibrations produced in elastic rods under longitudinal impact and Young (1807) and Cox (1849) derived simple relations for the transverse deflections of beams. Herz (1881) established a contact law describing the contact between solids. Sears (1908) and Timoshenko (1913) used this theory for impact problems. In 1960 Goldsmith published his famous work 'Impact, the theory and physical behaviour of colliding solids', still an important collection of impact theories. Only recently high speed equipment became available to monitor the motions, stresses and strains during impact. Impact remained of importance, especially for military applications and crashworthiness, but it also gained much interest as an important damage cause for composite materials.

3.3 The deformation process during elastic impact

The elastic impact of a projectile on a target can be described as follows. On contact, a transient compressive normal stress wave is initiated. It propagates to the back face of the plate. At interfaces with a mechanical impedance mismatch between different materials a part of the wave will be transmitted and a part will be reflected. Also at the back face the compressive wave will reflect as a tensile stress wave, and it may produce damage (spallation) in the plate. The area of the plate where incoming stress waves travel through the thickness will have a conical shape (see figure 3.2). After a few microseconds a transient bending wave will be formed, which travels to the supports of the plate. After tens of milliseconds the whole plate will show its structural response, deflecting under the impact loading. The deformation in the plate will be a combination of a local Herzian indentation under the projectile and a global deflection causing bending and stretching of the plate. If the deflection is smaller than half the plate thickness, bending stresses will

35

prevail. For larger deflections the membrane deformation will become more dominant. The plate will be excited in its eigenfrequencies. After impact it will still vibrate. This means that although the impact is elastic, a part of the kinetic energy of the impactor will be transferred to the plate.

One of the deformation modes (Herzian indentation, stress waves, global response, higher order vibrations) may dominate the deformation process. Fracture may be caused by one of them.

1. If the contact time is short, such that the stress waves do not reach the boundaries of the plate during impact, the process will be dominated by stress waves.

2. If the stiffness of the plate is large, and/or the impact energy relatively small, the global deflection can be neglected. The deformation is then mainly a kind of a Herzian indentation.

3. If the mass of the plate is small relative to the impactor, the effect of the higher order vibrations will be small and the deformation will be in a global quasi-static mode. For masses of the plate in the order of the impactor mass the higher order vibrations become more important.

The initial kinetic energy of the impactor will be transformed into internal strain energy and surface energy of the target and of the projectile. If the projectile has the shape of a bar, the stress state in the projectile will be approximately one-dimensional. Also in the projectile a compressive wave starts to propagate at initial contact. This compressive wave travels to the rear of the projectile and will be reflected as a tensile wave. This tensile wave will interfere with the incoming compression wave. The stress in the projectile will become inversely proportional to the distance to the contact point, the free end will be stress free.

3.4 Impact variables

The impact loading of a projectile on a plate can be characterized by the following variables:

projectile: 1. nose shape, evidently a sharp object will (in

general) more easily perforate than a blunt object.

2. impactor mass

3. impact velocity, the impact velocity will be related
   to the initial strain rate in the target.

4. material, a deforming projectile will cause less
   damage in the target than a rigid projectile.

5. obliquity, this is defined as the angle of impact. If
   the obliquity is smaller than 90^0, the loading on
   the target will be a combination of a normal
   pressure and a shear load. The projectile has to
   travel a larger distance through the target, and
   consequently the perforation velocity will be
   higher, but the damaged zone will be larger and the
   residual strength will be lower.

target: 1. boundary conditions, the plate may be simply
   supported or clamped, or may have boundary
   conditions somewhere between those extremes.
   A clamped plate will show more damage than
   a simply supported plate at the same impact energy.

2. material

3. dimensions: width, thickness, a wide plate will have
   a larger area over which to spread the impact energy. This
   leads to less damage than in a small plate (if the
   contact time is long enough for the stress waves to
   travel to the supports). The thickness will be
   related to the strains at maximum deflection. The
   dimensions of the target are also related with
   the mass to be accelerated by the projectile.

For the perforation of a target the thickness of the target will be a very
important parameter. In general the following classification is used
(regimes 2-4 are from Wilbeck et al.[8]):

1. semi-infinite target having one surface, e.g. meteors impacting the
   moon.

2. thick targets, the rear surface (or distal surface) has an influence in
   the penetration process only after the projectile has travelled a

substantial distance into the target.

3. intermediate targets: the rear surface exerts considerable influence on the penetration process during most of the impact event.

4. thin targets: the rear surface is so near the impact surface that there are no stress or deformation gradients throughout the plate thickness.

3.5 Impact regimes

The kind of physical phenomena which are observed during impact is dependent on the initial velocity (and related with this the strain rate in the material) and material of the impactor and the target and target thickness. In the literature various parameters are found which describe the severeness of impact and the impact regimes in which the same kind of physical phenomena take place.

The nature of the phenomena which can be observed during an impact are very much dependent on the impact regime. The analytical solution techniques for impact depend on the physical model which can be used. They are similar in an impact regime.

In general the following regimes can be distinguished, independent of the kind of parameter used:

1. elastic, quasi-static regime

2. plastic regime

3. hydrodynamic regime: the material strength can be neglected

4. hypervelocity regime: vaporization, explosion.

The most widely used parameter to describe an impact event is the kinetic energy of the impactor relative to the target. This parameter does not incorporate the material properties of the impactor and the target, but it gives a good impression of the intensity of the impact, e.g. a falling tool can have a kinetic energy in the order of 5 J, while an object hitting the front of a train may be associated with a kinetic energy of about 10,000 J.

Another important parameter is the impact velocity of the projectile and the corresponding strain rate in the target. Relevant material properties like the yield stress, Young's modulus and the ultimate stress can depend on the strain rate. Zukas et al.[7] (table 3.1) give an indication of the

impact regimes as defined by the strain rate, for high strength materials like aluminium, steels, etc. The table shows that the material behaves like a fluid in a certain high energy regime, while at still higher impact velocities the material starts to vaporize. The high velocity regimes are important e.g. for the impact of meteorites on spacecraft.

It is evident that a material like plasticine will show a hydrodynamic kind of impact at much lower impact velocities than steel for example. Therefore Johnson[4] introduced a non dimensional parameter $\rho v^2 / \sigma_y$ [1], with ρ as the density of the material, v as the projectile velocity and σ_y as the yield stress of the material. The parameter $\rho v^2 / \sigma_y$ is called the <u>damage</u> <u>number</u>. The regimes given by Johnson are presented in table 3.2. ρv^2 represents the dynamic pressure at the projectile target interface during penetration. The weaknesses of the damage number are also given by Johnson: in elastic situations and in the hypervelocity regimes the damage number will not be a relevant quantity, and the nose shape and mechanical properties of the projectile are not included. However, the damage number gives a good indication of the the impact regimes.

Wilbeck et al.[8] conclude that the major drawback of the damage number is the lack of differentiation between projectile and target materials. Wilbeck suggests to use a pair of parameters to describe an impact event. He differentiates between 9 different impact regimes, based on pairs of parameters p/σ_p and p/σ_t, with p as the impact pressure, σ_p as the projectile strength and σ_t as the target strength. Examples of impact problems in different regimes are presented in table 3.3.

With increasing magnitude of the impact the following material properties will dominate the problem[8]:

1. elastic stress-strain behaviour

2. plastic stress-strain behaviour

3. density

4. decrease of compressibility with increasing pressure

5. thermal properties.

---

1) Such a parameter which describes the regime of impact can be compared with the Reynolds number in aerodynamics.

For the impact phenomena related with damage tolerance of (composite) aircraft structures it is convenient to describe the impact regimes on basis of the devices needed to reach a certain impact velocity. We propose the following classification:

1. quasi-static loading: 'static' loading by a hydraulic testing machine.

2. very low-velocity impact: (primary) elastic and linear deformation, drop weight testing with drop heights of several centimeters.

3. low-velocity impact: the penetrator may be considered to be rigid, impact velocity in the order of 10 m/s, drop weight or pendulum impact testing.

4. high-velocity impact: gas gun impact testing, impact velocities in the order of 100 m/s.

5. ballistic impact: both projectile and target may show extensive deformation, impact velocity in the order of 500 m/s, powder guns.

6. hypervelocity impact: extremely high impact velocities of 5000 m/s and higher, electromagnetic guns.

3.6 Energy transformations

Impact is typically a process in which energy plays an important role for the description of the process. The kinetic energy of the impactor at the beginning of the process is transformed into other types of energy. When the impactor loses kinetic energy, its kinetic energy is absorbed and dissipated during impact by the following energy terms:

1. kinetic energy of the target

2. internal elastic and plastic strain energy of the target and the projectile

3. fracture, surface energy of the target and projectile

4. material damping of target and projectile material (heat dissipation)

5. acoustic radiation of the plate

6. friction between projectile and target and at the supports of the plate (heat dissipation)

7. deformation (strain energy) of the supports of the target.

When no perforation occurs, the kinetic energy has to be absorbed by the target during impact as internal energy. This means that the energy absorbing capacity of a material is an important parameter. Table 3.4 shows the energy until fracture of different materials. In this table the maximum internal energy per unit of volume (area under the stress-strain curve) until fracture is given for various unidirectional composite materials with a fibre volume fraction of 50%, Al 2024-T3 and GLARE. With this table a ranking of the materials for impact properties is not possible, because the damage and residual strength after impact are also dependent on the stiffness of the material and on strain rate effects. The stiffness of the material determines how the internal energy will be distributed over the plate, and thus the concentration of this energy around the impact point. However, the table gives a first indication. The U_f/ρ value of the R-glass fibre is promising if compared to the value for Al 2024-T3, a metal which is able to absorb energy by plastic deformation. It is important to note that the values given in table 3.4 for aramid, carbon, etc., are strictly unidirectional fibre properties; a realistic composite structure has cross-plied fibres in various directions. Table 3.4 only illustrates the fibre dominated properties. Moreover, the impact behaviour is also highly dependent on the occurrence of delamination, and thus on the interlaminar fracture toughnesses G_{Ic} and G_{IIc}, which are governed to a large extent by matrix, not fibre, performance. Table 3.4 indicates potentials, and gives an idea of the brittleness of the various materials, but the reality of impact is more complicated.

3.7 Strain rate effects

metallic materials
The mechanical properties of a material, like the yield stress and ultimate stress, are dependent on the strain rate. This is a rather complicated and still controversial subject. The deformation of a material can be expressed by a constitutive equation:

$$f(\sigma, T, \varepsilon, \dot{\varepsilon}) = 0 \qquad\qquad (3.1)$$

Many of these equations were proposed in the literature. Some are empirical (e.g Johnson and Cooke), and other ones are semi-empirical (e.g. Zerelli and Armstrong)[15]. It is very difficult to derive equations describing the macroscopic processes based on dislocation mobility. A constitutive equation relating macroscopic behaviour and the physical processes which control plastic deformation is still a goal to be reached. The thermal activation is generally accepted as a rate controlling mechanism. A so-called 'effective temperature' is used to include both the temperature and the strain rate in one parameter[8]. Also 'dislocation drag' is mentioned as a cause of the increase of the yield stress at high strain rates[15].

Constitutive equations are used in computer finite element and finite difference codes. For example, the empirical Johnson and Cooke relationship is[15]:

$$\sigma(T,\varepsilon,\dot{\varepsilon}) = (A + B \ \varepsilon^n) \left[1 + C \ln \frac{\dot{\varepsilon}}{\dot{\varepsilon}_0} \right] \left[1 - \frac{T}{T_{melt}} \right] \qquad (3.2)$$

with the material constants A, B, C, n, T_{melt} and $\dot{\varepsilon}_0$. Relatively simple relationships are shown to be adequate for computer modelling.

Different regions of the material behaviour can be distinguished, as shown by the empirical results for mild steel in figure 3.3. The mechanical properties are generally not sensitive to small variations of the strain rate: the order of magnitude of the strain rate is important and the yield stress is generally presented as a function of the logarithm of the strain rate. Quasi-static loading is usually applied at strain rates of about 10^{-3} s^{-1}, whereas drop weight (Charpy and Izod) tests induce a strain rate of $10^2 \ s^{-1}$ in a material at the notch root[14].

The first region (region I) in figure 3.3 is the athermal region[15]. In this regime the yield stress is nearly independent of the strain rate. The energy barriers to be overcome for dislocation movements are relatively high, and thermal vibrations are hardly effective.[23]. Only externally applied stresses will cause glide of dislocations. The higher the temperature, the lower the boundary where the strain rate becomes important. The relationship between the yield stress and the logarithm of

the strain rate is linear in the second (thermal) region (region II in figure 3.3). In this region thermal activation plays a dominant role. The barriers in the crystals can be overcome by a combination of the applied stress and thermal activation[23]. For higher strain rates (region IV in figure 3.3) the relationship between yield stress and the strain rate becomes linear, and the relation between yield stress and the logarithm of the strain rate exponential. In this region viscous drag becomes dominant. At the moment reliable experiments with strain rates up to 5.10^5 s^{-1} are possible, and this maximum strain rate is still increasing.

No strong strain rate dependence was reported for the high-strength aluminium alloys[23]. Al 7075-T73 is still in the athermal region at a strain rate of $\dot{\varepsilon}$ = $5*10^5$ s^{-1} (figure 3.4). Weaker alloys like Al 1100-0 (technically pure Al, annealed) and Al 5454-0 (Al-Mg alloy, annealed) exhibit a stronger strain rate dependence. Figure 3.5 shows the elongation (a measure for the ductility) at failure for different aluminium alloys. The stress-strain curves of Al 2024-T4, Al 6063 and Al 7075-T651 for a quasi-static and a high strain rate are presented in figure 3.6.

composites

Composite materials also show a strain rate dependence, but there is not much data available. The strain rate dependence of carbon/epoxy in the fibre direction is small. Harding and Welsh[22] reported the following results for carbon/epoxy:

$\dot{\varepsilon}$ (s^{-1})	E (GPa)	σ_u (GPa)
$5*10^{-4}$	145	1.21
7	145	1.26
450	149	1.14

For glass/epoxy a relatively large strain rate dependence was measured, as shown in figure 3.7. The energy absorbed per unit of volume is presented in table 3.5. This was also found by Chiai and Moore[9] and Caprino et al.[12]. An explanation for this effect was not given. In chapter 9 of this thesis high strain rate tensile and puncture test results ($\dot{\varepsilon}$ $\cong$ 10^2 s^{-1}) on GLARE, aramid ARALL and carbon/ thermoplastic composites will be presented.

Woven fibre reinforced laminates show a larger strain rate dependence than unidirectional materials[16,28]. Both the stiffness and the strength of woven material are higher, probably due to a dynamic effect in the stretching of the 'kinks' in the fabrics.

Matrix dependent properties like the interlaminar shear strength (important for the delamination caused by impact loading) will also depend on the strain rate. Table 3.5 also shows the results of tensile tests with a loading direction of 45^0 relative to the fibre direction. For this direction shearing occurs and the matrix plays an important role. The energy absorption at higher strain rates is in this case three times the quasi-static energy absorption.

At high strain rates the matrix material may become more brittle. Large reductions of the G_{Ic} values were measured, see figure 3.8. Berglund[26] observed a stick-slip mechanism in carbon/PEEK (thermoplastic) material. On the fracture surface brittle and ductile fracture zones were found. Berglund proposed that the ductile zone corresponded with stable crack growth, and that at some places the crack growth stopped at certain barriers. Consequently the load on the specimen rose, which caused an unstable 'slip' of the crack over the barrier with a high crack tip velocity. The 'slip' resulted in a zone with brittle fracture.

Sayers and Harris[24] performed impact tests on carbon/epoxy interlaminar shear (ILS) specimens (standardized three point bending test of a small rectangular sheet specimen with shear failure). They reported a reduction of 30% of the quasi-static ILS value at an impact velocity of 4.27 m/s.

3.8 Dynamic fracture

If failure takes place under impact loading of a structure, the crack will initiate and grow under dynamic conditions. The classical way to study the dynamic fracture of a metallic material is the Charpy-V notch test: a dynamic bend test on a notched beam specimen. This test is still used for the ranking of different materials (also of composite materials, see section 4.1). It is widely used for the determination of the ductile-to brittle transition temperature of steels. Instrumented Charpy tests are used to differentiate between the energy needed to initiate and to propagate a crack. The relationship between Charpy-V notch energy values

and fracture mechanics concepts like K_{Ic} is difficult to determine. Therefore instrumented Charpy tests are performed on fatigue precracked specimens[14]. The crack opening displacement, the load on the specimen and the crack length are recorded as a function of time. At relatively high impact velocities even a one point bending test is performed[14].

Three aspects of dynamic fracture are investigated: crack initiation, crack propagation and crack arrest under dynamic loading. The dynamic fracture toughness is written as K_{ID}. This dynamic fracture toughness may be higher or lower than the static K_{Ic} value[5].

3.9 Impact on aircraft structures

The main theme of this thesis is related to the impact properties of aircraft materials and structures. During the life of an aircraft damage will occur due to fatigue, corrosion and accidental (impact) damage. These types of damage have to be considered during the design process for reasons of safety. It is also important for economical reasons, because the damage has to be detected and repaired during maintenance.

For the present study the repairs of the fuselages of 71 Boeing 747 aircraft of airlines of 17 countries with an average life of 29,500 flying hours were classified and the location in the aircraft was determined[2]. The aim was to compare the importance of the three types of damage. Only the primary structure was considered. The damage to the floor structure and the wear of the door hinges were not taken into account. The analysis was limited to the damage reports of the skin, stringers, frames, clips, doublers, bulkheads, etc. The distribution of the 688 repairs over the damage types was:

(fatigue) cracks	396 repairs (57.6 %)
corrosion	202 repairs (29.4 %)
impact damage	90 repairs (13.0 %)

Scratches and lightning strike damage (low numbers), are not included in these figures.

---

2) private information Royal Dutch Airlines KLM

The actual number of impact damages is probably higher because not all small dents were repaired.

Figures 3.9 to 3.11 show the locations of the damage. For each damage type several regions can be indicated where the damage is concentrated. The fatigue damage was mainly present in the bulkhead of the nose wheel well, the splice at the canted bulkhead, around entrance door no. 1 (section 41) and in the APU section. The corrosion damage was mainly found in the lower part of the fuselage, especially around doors and at the canted pressure panel. Impact damage was mainly located around the doors, on the nose of the aircraft (hail strike?), in the cargo compartments and at the tail (due to tail scrape over the runway).

Data on damage caused by impact for the Lufthansa fleet were given by Gökgöl[18]. The impact damage of the tail surfaces was monitored during a period of 14 months. On a fleet of 114 aircraft (314,539 flying hours and 207,289 flights in 14 months) inspectors found the following damage:

	low velocity impact damage	bird impact	other impact
Fin box structure and leading edge	1	1	0
Horizontal stabilizer and leading edge	1	0	15
Elevator	2	0	5
	4	1	20

It includes 25 cases of impact damage on the tail surfaces of 114 aircraft in 14 months. For the total aircraft this number will be higher. Apparently impact is a frequently occurring phenomenon in service.

The data of the Boeing 747 and the Lufthansa tailplanes indicate that impact damage has to be seriously taken into account during the development of new materials (like ARALL laminates) and during the design and certification process. Impact damage will regularly happen in service. It must be possible to find the damage easily and to repair it with simple tools. The structure has to be damage tolerant: the aircraft has to be able

to fly with (small) dents and (small) damage. Because of the number of damages occurring it is not economical to repair each small dent or damage when it is detected. Generally, small dents are marked on the structure. If a crack is not found it will be repaired during the next major check when it exceeds a certain depth.

3.10 Causes of impact damage on aircraft structures

Impact damage of aircraft is caused by the following sources:

1. runway debris

This is important for lower parts of the aircraft behind the landing gear. It is an especially important criterion for wing flaps which are sandwich structures with a thin damage sensitive facing. The weight (several grams) and the dimensions of the objects (1 to 2 cm diameter) are relatively small, but their velocity is relatively high (in the order of 60 m/s). Generally the structure will not be struck by runway debris normal to the surface.

2. hail

An aircraft can encounter a hailstorm on the ground or in the air. Hail encounters are characterized by multiple impacts. The diameter of the hailstones may vary between 0.3 and 15 cm. The shape of the hail stones with a diameter smaller than 2 cm is conical, for larger sizes the hail stones have an oblate spherical shape[21]. On the ground the upper surfaces will be exposed, in the air especially the front parts: the fuselage nose and the leading edges of the wings and tail surfaces. A hail stone will often be shattered during impact. This means that this projectile is able to absorb a part of its own kinetic energy. In flight, while parts of the fuselage will be struck under a certain angle, the leading edges will locally have normal impacts. In flight the fuselage will be under pressure, making the impact more dangerous if damage is created. On the ground the impact velocity will be smaller, but it still may be considerable (varying between a velocity of about 25 m/s for a hail diameter of 2 cm and 60 m/s for diameters of 14 cm). In flight it is in the order of several hundreds of meters per second.

An example of a hailstorm on the ground: on 15 January 1980 in South Africa, hailstones as large as tennis balls struck several types of aircraft on the ground. Holes were found on a DC-10 in sandwich structures, and deep occurred dents in the upper surfaces of the structure. Most of the dents were not repaired because the aircraft's (aerodynamic) performance was not affected.

3. maintenance damage

Maintenance damage found during checks varies from saw cuts made during modifications of previous maintenance to dents and delaminations caused by dropped tools. Obviously, external upper surfaces and internal lower surfaces will be struck by dropped tools. Maintenance damage also includes walking in no-step areas. Generally the mass of dropped tools will be in the order of 1 to 2 kg, the impact velocity about 5 m/s. This type of damage is especially of importance for composite materials, because it can be hardly visible, while it reduces the strength significantly, which is a very bad combination.

4. collisions between service cars or cargo and the structure

Figure 3.12 shows an example of very severe damage on a DC-9 caused by a service car. As illustrated by this figure it generally happens near access doors in the fuselage. Cargo handling damage also occurs in cargo compartments where the fuselage is struck by containers. This type of damage is the predominant one for aircraft structures. The velocity is low, the impactor mass is relatively high. When this damage is not reported and if it is not detected because it is relatively small, the aircraft must be able to fly with this damage. If it is found and is small, the aircraft has to fly with it until the next service check. Whether a dent without a crack will be repaired depends on the depth and dimensions of the dent (the limits are given in the repair manual). Maintenance damage may be very severe when the striking object is sharp and piercing.

5. bird strike

Bird strike is a significant design criterion for leading edges of wings and tailplanes, the nose of the fuselage including the cockpit windows and the engines. It has to be proven (as part of the qualification of aircraft engines) that a bird strike in the engine will have no catastrophic

results. The striking bird is relatively weak and its velocity relative to the structure is high.

6. ice from propellers striking the fuselage

Ice from propellers may strike the fuselage. The Fokker 50 has two thermoplastic composite (aramid/polyetherimide) protection plates on the fuselage in the vulnerable areas to protect the fuselage from impacting ice.

7. engine debris

The chance of an uncontained engine burst is 1 per 10^6 flying hours, the chance that the aircraft structure will be hit is 1 per 8.5[11]. These figures do not directly indicate that engine debris may be a serious problem. However, Mangano[10] gives a rate of 30 uncontained engine bursts per year in the American civil aviation. The broken parts of rotating disks in the engine will be deflected in its flight when it perforates the casing (see figure 3.13). Several studies have been done on casings which are able to withstand broken disks due to engine bursts. Rolls Royce studied the application of aramid weave in the casing, because this material is able to spread the deformation over a larger area as a result of its fibrous nature in comparison to metals which deform locally and will be perforated[19].

Engine fragments hitting the aircraft structure will cause serious damage. Half a fan blade may weigh several kg's, half an engine disc 60 kg's[20]. When the fragment hits the structure during flight, the cabin is pressurized. According to Davis and Sakata[20] residual strength calculations for design and certification purposes have to reckon with a damage, which is not less than 2.6 times the dimensions of the engine fragment. The dimensions of half a fan blade is approximately 90 x 20 cm[20].

8. tire shrapnel from tread separation and tire rupture

This is especially important for the area in and around the wheel wells. Hydraulic and fuel lines in the wheel wells have to be able to withstand this type of impact.

9. ballistic impact

This type of damage is of course mainly a design aspect for military aircraft. These aircraft have to get home with heavy damage. It may be important for terrorists actions in the cabin of commercial aircraft.

10. crashworthiness

The impact loading during a crash is different from the other types of impact mentioned above. The design for crashworthiness is aimed at the survival of the occupants by minimizing the decelerations. The right materials and structure have to be chosen such that a maximum amount of energy can be absorbed by the structure. Crashworthiness is especially of importance for helicopter structures. This structure has to protect its occupants during crashes from relatively low heights.

Lockheed established composite fuselage impact criteria for a L-1011 type of aircraft (see table 3.6)[20]. The most frequent cause of impact damage are collisions and maintenance damage. They take place in the low velocity impact regime. Therefore the present study is limited to low velocity impact events.

For the design and material development the following impact aspects have to be considered (as mentioned before in section 2.2):

1. damage resistance   The material and structure have to be able to
   absorb impact energy with as little damage as possible.

2. damage tolerance   In the presence of damage the residual static strength
   has to be high, the damage accumulation (fatigue, moisture ingress,
   etc.) has to be small.

3. inspectability   The damage that will inevitably occur has to be found
   easily. Internal delamination of composite materials is harder to detect
   than dents in aluminium alloys. Criteria have to be developed for the
   decision to repair the damage or not.

4. repairability   When the damage has to be repaired (this depends on the
   damage tolerance of the material and the structure, and the aerodynamic
   and cosmetic aspects) one has to be able to perform the repairs with
   simple tooling. Field repairs may be required under rather primitive
   circumstances.

The present study will especially consider the damage resistance   (the

impact tests in part II) and damage tolerance (part IV) of various aircraft materials.

3.11 Conclusions

Impact is a process with many physical aspects: stress waves, vibrations, dynamic cracking, strain rate effects, etc. The nature of the phenomena involved is highly depending on the impact regime. The impact regime depends on the impact velocity, impactor mass and material and the target material. Impact has many variables: impactor nose shape, impactor mass, impactor material, boundary conditions of the target, etc. For aircraft structures impact damage is important. It is one of the three types of damage found during maintenance ((fatigue) cracks, corrosion and impact damage). In flight the aircraft may be struck by high velocity projectiles while the structure is loaded: in hailstorms, by engine fragments or ballistic impact. On the ground the impact velocity generally will be low and the chance of occurrence will be high. The consequences of impact loading should be part of material development and design of aircraft structures. The following aspects have to be considered: damage sensitivity, damage tolerance, inspectability and repairability.

Low-velocity impact due to small collisions and maintenance damage is the most frequent source of impact damage. The present study considers this type of impact. Especially the damage resistance (part II of this report) and damage tolerance (part IV) of aircraft materials will be treated.

References

1. MacLean, J.; De Historische ontwikkeling der stootwetten
    van Aristoteles tot Huygens, diss., VU Amsterdam, 1959.
2. Goldsmith, W.; Impact, the theory and physical behaviour
    of colliding solids, Edward Arnold Publishers, London, 1960.
3. Foreign object impact damage to composites, ASTM STP 568, 1973.
4. Johnson, W.; Impact strength of materials, Edward Arnold, London, 1972.
5. Macaulay, M.; Introduction to impact engineering, Chapman and Hall, London, 1987.
6. Awerbuch, J; Impact damage in composite materials, Composite materials

workshop, Katholieke Universiteit Leuven, 1984.

7. Zukas, J.A.; Nicholas, T.; Swift, H.F.; Greszczuk, L.B.; Curran, D.R.; Impact dynamics, John Wiley & Sons, New York 1982.

8. Wilbeck, J.S.; Anderson, C.E ; Wenzel, A.B.; Westine, P.S.; Lindholm, U.S.; A short course on penetration mechanics, Southwest Research Institute, 1986.

9. Chiao, T.T.; Moore, R.L.; Strain rate effect on the ultimate tensile stress of fiber epoxy strands, in: Carbon reinforced epoxy systems, ed. C.J. Hilado, Technomic USA, pp.1-4, 1974.

10. Magano, G.J.; Studies of engine rotor fragment impact on protective structure, in: Specialists meeting on impact damage tolerance of structures, AGARD CP 186, 1975.

11. McCarthy, D.; Definition of engine debris and some proposals for reducing potential damage to aircraft structure, in: Specialists meeting on impact damage tolerance of structures, AGARD CP 186, 1975.

12. Caprino, G.; Crivelli Visconti, I; Di Ilio, A; Composite materials response under low-velocity impact, Composite structures; Vol. 2, pp.261-271, 1984.

13. Avery, J.G.; Design manual for impact damage tolerant aircraft structure, AGARD AG 238, 1981. 14. Shockey, D.; Recent progress in dynamic fracture testing and treatment, in : Impact loading and dynamic behaviour of materials, ed. C.Y. Chiem et al., pp.3-21, DGM Verlag 1988.

15. Harding, J.; Material behaviour at high rates of strain, in: Impact loading and dynamic behaviour of materials, ed. C.Y. Chiem et al., pp.23-42, DGM Verlag, 1988.

16. Harding, J.; Saka, K.; Taylor, M.E.C.; The effect of strain rate on the tensile failure of woven-reinforced carbon/glass hybrid composites, in: Impact loading and dynamic behaviour of materials, ed. C.Y. Chiem et al., pp.515-522, DGMVerlag, 1988.

17. Burtow, C.G. et al.; The response of 7075-T73 aluminium alloy at high rates of strain, in: Impact loading and dynamic behaviour of materials, ed. C.Y. Chiem et al., pp.557-564, DGM Verlag, 1988.

18. Gökgöl, O.; A310-300 CFRP fin damage tolerance demonstration, 7th international SAMPE conference, Munich, 1986.

19. Stewart, I.F.; The use of Kevlar on aero-engine fan containment casings, in: Impact loading and dynamic behaviour of materials, ed.

C.Y. Chiem et al., pp.549-556, DGM Verlag 1988.

20. Davis, G.W.; Sakata, I.F.; Design considerations for composite fuselage structure of commercial transport aircraft, NASA CR-159296, 1981.

21. Hayduk, R.J.; Hail damage to typical aircraft surfaces, J. Aircraft, vol.10, no.1, pp.52-55, 1973.

22. Harding,J.; Welsh, L.M.; A tensile testing technique for fibre-reinforced composites at impact rates of strain, J. materials science, Vol.18, pp.1810-1826, 1983.

23. Burstow, C.G.; Lovell, M.C.; Rodgers, A.L.; Mechanisms of dislocation motion in 7075-T73 aluminium alloy at strain rates round 10^5 s^{-1}, in: Mechanical properties of materials at high rates of strain, Proceedings of the fourth international conference on the mechanical properties of materials at high rates of strain, pp.317-322, Oxford, 1989.

24. Sayers, K.H.; Harris, B.; Interlaminar shear strength of a carbon fibre reinforced composite material under impact conditions, in: Carbon reinforced epoxy systems, ed. Hilado, C.J.; pp.80-84, Technomic, U.S.A.; 1974.

25. Smiley, A.J.; Pipes, R.B.; Rate effects on mode I interlaminar fracture toughness in composite materials, J.Composite materials, Vol.21, pp.670-687, 1987.

26. Berglund, L.; Fracture toughness of carbon fiber/PEEK composites, Linköping University, 1987.

27. Kawata, K.; Hashimoto, S.; Sekino, S.; Takedo, N.; Macro- and micro-mechanics of high-velocity brittleness and high-velocity ductility of solids, IUTAM Symposium Tokyo, Japan, 1985.

28. Chiem, C.Y.; Liu, Z.G.; The relationship between tensile strength and shear strength in composite materials subjected to high strain rates, J.Eng.Materials and technology, Vol.110, pp.191-194, 1988.

strain rate s^{-1}	impact velocity m/s	possible effects
< 10	< 50	primarily elastic, some local plasticity
$10-10^3$	50-500	primarily plastic
10^3-10^4	500-1000	viscous material strength significant
10^5-10^6	1000-3000	fluid behaviour in materials, pressures approach or exceed material strength, density a dominant parameter
10^6-10^7	3000-12000	hydrodynamic material compressibility can not be ignored
$> 10^7$	> 12000	explosive impact, colliding solids vaporize

table 3.1 Impact regimes for high strength materials[7]

impact velocity m/s (ft/s)	damage number	regime
0.762 (2.5)	10^{-5}	quasi-static elastic
7.62	10^{-3}	plastic behaviour starts
76.2	10^{-1}	slow bullet speeds
762	10^1	extensive plastic deformation ordinary bullet speeds
7620	10^3	hypervelocity impact

table 3.2 Impact regimes characterized by the damage number[4]

$$\rho/\sigma_y \cong 1.7.10^{-5} \text{ kg/Nm}$$

	$\dfrac{p}{\sigma_t} \ll 1$	$\dfrac{p}{\sigma_t} \cong 1$	$\dfrac{p}{\sigma_t} \gg 1$
$\dfrac{p}{\sigma_p} \ll 1$	impact of two billiard balls collision of ball and bat		flight water penetration
$\dfrac{p}{\sigma_p} \cong 1$		armour penetration	
$\dfrac{p}{\sigma_p} \gg 1$	raindrops on auto windshield bird impact on aircraft lead bullets striking steel		hypervelocity impact of meteorites impact of colinear water jets

<u>table 3.3</u> Matrix of impact regimes[8]

material	σ_u MPa	E MPa	ε_u %	ρ kg/dm^3	U_f 10^{-3}J/mm^3	U_f/ρ J/g
aramid	1400	62500	2.3	1.30	16.1	12.4
dyneema	1500	55000	2.9	1.07	21.8	20.4
carbon T-300	1500	150000	1.0	1.48	7.5	5.1
E-glass	1700	36500	4.6	1.89	39.1	20.7
R-glass	2200	43000	5.4	1.85	59.4	32.1
Al 2024-T3	450	72000	12	2.78	56	20.7
GLARE 2 (2R33)	1230	65600	5.1	2.52	37.8	15.0

<u>table 3.4</u> Mechanical properties and absorbed energy until failure
of various composite materials (unidirectional fibres in epoxy,
fibre volume fraction 50%), 2024-T3 and GLARE.

strain rate	energy absorbed per unit of volume $(10^{-3}J/mm^3)$		
	carbon/epoxy	glass/epoxy	
	$\phi = 0^o$	$\phi = 0^o$	$\phi = 45^o$
low rate (quasi-static)	4.6	4.1	11.3
intermediate rate $(7\text{-}20\ s^{-1})$	5.3	10.5	19.8
impact rate $(800\text{-}1000\ s^{-1})$	5.0	18.5	32.9

table 3.5 Energy absorbed per unit of volume for glass/epoxy and carbon/epoxy at different strain rates[22].
ϕ = loading direction relative to the fibre direction

hazard	load condition at impact	weight and size	impact velocity (m/s)	impact angle (^{o})
birds	inflight	1.8 kg	180	17 to 42
hail	on ground inflight gusts		270	90 9 to 90
runway debris (gravel, bolts and ice)	on ground	1.27 cm Dia. Al. spheres	60	18 to 34
tools	on ground	0.453 kg hemisphere 2.54 cm Dia	6	90
engine debris	inflight	1/2 disc: 59 kg, 86x20 cm 1/2 blade: 2.7 kg, 25 cm long	126 366	90 90
tire shrapnel	takeoff and landing	56 x 22 x 1.3 cm^3 rubber 2.54 kg	64	20 to 90

table 3.6 composite fuselage impact criteria, Lockheed L-1011, after G.W. Davis and I.F. Sakata[20].
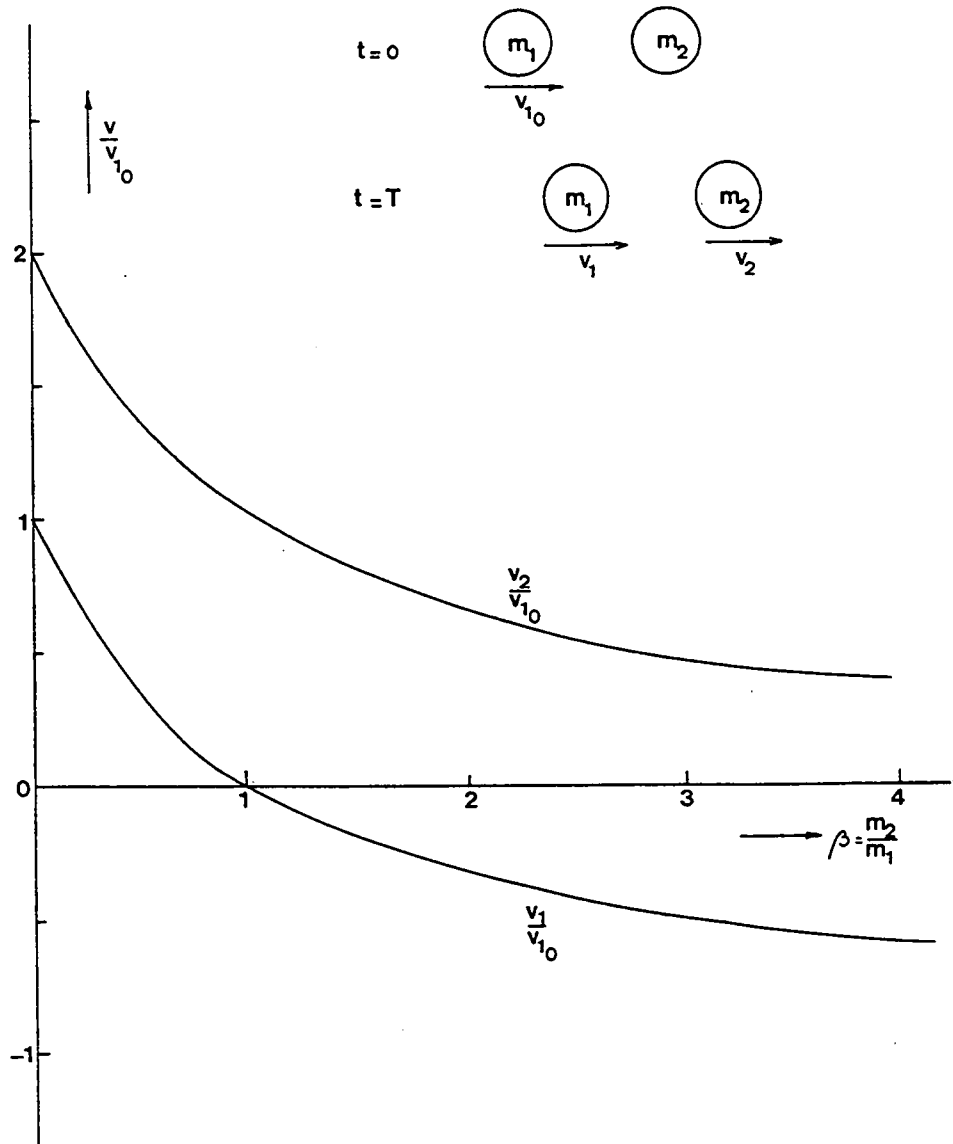
figure 3.1 The velocities after impact of two masses as function
of the ratio of the two masses, based on the classical
impact theory (conservation of momentum and kinetic energy).

t = 0

incoming compressive stress waves

bending wave

global structural response
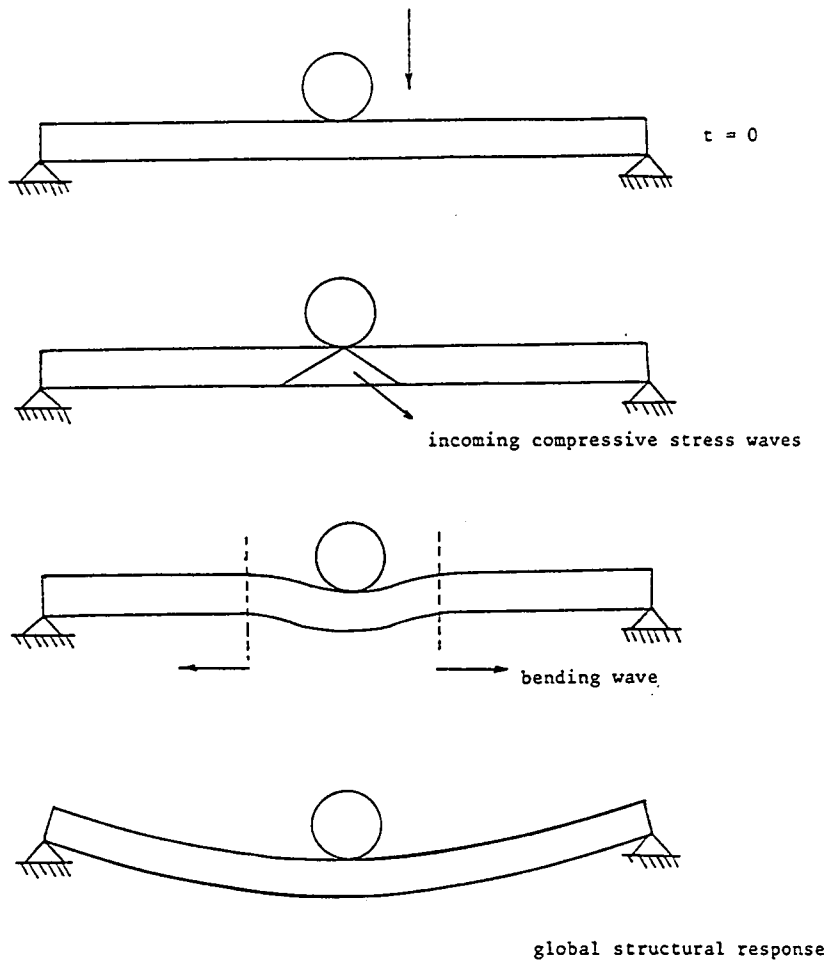
figure 3.2 The deformation process during the impact of a sphere on a plate.
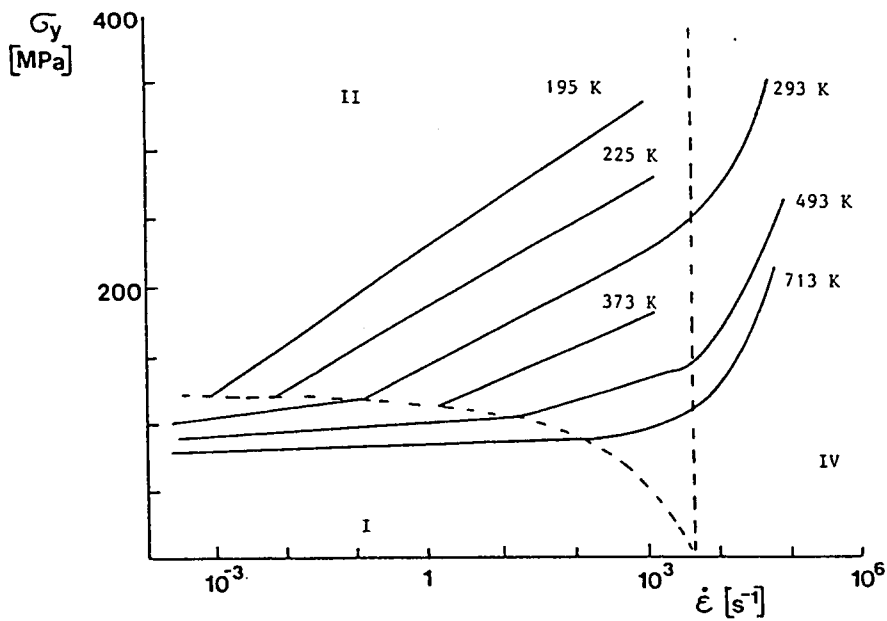
figure 3.3 Effect of temperature and strain rate on the yield stress of mild steel (empirical, ref.15).

figure 3.4 Yield stress vs. strain rate at 20^{0}C for Al.7075-T73 (ref.17).

figure 3.5 Effect of strain rate on the ductility of several aluminium alloys (ref.8).
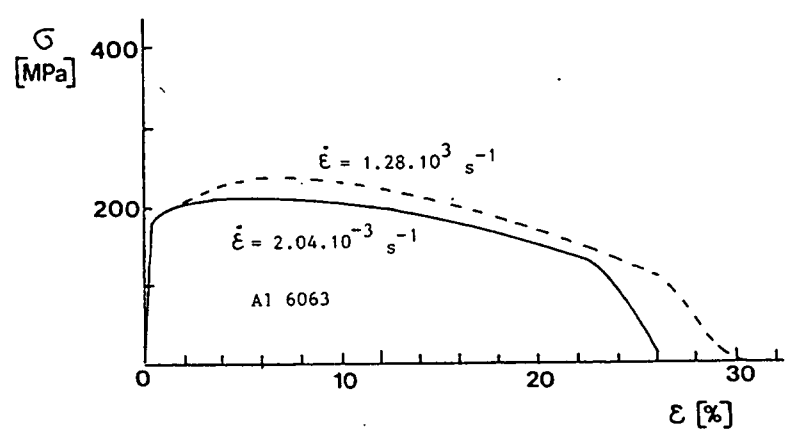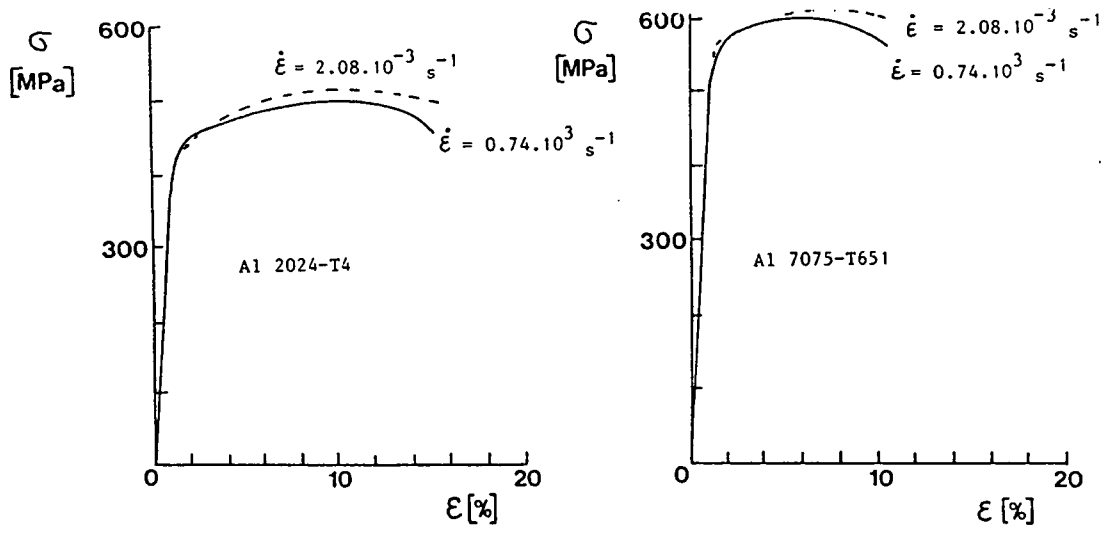
figure 3.6 Stress strain curves for different aluminium alloys, quasi-static and high strain rate loading (ref.27).
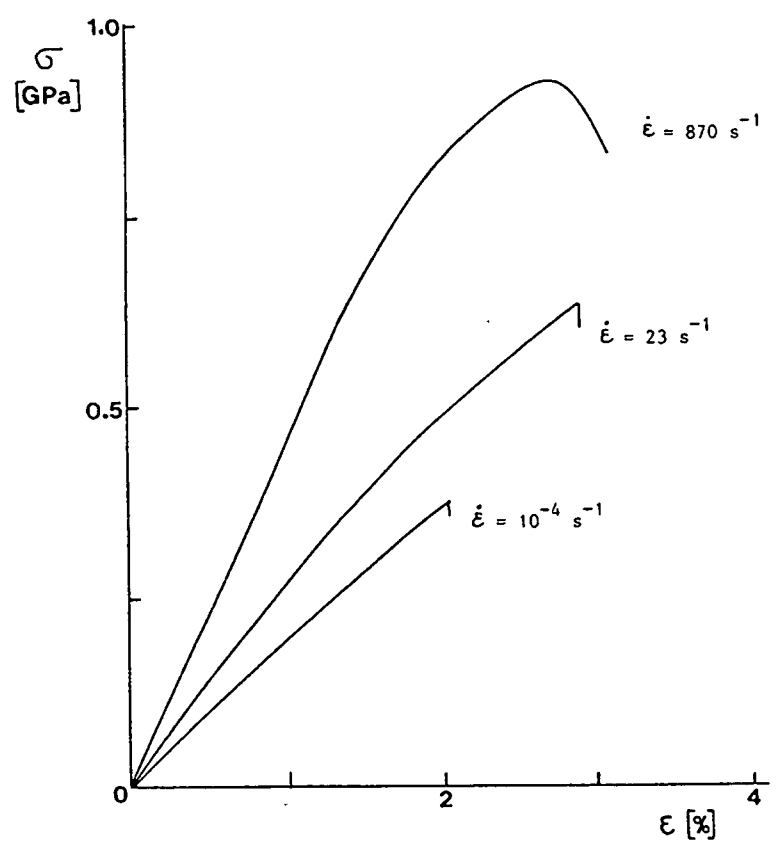
figure 3.7 Stress-strain curves of E-glass-epoxy at different strain rates (ref. 22).
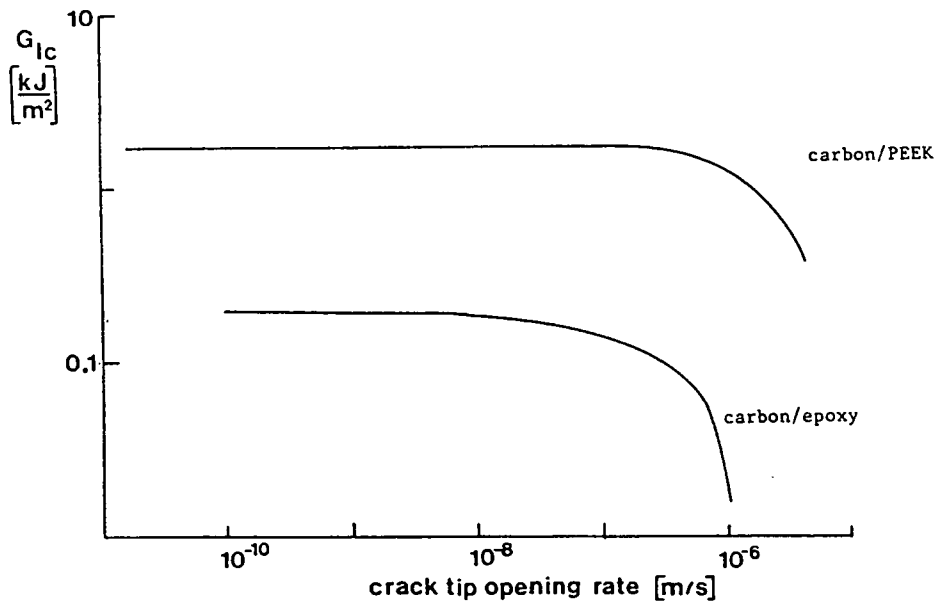
figure 3.8 Mode I fracture toughness as function of the crack tip opening rate (ref.25).
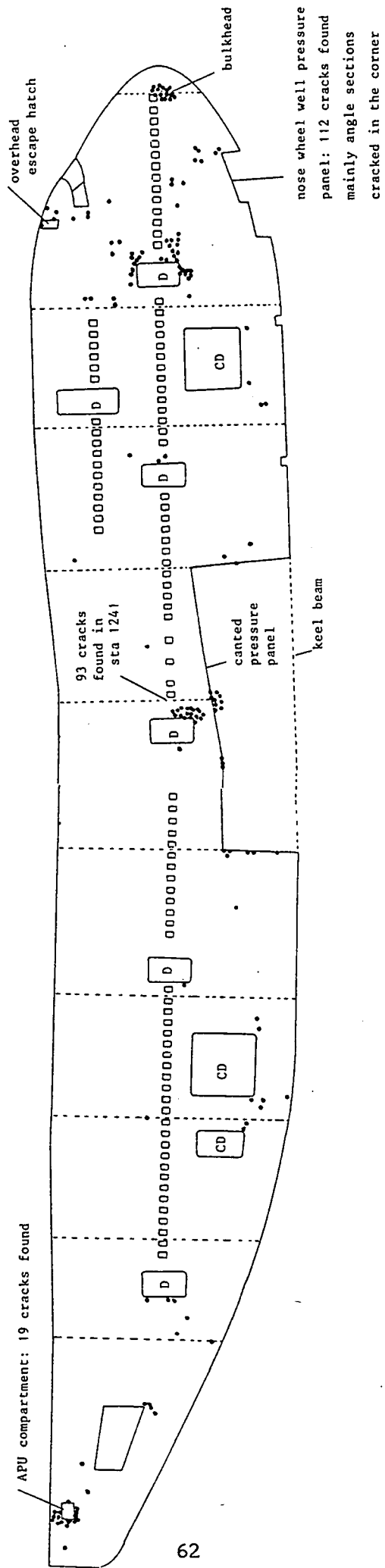
figure 3.9 The location of repaired (fatigue) cracks in 71 B747 aircraft.

Labels within the figure:

overhead escape hatch

bulkhead

nose wheel well pressure panel: 112 cracks found mainly angle sections cracked in the corner

93 cracks found in sta 1241

canted pressure panel

keel beam

APU compartment: 19 cracks found
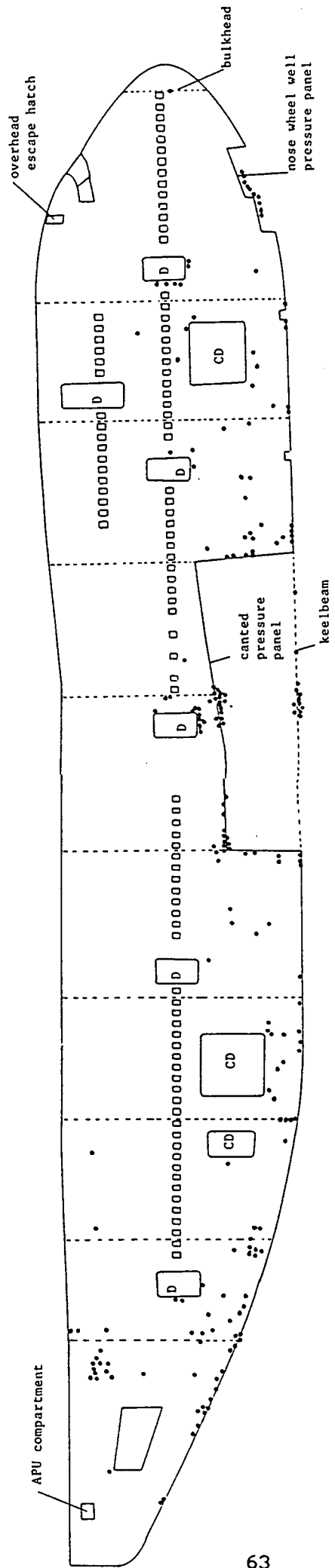
figure 3.10 The location of repaired corrosion damage in 71 B747 aircraft.

Labels in figure: overhead escape hatch, bulkhead, nose wheel well pressure panel, canted pressure panel, keelbeam, APU compartment, D, CD
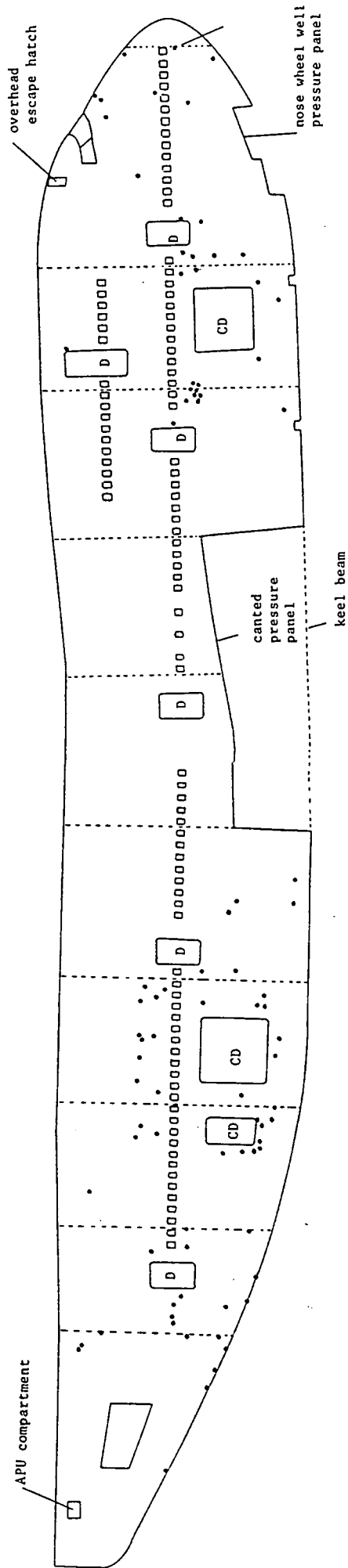
figure 3.11 The location of repaired impact damage in 71 B747 aircraft.

overhead escape hatch

nose wheel well pressure panel

canted pressure panel

keel beam

APU compartment

D

CD

64
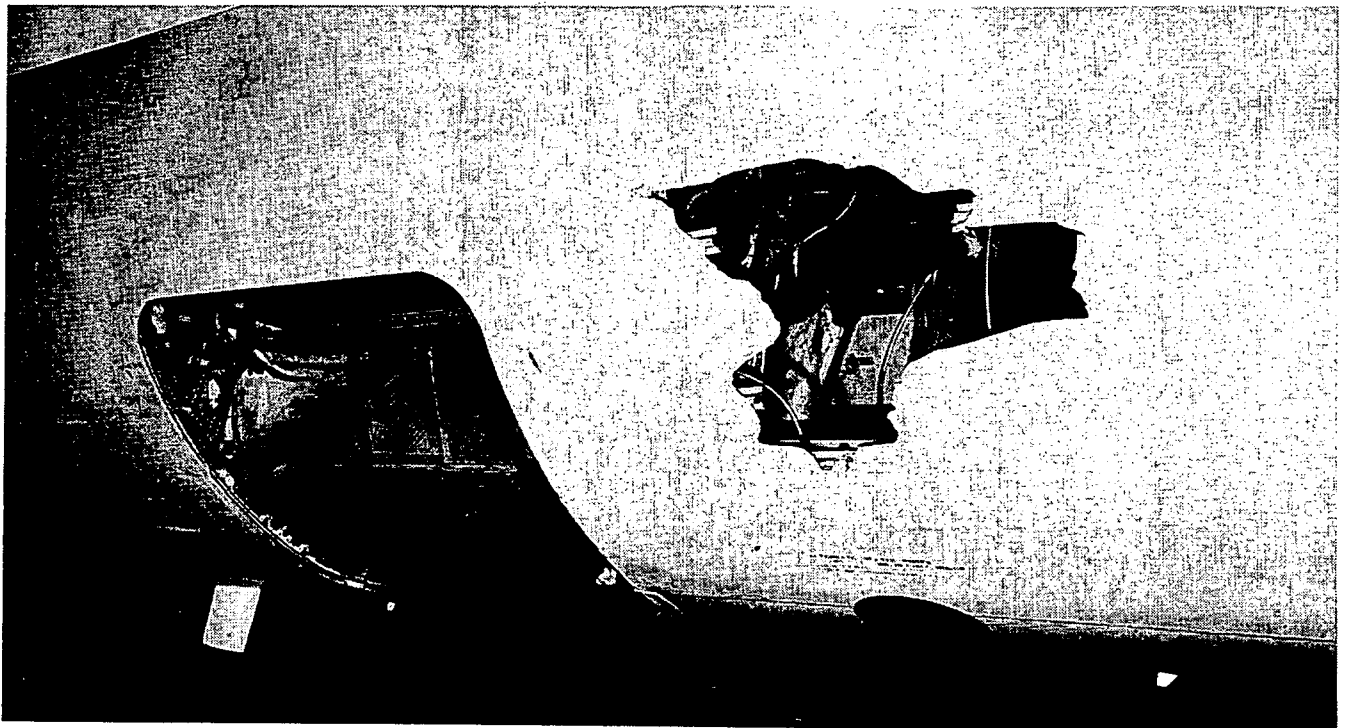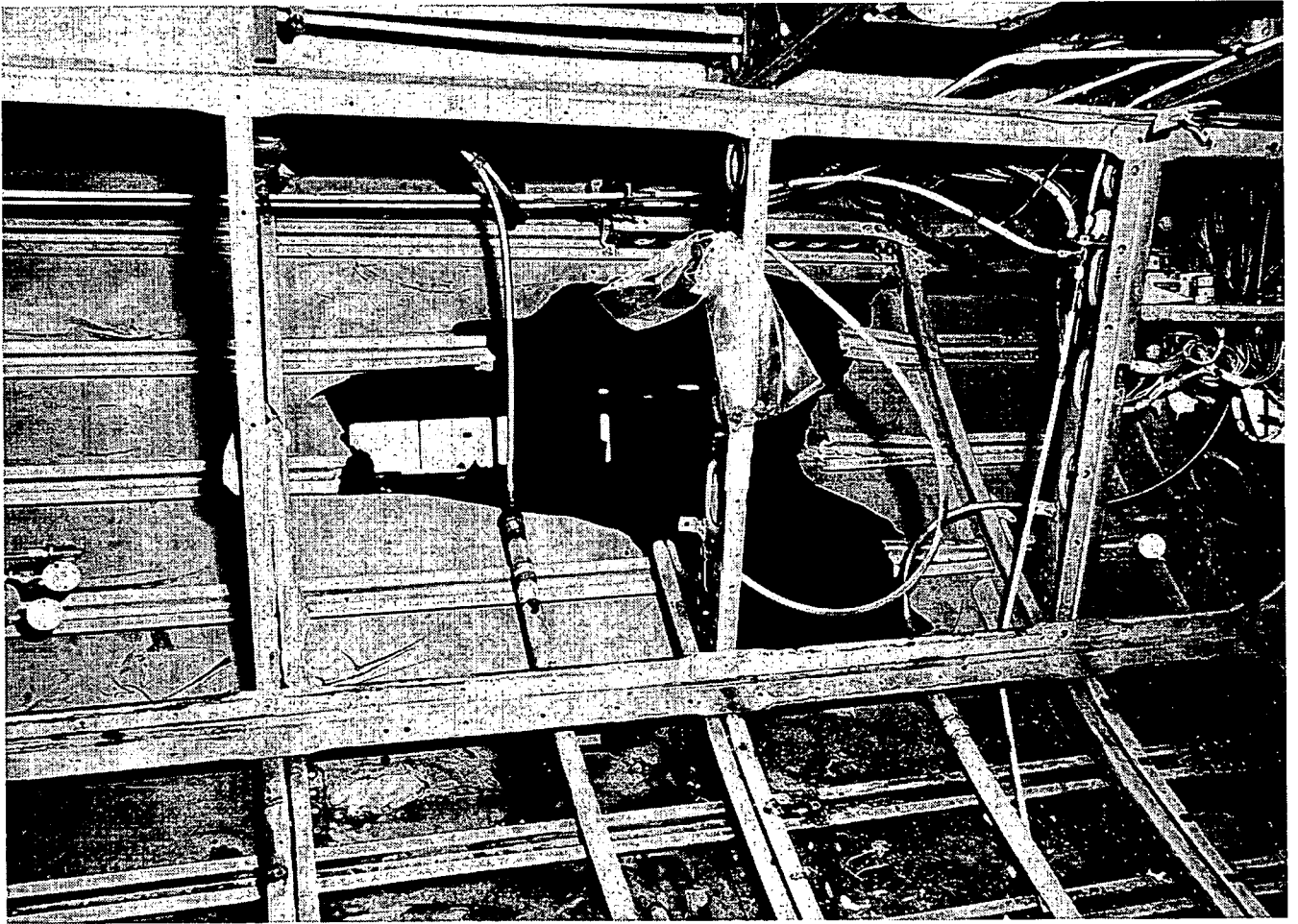
figure 3.12 An example of heavy damage due to cargo handling.
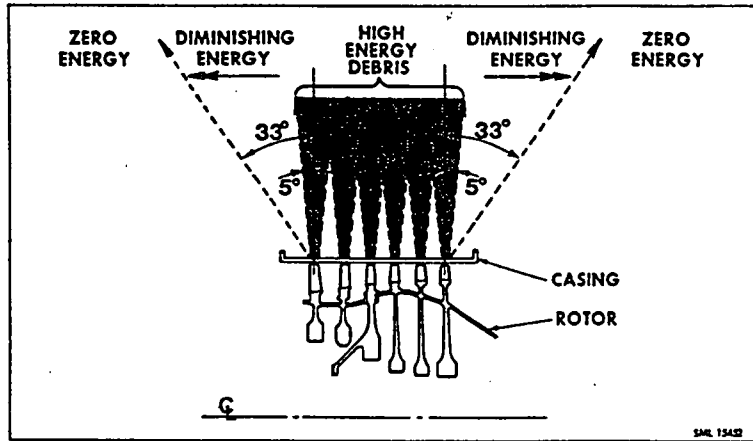
figure 3.13 Direction and energy of emerging engine debris (ref.11).

PART II IMPACT EXPERIMENTS

67

chapter 4 Impact experiments: introduction and literature survey

4.1 History

The reference list at the end of this chapter shows that many studies on impact of composites have recently been published. Impact tests (Charpy and ballistic) were performed on metals for many years, but impact testing of composites started at a much later time. As discussed in chapters 2, the impact strength of composites is an important design criterion for these materials. In the seventies the testing of composites started. The symposium on 'Foreign object damage to composites' in 1973[41] was a milestone. Since it was realized that impact damage can lead to a serious limitation of the application of composite materials, much effort was spent on this subject. The work done at the Langley Research Center of the NASA in the late seventies became well-known (for example ref. 66). Most of the research has been done in the eighties. After ten years Sjöblom (1988) concludes that 'the field of impact on composite structures is still in its infancy'[44]. Many tests have been done on various materials, but there is still a lack of understanding of the processes involved and the effects of the material properties on the damage and residual strength after impact. It is not clearly understood how the damage initiates and how the damage modes (like delamination and matrix cracking) are related. There is no commonly accepted analytical approach and no generally accepted test method.

In the early years of impact testing on composite materials, the Charpy and Izod tests were used after the testing procedures for metals. Although these tests are easy to perform and represent a simple loading on the material, it was later realized that the test conditions are too far from realistic application conditions of the composite in a structure[28]. However, the instrumented or non instrumented Charpy tests have still recently been used to test composite materials[2,10,19,35,38,39,58,60,61]. Typical absorbed Charpy energy values for some materials are given in table 4.1. This table shows that the aramid (Kevlar) and S-glass composites have substantially higher Charpy energy values than typical aerospace aluminium alloys.

Drop weight impact testers and gas guns have become popular for impact tests on plate materials . Still there is a large variation in projectile shapes (mainly hemispherical, but with a large variation in diameters, although a diameter of 12.7 mm (0.5 inch) is often used), specimen geometries, dimensions and boundary conditions and instrumentation. Unfortunately there is not a universal way to interpret the results, because there are several parameters involved to rank the materials (see section 4.2), and because the interpretation depends on the application of the material.

4.2 Literature results

Most of the studies were done to compare different materials, some of the studies have the aim to improve the understanding of the impact process[3,5,27,30,40,44,56]. Several ways have been tried to improve the impact behaviour: new fibres[1,21,49,63], tougher resins[8,42,63], hybridization[19,21,25,35], stitching[13], 3-D composites[31], thermoplastics[4,14,18,70], adding metallic wire sheet[6], adhesive layers between layers with different orientations (interface toughening)[16,50] and the application of fabric face sheets on a base laminate built up from unidirectional (UD) layers[17]. Relatively few studies were done to obtain insight into the impact process and to develop analytical tools.

Figure 4.1 shows three of the basic failure modes found in composites. Delaminations dominate the behaviour with short spans, thick laminates or laminates with low interlaminar shear strength. Flexural failures are found in thin laminates, i.e. with a low thickness relative to the span of the specimens. Penetration of the type as indicated in figure 4.1 will occur in thick specimens at sufficiently high velocities such that the specimen cannot respond quickly enough (shear failure by plugging)[23]. Figure 4.2 shows the typical load-time curves for flexural and interlaminar shear failure. Other failure modes are matrix cracking and matrix splitting parallel to the fibres. These types of failure generally lead to branching into delaminations as shown in figure 4.3 for thermoplastic and thermosetting carbon composites. The delamination generally occurs between layers with different orientations and runs in the fibre directions of the adjacent plies.

For impact tests on sheet or plate specimens the following parameters can be used to rank different materials:

1. The residual strength[4,13,14,18,52,54,55] and the fatigue behaviour[48,65] after impact.

2. The energy needed for the first damage (or the energy needed to cause barely visible impact damage) describes the sensitivity of the material for damage.

3. The damaged area[4,13,37]. This quantity is usually determined by a C-scan for composite and laminated materials. In structural applications, this area has to be small for cosmetic reasons, and to allow small repairs.

4. The permanent deflection after impact is especially important for metals. This permanent deformation is in general small for composite materials. For the detection of damage it is favourable to have some permanent indentation after impact[14].

5. The amount of absorbed energy during impact[44] is an important parameter. It is related to the damage caused by the impact. During a fully elastic impact without damage nearly all the internal energy is returned to the impactor, in this case the energy restitution coefficient (= ratio of the velocity after impact and the initial impact velocity) is approximately equal to 1.

6. The critical velocity[5,11,29] is the perforation threshold. For velocities below the critical velocity the plate will stop the projectile. The critical velocity is especially of importance for ballistic and protection applications.

A summary of various observations from the literature is given below. It illustrates the complexity of impact testing and evaluation of the results.

fibres

1. Composites with polyethylene fibres (Dyneema[1] and Spectra 900[21]) are able to absorb much energy in comparison with composites with E-glass, carbon and aramid fibres.

2. The E-glass fibre shows a strain rate dependent behaviour during a drop weight test with respect to the force-displacement curve[3]. An increase of the impact strength (maximum force which can be sustained by the specimen during an impact) of 70% was measured[3] at higher strain rates.

3. Hybridization (combination of a brittle fibre and a fibre with a better energy absorption capability, see table 3.4) carbon/glass[25], polyethylene/carbon[21], aramid/carbon[19]) increases the absorbed energy during impact.

4. With E-glass composites a higher critical velocity (penetration velocity) can be reached for the same surface density as for steel and aluminium[29].

5. A lower fibre volume fraction increases damage tolerance[55,64].

6. The maximum force and the corresponding absorbed energy during perforation progresses from carbon/epoxy (relatively low) to aramid/epoxy, to E-glass/epoxy (relatively high)[28]. No data were found on the behaviour of the behaviour of the stronger R- and S-glass composites.

7. A fabric sheet on a UD base laminate does not reduce the area of delamination, but prevents delamination growth under cyclic loading[17].

matrix

8. PEEK matrix material (a thermoplastic) shows a strain rate dependent behaviour with respect to the damaged area as a function of the impact energy[4]. This material shows an improvement relative to epoxies with respect to the residual tensile and compression strength after impact until perforation[4,14]. The compressive strength is significantly improved[18]. This thermoplastic material exhibits more indentation after impact, which makes detection easier[4]. Empirical evidence obtained at high impact velocities indicates a diminished improvement of the residual strength properties relative to thermosetting composites, because of the large strain rate dependence of the material[64,65].

9. Interface toughening by adding adhesive between two fibre orientations suppresses delamination[16,50].

damage

10. Tough matrices in thin laminates hardly enhance the damage resistance

because the behaviour is fibre dominated. The shear strength of the matrix controls the onset of delamination, whereas fibre strength controls the onset of penetration. Excessively tough matrices may lead to brittle composites[8].

11. Stitching[13] and the use of 3–D woven composites[31] improve the residual strength after impact and reduce the damage.

12. Delamination will be initiated by branching of matrix cracks[16]. There is an interaction between matrix cracks and delamination[27,40] (see also figure 4.3).

13. An initial tensile stress on the material reduces the energy needed for the first damage, but beyond a certain impact energy level it may help in containing delamination[24].

14. The damage due to one large impact is larger than that of several small impacts with the same total impact energy. During repeated impact with a constant impact energy, the amount of additional damage decreases[37,57].

experimental

15. Charpy impact tests have a limited value for structural materials.

16. The dynamic fracture toughness determined by Charpy tests depends on the impact velocity due to dynamic effects in the test technique[58].

17. Instrumented impact testing is especially necessary to obtain data to verify impact models and to obtain insight into the impact problem. However, it is not always necessary to do instrumented impact tests; for structural materials it will often be sufficient to determine the impact energy threshold of the first (visible) damage, to determine the damaged area as a function of the impact energy, and to determine the residual strength as a function of the impact energy. In general, researchers are too optimistic in stating the relevance of instrumented impact testing. Instrumented impact tests are especially important for the modelling of the impact behaviour, but the measured data will only be meaningful if an analytical model is developed.

18. It is difficult to indicate the point of first (fibre) failure in the load-deflection or load-time curve. Local failure may occur before the first significant load drop. Penetration is easily discovered by a dramatic load drop[47,62]. The load-time or load-deflection curve may be obscured by the dynamic behaviour of the impactor. Additional strain measurements in

the specimen may improve instrumented impact testing. And also the measurement of the stresses in the support of the specimen may lead to better results. These types of tests were not found in literature.

19. Under certain circumstances multiple contacts are possible during impact[30]. This means that the contact between impactor and specimen is lost several times during the impact process.

4.3 Conclusions

General trends derived from various observations are:

- Impact problems have been tackled mainly by empirical means. Due to the large number of significant variables, a consistent picture on impact damage of composites is emerging slowly.

- Impact testing as an empirical approach is far from easy. The evaluation of the results is difficult.

A lot of work remains to be done on the material behaviour during impact. It is also necessary to establish standardized test methods based on a firm basis of physical concepts and analysis.

references

1. Gorp, E.H.M. van; Dingenen, J. van; Nieuw versterkingsmateriaal voor nieuwe materiaalcombinaties, I^2 werktuigbouwkunde, 6/7, pp.23-26, 1989.

2. Hoover, W.R.; Guess, T.R.; The dynamic fracture toughness of carbon-carbon composites, J.composite materials, Vol.7, pp.334-347, 1973.

3. Caprino, G.; Crivelli Visconti, I.; Di Ilio, A.; Composite materials response under low-velocity impact, Composite structures Vol.2, pp.261-271, 1984.

4. Godwin, E.W.; Davies, G.A.O.; Impact behaviour of thermoplastic composites, in: CAD in composite material technology, Ed. Brebbia, C.A.; Wilde, W.P. de; Blain, W.R.; Int. Conf. Southampton, 1988.

5. Ross, C.A.; Sierakowski, R.L.; Studies on the impact resistance of composite plates, Composites, July 1973.

6. Wrzesien, A.; Improving the impact resistance of glass-fibre composites,

Composites, July 1972.

7. Awerbuch, J.; Hahn, H.T.; Hard object impact damage of metal matrix composites, J.composite materials, Vol.10, 1976.

8. Elber, W; The effect of matrix and fiber properties on impact resistance, in: Tough composite materials, NASA CP 2334, pp.99-121, 1983.

9. Dorey, G.; Sigéty, P.; Stellbrink, K.; 't Hart, W.G.J.; Impact damage tolerance of a carbon fibre composite laminate, Royal Aircraft Establishment, Technical report 84049, Garteur/TP-007, 1984.

10. Adams, D.F.; Impact response of polymer-matrix composite materials, in: Composite materials: testing and design (fourth conference), ASTM STP 617, pp.409-426, 1977.

11. Davies, C.K.L.; Turner, S.; Williamson, K.H.; Flexed plate impact testing of carbon fibre-reinforced polymer composites, Composites, Vol.16, No.4, pp.279-285, 1985.

12. Kida, S.; Oda, J.; Fracture behaviour of brittle plates and cylindrical shells subjected to concentrated impulse loading, Exp. Mechanics, June, pp.158-163, 1987.

13. Dexter, H.B.; Funk, J.G.; Impact resistance and interlaminar fracture toughness of through-the-thickness reinforced graphite/epoxy, AIAA/ASME/ASCE/AMS 27th structures, structural dynamics and material conference, pp.700-709, May 1986.

14. Brandt, J.; Warnecke, J.; Influence of material parameters on the impact performance of carbon-fibre-reinforced polymers, in: High tech-the way into the nineties, ed. Brunsch, K.; Gölden, H.D.; Herkert, C.M.; pp.251-260, Elsevier Science Publishers, B.V., Amsterdam, 1986.

15. Dorey, G.; Sigéty, P.; Stellbrink, K.; 't Hart, W.G.J.; Impact damage tolerance of carbon fibre and hybrid laminates, Royal Aircraft Establishment Technical report 87057, Garteur TP-037, 1987.

16. Rechak, S.; Sun, C.T.; Optimal use of adhesive layers in reducing impact damage in composite laminates, in: Composite Structures 4, Volume 2, ed. Marshall, I.H.; pp.2.18-2.31, Elsevier Applied Science, 1987.

17. Hart, W.G.J.; Impact/fatigue performance of a $(\pm 45_2, 0_4)_s$ type carbon/epoxy laminate, National Aerospace Laboratory NLR, NLR TR 85108 U, 1985.

18. Dorey, G.; Bishop, S.M.; Curtis, P.T.; On the impact performance of

carbon fibre laminates with epoxy and peek matrices, Int. Symposium on composites: materials and engineering at the University of Delaware, 1984.

19. Helfinstine, J.D.; Charpy impact of unidirectional graphite/aramid /epoxy hybrid composites, in: Composite materials: testing and design (fourth conference), ASTM STP 617, pp.375-388, 1977.

20. Butcher, B.R.; Fernback, P.J.; Impact resistance of unidirectional CFRP under tensile stress: further experimental variables, Fibre science and technology Vol.14, pp.41-58, 1983.

21. Adams, D.F.; Zimmerman, R.S.; Static and impact performance of polyethylene fiber/graphite fiber hybrid composites, SAMPE journal November/December, pp.10-16, 1986.

22. Caprino, G.; Residual strength prediction of impacted CFRP laminates, J.composite materials, Vol.18, November 1984.

23. Dorey, G.; Impact damage in composites - development, consequence and prevention, 6th conference on composite materials, ICCM & ECCM, Vol.3, pp.3.1-3.26, 1987.

24. Sankar, B.V.; Sun, C.T.; Low-velocity impact damage in graphite-epoxy laminates subjected to tensile initial stresses, AIAA journal, Vol.24, No.3, pp.470-471, 1986.

25. Marom, G.; Drukker, E.; Weinberg, A.; Banbaji, J.; Impact behaviour of carbon/Kevlar hybrid composites, Composites, Vol.17, No.2, pp.150-153, April 1986.

26. Aleszka, J.C.; Low energy impact behavior of composite panels, J.Testing and evaluation, Vol.6, No.3, pp.202-210, May 1978.

27. Joshi, S.P.; Sun, C.T.; Impact induced fracture in a laminated composite, J. composite materials, Vol.19, pp.51-66, 1985.

28. Winkel, J.D.; Adams, D.F.; Instrumented drop weight impact testing of cross-ply and fabric composites, Composites, Vol.16, No.4, pp.268-278, 1985.

29. Batchelor, J.; Carrington, P.J.; Impact considerations and performance for FRP on British Rail, British Rail TM PDU 81, 1980.

30. Takeda, N; Sierakowski, R.L.; Malvern, L.E.; Studies of impacted glass fiber-reinforced composite laminates, SAMPE Quarterly, pp.9-17, January 1981.

31. Ko, F.K.; Hartman, D.; Impact behavior of 2-D and 3-D glass/epoxy composites, SAMPE journal, pp.26-30, July/August 1986.

32. Khetan, R.P.; Chang, D.C.; Surface damage of sheet molding compound panels subject to a point impact loading, J. composite materials, Vol.17, pp.182-194, March 1983.

33. Chaturvedi, S.K.; Sierakowski, R.L.; Effects of impactor size on impact damage-growth and residual properties in a SMC-R50 composite, J. composite materials, Vol.19, pp.100-113, March 1985.

34. Dharan, C.K.H.; Beardmore, P.; The resistance of graphite fiber-reinforced composites to impacts, in: Failure modes in composites III, Ed. Chiao, T.T.; Schuster, D.M.; New York 1976.

35. Adams, D.F.; Perry, J.L.; Static and impact behavior of graphite/epoxy composite laminates containing third-phase reinforcement materials, J. Testing and evaluation, Vol.5, No.2, pp.114-123, March 1977.

36. Voelker, M.J.; Low temperature impact properties of long fiber thermoplastic composite molding materials, 20th international SAMPE Technical Conference, pp.144-148, September 1988.

37. Wyrick, D.A.; Adams, D.F.; Damage sustained by a carbon/epoxy composite material subjected to repeated impact, Composites, Vol.19, No.1, pp.19-27, January 1988.

38. Hsu, P.; Song, H.C.; Chang, Z.H.; On the impact properties of fibre composites and their hybrid materials, in: Computer aided design in composite material technology, Ed. Brebbia, C.A.; Wilde, W.P. de; Blain, W.R.; Proceedings of the international conference, pp.395-401, Southampton, 1988.

39. Toland, R.H.; Impact testing of carbon-epoxy composite materials, in: instrumented impact testing, ASTM STP 563, pp.133-145, 1974.

40. Liu, D.; Malvern, L.E.; Matrix cracking in impacted glass/epoxy plates, J. Composite materials, Vol.21, pp.594-609, July 1987.

41. Foreign object impact damage to composites, ASTM STP 568, 1973.

42. Boll, D.J.; Bascom, W.D.; Weidner, J.C.; Murri, W.J.; A microscopy study of impact damage of epoxy-matrix carbon-fibre composites, J.Materials Science, Vol.21, pp.2667-2677, 1986.

43. Buynak, C.F.; Moran, T.J.; Donaldson, S.; Characterization of impact damage in composites, SAMPE Journal, pp.35-39, March/April 1988.

44. Sjöblom, P.O.; Hartness, J.T.; Cordell, T.M.; On low-velocity impact testing of composite materials, J. Composite materials, Vol.22, pp.30-52, January 1988.

45. Rotem, A.; Residual flexural strength of FRP composite specimens

subjected to transverse impact loading, SAMPE Journal, pp. 19-25, March/April 1988.

46. Joneja, S.K.; Newaz, G.M.; Fracture toughness and impact characteristics of a hybrid system: glass-fiber/sand/polyester, in: Effects of defects in composite materials, ASTM STP 836, pp.3-20, 1984.

47. Teti, R.; Langella, F.; Crivelli Visconti, I.; Caprino, G.; Impact response of carbon cloth reinforced composites, ICCM V, pp.373-381, 1985.

48. Johnson, W.S.; Impact and residual fatigue behavior of ARALL and AS6/5245 composite materials, NASA Technical Memorandum 89013, 1986.

49. Buchanan, D.L.; McClellan, P.S.; Structural evaluation of high strain fiber and resin composite material systems, Air Force Wright Aeronautical Laboratories, AFWAL-TR-86-3007, 1986.

50. Hirschbuehler, K.R.; An improved 270°F performance interleaf system having extremely high impact resistance, SAMPE Quarterly, Vol.17, No.1, pp.46-49, October 1985.

51. Blaricum, T.J. van; Bates, P.; Jones, R.; An experimental investigation into the effect of impact damage on the compressive strength of step lap joints, Eng. Fracture Mechanics, Vol.32, No.5, pp.667-674, 1989.

52. Banthia, N.; Mindess, S.; Bentur, A.; Pigeon, M.; Impact testing of concrete using a drop-weight impact machine, Experimental mechanics, pp.63-69, March 1989.

53. Tanaka, T.; Kinoshita, K.; Nakayama, H.; Fatigue crack growth and microscopic crack opening behaviour under impact fatigue load, Int. J. Fatigue, pp.117-123, March 1989.

54. Loriot, G.; Cardamone, J.C.; Essais de choc instrumentes sur composites reinforces de fibres de carbonne, Centre d'Essais Aeronautique de Toulouse, Proces-verbal de l'essai No m6 582500.

55. Manders, P.W.; Harris, W.C.; A parametric study of composite performance in compression-after-impact testing, SAMPE Journal Noverber/December, pp.47-51, 1986.

56. Wu, H.T.; Springer, G.S.; Measurements of matrix cracking and delamination caused by impact on composite plates, J. Composite materials, Vol.22, pp.518-531, June 1988.

57. Wyrick, D.A.; Adams, D.F.; Residual strength of a carbon/epoxy composite material subjected to repeated impact, J. Composite materials, Vol.22, pp.749-765, August 1988.

58. Kinloch, A.J.; Kodokian, G.A.; Jamarani, M.B.; Impact properties of epoxy polymers, J. Materials science, Vol.22, pp.4111-4120, 1987.

59. Wu, J.S.; Friedrich, K.; Grosso, M.; Impact behaviour of short fibre/liquid crystal polymer composites, Composites, Vol.20, No.3, pp.223-233, May 1989.

60. Plati, E.; Williams, J.G.; The determination of the fracture parameters for polymers in impact, Polymer engineering and science, Vol.15, No.6, pp.470-477, June 1975.

61. Golovoy, A.; Cheung, M.F.; Oene, H. van; The impact behaviour of glass and carbon fiber composites, Polym.Plast.Technol.Eng., Vol.23, No.2, pp.217-227, 1984.

62. Johnson, A.E.; Moore, D.R.; Prediger, R.S.; Reed, P.E.; Turner, S.; The falling weight impact test applied to some glass-fibre reinforced nylons, part 2 Some results and interpretations, J. Material science, Vol.22, pp.1724-1732, 1987.

63. Curtis, P.T.; An investigation of the mechanical properties of improved carbon fibre composite materials, Royal Aircraft Establishment, Technical Report 86021, 1986.

64. Hart, W.G.J. 't; Frijns, R.H.W.M.; Damage tolerance properties of new carbon composites, NLR Technical Publication TP 89032 L, 1989.

65. Hart, W.G.J. 't; Frijns, R.H.W.M.; Delamination growth in improved carbon composites under constant amplitude fatigue loading, NLR Technical Publication TP 89008 L, 1989.

66. Card, M.F.; Rhodes, M.D.; Graphite-epoxy panel compression strength reduction due to local impact, Effect of service environment on composite materials, AGARD 50th Meeting of the structures and materials panel specialists meeting, 1980.

67. Reed, P.E.; Turner, S.; Flexed plate impact, part 7. Low energy and excess energy impacts on carbon fibre-reinforced polymer composites, Composites, Vol.19, No.3, pp.193-203, May 1988.

68. Wardle, M.W.; Tokarsky, E.W.; Drop weight impact testing of laminates reinforced with Kevlar aramid fibers, E-glass, and graphite, Composites technology review, Vol.5, No.1, pp.4-10, 1983.

69. Johnson, S.R.; Sun, C.T.; Impact damage in polyimide composite laminates, 33rd int. SAMPE symposium, pp.1200-1207, 1988.

70. Spamer, C.T.; Brink, N.O.; Investigation of compression strength after impact properties of carbon/PPS and carbon/APC-2 thermoplastic

materials, 33rd int. SAMPE symposium, 1988.

material description	total energy (kJ/m^2)
boron/epoxy (60% fibre volume)	78
Modmor II carbon/epoxy (55% fibre volume)	113
Kevlar 49 aramid/epoxy (65% fibre volume)	694
S-glass/epoxy (72% fibre volume)	694
4130 steel alloy	593
Al 2024-T3	84
Al 6061-T6	153
Al 7075-T6	67

table 4.1 Typical total energy values for various
materials-standard Charpy-V notched impact tests[10].

interlaminar shear failure

flexural failure

penetration (plugging)
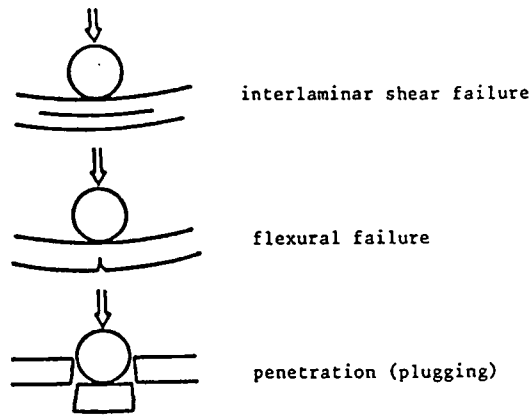
figure 4.1 The primary failure modes of composite laminates under impact loading (ref.23).
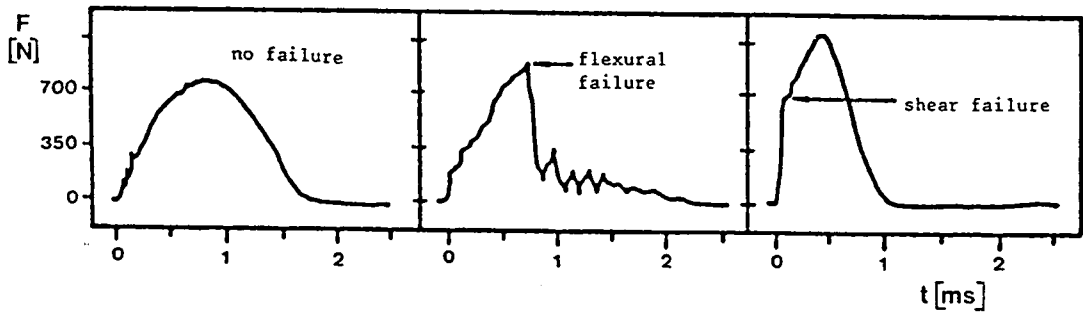
figure 4.2 Load-time records during drop weight impact on CFRP laminates (ref.23).
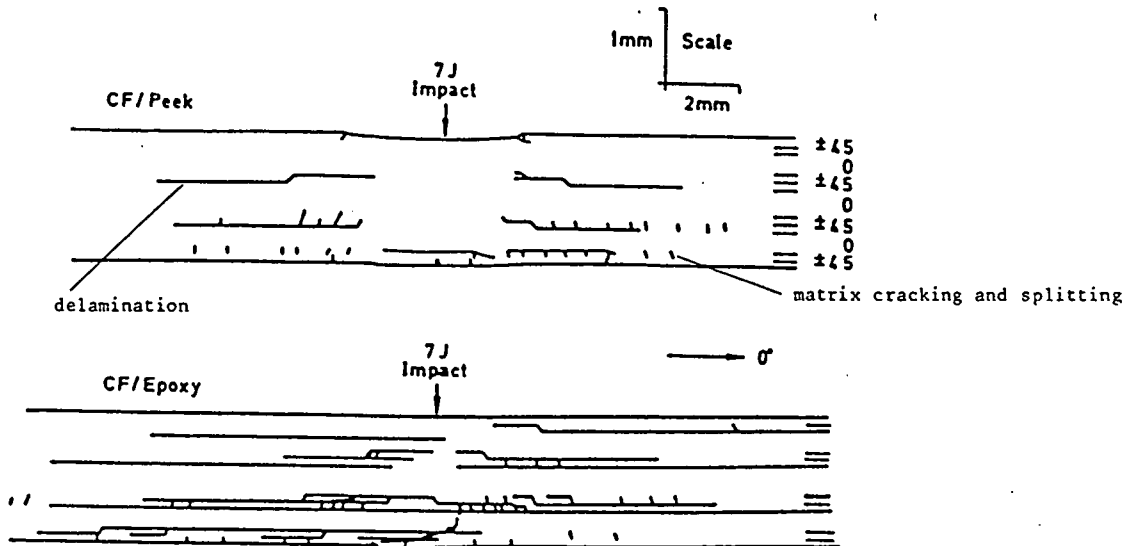
figure 4.3 Matrix cracks and splitting branching into delamination, schematics of internal damage caused by drop weight impact on laminates of carbon/PEEK and carbon/epoxy (ref.23).

81

chapter 5 Instrumented impact testing, a description of the b2-impact tester

5.1 Introduction

Impact testing is not as straightforward as, for example, a tensile test. This chapter gives the background of instrumented impact testing and a description of the impact tester developed, built and used in the present study. It is called the b2-impact tester after the code number for the Production and Materials section (b2) of the Faculty of Aerospace Engineering of the Delft University of Technology.

Impact tests are done on materials and structures to determine their sensitivity for damage caused by striking objects. The classical Charpy and Izod tests are used to measure the impact fracture energy of materials. The results of such impact tests are mainly comparative in nature and in general cannot be used as design data. They characterize, however, the brittle or ductile material behaviour. The Charpy and Izod test are not suitable to simulate the impact of an object on an aircraft structure composed of sheet materials. The sheet materials tested in this study were clamped and hit by a well-defined impactor.

The development of fast data acquisition instruments has made it possible to carry out instrumented impact tests in order to obtain information about the behaviour of the material during impact, instead of studying only the damage in the specimen after impact. It enables a discrimination between damage initiation and damage propagation. The instrumentation is complex, mainly because the duration of the event is very short (in the order of a few milliseconds). Dynamic effects may disturb the measured data because of the dynamic behaviour of the force and displacement transducers, the data acquisition system, the clamping and supports of the specimen and the interaction between the impactor and the specimen.

This chapter gives a description of:
- the mechanical part of the b2-impact tester (5.2)
- the instrumentation of the b2-impact tester (5.3)
- problems associated with the instrumentation (5.4)

- data processing (5.5).

The test program on several aircraft materials and the results obtained are presented in part II, chapters 6 to 8.

5.2 Test geometry and mechanical part of the b2-impact tester

5.2.1 The type of the impact tester

Four types of impact testers can be distinguished: the drop tower type, the pendulum, the air gun and the Hopkinson type pressure bar technique. The types are illustrated by figure 5.1.

The pendulum is the classical method for impact testing (figure 5.1a). Figure 5.1a shows a Charpy impact tester and the pendulum impact tester of the US Air Force Materials Laboratory[10]. The pendulum has some advantages: the residual energy of the impactor can be easily determined by measuring the angle of rebound, the motion of the impactor can be easily controlled and the impactor can easily be caught after impact. The influence of the gravity is small, because the impact is horizontal.

If higher impact velocities are needed an air gun can be used (figure 5.1b). The pressure vessel of this tester is filled with compressed air. The plastic membrane is burned through by electrical wires, and the projectile (indentor) is accelerated by the expanding air. After leaving the barrel, the velocity of the projectile is measured by the photocell velocity meter. The specimen is placed before the barrel of this air gun. The impactor mass used in these guns is relatively low, and generally these tests are not instrumented.

The Hopkinson pressure bar technique is a rather complicated type of testing. In the case of a plate specimen this device consists of an input bar with two strain gages, which is attached to the specimen. The input bar will be hit by a striker, and a stress wave will start to travel in the bar. At the specimen a part of the wave will be reflected, and a part will excite the plate. The load on the plate as function of time can be derived from the signals of the strain gages.

It is not a common technique. It requires a one dimensional stress wave analysis of the input bar by which the forces and displacements can be calculated, without assuming a quasi-static equilibrium. This type of testing is generally applied for high strain rate tensile, compression or torsion tests.

The Hopkinson pressure bar is a rather complicated type of testing, and the indirect loading on the specimen by an input bar is less realistic than with the other test methods.

For the tests in this study a drop weight impact tester was chosen. Compared with the pendulum tester the drop weight tester has several advantages. It is easier to reach a higher impact velocity, depending on the available height for dropping. In our laboratory a drop height of 12 m could be used. The tester needs less laboratory floor compared with a pendulum tester. Compared with the gas gun it is easier to instrument the drop weight impact tester. The drop weight tester covers the most important velocity range of low-velocity maintenance damage (see chapter 3). The drop weight tester used for the present study (the 'b2-impact tester') is discussed in the next section.

5.2.2 Mechanical part of the b2-impact tester

The principle of a drop weight impact tester is simple: an impactor with a certain weight and a known nose shape is dropped from a adjustable height, and at the end of its fall it will strike a specimen with a well defined clamping condition.

The impact tester designed and built as a part this study is shown in figures 5.2 and 5.3. The operation of the tester is as follows.

1. The impactor (A in figure 5.2, more detailed in figure 5.4) is lightly clamped by two springs (friction clamping) in a carriage (B). This is done to prevent the impactor from dropping out of the carriage during its fall.

2. The carriage is released by pulling the impactor with the grip into a conical fixture (O).3. This fixture can be adjusted by a cable for the desired drop height.

4. The main function of the carriage is to guide the impactor during the fall along two pipes (P).

5. At the end of the fall the carriage is stopped by two dampers. The impactor continues its motion, it interrupts the clamping of the two springs and strikes the specimen.

6. A 12 m long electrical cable (Q) is connected with the carriage to enable measurements of the contact force. The connection between the cable on the carriage and the load cell in the impactor was established by a thin wire which does not influence the motion of the impactor.

7. After impact the impactor is caught by the springs in the carriage to avoid a second impact.

The mass of the impactor can be varied, by adding mass between the nose and the reflector disc, and at the end of the impactor between the grip and the pipe. The mass of the impactor can be varied between 0.3 and 0.5 kg. The impactor nose with the load cell can be changed. The maximum drop height is approximately 12 m, the maximum velocity which can be reached is approximately 12 m/s. The clamping with the specimen (see figure 5.5) is mounted on a heavy steel table with bolts in T grooves of the table. The dimensions of the table are 1 x 0.8 m. On the table also a device can be clamped for biaxial initial loading of the specimen.

5.2.3 Test geometry

The test geometry is very important, because it is not easy to compare impact tests done with different projectile nose shapes or different plate boundary conditions. The test geometry includes the shape of the impactor, the dimensions and the shape of the specimen, and the boundary conditions of the specimen. The Charpy and Izod tests are well-known to measure the energy needed to break a beam specimen by a pendulum, figure 5.1. Standards also exist for drop weight tests on sheet materials (e.g. ASTM D 3029), but in the literature no generally accepted standard is found. ASTM D 3029 describes three dimensions of circular clamped specimens (method F): diameters 3.81 cm (method FB), 7.62 cm (method FA), and 12.7 cm (method FC) and three nose radii of the impactor (tubs): 6.35 mm (method FB), 7.94 mm (method FA), and 19.05 mm (method FC). ASTM D 3029 also mentions a geometry (method G) in which a mass strikes an impactor positioned on the plate. For

this method simply supported specimens are recommended.

In general the tests in this study were performed on a specimen with a clamped circular test area with a diameter of 80 mm (as shown in figure 4.5) or with a clamped square area 100x100 mm^2. The tip radius of the impactor was 7.5 mm. The diameter of the circular specimen is close to one of the recommended geometries of the ASTM test method (method FA). To obtain realistic conditions, the clamped width of the specimen was selected to be in the order of the stiffener spacing in an aircraft structure.

5.3 Instrumentation of the b2-impact tester

5.3.1 Introduction

The impact process can be described by the following functions of time:
1. the <u>contact force</u> between impactor and specimen,
2. the <u>velocity</u> of the impactor
3. the <u>displacement</u> of the impactor. and
4. the <u>strain</u> in the specimen.

The strain at a certain point of the specimen was measured directly. The other three quantities were measured directly or were derived from other measured quantities. In this study two methods were followed:

(i) Measurement of the <u>contact force</u> by a load cell as function of time, the acceleration is derived from this force with Newton's law of motion. This acceleration is integrated in time to obtain the velocity as function of time. The displacement is calculated by a second integration: the integration of the velocity-time function.

(ii) Measurement of the <u>displacement</u> by a displacement transducer as function of time. This function is differentiated to obtain the velocity-time curve. This latter function is differentiated to the acceleration-time curve.

The formulation of these two methods are:

(i) measurement of the contact force

1. contact force between impactor and specimen F vs. time t.

This contact force is measured, and the acceleration of the impactor is calculated with Newton's law of motion:

$$F(t) = m_p \, a(t) + m_p \, g \qquad (5.1)$$

with a as the acceleration, F as the contact force and m_p as the impactor mass, and g as the acceleration of gravity.

2. velocity of the impactor v vs. time

$$v = v(t) = v_0 - \int_0^t a(\tau) \, d\tau = v_0 - \frac{1}{m_p} \int_0^t F(\tau) \, d\tau + g \, t \qquad (5.2)$$

For this integration the impact velocity v_0 is needed.

3. displacement of the impactor s vs. time

$$s = s(t) = \int_0^t v(\tau) \, d\tau \qquad (5.3)$$

If the indentation of the specimen is small and as long as there is contact between the impactor and the specimen (F > 0), the displacement of the impactor will be approximately equal to the central deflection of the specimen:

$$s(t) \cong w_0(t) \qquad (5.4)$$

(ii) measurement of the displacement

1. displacement s of the impactor as function of time

87

The function s(t) is measured directly.

2. velocity v as function of time

The velocity of the impactor is derived from:

$$v(t) = \frac{ds}{dt} = \dot{s}(t) \tag{5.5}$$

3. contact force as function of time

$$F(t) = - m_p \ddot{s}(t) + m_p g \tag{5.6}$$

The next section (5.3.2) describes the measurement of the impact velocity, needed for the integration of the force-time curve(equation 5.2). The measurement of the contact force, the displacement and the strain is discussed in sections 5.3.3, 5.3.4 and 5.3.5 respectively. The measurement is done by a computer, as is briefly described in section 5.3.6. Some problems which may be associated with the instrumentation are discussed in section 5.4:

1. The specimen is mounted in a clamp which is connected with the other parts of the impact system. The elastic compliance of the test set-up will have an influence on the measured force-time curve (section 5.4.1)

2. The load cells are statically calibrated, while they are dynamically loaded during the impact process (section 5.4.2).

3. The measured force-time curve will not be a smooth curve. This may be due to vibrations in the test system or noise of the instrumentation (section 5.4.3).

Finally the data processing computer program will be described in section 5.5.

5.3.2 Impact velocity measurement

The reflector disk on the impactor (see figure 5.4) interrupts the infrared beams which shine on infrared photo transistors A and B, see figure 5.6.

The time between the darkening of the transistors is measured by a counter with a frequency of 1 MHz. The distance between the two pairs is 30.0 mm. The counter measures the time between the darkening of the two photocells. This means that an average velocity $\bar{v}$ is measured. It can be derived that the relationship between $\bar{v}$ and the actual impact velocity v_c is:

$$\bar{v} = g \frac{AB}{\sqrt{v_c^2 - 2\,g\,BC} - \sqrt{v_c^2 - 2\,g\,AC}} \qquad (5.7)$$

It assumes that the acceleration of the impactor is equal to the acceleration of gravity, and that friction is negligible. Figure 5.6 shows this relation between the measured velocity and the actual impact velocity for different values of the distance BC (distance between the lower infrared beam and the specimen). During the tests this distance is smaller than 5 cm. It implies that the impact velocity does not need a correction for impact velocities larger than 3 m/s (corresponding to the low impact height of approximately 45 cm) because the inaccuracy according to equation 4.5 is smaller than 1%.

5.3.3 Force measurement

5.3.3.1 Load cell in the impactor

The force transducer measures the strain (force) at a point of the impactor above the contact point. To obtain the contact force a correction factor is needed, which can be easily derived to be:

$$F_{contact} = \frac{m_p}{m_p - m} F_{measured} \qquad (5.8)$$

with: $F_{contact}$ as the contact force,
$F_{measured}$ as the measured force,
m_p as the total impactor mass,
and m as the mass of the impactor between the strain gages and

the contact point.

The mass m is 22.8 g, the total impactor mass in most tests was 325 g. The correction factor then is 1.075.

An integral load cell/nose tip was applied (see figure 5.4) to avoid disturbances in the force-time curve caused by vibration of the nose tip relative to the load cell (this will be discussed in section 5.4.3).
The load cell was made of stainless steel. A complete Wheatstone bridge (four gages) was mounted on the load cell. Two of the gages are in the direction of the load and compensate for bending of the transducer, and two gages are mounted in the transverse direction to complete the bridge. The load is measured close to the nose of the projectile (in order to make m in equation 5.8 small). The load cell was statically calibrated. It was calibrated with the long cable needed to reach the drop height of 12 m, to include the resistance of this cable. The force transducer is connected with a DC amplifier Peekel type GRL 1. The Wheatstone bridge has to be balanced before testing. Because it is not possible to make the output exactly zero, it is better to allow a small negative output which can be measured by the computer during initialization before testing and subtracted from the measured signal (The ADC in the computer can only measure negative signals, see section 5.3.6).

5.3.3.2 Comparison of the force measured by the load cell in the impactor with the force derived from an acceleration transducer

Before the impact tester described in this chapter was built, a comparison was made between the measurement by the load cell and the measurement by an acceleration transducer. In these tests the load cell had a different shape than that shown figure 5.4: the load cell and the tip were not integrated. The load cell of Al 7075-T6 had an outer diameter of 15 mm and an inner diameter of 8 mm. This load cell is also discussed in section 5.4.3.

The tests were part of the experimental verification of an elastic impact model described in chapter 12. Impact tests were performed with very low velocities, by adopting impact heights of 1, 2 and 3 cm. The tests were carried out on specimens with a clamped square test area of 100x100 mm^2 of

Al 2024-T3 with a thickness of 1 mm and aramid ARALL with a thickness of 0.8 mm. A small test set-up was made as shown in figure 5.7, with the load cell near the tip and the acceleration transducer at the top if the impactor. The aim of these tests was a comparison of the output of both transducers.

The results are shown in figure 5.8 and 5.9. It is clearly visible that the acceleration transducer indicates much greater vibrations in the first part of the impact. The vibrations are more severe for higher impact velocities and for the stiffer monolithic aluminium specimen. They are due to resonant vibrations of the acceleration transducer. According to the specifications the resonant frequency is 42 kHz, and the maximum frequency which could be measured (which is far enough below the resonant frequency according to the specifications) is 12.6 kHz. The frequency of approximately 5 kHz in the signal of the load cell which can be distinguished in figure 5.8 could be influenced by the stiffness of the specimen. The frequency in the load cell signal of figure 5.9 is smaller than in figure 5.8.

The acceleration transducer directly measures the acceleration of the impactor, while the load cell measures a strain which can be related to the contact force and the acceleration. It was concluded that the signal of the load cell followed the signal derived from the acceleration transducer quite well.

5.3.3.3 Load cells under the clamping

Another method to measure the contact force (which is not found in the literature), is by load cells under the specimen clamps. This method can be advantageous because it eliminates the long 'moving' wire connected to the load cell in the impactor.

Figure 5.5 shows the clamping with the load cells used in this study. (The measurement of the force under the clamping was optional and it was not always used during the tests). First the -4 load cells of this table were made of Al 7075-T6, to obtain sufficient output. However, in this case the vibration of the table became too dominant. Calculations with the mass-spring model discussed in section 5.4.1 indicated that it would be more appropriate to make the load cells stiffer (i.e. of steel) and to

amplify the signal. At high impact velocities and relatively stiff specimens, the vibration of the clamping starts to dominate again as shown in figure 5.10. The force acting on the 'clamping table' can be derived from this curve, by the analysis of a simple mass-spring model (figure 5.11). The mass on top of the load cells is M = 7.56 kg (including the bolts and neglecting the mass of the specimen). The stiffness of the system is approximately equal to four times the stiffness of a single load cell (the clamping is supported by 4 load cells, figure 5.5). The load cell is a hollow steel cylinder with an outer radius of 6 mm and an inner radius of 3.25 mm.

The equation of motion of the mass-spring system is:

$$M \frac{d^2w}{dt^2} + k w = F \qquad (5.9)$$

with F as the actual contact force and k as the stiffness. The measured force F^* will be equal to:

$$F^* = k w \qquad (5.10)$$

The actual contact force can therefore be calculated from:

$$F = \frac{T^2}{4\pi^2} \frac{d^2F^*}{dt^2} + F^* \qquad (5.11)$$

with T as the period of the vibration:

$$T = 2\pi \sqrt{\frac{M}{k}} \qquad (5.12)$$

The calculated period T is 0.325 ms, the measured value (figure 5.10) is 0.305 ms. The latter value was used for the correction of the measured force. The correction (equation 5.11) needs the numerical calculation of the second derivative of the measured force F^*. The Lanczos method was used as will be discussed in section 5.5.4. Figure 5.12 shows one of the corrected force-time curves. The large fluctuations in the force-time curve measured by the load cells in the clamping are removed, and the curve is close to the curve measured by the load cell in the impactor.

5.3.4 Displacement measurement

An infrared displacement measuring system was developed to measure the displacement of the impactor. The transducer consists of 6 infrared transmitters (LED's) and one photocell. The transmitters are positioned around the photocell as is indicated in figure 5.13. The infrared signal is reflected from a disk which is mounted on the projectile, see figures 5.2 and 5.4. The disk was made of mat white plastic. It had to be cleaned regularly to assure a constant reflection. The intensity of the signal measured by the photocell is a measure for the distance to the disk. The system can also be used to trigger the sampling of the force and displacement signal: when a critical distance is reached, the sampling is started. This triggering can also be done by the photocells of the velocity measurement.

The displacement-output curve is not linear, see figure 5.14. The curve was approximated by a fifth order polynomial. Frequent checks are done to assure that this curve did not change, e.g. due to a diminishing reflection capability of the disk.

5.3.5 Strain measurement

To obtain direct information on the behaviour of the specimen, the strain in the specimen was measured by strain gages. The signal was amplified by a DC amplifier, which was connected with the analog-digital converter in the computer.

5.3.6 Analog-digital converter (ADC) and personal computer

The ADC is an extension board for the personal computer. It was designed and built at the Delft University (Faculty of Electronic Engineering). The ADC samples the signal with a frequency of 1 MHz, (= 10^6 samples per second). It has a resolution of 8 bits (0-255) and an internal memory of 32 kbyte (32,000 data points). Two ADC's are used: one for the force signal from the load cell in the impactor, and the other one for the displacement signal. In some experiments the second one was used for the the clamping load cells or a specimen strain signal. The displacement transducer had to

be shielded to avoid light from the surrounding shining in the transducer. This shielding was rather problematic, while large errors could be introduced by light shining in the transducer. Therefore in many cases only the signals of the clamping and the load cell in the impactor were measured.

The ADC can be initiated and read from a Turbo Pascal program and after reading the data can be handled as ordinary program data. The input of the ADC has to be between zero V (=0) and -0.5 V (=255). For a more detailed description of the ADC see Franken [12].

The ADC boards are inserted in an IBM XT personal computer. A program is written (see section 5.5.6) to initialize the settings of the ADC, to read the sampled signal, to store it on floppy disk (together with specimen data and calibration factors), and to process the data on basis of the range settings and the masses.

5.4 Discussion of the problems associated with the instrumentation

5.4.1 The elastic compliance of the impact system

During impact, in addition to deforming the specimen, some of the kinetic energy of the impactor is stored as elastic energy of the clamps and anvil (table) of the test system (see figures 5.2 and 5.5). Mark-Markowitch et al.[4] and Ireland[3] corrected the integrated force signals (equations 5.2 and 5.3) for the elastic compliance of the system. The compliance of the system can be determined by with a 'low blow test' (an elastic impact test with a low impact velocity) on a specimen with a known compliance[1]. In general it will be better to use a system with high stiffness such that this correction is not necessary. A high stiffness and mass are also needed to avoid or minimize vibration effects that may disturb the measured force-time curve.

The analysis of an impact by the use of a mass-spring model is described by e.g. Cain[2] and William and Adams[19]. A simpler approach will be given

---

[1] The accuracy of the measured compliance of the system can be expected to be low, because this compliance is very large relative to the compliance of the specimen.

here.

The impact on a specimen and its interference with the elastic compliance of the system can be described by a two degree of freedom system as shown in figure 5.15. The impactor mass m_p with an initial velocity v_0 accelerates a specimen with an effective mass m_1 and compliance c_1. The support of the specimen has a compliance c_2 and an effective mass m_2. The support is connected with an anvil which is considered rigid. The effective mass[2] of the specimen is in our case small compared with the mass of the impactor and can be neglected.

The equations of motion of this lumped mass system are:

$$m_p \frac{d^2 w_1}{dt^2} + c_1(w_1 - w_2) = 0$$

$$m_2 \frac{d^2 w_2}{dt^2} - c_1(w_1 - w_2) + c_2 w_2 = 0 \qquad (5.13)$$

with the initial conditions (at t=0: $w_1 = 0$, $w_2 = 0$, $\frac{dw_1}{dt} = 0$) the solutions of these equations can be written as:

$$w_1 = a_1 \sin \omega_1 t + a_2 \sin \omega_2 t$$

$$w_2 = r_1 a_1 \sin \omega_1 t + r_2 a_2 \sin \omega_2 t \qquad (5.14)$$

with:

$$\omega_{1,2}^2 = \frac{m_p(c_1 + c_2) + c_1 m_2}{2 m_p m_2} \pm \sqrt{\left[\frac{m_p(c_1 + c_2) + c_1 m_2}{2 m_p m_2} \right]^2 - \frac{c_1 c_2}{m_p m_2}}$$

and:

$$r_1 = 1 - \frac{m_p \omega_1^2}{c_1}$$

---

[2] The effective mass is smaller than the real mass of the plate, this will be discussed in chapter 12.

95

$$a_1 = \frac{r_2 \, v_0}{(r_2 - r_1) \, \omega_1}$$

$$a_2 = \frac{-r_1 \, v_0}{(r_2 - r_1) \, \omega_2}$$

Ideally, if the support is rigid ($c_2 = 0$) and the mass m_2 is large, the response of the target will be:

$$w_1 = v_0 \sqrt{\frac{m_p}{c_1}} \, \sin\left[\sqrt{\frac{c_1}{m_p}} \, t \right] \qquad (5.15)$$

The force on the impactor was compared with this ideal situation. During the tests in this study the compliance of the specimens was in the order of 1 kN/mm, the impactor mass was approximately 0.3 kg, the mass of the clamping device was in the order of 7 kg. For the compliance of the clamping 10 and 100 kN/mm were adopted to estimate possible effects. The first value is a worst case, the latter one is more realistic. Figures 5.16 and 5.17 show the contact force which will be measured (dotted line) compared with the ideal one (m_2 large and $c_2 = 0$, solid line). It can be concluded that under realistic conditions the effect of the elastic compliance of the system will be small.

5.4.2 Dynamic calibration of the load cell

The load cells of the b2-impact tester are calibrated in a static way. This calibration is performed by placing a load cell in a hydraulic testing machine and by measuring the relation between the load on the cell and the output of the strain gage amplifier. From a physical point of view, a correction factor may be needed because the adhesive of the strain gages may exhibit a different behaviour under dynamic loading compared with static loading.

It can be proven that the dynamic calibration was not necessary by considering the correspondence between the contact force derived from the

load cell and from the acceleration transducer (figures 5.8 and 5.9) and with the fact that the displacements obtained by integration of the force signal (equations 5.2 and 5.3) agreed with the directly measured displacement curves.

In the literature a correction is proposed for dynamic response. The following equation is used as an approximate method to include dynamic effects[10]:

$$\int -F_{actual} \, dt = m_p \, (v_r - v_0) = C \int -F_{measured} \, dt \qquad (5.16)$$

with: F_{actual} as the actual contact force

$F_{measured}$ as the measured contact force

m_p as the impactor mass

v_r as the velocity of the impactor after impact

v_0 as the impact velocity

C as the dynamic calibration factor.

The impact and rebound velocity are measured by the photocells and light emitting diodes. The correction factor will be:

$$C = \frac{m_p (v_r - v_0)}{\int -F_{measured} \, dt} \qquad (5.17)$$

Hudock[10] gives typical values of C between 0.90 and 0.99. Markowitch et al.[4] state that the calibration factor can be checked by a 'low blow test'. In this case the velocity has to be zero when the force reaches a maximum. Whether the dynamic correction factor is really needed is questionable. Equation (4.15) assumes that the correction factor is constant during the impact event, which can not be expected for a dynamic influence. Further it is possible that C is not equal to 1 because of other inaccuracies of the test system: equation (5.17) incorporates twice the inaccuracy of measuring the velocity and the inaccuracy in the integrated contact force. In view of the above arguments the equation was not used in

this study.

5.4.3 Vibration and noise in the force signal

A measured force-time curve never will be a smooth curve. This will not only be caused by noise of the amplification system, but also by other sources. The contact force between projectile and specimen will always be measured indirectly, either as a strain in the impactor or in an acceleration transducer. A part of the vibrations can therefore be attributed to resonance of the impactor and the transducer.

The following sources of vibrations can be distinguished:
1. inertial loading: this phenomenon may cause high peak loads in the initial phase of the impact process.
2. vibrations of the specimen: the specimen will be excited by the impactor.
3. ringing: these are vibrations due to the Herzian indentation of the specimen.
4. vibrations in the impactor: stress waves start to travel in the impactor and the impactor later will start to vibrate in its resonance frequency.

These sources will be discussed in this section.

initial inertial loading

Before impact the specimen displacement velocity is zero. As a result high initial inertial loads are present during approximately the first 20 to 30 micro seconds of the impact process. It can cause high peak loads and load drops with a temporary loss of contact between projectile and plate. The plate has to be accelerated from rest to the velocity of the impactor, which may cause relatively high initial loads.

Saxton et al.[7] show a figure (figure 5.18) to explain what happens in the first micro seconds of the impact. The specimen velocity rapidly increases and then becomes equal to the velocity of the impactor. The inertial load is very high shortly after the first contact. Afterwards it drops when the mechanical load due to the deflection of the specimen is reached. According

to figure 5.18 the inertia load on the specimen directly starts at a high load. That must be wrong because at t=0 the inertial force will be zero, but it will rise rapidly. A peak load at initial contact was also mentioned by Hoover and Guess[14]. It will not always be measured due to the limited frequency response of the measuring system. Due this limited frequency response high frequency oscillations and loads with a short rise time (e.g. inertial load peaks or load fluctuations due to fracture in the specimen) may lead to inaccurate measurements.

vibration of the specimen

Vibration of the specimen will influence the force-time curve, especially after changes of the load e.g. at fracture. Ireland[3] states that the first three eigenmodes dominate in the force-time curve.

Figures 5.8 and 5.9 illustrate the effect of specimen vibrations on the the load-time curve. The contact forces measured by the load cell (solid line) based on strain gages, and by an acceleration transducer, are plotted for Al 2024-T3 and ARALL respectively. The fluctuations in the dotted lines were already discussed in section 5.3.3.2. The output of the load cell (solid lines) for the Al 2024-T3 plate shows a vibration with a higher frequency than the vibration in the corresponding curve for ARALL. This corresponds with the lower stiffness of the ARALL material. We may conclude that the higher eigenfrequencies of the plate are measured by the load cell.

ringing

Another vibration effect is called 'ringing': a vibration caused by the indentation stiffness of the specimen. This phenomenon will be discussed in chapter 12 (impact modelling). This effect can be minimized by putting tape between impactor and plate. The tape influences the force peaks in the force-time curve, and only will have a small effect on the deflection and failure of the specimen. The tape was not used in this study because it only had a small effect on the force-time curves.

vibrations in the impactor

Vibrations in the impactor can be another source of fluctuations in the force-time curve. The impactor used in this study first had a steel nose which was screwed on an Al 7075-T6 load cell. At relatively high impact velocities with relatively stiff specimens the force-time curve was heavily distorted because the nose vibrated relative to the load cell. The vibration could be influenced by a tighter attachment of the nose to the load cell.

An example of a heavily distorted signal is shown in the contact force-time curves in figures 5.19 and 5.20 (the filtered curves in these figures will be discussed in section 5.5.2). The frequency spectrum (figure 5.21) revealed that the signal had dominant frequencies around 3 and 7 kHz, independent of the target support and dimensions, and independent of the impact velocity. As said before the amplitude of the vibrations could be minimized by attaching the nose more tightly to the load cell. However, the vibrations reappeared at higher impact velocities or after several impacts because the attachment was loosened. It then was decided to make an integral load cell/nose tip of stainless steel as shown in figure 5.4. After this modification the force-time curve became smooth, and the peaks in the frequency spectrum disappeared, see figure 5.22 and 5.23.

Vibrations in the force-time curve can also be caused by travelling stress waves in the impactor. A model to illustrate this will be derived here.
The one dimensional motion of stress waves in a cylindrical bar is described by (e.g. Kolsky[15]):

$$\frac{\delta^2 u}{\delta t^2} = \frac{E}{\rho} \frac{\delta^2 u}{\delta x^2}$$
(5.18)

where $u(x,t)$ is the displacement of coordinate x at time t. We will determine the solution of this equation for a prescribed function in time of u_0 (the interface between the impactor and the sheet specimen). An exact solution of equation 4.17 can not easily be derived for this situation.
A numerical solution can be obtained by integration by substituting:

$$\frac{\delta^2 u}{\delta t^2} = \frac{1}{(\Delta t)^2} \left[u(x,t+\Delta t) + u(x,t-\Delta t) - 2u(x,t) \right]$$

(5.19)

$$\frac{\delta^2 u}{\delta x^2} = \frac{1}{(\Delta x)^2} \left[u(x+\Delta x,t) + u(x-\Delta x,t) - 2u(x,t) \right]$$

with Δt as the time step of integration, Δx as the step in x direction, see figure 5.24.

This leads to:

$$u(x,t+\Delta t) = \frac{E}{\rho} \frac{(\Delta t)^2}{(\Delta x)^2} \left[u(x+\Delta x,t) + u(x-\Delta x,t) - 2\,u(x,t) \right]$$
$$- u(x,t-\Delta t) + 2\,u(x,t)$$

(5.20)

The projectile strikes the target at t = 0, with an impact velocity v_0. x = 0 corresponds with the contact point. The boundary conditions are:

$$u(x,-\Delta t) = -v_0 \Delta t$$

$$u_0 = u(0,t) = v_0 \frac{t_c}{\pi} \sin\left(\frac{\pi\, t}{t_c} \right)$$

(5.21)

(a sinusoidal displacement-time curve is assumed, which is
realistic for a linear elastic impact, see chapter 12)

$$u((N-1)\Delta x,t) = u(N\Delta x,t) \qquad \text{(stress free end)}$$

The variables of this model are: contact time t_c, wave velocity $\sqrt{\frac{E}{\rho}}$, length of the impactor, impact velocity and the integration steps Δx and Δt. A wave velocity of 5100 m/s was taken, approximately corresponding with the value for steel and aluminium. Further an impact velocity of 5 m/s and a contact time of 4 ms was substituted. Different integration steps were tried to assure an accurate and stable solution, 50 integration points in x direction and $\Delta t = 1*10^{-7}$ s was sufficient.

Figure 5.25 shows how the stress wave travels to the end of the impactor, for an impactor length of 50 cm. The strain is calculated from:

$$\varepsilon(x+0.5\Delta x,t) = \frac{u(x+\Delta x,t) - u(x,t)}{\Delta x}$$ (5.22)

At t = 0.175 ms the strain is linearly dependent on the coordinate x.

Figure 5.26 shows the strain at 5 cm above the contact point (in the load cell at the strain gages of the load cell) as a function of time, for an impactor length of 50 cm. The measured contact force will be proportional to the strain measured in the load cell. The maximum time in figure 5.26 corresponds with half the total contact time. At that moment the contact force reaches a maximum. The displacement-time function is sinusoidal, therefore also the contact force (which is proportional with the strain) should have this shape. The disturbance due to the vibration of the impactor is clearly visible in figure 5.26. This curve shows the possible effect of stress waves on the measured signal. The influence becomes smaller if the impactor is shorter. Figure 5.27 shows the strain at x = 5 cm for an impactor length of 10 cm.

In reality the situation will be far more complex. Trubshaw[16] recommends to split a striker into several short pieces to increase the resonant frequency. The impactor used in this study is shown in figure 5.4. It consists of several parts of different materials and it is not a cylindrical bar. Although the impactor is axisymmetrical, it certainly cannot be considered as one-dimensional. At the interface between the load cell and the reflector disk a part of the waves will be reflected at the boundary steel-plastic (PVC), a part will travel through the disk and a part will travel through the steel thread to the steel tube.

To determine the lowest resonant frequency of the impactor, it was dropped with an impact velocity of 1.41 m/s on a ceramic tile which can be considered as a rigid target. Figure 5.28 shows the load-time curve indicating the impact, rebound and the vibration of the impactor after rebound. The frequency spectrum is shown as figure 5.29, the lowest resonant frequency is approximately 13.0 kHz. Trubshaw[16] states that the striker/transducer system generally has a resonant frequency of 4-10 kHz. The resonant frequency of our impactor is therefore satisfactory.

5.5 Data processing of the b2-impact tester

The data processing in most tests is based on the measured force signal, F(t), and the measured displacement, s(t). The acceleration can be obtained from F(t) (see equation 5.1), and integration then produces the velocity v(t), while a second integration gives the displacement, s(t). Similarly the measured displacement signal s(t) can be used to obtain v(t) by differentiation. Another differentiation gives the acceleration a(t), from which the force F(t) can be calculated. The data processing includes all the above steps, which implies a redundancy of the results obtained. However, certain steps imply a loss of accuracy, partly due to problems involved in the processing of the numerical data. In this sub-chapter we will first indicate the various functions either directly measured or calculated, i.e. F(t), s(t), v(t) and absorbed energy U(t) as well as some characteristic quantities derived from these time functions. The problems related to data processing are discussed (filtering, integration, differentiation).

5.5.1 Relevant curves and quantities

An example of a set of measured data of a (single) impact test is given in figure 5.30.

The following curves can be determined in an impact test:

1. force vs. time. The contact force between impactor and specimen reaches a maximum at maximum deflection of the plate at the point where the velocity of the impactor is zero, or at the maximum load that can be sustained by the specimen, the failure load. After the maximum the load drops to zero at the point where contact between projectile and plate is lost.

2. velocity vs. time. The velocity drops to zero and becomes negative, which implies that rebound of the impactor occurs.

3. displacement vs. time. If the velocity-time curve is integrated the displacement-time curve is obtained.

4. force vs. displacement. This curve can be used to observe the failures in the specimens, because a significant load drop at an increasing deflection means failure of the specimen. When specimen failure occurs, the curve consists of two parts: a part needed to initiate cracking

until the point of the first significant load drop, and a part that corresponds with crack propagation.

5. energy vs. time. The absorbed energy by the specimen is plotted as function of time (not plotted in figure 5.30). If the projectile rebounds after impact, the maximum absorbed energy will be equal to the impact energy. If perforation or complete failure of the specimen occurs, the maximum absorbed energy will be less than the impact energy. The absorbed energy at the first significant load drop is equal to the impact energy needed to create cracking of the specimen. The energy needed to propagate the crack is a measure for the brittleness of the material.

6. energy vs. displacement. Both the force-displacement curve and the energy-displacement curve can be used to compare impacts at different impact energies with a (quasi) static loading of the specimen. Because the energy-displacement curve is an integrated curve the curve is rather smooth and can be better compared with a static energy-deflection curve than the force-displacement curve.

Apart from the curves some (extreme) force, velocity and displacement quantities will also give an indication of the material behaviour:

1. maximum displacement. The maximum displacement which corresponds with the maximum deflection of the specimen will be related to the maximum induced strains in the target.

2. maximum force. If fracture occurs this force will be equal to the maximum force which can be sustained by the target.

3. velocity restitution and energy restitution coefficient. If the impactor rebounds, the velocity after impact is the velocity at the moment that the contact between projectile is lost (at F(t)=0). The velocity after impact v_r will be related to the energy absorbed by the specimen, and thus will be related to the damage in the target.
The velocity restitution coefficient is defined as:

$$e_v = \frac{|v_r|}{v_o} \qquad (5.23)$$

and the energy restitution coefficient as:

104

$$e_T = \frac{\frac{1}{2} m_p v_r^2}{\frac{1}{2} m_p v_0^2} = \frac{v_r^2}{v_0^2} = c_v^2 \qquad (5.24)$$

4. absorbed energy at fracture. The absorbed energy at fracture is the area under the force-deflection curve at fracture as indicated in figure 5.31. The energy is a measure for the impact damage resistance of the material.

5. damage propagation energy. The propagation energy compared with the fracture energy is a measure for the brittleness of the material. The damage propagation energy can only be measured if complete perforation of the specimen occurs.

6. contact time. The contact time is related to the stiffness of the specimen. A short contact time corresponds with a relatively stiff specimen.

7. permanent deflection. The permanent deformation of a metallic material is related to the absorbed energy. It can be a measure for the visibility of the damage after impact on a structure. This permanent deflection can be measured by the displacement transducer after impact.

5.5.2 Digital filtering

Hardware filtering (filtering of the analog signal by electronic means) can be performed to remove high frequencies and to reduce errors due to sampling. This type of filtering was not applied here. Digital filtering was implemented, which is a post filtering technique. The advantage of this type of filtering is that the original signal remains available.

Different ways of filtering are possible. Adam et al.[8] describe two digital filtering methods. One way of digital filtering is by doing a least square fit to 9 points and calculating the middle point from the fit. Another way is to calculate each data point using a moving average method. In this method the average value y (= filtered data point) of a data point x ($0 \leq x \leq 255$) is obtained by:

$$y_{n+0.5m} = \frac{1}{m+1} \sum_{k=n}^{n+m} x_k \qquad \text{with m is even} \qquad (5.25)$$

This last method has proven to be a simple and satisfactory method for smoothing of the original data[16]. One has to be careful to avoid distortion of a force-time curve of a brittle failure, because in this case the peak of the force will be rounded. A more complicated way to filter the data is the use of the Fourier transform[2]. In this case the filtering can be expressed in the frequency domain as:

$$y(\omega) = H(\omega)\,X(\omega) \qquad (5.26)$$

With $y(\omega)$ as the filtered signal, $X(\omega)$ as the original signal and $H(\omega)$ as the transfer function (filter).

In the present study a filtering technique was implemented based on the technique described by Fasanella[13] and used for the filtering of the Full-Scale Transport Controlled Impact Demonstration of the NASA. The digital high pass filter is shown in the frequency domain in figure 5.32a. This filter is flat to the cutoff frequency f_c and then rolls off until it attenuates all frequencies above the terminal frequency f_t. This means that frequencies higher than f_c and smaller than f_t are partly removed and frequencies higher than f_c are completely removed. The function which defines the roll off of the filter in the frequency domain is taken as a cosine function. In this case it can be derived that the inverse Fourier transform is given by:

$$h(t) = \frac{1}{2\pi} \int_{-\infty}^{\infty} e^{i\omega t}\,H(\omega)\,d\omega = \frac{\pi}{2t} \left[\frac{\sin \omega_t t + \sin \omega_c t}{\pi^2 - (\omega_t - \omega_c)^2 t^2} \right] \qquad (5.27)$$

with $\omega_t = 2\pi f_t$, $\omega_c = 2\pi f_c$. We consider m equally spaced data points (d_1,t_1), (d_2,t_2), ... (d_m,t_m), were $t_n = n \Delta t$. We define $\bar{h}_n$ as the nth normalized coefficient:

$$\bar{h}_n = \frac{h_n}{\sum\limits_{l=-N}^{N} h_l}$$

(5.28)

We denote the N+1 filtered data point d'_{N+1} obtained by a summation which is a Fourier convolution integral:

$$d'_{N+1} = \sum_{n=-N}^{N} \bar{h}_n d_{N+n+1} = \bar{h}_{-N} d_1 + \ldots \bar{h}_0 d_{N+1} + \ldots \bar{h}_n d_{2N+1}$$

(5.29)

Fasanella states that for a 1% accuracy the number of points to calculate a filtered data point has to satisfy the following condition:

$$N \geq \frac{2}{\Delta t \, (f_t - f_c)}$$

(5.30)

Based on this theory given by Fasanella, also a notch filter (filter to remove frequencies in a certain band) was derived as shown in figure 5.32b. The notch filter removes frequencies between two frequencies f_{t1} and f_{t2}. It can be derived that:

$$h(t) = \frac{\pi}{2t} \left[\frac{\sin \omega_{t1} t + \sin \omega_{c1} t}{\pi^2 - (\omega_{t1} - \omega_{c1})^2 t^2} - \frac{\sin \omega_{t2} t + \sin \omega_{t2} t}{\pi^2 - (\omega_{t2} - \omega_{c2})^2 t^2} + \right.$$

$$\left. \frac{\sin \omega_{t3} t + \sin \omega_{t3} t}{\pi^2 - (\omega_{t3} - \omega_{c3})^2 t^2} \right]$$

(5.31)

The effect of digital filtering is shown in figure 5.19 and 5.20. The distorted signal, due to the vibration of the nose tip relative to the load cell in the impactor, was filtered. In figure 5.19 the frequencies higher than 6 kHz are removed from the signal, these frequencies around 6 kHz correspond with one of the peaks in the frequency spectrum (figure 5.21). Figure 5.20 shows the effect of removing the frequencies higher than 3 kHz. The influence of the filtering on the velocity-time and displacement-time curves is small.

5.5.3 Numerical integration

The force signal can be integrated (equations 5.2 and 5.3) to obtain the velocity and displacement and absorbed energy of the specimen:

$$v(t_1) = v_0 + g\, i\, \Delta t - \frac{1}{m_p} \left[\sum_{n=0}^{1} F(n)\Delta t \right]$$

$$s(t_1) = v_0\, i\, \Delta t + \frac{1}{2} g(i\, \Delta t)^2 - \frac{1}{m_p} \left[\sum_{m=0}^{1} \left[\sum_{n=0}^{m} F(n)\Delta t \right] \Delta t \right]$$

$$U(t_1) = \frac{1}{2} m_p v_0^2 - \frac{1}{2} m_p v(t_1)^2$$

(5.32)

with: v as the velocity,

    Δt as the sample time (= 1 μS),

    F as the contact force,

    m_p as the impactor mass,

    i as the number of samples at t_1,

    U as the absorbed energy

and v_0 as the impact velocity.

This simple form of integration is possible because the sample frequency is high enough, it is not necessary to use for example the Simpson rule.

5.5.4 Numerical differentiation

The displacement signal has to be differentiated to obtain the velocity and the acceleration, the strain signal has to be differentiated to obtain the strain rate, and the force measured in the clamping has to be differentiated to correct this signal (equation 5.11).
Numerical differentiation is far more complicated than integration. Integration is not so sensitive for small amounts of noise over the signal.

However, differentiation of signals may lead to large fluctuations of the differentiated signal. Several methods of differentiation were tried for the present study. The best one was found in Hu and Chen[9]. They describe the Lanczos[18] convergence factor method. The signal is represented by a Fourier series, and the differentiated signal is obtained by a term-by-term differentiation. Convergence factors are needed to reduce the adverse effect of the high harmonics in the differentiated Fourier series. The signal is expressed by its Fourier series:

$$f(t_i) = \frac{1}{2} a_0 + \sum_{n=1}^{N} (a_n \cos \frac{2n\pi}{T} t_i + b_n \sin \frac{2n\pi}{T} t_i)$$
$$\text{for } 0 \le t_i \le T \qquad (5.33)$$

with the Fourier coefficients:

$$a_n = \frac{2}{T} \sum_{i=1}^{I} f(t_i) \cos \frac{2n\pi}{T} t_i (\Delta t) \qquad \text{for } n = 0,1,2,\ldots N$$

$$b_n = \frac{2}{T} \sum_{i=1}^{I} f(t_i) \sin \frac{2n\pi}{T} t_i (\Delta t) \qquad \text{for } n = 1,2,\ldots N$$

with: t_i as the sampled time,

   N as the total number of harmonics in frequency domain

   n as the frequency index, 1,2...N

   i as the time index, 1,2,3..I

   I as the total number of data points in the time domain

   Δt as the time increment

If the Fourier series are simply differentiated term by term, this leads to a strong fluctuation of the differentiated signal, because of the high harmonics. Lanczos[18] describes a correction factor σ_k by which every differentiated Fourier term has to be multiplied ('attenuation factors') to reduce the large errors caused by the differentiation of the Fourier series:

$$\sigma_n = \frac{\sin \pi k/n}{k\pi/n} \qquad (5.34)$$

The second derivatives are obtained by multiplication of the same factor squared. The first two derivatives are:

$$f'(t_i) = -\frac{2N}{T} \sum_{n=1}^{N} a_n (\sin \frac{2n\pi}{T} t_i)(\sin \frac{n\pi}{N}) +$$

$$\frac{2N}{T} \sum_{n=1}^{N} b_n (\cos \frac{2n\pi}{T} t_i)(\sin \frac{n\pi}{N})$$

$$\text{for } 0 \leq t_i \leq T$$

$$f''(t_i) = -\frac{4N^2}{T^2} \sum_{n=1}^{N} a_n (\cos \frac{2n\pi}{T} t_i)(\sin^2 \frac{n\pi}{N}) -$$

$$\frac{4N^2}{T^2} \sum_{n=1}^{N} b_n (\sin \frac{2n\pi}{T} t_i)(\sin^2 \frac{n\pi}{N})$$

$$\text{for } 0 \leq t_i \leq T$$

(5.35)

The factors $(\sin \frac{n\pi}{N})/(\frac{T}{2N})$ are the Lanczos convergence factors[9].

5.5.5 Frequency spectrum

Two methods were implemented to calculate a frequency spectrum of a measured signal. The first one is a frequency analysis based on a fast Fourier transform. This method is available in the Numerical Toolbox of Turbo Pascal[20]. The second one calculates the coefficients of the Fourier terms of the signal (equation 5.33). The frequency spectrum is obtained by plotting c_n as function of the frequency, with c_n as[9]:

$$c_n = \sqrt{a_n^2 + b_n^2}$$

(5.36)

Examples of frequency spectrums determined in this way have already been shown in this chapter (e.g. figure 5.21).

5.5.6 The measuring and processing program

The program is written in Turbo Pascal. It is based on a menu system. It consists of one main program, 4 separate programs and one part with subroutines for the plotting of data.

The structure of the program is as follows:

```
                              ┌──────────────┐
                              │ main program │
                              └──────────────┘
        ┌──────────────┬───────────────┬───────────────┐
 ┌──────────────┐ ┌──────────────┐ ┌──────────────┐ ┌──────────────┐
 │   testing    │ │  read data   │ │ data reading │ │ data reading │
 └──────────────┘ │  or filtered │ └──────────────┘ └──────────────┘
        │         │  data        │        │                │
 ┌──────────────┐ └──────────────┘ ┌──────────────┐ ┌──────────────┐
 │ data storage │        │         │  filtering   │ │  frequency   │
 └──────────────┘ ┌──────────────┐ └──────────────┘ │  analysis    │
                  │   data       │        │         └──────────────┘
                  │  processing  │ ┌──────────────┐        │
                  └──────────────┘ │  store       │ ┌──────────────┐
                         │         │  filtered    │ │ spectrum plot│
                  ┌──────────────┐ │  data        │ └──────────────┘
                  │  plot data   │ └──────────────┘
                  └──────────────┘
```
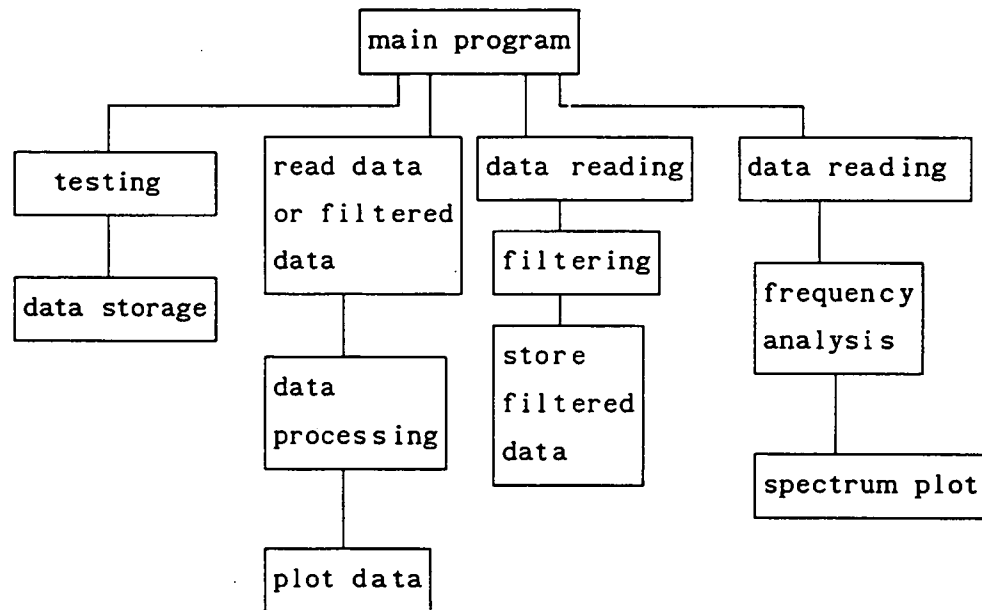
Four similar programs are available for the following signals:
- force from impactor and displacement
- force from impactor and from clamping
- force from impactor and strain in the specimen
- force from impactor only
- force from clamping and strain in the specimen

An example of measured data is given in figure 5.30 (force from impactor and displacement). The full curves are derived from the signal measured with the load cell, the dotted curves are derived from the displacement signal.

5.6 Summary

A drop weight impact tester was designed and built for the present study (the 'b2-impact tester). The instrumentation of the tester was developed.

The displacement of the impactor can be measured as a function of time by an infrared sensor (section 5.3.4). The contact force is measured by a strain gage load cell at the tip of the impactor, or by load cells positioned under the clamping of the specimen (section 5.3.3). The strain in the specimen can be measured by strain gages. The signals are measured and processed by a computer.

The signal of the load cell can be processed to obtain velocity-time and displacement-time curves. The displacement as a function of time can be processed to obtain velocity-time and force-time curves (section 5.3.1).

The impact velocity is measured by photo transistors which are connected with a counter. In this way an average velocity before impact is obtained, but it is accurate enough to represent the impact velocity (section 5.3.2).

Several problems associated with the instrumentation are discussed. The force measured by the load cells under the clamping is obscured by vibrations of the clamping (mass-spring system) and has to be corrected (section 5.3.3.3). The influence of the elastic compliance of the test system is analytically estimated and appears to be small (section 5.4.1). The dynamic calibration of the load cell is discussed (section 5.4.2), but it is not applied in this study. Different sources of vibration and noise in the force signal are treated (section 5.4.3). Vibrations were experimentally studied for the b2-impact tester by a frequency analysis. The vibrations observed in the force-time curves can be due to initial inertia loading, resonance vibration of the specimen, ringing and vibrations in the impactor.

The various curves and quantities to be derived from the impact data are discussed (section 5.5.1). A summary of processed data of a single impact test is given in figure 5.30. Digital filtering, numerical integration and differentiation and frequency analysis are necessary to derive the processed data (section 5.5.2 to section 5.5.5).

references

1. Cheresh, M.C.; McMichael, S.; Instrumented impact test data interpretation; Instrumented impact testing of plastics and composite materials, pp.9-23, ASTM STP 936, 1986.

2. Cain, P.J.; Digital filtering of impact data, Instrumented impact testing of plastics and composite materials, pp.81-102, ASTM STP 936,

1986.

3. Ireland, D.R.; Procedures and problems associated with reliable control of the instrumented impact test, Instrumented impact testing, pp.3-29, ASTM STP 563, 1974.

4. Mark-Markowitch, M.; Rosenthal, Y.; Adam, G. Experience with a digitized instrumented impact testing system, J.of testing and evaluation, Vol.15, No.5, pp.265-273,1987.

5. Agarwal, B.D.; Analysis and performance of fibre composites pp. 246-287, New York, 1980.

6. Gardiner, D.S.; Pearson, L.H.; Acoustic-emission monitoring of composite damage occurring under static and impact loading, Exp.Techniques, Nov., pp.22-28, 1985.

7. Saxton, H.J.; Ireland, D.R.; Server, W.L.; Analysis and control of inertial effects during instrumented impact testing, Instrumented impact testing, pp.50-73, ASTM STP 563, 1974.

8. Adam, G.; Rosenthal, Y.; Mark-Markowitch, M.; Computer-assisted instrumented-impact testing, Exp. Techniques, Sept., pp.24-26, 1986.

9. Hu, A.S.; Chen, Han-Tau; Frequency response and differentiation requirements for impact measurements, The shock and vibration bullitin, part 2, Sept. 1978, pp.123-130, Naval Research Laboratory, Washington D.C., 1978.

10. Hudock, M.F.; Low velocity impact testing operator's manual AFWAL/MLBC, Wright Patterson Air Force Base, 1986.

11. Standard test methods for impact resistance of rigid plastic sheeting or parts by means of a tub (falling weight), D 3029 - 84, ASTM.

12. Franken, J.; Fast AD-converter for IBM-PC (in Dutch), TU Delft, May, 1988.

13. Fasanella, E.L; Digital filtering and acceleration pulse interpretation, Full-scale transport controlled impact demonstration, pp.103-123, NASA CP 2395, 1985.

14. Hoover, W.R.; Guess,T.R.; The dynamic fracture toughness of carbon-carbon composites, J.composite materials, Vol.7, pp.334-347, 1973

15. Kolsky, H.; Stress waves in solids, Dover Publications, New York, 1963.

16. Trubshaw, R.N.; Resonance and signal conditioning in instrumented impact testing, Polymer testing, vol.6, pp.387-401, 1986.

17. Li, R.K.Y.; Harding, J.; Studies of transverse impact damage in

composite materials using a Hopkinson type pressure-bar technique, 6th conf. on composite materials ICCM & ECCM, vol.3 1987.

18. Lanczos, C; Applied analysis, Prentice Hall, 1956.

19. Williams, J.G.; Adams, G.C.; The analysis of instrumented impact tests using a mass-spring model, Int.J.of Fracture, vol.33, pp.209-222, 1987.

20. Anon.; Turbo Pascal, Numerical Toolbox, Borland.

21. Martin, Th. M. E.; Balette, J.J.; Quenisset, J.M.; Compliance calibration during instrumented Charpy impact testing, Eng. Fracture Mech., Vol.37, No.4, pp.831-838, 1990.

Charpy tester
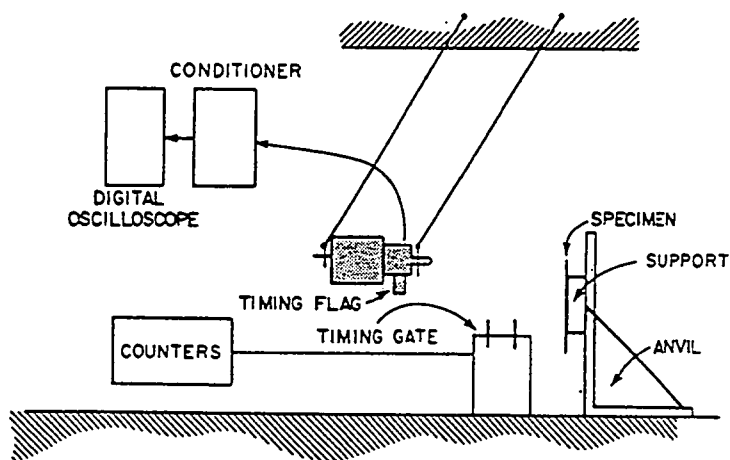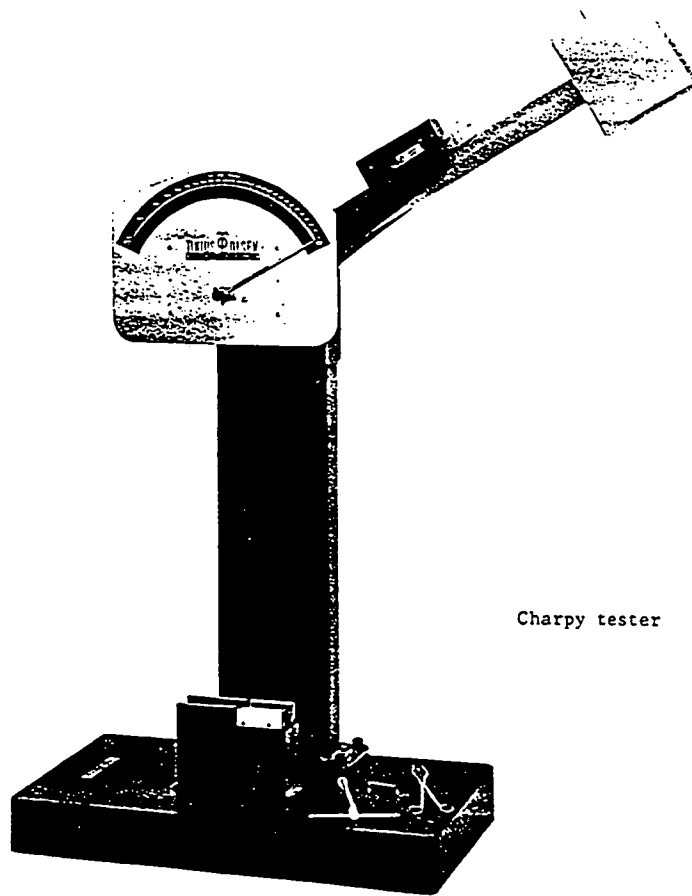
U.S. Air Force

figure 5.1a Pendulum type impact testers.

PRESSURE
METER

PRESSURE VESSEL

PLASTIC
MEMBRANE

PHOTOCEL
VELOCITY METER

PROJECTILE

ELCTRICAL WIRES

AIR GUN

POLYAMID

ALUMINIUM BALL
MASS: 22 g

24.5

12.7

INDENTER

figure 5.1b Air gun.

striker

input bar

strain gage I

strain gage II

clamping

specimen

v_0
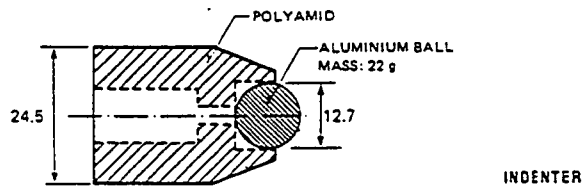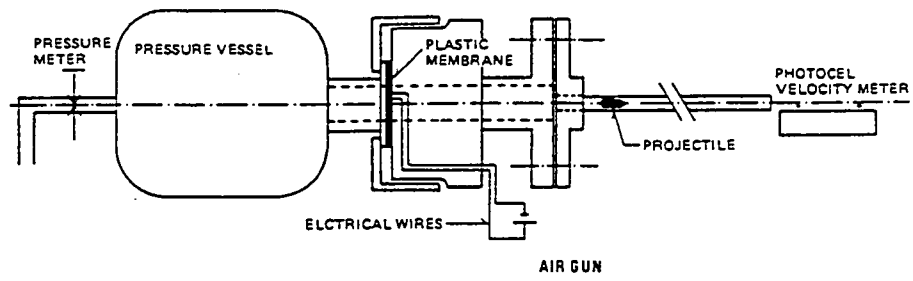
Hopkinson type pressure bar
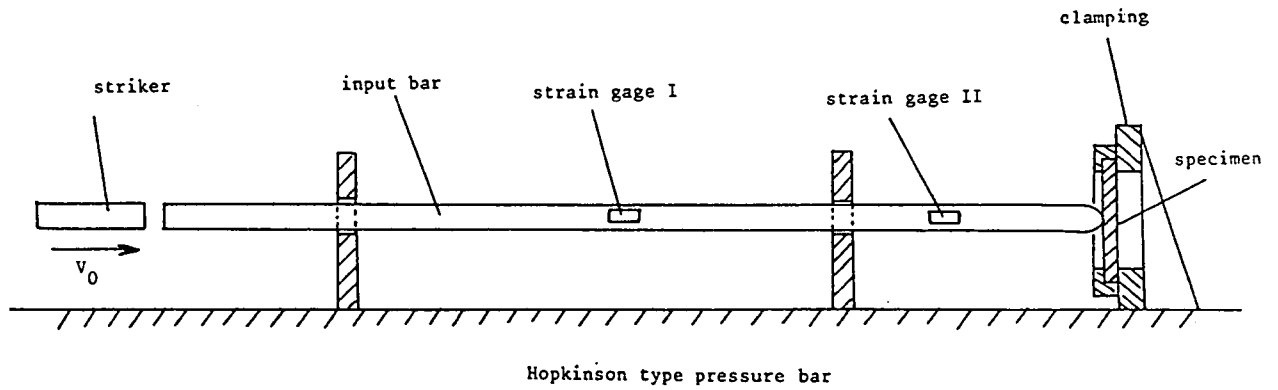
figure 5.1c Hopkinson type pressure bar.

116
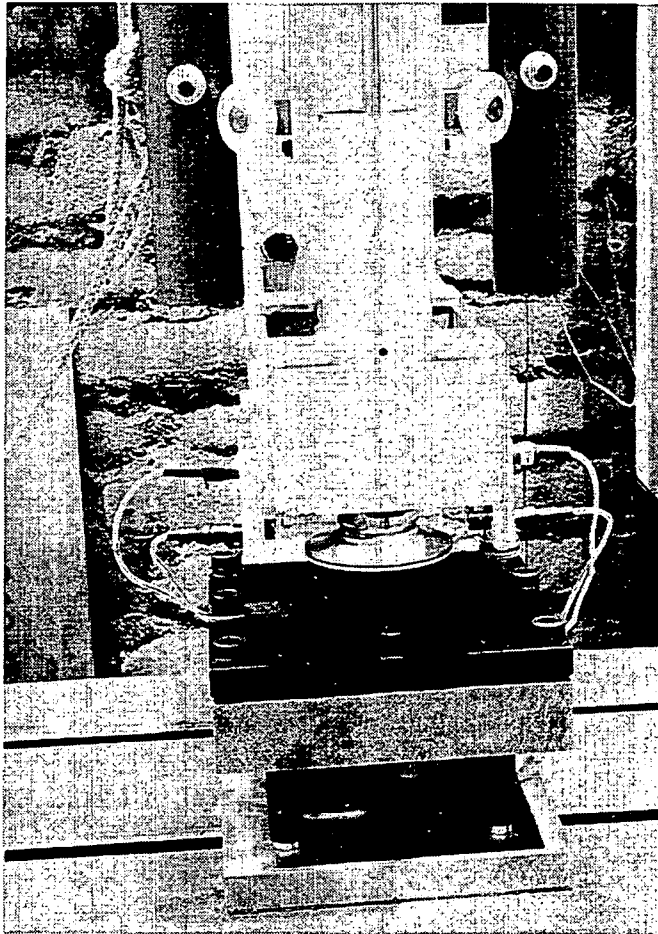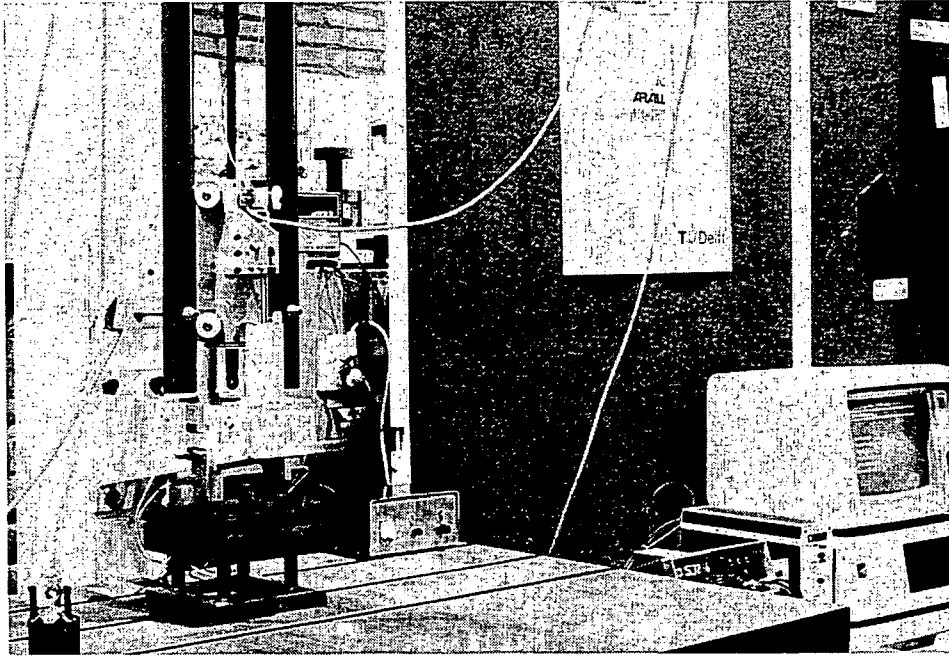
figure 5.2 The b2-impact tester.

A. load cell
B. carriage
C. dampers
D. pistons
E. release mechanism
F. photo cells
G. displacement transducer
H. clamping
I. counter
J. strain gage amplifier
K. triggering and amplifier
L. strain gage amplifier
M. A/D converter
N. PC
O. fixture
P. pipe
Q. long electrical cable
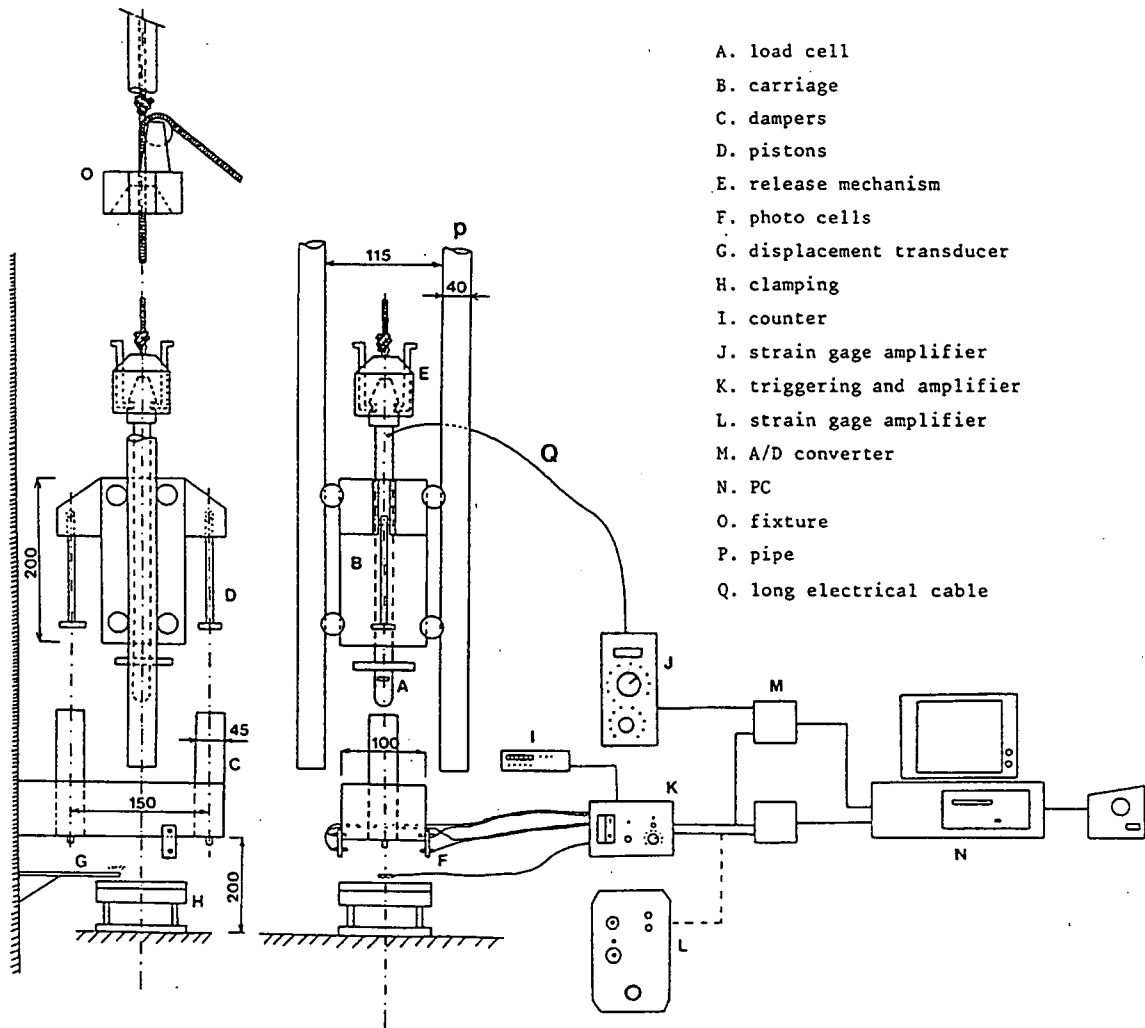
figure 5.3 The B2 impact tester.
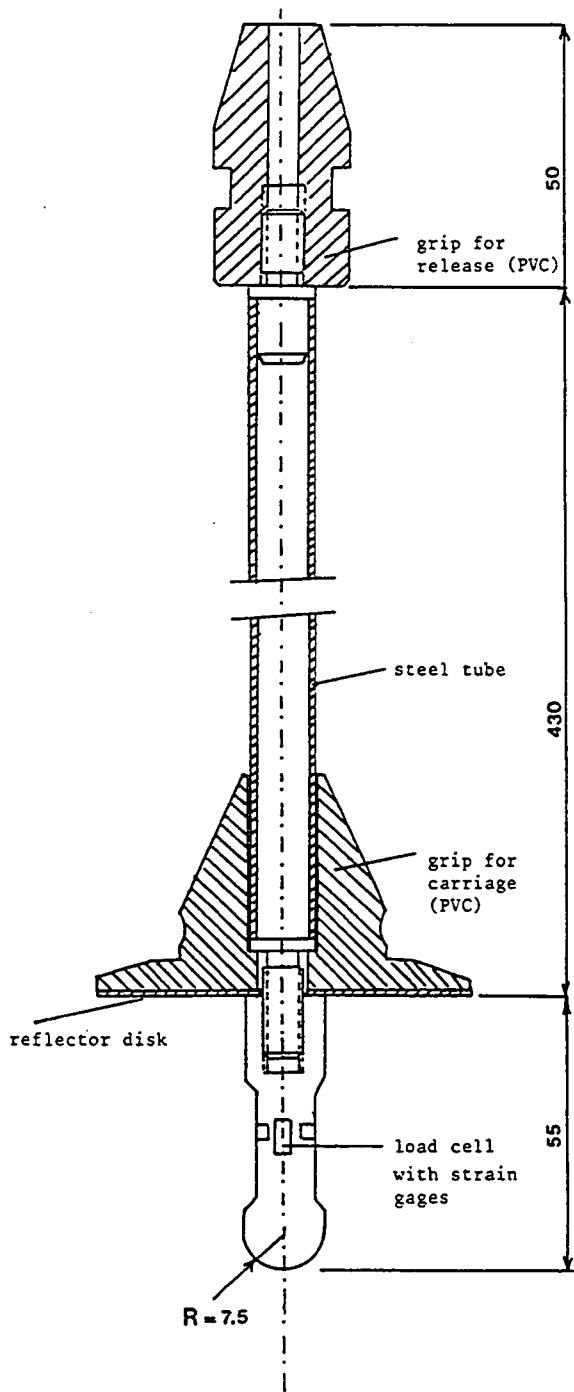
figure 5.4 The impactor used in this study.
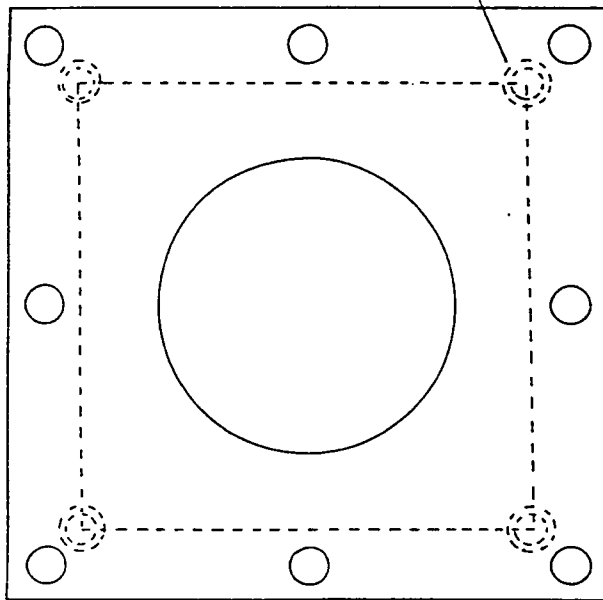
figure 5.5 The clamping used in this study.

position of the load cells

160
120
80
12
15
105
30
35

specimen
load cell
6.5
heavy steel table

120
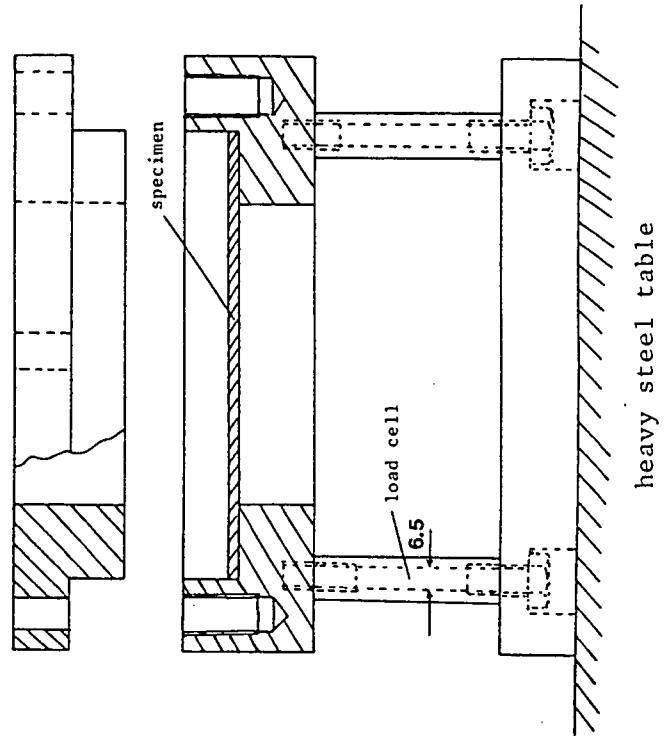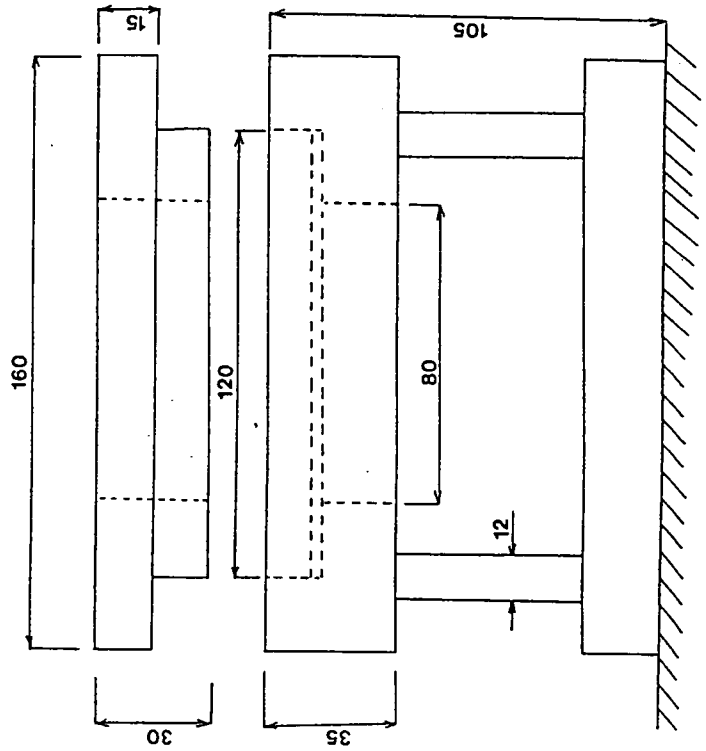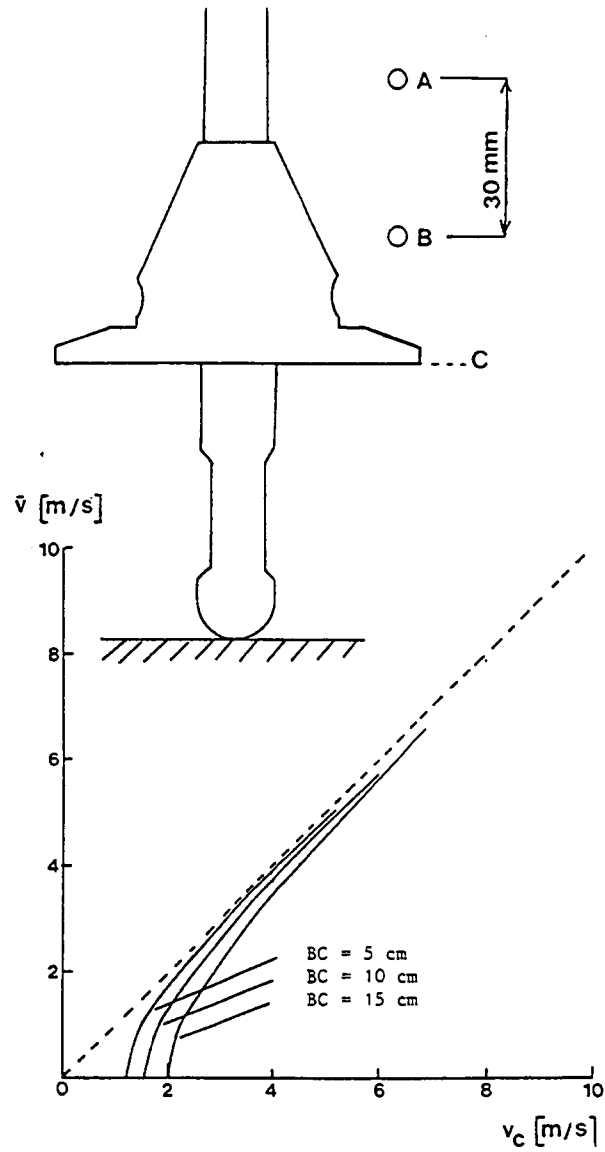
figure 5.6 Measured mean velocity $\bar{v}$ between the photo transistors A

and B as function of the real impact velocity at the specimen v_c

(acceleration = g = 9.81 m/s^2).
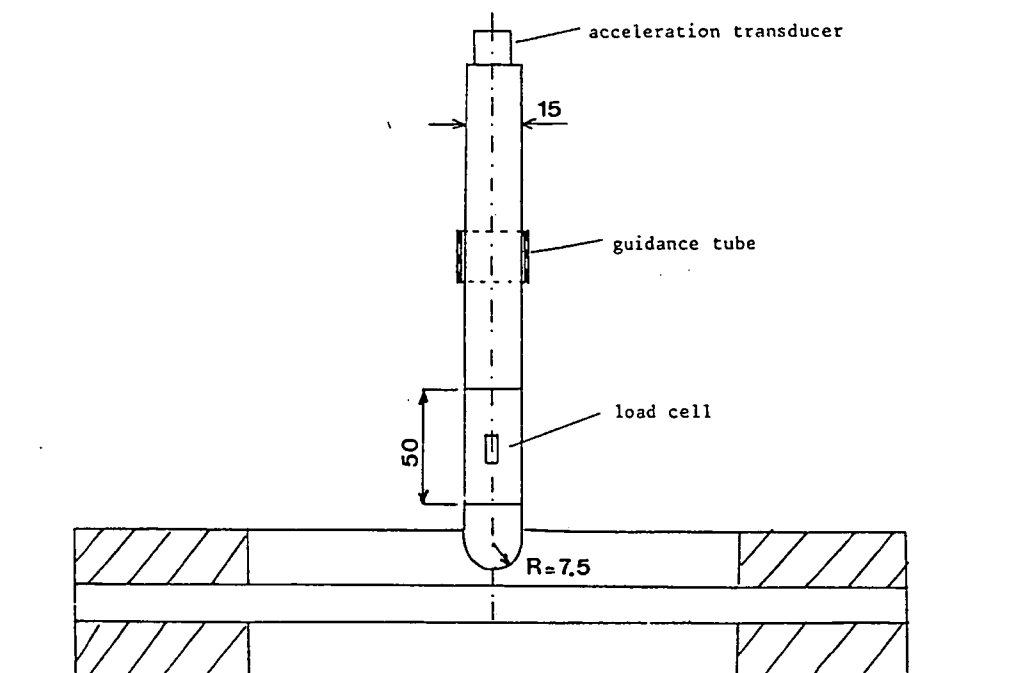
figure 5.7 Small very low-velocity impact tester for a comparison of
the force derived from the signal of an acceleration transducer and of a
load cell.
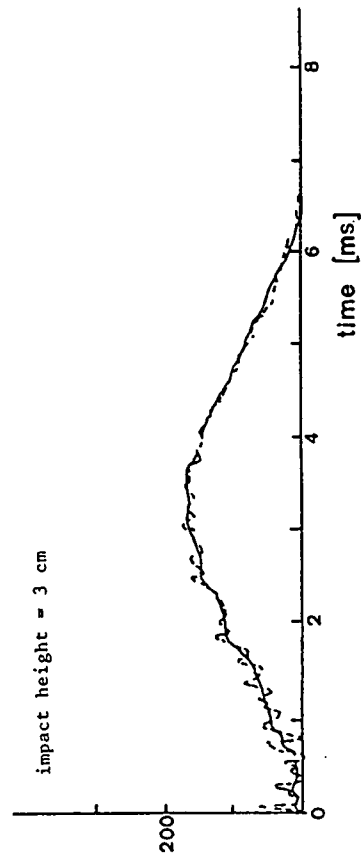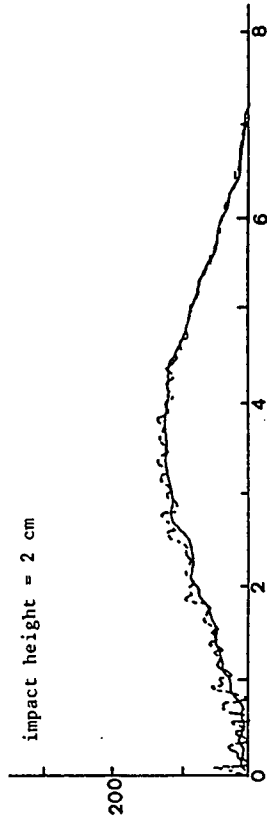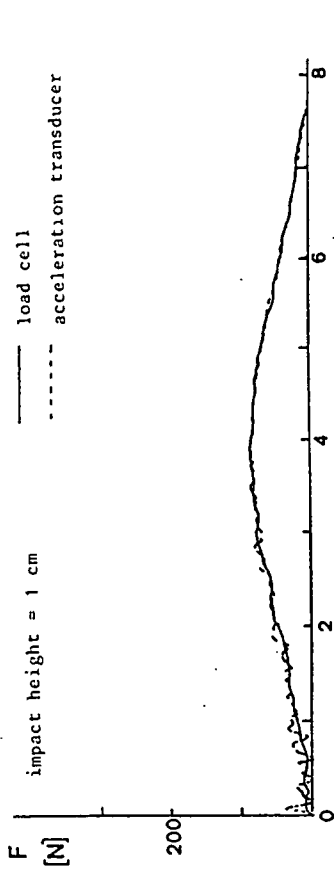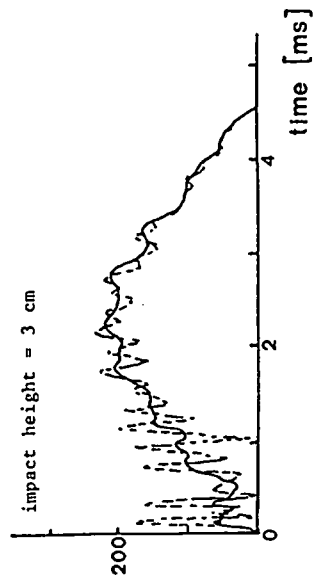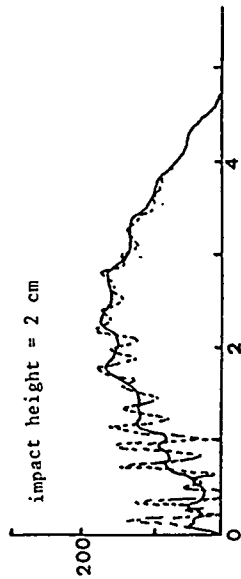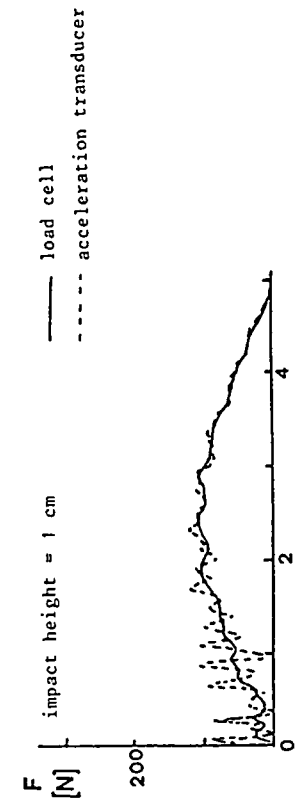
figure 5.8 Force-time curve of an impact on a 100x100 mm clamped Al 2024-T3, t= 1mm specimen. Comparison of the load measured by a strain gage load cell and an acceleration transducer.

figure 5.9 See figure 5.8, ARALL specimen (2H32, t = 0.8 mm).
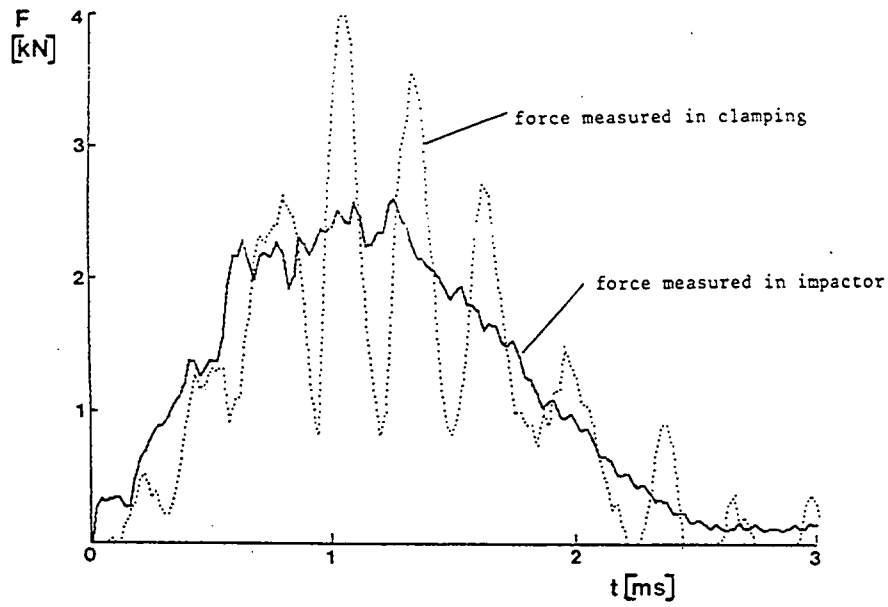
figure 5.10 The contact force measured in the impactor and the
measured force in the clamping.
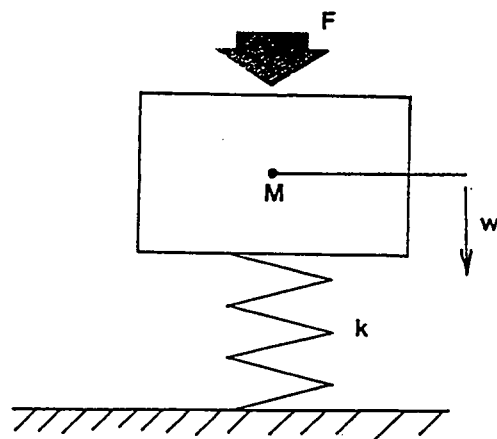
figure 5.11 Mass-spring model for the clamping of the specimen.
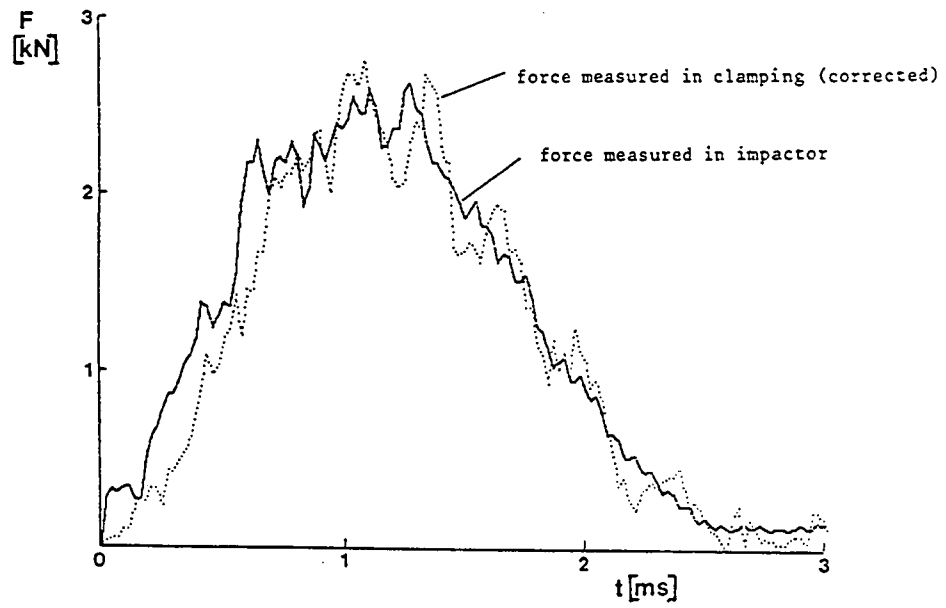
figure 5.12 Result of the correction of the force measured by the clamping (see: figure 5.10).
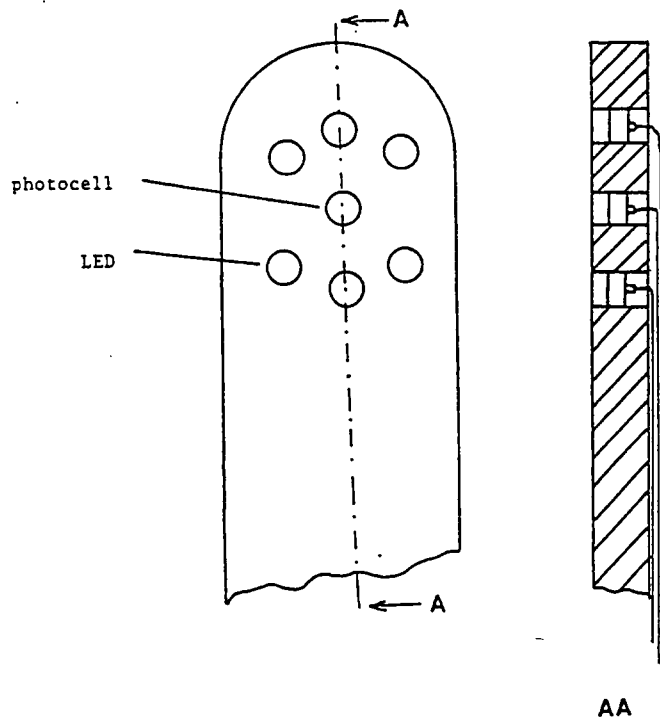
figure 5.13 The displacement transducer used in this study.
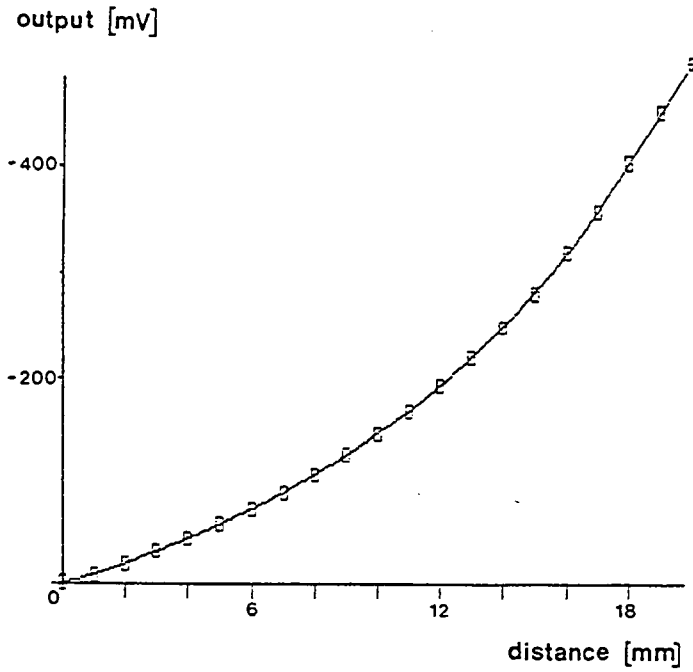
figure 5.14 The measured output of the displacement transducer as function of the distance.
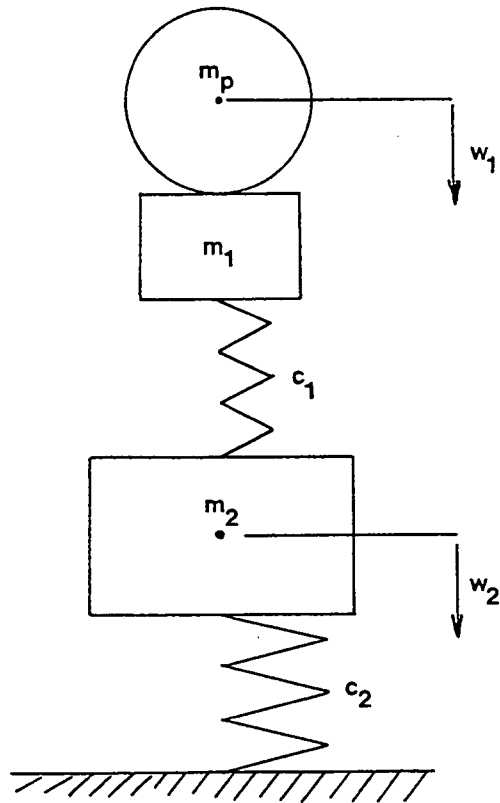
figure 5.15 Two degree of freedom system.

126
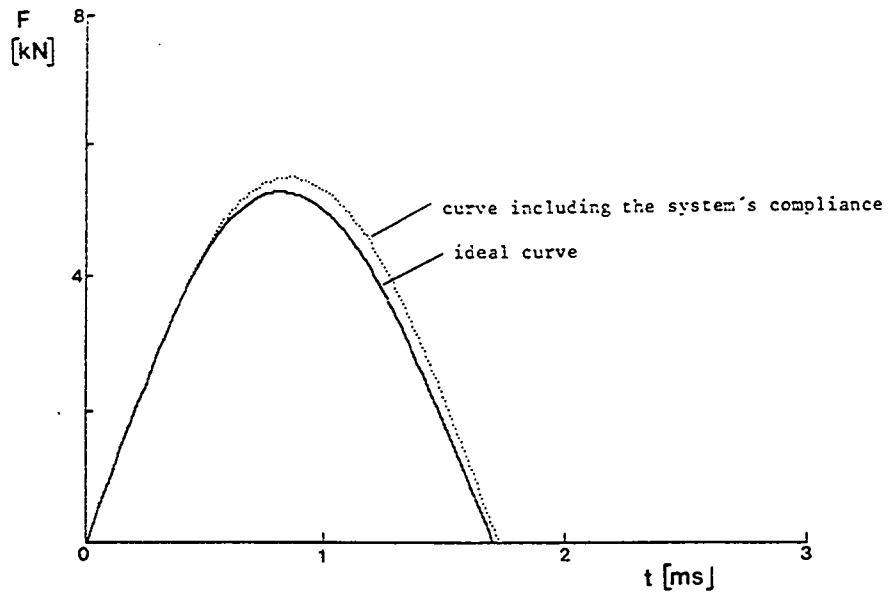
figure 5.16 The ideal contact force-deflection curve (c_2=0, $m_2 \to \infty$) compared with the curve for c_2= 10 kN/mm and m_2= 7 kg (c_1=1 kN/mm, v_0= 10 m/s, m_p=0.3 kg).
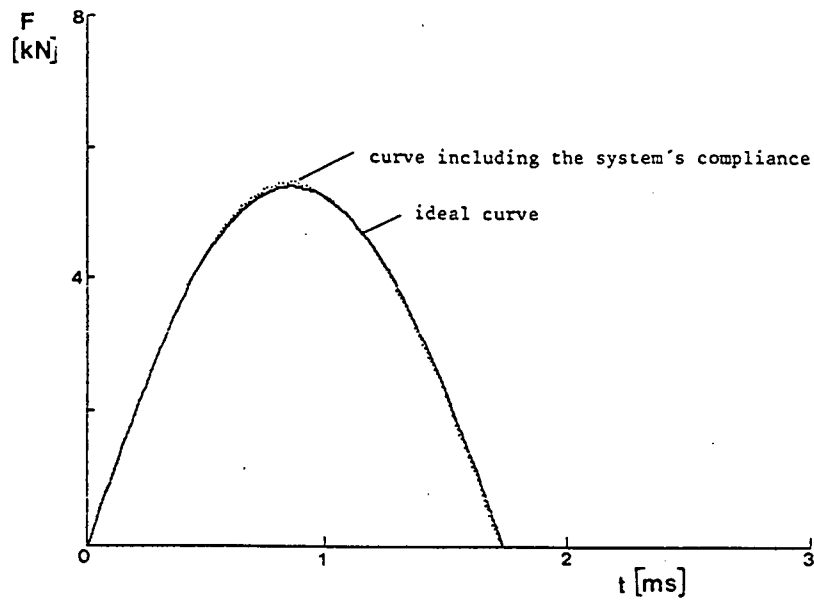
figure 5.17 See figure 4.15, c_2= 100 kN/mm, m_2= 7 kg (c_1= 1 kN/mm, v_0= 10 m/s, m_p = 0.3 kg)
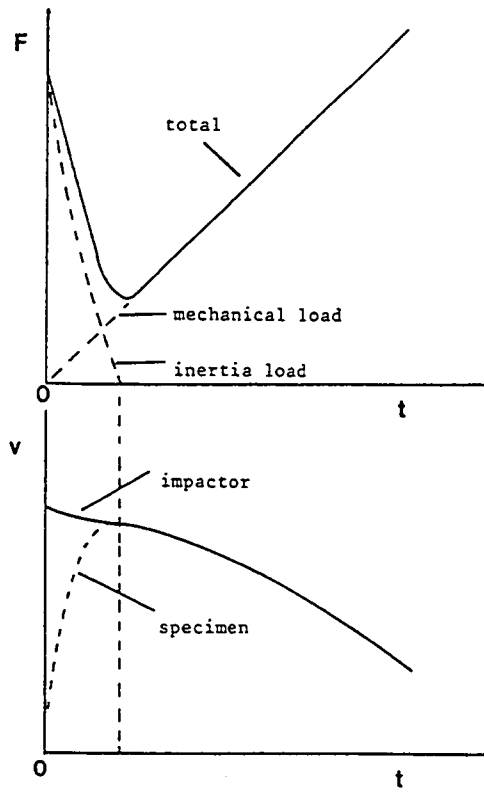
figure 5.18 Load-time and velocity-time curves during the first micro seconds after initial contact (ref.7).
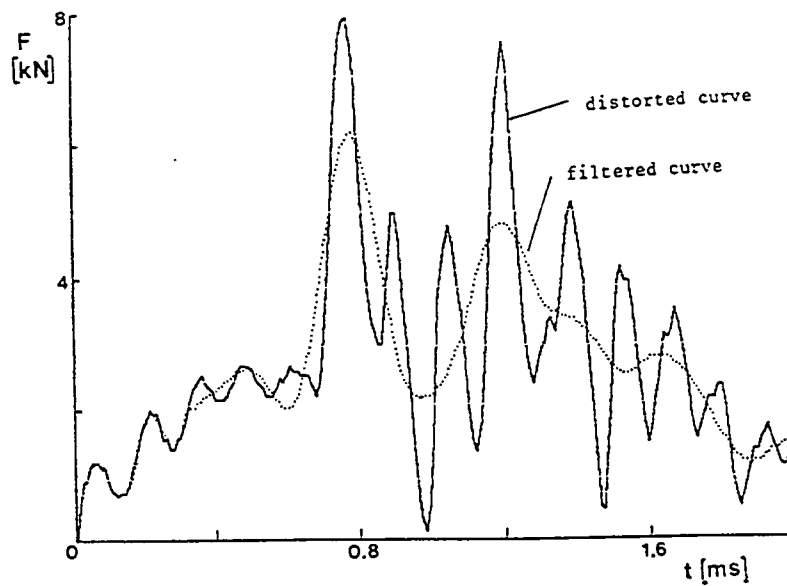
figure 5.19 Distorted and filtered force-time curve (filter: N=670,

f_c = 3000 Hz, f_t = 6000 Hz)
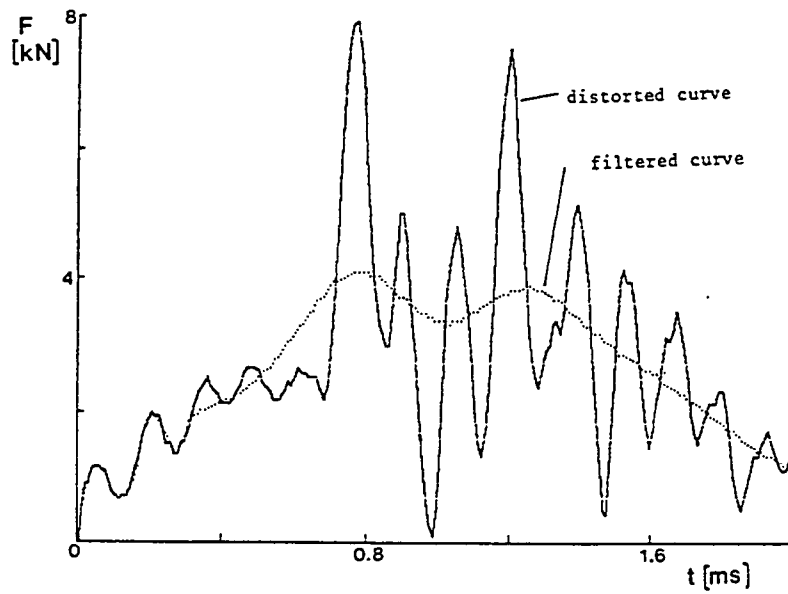
figure 5.20 See figure 5.19 (filter: N=670, f_c = 100 Hz, f_t = 3000 Hz).
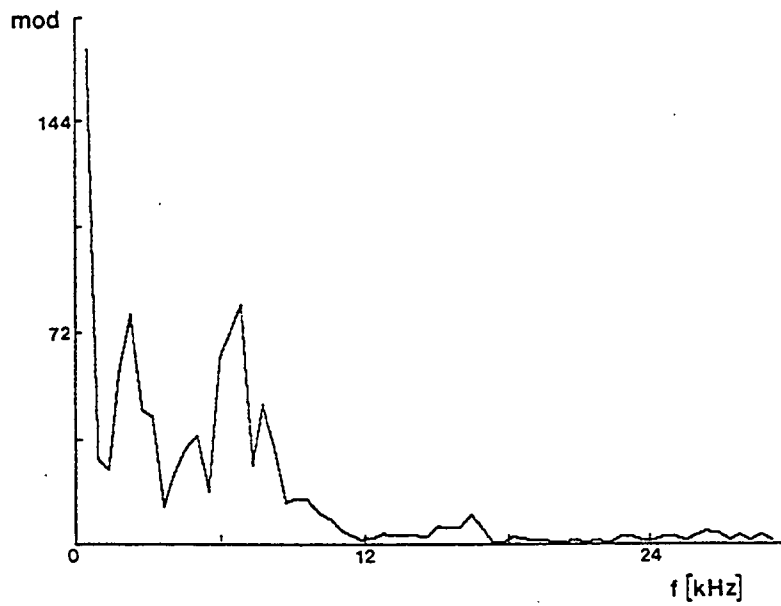
figure 5.21 Frequency spectrum of the distorted signal of figures 5.19 and 5.20.
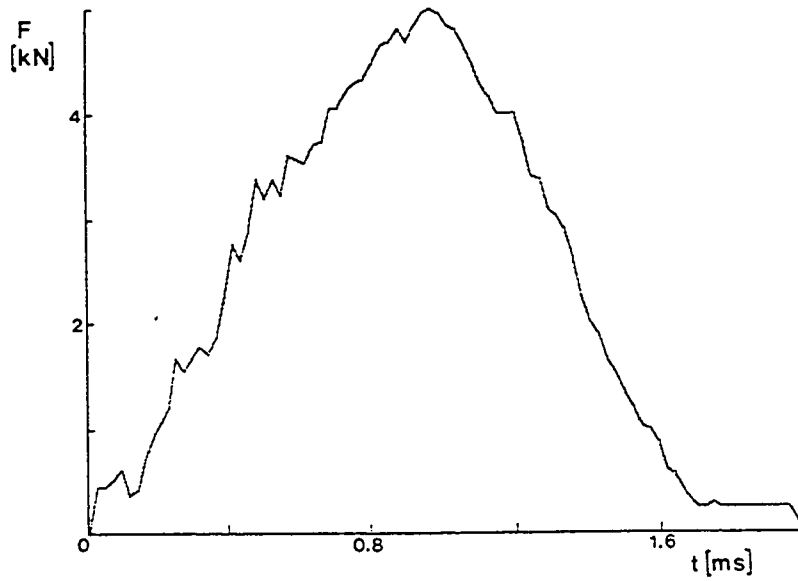
figure 5.22 Example of a force-time curve after modification of the load cell (compare to figure 5.19).
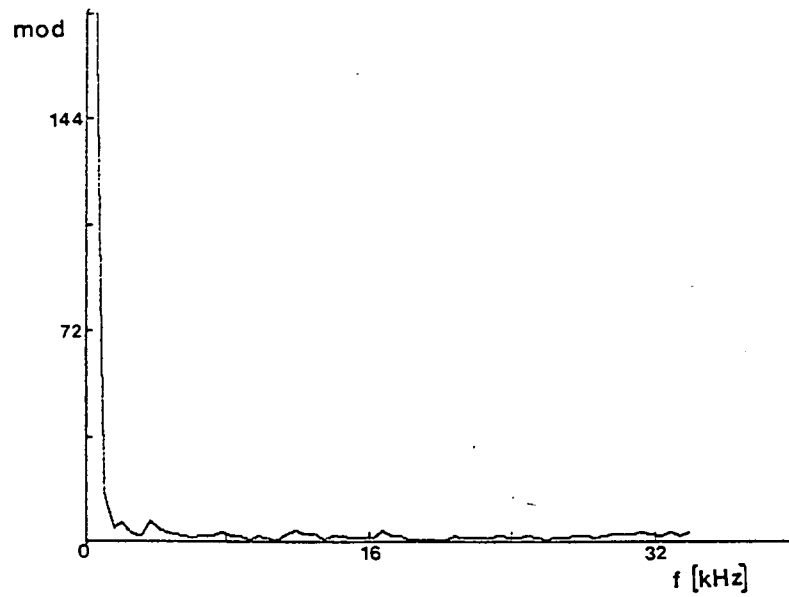
figure 5.23 Frequency spectrum of the force-time curve of figure 5.22.

130
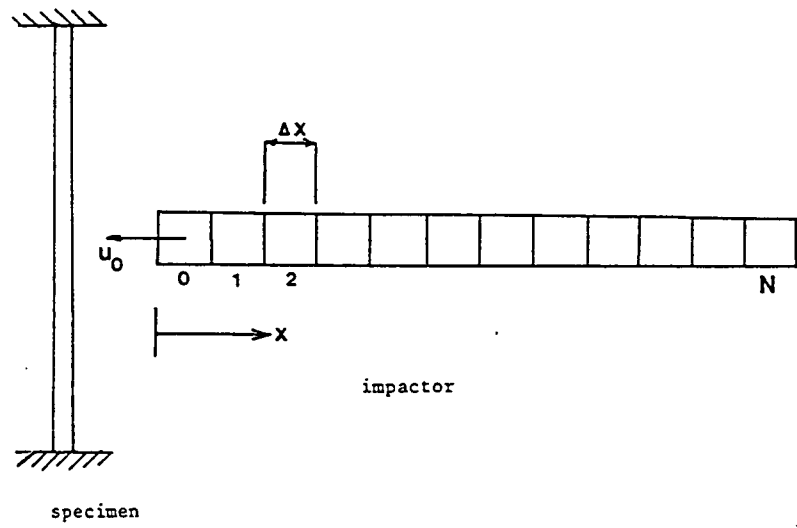
figure 5.24 A model of the impactor for stress wave analysis.
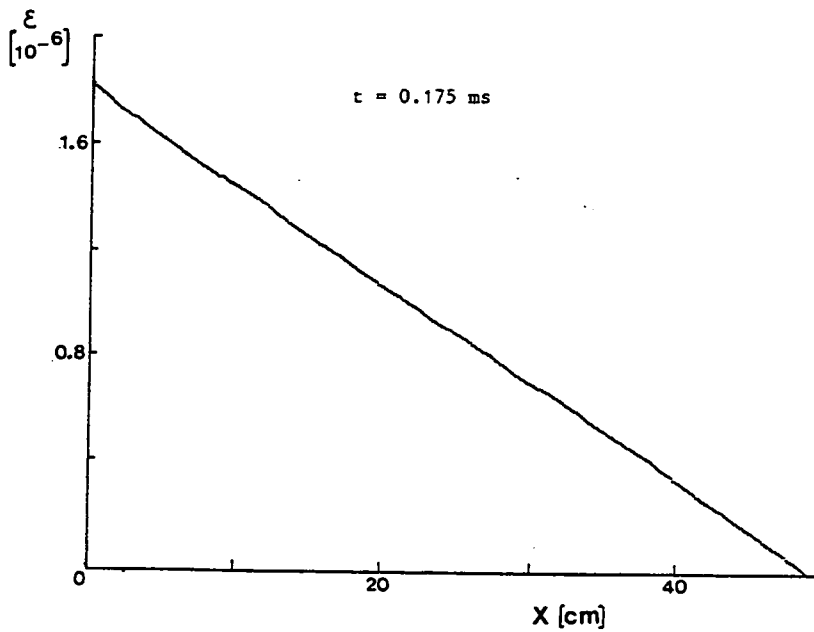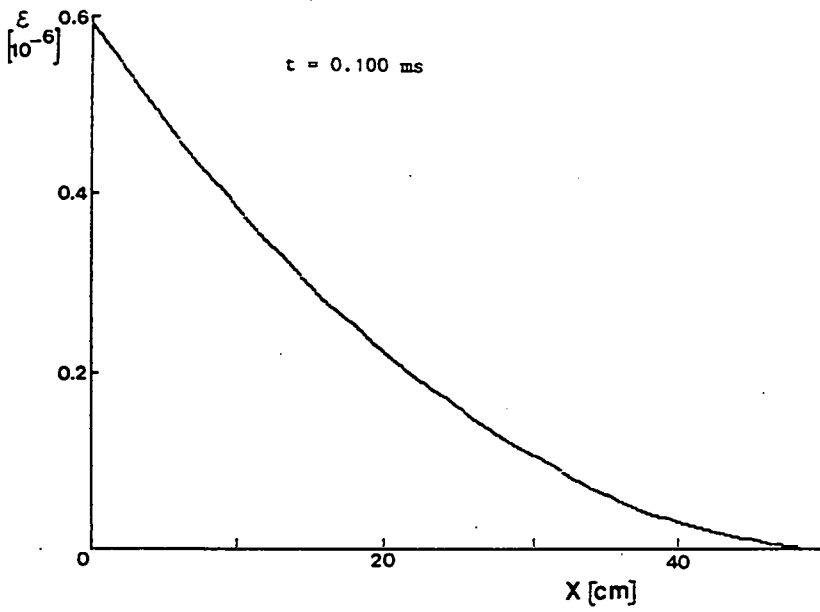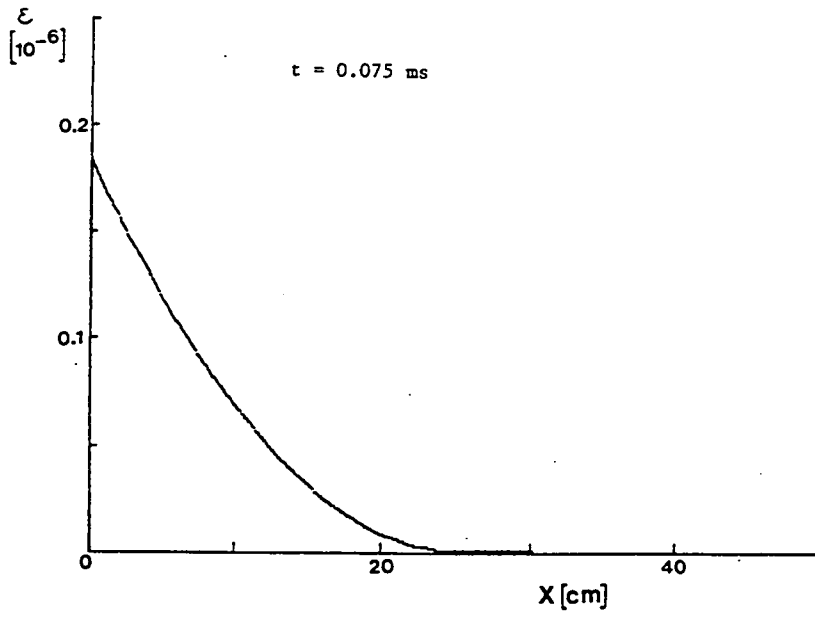
figure 5.25 Travelling
stress wave to
the end of the impactor
($\sqrt{\dfrac{E}{\rho}}$ = 5100 m/s, v_0 = 5 m/s,
t_c = 4 ms)
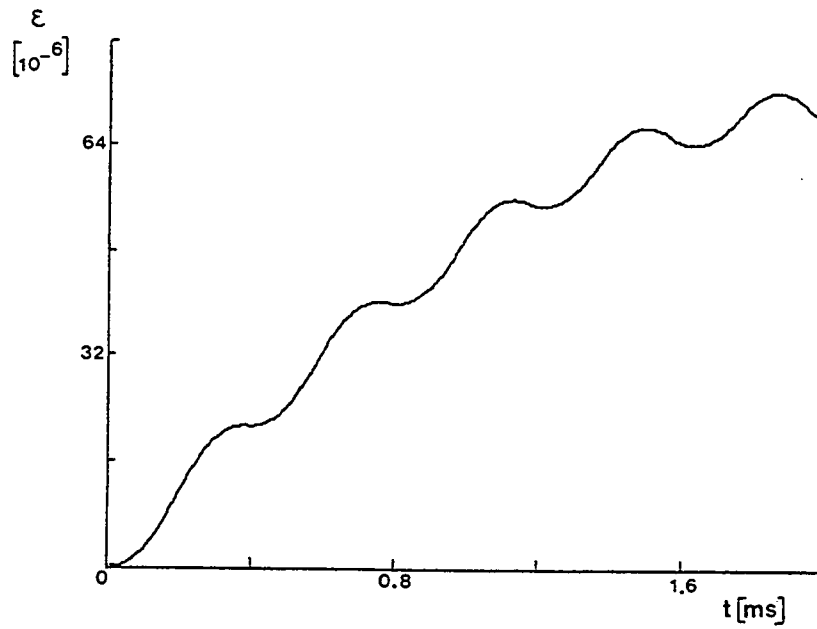
figure 5.26 Strain in the impactor at x= 5 cm, impactor length= 50 cm,

$\sqrt{\dfrac{E}{\rho}}$ = 5100 m/s, v_0= 5 m/s, t_c = 4 ms.
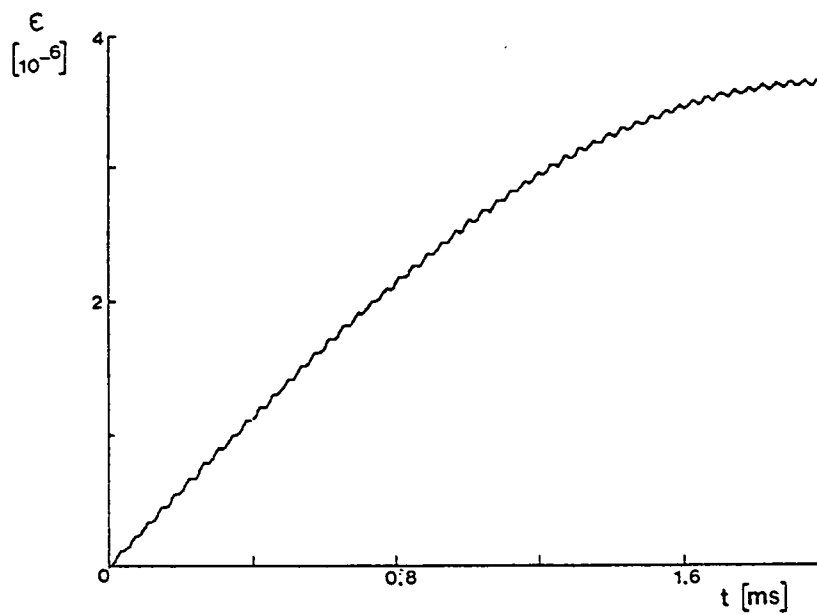
figure 5.27 Strain in the impactor at x= 5 cm, impactor length= 10 cm,

$\sqrt{\dfrac{E}{\rho}}$ = 5100 m/s, v_0= 5 m/s, t_c = 4 ms.
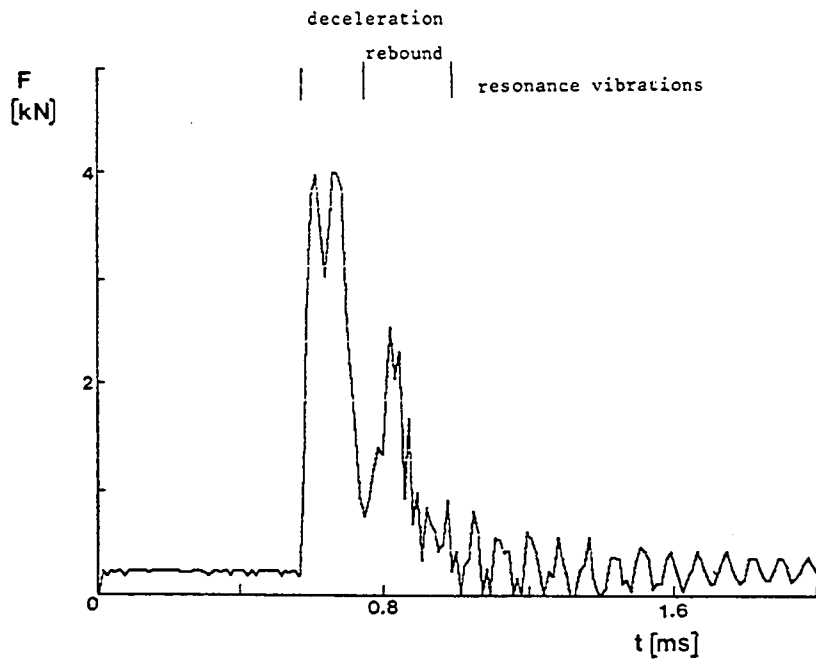
figure 5.28 Impact of the impactor used in this study on a ceramic tile, v_0= 1.41 m/s.
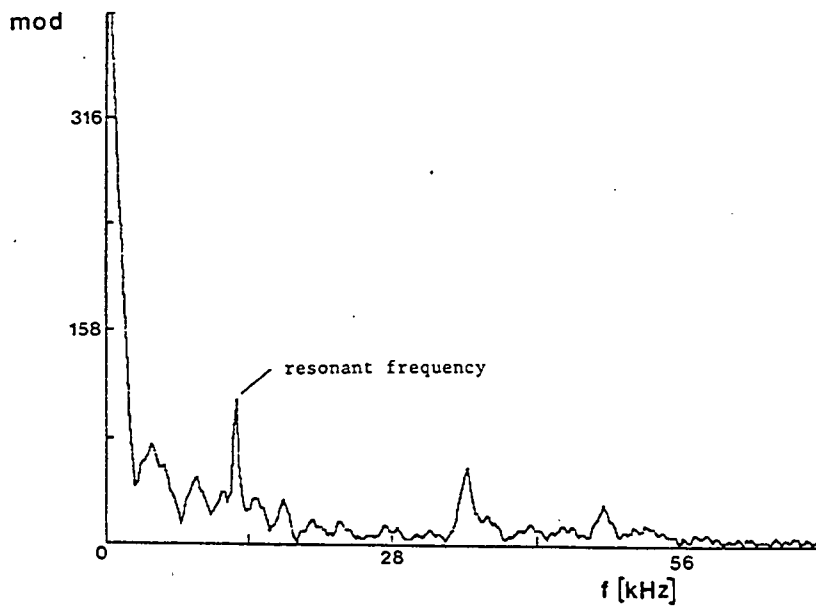
figure 5.29 Frequency spectrum of the load-time curve of figure 5.28.

134

figure 5.30 Example of a data set of a single impact test.

EXPERIMENTAL IMPACT DATA

operator:	anne	impact velocity (m/S):	0.76
date:	29/7/88	impact energy (J):	0.15
specimen:	ar1	velocity after impact (m/S):	-0.39
thickness (mm):	0.8	absorbed energy (J):	0.11
impactor shape:	r7.5	max. displacement (mm):	1.56
impactor mass (g):	533	permanent deflection (mm):	1.40
clamping width (mm):	80	max. force (kN):	0.18
prestress (MPa):	0	velocity restitution coefficient:	0.520
displacement range (mm):	6	energy restitution coefficient:	0.270
strain range (mstr/1000):	2	contact time (mS):	5.45
force cal.factor (kg/mV):	0.48075		

135
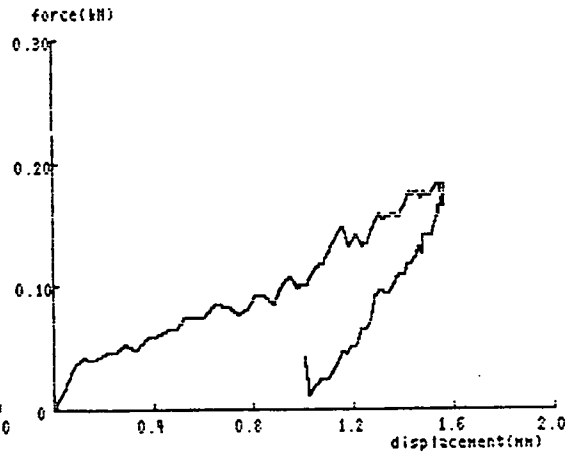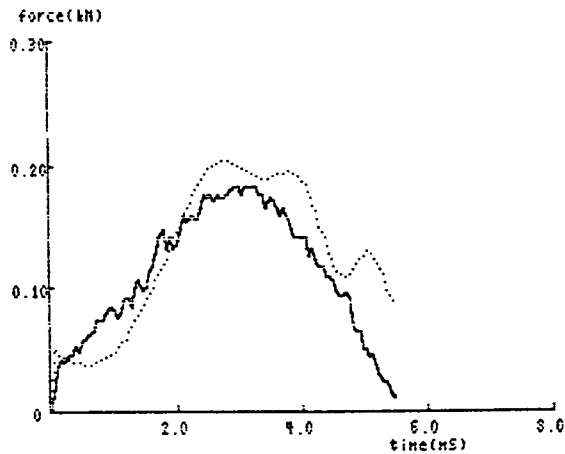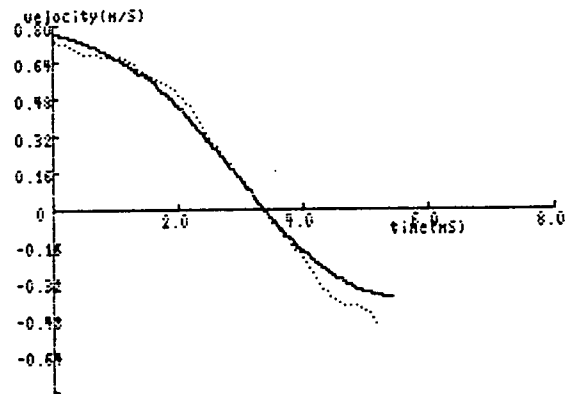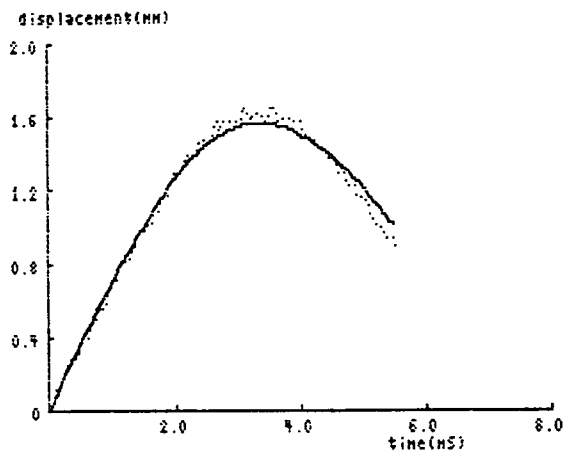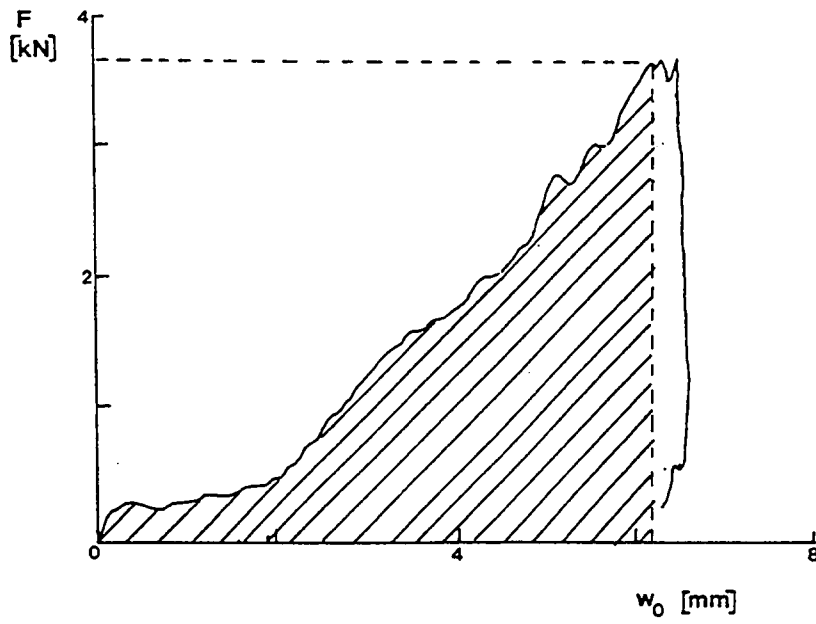
figure 5.31 The absorbed energy at fracture.
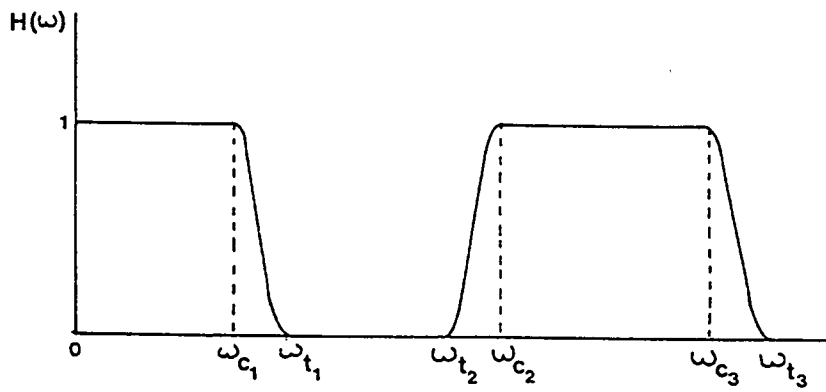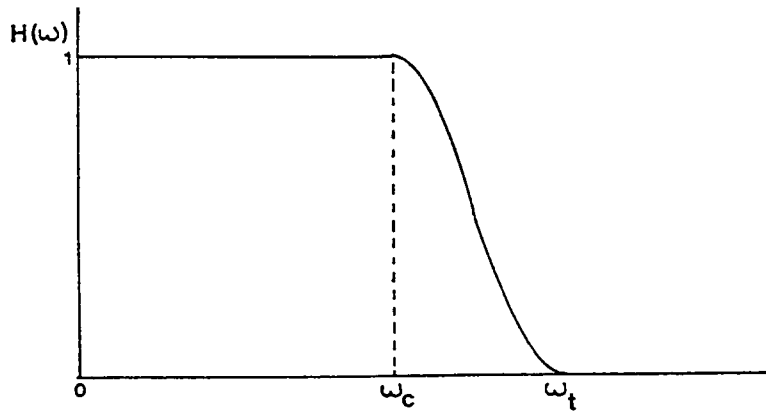
figure 5.32 High pass filter (a) and notch filter (b).

chapter 6 Impact tests on sheet materials with a square test area

6.1 Introduction

differences between chapters 6 and 7

In chapters 6 and 7 the results of impact tests on unloaded sheet materials are discussed. The impact models which were found in the literature generally describe an impact loading on a rectangular plate. The straight boundaries of a rectangular or square test area makes the formulation of the model (for orthotropic material) easier than for a circular area. Therefore tests were performed on specimens with a clamped square tests area. The results of these tests are discussed in the present chapter.

A specimen type with a circular test area is generally used according to the literature. It is also normalized (ASTM D 3029). This specimen type is used to determine the damage resistance of various types of aluminium alloys, ARALL laminates and composites. The results of these tests are discussed in chapter 7. In this chapter the results of a wider range of materials are described than in chapter 6. For example: the tests on specimens with a square test area were only done on aramid ARALL, whereas in chapter 7 the results of tests on ARALL with glass and carbon fibres are given also.

impact damage definition in chapters 6 and 7

Figure 6.1 shows typical (static and dynamic) force-deflection curves for monolithic Al alloys and for composites and ARALL. The force at first failure is designated with F_f. The corresponding deflection and absorbed energy (= area under the force-deflection curve) are $w_{o,f}$ and U_f respectively. U_f is called 'the energy at first failure'. At maximum force the force is F_u (ultimate load), and the deflection and the absorbed energy $w_{o,u}$ and U_u respectively.

Monolithic Al alloys, composites and ARALL show a different behaviour with respect to damage accumulation:

1. *Monolithic aluminium* has a rising force-deflection curve until failure. Until first failure the specimen only shows plastic deformation. First failure occurs at maximum force (= ultimate load) that can be sustained by

the specimen. After fracture the force drops rapidly: a hole will be created and the indentor is pushed through the plate.

2. *Composites* show matrix failure and delamination before the first load drop (point of 'first fibre failure'). At the 'first failure load' F_f a significant load drop occurs due to fibre fracture. This fibre fracture starts at the side opposite to the loaded side and progresses inwards. Meanwhile the force rises again until the ultimate load F_u is reached.

3. *ARALL laminates* have a force-deflection curve which is similar to that of the composites. For some ARALL types however, the first failure occurs at ultimate load as for monolithic aluminium.

Before the first load drop in the force-deflection curve a region of the prepreg layer around the centre of the specimen shows some micro-cracking: small cracks in the adhesive.

At 'first failure' (F_f, the first load drop) the fibre and/or the outer aluminium layer will fail. Always when the fibre is critical a crack was also found in the outer aluminium layer opposite to the loaded side. When an aluminium critical failure occurs a crack will run in the rolling direction irrespective of the fibre direction. If the fibres underneath this layer also run is the rolling direction, they remain intact.

After 'first failure' the force rises until the ultimate load F_u is reached. At this point the indentor starts to perforate the specimen.

The 'cracklength' (2a) is defined as the length of the crack in the aluminium layers. With the 'damage width in the prepreg' the area of matrix cracking and delamination is meant, which is determined after chemical removal of the outer Al layers.

In the above descriptions it is assumed that sufficient impact energy is available for penetration of the specimen. If the energy is too low for penetration only a part of the curves in figure 6.1 is applicable.

6.2 The aims of the tests

Impact tests were performed on specimens with a square 100 x 100 mm^2 clamped test area, in order to obtain the following results:

1. A collection of experimental data for a verification of theoretical modelling (part three of this report). The force-time, velocity-time and displacement-time curves gathered by the testing of the specimens with a square test area will be used for a comparison with the calculations in chapter 12.

2. A comparison of the impact behaviour of monolithic aluminium 2024-T3, unidirectional aramid ARALL laminates and several thermoplastic composites. (In the next chapter also test results will be discussed of Al 7075-T6 (monolithic and ARALL), glass and carbon ARALL, cross-ply ARALL and thermosetting composites)

3. Insight in the impact process. Because the number of materials in this chapter will be relatively small (compared with chapter 7), a more complete description of the measured data can be given here.

4. A comparison between the behaviour during impact and the behaviour in quasi-static tests. The quasi-static tests are realistic for damage caused by objects with a low velocity and a high mass. Static and dynamic force-deflection, deflection-absorbed energy curves and fracture energies are compared.

6.3 Test method

The specimens were clamped between two Al 7075-T6 frames by 12 bolts which were inserted through bolt holes in the specimen, see figure 6.2. The opening of the frames was 100 x 100 mm^2, the dimensions of the specimens were 150 x 150 mm^2.

In order to explore the significance of the specimen clamping static force-deflection tests were carried out on Al 2024-T3 (t=1 mm) specimens. The following conditions were compared:
- the specimen supported on one of the frames,
- loosely clamped by the bolts (torque $\cong$ 5 Nm) between two frames
- clamped by the bolts with a torque of 10, 20 and 30 Nm.

The results in figure 6.3 show the influence of the clamping of the specimen. Apparently a loose clamping should be avoided. The deformation shape of the plate as drawn schematically in figure 6.4 has to be suppressed: the deflected sheet tends to lift the clamping plates. The influence of the specimen clamping will also be discussed in the next

chapter for a circular test area.

The frame with the clamped specimen (figure 6.2) was mounted on the heavy table of the impact tester. The same frame was used to perform quasi-static tests for a comparison with the results of the dynamic tests. The loading rate during the quasi-static tests was approximately 1 mm/min.

The impactor mass was 302 g, the tip radius was 7.5 mm.

The contact force and the displacement of the impactor were measured. For specimens with strain gages the contact force and the strain were measured during impact.

The force-displacement and force-time measurements give information on the load acting on the specimen. In order to compare this with the strains in the material, strains were measured by strain gages. Two strain gages were mounted on a statically loaded quasi-isotropic carbon/PEI specimen with the lay-up $[0,\pm45,90]_s$ and on a cross-ply carbon/PEI specimen with the lay up $[0/90]_{2s}$, at the non loaded side. Figure 6.5 shows the position of the gages. The gage length was 2 mm. Three quasi-isotropic and six cross-ply carbon composites were dynamically tested with one strain gage on each specimen in the off-centre position (number 2) indicated in figure 6.5 (20 mm from the impact point). The strain gages of the impact specimens were not mounted in the centre because the strain gradient in this region is very high, and it was not possible to control the impact point accurately enough (within 1 mm from the centre of the specimen).

The following types of data were determined in the static tests:

1. The force-deflection curves.
2. The force and deflection at first failure, and at ultimate load.
   First failure is accompanied by a dip in the force-deflection curve (figure 6.1).
3. The force-deflection curves were numerically integrated to obtain the absorbed energy at first failure and at ultimate load.
   The absorbed energy at first failure is the more important result.
   The absorbed energy at ultimate load is a measure for the resistance against perforation.

The damage in a specimen (as was defined in section 6.1) after impact was characterized by:

1. The <u>damage width</u>: defined as the diameter of the smallest circle
   around the damaged area in the material. For ARALL the damaged area was
   considered to be the region of delamination and matrix cracking, visible
   after removal of the outer layers by etching. The composite specimens
   were C-scanned to reveal the delaminated area.

2. The <u>crack length</u> in the monolithic aluminium and ARALL, visible
   at the outside. This crack length is smaller than the damage width,
   but it is especially the crack length which will determine the
   residual tensile strength.

3. The <u>permanent deflection</u> after impact. After an impact test the
   permanent deflection of the specimens was determined at the side of
   impact. It was done by a displacement transducer, on the specimen still
   mounted in the frame. The specimens showed (limited) spring-back when
   they were removed from the frame.

4. The damage will be related to the energy absorbed by the specimen
   as is expressed by the <u>velocity restitution coefficient</u> (ratio if impact
   and rebound velocity).

6.4 Materials

The following materials were tested:

material	t	number of specimens		details
	(mm)	static	dynamic	
Al 2024-T3	1.25	2	10	
	1.35		6	chemically milled from t=1.5 mm
ARALL 2H33	1.35	2	15	fibre volume fraction of prepreg 50%
carbon/PEI	1.70	1	9	lay-up $[0,\pm45,90]_s$
aramid/PEI	1.70	1	9	ditto
E-glass/PEI	1.70	1	9	ditto
carbon/PEI	1.65	2	9	lay-up $[0/90]_{2s}$
carbon/PEI	5.00	1	9	lay-up $[0,\pm45,90]_{3s}$

The matrix of the thermoplastics was polyetherimide (PEI), with a fibre
volume fraction of 45%.

The specimens of each type of the thermoplastic laminates were consolidated in one batch in an autoclave. The stacked carbon and E-glass prepregs were heated to 270 ^{0}C, the aramid prepregs to 240 ^{0}C, both for 30 minutes, under a pressure of 5 bar. The cooling was done to 160°C under the pressure of 5 bar, and after that to room temperature at ambient pressure.

The thermoplastic composite specimens were C-scanned before testing to reveal possible delaminations. The stiffnesses and the Poisson 's ratio's of unidirectional thermoplastic layers were determined by tensile tests, the in-plane shear modulus was determined by torsion tests. Also the densities of the materials were determined, see table 6.1.

6.5 Results

6.5.1. Description of the impact damage

Al-alloy specimens

In the range of the impact energies used in this chapter (T < 17 J), the aluminium specimens showed plastic deformation only; no cracking was observed. The statically loaded specimens failed beside the centre, at the edge of the contact zone, as shown in figure 6.6.

aramid ARALL specimens

The aramid ARALL specimens deformed plastically at low impact energies, which makes the detection of the impact damage easy, if compared with the thermoplastic composite materials. The out-of-plane deformation pattern is not axisymmetrical, due to the anisotropy of the material. The permanent deflection of the plate reaches a maximum in a plane through the centre, parallel to the fibre direction and perpendicular to the plate. C-scanning of the ARALL specimens was not possible because the plastically deformed bulge reflects the ultrasonic signal. The aramid ARALL specimens were chemically removed by etching after testing in order to reveal the damage of the aramid layers. Figure 6.7 shows the damage of the prepreg layer.

At low impact energies (T < 4 J) plastic deformation occurs and the aramid layers show some signs of matrix cracking and splitting.

At higher impact energies (T > 5 J) the maximum strain of the aramid fibres will be reached, the outer aluminium layer at the convex side of the dent is attached to the aramid layer and will also crack perpendicular to the

fibre direction. Fibre breakage and cracking of the aluminium layer(s) always occurred simultaneously.

At higher impact energies (T > 8 J) also the middle and inner (concave) layers will crack. The inner and middle layers break at another point than the outer layer, as shown in figures 6.8 and 6.9. The inner (concave) layer cracks at the edge of the contact region, the outer (convex) layer starts to crack near the centre of impact. In the thickness direction the crack shifts step wise away from the centre of impact to the edge of the contact region (figure 6.9). The aramid layers are broken, and the prepreg has some minor spots of delamination.

At still higher impact energies (T > 9 J) the crack branches, and the cracks propagate parallel to the fibre direction. A typical damage propagation is shown in figure 6.10. In this way a lip is created which is pressed aside by the impactor. At the opposite side of the lip a crack is formed running from the centre of impact outwards parallel to the fibres.

thermoplastic composite specimens

The first damage which occurs in the thermoplastic composite specimens at relatively low impact energies (T < 2 J) is delamination. Especially the aramid specimens show extensive delamination, which propagates along the fibre directions (figure 6.11). This damage is followed by splitting and fibre breakage at higher impact energies (T > 5 J). At the front side an indentation is visible due to the plastic deformation of the matrix. This is typical for composites with thermoplastic resins. The damage of quasi-isotropic carbon/PEI, E-glass/PEI and aramid/PEI is shown in the figures 6.12 to 6.14.

The crack length and the damage width of the aramid ARALL specimens are shown in figure 6.15. The damage width is defined as the diameter of the smallest circle around the impact damage. The damage width for thermoplastic specimens is drawn in figure 6.16.

The minimum energy to initiate the damage modes are given in table 6.2.

6.5.2. Description of the impact process

The displacement and velocity curves had typical smooth shapes: approximately a sine shape for the deflection curve and a cosine shape for

the velocity vs. time curve. The velocity will have a cosine shape (figure 6.17): the velocity will drop to zero, the projectile will rebound and thus the velocity becomes negative. The velocity-time curve can be approximated by a shifted cosine:

$$
v = \frac{v_0 + v_r}{2} + \frac{v_0 - v_r}{2} \cos\left(\frac{\pi t}{t_c}\right) \tag{6.1}
$$

with v_0 as the impact velocity, v_r as the velocity after impact and t_c as the contact time.

In figure 6.17 a typical measured curve is compared with this approximation.

The force-time curves were not smooth, figure 6.18 shows a typical force-time curve for a specimen with extensive fibre failure (the force drops rapidly after reaching the maximum). Figure 6.19 shows a typical detail of the first part of a force-time curve. This typical behaviour was not yet described in literature. At initial contact a relatively high contact force is excited on the plate: the specimen has to be accelerated from rest. During the first millimeters of the deflection of the plate the stiffness of the plate will be very low. The plate is pushed forward at a rapidly fluctuating force, the force drops and the contact between projectile and plate is lost.

At larger deflections the membrane reaction of the sheet will become important and consequently the stiffness increases.

This phenomenon is comparable with the impact of a large mass on an object with a relatively low mass. During the initial 0.2 to 0.3 ms the contact force may be very low. Care has to be taken not to miss this first part of the force-time curve. It may lead to large errors in the integrated displacement-time curve, because the velocity is still very high (approximately equal to the impact velocity). After this first 0.2 to 0.3 ms the resistance of the specimen starts to increase, the contact between impactor and plate will remain for the rest of the impact process. The loading part of the force-time curve shows fluctuations caused by the vibration of the specimen. The unloading part after maximum force may be

relatively smooth.

The measured maximum strain 20 mm from the impact centre (see figure 6.5) as a function of the impact energy is shown in figure 6.20 for carbon/PEI. The maximum strain as function of the maximum central displacement for these materials is drawn in figure 6.21. In this figure also the quasi-static strain-displacement curves are presented.

The strain-time curves and the contact force-time curves for quasi-isotropic carbon/PEI laminates are shown in figure 6.22. These relationships for cross-ply carbon/PEI are presented in figures 6.23, 6.24 and 6.25. Both the force-time and the strain-time curve were not filtered. The frequency spectrum of the strain-time curve of a cross-ply carbon/PEI specimen is presented in figure 6.26. The two peaks in this spectrum corresponds with the higher order vibrations during impact. The higher order vibration has a frequency of approximately 2.7 kHz; the resonant frequency of the specimen after impact is approximately 0.9 kHz.

The maximum central deflection during impact is shown in figure 6.27 (for monolithic aluminium and aramid ARALL laminates) and in figures 6.28 and 6.29 (for thermoplastic specimens). In these figures also the permanent central deflection after impact is indicated. To illustrate the effect of the specimen thickness, the relation between maximum deflection and impact energy is also shown in figure 6.30 for carbon/PEI and aluminium.
The maximum force during impact is shown in figure 6.31 (for aluminium and aramid ARALL) and in figure 6.32 (for the thermoplastic specimens).

The contact time of projectile and specimen is shown as function of the impact energy in figure 6.33. The velocity restitution coefficient (as defined in chapter 5) is given in figure 6.34.

Table 6.3 shows the ultimate energies and the ultimate displacements, i.e. the values at ultimate load during perforation under impact loading.
They are determined from two specimens for each material. Examples of force-displacement curves of the specimens are presented as figure 6.35.

6.5.3. Quasi-static loading and impact loading

Figure 6.36 shows the load-deflection curves during quasi-static loading. The E-glass/PEI material was not statically tested. The aramid ARALL and thick carbon/PEI specimens showed (audible) fibre failure before ultimate load, the fibres of the other specimens failed at ultimate load. The first dip in the force deflection curve of the thick carbon specimen is probably caused by delamination, which causes a decrease of the stiffness of the plate. Figure 6.37 illustrates the effect of the lay-up of carbon/PEI on the force-deflection curve. Figures 6.38 and 6.39 show the measured strains under quasi-static loading. Table 6.4 gives the energies for first and final failure of the specimens during quasi-static loading. The force-deflection and energy-deflection curves of the quasi-static and dynamic loading are given for various impact energies in the figures 6.40 to 6.44.

6.6 Discussion

The results of the various impact tests have revealed a number of systematic trends, which are summarized below.

comparison between aramid ARALL and Al 2024-T3

The behaviour of aramid ARALL resembles the behaviour of the thermoplastic composite materials. This is caused by the relatively brittle behaviour of the aramid fibre. The material is relatively sensitive to impact damage as compared with conventional Al 2024-T3. Under dynamic loading aramid ARALL showed fibre failure at energies higher than 5.4 J, whereas the monolithic material did not show cracking even at 16 J. The static values were 6.1 and 39.8 J for aramid ARALL and Al 2024-T3 respectively (table 6.4). The energy needed to initiate fibre failure is important because fibre failure will have a strong influence on the tensile strength after impact.

The maximum central deflection during impact for aramid ARALL and monolithic materials is significantly larger than the height of the dent after impact (figure 6.27). The difference between maximum deflection during impact and the permanent deflection becomes smaller for ARALL, because less elastic energy is stored and more energy is needed for plastic

deformation and failure.

The maximum central deflection during impact and the permanent central deflection are significantly larger for aramid ARALL than for monolithic material with the same thickness (figure 6.27). This is caused by the lower stiffness of aramid ARALL material, especially perpendicular to the fibre direction.

The maximum force during impact of ARALL laminates and monolithic aluminium are approximately equal (figure 6.31). Also the difference between the contact forces of monolithic aluminium/aramid ARALL and the thermoplastic composites is small (figures 6.31 and 6.32). The maximum contact force is less influenced by a difference in (bending) stiffness of the material. Monolithic Al with a thickness of 1.25 and 1.35 have an equal maximum force during impact (figure 6.31).

comparison between aramid ARALL and composites

The minimum impact energy needed to cause fibre failure in ARALL laminates with aramid fibres is close to the values for the thermoplastic composites (table 6.2). This is caused by the fibre critical behaviour of aramid ARALL.

A comparison of figures 6.15 and 6.16 shows that the damage width of the thermoplastic composites is much larger than the damage width of aramid ARALL. This is caused by the fact that the prepreg layers in ARALL are closer to the neutral line than the fibre/PEI layers in the thermoplastics. Consequently the stresses are smaller. Moreover, the prepreg layers in ARALL laminates are supported by the aluminium layers. Matrix cracks can not grow through the thickness, which also limits the extent of the delamination. The large delaminations which are noted in aramid/PEI, do not occur in aramid ARALL.

Aramid/PEI has the largest damaged area because of the bad adhesion between aramid and PEI, followed by E-glass/PEI and carbon/PEI. If we consider the minimum energy to initiate the various damage modes (table 6.2), E-glass/PEI shows the best behaviour of the thermoplastics. This is caused by the high energy absorbing capability of E-glass fibres (see table 3.4).

147

observation on impact damage in aramid ARALL

The damage width in the aramid layers of aramid ARALL is larger than the externally visible damage in the form of cracking of the aluminium layers (figure 6.15). The crack in ARALL will initiate in the outer fibre layer (at the convex side of the dent, where the highest strains occur), forcing the aluminium layer at the convex side of the dent to crack also. At higher impact energies a through crack will be created. However, this means in general that the first crack at low impact energies will be present at the inner side of the aircraft structure. This makes the detection of the crack more complicated, although a dent will be clearly visible on the outer (impact) side of the structure.

comparison between static and dynamic tests

A comparison of the material behaviour under static and dynamic loading can be made by summarizing the relevant data of tables 6.2 to 6.4, see the two tables below. Comparing table 6.2 and 6.4 we may conclude that the fibres in aramid ARALL, carbon/PEI and aramid/PEI failed at lower impact energies than the energy needed to cause fibre failure under quasi-static loading:

material	minimum energy to initiate fibre failure U_f (J)	
	quasi-static	impact
aramid ARALL	6.1	5.4±0.2
carbon/PEI	6.1	5.6±0.2
aramid/PEI	7.1	6.7±0.2

However, the difference between the failure energy for impact and quasi-static loading is relatively small (E-Glass/PEI was not tested statically).

Comparing table 6.3 and 6.4 for ultimate values it can be concluded that the energy absorbed during impact at ultimate load for ARALL is approximately equal to the static value, for aramid/PEI it is somewhat lower, for carbon/PEI it is higher:

materials	values at ultimate load			
	quasi-static		impact	
	F_u (kN)	U_u (J)	F_u (kN)	U_u (J)
aramid ARALL	3.5	9.3	3.4	9.5
carbon/PEI, q.i.	3.1	6.1	3.0	8.0
carbon/PEI, c.p.	1.6	2.5	1.5	2.9
aramid/PEI	2.4	7.1	2.9	6.6

A second way to compare static and dynamic loading is by a comparison the force-deflection and absorbed energy-deflection curves. The force-deflection curve for monolithic aluminium under impact loading is approximately equal to the quasi-static curve (figure 6.40). The dynamic force-deflection curves of ARALL, carbon/PEI and aramid/PEI tend to be higher than the quasi-static curves (figure 6.41 to 6.43). This means that the specimens tend to respond more stiffly at increasing impact energy. This tendency can also be discovered in the absorbed energy-deflection curves. The absorbed energy at a certain deflection tends to be higher for higher impact energies. However, in general the static curves are still fairly close to the dynamic curves.

comparison of various thermoplastic composites

E-glass/PEI had the highest minimum impact energy causing fibre failure of the thermoplastic composites, followed by aramid/PEI and carbon/PEI (table 6.2). For impact energies higher than this minimum cracking energy carbon/PEI had the smallest damage width followed by E-glass/PEI and aramid/PEI (figure 6.16). Carbon/PEI shows fibre failure at lower energies than E-glass/PEI, but because of this the damage size is more limited.

thickness effects

The effect of the thickness on the impact properties is significant. Figure 6.30 shows the maximum central deflection during impact of monolithic aluminium with a thickness of 1.25 and 1.35 mm. The contact force is less influenced by the thickness (figure 6.31).

The increase in thickness of 1.7 to 5.0 mm of carbon/PEI changed the damage mode at the lowest absorbed energy during quasi-static loading from fibre failure to transverse shear (delamination, figure 6.36). The absorbed

energy at fibre failure was increased from 6.1 J to 26.9 J (ratio 4.4) by a thickness increase of almost 3x.

contact time and velocity restitution coefficient

The contact time of projectile and specimen as a function of the impact energy had a minimum (figure 6.33). For higher impact energies the projectile starts to perforate and consequently the contact time increases.

The velocity restitution coefficient curve of aramid ARALL and monolithic material shows a large difference with the curves of the thermoplastic composites (figure 6.34), because of the plastic deformation of these materials. The thermoplastics behave more elastically, but show a large decrease of the velocity restitution coefficient for impact energies high enough to cause fibre failure. The behaviour of aramid ARALL resembles that of monolithic aluminium.

quasi-isotropic vs. cross-ply lay-up

A comparison can be made between the quasi-isotropic lay-up and the cross-ply $[0/90]_{2s}$ lay-up of carbon/PEI. The quasi-isotropic lay-up showed better impact behaviour (tables 6.3 and 6.4 and figure 6.37). This is caused by the fact that the strain in the centre of the specimen was higher for the cross-ply specimen (figure 6.38). An opposite trend was found for the strain gage at 20 mm from the loading point (quasi-static: figure 6.20, dynamic: figure 6.39). This means that the absorbed energy in the cross-ply specimen will be more concentrated around the impact centre than in the quasi-isotropic specimen. At 20 mm from the impact centre the strain is approximately 10% of the strain at the centre of the specimen for the quasi-isotropic and the cross-ply specimens.

dynamic specimen response

The measured strains 20 mm from the centre became negative in the first microseconds of impact (figures 6.22 to 6.25).

The measured strain-time curves at different impact energies show a similarity in their higher order vibration. This is also the case for the force-time curves at different impact energies.

Both the force-time and the strain-time curves show the same higher order vibrations of the specimen. The higher order vibrations are especially

clear in the curves of the cross-ply carbon/PEI specimens. The vibration frequency after impact is smaller than the frequency of the higher order mode during impact. Both frequencies are clearly visible in the frequency spectrum (figure 6.23).

The energy absorption by the higher order vibrations may cause the somewhat higher apparent stiffness during impact compared with the quasi-static loading case.

The force-time curves showed an inertia effect in the first phase of the impact. See section 6.4.2. The duration of this phase corresponds with the duration of the negative strain.

6.7 Conclusions

1. Aramid ARALL is relatively sensitive to impact damage compared with monolithic aluminium, due to the brittle behaviour of the aramid fibre. The minimum impact energies which are needed to cause fibre failure in aramid ARALL and thermoplastic composites are approximately equal. The failure behaviour of aramid ARALL is dominated by the fibres: when their failure strain is reached, cracking will occur, both in the fibre and aluminium layers.

2. E-glass/PEI has the highest impact energy needed to cause fibre failure of the thermoplastics, followed by aramid/PEI and carbon/PEI. This ranking corresponds with the ranking of fracture energies of the fibres (table 3.4). Carbon/PEI has the smallest damaged zone, because this material shows early fibre failure. The damage zone of aramid ARALL was significantly smaller than the zone of the thermoplastics.

3. The force-deflection curves and the absorbed energy-deflection curves are approximately equal for quasi-static and dynamic loading. The force and energy values for dynamic loading tends to be somewhat higher than for static loading for the same deflection, indicating an increase in stiffness.

The absorbed energy of the plates at ultimate load during perforation is approximately equal to the absorbed energy at ultimate force during quasi-static perforation. The ultimate force and the corresponding

displacement are approximately equal for quasi-static and dynamic loading. The impact energy needed to initiate fibre failure tends to be lower than the quasi-static value.

material	c_{11} (GPa)	c_{22} (GPa)	c_{12} (GPa)	c_{66} (GPa)	t_{ply} (mm)	ρ (kg/m^3)
E-glass/PEI	43.6	18.8	5.07	6.52	0.161	1883
carbon/PEI	103.1	5.46	1.65	4.06	0.206	1515
aramid/PEI	53.0	4.88	1.64	2.24	0.215	1328

table 6.1 Stiffness matrix of a ply, ply thickness and density of the tested thermoplastic composites.

material	t (mm)	minimum impact energy (J) for:		
		delamination	splitting	fibre breakage
ARALL 2H33	1.35	4.1 ± 1.5	< 0.8	5.4 ± 0.2
E-glass/PEI	1.75	1.9 ± 0.8	8.4 ± 0.9	8.4 ± 0.9
aramid/PEI	1.76	1.3 ± 0.2	1.4 ± 0.1	6.7 ± 0.2
carbon/PEI (q.i)	1.70	< 5.4	5.6 ± 0.2	5.6 ± 0.2

table 6.2 The minimum impact energy needed to initiate the damage modes for the tested materials (q.i. = quasi-isotropic).

material	t (mm)	U_u (J)	F_u (kN)	$w_{o,u}$ (mm)
ARALL 2H33	1.35	9.5	3.4	6.4
E-glass/PEI	1.75	8.4	3.8	5.3
aramid/PEI	1.76	6.6	2.9	5.0
carbon/PEI, q.i.	1.70	8.0	3.0	5.7
carbon/PEI, c.p.	1.65	2.9	1.5	4.0

table 6.3 The ultimate values of the absorbed energy U_u, the force F_u and the displacement $w_{o,u}$ during the perforation of the specimens under impact loading (if it is large enough for perforation).

153

material	t	first (fibre) failure			ultimate strength		
	(mm)	F_f	$w_{0,f}$	U_f	F_u	$w_{0,u}$	U_u
		(kN)	(mm)	(J)	(kN)	(mm)	(J)
Al 2024-T3	1.25	9.2	10.9	39.8			
ARALL 2H33	1.35	2.9	5.6	6.1	3.5	6.4	9.3
aramid/PEI	1.76	2.4	7.1	7.1			
carbon/PEI,q.i.	1.70	3.1	5.5	6.1			
carbon/PEI,q.i.	5.00	5.3	3.0	8.1	9.7	5.2	26.9
carbon/PEI,c.p.	1.65	1.6	4.0	2.5			

table 6.4 Results of the quasi-static tests (q.i.= quasi-isotropic, c.p.=cross-ply).
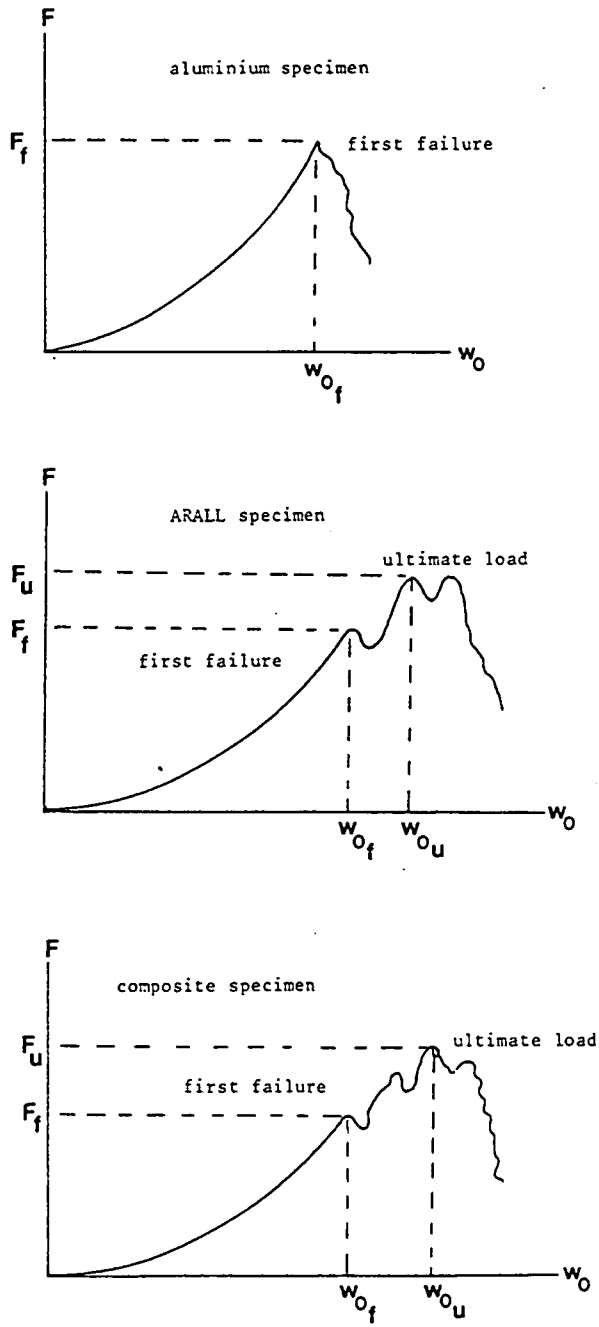
figure 6.1 Typical force-deflection curves.
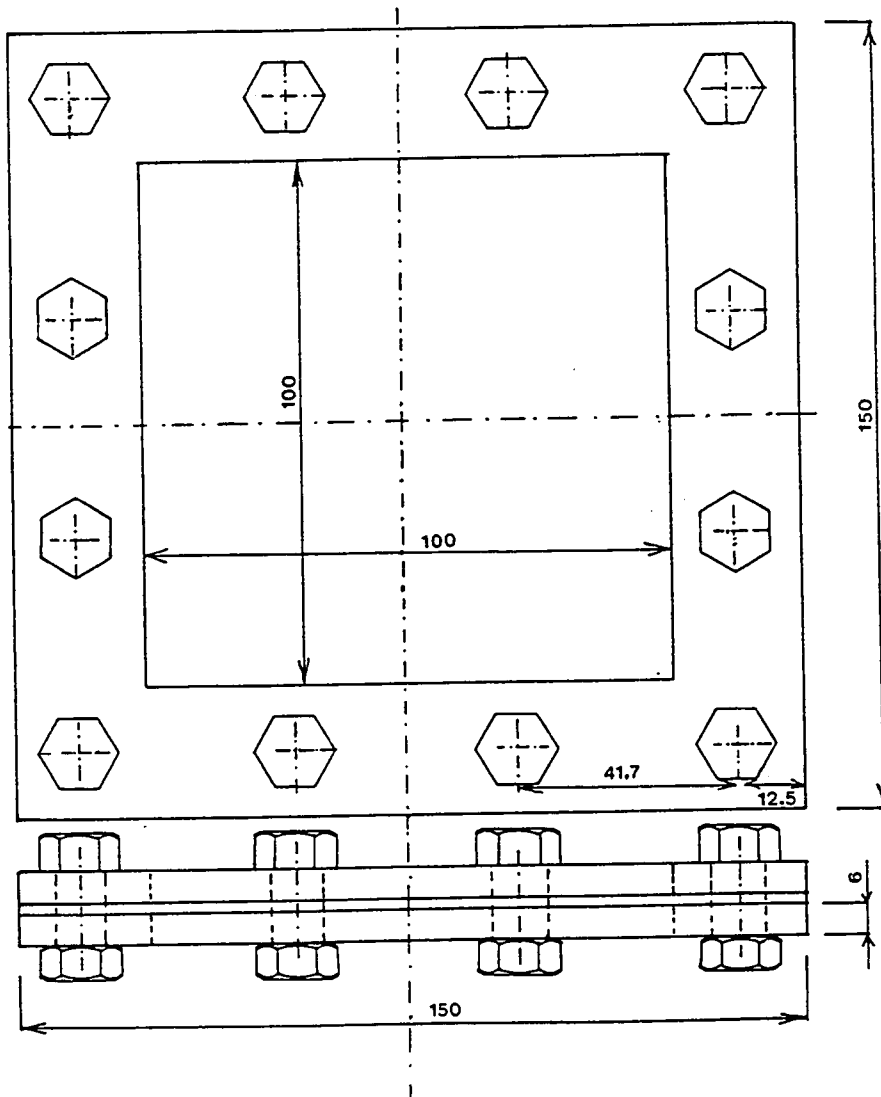
figure 6.2 The clamping used for the specimens with a square test area

156
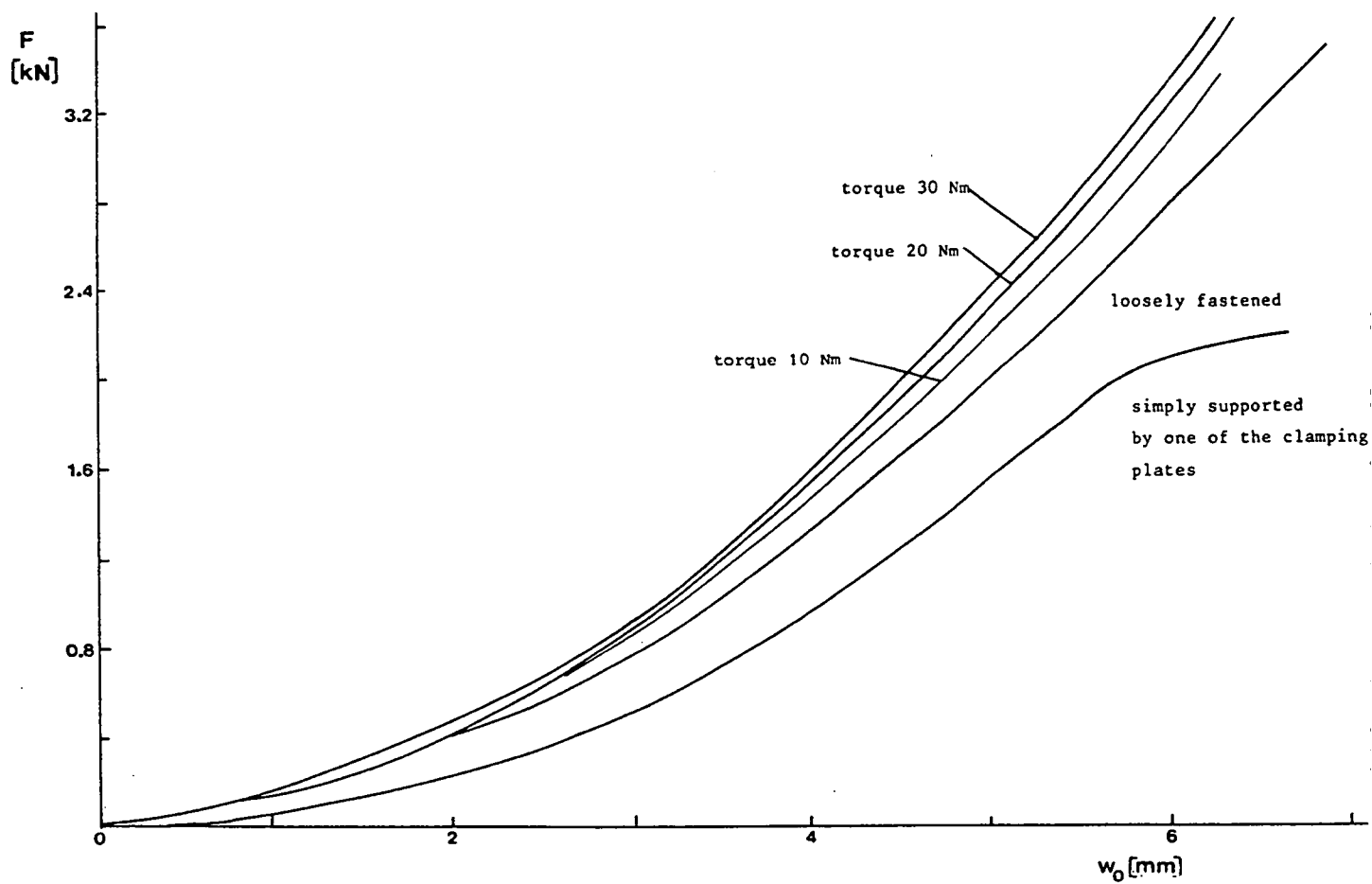
figure 6.3 The effect of the clamping conditions of an Al 2024-T3 (t=1 mm) specimen on the force-deflection curve.
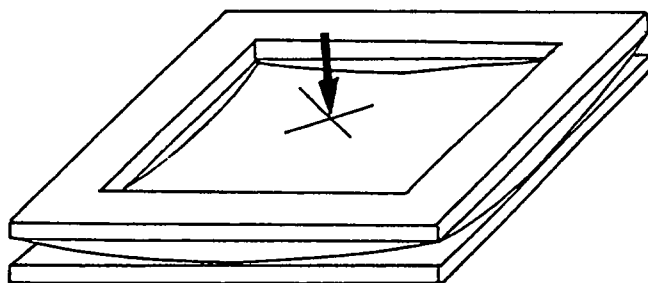
figure 6.4 The deformation mode which has to be suppressed by the clamping plates.
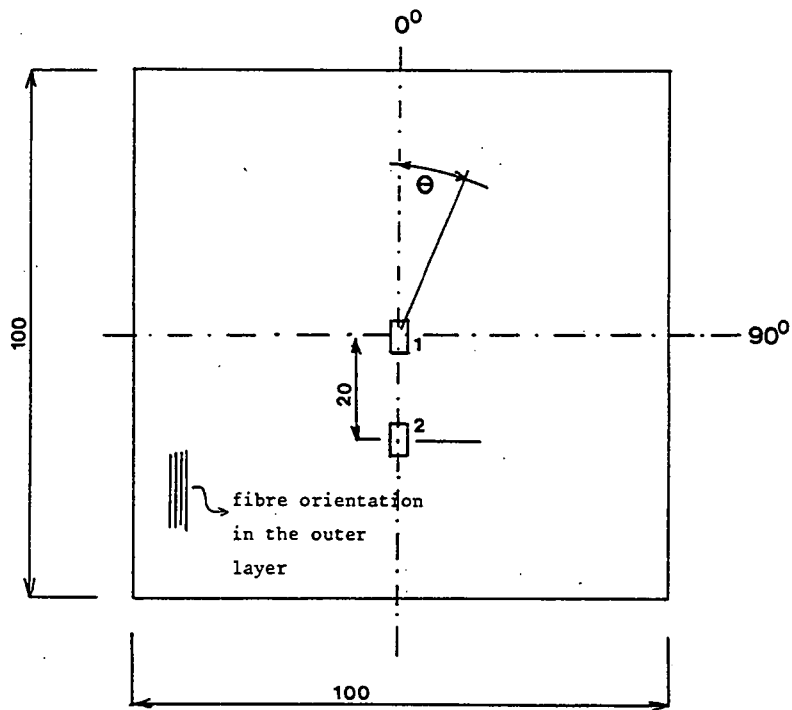
figure 6.5 The position of the strain gages.
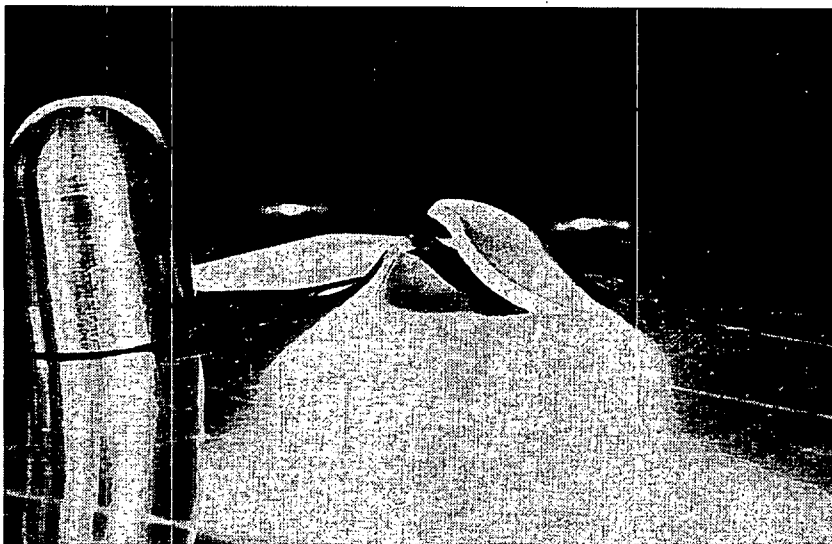
figure 6.6 The quasi-static failure mode of the monolithic Al 2024-T3 (t=1.25 mm) specimen (dimensions to be compared with the impactor tip radius R=7.5 mm).
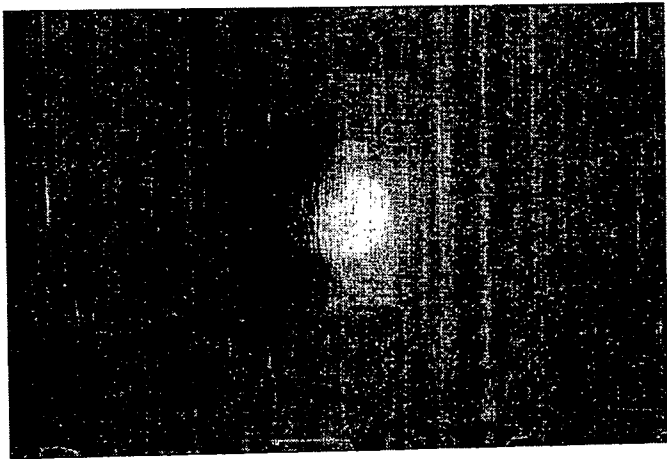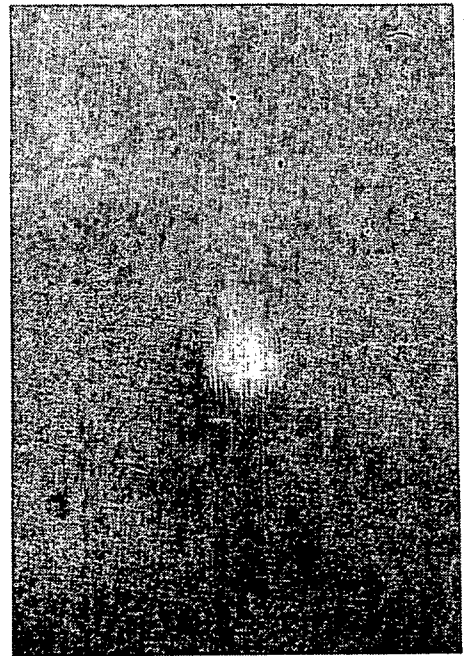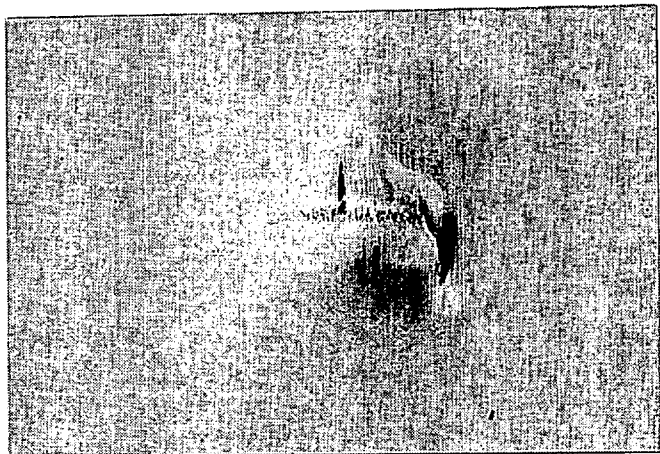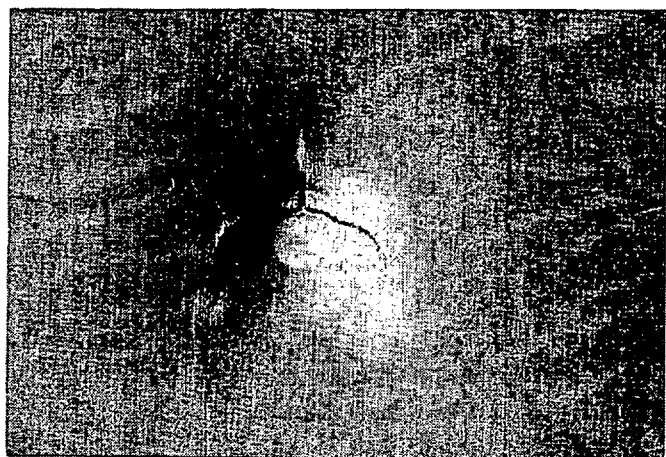
figure 6.7   The damage in
the prepreg layer of aramid
ARALL 2H33 revealed after
removing Al layer (etching)
a. 5.3 J, convex side
b. 8.4 J, concave side
c. 16.8 J, convex side
d. 16.8 J, concave side

159
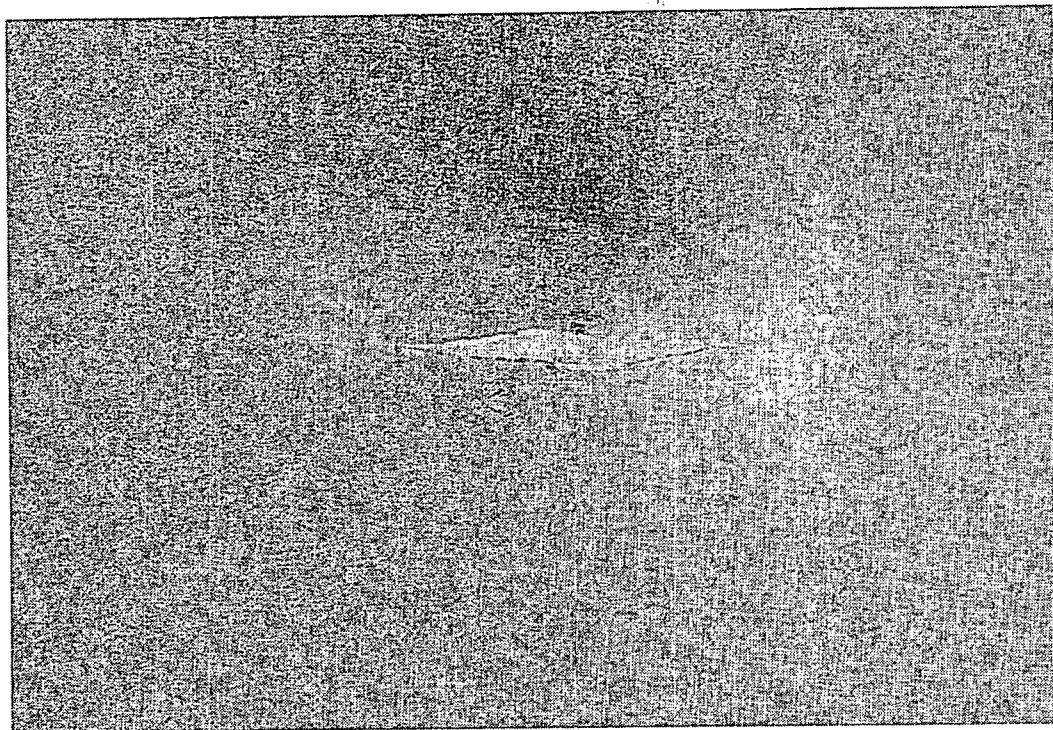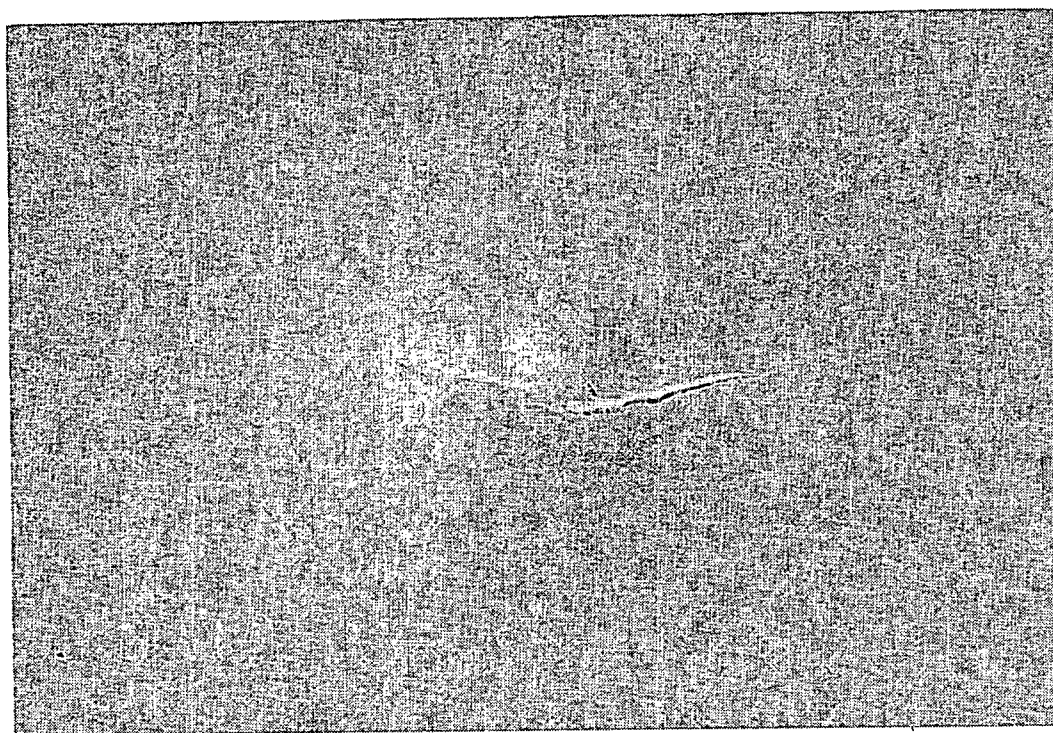
figure 6.8 Impact damage in aramid ARALL (9 J).
          a. convex (not loaded) side
          b. concave (loaded) side
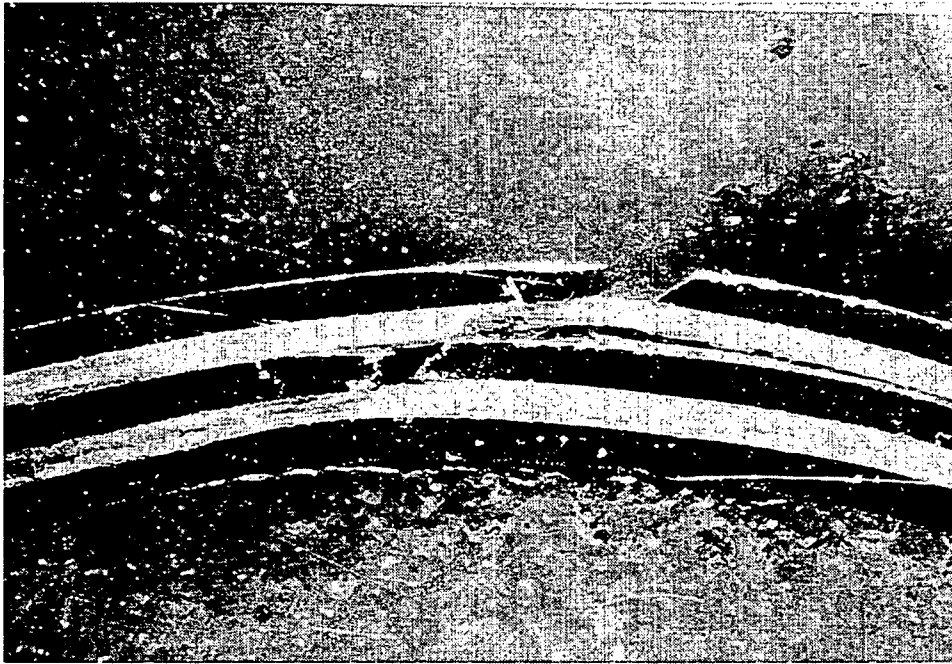
figure 6.9 Cross-section of impact damage in aramid ARALL (9.5 J): the crack shifts from the centre of the dent on the convex side, to the edge of the contact area on the concave side. fibre direction: ⟵⟶
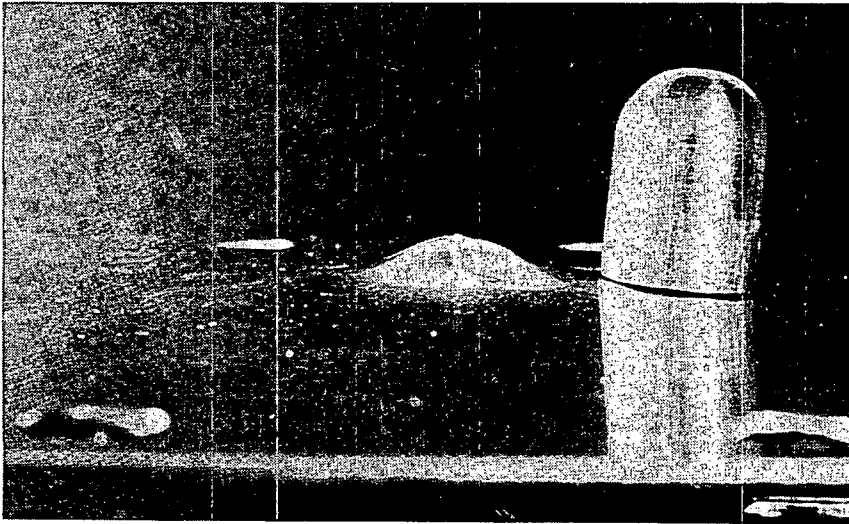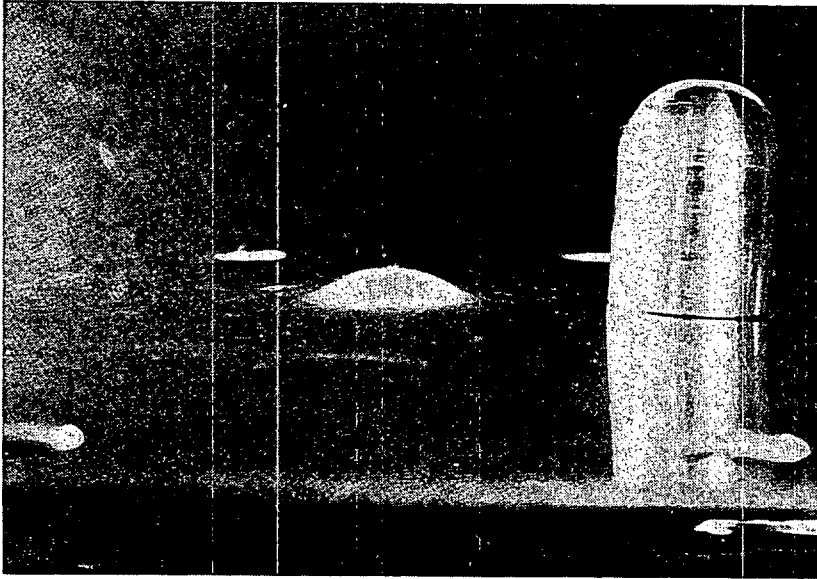
figure 6.10 Bulge with
crack in aramid ARALL
(dimensions to be compared
with impactor tip radius
R=7.5 mm)
a. 9.0 J
b. 12.0 J (crack branches)

figure 6.11 Delamination
in aramid/PEI, below outer
surface running in fibre
direction.
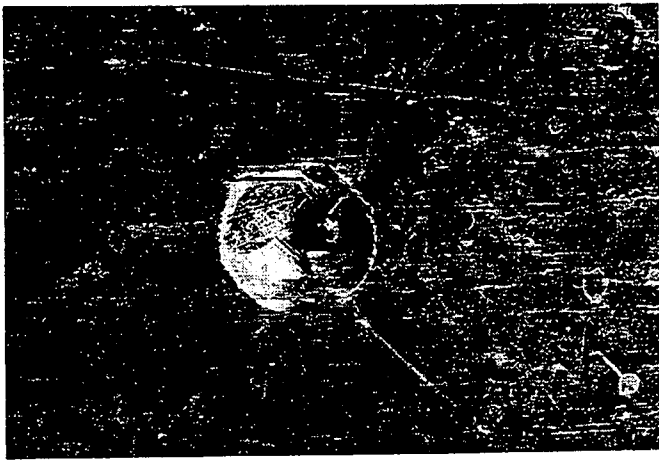
a
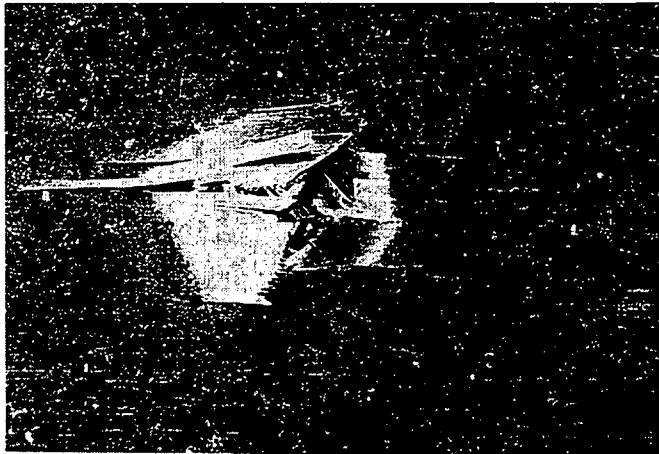
b
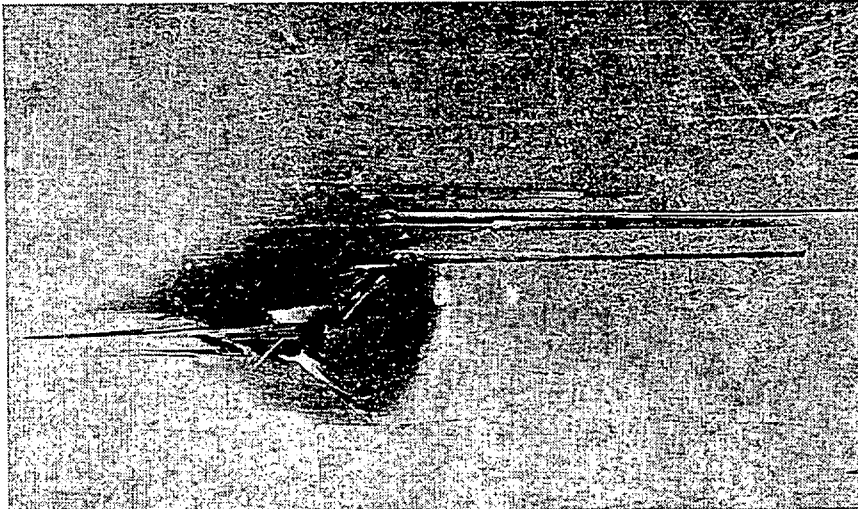
figure 6.12 Impact damage in carbon/PEI

    a. 14.3 J, concave (loaded) side
    b. 14.3 J, convex (not loaded) side
    c. 8.3 J, convex (not loaded) side
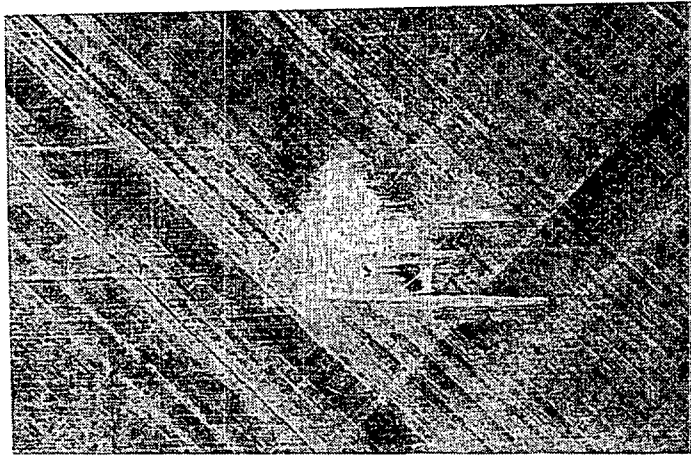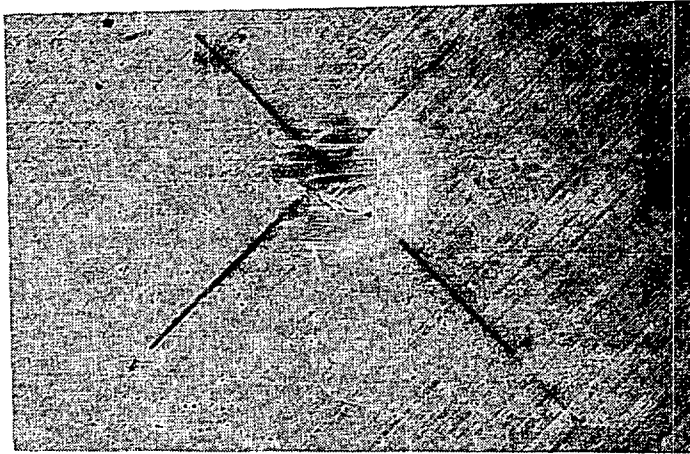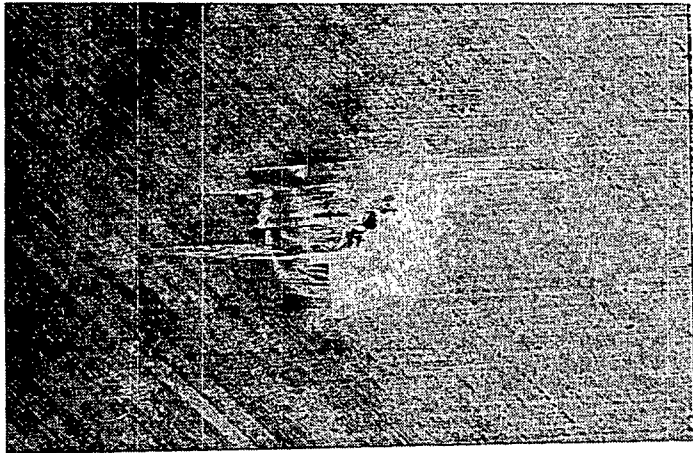
figure 6.13 Impact damage in E-glass/PEI
                 a. 9.9 J, convex (not loaded) side
                 b. 14.8 J, concave (loaded) side
                 c. 14.8 J, convex (not loaded) side
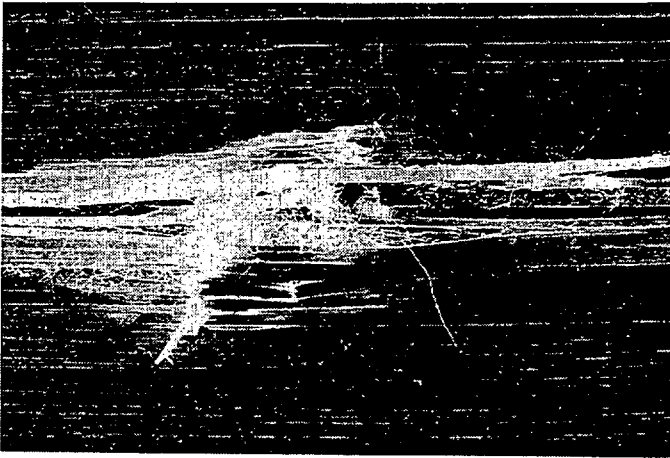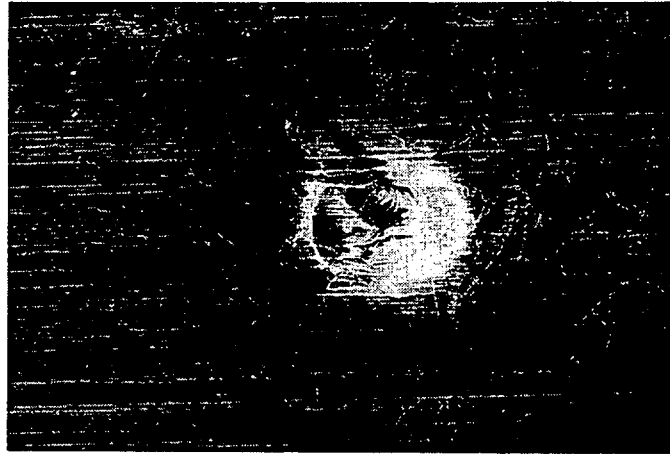
figure 6.14 Impact damage in aramid/PEI.

          a. 6.8 J, convex (not loaded) side

          b. 11.4 J, convex (not loaded) side

          c. 11.4 J, concave (loaded) side
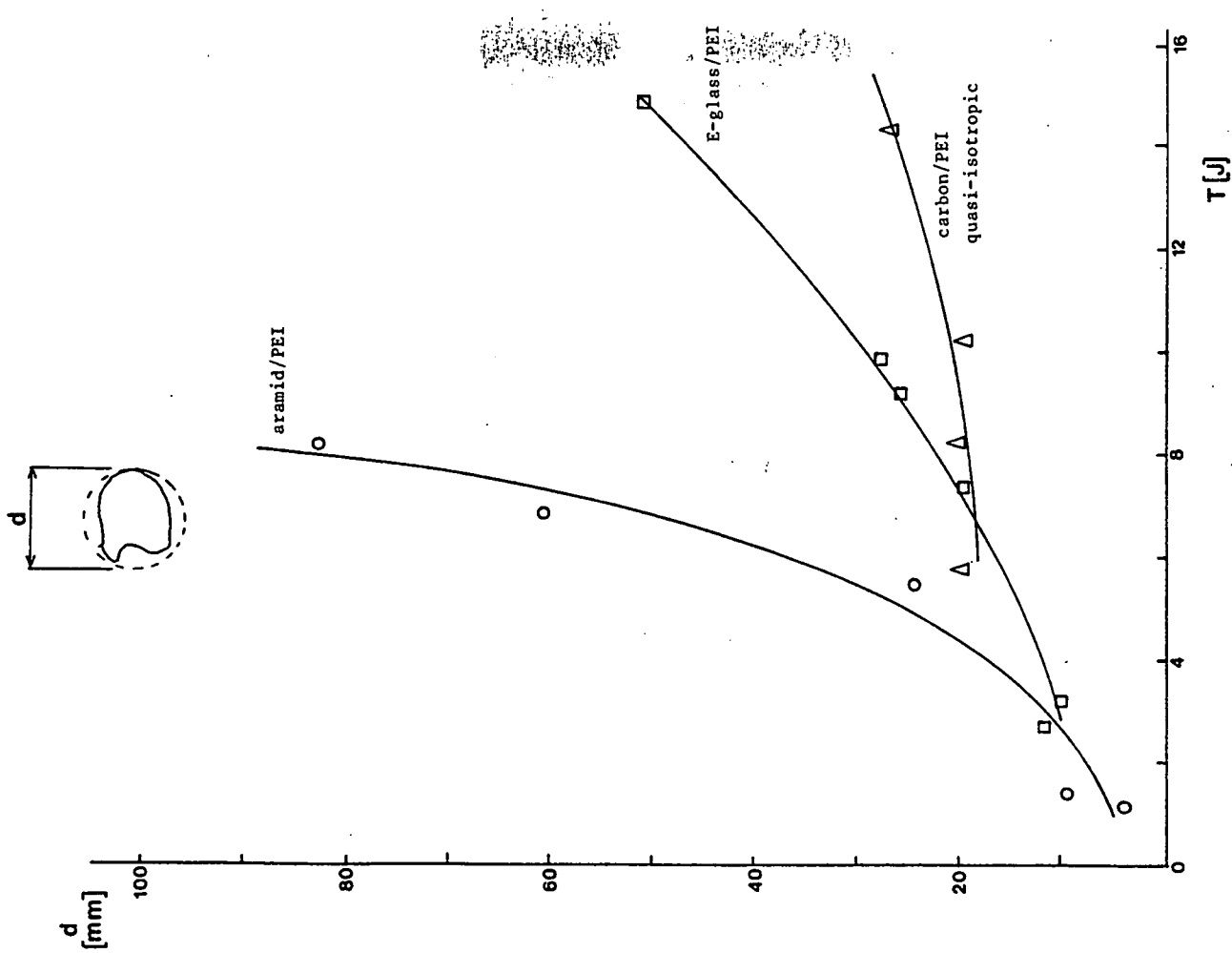
figure 6.16 Damage width d in thermoplastic composites as function of the impact energy T.
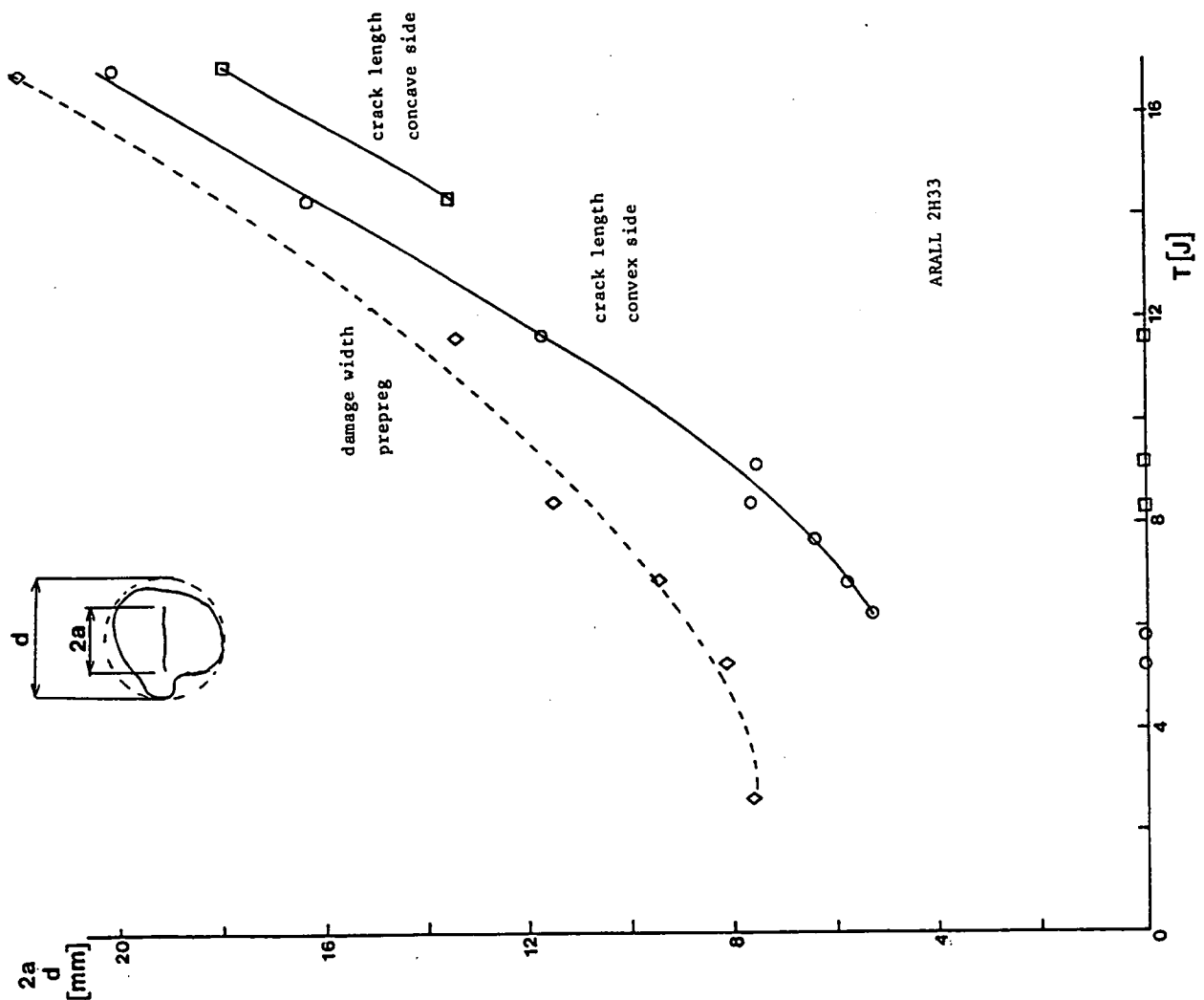
figure 6.15 Crack length 2a and damage width d in aramid ARALL vs. the impact energy T.
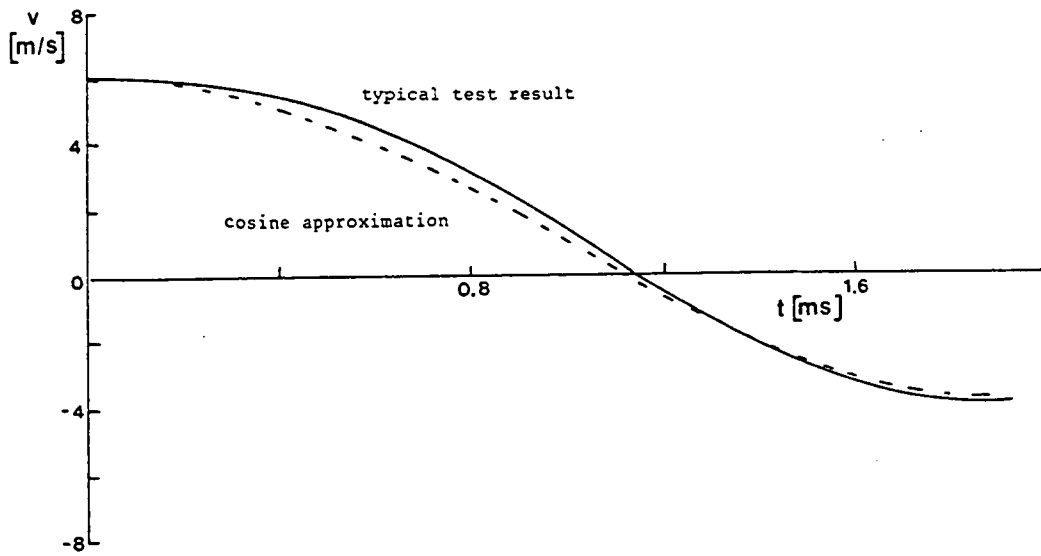
figure 6.17 Typical velocity-time curve with a cosine approximation.
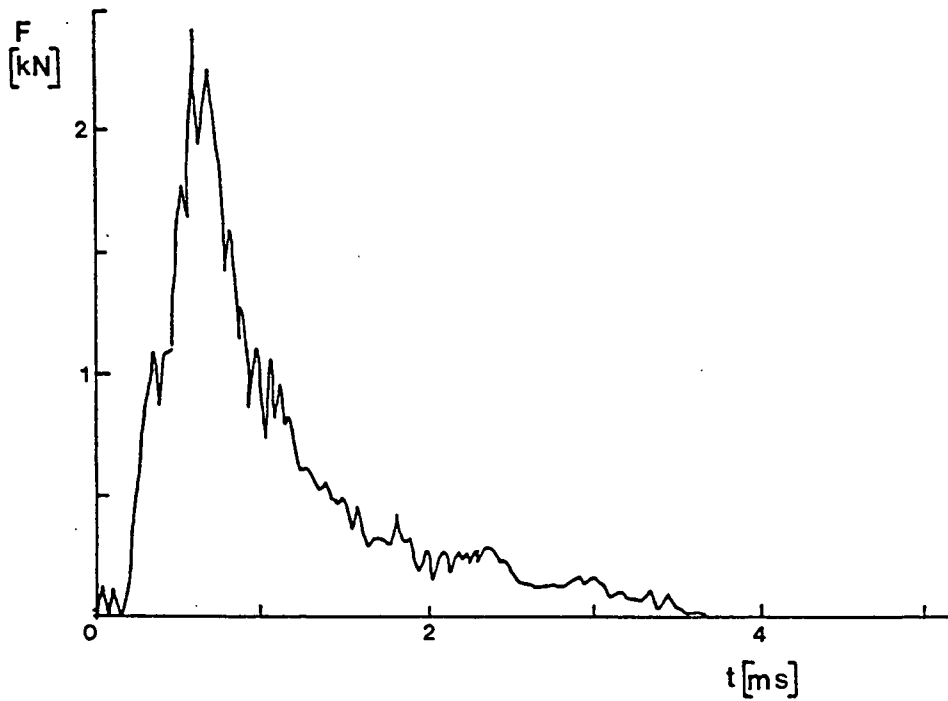
figure 6.18 Typical contact force-time curve for a specimen with extensive fibre failure.
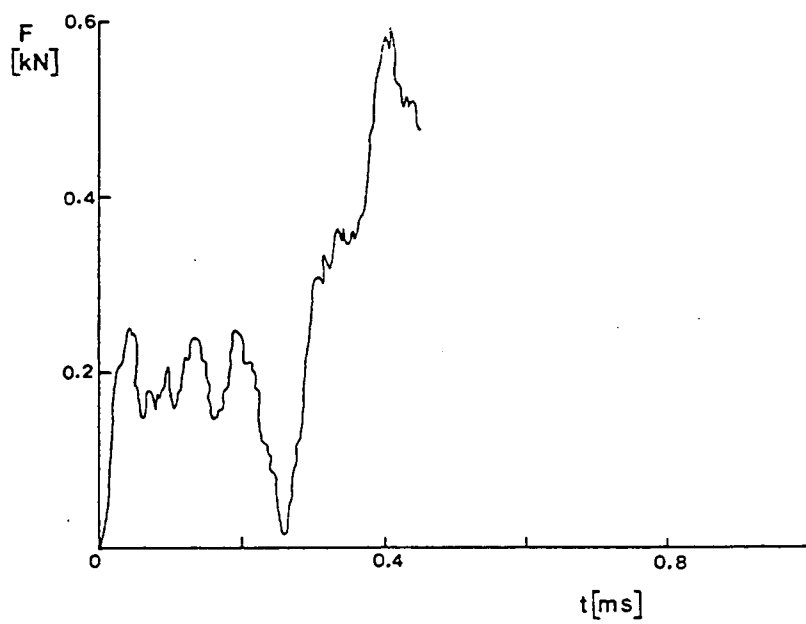
figure 6.19 Typical initial part of a contact force-time curve.
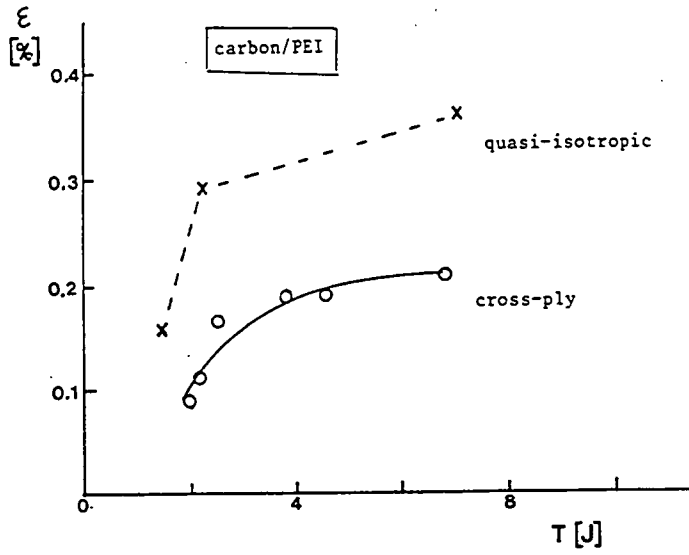
figure 6.20 The maximum measured strain ε vs. the impact
energy T̄ for carbon/PEI specimens.
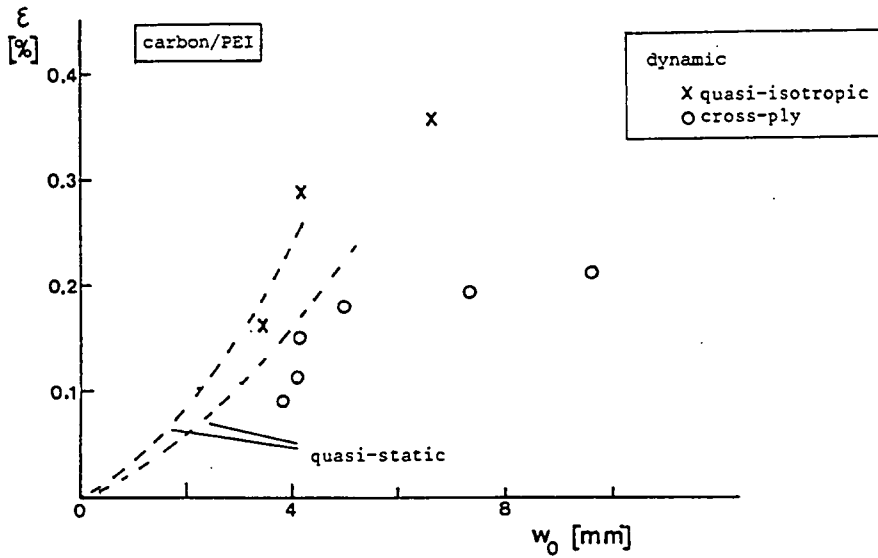
figure 6.21 The strain ε at 20 mm from the centre as function of the
deflection of the carbon/PEI specimens under impact and
quasi-static loading.
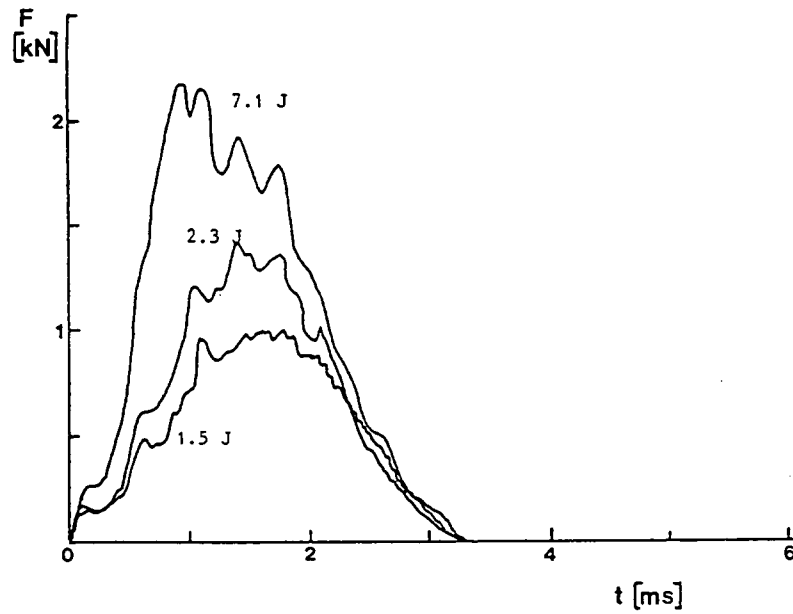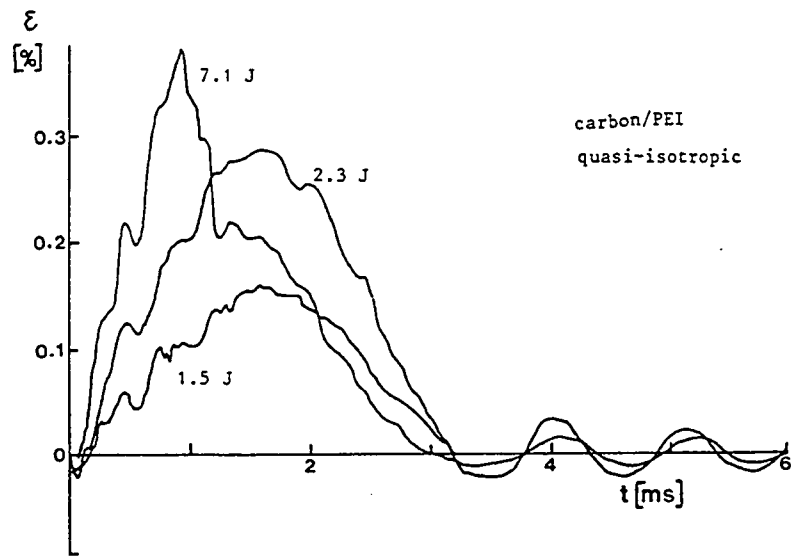
figure 6.22 Strain-time and contact force-time curves for
quasi-isotropic carbon/PEI at different impact energies.
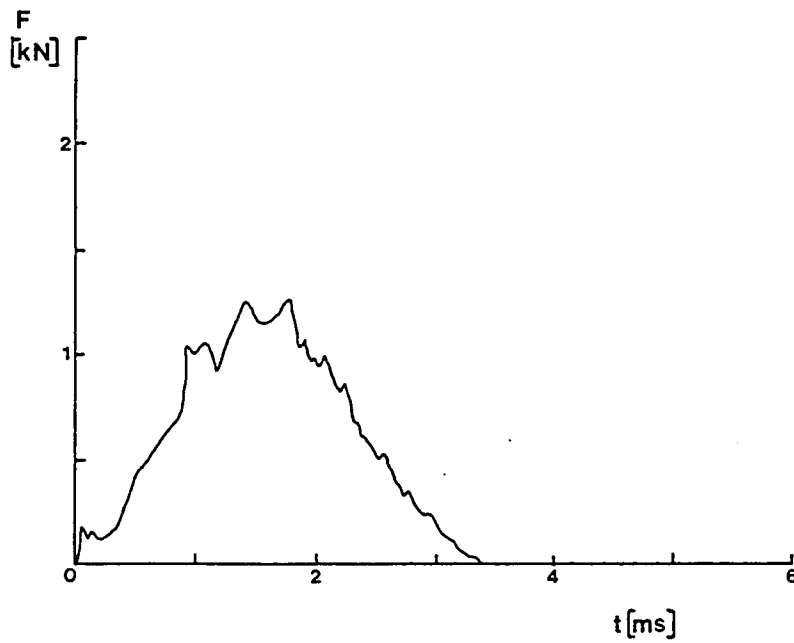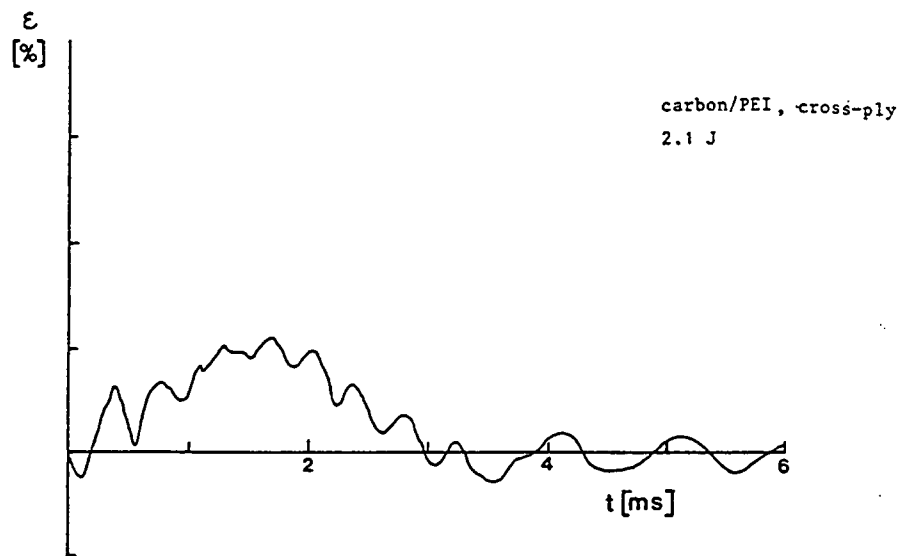
figure 6.23 Strain-time and contact force-time curves for cross-ply
carbon/PEI at an impact energy of 2.1 J.

171
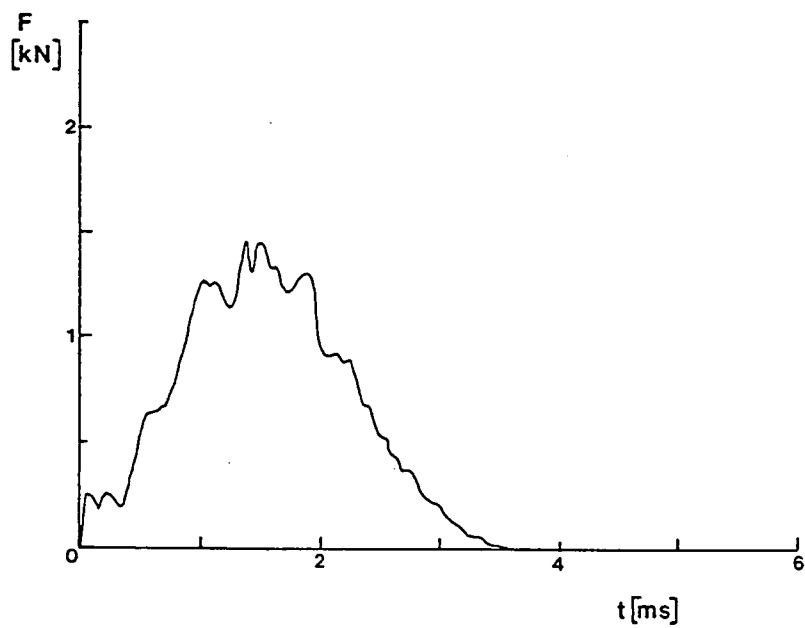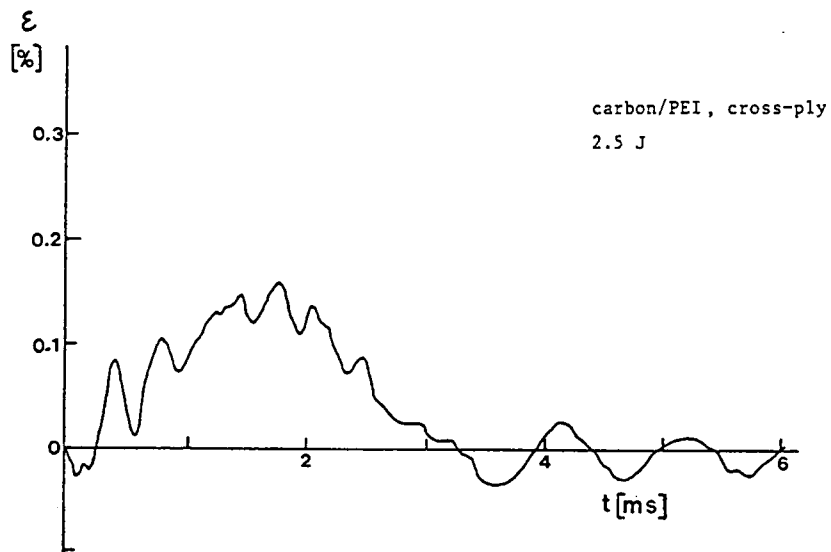
figure 6.24 Strain-time and contact force-time curves for cross-ply
carbon/PEI at an impact energy of 2.5 J.
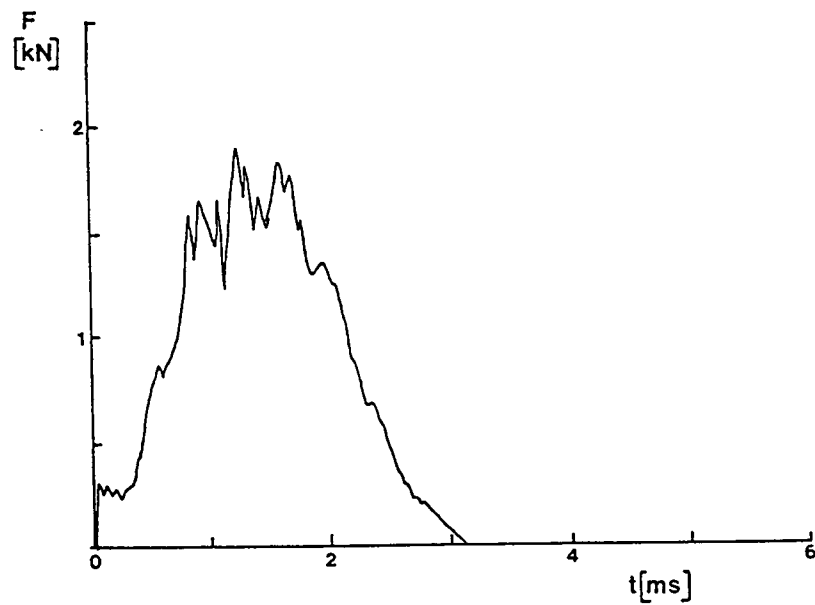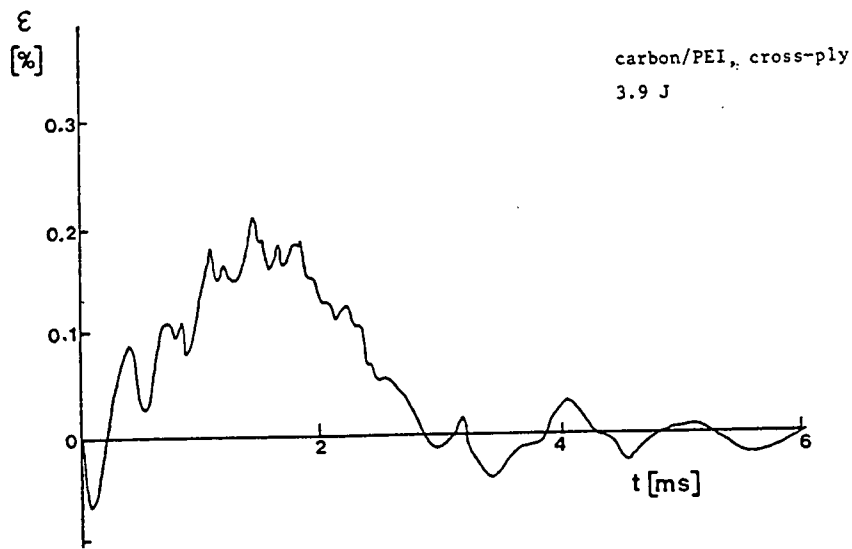
figure 6.25
Strain-time and
contact force-time
curves for cross-
ply carbon/PEI,
impact energy 3.9 J
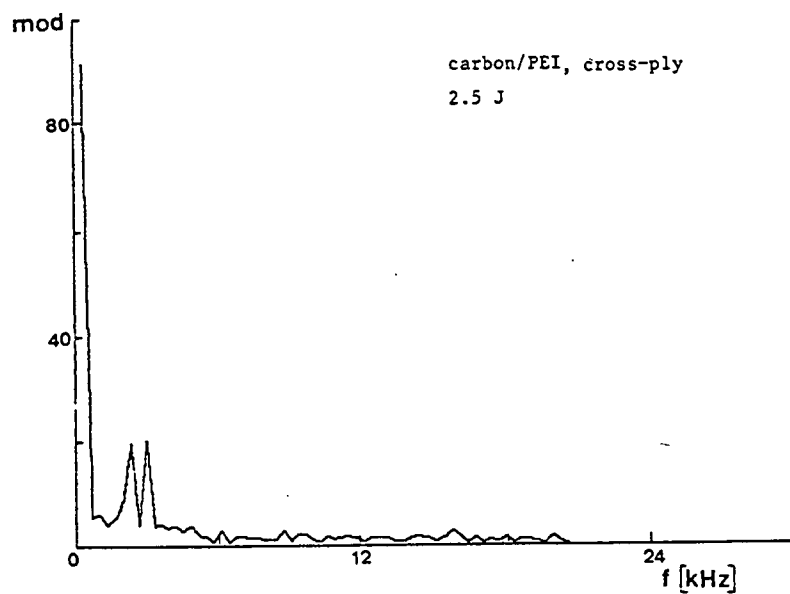
figure 6.26
Frequency spectrum
of the strain-time
curve of fig.6.23.

figure 6.28 The maximum central deflection during impact and the permanent central deflection after impact as function of the impact energy T, for thermoplastic composites.
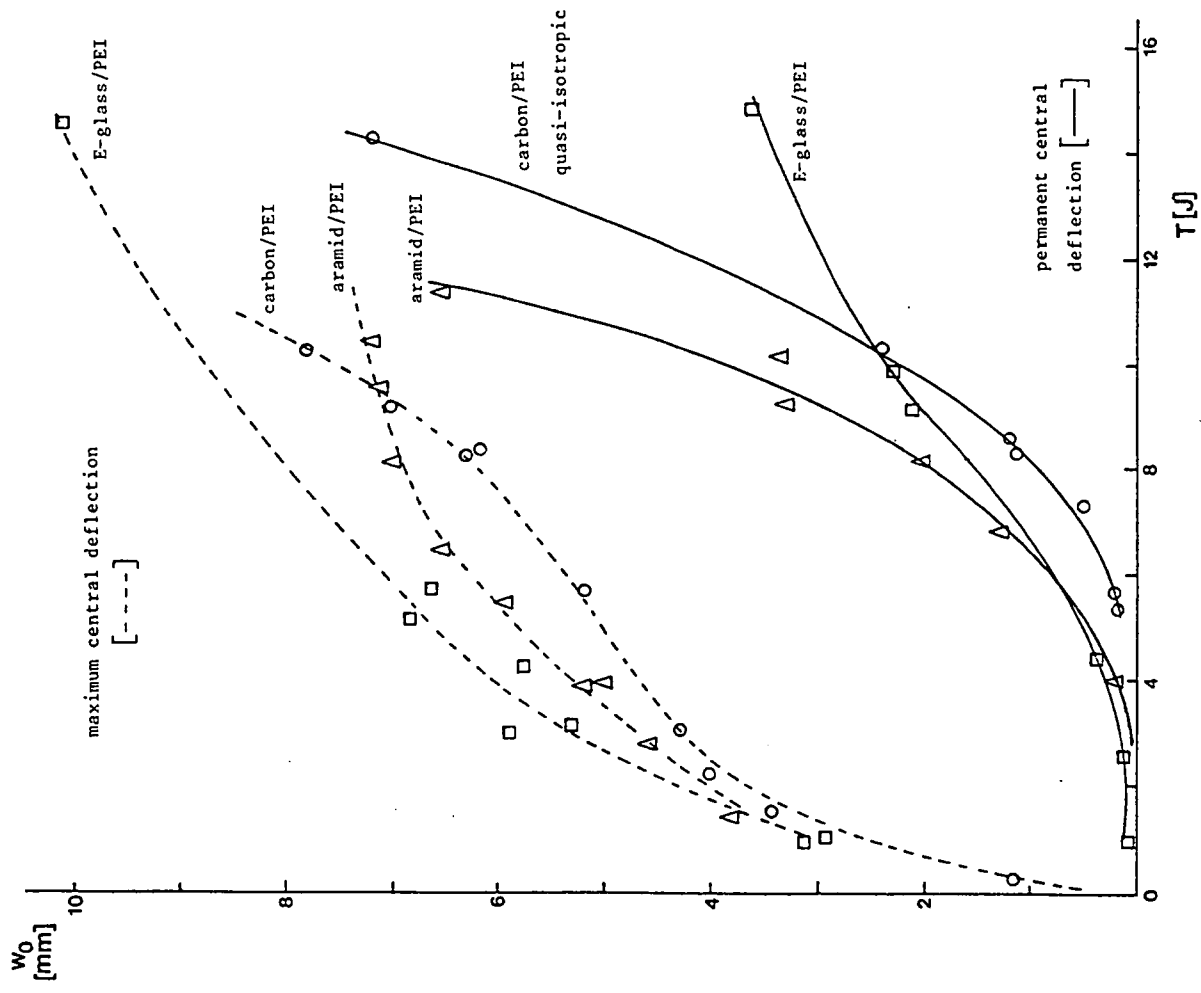
figure 6.27 The maximum central deflection during impact and the permanent central deflection after impact as function of the impact energy T, for aramid ARALL and monolithic aluminium.
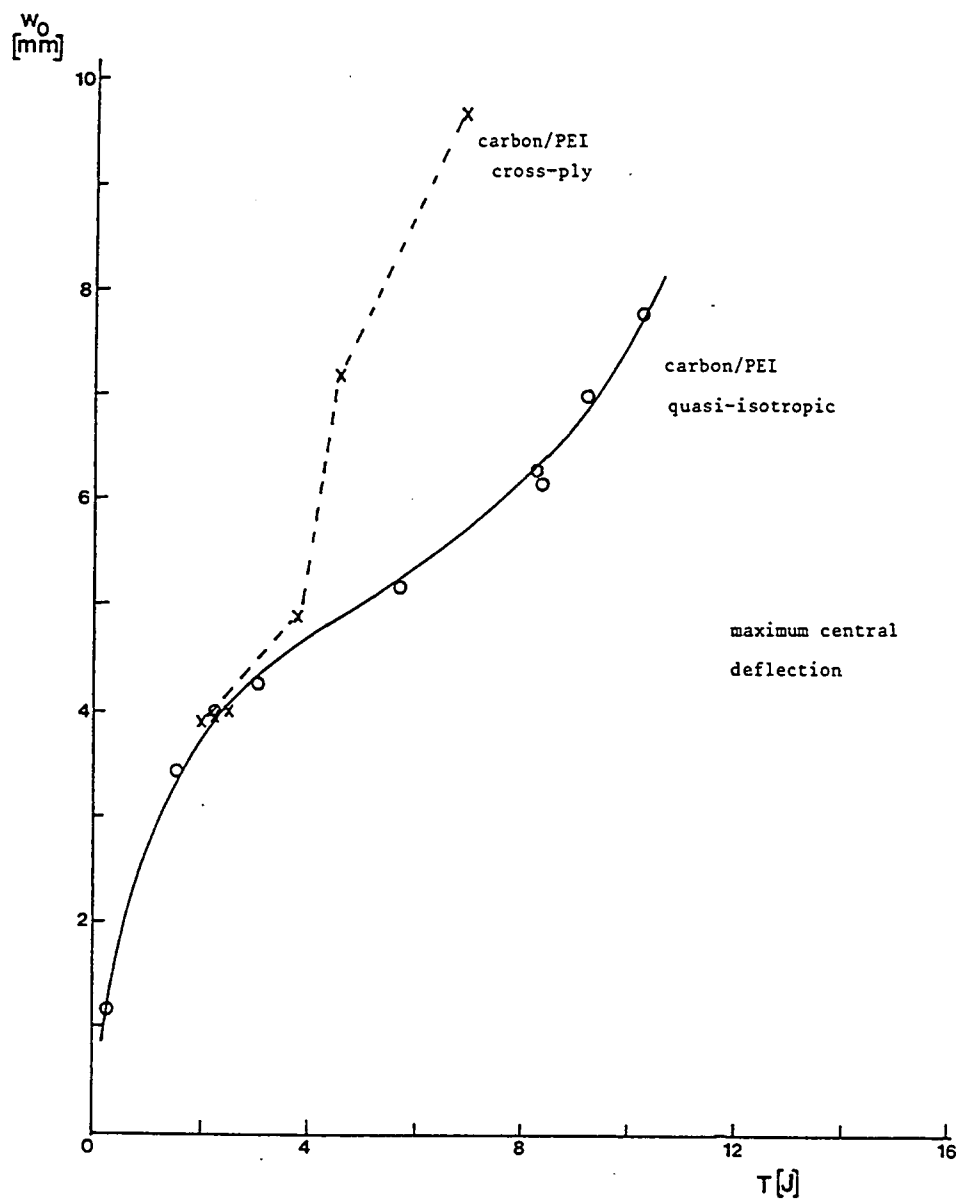
figure 6.29 The maximum central deflection during impact as function of the impact energy T, for the quasi-isotropic and cross-ply carbon/PEI specimens.

figure 6.30 The maximum central deflection during impact as function of the impact energy T of the monolithic aluminium and quasi-isotropic carbon/PEI specimens with two thicknesses.
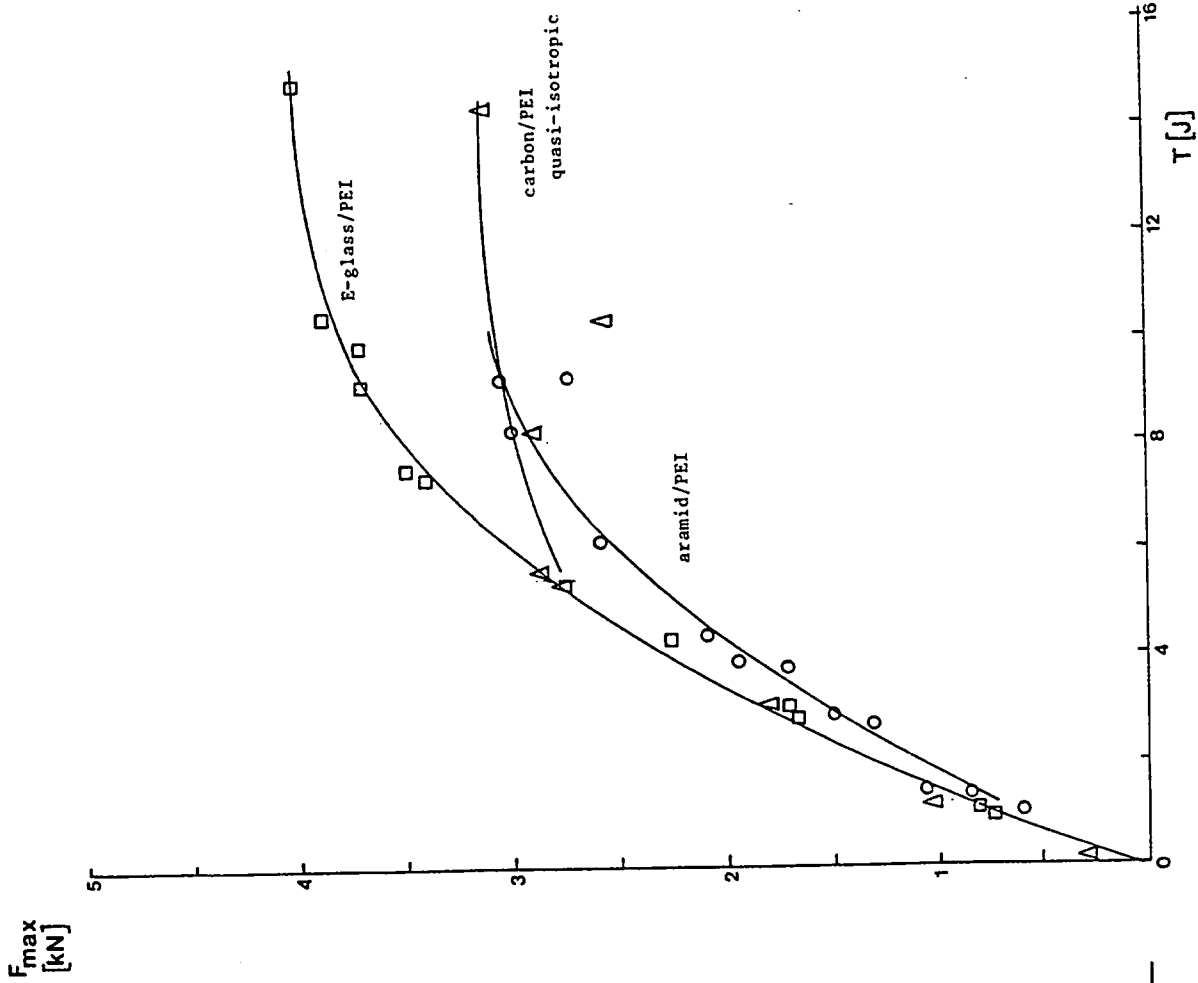
figure 6.32 The maximum force during impact as function of the impact energy T for the thermoplastic composite specimens.
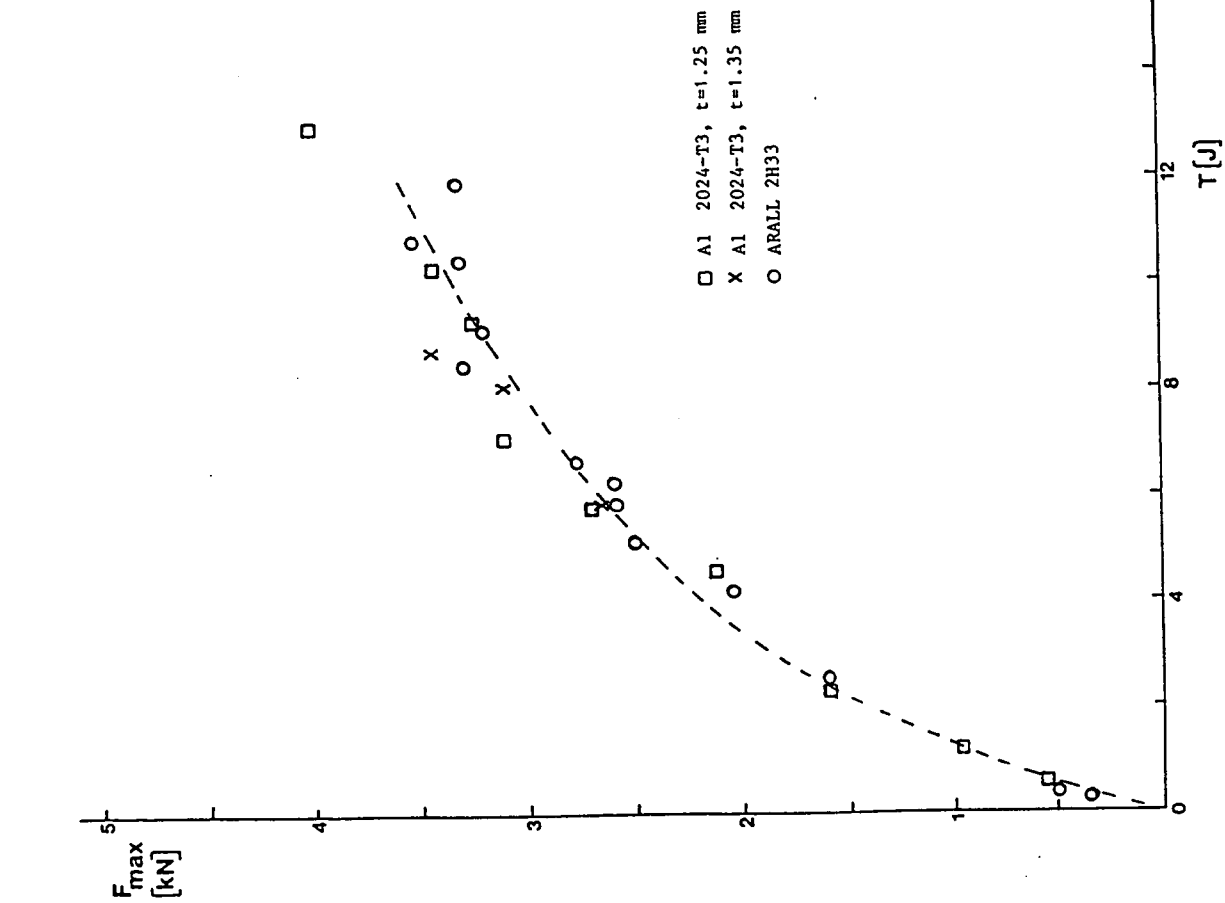
figure 6.31 The maximum force during impact as function of the impact energy T for the monolithic aluminium and aramid ARALL specimens.

□ Al 2024-T3, t=1.25 mm
X Al 2024-T3, t=1.35 mm
O ARALL 2H33

177
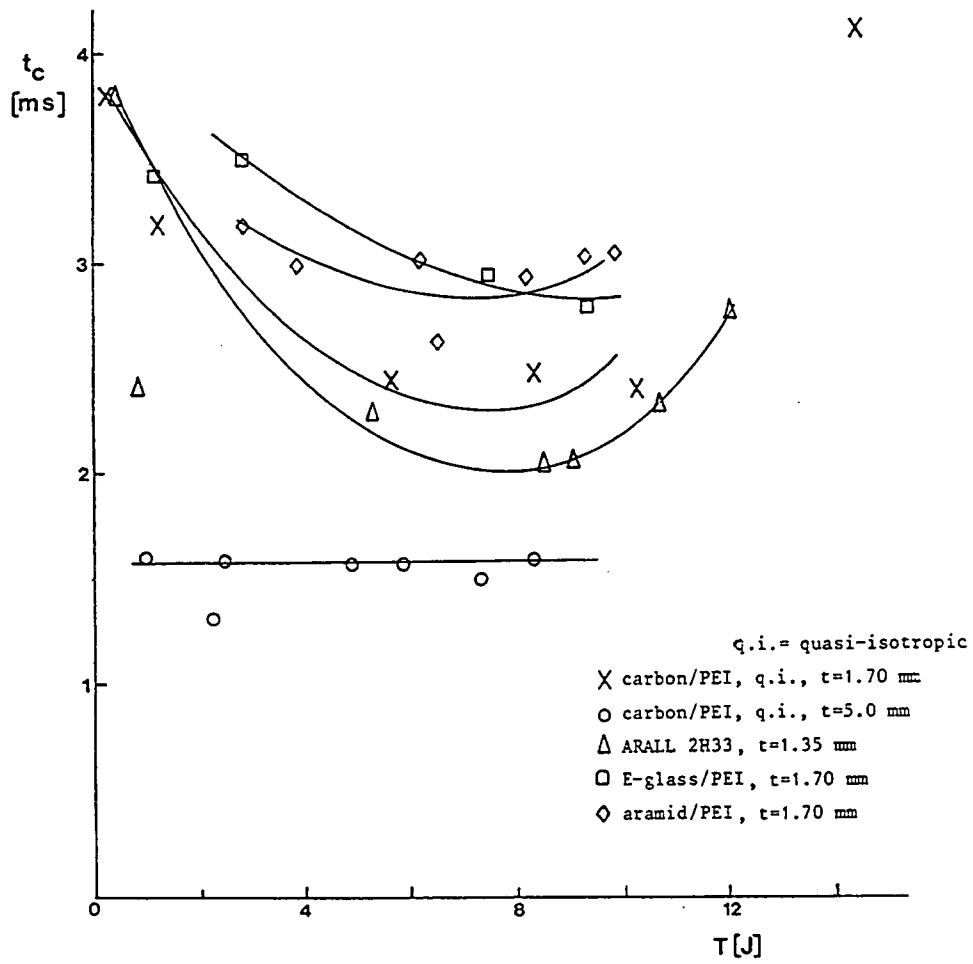
figure 6.33 The contact time as function of the impact energy T.
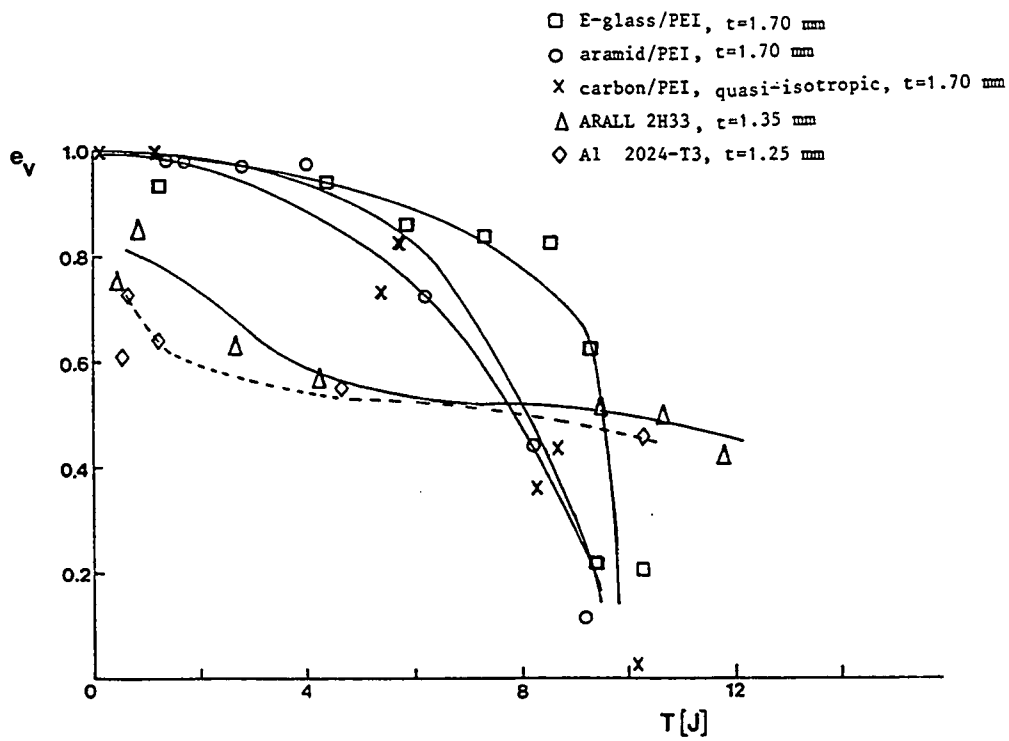
figure 6.34 The velocity restitution coefficient as function of the
impact energy T.

179
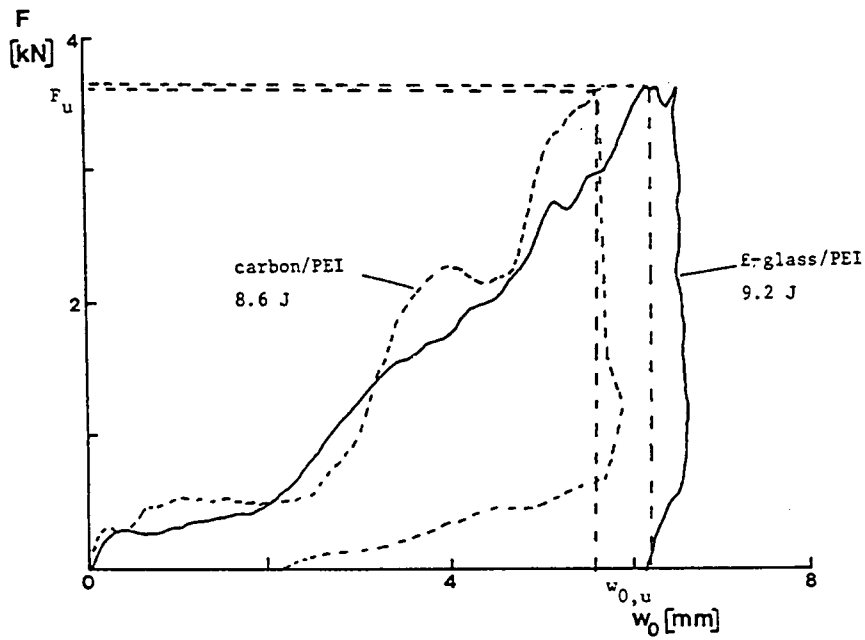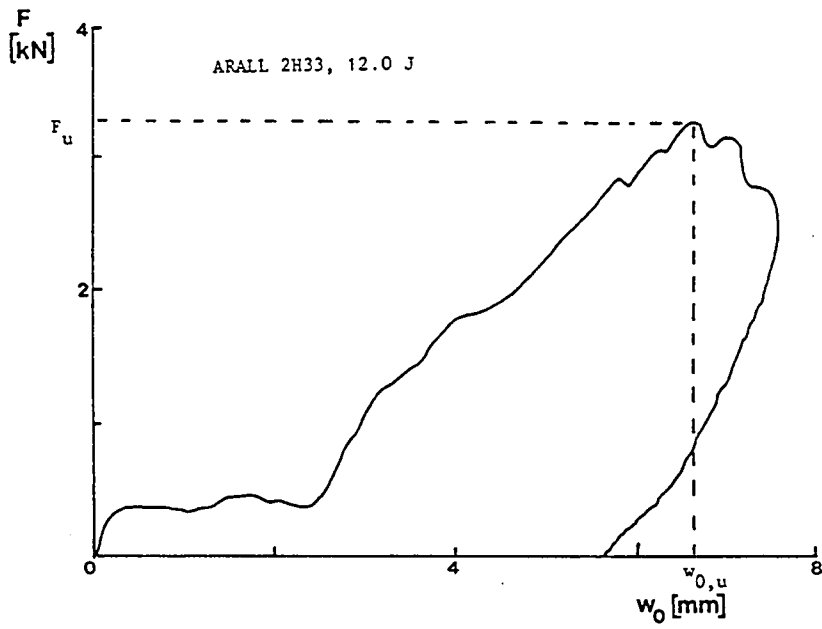
figure 6.35 Dynamic force-deflection curves for perforated
specimens, with ultimate values.
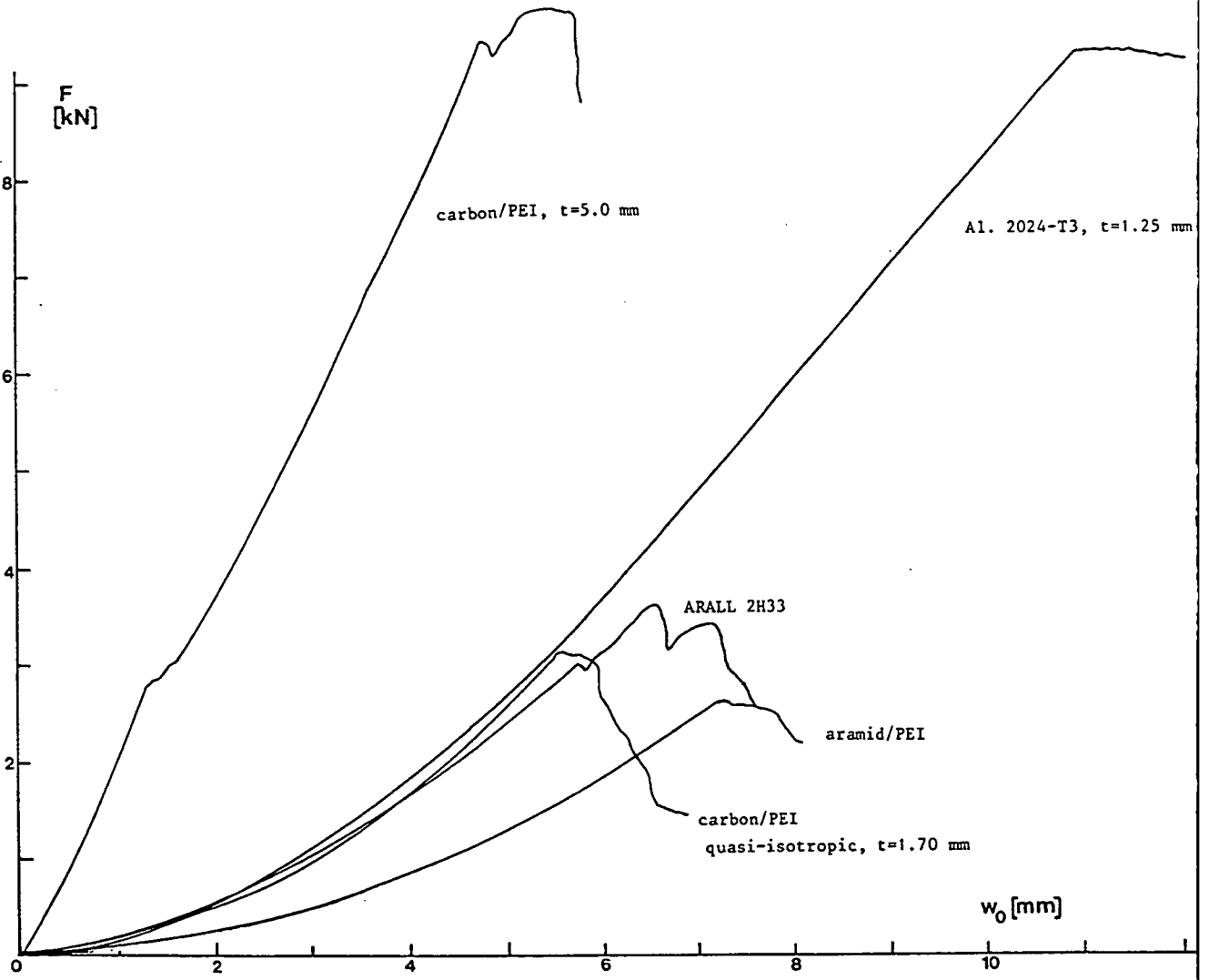
figure 6.36 Quasi-static force-deflection curves.
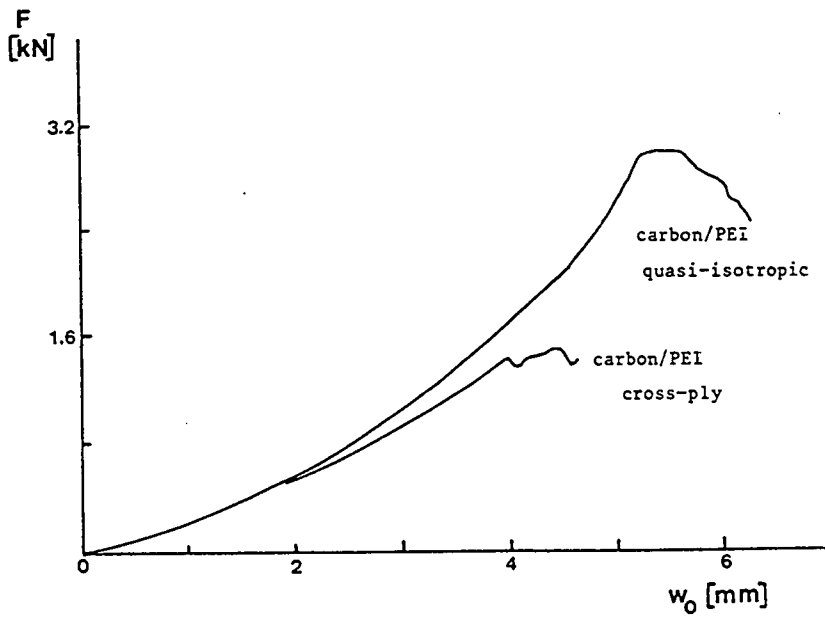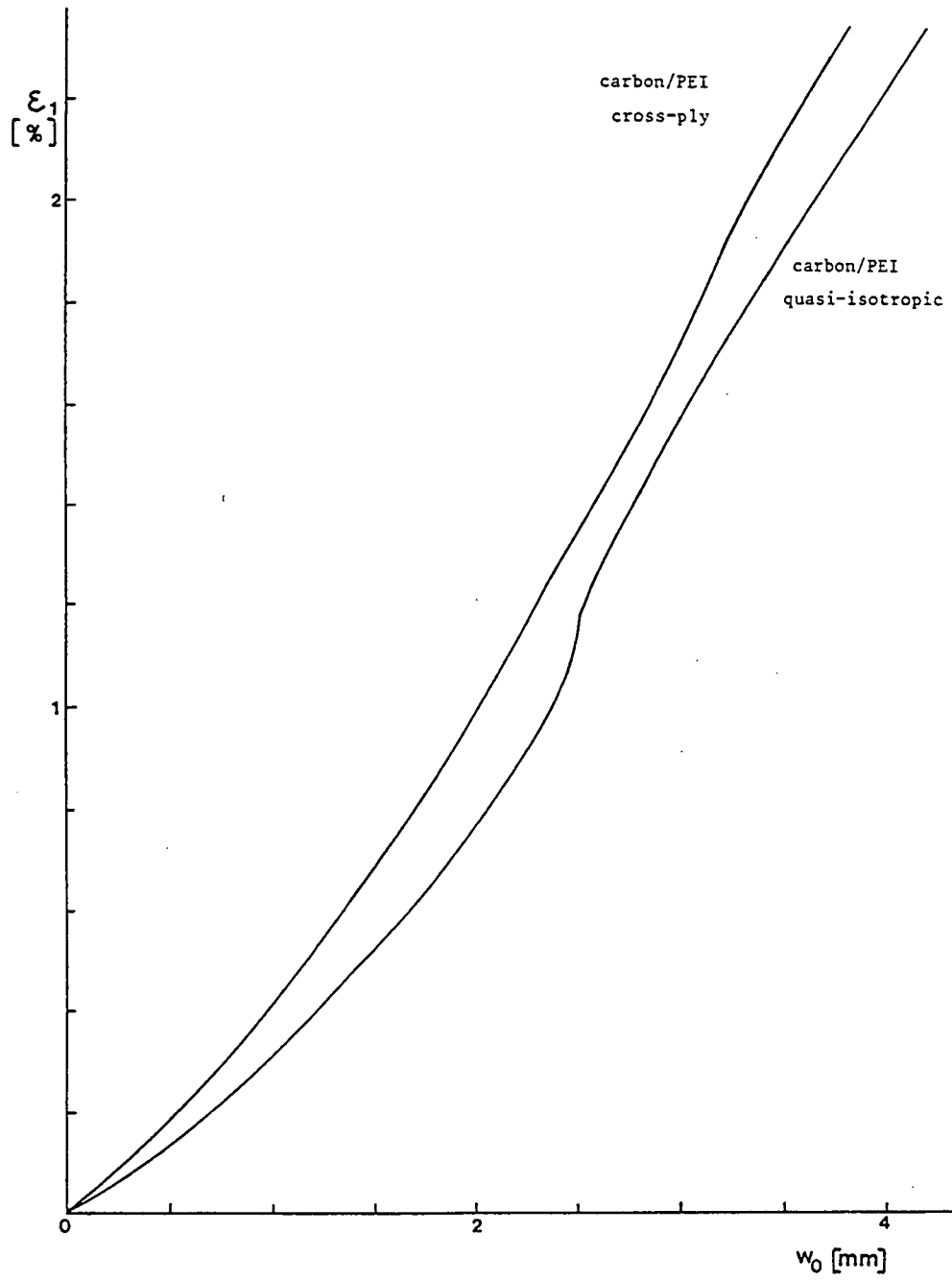

figure 6.37
Quasi-static force-deflection curves

181

figure 6.38 Central strain vs. deflection during quasi-static
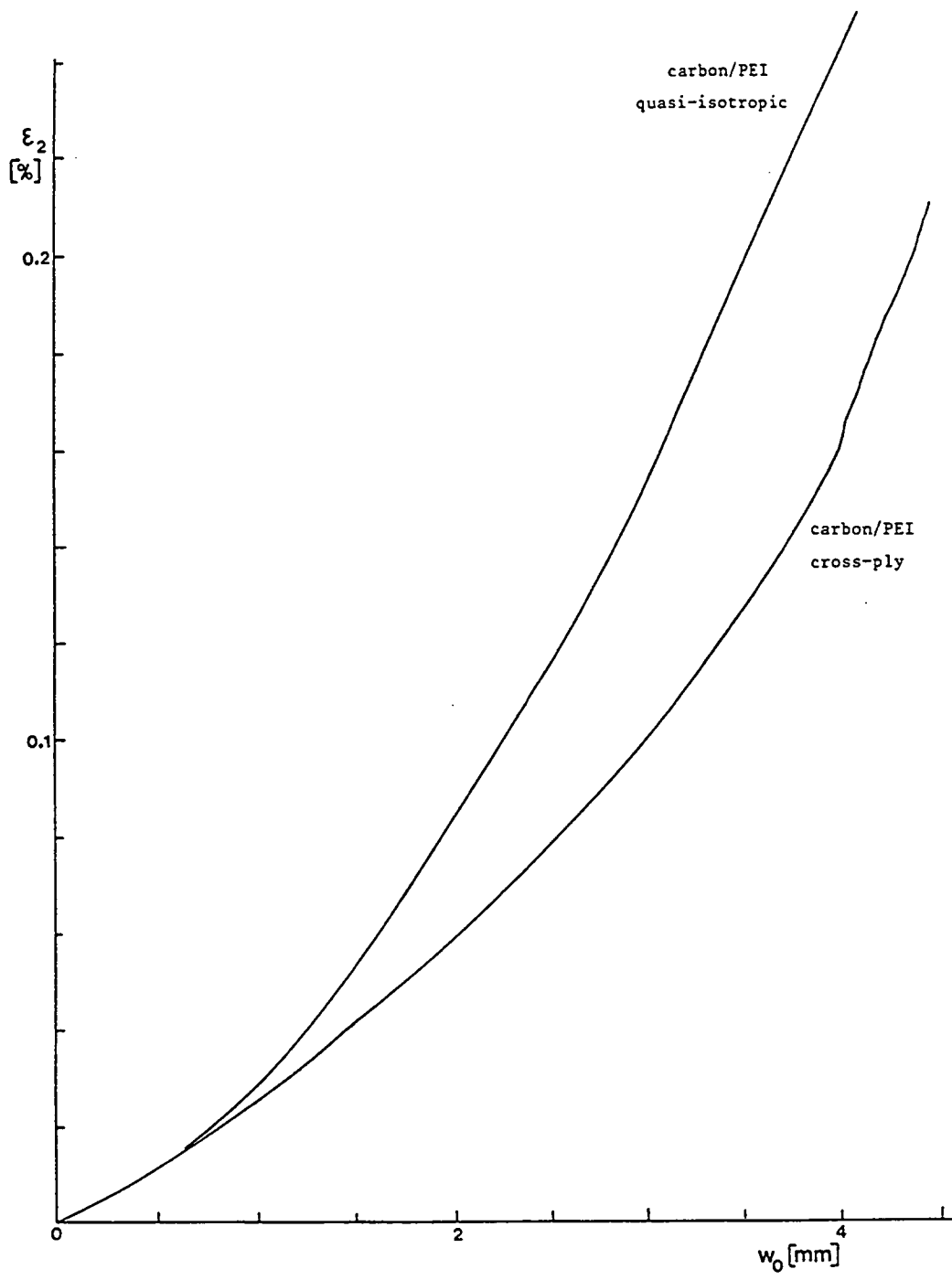loading of carbon/PEI specimens.

figure 6.39 Strain 20 mm from the loading point vs. deflection during quasi-static loading of carbon/PEI specimens.
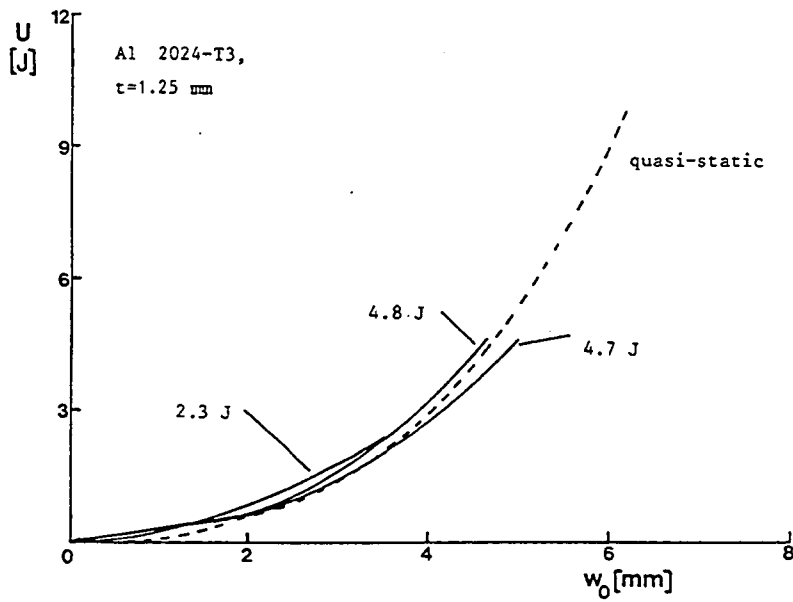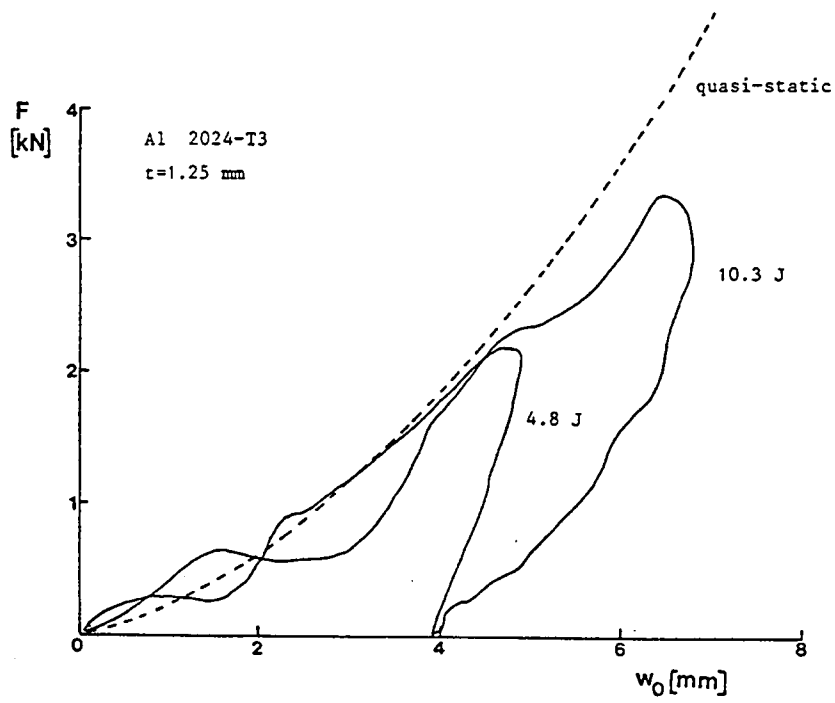
figure 6.40 Comparison of quasi-static and dynamic force-deflection
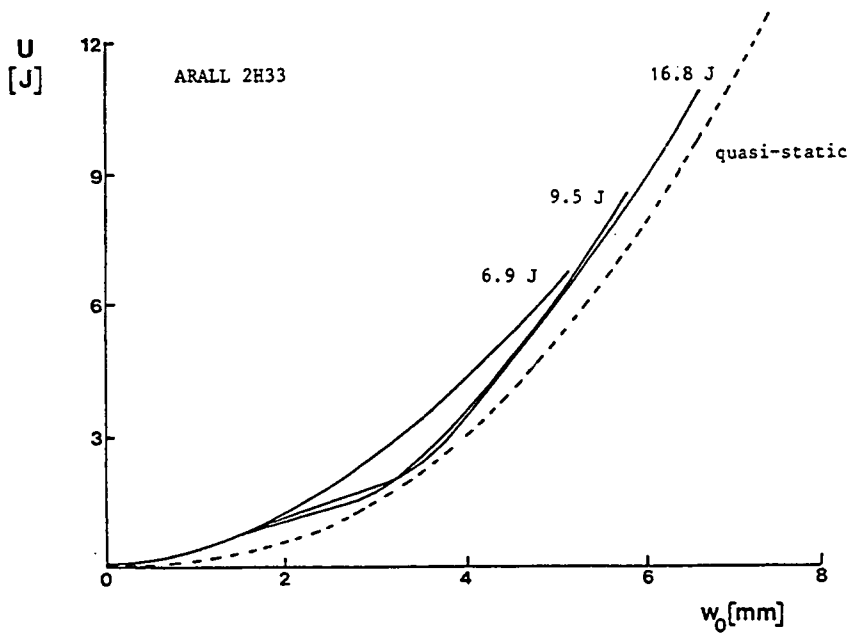and absorbed energy-deflection curves for monolithic Al 2024-T3.

figure 6.41 Comparison of quasi-static and dynamic force-deflection and absorbed energy-deflection curves for aramid ARALL.

185

figure 6.42 Comparison of quasi-static and dynamic force-deflection and absorbed energy-deflection curves for carbon/PEI.
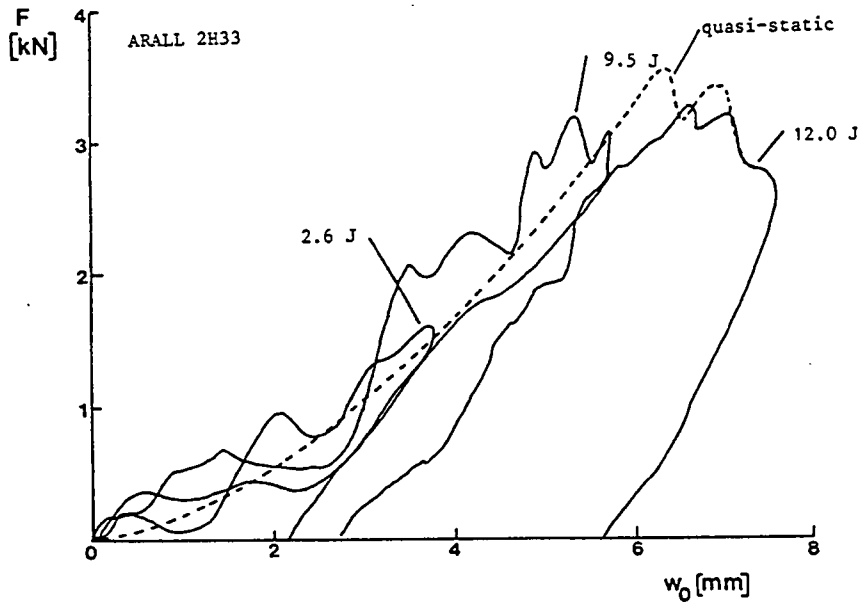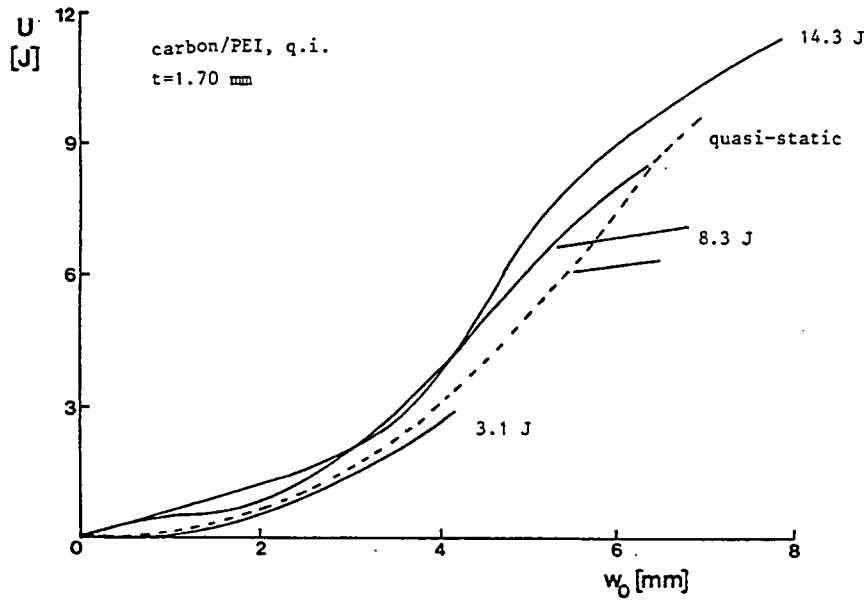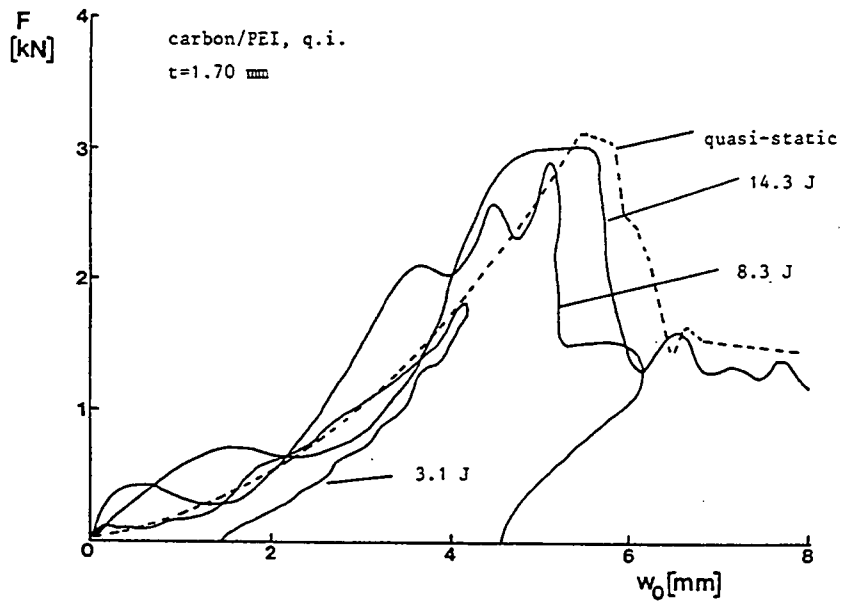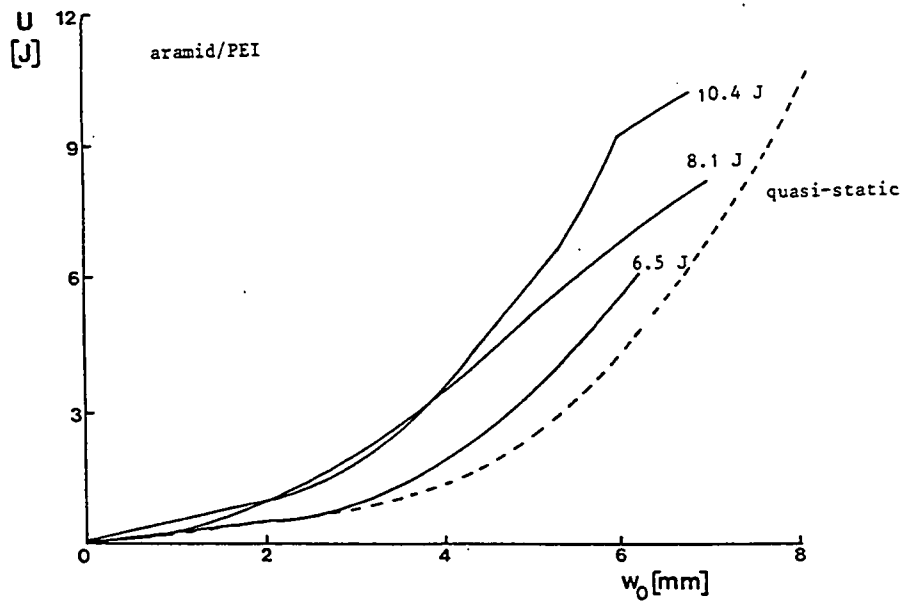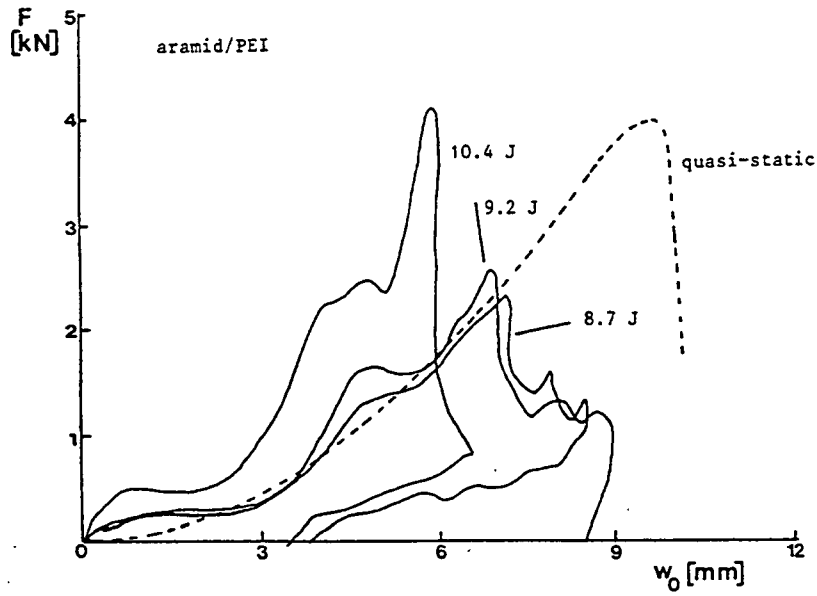
figure 6.43 Comparison of quasi-static and dynamic force-deflection
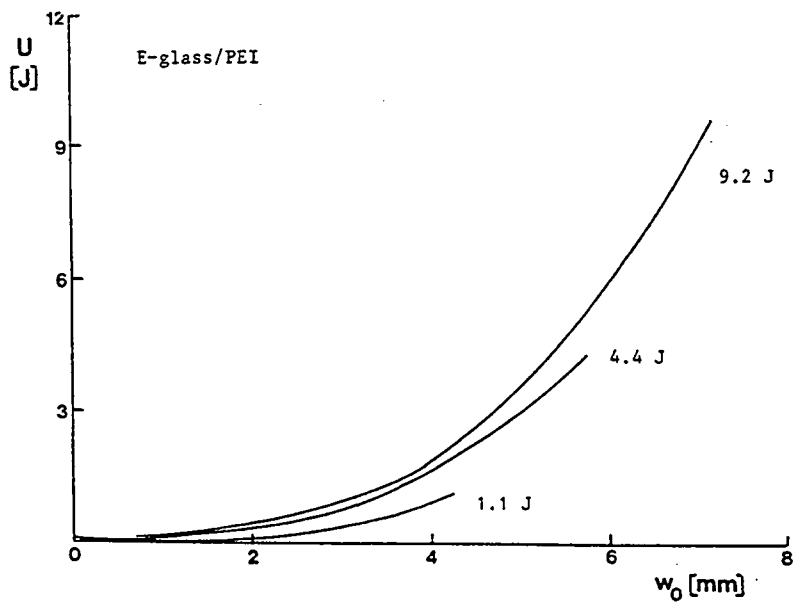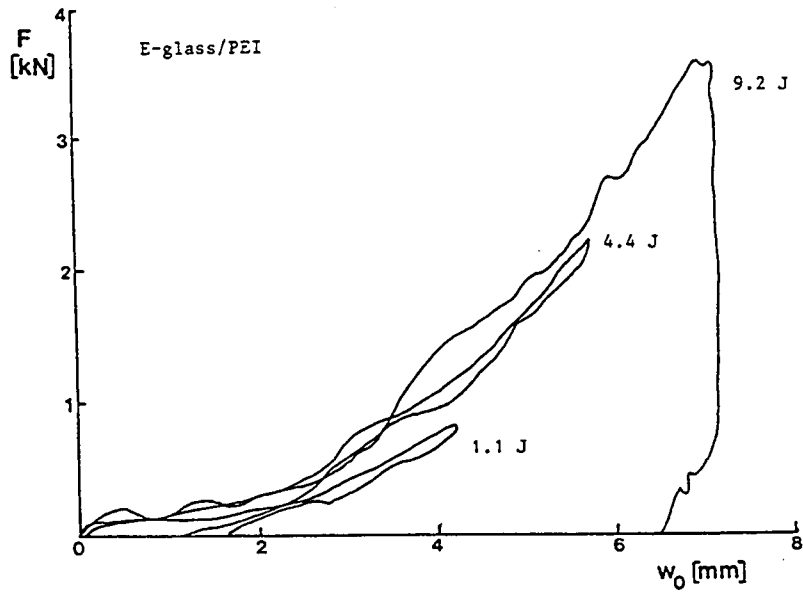and absorbed energy-deflection curves for aramid/PEI.

figure 6.44 Comparison of quasi-static and dynamic force-deflection
and absorbed energy-deflection curves for E-glass/PEI.

Chapter 7 Impact tests on specimens with a circular test area

In this chapter the results are discussed of impact tests on a larger number of different materials, with a normalized circular test area (ASTM D 3029, method FA). A description of the materials is given in section 7.1.

Quasi-static tests are also carried out. Such tests give accurate results with a small number of specimens. Moreover, they are easy to perform. Static loading can still be realistic, e.g. to simulate low velocity impact of service cars on aircraft structures. The results of the static tests are discussed in section 7.2. The results of the dynamic tests are presented in section 7.3, with a comparison to the static results (the maximum deflection- impact energy curves and the energy at first failure.

The force-deflection and impact energy-maximum deflection curves gathered in this chapter will be used for a comparison with the theoretical model in chapter 12.

7.1 Materials

A large range of materials in four categories was tested:

1. Monolithic Al-alloys (Al 2024-T3 and 7075 T6)
2. ARALL laminates (three types of fibres, different prepregs)
3. Composites built up from various prepregs
4. Polycarbonate, as a typical impact damage resistant material

A survey of the prepregs is given in table 7.1, with additional information on adhesive properties and fibre properties in tables 7.2 and 7.3 respectively.

As shown by table 7.1 three types of fibres were used, viz. high modulus aramid fibres (TWARON produced by AKZO), glass fibres (E-glass fibres and advanced R-glass (produced by Saint Gobain) and S_2 glass fibres (produced by Owens & Corning) and modern carbon fibres (T800 H obtained from Torayca and IM 600 from Tenax).

The large variety of prepregs tested is a result of development investigations on improved ARALL laminates (see also Roebroeks[1]). For that reason aramid fibres were used as UD fibres and as a weave. Another

option was to use the thermoplastic adhesive (PEI = polyetherimide). In a cooperation with the glass fibre producer (Saint Gobain) and an adhesive producer (Ciba Geigy) different types of glass fibre/adhesive combinations have been considered for application in GLARE. Moreover, there was a strong need for thinner prepreg layers (i.e. 0.1 mm instead of 0.2 mm) in view of cross-ply applications in GLARE.

Several types of composites were tested:

a. To compare ARALL with pure composites, cross-plies were tested of several thicknesses with the same fibre/adhesive system as the ARALL laminates. Cross-plies were tested with R-glass (R_2, R_3, R_4, R_5, see table 7.1) and carbon (C_2, see table 7.1) prepregs.

b. Thermosetting composites were tested with the Tenax HTA 12000 fibre, fibre volume fraction 50%. The strength of this fibre is 3970 MPa, the stiffness is 240 GPa, the strain to failure 1.65%.

The matrix was a non-modified epoxy.

c. Thermoplastic composites, matrix material polyetherimide (PEI).

Fibres: -carbon Hercules graphite fibre AS-4 (strength 3690 MPa, stiffness 230 GPa), fibre volume fraction 42%. Both square weave and unidirectional prepregs were tested.

-aramid Twaron HM (properties: see table 7.3). Both square weave and unidirectional prepregs were tested.

Fibre volume fraction: 42%.

As a typical impact resistant material polycarbonate (two thicknesses) was tested.

7.2 Quasi-static loading

7.2.1 Test method

The standard configuration was used: indentor radius R=7.5 mm and radius of the test area a=40 mm. The square specimen with the dimensions of 150x150 mm^2 was clamped between two clamping plates (schematically shown in figure 7.1a). The clamping was established by bolts through the clamping plates just beside the specimen. The specimens were loaded with a rate of

approximately 1 mm/min.

Figure 7.1b shows the effect of the clamping conditions on the force-deflection curve. It was relatively easy to fully clamp the specimen, in contrast with the square specimens (see figure 6.2). A square specimen will have a deformation mode which tends to lift the clamping plate (figure 6.3), whereas a circular boundary of the test area will fit better to the deflection shape of the specimen. A sharp imprint in the specimen caused by the clamping plate at the edge of the clamped area was observed. This showed that the slipping of the specimen was constrained.

7.2.2 Results

The difference between the force-deflection curves of monolithic Al-alloys, composites and ARALL was already discussed in section 6.1.

Tables 7.4 to 7.9 give the force, deflection and absorbed energy values at first failure and the values at ultimate load (if applicable). These tables deserve some careful examination. Tables 7.4 to 7.9 show the effects of the fibre and alloy type, fibre orientations and thickness of the ARALL laminates. The tables also offer a comparison between the behaviour of ARALL with composites and monolithic aluminium. This will be discussed with some illustrations below.

A. Observations on the force-deflection curves

Al 7075 ARALL vs. Al 2024 ARALL
Differences between the force-deflection curves of ARALL 2H32 (Al 2024-T3), 7H32 (Al 7075-T6) and 2S32 (Al 2024-T3) are illustrated by figure 7.2. The influence of the alloy type on the force-deflection curve until first failure is small.

fibres in ARALL
The effect of three types of fibres on the force-deflection curves is shown in figure 7.3, where the curves are drawn for ARALL 2H32 (aramid), $2R_4{}^232$ (R-glass), $2C_2{}^232$ (carbon) and monolithic aluminium 2024-T3. Until fibre

failure the influence of the fibre type on the curve is small. The carbon ARALL fails first (fibre failure), followed by aramid ARALL (fibre failure), R-glass ARALL (aluminium failure, fibres intact) and monolithic aluminium.

poststretching

Poststretching of ARALL lowers the energy absorption capability as shown in figure 7.4 for ARALL 7H32 (no poststretch) and 7H32,.42 (0.42% poststretch). ARALL 7H32 has a fibre critical failure. Poststretching causes an initial tensile stress in the fibres, and therefore causes a reduction of the energy at first failure.

monolithic aluminium vs. GLARE

Aluminium laminates with R-glass fibres may behave better than monolithic aluminium. A comparison between the force-deflection curves of monolithic aluminium and GLARE $2R_4{}^2 33/C55$ is made in figure 7.5. Both materials have approximately the same thickness. The GLARE variant shown in the figure has a higher absorbed energy value at first failure than the monolithic material. The stiffness of the GLARE specimen is lower than of Al 2024-T3 (see also figure 7.3), but the deflection at first failure is higher.

cross-ply composite vs. GLARE

Figure 7.6 compares the behaviour of a typical ARALL variant and a cross-ply composite with the same fibre/matrix system and thickness. The composites fail at lower absorbed energy values. The dip at first failure in the force deflection curve of these materials is relatively small, it is accompanied by clearly audible cracking of the fibres.

thickness effect

In general an increase in thickness of a material will cause an improved energy at first failure. However, increase in thickness may reduce the absorbed energy at failure (table 7.4 and figure 7.9). This is the case for monolithic aluminium as well as for some ARALL types. For monolithic material it may be partly due to the fact that material with a different thickness may not have the same material properties.

However, also another mechanism will be important. Figure 7.7 shows the effect of adding fibre adhesive layers to GLARE with two aluminium layers $2R_4{}^x32$ (x = number of intermediate prepreg layers, if x is omitted x=1). As shown in figure 7.7 the specimen thickness is then increased. The average stiffness is thus increased, but the force and deflection at failure (in the Al sheets) is decreased. For a given deflection the thicker material will have higher strains in the material. This means that the failure strain will be reached at a lower deflection for a thicker material. In this way the total absorbed energy can be lower than for a thinner material which fails at a higher deflection.

The thickness of the aramid ARALL was increased to see whether an interlaminar shear type of failure would occur. Figure 7.8 shows the force-deflection curves of aramid ARALL 2H3x with different thicknesses, obtained by adding prepreg and aluminium layers (x = number of aluminium layers). In this figure it is remarkable that the load at failure rises for increasing thickness, while the deflection at failure is approximately constant. The tendency of a larger variation of the force than of the deflection at failure for a variation of the sheet thickness is also found for other materials in tables 7.4 to 7.9. The 2H38 (8 Al layers) and 2H310 (10 Al layers) aramid ARALL materials showed a typical change of the stiffness at a deflection of 1 mm, which may be associated with interlaminar shear failure. However, the delaminated area visible after removal of the aluminium layers by etching, was small (diameter of 15 mm) and approximately limited to the contact area between indentor and plate.

B. Observations on the absorbed energy at first failure

monolithic aluminium vs. ARALL

The comparison in figures 7.9 and 7.10 of monolithic aluminium and GLARE is important. Results of GLARE with two types of fibres are presented (R_2 and R_4, see tables 7.1 and 7.3). Figure 7.9 shows the energy at first failure vs. the sheet thickness. In figure 7.10 this quantity is plotted as a function of the surface density ρ_s (to take into account the lower density of aramid ARALL relative to GLARE and monolithic aluminium). In these figure the effect of two different types of R-glass fibres (R_2 and R_4) in

193

GLARE is evident. For the GLARE variants with the R_4 prepreg (RA 9041 fibre: σ_u =5200 MPa, ε_u = 5.9%) the absorbed energy at first failure was $\approx$1.5x the energy for GLARE with the R_2 prepreg (RC 10 fibre: σ_u = 3270 MPa, ε_u = 3.8%). The GLARE variant with the R_4 prepreg has first failure energies similar to those of the monolithic material. The behaviour of the R-glass ARALL types is superior to the aramid ARALL variants.

pure composites vs. ARALL

In figures 7.11 and 7.12 the energy at first (fibre or aluminium sheet) failure and the ultimate energy values (energy at ultimate load) are plotted as a function of the sheet thickness and of the surface density respectively. The behaviour of ARALL laminates is compared to the behaviour of cross-ply composites (both with R_2 prepreg). In figure 7.12 the first failure energies are plotted as a function of the surface density to take into account the lower density of the composites. The absorbed energy vs. the sheet thickness for the R_4 prepreg and the carbon prepreg C_2 are plotted in figures 7.13 and 7.14 respectively. The ARALL materials exhibit higher absorbed energy at first fibre failure than the corresponding cross-ply composites. Probably it is favourable to have an Al outer layer, because their failure strain will be higher. The R-glass composites are superior to the carbon prepreg composites in absorbing energy until ultimate load.

cross-ply composites

The absorbed energy at fibre failure and the ultimate absorbed energy are presented in figures 7.15 and 7.16 (R-glass and carbon respectively), to compare the cross-ply composites of the various prepregs. The R-glass composites with the RA 9041 fibre (R_3, R_4 and R_5) have similar first failure energies, although there is a difference in fibre volume fraction and resin (see: table 7.1). The absorbed energy at first failure of the RC 10 R-glass fibre composites (R_2) is 50% lower.

The thermoplastic carbon composite had a somewhat higher absorbed energy at first failure and at ultimate load than the thermoset (figure 7.16), but the difference is small. The failure behaviour is dominated by the fibre.

histograms for one thickness

To compare the energy values of the materials for one thickness, figures 7.17 and 7.18 show histograms for t=0.8 and (approximately) 1.4 mm.

Figure 7.17 shows that the absorbed energy at first failure of the cross-ply ARALL variants is slightly smaller than for the unidirectional carbon and R-glass ARALL types. This is also true for the ARALL variants with the R_2 fibre (RC 10) in figure 7.18 (unidirectional GLARE $2R_2^2 33$ and cross-ply GLARE $2R_2^2 33/C55$). The opposite trend was found for the R_4 fibre (RA 9041, $2R_4^2 33$ and $2R_4^2 33/C55$ in figure 7.18). This material showed first failure at ultimate load.

It is also remarkable (see figure 7.18) that the ARALL laminates with the stronger RA 9041 fibre (R_4 and R_5 prepreg) showed fibre failure only at ultimate load, while the weaker fibre (R_2 prepreg) failed below the ultimate load.

failure modes in ARALL

There are two types of failure which were found in the ARALL laminates (as indicated in tables 7.4 to 7.9): fibre critical failure and aluminium critical failure. In the tests of chapter 6 only fibre critical behaviour was observed, because only aramid ARALL was tested. The GLARE variant of ARALL shows fibre critical or aluminium critical behaviour depending on the type of glass fibre and the lay-up. In carbon ARALL only fibre critical behaviour was observed. For cross-ply ARALL laminates it is sometimes difficult to discriminate between both types of failure.

An aluminium critical failure will cause a crack in the rolling direction, first at the convex (not loaded) side of the specimen. It is not necessarily followed by fibre failure and the load can further increase. A fibre critical failure will have a crack perpendicular to the fibre direction. The fibre direction is usually the rolling direction of the aluminium layers. No fibre failure was observed without aluminium failure. This means that if the fibres run in the rolling direction of the specimen, the visible crack on the convex side will run perpendicular to the rolling direction in the case of fibre critical failure.

195

In an ARALL laminate with two aluminium layers and one intermediate unidirectional prepreg layer (2/1 lay-up), the difference between the two types of failure is clearly visible. The visible damage at the outside of the specimens is shown in figure 7.19.

Cross-sections of the sheet materials (2/1 lay-up) with the cracks are given in figures 7.20 and 7.21, for a fibre critical failure and an aluminium critical failure respectively. In the case of fibre failure (figure 7.20) a crack runs from the boundary of the contact area at the side of the indentor, to the opposite side near the centre of the specimen.

In the case of an aluminium failure in the 2/1 lay-ups (for the GLARE laminates, see figure 7.21), the crack runs through the cross-section in fibre direction at the edge of the contact area. If a crack is initiated, it will easily grow because there is a low restraint on crack opening. A large crack will be created. This crack grows towards the symmetry axis of the specimen as indicated in figure 7.22. The fibres remain intact.

energy restitution coefficient and permanent deflection

Some of the specimens were unloaded several times at several values of the deflection to determine the permanent part of the deflection and the amount of energy absorbed by plastic deformation.

A typical load-deflection curve is given in figure 7.23. After unloading from the force at w_0, a permanent deflection $\overline{w}_0$ will be present in the plate. Figure 7.23 shows how the elastic energy U_{el} was determined. To determine the elastic energy as a function of the deflection, the specimen was unloaded several times before final failure. In this way also the permanent part of the deflection $\overline{w}_0$ was determined as a function of w_0.

The energy restitution coefficient e_E (defined as the ratio of the elastic part of the absorbed energy released during unloading and the total absorbed energy) is given in figure 7.24 and 7.25 for aluminium alloys and ARALL respectively. It is remarkable that the energy restitution coefficient of the aluminium alloys neither depends on the thickness nor the alloy type. For energies higher than 3 to 4 J the e_E value is

approximately 0.5 for both monolithic aluminium and ARALL. The composites deform almost elastically until first fibre failure ($e_E \cong 1$).

The permanent deflection as a function of the absorbed energy is shown in figures 7.26 and 7.27 for ARALL and monolithic aluminium. Al 7075-T6 has a smaller dent after unloading than Al 2024-T3, but fails at a lower absorbed energy. The difference between the failure energies of Al 7075-T6 aramid ARALL and Al 2024-T3 aramid ARALL types is smaller. The S-glass ARALL laminate has a deeper dent after unloading than 2H32 aramid ARALL but the energy at failure is higher.

7.2.3 Discussion

thickness effect

In general the absorbed energy at first failure is improved by increasing the thickness of the material, but it is remarkable that it is not always improved. The absorbed energy at failure vs. the sheet thickness for monolithic aluminium shows a local maximum (figure 7.9). The absorbed energy at first failure of GLARE 2R32 is decreased by increasing the thickness (adding prepreg layers, $2R^232$ and $2R^332$, figure 7.7), but the effect is relatively small ($2R_432$: U_f = 11.4 J, $2R_4{}^332$: U_f = 9.6 J).

comparison ARALL and monolithic aluminium

ARALL generally has a smaller first failure energy than monolithic aluminium of the same thickness. This is especially true for ARALL with aramid and carbon fibres. With the R_4-glass prepreg it was possible to reach results comparable to the values for monolithic material, while some lay-ups showed even higher first failure energies (figure 7.9 and 7.10).

comparison of ARALL with various types of fibres

Although the carbon fibres have higher strength and an approximately equal strain to failure as the aramid fibre (and also an higher failure energy, see table 7.3), the ARALL variants with carbon fibres have a significantly lower energy until first failure than aramid ARALL (figure 7.17, table 7.5 and 7.7). Probably the higher stiffness of the material causes a higher concentration of the deformation around the loaded zone, and consequently

197

the absorbed energy at first failure is lower.

The ranking of the prepreg systems in ARALL (with respect to the absorbed energy at first failure) is as follows (as an illustration the energy values at first failure are given for a typical cross-ply ARALL with a thickness of 1.4 mm, and a unidirectional ARALL with a thickness of 0.8 mm):

code	fibre/adhesive	v_f (%)	U_f (J) t=1.4 mm	U_f (J) t=0.8 mm
R_4	R-glass RA 9041/DLS 1115	50	17.3	10.4
R_5	R-glass RA 9041/DLS 1115	55	15.4	
R_3	R-glass RA 9041/DLS 1095	60	9.07	
R_2	R-glass RC 10 P109/DLS 1095	60	7.72	7.34
H	aramid Twaron HM/AF 163-2	47	6.0	4.25
C_2	carbon T800H/Fibredux 924C	56		2.51
C_1	carbon IM 600/Fibredux 924C	58		2.3

The ranking of the fibres in the prepregs in ARALL is according to the ranking of the area under the stress-strain curve until fracture of the fibres (fracture energy). The ranking is shown in

figures 7.17 and 7.18. The application of

the RA 9041 fibre implies a large improvement of the properties relative to the RC 10 fibre, as might be expected from the fibre properties (table 7.3).

It is remarkable that the RA 9041/DLS 1115 system with a fibre volume fraction of 55% (R_5) has a lower failure energy than the system with a fibre volume fraction of 50% (R_4). (Compare this with the very good behaviour of the thinner material with adhesive only and no fibres: 2AF33, t=1.32 mm in table 7.7, failure energy 14.8 J). Adding fibres to the laminate will not always have a positive effect on the damage resistance.

The relatively large influence of a more brittle adhesive (DLS 1095, R_3) compared with the tougher DLS 1115 (R_4) is also remarkable.

The type of the fibre has only a minor influence on the elastic part of the absorbed energy, see figure 7.25. The type of aluminium also has a small influence on this quantity (figure 7.24 and 7.25). The permanent deflection is more affected by the fibre and alloy type (figure 7.26 and 7.27). During plastic deformation the difference in strain hardening between Al 2024-T3 and 7075-T6 become important, and the interaction between fibre and metal layers becomes more significant.

A cross-ply ARALL variant will not always have an improved first failure energy compared with a unidirectional variant. The cross-ply ARALL types with aramid had a better performance than the unidirectional aramid ARALL types; the same was true for the (high strength) R_4-glass GLARE variants. Both the R_2-glass and the carbon C_2 ARALL variants showed the opposite behaviour (table 7.5 to 7.7 and figures 7.17 and 7.18). This can explained as follows. The presence of fibres in a direction increases the stiffness in that direction which is favourable (more area under the force-deflection curve), but also limits the failure strain in that direction. One of the two effects will win.

comparison of ARALL and composites

The ARALL laminates have a higher energy at first fibre failure than the corresponding cross-ply composite with the same fibre/matrix system. This is probabaly due to the favourable effect of having an aluminium layer at the outside of the material, because the maximum strains will be reached in the aluminium layer at the convex (not loaded) side.

The cross-ply composites with R-glass have a higher absorbed energy value at ultimate load than the monolithic Al 2024-T3 and the ARALL laminates: the material has a high resistance against perforation.

comparison of various composites

The ranking of the cross-ply composites is (figure 7.15 and 7.16):

code	fibre/adhesive	v_f (%)	
R_4	R-glass RA 9041/DLS 1115	50	small difference in first failure energy
R_5	R-glass RA 9041/DLS 1115	55	
R_3	R-glass RA 9041/DLS 1095	60	
R_2	R-glass RC 10 P109/DLS 1095	60	
C_2	carbon T800H/Fibredux 924C	56	

This ranking is the same as for the prepreg systems in ARALL.

The thermoplastic material has a somewhat higher energy at first failure than the thermoset. Especially the ultimate energy value is higher (see figure 7.16). The first failure energy of the carbon composites is very low compared to the R-glass composites, monolithic aluminium and ARALL.

comparison of Al 2024-T3 and 7075-T6

Monolithic Al 7075-T6 has 1/3 of the energy until failure of Al 2024-T3. This is directly related to the smaller area under the stress-strain curve of Al 7075-T6 compared to Al 2024-T3. The type of the alloy of the aluminium layers in aramid ARALL does not have a large influence on the first failure energy because of the fibre dominated failure behaviour (table 7.5). It might be expected that this will be different for the glass variant of ARALL with aluminium critical failure. In other words for GLARE the application of Al 7075-T6 might lead to a less favourable impact damage resistance than with Al 2024-T3.

polycarbonate

The behaviour of polycarbonate shows that a lot of energy can be stored in a material with a high strain to failure. This material absorbed much energy, not by a high ultimate load, but due to a large possible deflection. Compare:

material	t(mm)	U_f (J)	deflection(mm)
polycarbonate	1.2	49	29
Al 2024-T3	1.2	<15	<7

The polycarbonate tested has a tensile strength of 65 MPa only, but a strain to failure of approximately 100%.

This illustrates that there are basically two ways for a material to absorb much energy until first failure:

a. A high strain to failure, in this way large deflections are possible until failure.

b. A high strength, to assure a high failure load.

The stiffness of the material (and the stress-strain curve after yield) determines the strain distribution in the deflected sheet and the shape of the force-deflection curve, the strength and strain to failure of the material determine the deflection at failure.

7.2.4 Conclusions

1. The absorbed energy at first (fibre) failure of ARALL with aramid fibres is significantly improved by using R-glass fibres instead of aramid fibres. The effect of the application of a type of fibre in ARALL on absorbed energy at first fracture of ARALL is directly related to the fracture energy of the fibre. The first failure energy of GLARE is of the same order as for monolithic aluminium, and it may even be better.

Aramid ARALL shows fibre critical failure. GLARE shows fibre or aluminium critical failure depending on the type of fibre and the lay-up.

2. ARALL laminates have a higher energy at first failure than the corresponding cross-ply composites with the same fibre/matrix system. Consequently ARALL laminates have a higher damage resistance than the composite material which makes the material more suitable for application.

The absorbed energy at ultimate load however, has the highest values for the R-glass composites: the R-glass composites have a high resistance against perforation.

3. A cross-ply aramid ARALL material will have a significant higher energy at first failure compared to the corresponding unidirectional type. A cross-ply GLARE variant will not always have a higher energy at first

failure than a unidirectional ARALL type, because the presence of fibres in a certain direction can reduces the strain to failure in this direction, and may lead to a smaller absorbed energy. The difference in the energy at first fracture values (which are a measure of damage resistance) between cross-ply GLARE and UD GLARE is not large.

4. Although the difference in fracture energy between the applied carbon and aramid fibres is relatively small (aramid: $2.3*10^{-3}$ J/mm^3, carbon: $1.8*10^{-3}$ J/mm^3), the carbon ARALL specimens have a significant smaller energy at first failure. This is probably caused by the stiffness of the fibre and the corresponding strain distribution in the deflected sheet.

5. In general an increase of the thickness of a material will lead to a higher absorbed energy until first failure. However, in some cases the energy at first failure is reduced by adding thickness to the material. A larger thickness increases the maximum strain in the deflected sheet for the same value of the deflection, and consequently reduces the deflection at first failure.

7.3 Impact loading

7.3.1 Test method and materials

Impact tests were performed on circular clamped specimens, to examine the damage as a function of the impact energy of various materials. The specimens were clamped in the device as discussed in chapter 5. The circular clamped area had a diameter of 80 mm, the impactor had a hemispherical tip with a radius of 7.5 mm and a mass of 325 g. The contact force derived from the load cell in the impactor and the load cells under the clamping were measured. Strain gages were mounted on some of the specimens.

Impact test results for materials marked with * in tables 7.4 to 7.9 will be presented. Results of impact tests on the following thermoplastic ARALL variants are also shown:

2H32/PEI,p with p (poststretch percentage) = 0, 0.2, 0.4, 0.6

2E32/PEI,p   with p = 0 and 0.5

For each material at least 7 specimens were tested at different impact heights.

7.3.2 Strain measurements

On some specimens strain gages were mounted in the centre (in the fibre direction of the ARALL material), in order to obtain information about the order of magnitude of the strain rate in the specimen during impact. Another aim of the strain measurements was to examine the behaviour of plastically deforming material, because the strain measurements in chapter 6 were done on elastically deforming composites (see section 6.4.2). As already mentioned in chapter 6, it was difficult to hit the specimen exactly in the centre. Only the valid results will be presented.

Due to the large induced strains the strain gages failed at relatively low impact energies (at measured strains of 5 to 6%).

Figures 7.28 and 7.29 show two examples of measured force and strain vs. time curves. The initial phase of the impact process (already mentioned in section 6.4.2) can also be distinguished here in the strain-time curve of the tests. The force-time and the strain-time curves show fluctuations during loading and a relatively smooth shape during the unloading part. After impact the strain becomes equal to the permanent strain in the plastically deformed dent (compare this with figure 6.22 for the elastic deformation of the carbon/PEI specimen a vibration around $\varepsilon=0$ is present after impact). The vibration after impact around this plastic strain is relatively small. This suggests that no internal residual elastic deformation in the plate is released after loss of contact with the projectile. The elastic spring back of the specimen occurs during the contact period of the specimen and the impactor. Therefore the displacement at the moment that the force is zero and the contact between projectile and specimen is lost, approximately corresponds with the measured permanent central deflection. The permanent strain is relatively large: half the maximum strain during impact or more.

The maximum strain rate during the impact was in the order of $10^2 \ s^{-1}$ as figure 7.30 shows. The strain rate shows large fluctuations.

7.3.3 Static vs. dynamic loading

Deflection-(impact)energy curves for quasi-static and dynamic loading are compared in figures 7.31 to 7.35. In figure 7.36 the quasi-static and dynamic force-energy curves for Al 2024-T3 are presented. In general the quasi-static curves describe the impact behaviour quite well. However, a significant difference between static and dynamic maximum central deflection may occur. The figures show that the initial part of the deflection requires little energy: the deflection-energy curve is relatively steep in the beginning of the curve. A relatively low energy of 1 J causes a deflection of the specimen in the order of 2x the sheet thickness.

In the curves also the first (fibre) failure is indicated. The R-glass cross-ply GLARE behaves better under dynamic loading, but aramid ARALL needs less impact energy to cause first fibre cracking than under static conditions. Also the R-glass cross-ply composites have a better dynamic behaviour.

Table 7.10 shows that the aramid (except 7H33) and UD R_1-glass GLARE fail at impact energies smaller than the quasi-static energy at first failure. Monolithic aluminium failed at impact energies near the quasi-static values. The same is true for the thermoplastic composites, and the carbon ARALL variants.

The cross-ply R-glass GLARE and the R-glass cross-ply composites failed at impact energies significantly higher than the quasi-static energy values. This is probably due do the strain rate dependence of the strength of the glass fibre. This strain rate dependent behaviour will be treated in more detail in chapter 11.

7.3.4 Comparison of impact damage in various materials

monolithic aluminium vs. ARALL

The energy at first failure of aramid ARALL like 7H32 is significantly smaller than of their monolithic counterpart (table 7.10), because of the brittle behaviour of the aramid fibre. The cross-ply R-glass GLARE has an energy at first failure in the order of the monolithic material or higher.

Until significant (fibre or aluminium) failure the energy restitution coefficient of ARALL is equal to or somewhat higher (more elastic deformation) than monolithic aluminium (figure 7.37 and 7.38). The higher energy restitution can be caused by the elastic behaviour of the fibres in ARALL.

Even at low energies the energy loss is fairly large (50 %). The energy restitution coefficient vs. impact energy curve is generally relatively flat.

The contact area (loaded area) was measured by placing a piece of carbon-paper on the specimen, and by dropping the impactor on the specimen with the attached carbon-paper. After impact a clear print of the loaded area is visible on the specimen. The contact area after impact of the ARALL specimens 2H32 (t=0.8 mm) is larger for a given impact energy than of monolithic aluminium Al 2024-T3 (t=1.0 mm) (figure 7.39). The relation between the width of this area and the impact energy is approximately linear. The effect of the rolling direction of aluminium on the shape of this area is small, in contrast with the influence of the fibre direction of the ARALL laminates. The deformation perpendicular to the fibre direction is larger than in fibre direction. The contact zone is therefore elliptical with the long axis perpendicular to the fibre direction.

The maximum central deflection during impact of ARALL is larger than for monolithic aluminium (figures 7.40 and 7.41), because of the lower stiffness of the material. The permanent central deflection after impact of aramid ARALL is also larger than for the aluminium alloy, especially after first fibre failure (figure 7.42). The permanent central deflection of R-glass GLARE may be smaller than for monolithic material (figure 7.41), due to the elastic deformation of the fibres which is released during spring back.

At low energies a zone in ARALL is observed with small cracks in the matrix

material. This causes some fading (white spots) on this fibre layer (figure 7.43a). These spots are zones with matrix cracks, see figure 7.43b.

Delamination in GLARE is visible after removal of the outer aluminium layers by etching as a 'bubble' (a thin film of adhesive disbonded from the fibres) on the prepreg layer. The delamination will take place in the prepreg between fibre and adhesive at the outside of the prepreg (convex side), or between two crossed prepreg layers.

Figure 7.44 shows the crack length vs. the impact energy for Al 7075-T6 and aramid ARALL 7H32. The crack length in 7H32 is larger than in the monolithic material at equivalent impact energy levels. Moreover cracks occur in 7H32 at significantly lower impact energy levels than in the monolithic material.

Al 7075-T6 vs. Al 2024-T3 in monolithic and ARALL material

The damage width of the prepregs of 7075-T6 ARALL and 2024-T3 ARALL at low energies are similar (figure 7.45). The 7075-T6 aramid ARALL types have the same sensitivity for cracking as 2024-T3 aramid ARALL, because failure is dominated by the fibre (table 7.10). Figure 7.46 shows that the crack length visible at the outside in the metal layers of 7075-T6 ARALL may be larger than in 2024-T3 ARALL, because 7075-T6 is a more brittle material. However, in both materials a hole with approximately the same diameter will be punched for high impact energies (12 J).

The aramid ARALL 7H32 (Al 7075-T6) has a slightly smaller (permanent) central deflection than the 2H32 (Al 2024-T3, figure 7.47). For the thicker 2H33 and 7H33 material the same trend was found (figure 7.48). This is caused by the difference in stress-strain curve between Al 2024-T3 and 7075-T6. The stress at a certain strain for Al 7075-T6 is higher than for Al 2024-T3, which means that in a sheet specimen at a certain deflection more energy will be stored in Al 7075-T6 than in 2024-T3. Consequently the permanent deflection for a certain energy is for Al 7075-T6 smaller than for 2024-T3 (see also figure 7.26 and 7.27 for the static loading).

Figure 7.49 shows the permanent central deflection of Al 7075-T6 and Al 2024-T3 as a function of the impact energy. Until failure the permanent

deflection of Al 7075-T6 is smaller.

thickness effect

Material with a smaller thickness will have a larger energy restitution, until first failure (figure 7.50). This is the case for aramid ARALL as well as for monolithic Al 2024-T3. This is not an expected trend, because it may be thought that a thicker material will show more elastic deformation and consequently a higher energy restitution. It can be explained by the fact that the thicker material will have more plastic deformation at the outside of the material where it is bent around the radius of the impactor. For static loading the difference in energy restitution is very small (figure 7.24 for Al 2024-T3).

The damage width (delamination) in the R_2-cross-ply composites was not much dependent on the thickness (figure 7.55).

cross-ply vs. unidirectional ARALL

A cross-ply aramid ARALL variant has approximately the same maximum central deflection during impact as a unidirectional one, but its permanent central deflection is somewhat smaller. This is due to the fact that first cracking is postponed (figure 7.51).

A cross-ply ARALL variant will have a smaller crack length after an impact than a unidirectional one. The fibres provide a restraint on the growth of the crack. This effect is especially pronounced in GLARE, where the addition of cross-plied fibres will have a significant influence because the crack will occur in fibre direction (figure 7.46). For aramid ARALL the effect may be relatively large as well (figure 7.52).

fibre type in ARALL laminates

The type of fibre in ARALL until first failure has a small influence on the maximum central deflection during impact (figures 7.40, 7.41, 7.53). For the permanent deflection after impact there is more influence. The ranking

207

for increasing permanent deflection is: carbon, glass, aramid fibre (figures 7.40, 7.53 and 7.54). Carbon ARALL will fail first and then shows considerable deformation, followed by aramid ARALL and GLARE.

GLARE will have a smaller damage width of the prepreg than the carbon and aramid ARALL types. A tougher resin decreases this damage width (figure 7.55, R_6:AF 163-2, R_4: DLS 1115 adhesive, which is tougher than AF 163-2). Because 2R33/C55 will show fibre failure at relatively high energies, a considerable area of delamination may be formed until fibre failure. This is in contrast with the behaviour of aramid and carbon ARALL: their damage width is dominated by fibre failure.

ARALL vs. thermoplastic composites

ARALL has a much larger permanent deflection than the thermoplastic composites because of the plastic deformation in this material (figure 7.53).

In general the damage width of ARALL will be smaller than for thermoplastic composite materials (figure 7.56).

poststretch percentage of ARALL

Aramid ARALL 2H32 was tested at 0, 0.2, 0.4 and 0.6 % poststretch. The poststretch percentage did not influence the maximum central deflection (figure 7.57) or the maximum force during impact. The absorbed energy at ultimate load (perforation) during impact decreases with increasing poststretch percentage (figure 7.58). The crack length after first failure after impact is not dependent on the percentage of poststretch (figure 7.59).

thermoplastic ARALL

Thermoplastic ARALL is a new development for high temperature applications and as a material with a high formability at elevated temperature. A small test series was carried out on impact properties which showed some

208

remarkable results. The applied fibres were: E-glass and high modulus aramid, the adhesive was polyetherimide (PEI). Aramid ARALL 2H32/PEI (fibre volume fraction of the prepreg 38 %) and E-glass ARALL 2E32/PEI (fibre volume fraction of prepreg 46 %) were tested.

The thermoplastic ARALL was bonded and consolidated at 240 $^{\circ}$C for 20 min. This causes some loss of ductility for the Al 2024-T3 material. The material condition became similar to the T8 condition. The higher curing temperature also caused higher internal stresses compared with thermosetting ARALL:

material	internal stress (MPa)	
	Al layers	prepreg layer
2H32	32	-87
2H32/PEI	69	-189

Both effects are negative for the energy absorption capability of the aluminium layers. Therefore the 2H32/PEI material showed aluminium failure in fibre direction instead of fibre failure during impact (like ARALL 2H32). Poststretching of 2H32/PEI to 0.4 %, introduces tensile stresses in the fibres high enough to cause the fibres to be the weakest link again, i.e. fibre cracking.

The maximum and permanent central deflection were not influenced by the PEI matrix. The impact energy at first failure was somewhat higher but close to the thermosetting variant. Figure 7.60 shows the crack length as a function of the impact energy. The crack length of the thermoplastic variant of ARALL was larger than in the thermosetting ARALL.

7.3.5 Impact tests on stiffened panels and a variation of the nose shape of the impactor

tests on stiffened aramid ARALL panels -

To compare the behaviour of specimens with a more realistic configuration, impact tests were performed on three 65 cm long aramid ARALL panels with a

cross section as shown in figure 7.61. The stiffeners were bonded on the skin with AF 163-2 (epoxy adhesive). The effective width of a subpanel between two stiffeners was taken equal to the clamped diameter of the specimens (80 mm). The panels were clamped at a span of 50 cm on two heavy bars on the clamping table of the impact tester. The span of 50 cm is approximately equal to the distance between two frames in an aircraft fuselage. The panels were impacted in their centre between two stiffeners, with impact energies of 4.5, 11.4 and 16.4 J.

Already during impact it was clear that the stiffness of the panel was much lower than the stiffness of the circular specimens: the frequency of the radiated sound during impact was much lower. The energy in the panels is spread over a larger area, the deflection during impact is larger (figure 7.62). The permanent deflection of the subpanel is smaller (figure 7.63), and the contact force during impact is smaller (figure 7.64). The panel failed at a considerably higher impact energy than the small circular clamped specimens.

The panel impacted at 11.4 J showed no cracking, whereas a circular clamped specimen failed at 3.7 J. The panel with the 16.4 J impact shows a relatively clean perforated elliptical hole with the dimensions 20x15 mm^2. The absorbed energy of the panel impacted at 16.4 J at ultimate load was 11.1 J, whereas a typical value of the circular clamped specimens was approximately 4 J.

nose shape

Some tests were performed with tip radii of the impactor of 5 and 7.5 mm and with sharp conical tips with top angles of 60^0 and 90^0.

The impactor with a tip radius of 5 mm caused a slightly smaller permanent central deflection than an impactor with a tip radius of 7.5 mm (figure 7.65).

A sharp object may cause a lot of damage in the unidirectional reinforced aramid ARALL (figure 7.66). The impactor with a top angle $\alpha = 60^0$ created a hole with a larger diameter than the impactor with $\alpha = 90^0$. The punched

hole in aramid ARALL 2H33 is considerably larger than in the monolithic material. The fibres are pushed aside by the sharp tip.

7.3.6 Conclusions

1. aramid ARALL, GLARE, monolithic aluminium

Aramid ARALL is relatively sensitive to impact damage as compared with the monolithic Al-alloy sheet material. Cross-ply aramid ARALL shows a significant increase of the energy needed to cause fibre failure during dynamic loading if compared to the UD aramid ARALL, but the damage resistance of the material remains poor.

Cross-ply GLARE has a significantly better behaviour under dynamic loading compared to static loading.

GLARE behaves similar to or even better than monolithic material. The permanent deflection of GLARE may be smaller than of monolithic material, because of more elastic deformation. Aramid ARALL has a larger permanent deflection after impact compared with monolithic aluminium.

2. strain measurement in ARALL during impact

During the first part of the impact the force-time curve shows a typical behaviour. The contact force is small, and the contact between impactor and plate may be lost (F = 0). This is probably due to the low stiffness of the specimens at small deflections: the specimen is pushed away by the impactor. This behaviour was also observed in the strain-time curve of the specimen.

After the impact on ARALL and monolithic material (at F = 0) the strain remains constant and is equal to the permanent strain in the specimen (figures 7.28 and 7.29)

The strain rate during the impact tests is in the order of 10^2 s^{-1} (figure 7.30).

3. damage in ARALL

The damage of the prepreg of aramid ARALL until fibre failure is mainly limited to matrix cracking: very little delamination does occur. After fibre failure the damaged zone is approximately limited to the zone of cracked fibres. In that case the damage width is approximately equal to the

crack length in the outer aluminium layers.

Matrix cracking is visible as a fading (white zone) in the prepreg layer. GLARE shows more delamination because the fibres remain intact until high impact energies, especially for cross-ply GLARE. Cross-ply GLARE $2R_6^2 33/C55$ with AF 163-2 adhesive has a damaged zone in the prepreg comparable with composites. If a tougher adhesive (DLS 1115) is applied the damaged zone is significantly smaller (figure 7.55).

4. dynamic vs. static loading

The dynamic (maximum) central deflection vs. (impact) energy curve of static and impact loading are in general comparable, especially at low impact energies. This curve will be calculated with the model presented in chapter 12.

Aramid ARALL fails at somewhat lower dynamic impact energies compared with static loading. Cross-ply GLARE and cross-ply R-glass composites fail at significantly higher energies under dynamic loading. This is probably caused by the strain rate dependence of the strength of the glass fibres, as will be treated in chapter 11.

5. Al 2024-T3 vs. 7075-T6

Monolithic and laminated Al 7075-T6 show a smaller (permanent) deflection and fail at a lower impact energy than Al 2024-T3. However. if the two alloys are applied in aramid ARALL, then Al 7075-T6/aramid ARALL fails at approximately the same impact energy as Al 2024-T3/aramid ARALL, because the failure is dominated by the fibre. The crack length in the more brittle Al 7075-T6 ARALL may be larger than in Al 2024-T3 ARALL, but at higher energies a hole with approximately the same diameter (somewhat larger than the diameter of the tip of the impactor) is cut in both materials.

6. thickness effect

Thin material has a higher energy restitution coefficient than thicker material until failure.

7. unidirectional vs. cross-ply ARALL

Cross-ply aramid and glass ARALL need a significant higher energy to crack

the material than UD variants, while a smaller permanent deflection remains after impact. However, cross-ply GLARE has approximately an equal energy at first failure as UD GLARE (compare $2R_1 32$ and $2R_1 32/C82$ and $2R_2^2 32$ and $2R_2^2 32/C55$ in table 7.10). It can be explained by considering the strain rate dependent behaviour of the glass fibre.

It is also noteworthy that the impact damage of the cross-ply ARALL variants leads to smaller cracks if compared to UD variants.

8. ARALL vs. composites

The damage width after impact in ARALL is generally smaller than in composite material (figures 7.55 and 7.56).

9. poststretching and thermoplastic ARALL

Poststretching of ARALL lowers the energy at first failure (figure 7.66), but it has no influence on the (permanent) deflection or the crack length after failure (figure 7.67). The behaviour of thermoplastic ARALL shows that the failure type (fibre or aluminium critical) can be influenced by poststretching.

10. panel vs. specimen

An impacted stiffened panel has a significantly higher maximum deflection during impact and a smaller permanent deflection after impact than a circular clamped specimen (figure 7.71). The minimum impact energy needed to induce failure is significantly higher for the stiffened panel.

11. nose shape of the impactor

An impactor with a tip radius of 5 mm causes a slightly smaller permanent central deflection than an impactor with a tip radius of 7.5 mm (figure 7.65).

A sharp impactor causes more damage in aramid ARALL than in monolithic material (figure 7.66).

reference

1. Roebroeks, G.H.J.J.; PhD-thesis, Delft Technical University, to be published.

fibres	fibre	adhesive	prepreg t(mm)	v_f(%)	code
aramid fibres (TWARON, high modulus)	1. UD	AF 163-2	0.2	47	H
	2. weave (50-50)	-		47	H/w
	3. weave (90-10)			45	H/90-10
	4. UD	PEI		38	H/PEI
glass fibres (UD only)	R-glass				
	5. RC 10 P109	AF 163-2	0.2	60	R_1
	6. ditto	DLS 1095		ditto	R_2
	7. RA 9041	DLS 1095		ditto	R_3
	8. ditto	DLS 1115	0.1	50	R_4
	9. ditto	DLS 1115		55	R_5
	10. RA 10 P109	AF 163-2		53	R_6
	S-glass				
	11. S_2-glass	AF 163-2	0.2	60	S
	E-glass				
	12. E-glass	PEI	0.2	46	E/PEI
carbon fibres (UD only)	13. IM 600	fibredux 924C	0.1	58	C_1
	14. T800 H	ditto	ditto	56	C_2
no fibres		AF 163-2	0.2	100	AF

table 7.1 Prepreg layers used in ARALL laminates

214

adhesive	manufacturer	curing temperature (^{0}C)	density (kg/dm^3)
AF 163-2	3M	120	1.15
DLS 1095	Ciba Geigy	ditto	1.20
DLS 1115	ditto	ditto	ditto
Fibredux 924C	ditto	180	1.15

table 7.2 Adhesive properties.

fibre	prepreg code(s)	E GPa	σ_u MPa	ε_u %	U_u 10^{-3}J/mm^3	ρ kg/dm^3	U_u/ρ J/g
aramid Twaron HM	H	125	2800	2.3	31	2.30	14
R-glass RC 10 P109	R_1, R_2	86	3270	3.8	62	2.54	24
R-glass RA 9041	R_3, R_4, R_5	89	5200	5.9	152	2.54	60
R-glass RA 10 P109	R_6	86	4100	4.8	98	2.54	39
S_2-glass	S	86	4600	5.3	123	2.54	48
carbon IM 600	C_1	300	6000	2.0	60	1.80	33
carbon T800H	C_2	294	5600	1.9	53	1.80	29

table 7.3 Fibre properties.

material	t (mm)	first failure F_f (kN)	first failure $w_{0,f}$ (mm)	first failure U_f (J)
2024-T3	0.30	1.67	7.0	4.82
	0.37	2.32	7.4	7.21
	0.50	3.82	9.1	14.7
	0.60	4.87	9.7	19.6
	0.80*	5.13	7.8	15.1
	1.02*	4.94	7.0	12.9
	1.40	6.08	6.3	15.1
	1.57*	6.67	6.3	16.6
7075-T6	0.86*	3.30	5.4	6.07
	1.00*	3.43	4.8	5.81

Al - alloys

table 7.4 Results of the quasi-static tests on aluminium alloys.
(* impact tests were also performed)

aramid ARALL

material	failure type	t	first failure			ultimate load		
			F_f	$w_{0,f}$	U_f	F_u	$w_{0,u}$	U_u
		(mm)	(kN)	(mm)	(J)	(kN)	(mm)	(J)
2H32	fibre	0.83*	2.31	5.1	4.25	-	-	-
2H42	ditto	1.0*	3.3	6.0	6.5	-	-	-
7H32	ditto	0.80*	3.0	5.6	5.8	-	-	-
2H33	ditto	1.35*	2.85	4.8	4.89	3.38	5.7	7.6
7H33	ditto	1.32*	2.88	4.5	4.86	3.37	5.1	6.7
2H33/90-10	ditto	1.35*	4.0	5.9	8.2	4.4	6.5	12.3
2H33/#	ditto	1.35*	3.1	5.1	6.0	4.0	6.3	10.1
2H33/w	ditto	1.36*	3.8	5.7	8.1	4.0	6.2	9.8
2H34	ditto	1.80	4.3	4.8	8.9	5.5	6.1	15.3
2H35	ditto	2.43	5.7	5.4	14.4	7.0	6.8	23.4
2H36	ditto	2.97	6.7	5.4	17.8	8.0	7.1	30.3
2H38	ditto	4.04	10.7	4.8	27.0	11.3	5.8	38.0
2H310	ditto	5.10	14.6	4.9	38.5	18.4	6.4	63.3

table 7.5 Results of quasi-static tests on aramid ARALL.
(* impact tests were also performed)

GLARE

material	failure type	t	first failure			ultimate load		
		(mm)	F_f (kN)	$w_{o,f}$ (mm)	U_f (J)	F_u (kN)	$w_{o,u}$ (mm)	U_u (J)
2S32	aluminium	0.90*	3.7	7.0	8.8	–	–	–
2S32/C64	?	1.24	6.7	8.1	18.9	–	–	–
2S33	aluminium	1.70	6.3	7.0	17.1	6.4	7.3	19.2
$2R_1 32$	aluminium	0.95*	3.69	6.7	8.77	–	–	–
$2R_1 32/C82$	ditto	0.97*	2.70	5.4	4.97	3.45	6.9	9.8
$2R_2 32$	fibre (!)	0.69	2.98	6.6	7.48	–	–	–
$2R_2^{\,2} 32$	aluminium	0.85*	3.18	6.3	7.34	–	–	–
$2R_2^{\,2} 32/C55$	aluminium ?	0.83*	2.98	5.8	6.08	–	–	–
$2R_2^{\,3} 32$	aluminium	0.95	3.08	5.98	6.66	–	–	–
$2R_2^{\,4} 32/C55$	fibre	1.10	3.98	6.6	9.46	–	–	–
$2R_2^{\,2} 33$	aluminium	1.36	3.98	5.7	8.95	5.25	7.2	15.6
$2R_2^{\,2} 33/C55$	fibre	1.37	3.78	5.4	7.72	4.33	6.1	10.6
$2R_2^{\,4} 33/C55$	fibre	1.80	4.92	5.5	11.3	5.8	7.3	21.9
$2R_3^{\,2} 33/C55$	aluminium	1.36	4.21	5.8	9.07	5.24	6.9	13.7
$2R_3^{\,4} 32/C55$	fibre	1.07	4.96	7.3	13.1	–	–	–
$2R_4 32$	aluminium	0.71	3.90	7.7	11.4	–	–	–
$2R_4^{\,2} 32$	ditto	0.87	3.82	7.2	10.4	–	–	–
$2R_4^{\,3} 32$	ditto	1.04	3.71	6.9	9.60	–	–	–
$2R_4^{\,3} 32/C73$	ditto	1.06	4.43	7.0	11.6	–	–	–
$2R_4 33$	ditto	1.14	5.20	7.1	13.7	–	–	–
$2R_4^{\,4} 32/C55$	fibre	1.15	5.86	8:4	18.3	–	–	–
$2R_4^{\,2} 33$	aluminium	1.45	5.59	6.9	15.0	–	–	–
$2R_4^{\,2} 33/C55$	fibre	1.45*	6.33	7.2	17.3	–	–	–
$2R_5^{\,2} 33/C55$	fibre	1.52	5.90	6.9	15.4	–	–	–
$2R_5^{\,4} 32/C55$	fibre	1.15	5.59	7.6	15.1	–	–	–
$2R_6^{\,2} 33/C55$	fibre(?)	1.41*	2.98	4.8	5.7	4.16	6.1	10.4

table 7.6 Results of the quasi-static tests on ARALL laminates with glass fibres (* impact tests were also performed).

217

CARE and metal laminates

material	failure type	t (mm)	first failure			ultimate load		
			F_f (kN)	$w_{0,f}$ (mm)	U_f (J)	F_u (kN)	$w_{0,u}$ (mm)	U_u (J)
$2C_1^2 32$	fibre	0.85	1.8	4.2	2.3	2.5	5.2	4.4
$2C_1^3 32$	ditto	0.98	2.04	4.3	3.0	2.2	4.5	3.5
$2C_2^2 32$	ditto	0.84*	1.73	4.1	2.51	2.33	5.8	5.89
$2C_2^2 32/C55$	ditto	0.85*	1.60	3.9	2.07	2.06	5.7	5.39
2AF33		1.32				5.4	7.6	14.8

table 7.7 The results of the quasi-static tests on ARALL laminates with carbon fibres and without fibres.
(* impact tests were also performed)

composites

prepreg	no. layers	t (mm)	first failure			ultimate load		
			F_f (kN)	$w_{0,f}$ (mm)	U_f (J)	F_u (kN)	$w_{0,u}$ (mm)	U_u (J)
R_2	7	0.94*	1.88	6.7	5.98	2.98	7.7	8.66
	9	1.20*	2.49	5.8	5.35	3.78	7.6	11.0
	11	1.45*	2.65	5.3	5.43	4.45	7.9	15.2
	15	1.96*	3.73	5.6	8.69	5.42	7.9	19.8
R_4	7	1.14	2.84	9.3	11.0	3.35	10.8	15.6
	9	1.24	3.80	9.4	13.4	4.30	10.5	18.1
	11	1.45	4.02	8.2	12.4	5.22	8.2	22.3
R_3	7	0.94	3.65	8.3	10.9	4.13	10.1	18.05
	9	1.22	3.53	7.5	9.35	4.28	9.8	18.53
R_5	7	1.04	3.24	8.7	10.6	3.67	10.0	15.24
C_2	9	1.20	0.71	2.4	0.65	2.22	5.3	5.01
	11	1.45	0.76	1.9	0.67	2.52	5.0	5.78
carbon/PEI	8	1.65	1.61	3.1	1.87	-	-	-
	12	2.75	2.51	3.0	3.66	4.10	5.9	13.0
	16	3.40	3.14	2.2	3.35	5.50	4.8	15.3

table 7.8 The results of the quasi-static test on the cross-ply composites.
(* impact tests were also performed)

composites

material/lay-up	t	first failure			ultimate load		
		F_f	$w_{0,f}$	U_f	F_u	$w_{0,u}$	U_u
	(mm)	(kN)	(mm)	(J)	(kN)	(mm)	(J)
UD carbon/PEI, lay-up:							
[0/60/-60/90/-60/60/0]	1.42*	2.5	4.7	4.3	–	–	–
[0/±60^0]$_s$	1.25	2.1	4.3	3.1	–	–	–
carbon weave/PEI, lay-up							
[0-90/±45/0-90/±45/0-90]	1.50*	1.4	3.1	1.7	2.4	4.7	4.8
UD aramid/PEI, lay-up:							
[0/45/90/45]$_s$	1.50	2.8	6.4	6.3	–	–	–
aramid weave/PEI, lay-up							
[0-90/±45$_2$]$_s$	1.47*	1.5	4.4	2.4	2.1	5.8	4.9
UD carbon/epoxy, lay-up							
[0/60/-60/90/-60/60]$_s$	2.00*	1.61	2.5	1.7	2.45	4.2	5.59
UD carbon/epoxy, lay-up							
[0/90]$_8$	2.75	2.67	2.6	3.4	3.53	4.2	8.42
polycarbonate	1.20	3.48	28.9	49	–	–	–
ditto	2.96	6.04	21.8	62	–	–	–

table 7.9 Results of the quasi-static tests on various composites.
(* impact tests were also performed)

219

material	t (mm)	static first failure energy(J)	impact energy(J) crack observed		dynamic/ static ratio	
			no	yes	min.	max.
Al 7075-T6	0.86	6.1	6.1	9.5	1.0	1.58
2H32	0.83	4.3	3.6	3.7	0.84	0.86
2H33	1.35	4.9	4.5	4.6	0.92	0.94
2H33/90-10	1.35	8.2	7.2	8.4	0.88	1.02
2H33/w	1.36	8.1	5.4	5.8	0.67	0.72
2H33/#	1.36	6.0	4.8	5.6	0.80	0.93
7H32	0.80	5.8	3.7	4.5	0.64	0.78
7H33	1.32	4.9	5.2	5.4	1.06	1.10
$2R_1 32$	0.95	8.8	4.7	6.4	0.53	0.73
$2R_1 32/C82$	0.97	5.0	9.2	11.7	1.84	2.34
$2R_2^2 32$	0.85	7.3	2.2	4.2	0.30	0.58
$2R_2^2 32/C55$	0.83	6.1	9.7	13.2	1.59	2.16
$2R_4^2 33/C55$	1.45	17.3		>24	1.39	
$2R_6^2 33/C55$	1.41	5.7		>9.0	1.58	
$2C_2^2 32$	0.84	2.5	2.2	4.2	0.88	1.68
$2C_2^2 32/C55$	0.85	2.1		< 5		2.38
UD carbon/PEI, lay-up:						
[0/60/-60/90/-60/60/0]	1.42	4.3	3.3	4.5	0.77	1.04
carbon weave/PEI	1.50	1.7	1.6	3.6	0.94	2.12
R-glass (R_2) cross-ply	0.94	4.0	13.3	16.3	3.33	4.08

table 7.10 Comparison of static and impact failure energies.
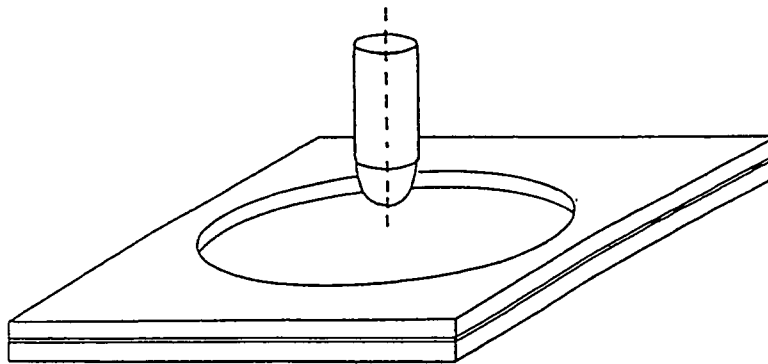
figure 7.1a The specimen with a circular test area between two clamping plates.
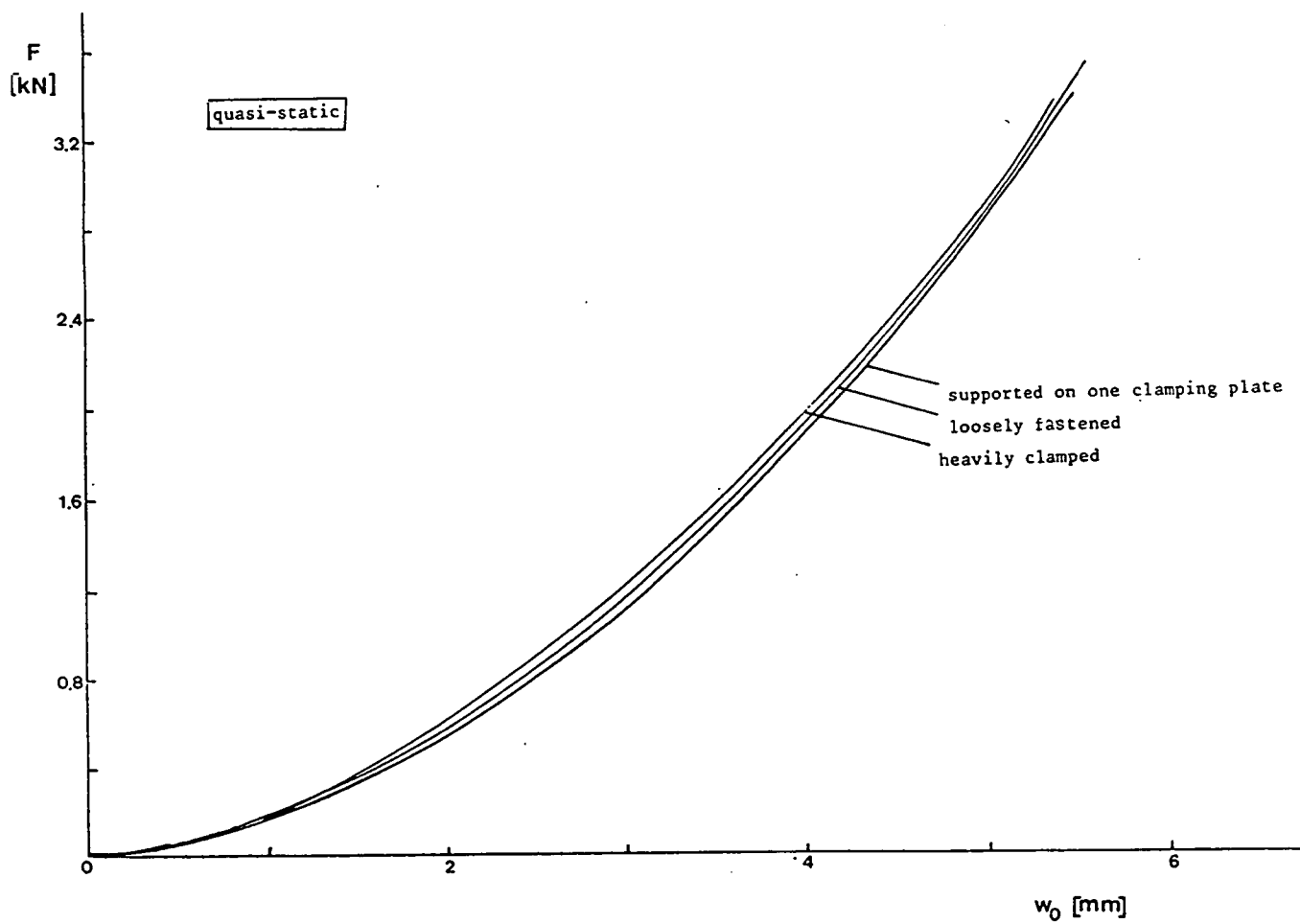
figure 7.1b Influence of the clamping conditions on the force-deflection curve of Al 2024-T3 (t=1 mm).
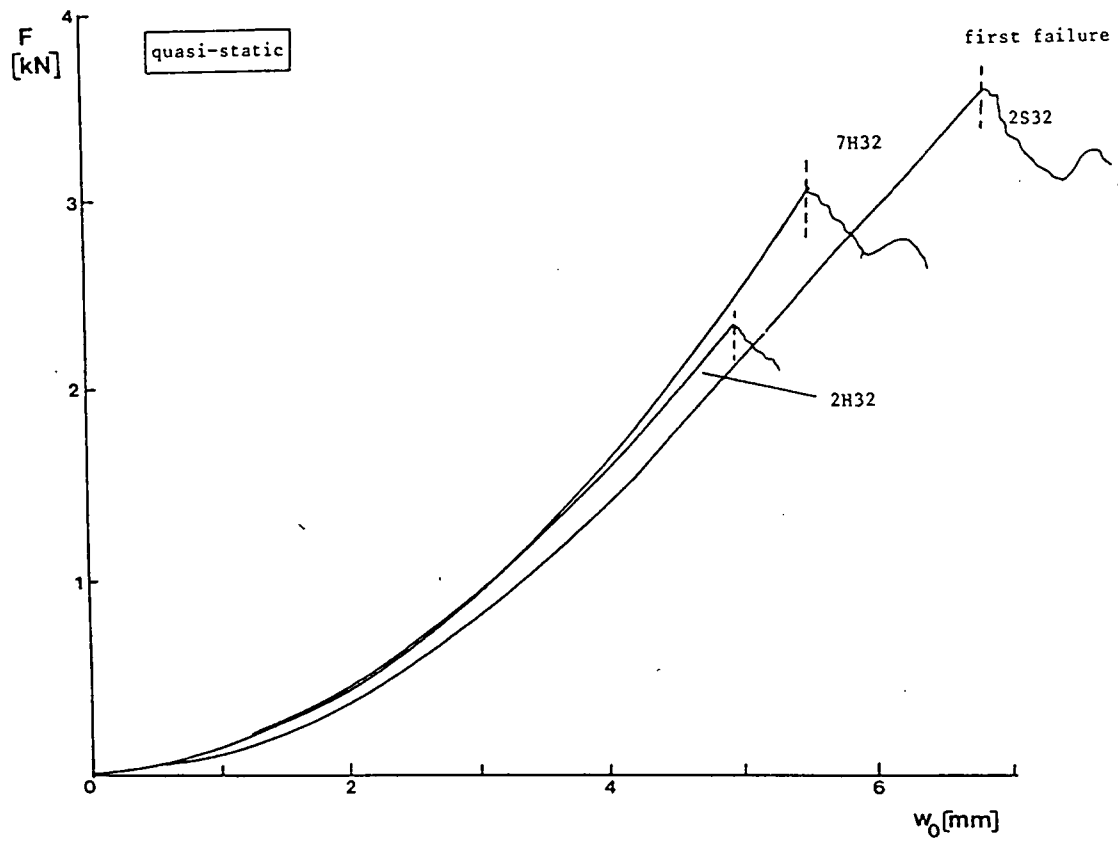
figure 7.2 Force-deflection curves of ARALL variants (2H32: aramid
ARALL with Al 2024-T3 layers, 7H32: aramid ARALL with Al 7075-T6
layers, 2S32: S-glass ARALL with Al 2024-T3 layers).
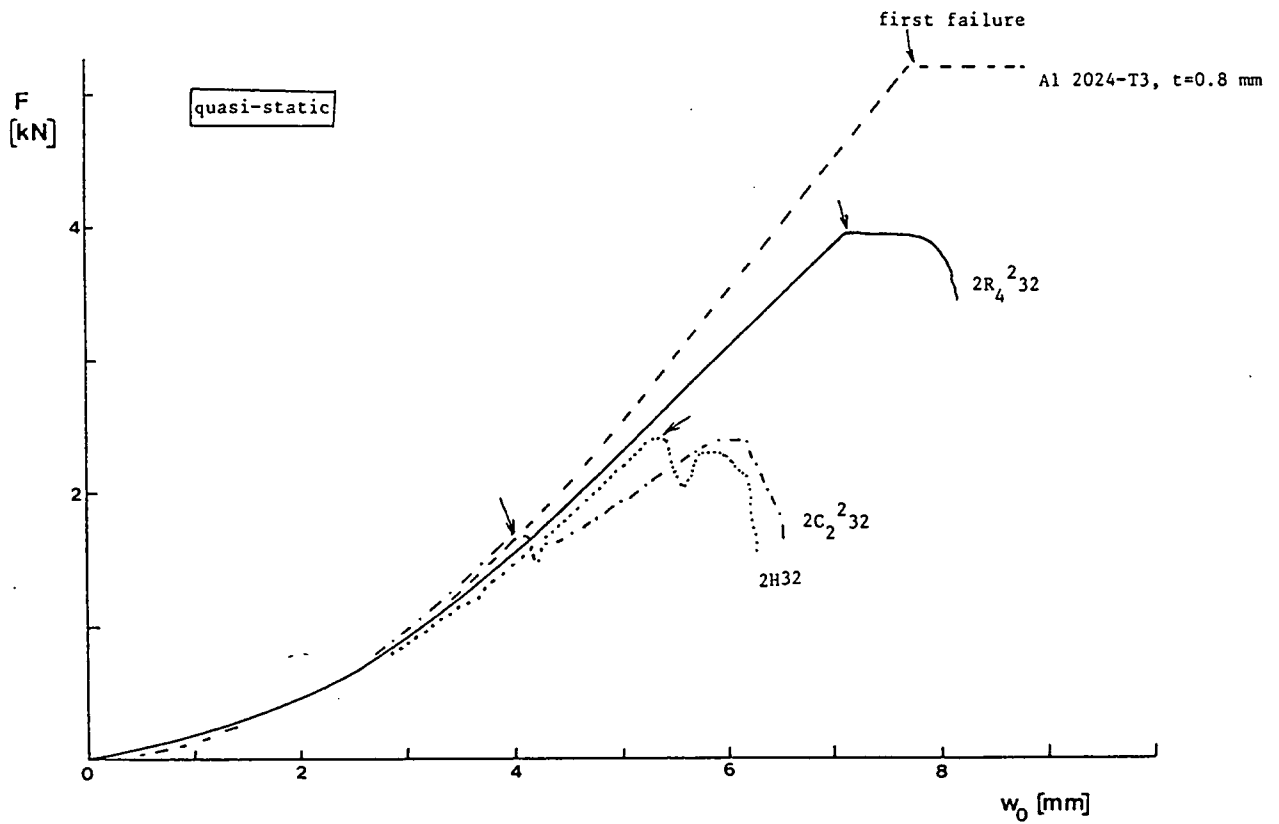
figure 7.3 The influence of the type of fibre in ARALL on the force-deflection curve; 2H32: aramid fibre, $2C_2^2 32$: carbon fibre, $2R_4^2 32$: R-glass fibre.
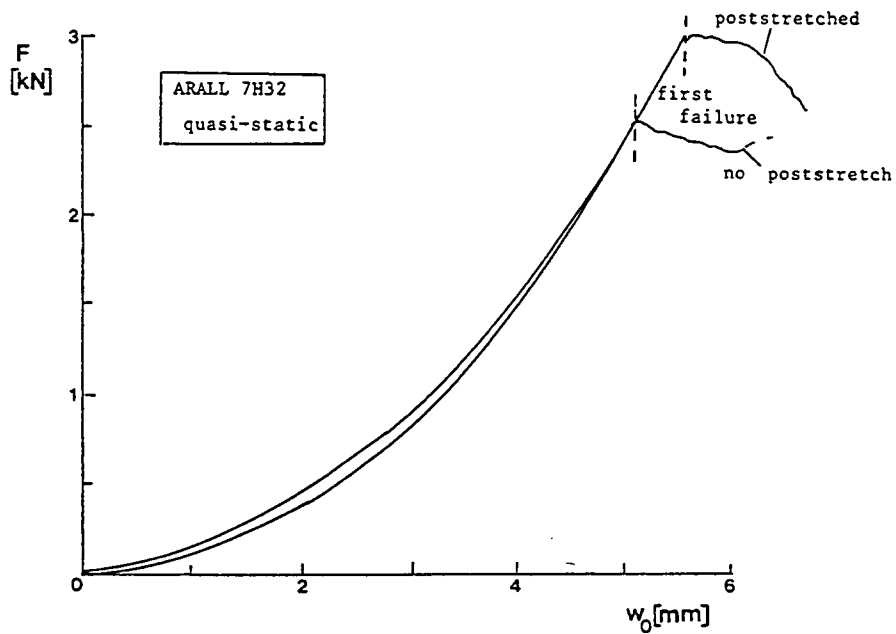
figure 7.4 The influence of poststretching on the force-deflection curve of aramid ARALL; 7H32: no poststretch, 7H32,0.4: 0.4% poststretch.
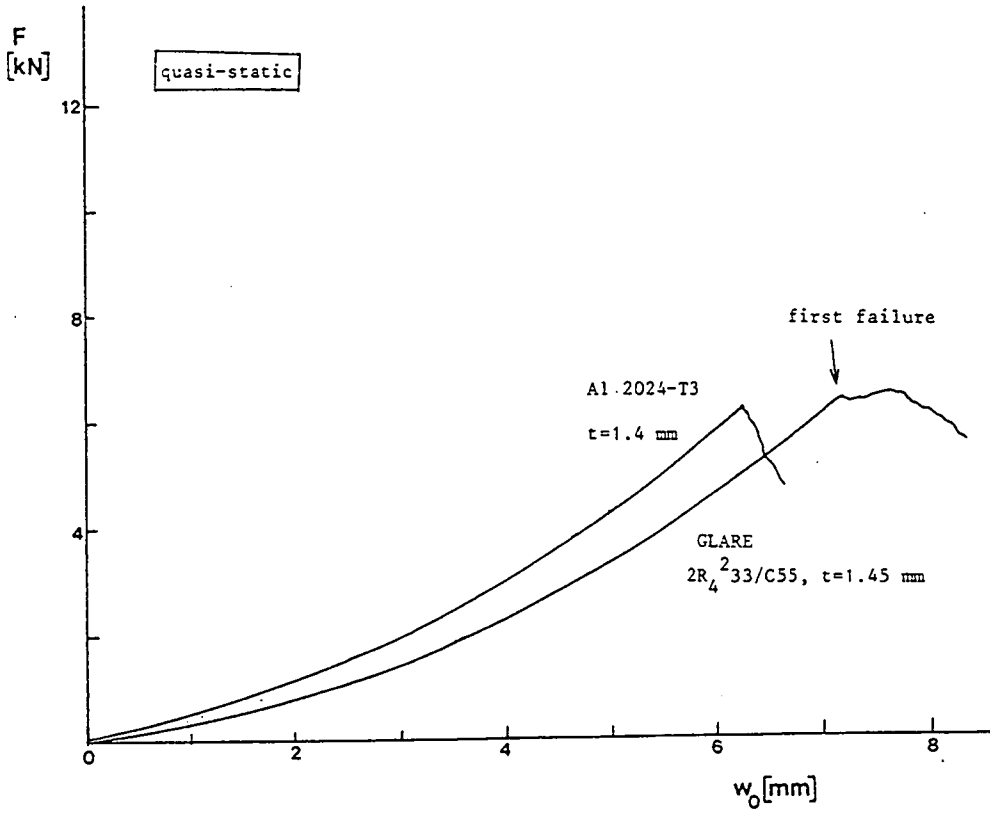
figure 7.5
Comparison of the
force-deflection
curve of Al 2024-T3
and GLARE.
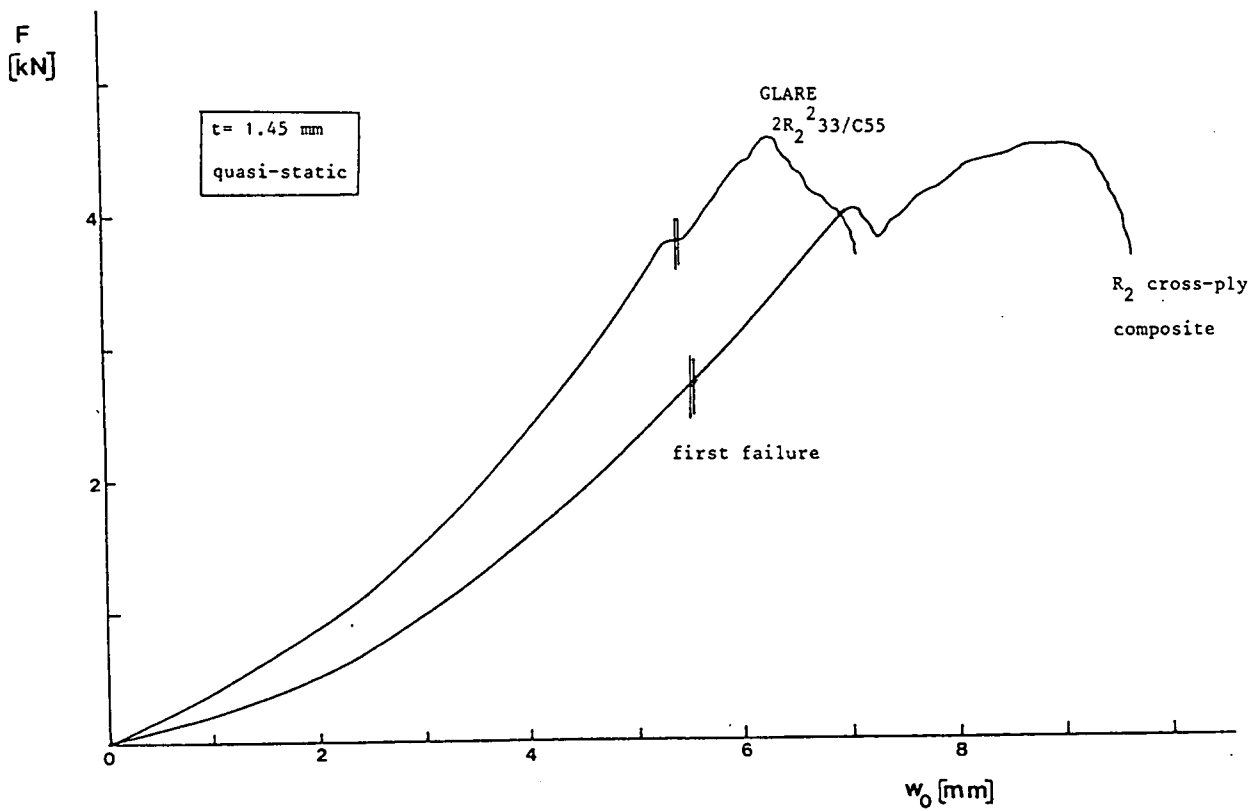
figure 7.6 Comparison of the force-deflection curves of GLARE and the
corresponding cross-ply composite.
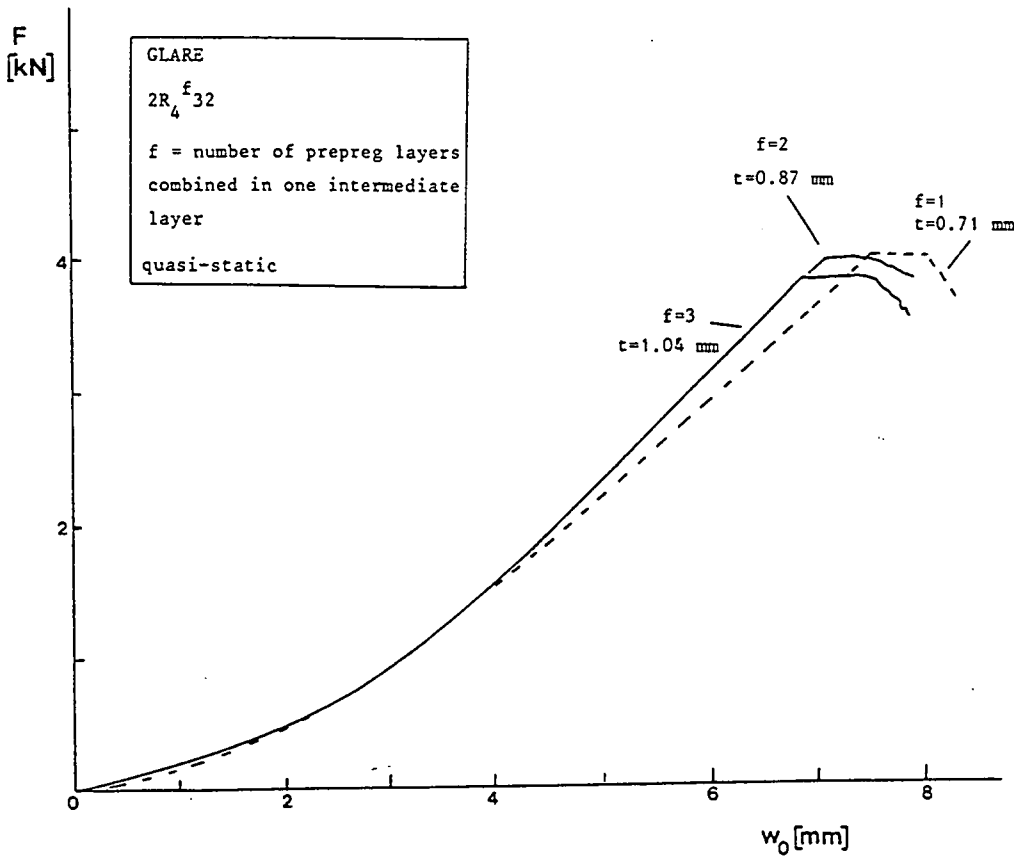
figure 7.7
The influence of adding
fibre/adhesive layers
to GLARE 2R32 on the
force-deflection curve

$2R_4{}^x32$: x=number
of prepreg
layers
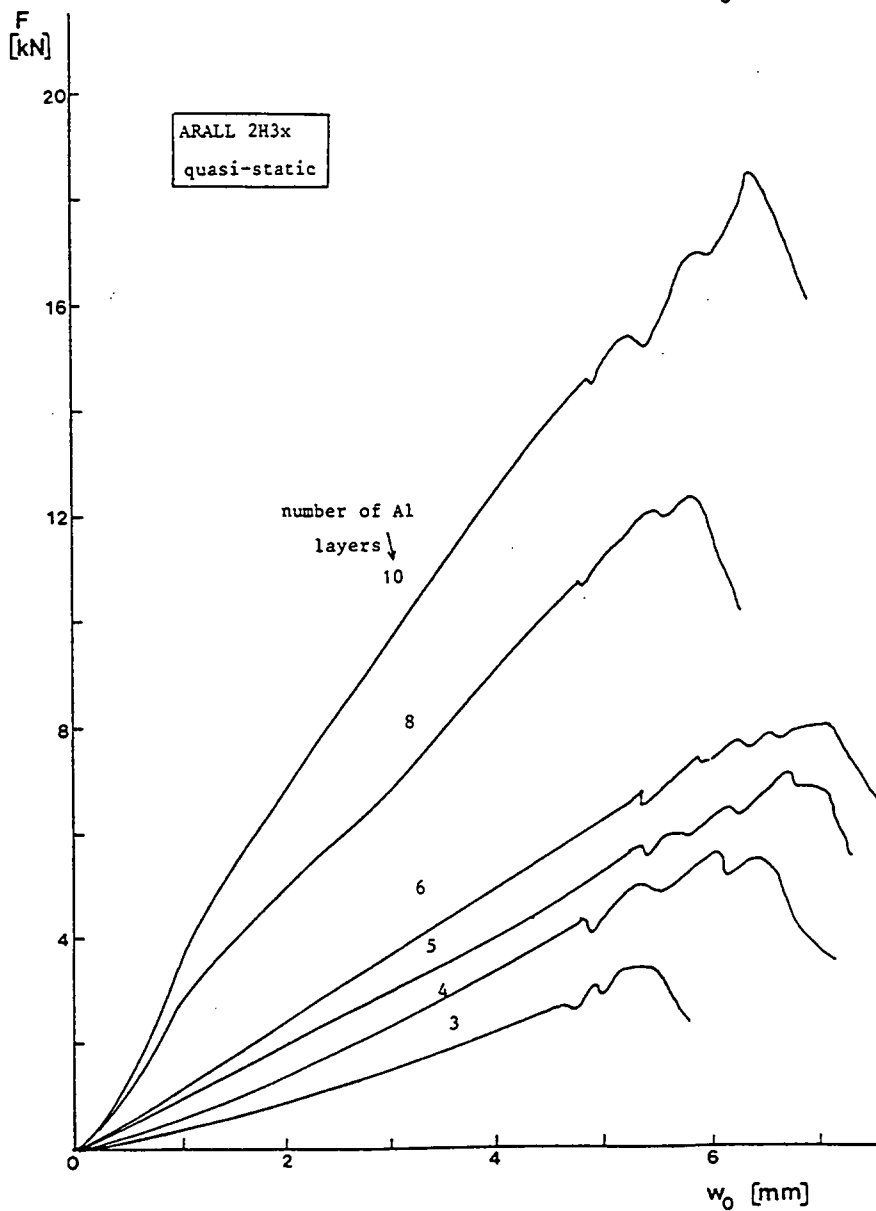
figure 7.8
Force-deflection curves
for aramid ARALL of
various thicknesses.

2H3x: x=number
of Al layers

225
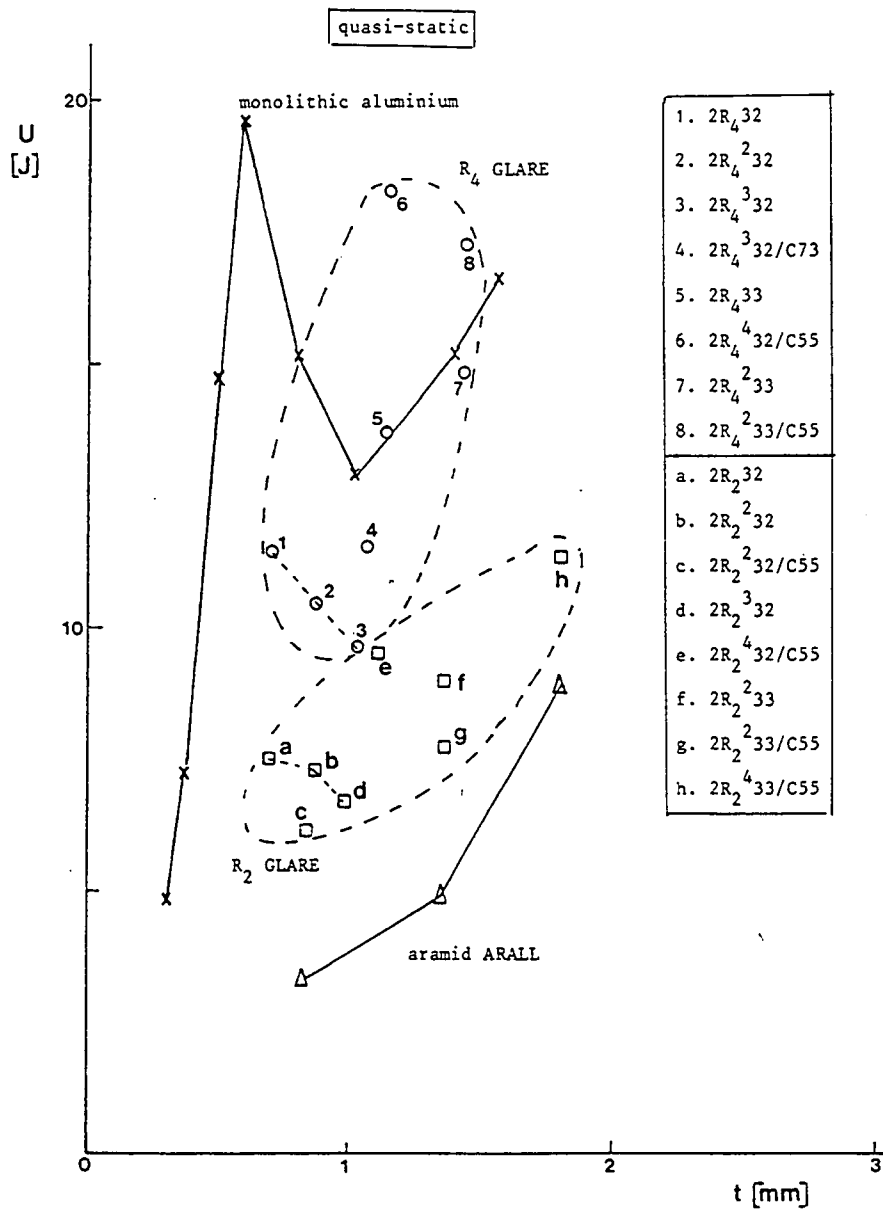
figure 7.9 The absorbed energy at fracture vs. the sheet thickness for monolithic aluminium Al 2024-T3, aramid ARALL and GLARE.

R_4 GLARE: RA 9041 fibre, σ_u = 5200 MPA, ε_u =5.9%

R_2 GLARE: RC 10 fibre, σ_u = 4100 MPa, ε_u =3.8%
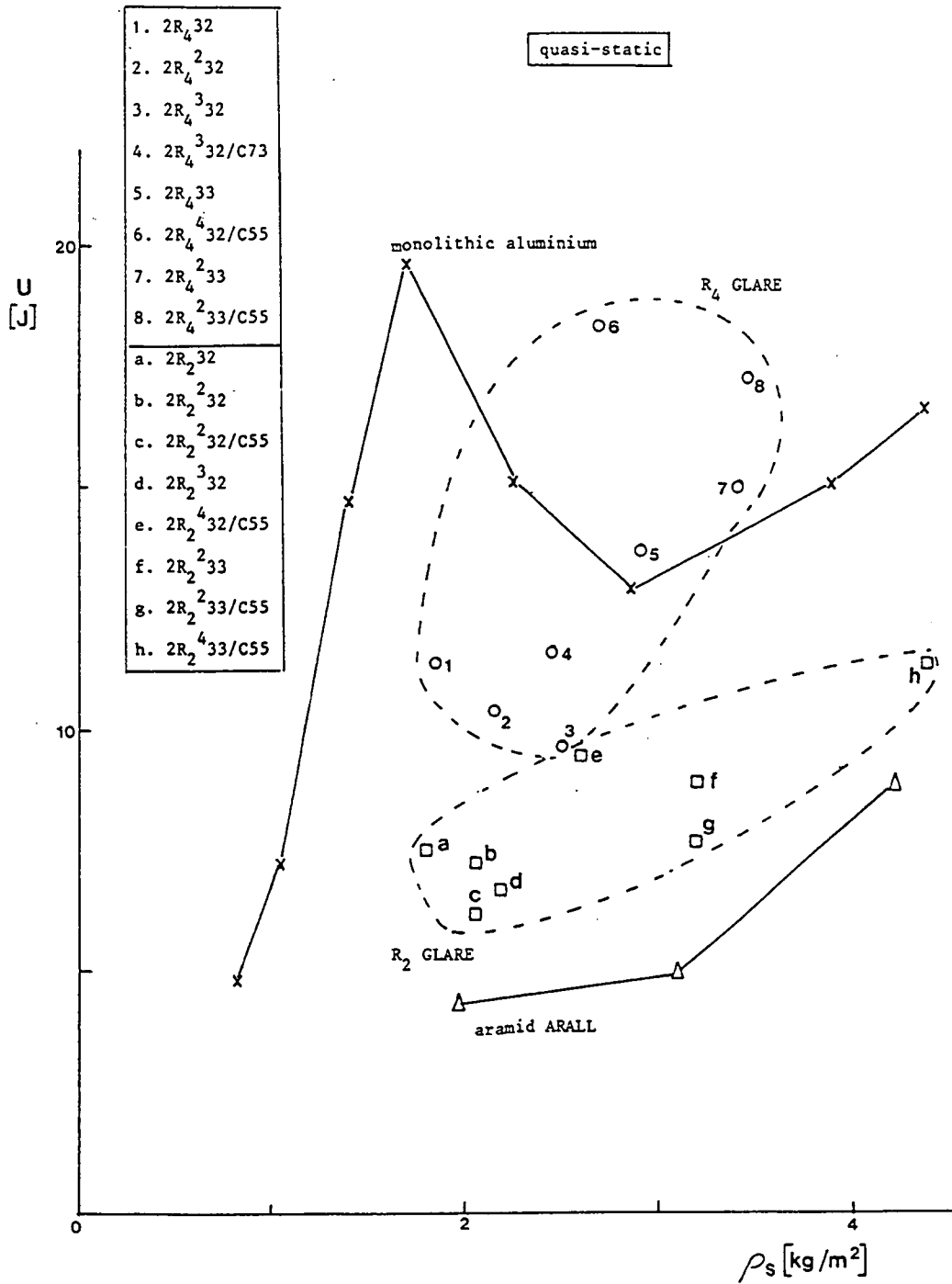
figure 7.10 The energy at fracture vs. the surface density for monolithic aluminium, aramid ARALL and GLARE.

R_4 GLARE: RA 9041 fibre, σ_u = 5200 MPA, ε_u =5.9%

R_2 GLARE: RC 10 fibre, σ_u = 4100 MPa, ε_u =3.8%
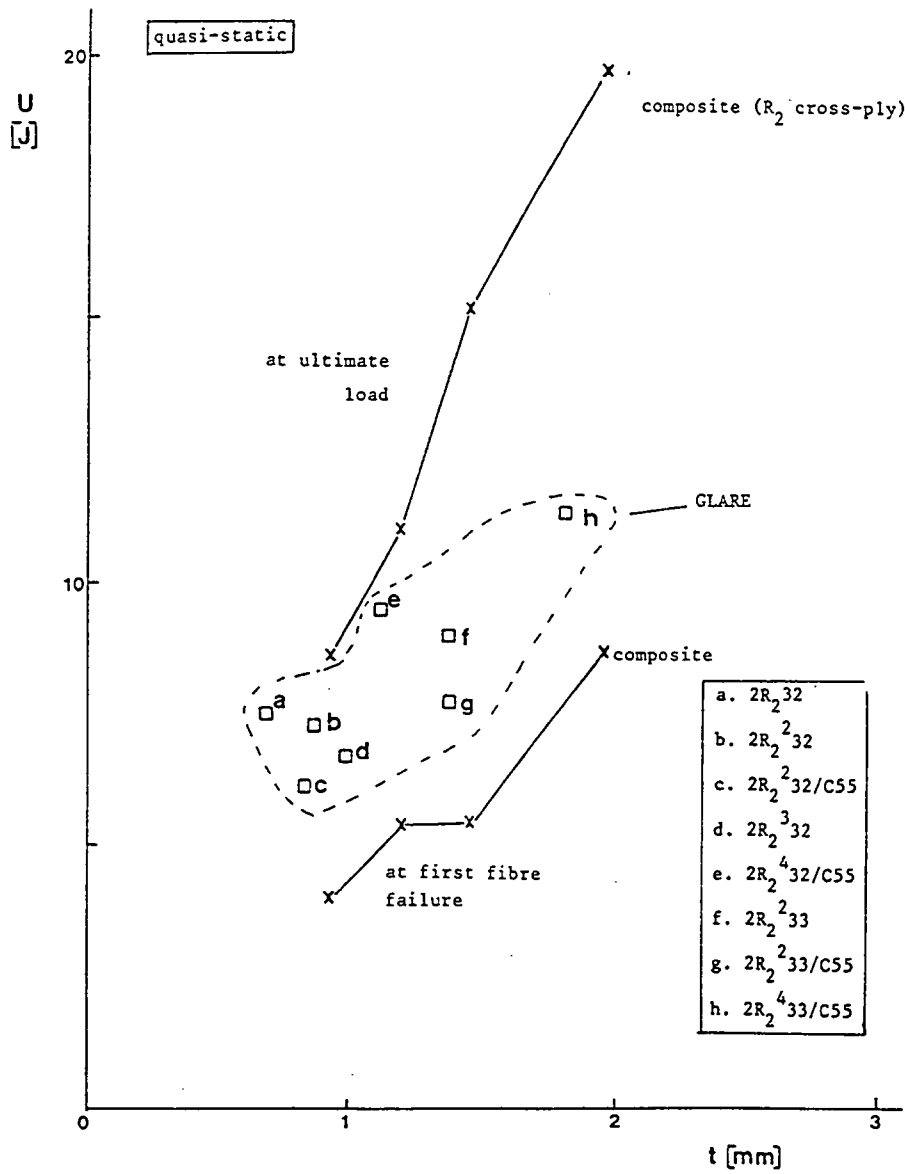
figure 7.11 The absorbed energy at first fibre fracture and at maximum load vs. the sheet thickness for cross-ply composites and GLARE.

quasi-static

a. $2R_2 32$

b. $2R_2{}^2 32$

c. $2R_2{}^2 32/C55$

d. $2R_2{}^3 32$

e. $2R_2{}^4 32/C55$

f. $2R_2{}^2 33$

g. $2R_2{}^2 33/C55$

h. $2R_2{}^4 33/C55$

at ultimate
load

composite
(R_2 cross-ply)

GLARE

composite

at first fibre
failure
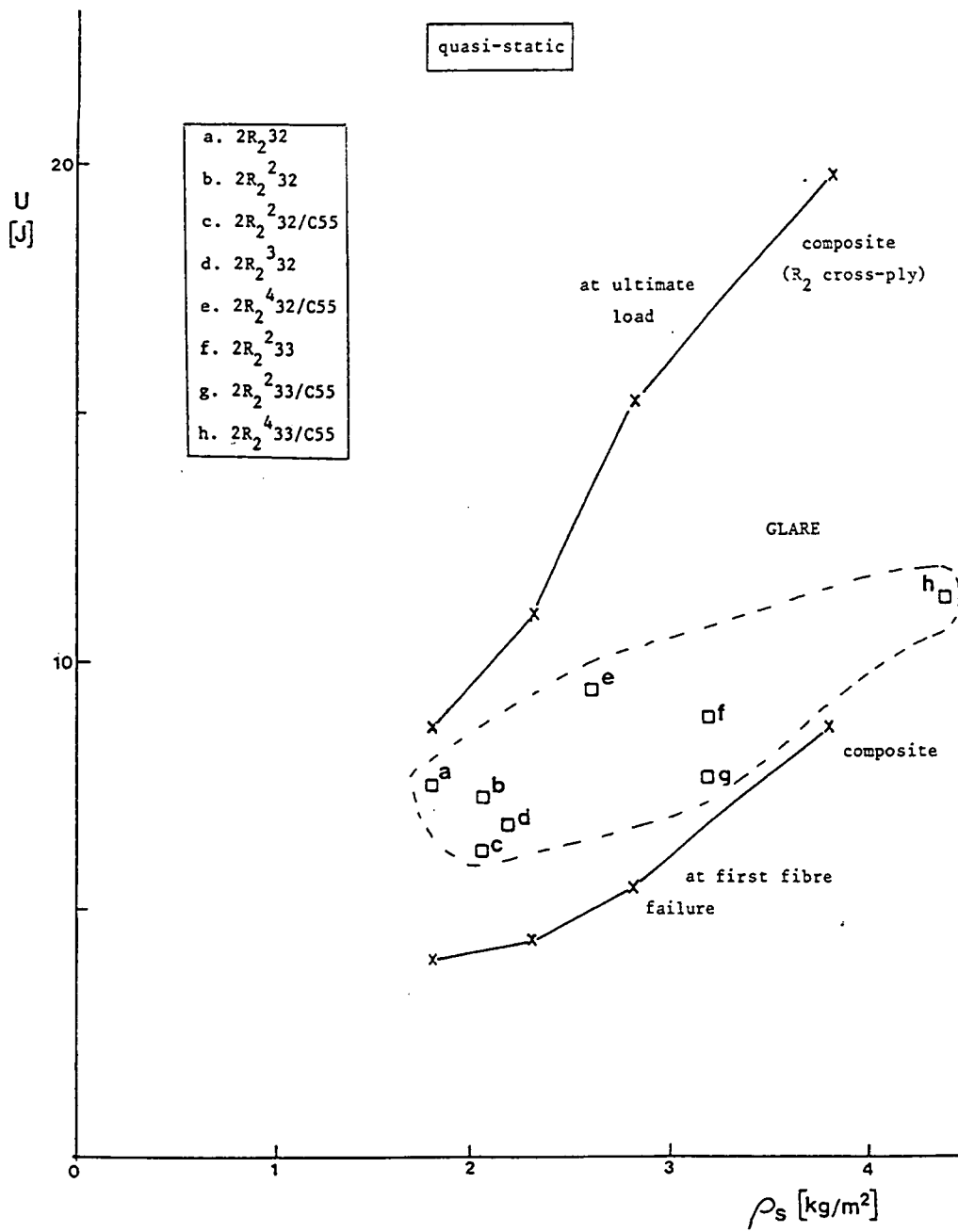
figure 7.12 The absorbed energy at first fibre fracture and at maximum load vs. the surface density for cross-ply composites and GLARE.

quasi-static

U
[J]

at ultimate
load

composite (R_4 cross-ply)

20

6 O
X

O 8

GLARE

X

O 7

O 5
X

composite
X at first
fibre failure

O 1

4 O

X

O 2

10

O 3

| 1. $2R_4 32$ |
| 2. $2R_4^2 32$ |
| 3. $2R_4^3 32$ |
| 4. $2R_4^3 /C73$ |
| 5. $2R_4 33$ |
| 6. $2R_4^4 32/C55$ |
| 7. $2R_4^2 33$ |
| 8. $2R_4^2 33/C55$ |

0   1   2   3

t [mm]
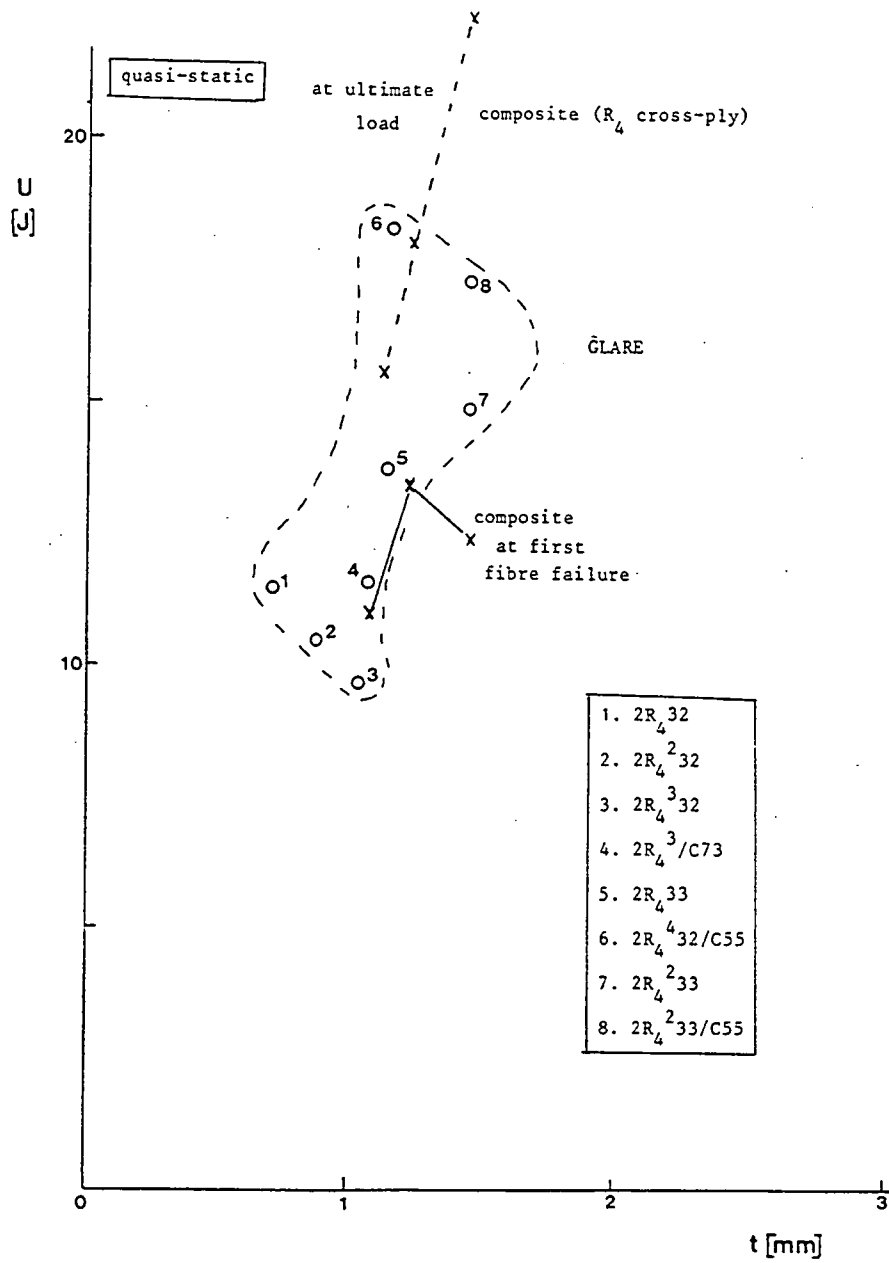
figure 7.13 The absorbed energy at first fracture and at maximum
load vs. the sheet thickness for cross-ply composites and GLARE.
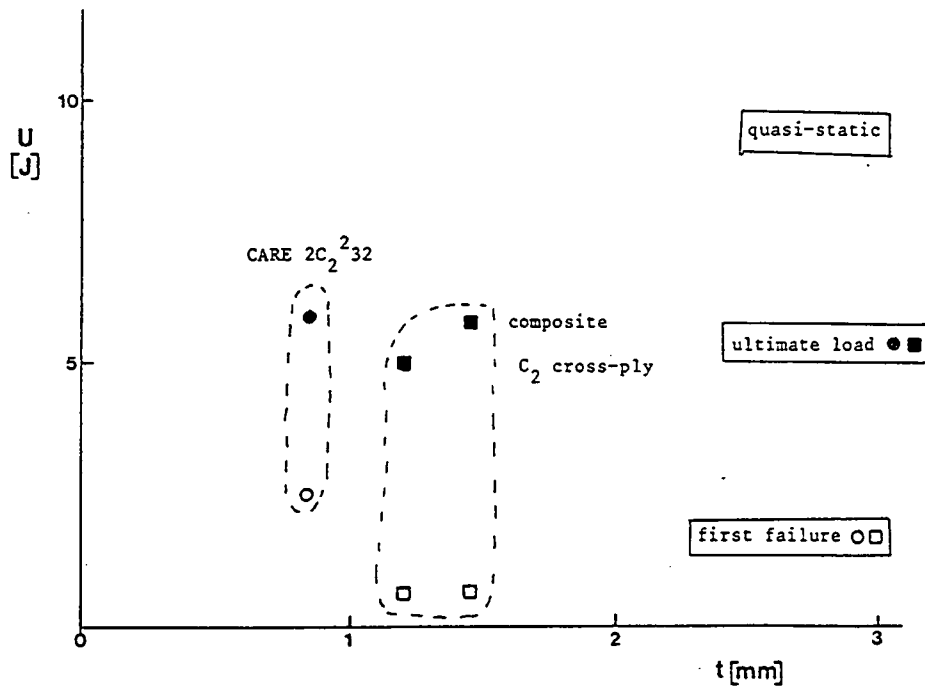
figure 7.14 The absorbed energy at first fracture and at maximum load for the carbon cross-ply composites and carbon ARALL $2C_2 32$.
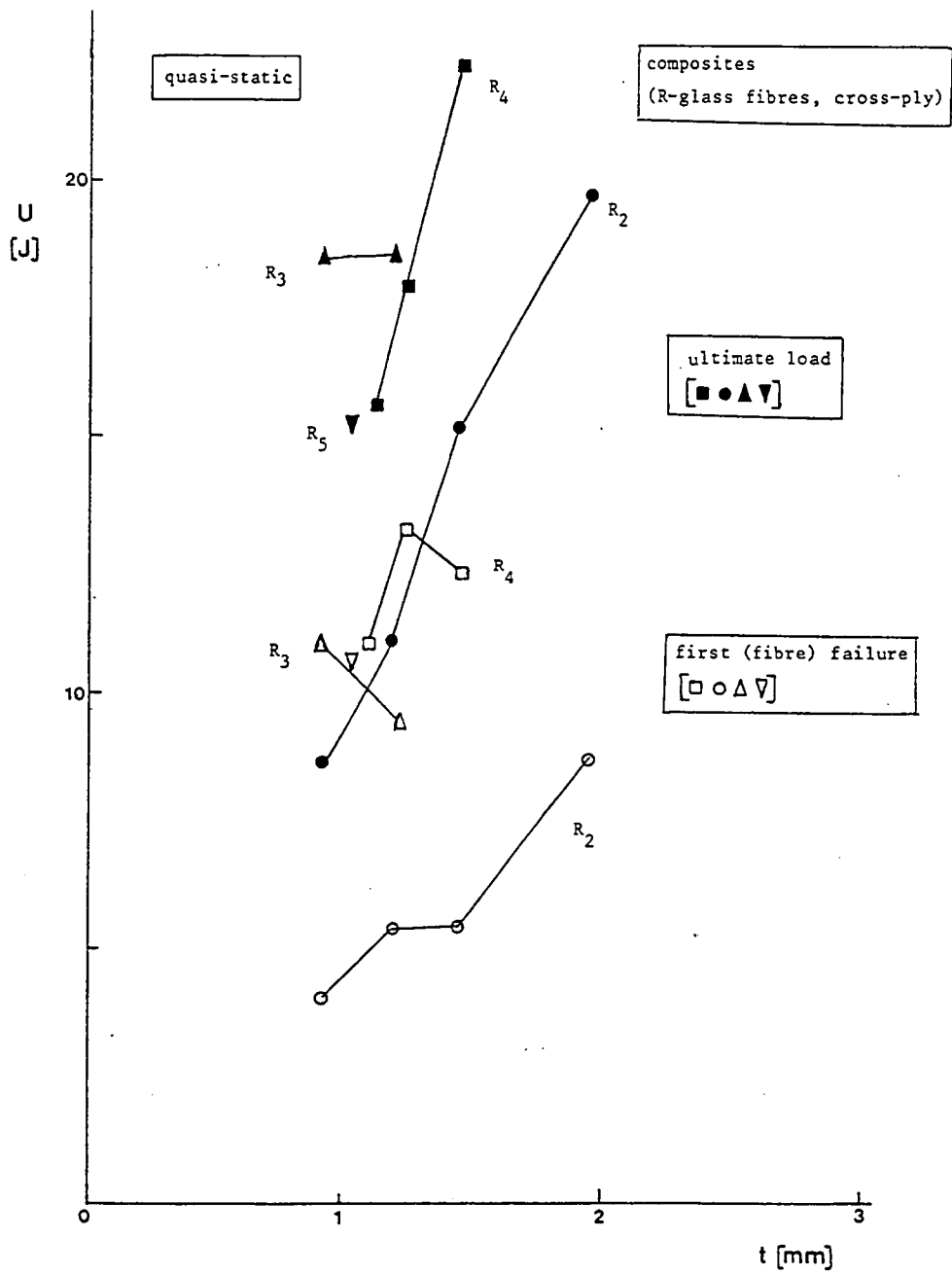
figure 7.15 The absorbed energy at first fibre fracture and at maximum force vs. the sheet thickness for the R-glass cross-ply composites.
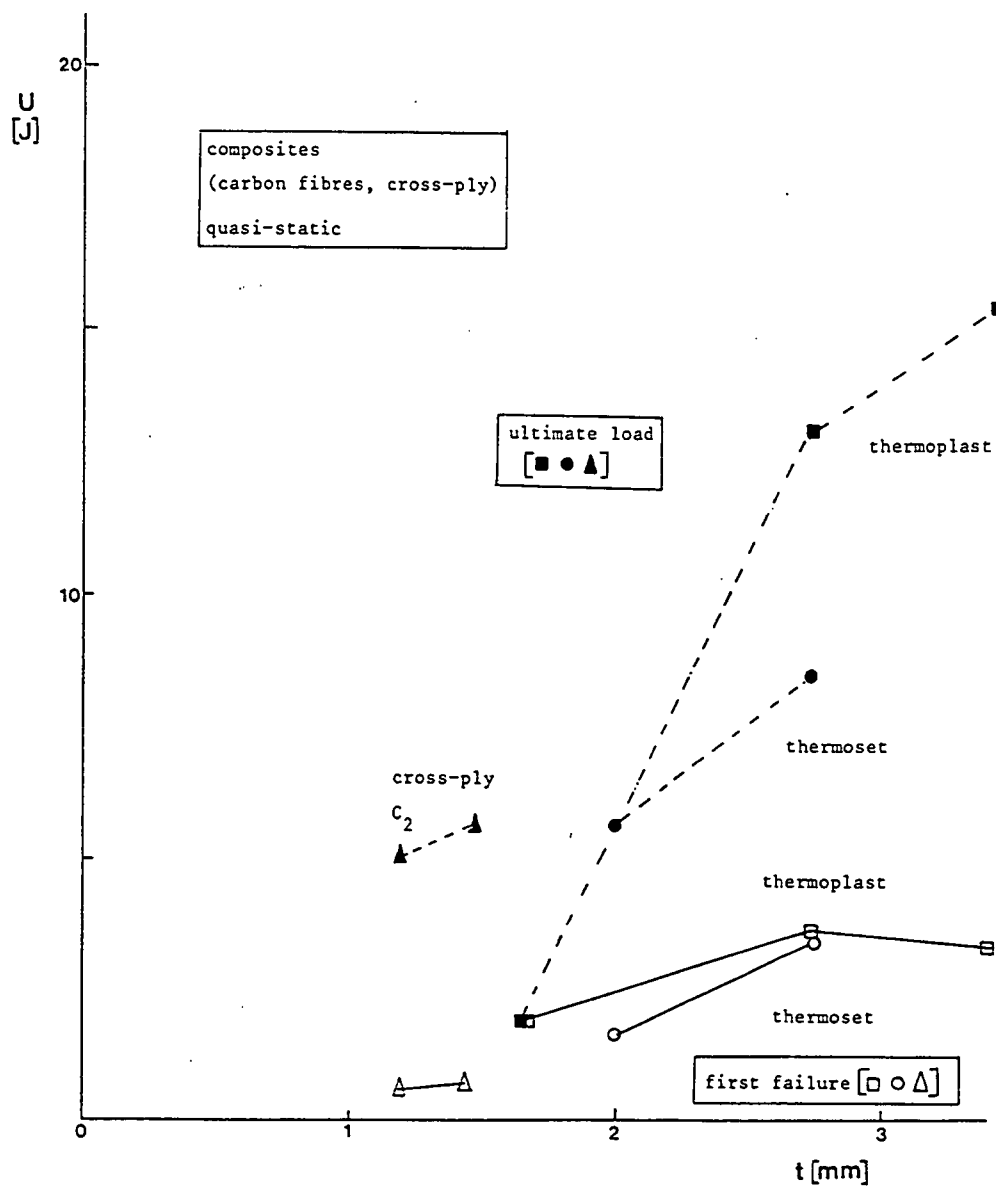
figure 7.16 The absorbed energy at first fibre fracture and at maximum force for the carbon thermoplastic and thermosetting composites.

quasi-static

Al 2024-T3, t=0.8 mm

$2R_4{}^232$

$2R_2{}^232$

$2R_2{}^232/C55$

GLARE

2H32

aramid ARALL

$2C_232$

CARE

$2C_232/C55$

U [J]

first failure   ultimate load
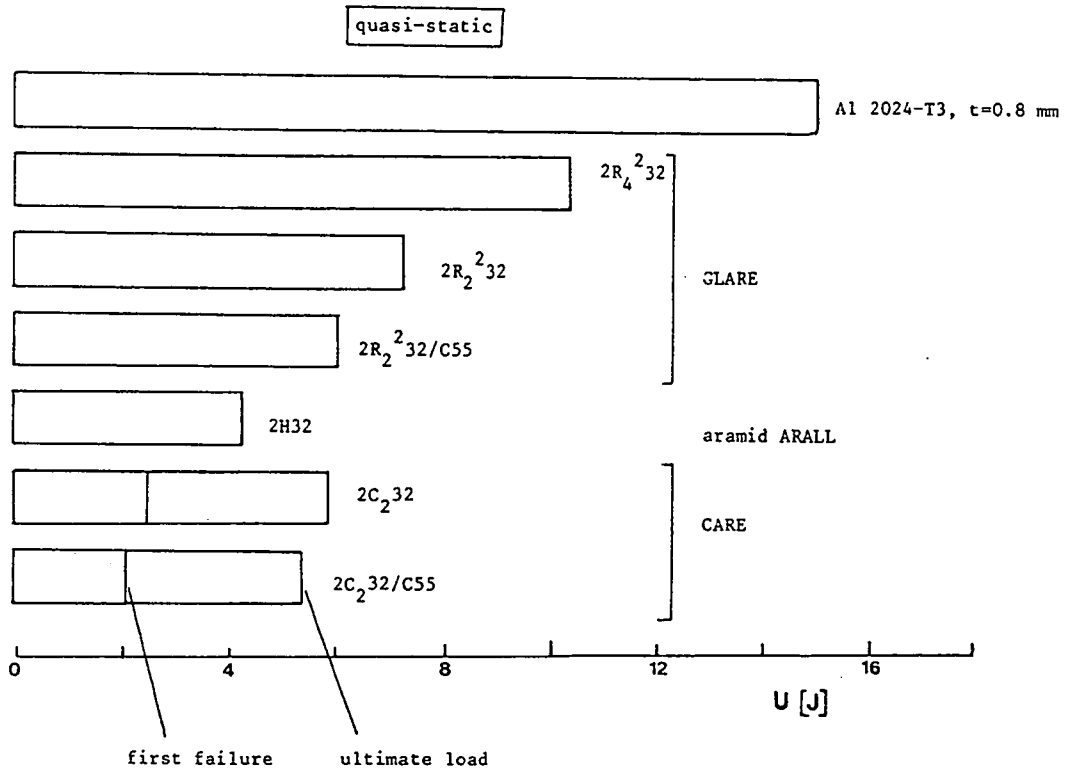
figure 7.17 The absorbed energy at fibre failure and at maximum load for monolithic aluminium and ARALL, with a thickness of 0.8 mm.

234

quasi-static

Al 2024-T3, t=1.4 mm

$2R_4^2 33$, t=1.45 mm

$2R_4^2 33/C55$, t=1.45 mm

$2R_2^2 33$, t=1.36 mm

$2R_2^2 33/C55$, t=1.37 mm

$2R_3^2 33/C55$, t=1.36 mm

$2R_5^2 33/C55$, t=1.52 mm

cross-ply R_2-fibre, t=1.45 mm

cross-ply C_2-fibre, t=1.45 mm

cross-ply R_4 fibre t=1.45 mm

GLARE

composites

U [J]

0   4   8   12   16   20

first failure

ultimate load
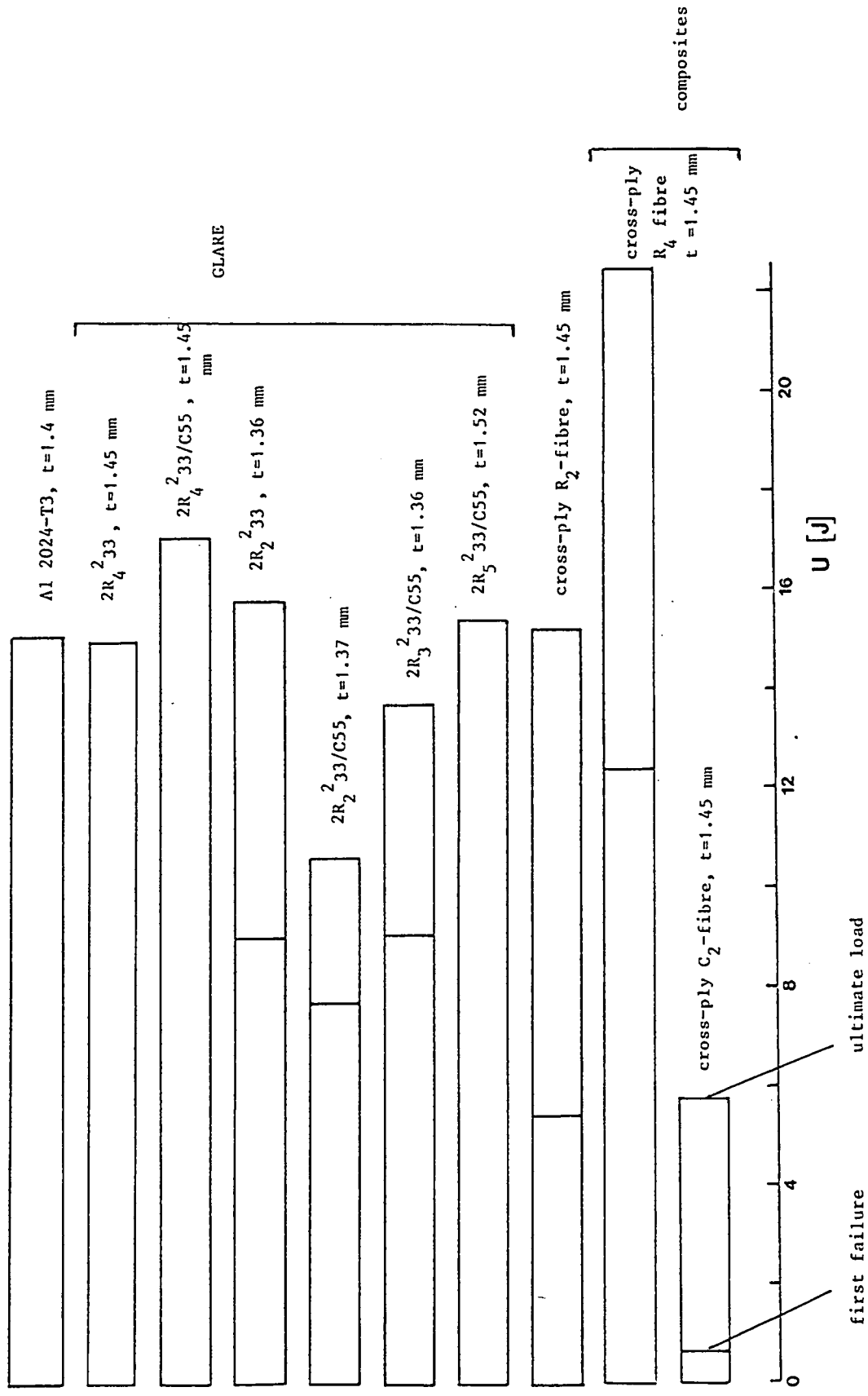
figure 7.18 The absorbed energy at fibre fracture and at maximum force for monolithic aluminium, ARALL and cross-ply composites, for a thickness of 1.4 mm.
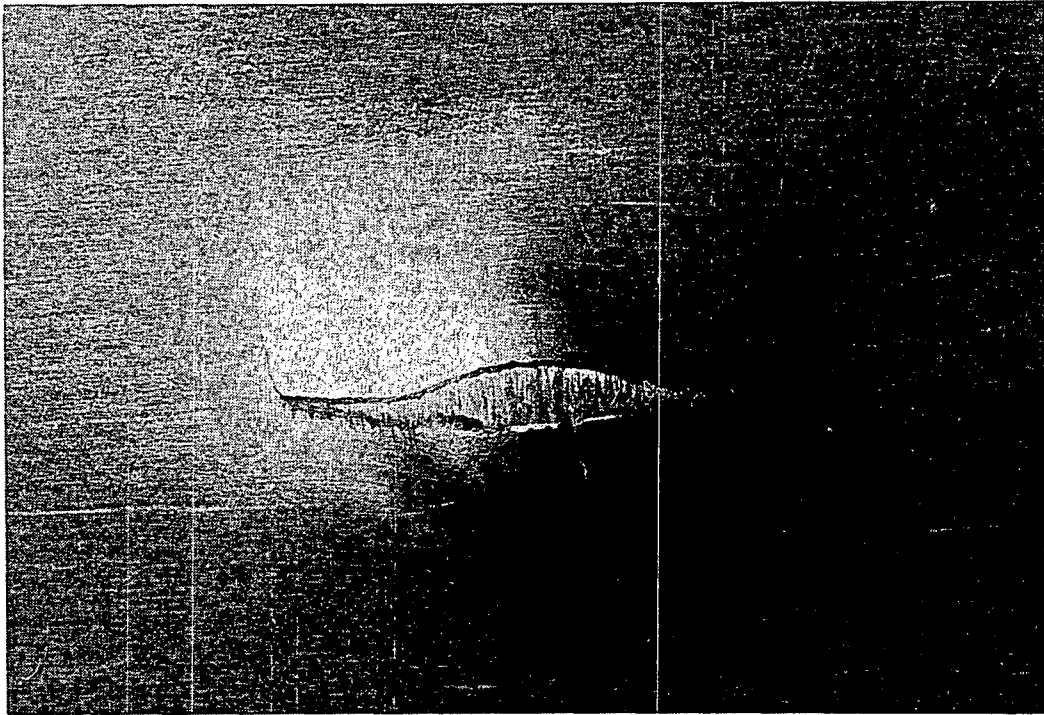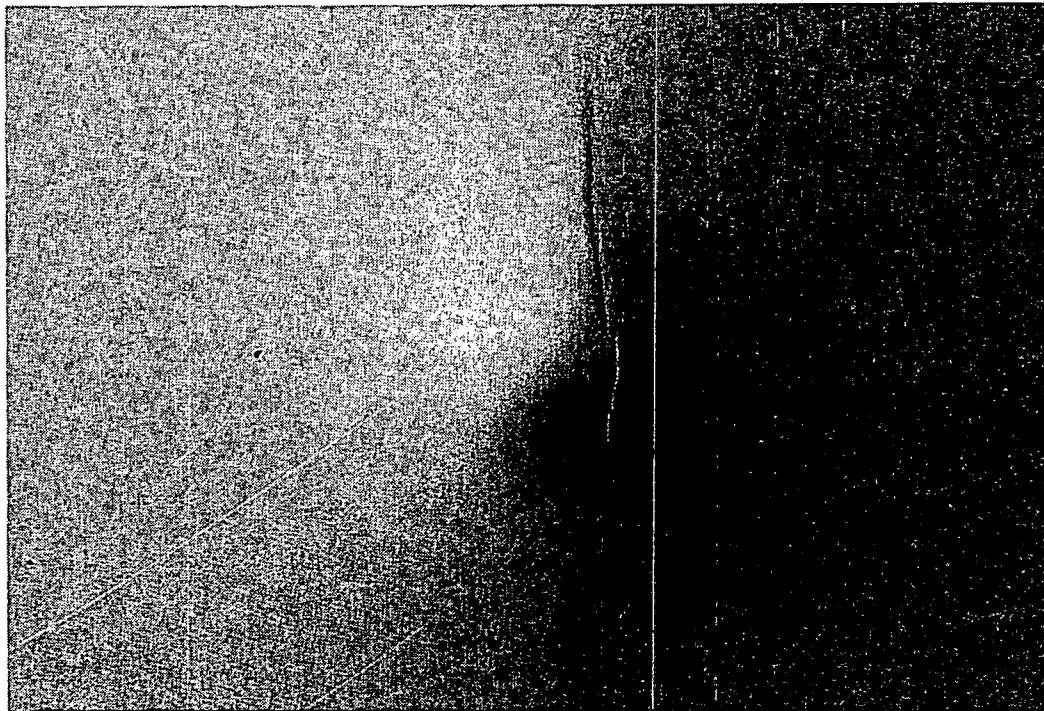
figure 7.19 Fracture modes in aluminium layer of ARALL
a. fibre critical, 2H32 aramid ARALL
b. aluminium critical, 2R32 GLARE. } fibre direction: ↕
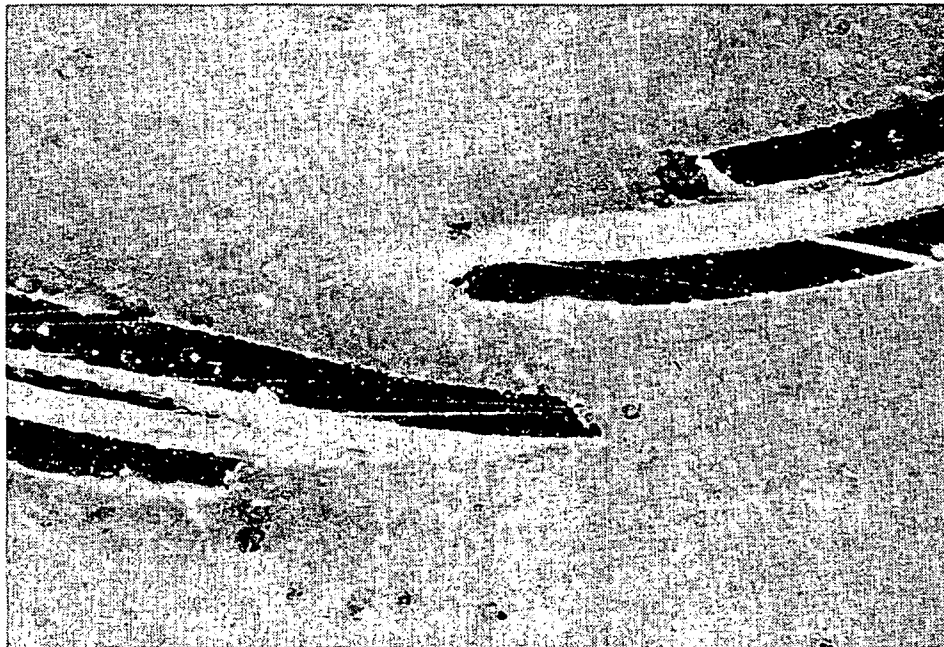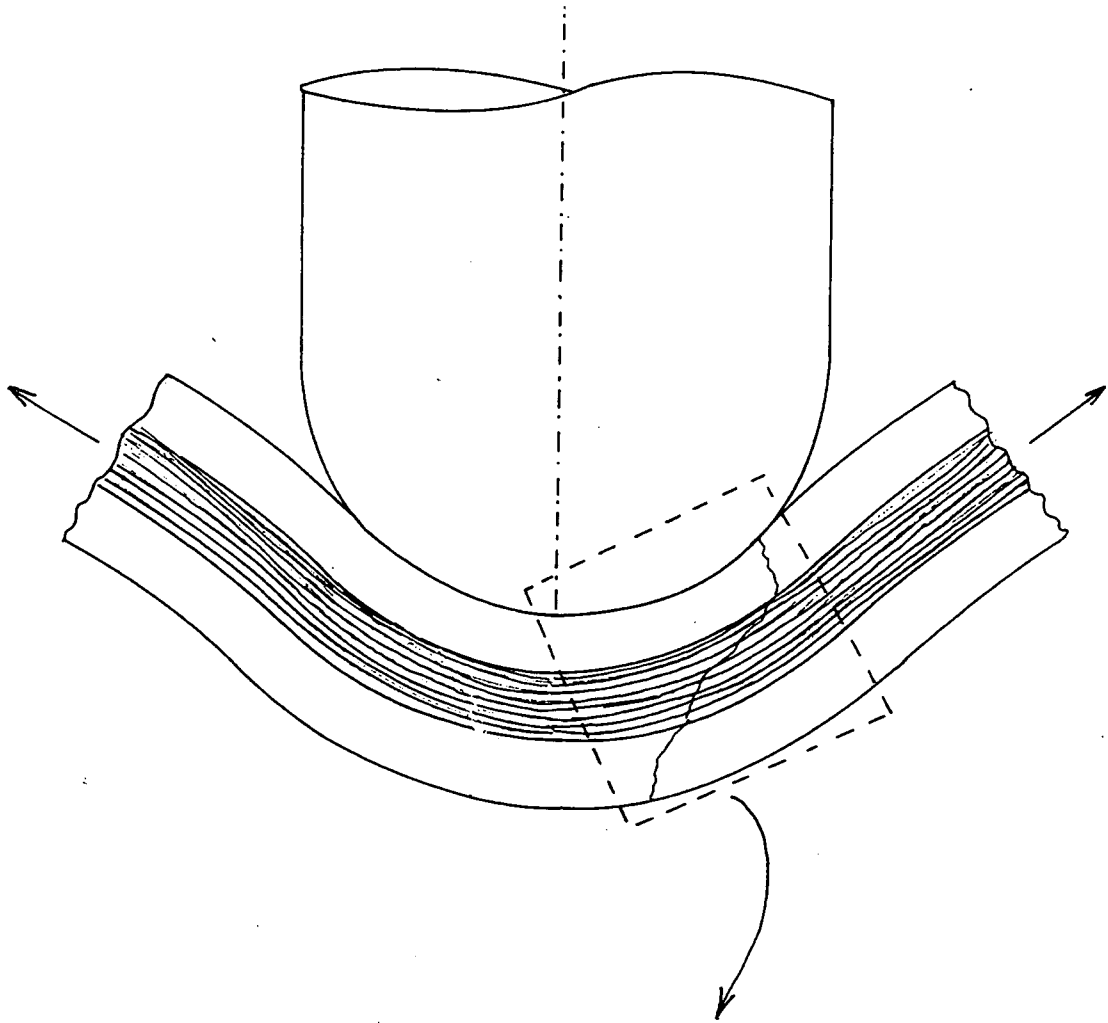
figure 7.20 Cross-section of an aramid ARALL specimen with fibre
critical fracture.
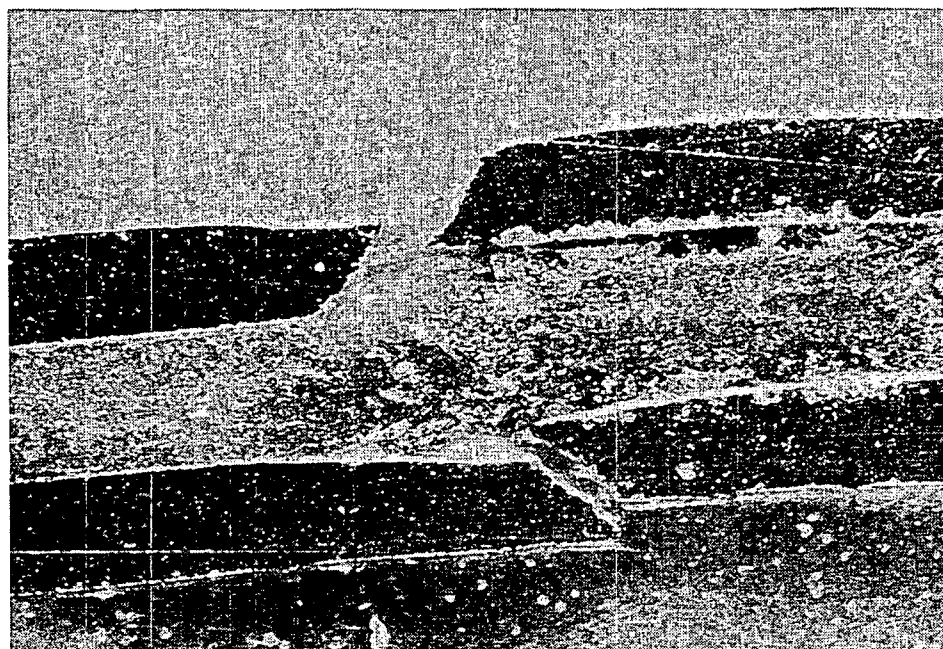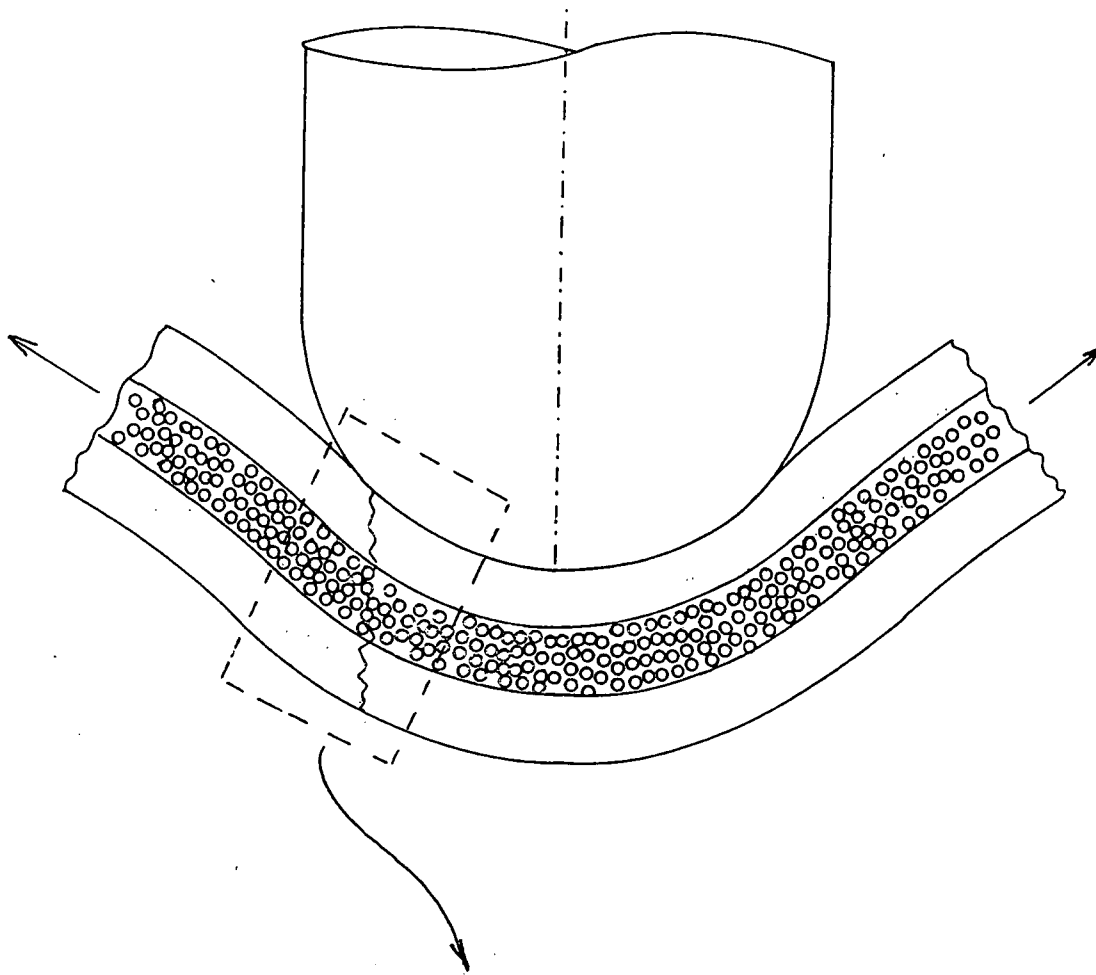
figure 7.21 Cross-section of glass ARALL (GLARE) specimen with aluminium critical fracture.
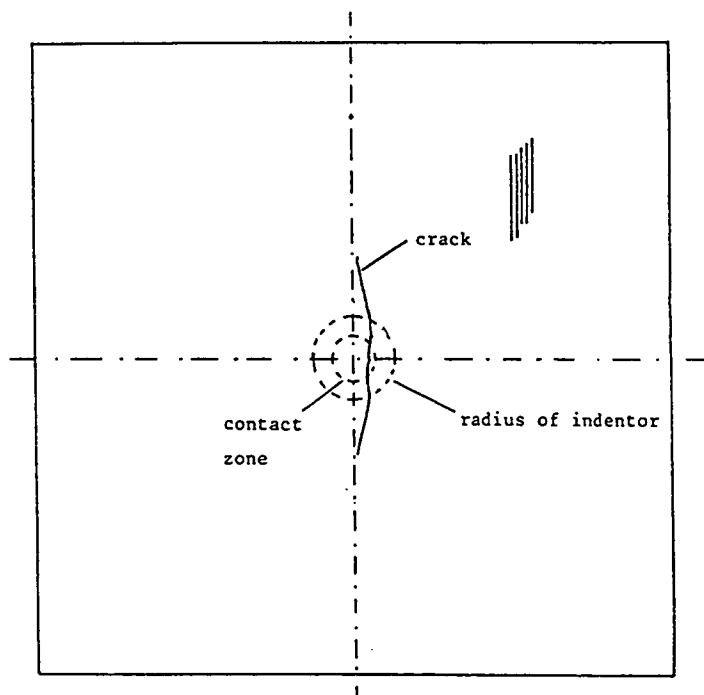
figure 7.22 Crack in unidirectional ARALL with aluminium critical fracture.
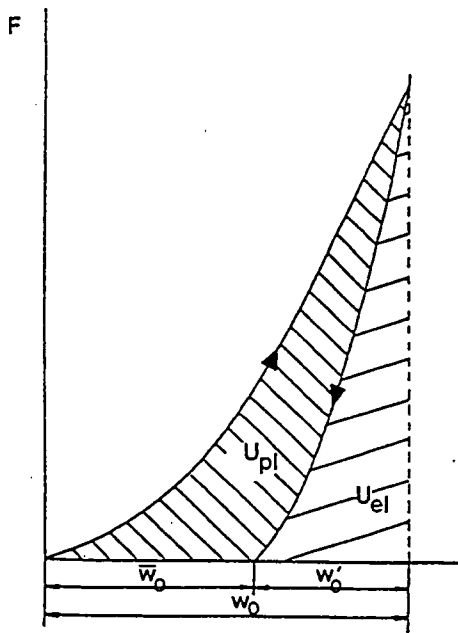
figure 7.23 Force-deflection curve with unloading path, with the

plastic energy U_{pl} the elastic energy U_{el}, the total central

deflection w_0, the elastic central deflection w_0' and the permanent

central deflection $\bar{w}_0$.
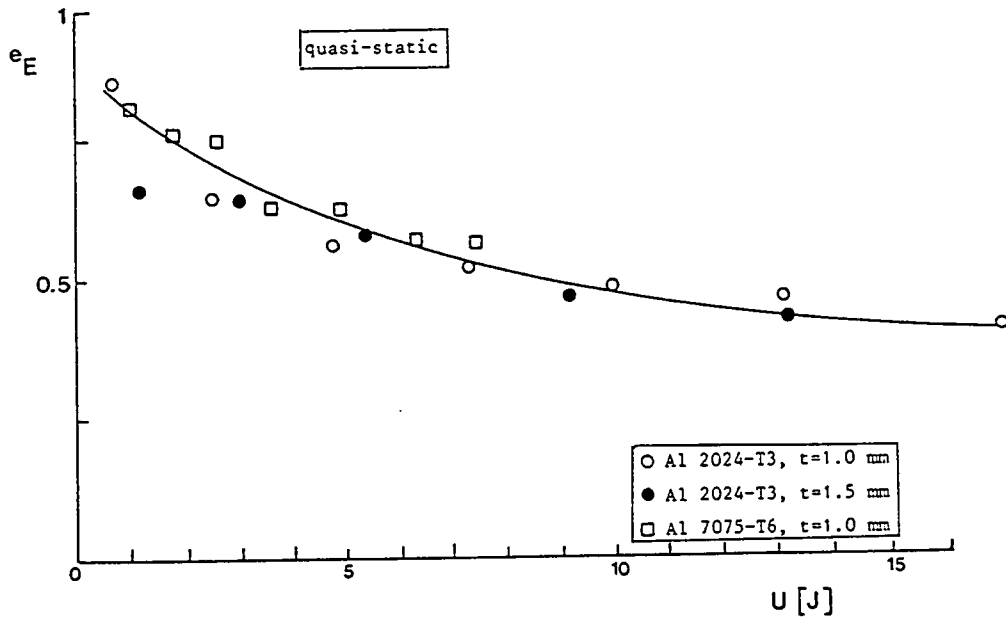
figure 7.24 Energy restitution coefficient vs. the absorbed energy for monolithic aluminum.
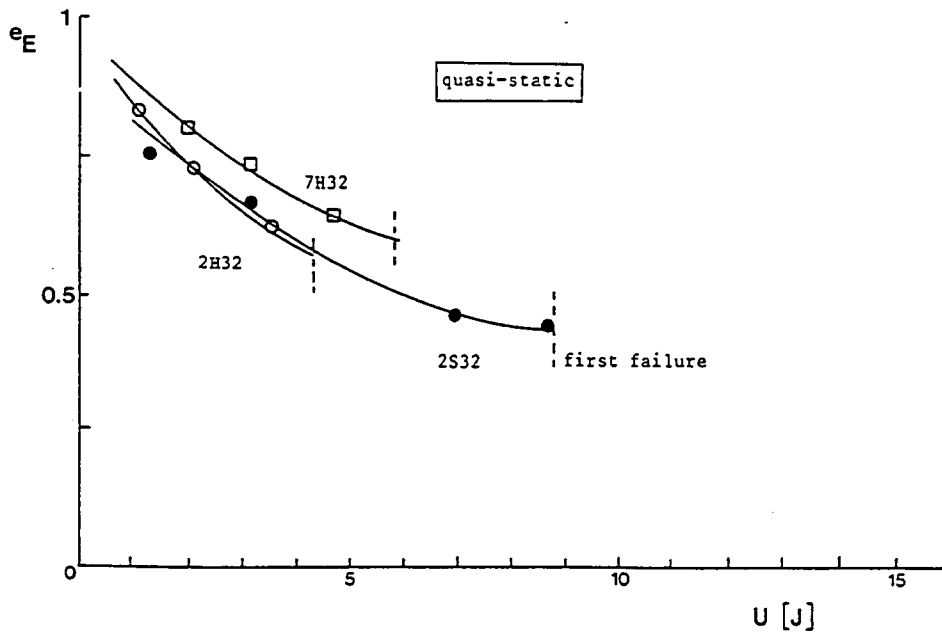
figure 7.25 Energy restitution coefficient vs. the absorbed energy for aramid ARALL, 7H32: Al 7075-T6 layers, 2H32: Al 2024-T3 layers.
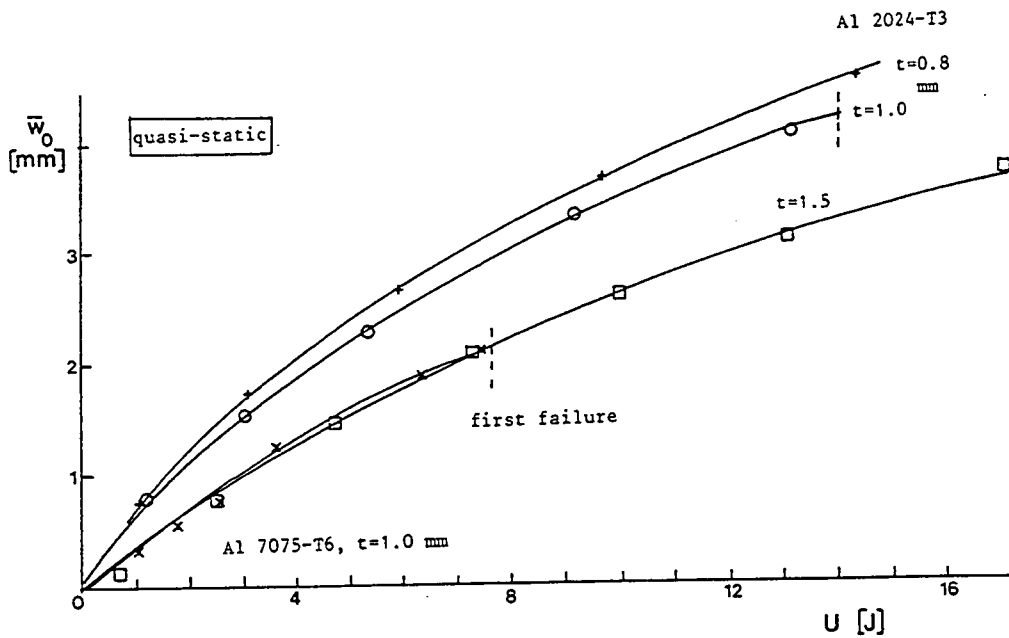
figure 7.26 The permanent central deflection vs. the absorbed energy for monolithic aluminium.
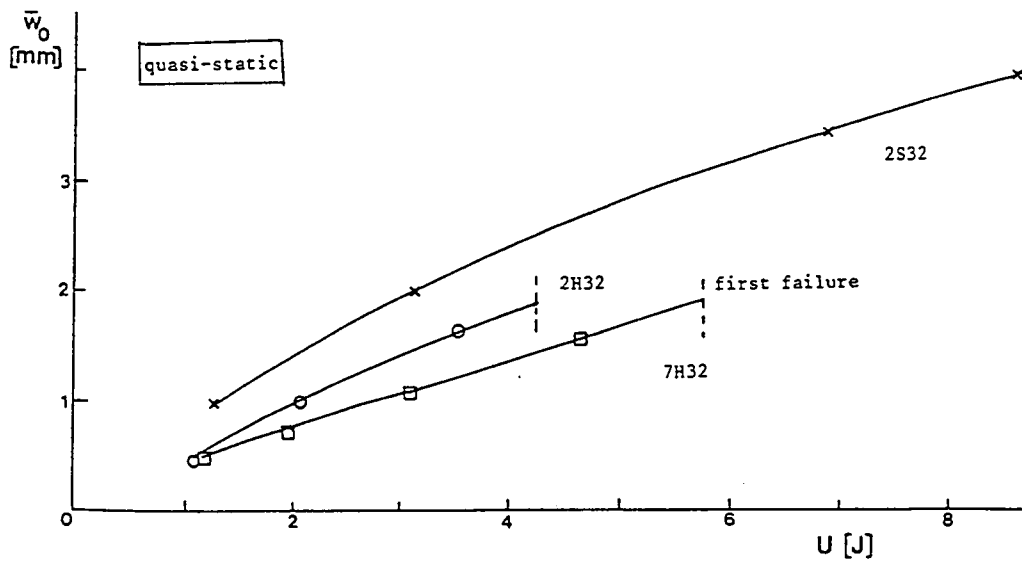
figure 7.27 The permanent central deflection vs. the absorbed energy for ARALL.

2H32 and 7H32: aramid ARALL
2S32: S-glass ARALL

242
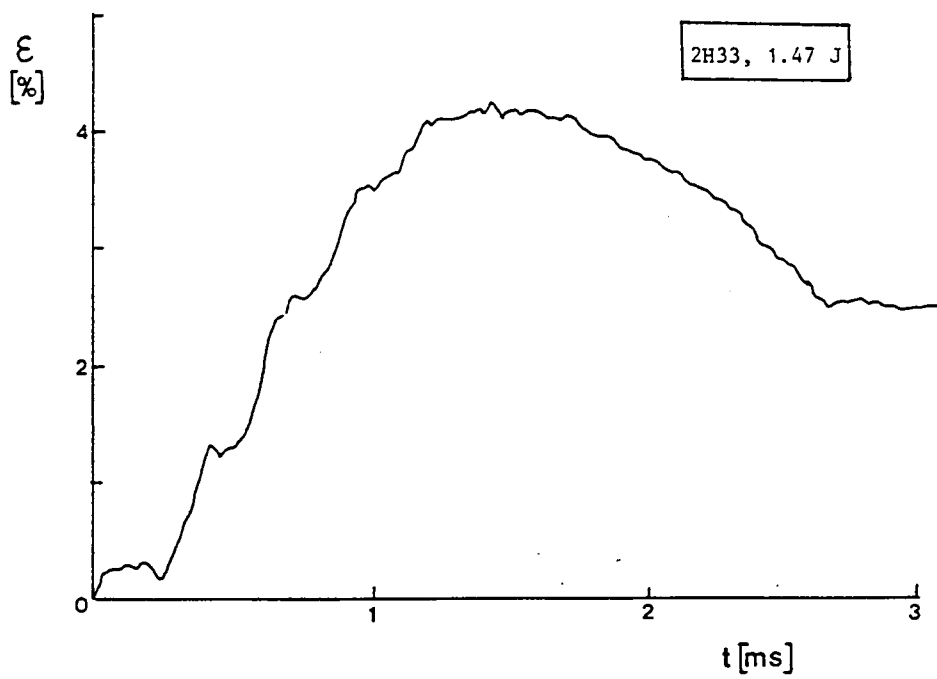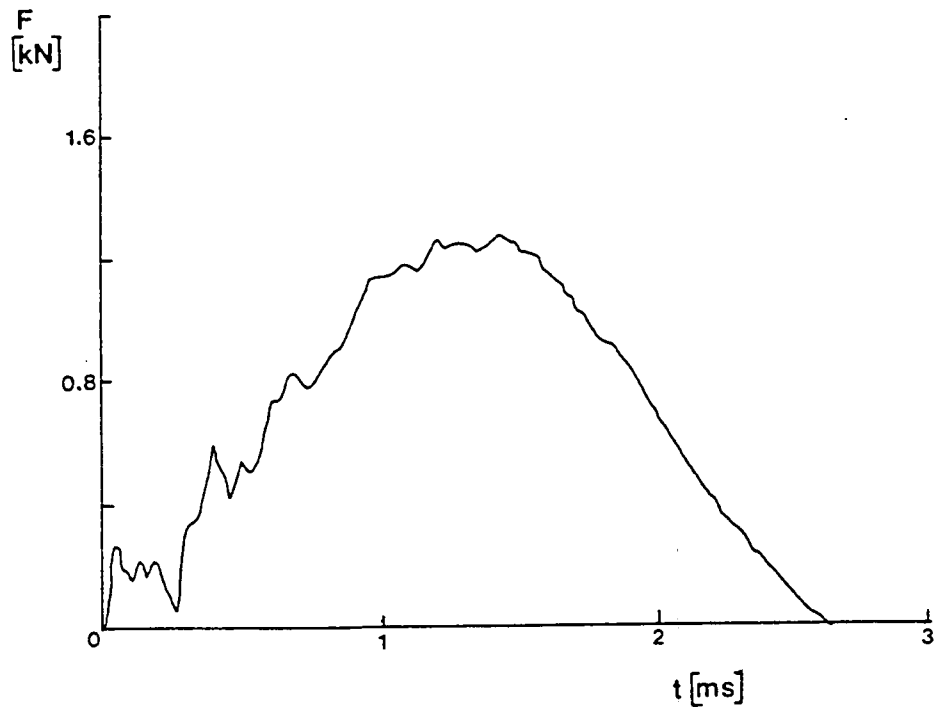
figure 7.28 Contact force- time and strain-time curves for aramid ARALL.
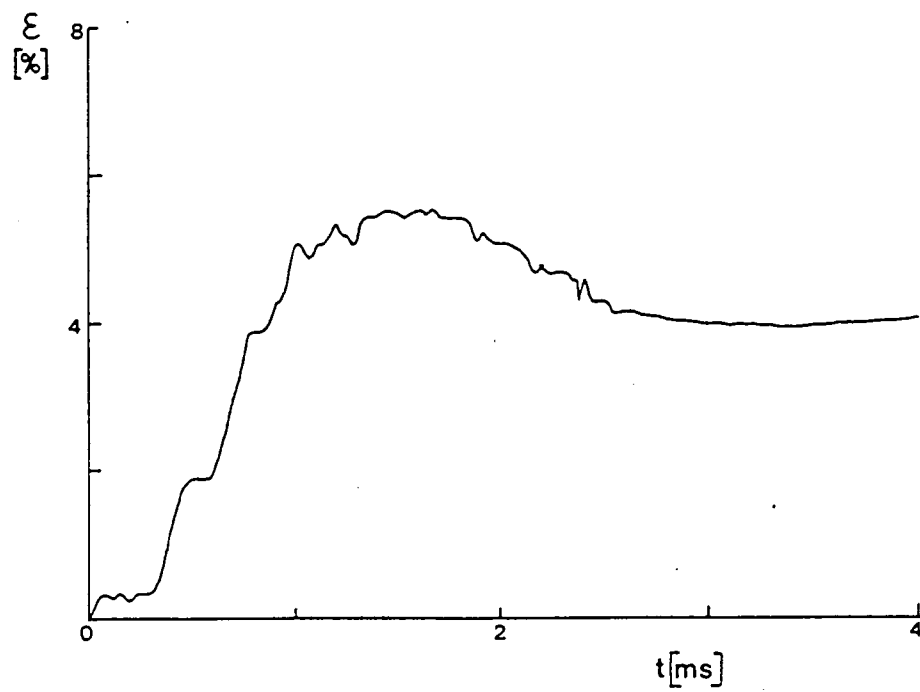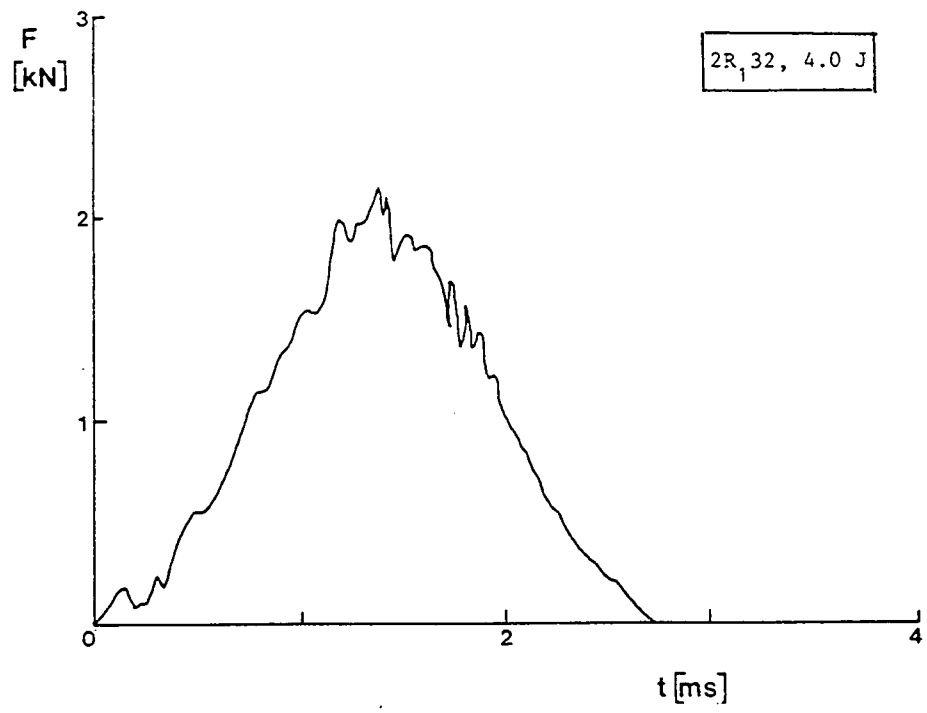
figure 7.29 Contact force- time and strain- time curves for GLARE.
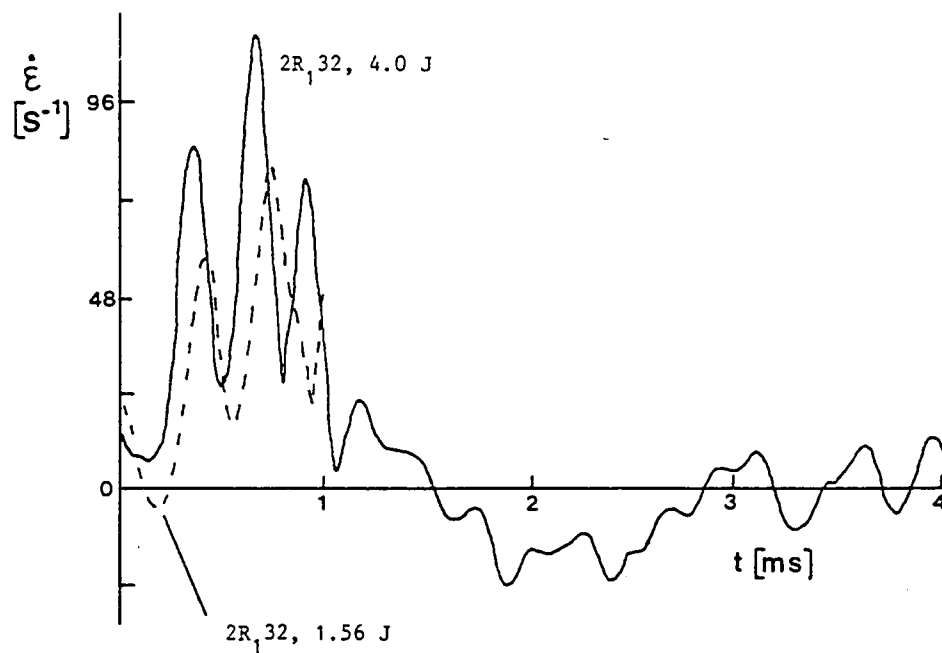
figure 7.30 Strain rate- time curve for GLARE specimens.
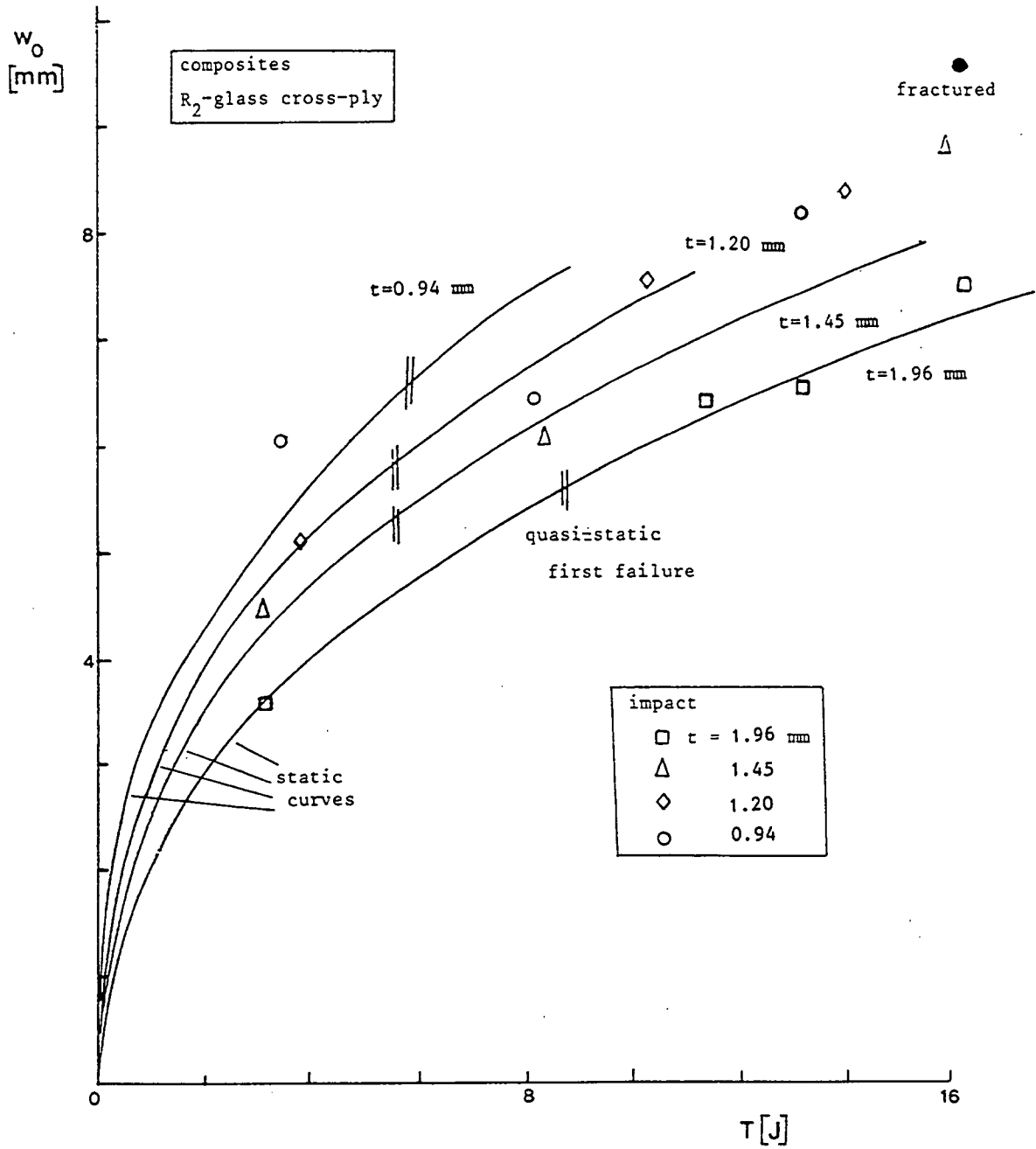
figure 7.31 Comparison of maximum central deflection during impact and quasi-static deflection vs. (impact) energy for R-glass cross-ply composites.
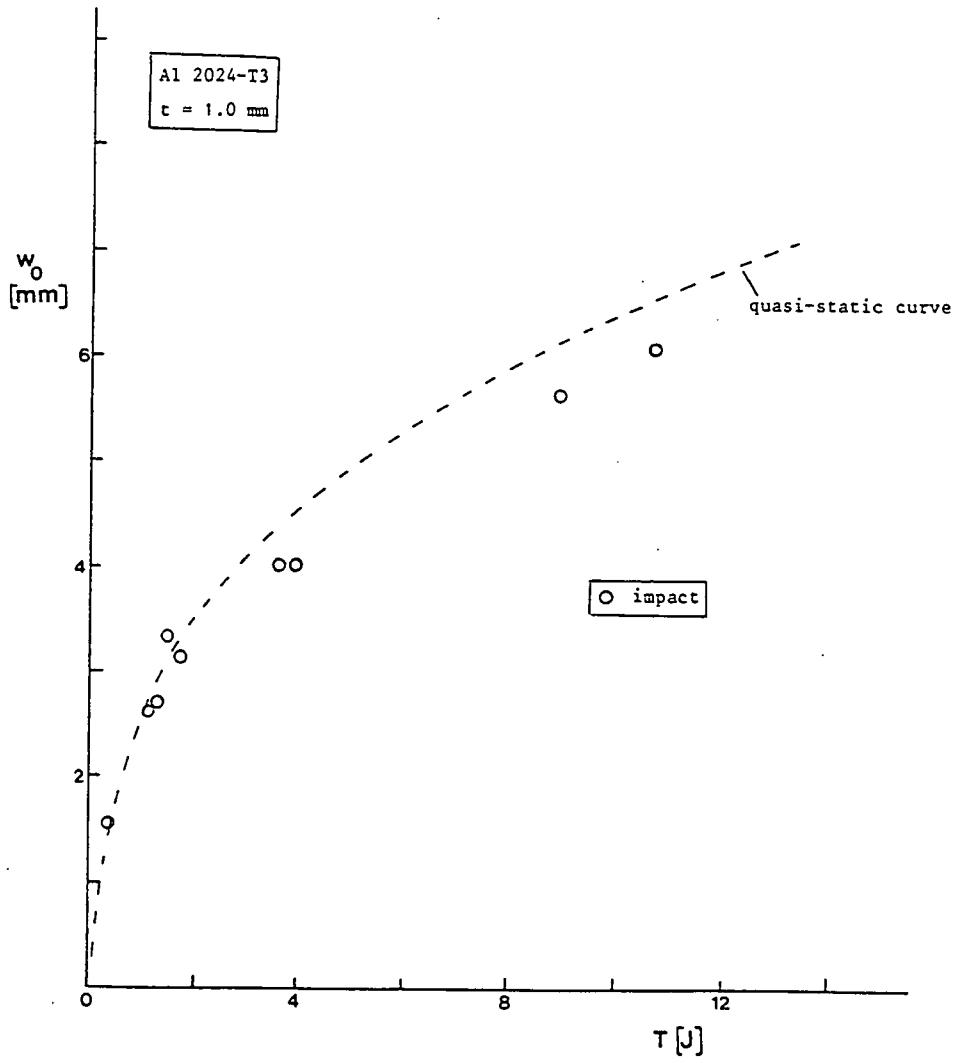
figure 7.32 Comparison of maximum central deflection during impact and quasi-static deflection vs. (impact) energy for monolithic aluminium.
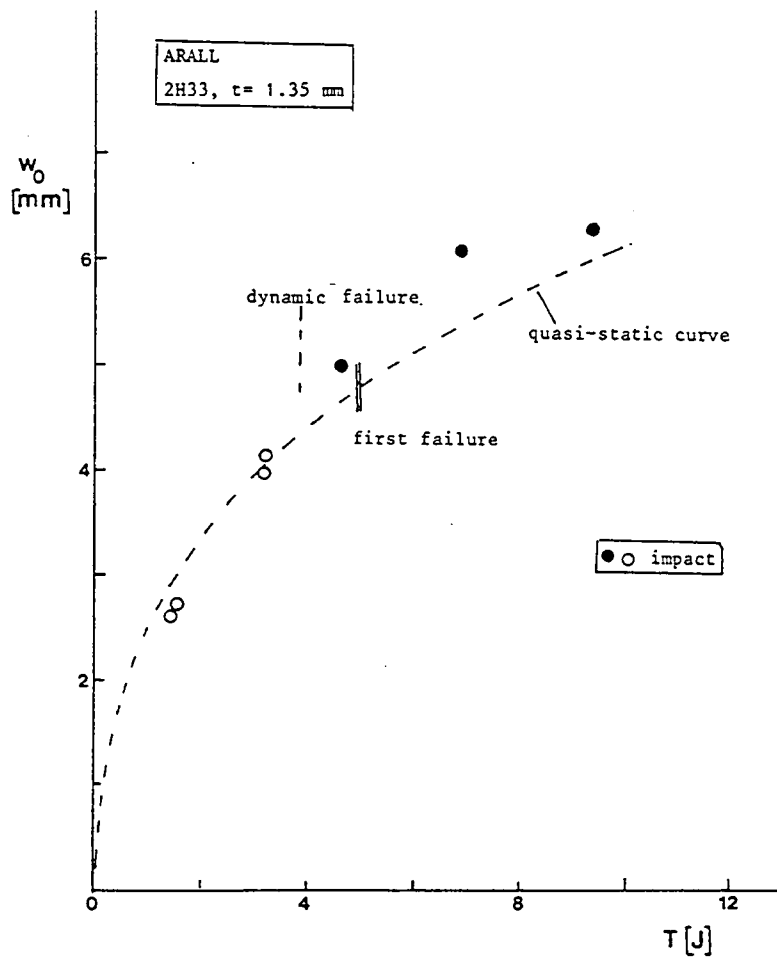
figure 7.33 Comparison of maximum central deflection during impact and quasi-static deflection vs. (impact) energy for aramid ARALL 2H33.
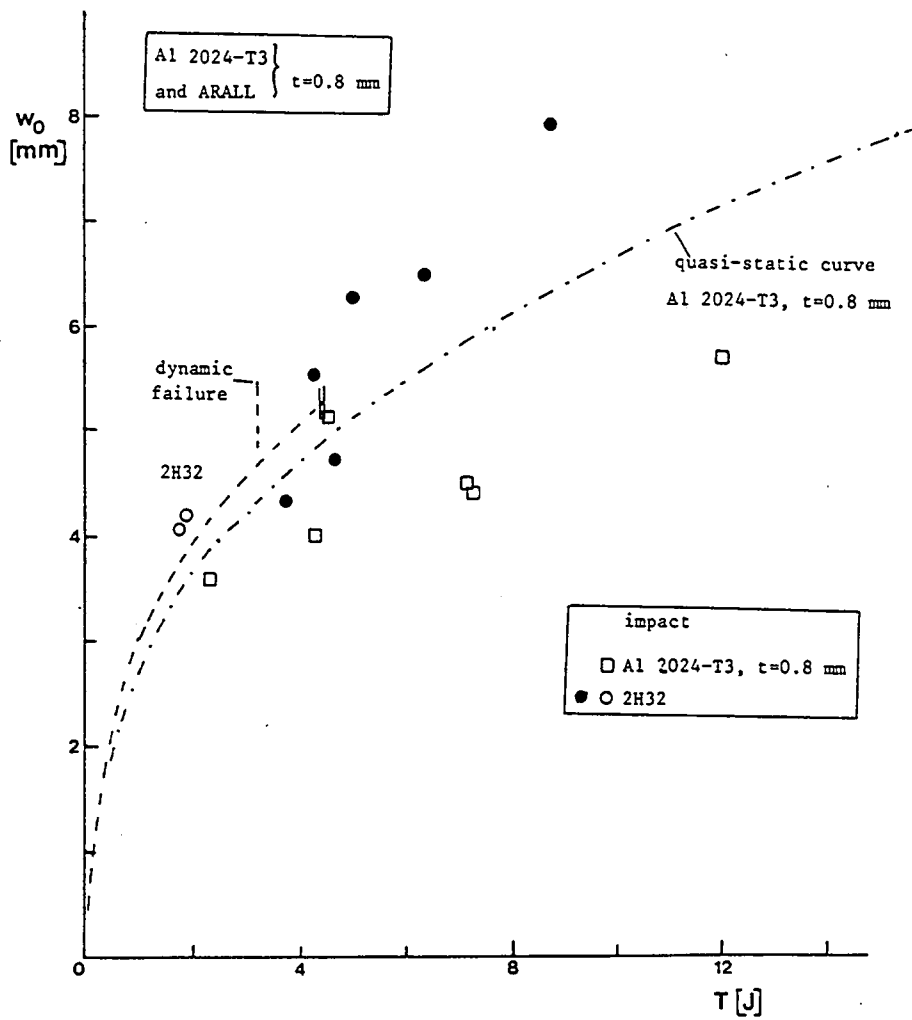
figure 7.34 Comparison of maximum central deflection during impact
and quasi-static deflection vs. (impact) energy for monolithic
aluminium and aramid ARALL 2H32.
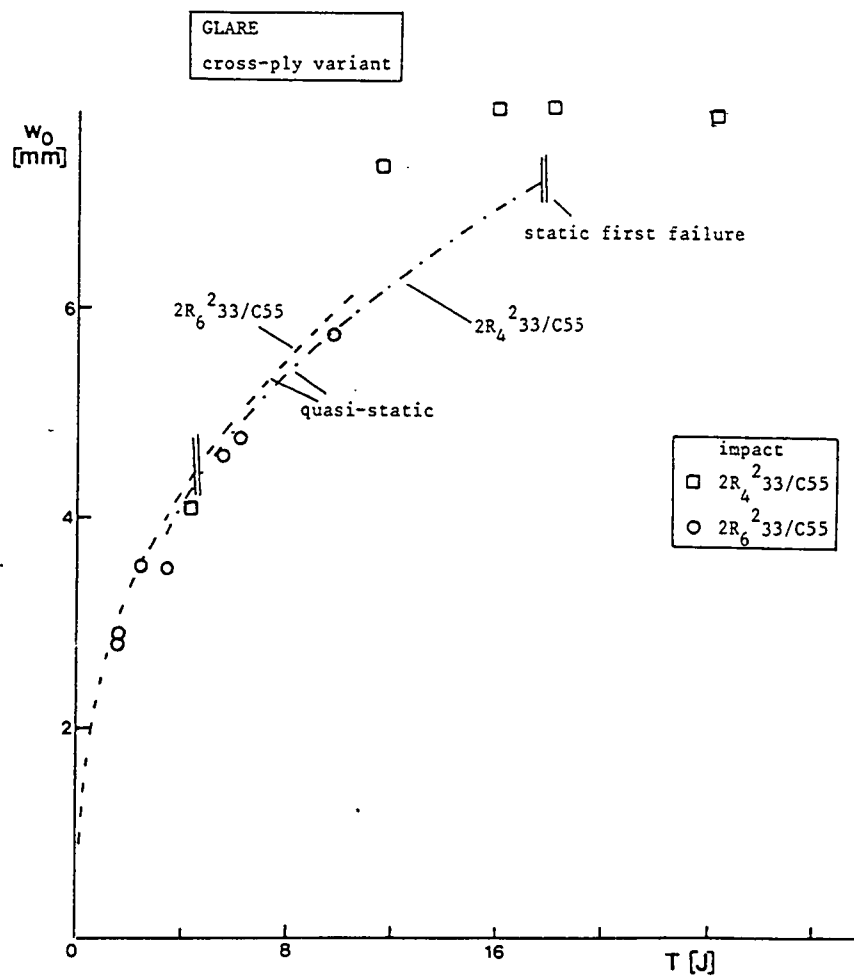
figure 7.35 Comparison of maximum central deflection during impact and quasi-static deflection vs. (impact) energy for GLARE.
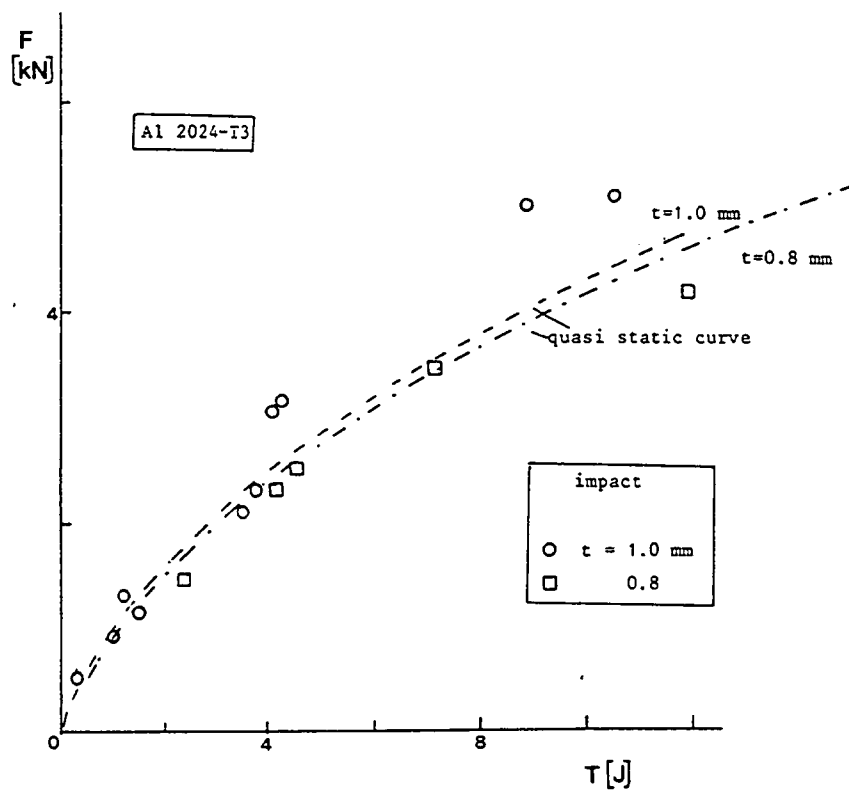
figure 7.36 Comparison of maximum contact force during impact and quasi-static force vs. (impact) energy for monolithic aluminium.
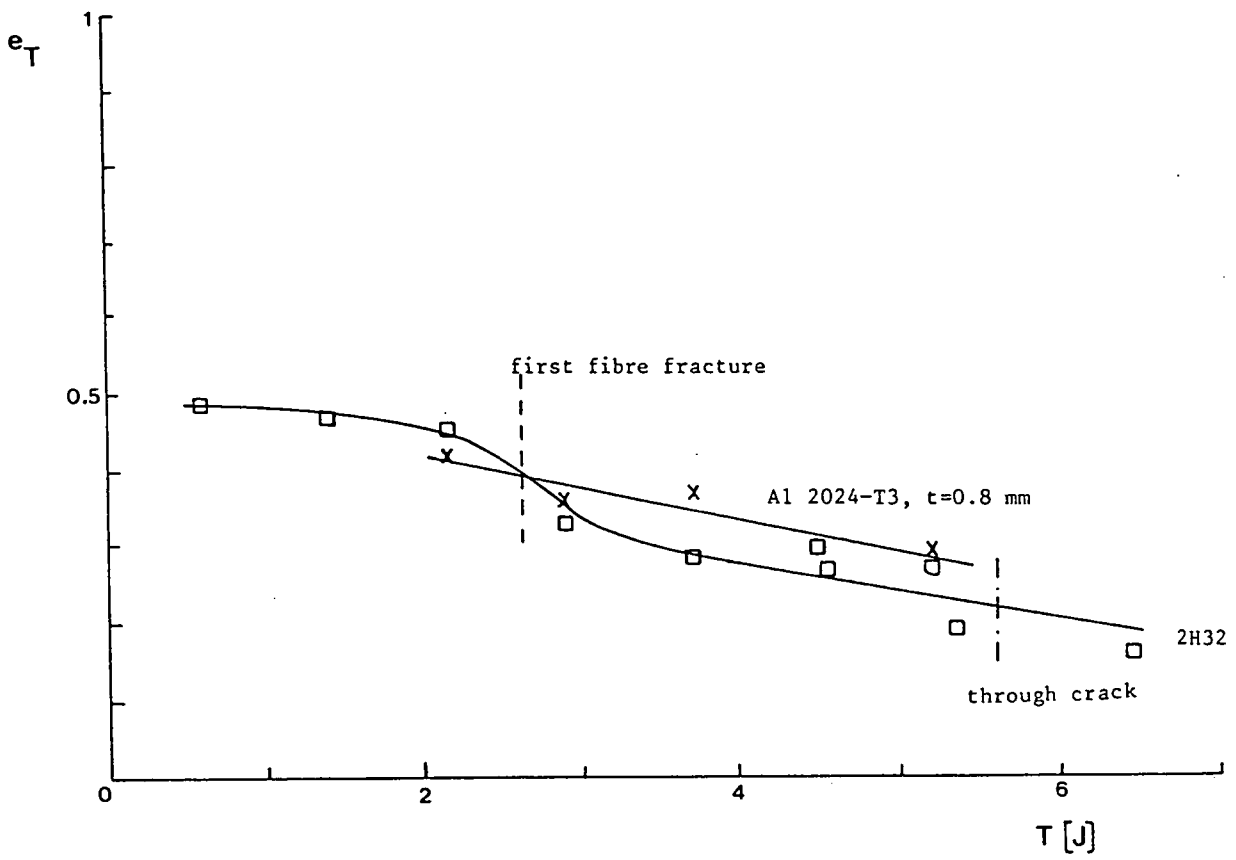
figure 7.37 The energy restitution coefficient as function of the
impact energy for monolithic aluminium and aramid ARALL 2H32.
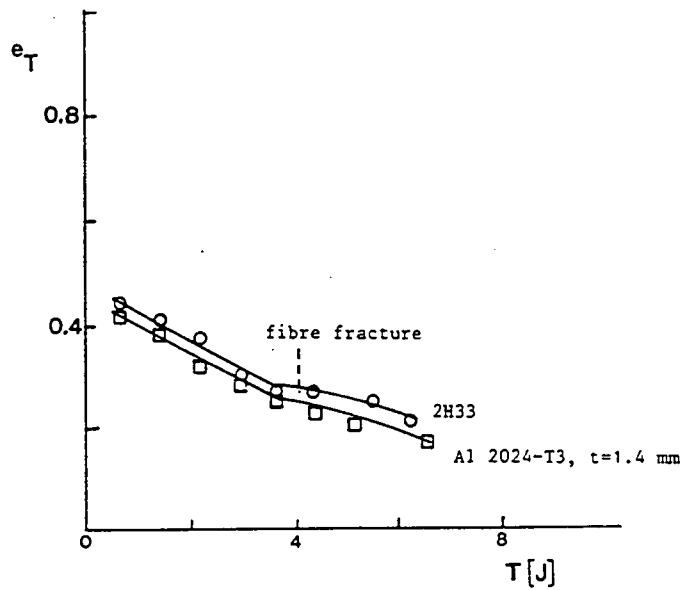
figure 7.38 The energy restitution coefficient vs. the impact energy
for monolithic aluminium and aramid ARALL 2H33.
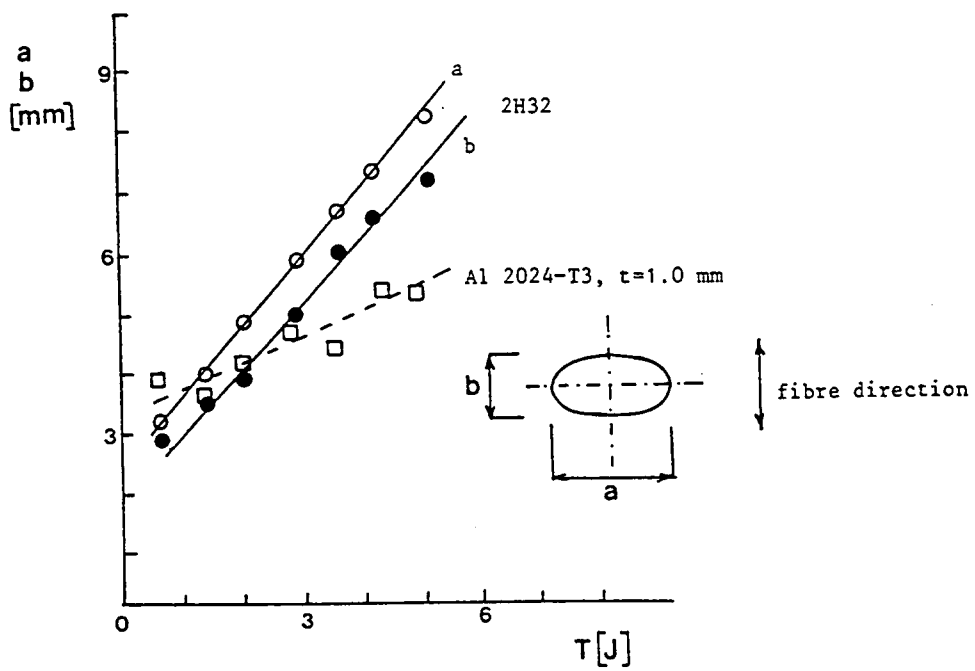
figure 7.39 The contact area after impact vs. the impact energy for monolithic aluminium and aramid ARALL 2H32.
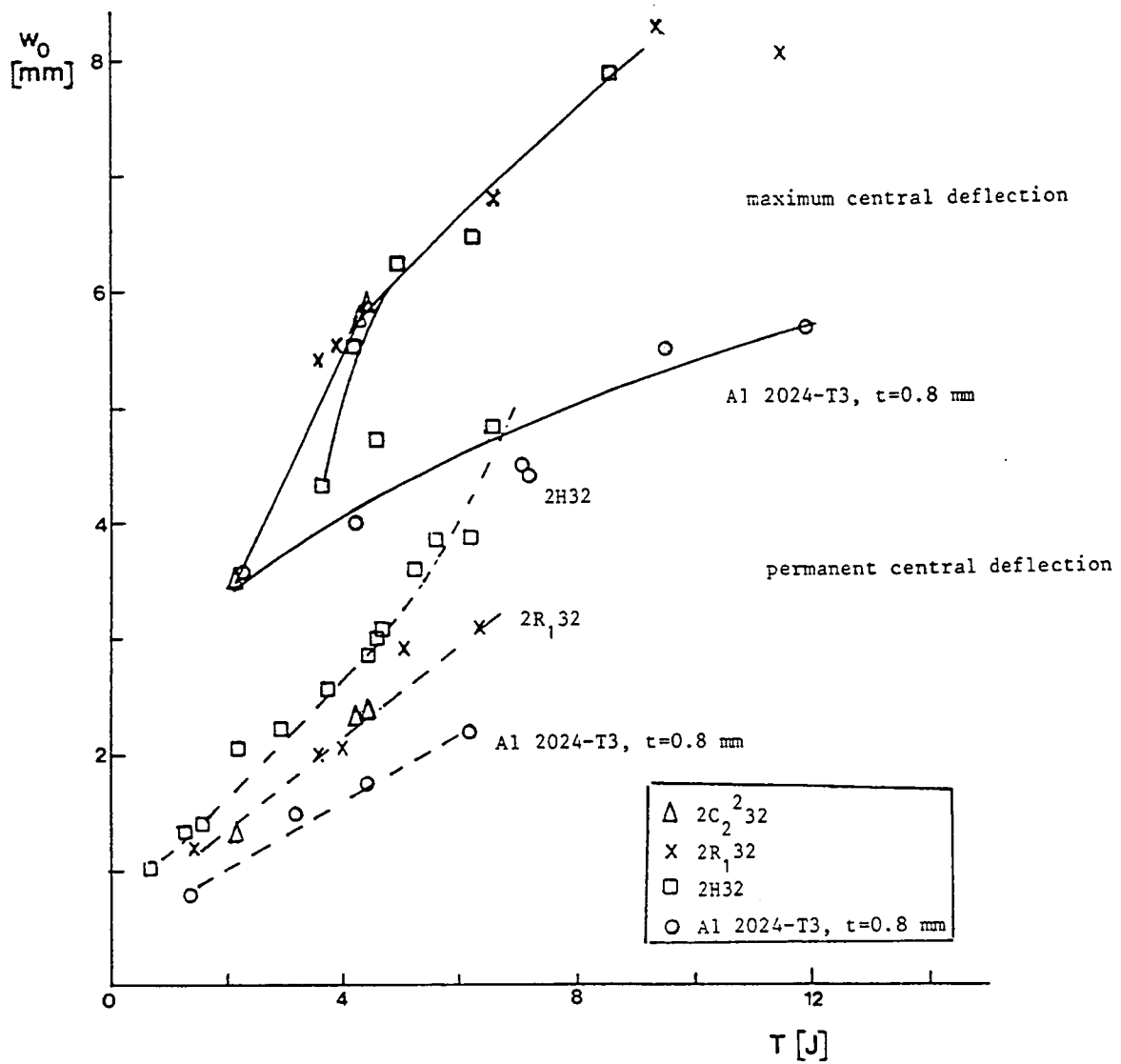
figure 7.40 The maximum and permanent central deflection of monolithic aluminium, aramid ARALL 2H32, GLARE $2R_1 32$, and CARE $2C_2{}^2 32$.
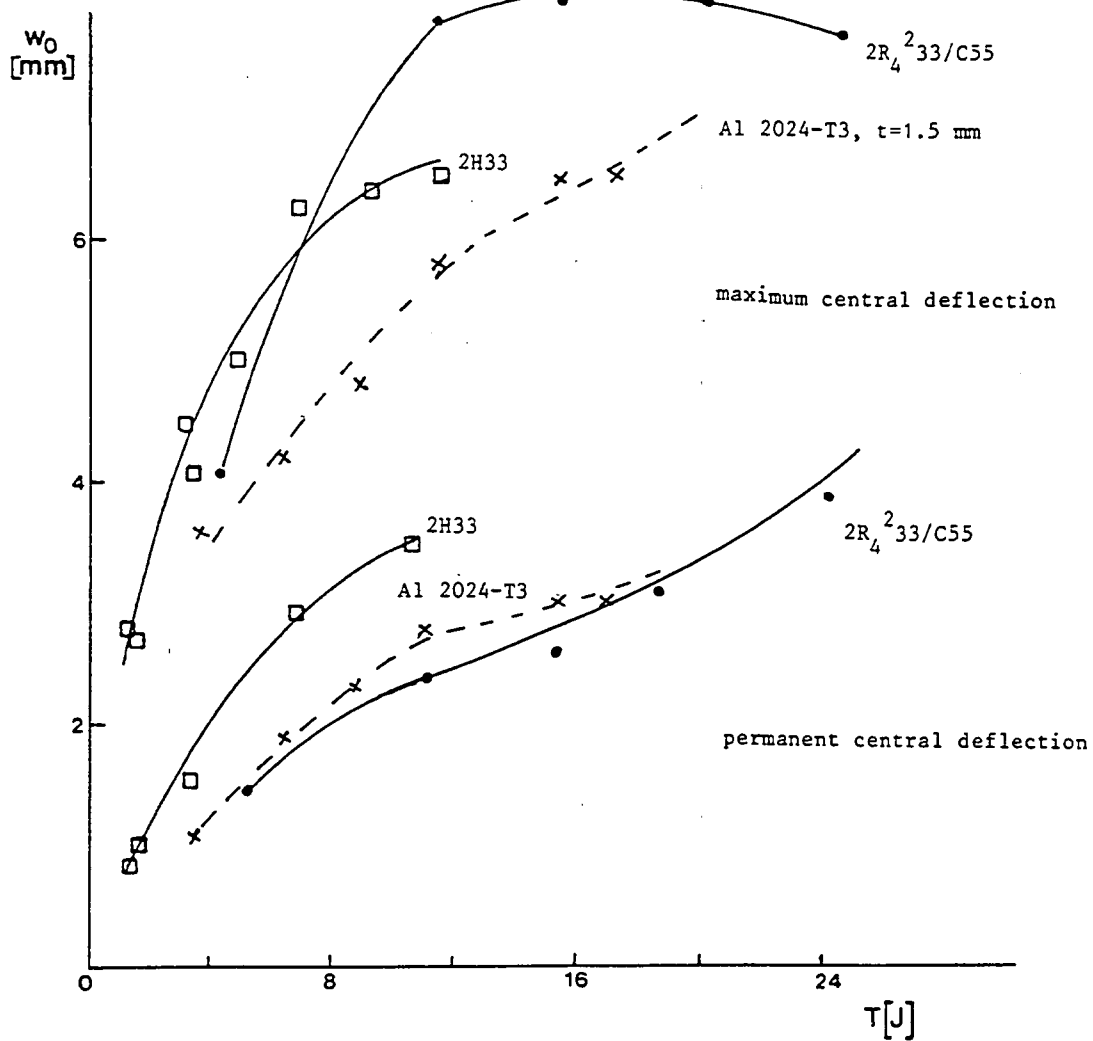
figure 7.41   The maximum and permanent central deflection of monolithic aluminium, aramid ARALL 2H33 and GLARE $2R_4^2 33/C55$.
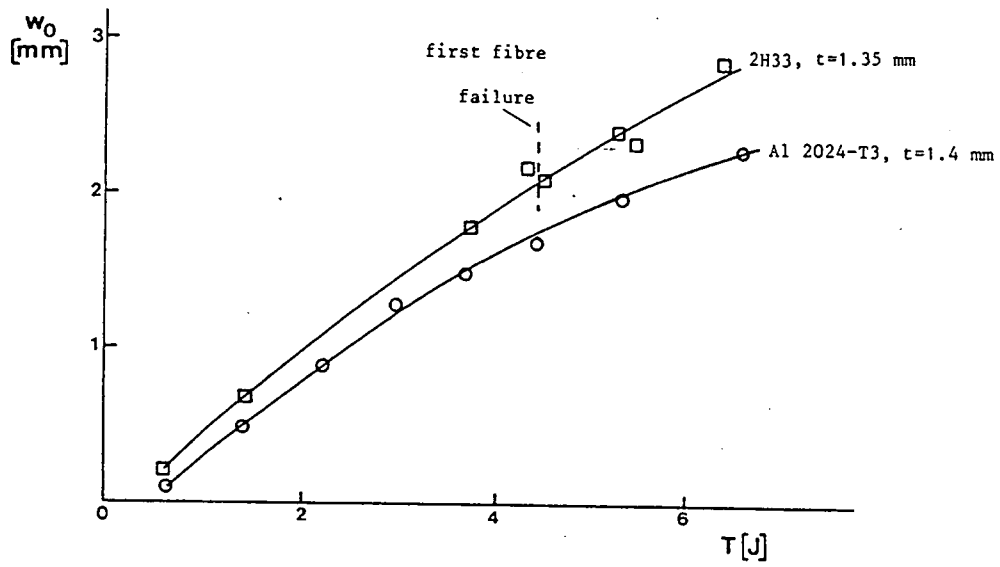
figure 7.42 The permanent central deflection after impact of
monolithic aluminium and aramid ARALL 2H33.

256
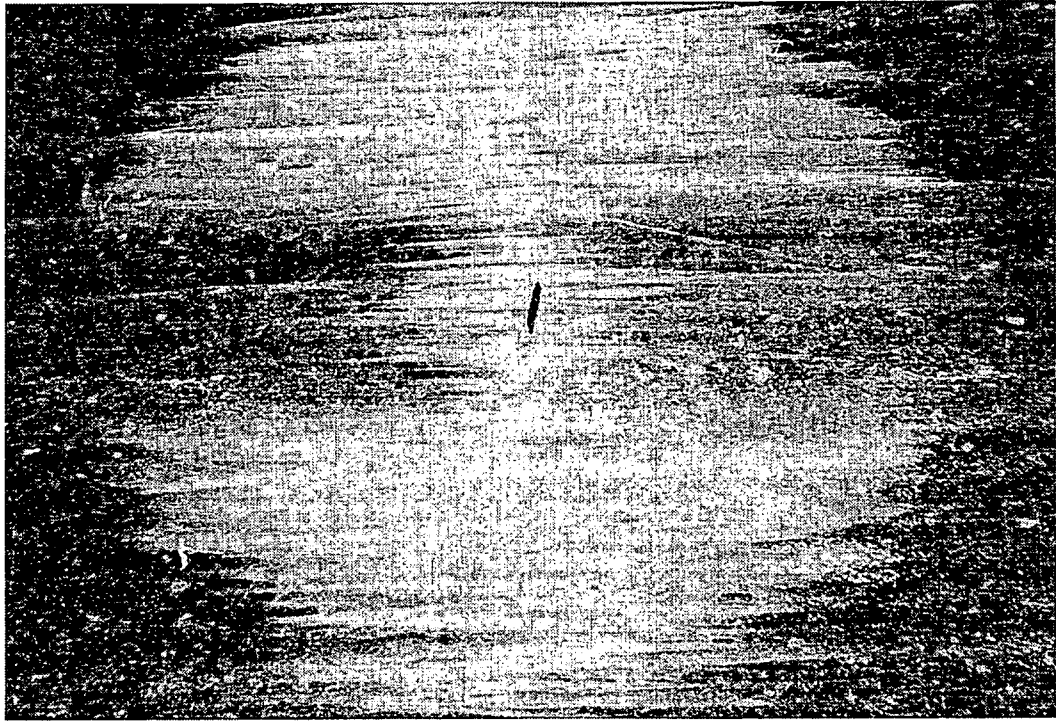
figure 7.43 Matrix cracking in aramid ARALL after removing the Al
layers (etching)

a. fading (white spot) of prepreg layer (20x)
b. detail: matrix cracks (3000x)

2a
[mm]

7H32

Al 7075-T6, t=0.8 mm
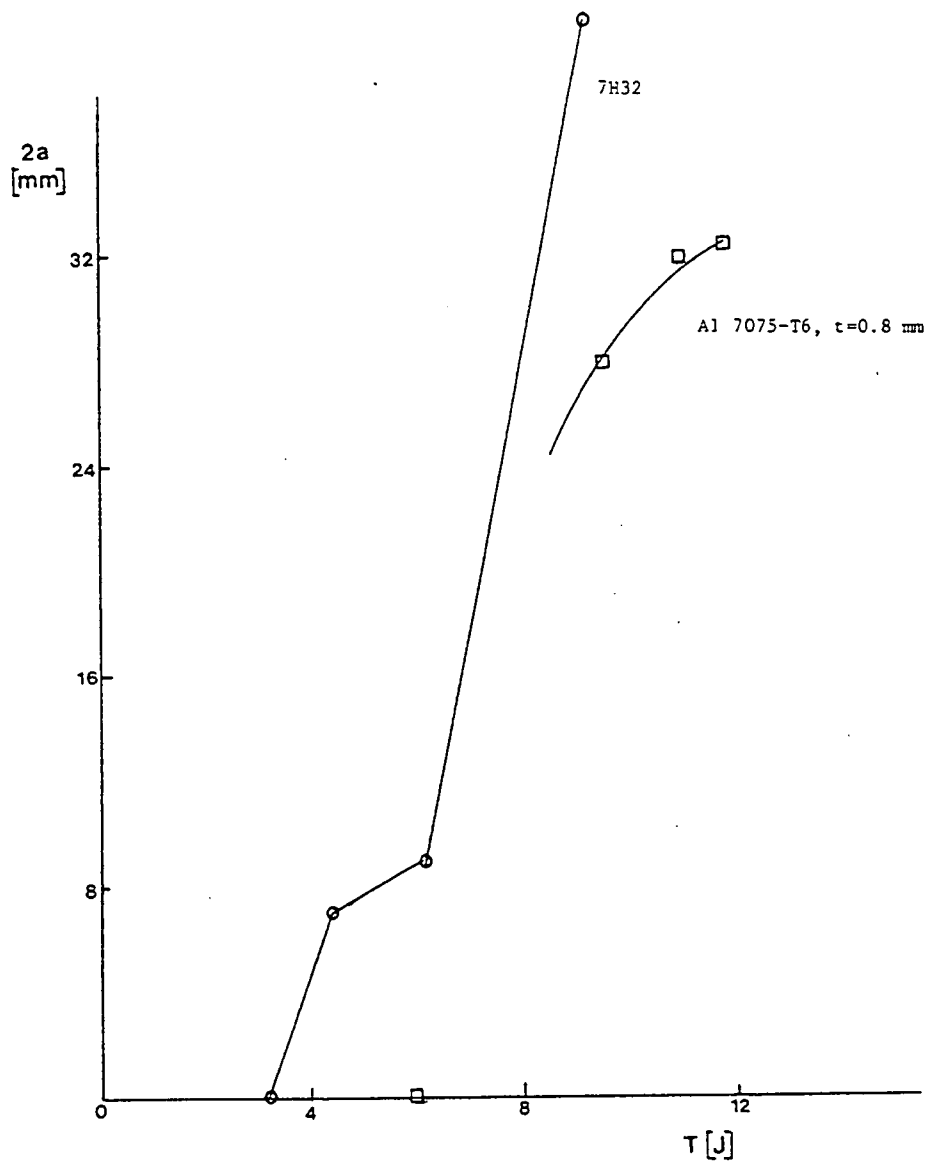
figure 7.44 The total crack length vs. the impact energy for aramid
ARALL 7H32 and monolithic aluminium.
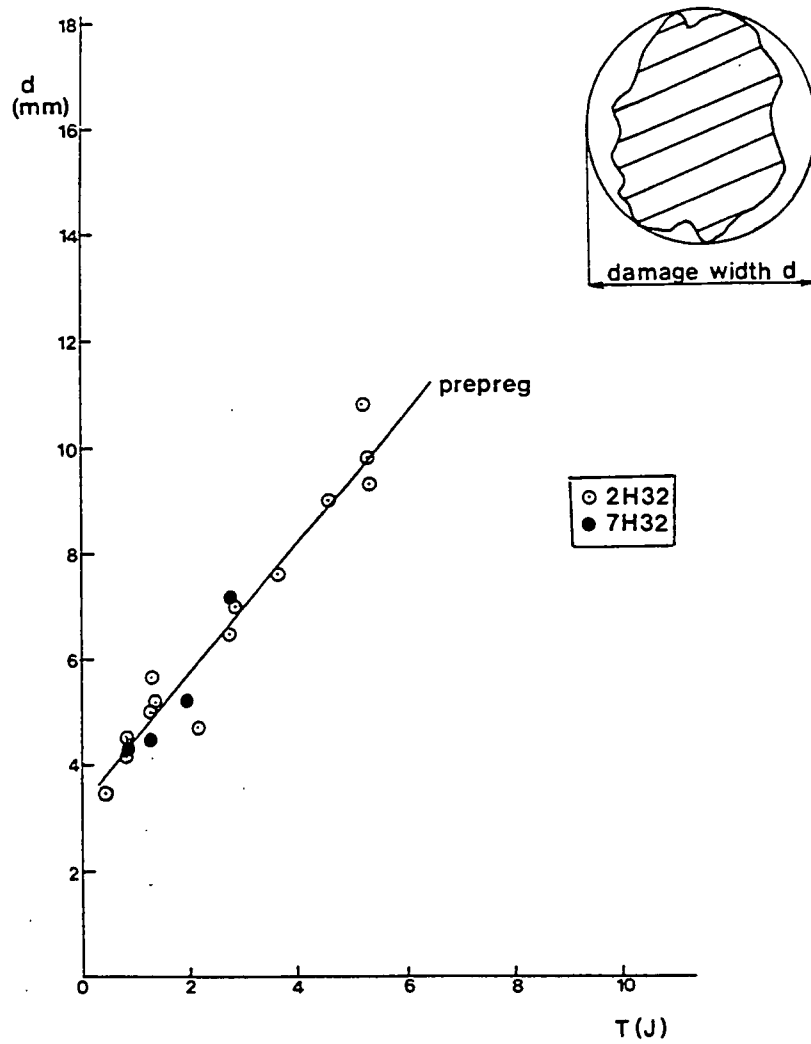
figure 7.45 The damage width in the prepreg layer vs. the impact
energy for two types of aramid ARALL.

2H32: Al 2024-T3 layers
7H32: Al 7075-T6 layers
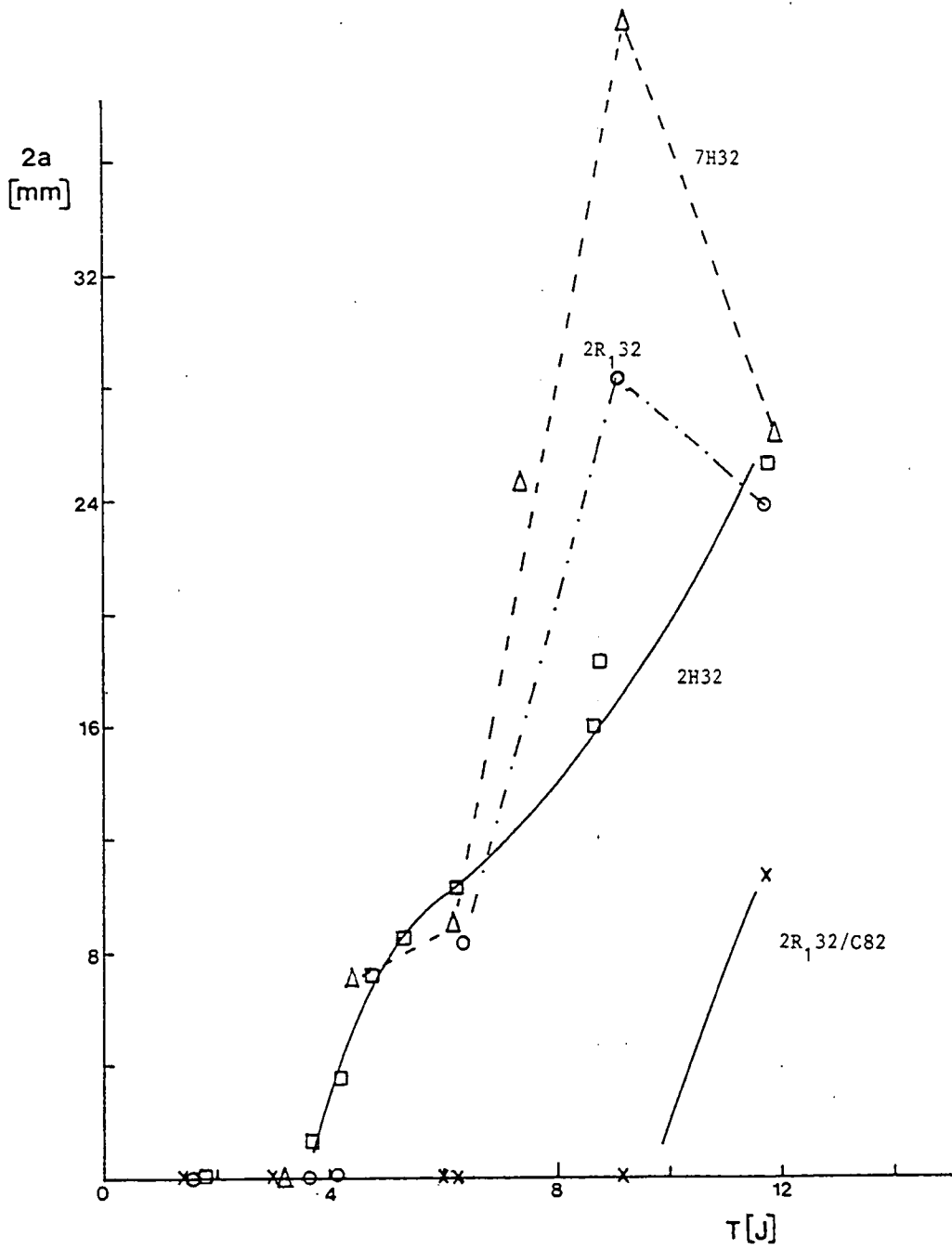
figure 7.46 The total crack length as function of the impact energy
for unidirectional aramid ARALL 2H32 and 7H32,
unidirectional GLARE 2R$_1$32 and cross-ply GLARE 2R$_1$32/C82
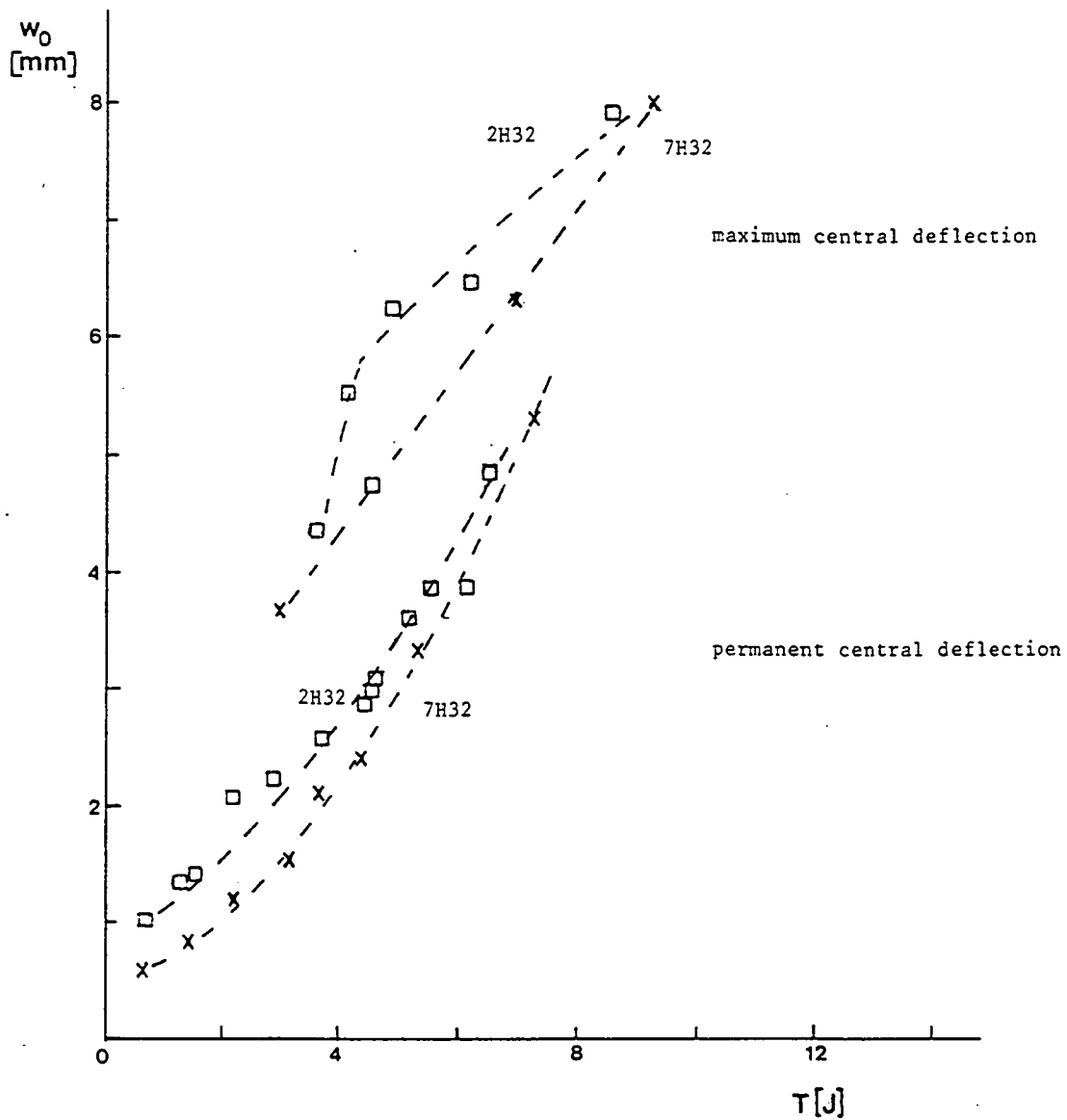
figure 7.47 The maximum central deflection during impact and the permanent central deflection for two types of aramid ARALL: 2H32 with Al 2024-T3 and 7H32 with Al 7075-T6 layers.
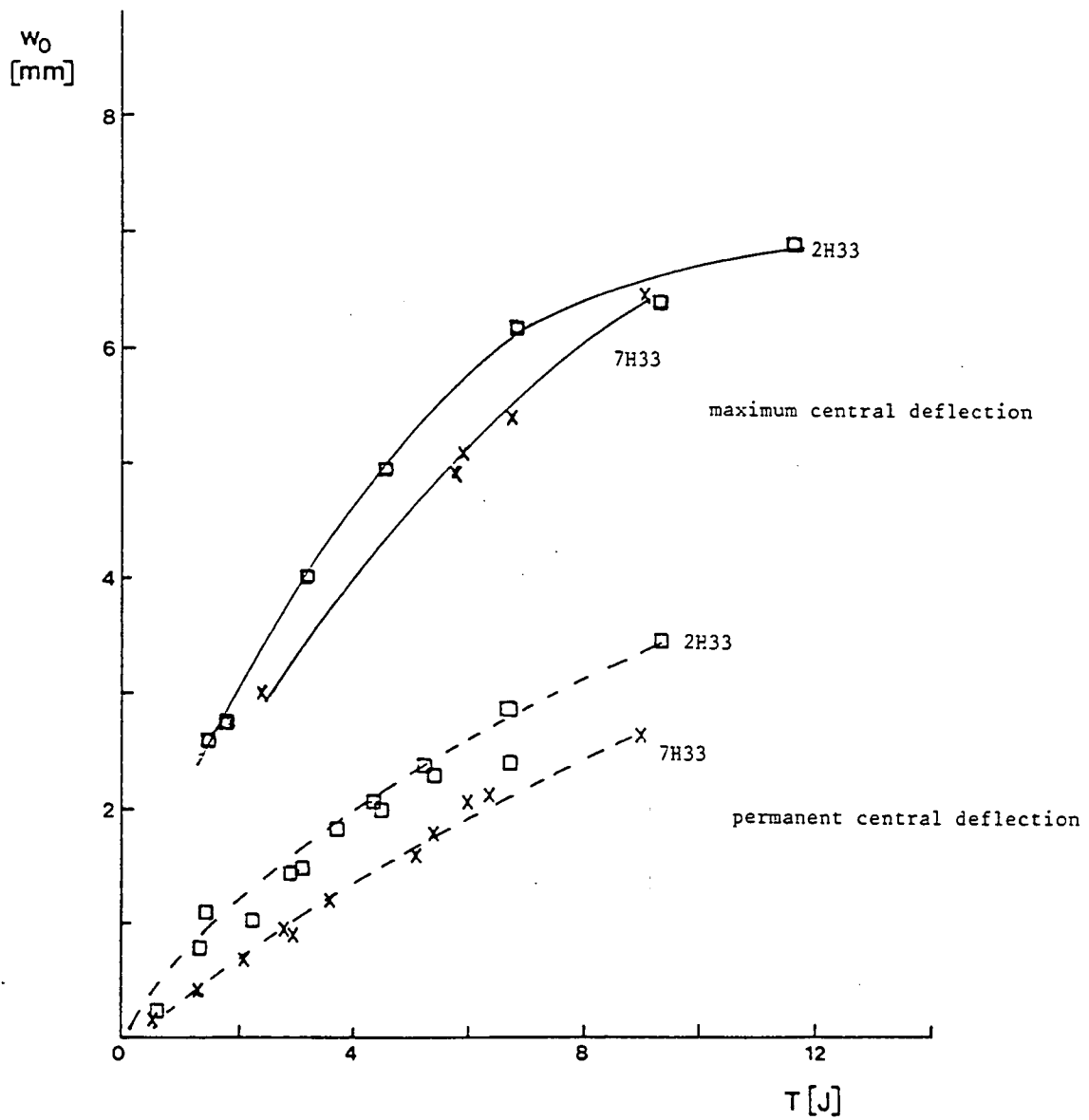
figure 7.48 The maximum central deflection during impact and the permanent deflection as function of the impact energy for two types of aramid ARALL: 2H33 with Al 2024-T3 and 7H33 with Al 7075-T6 layers.
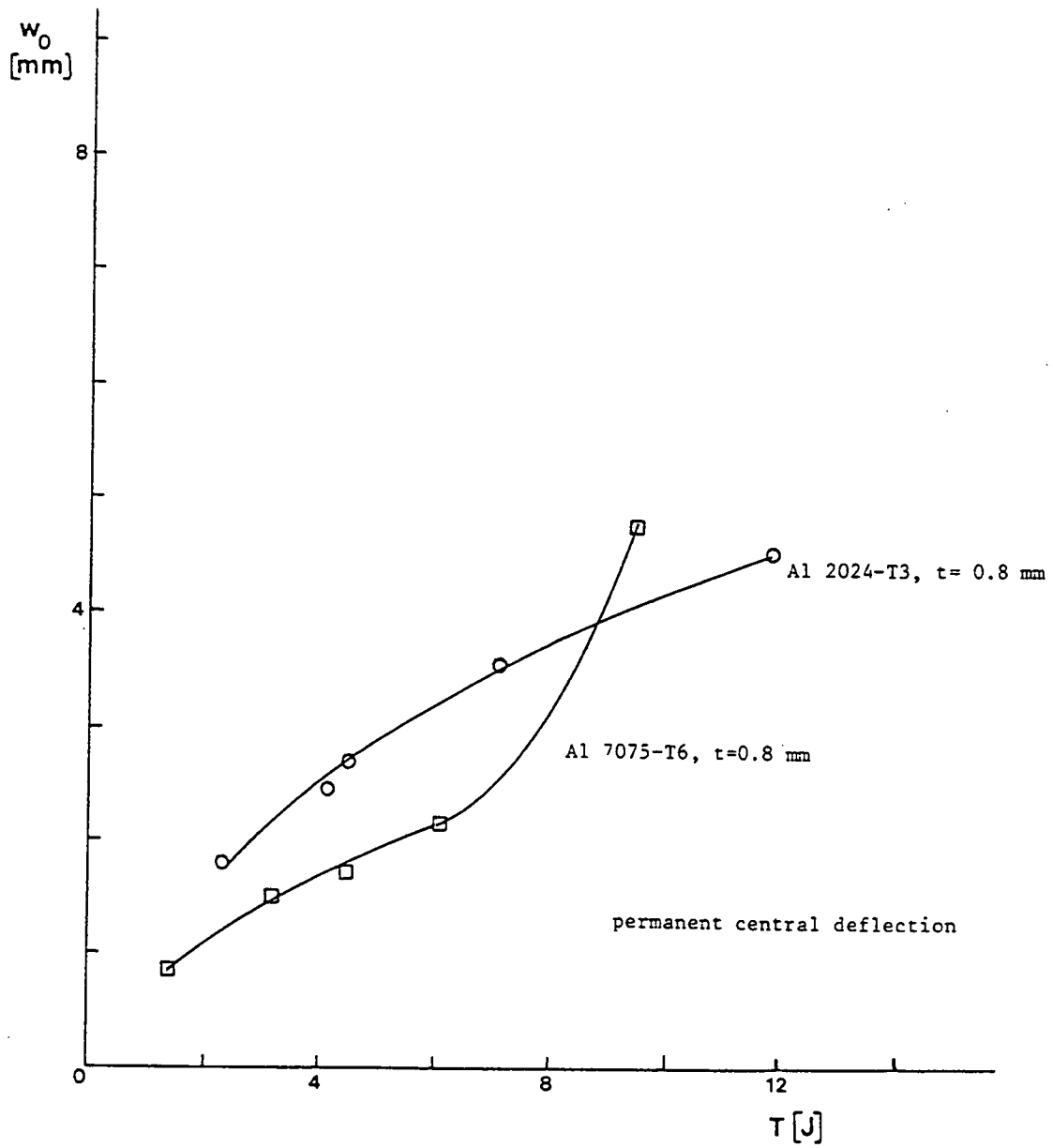
figure 7.49 The permanent central deflection as function of the impact energy for two types of monolithic aluminium.
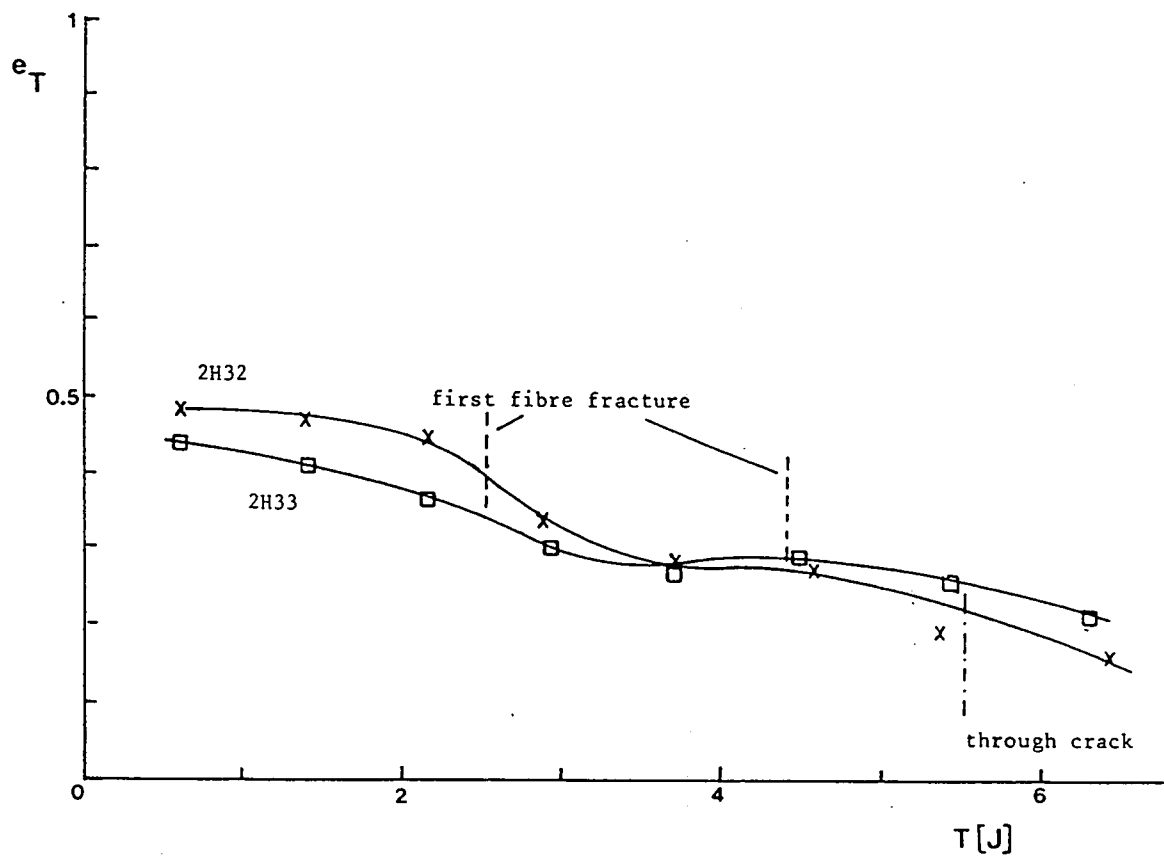
figure 7.50 The energy restitution coefficient as function of the
impact energy for two types of aramid ARALL.

2H32: t=0.8 mm
2H33: t=1.4 mm

W_0
[mm]

8

maximum central deflection

permanent central deflection

4

O	7H32
X	7H32/90-10
□	7H32/w

7H32/w

7H32/90-10

first fibre
fracture 7H32

0   4   8   12

T[J]
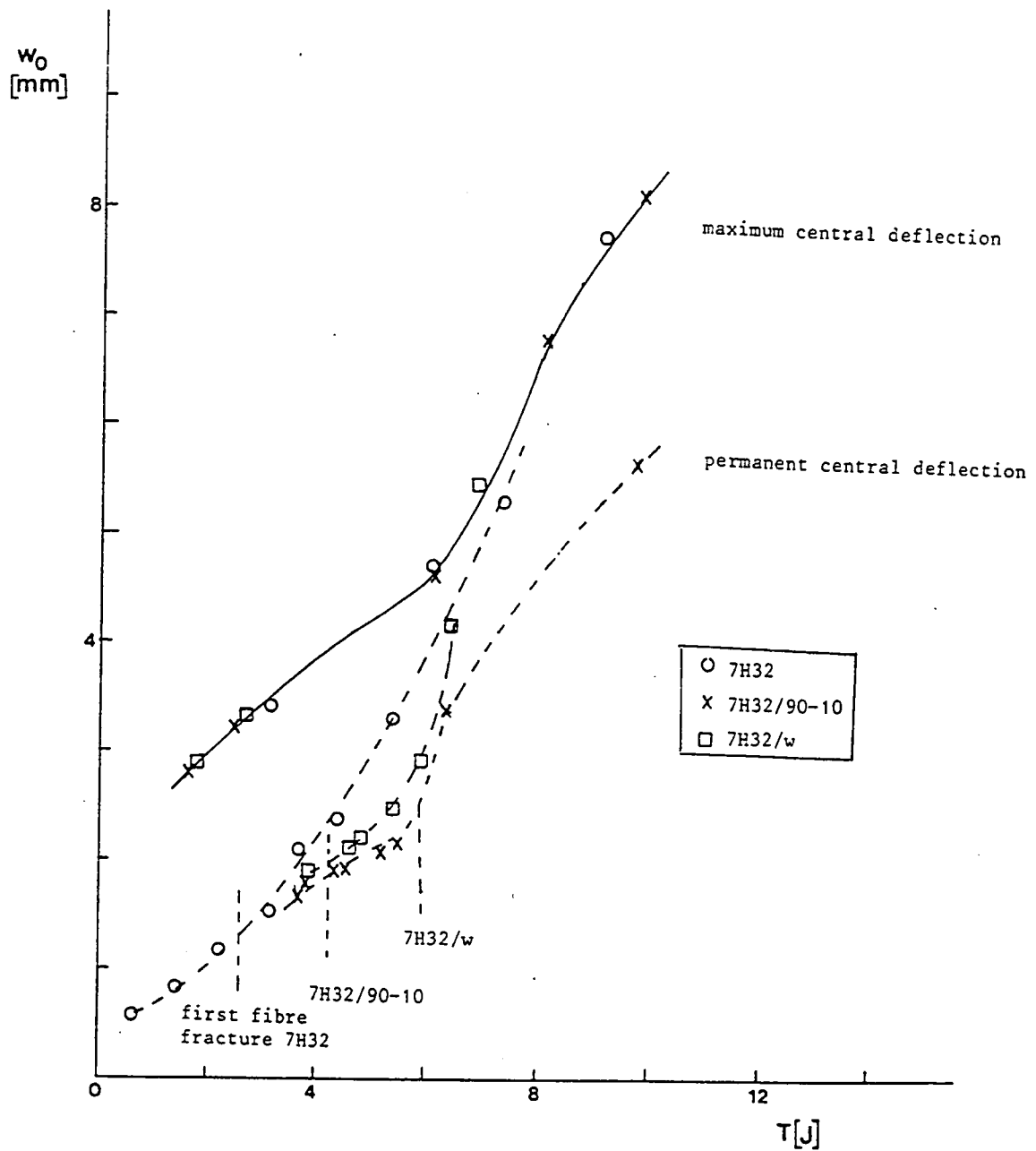
figure 7.51 The maximum central deflection and the permanent central
deflection as function of the impact energy for aramid ARALL.
        7H32: unidirectional prepreg
        7H32/90-10: prepreg with 90% of the fibres in one direction and
                        10% in a perpendicular direction
        7H32/w: prepreg with a weave
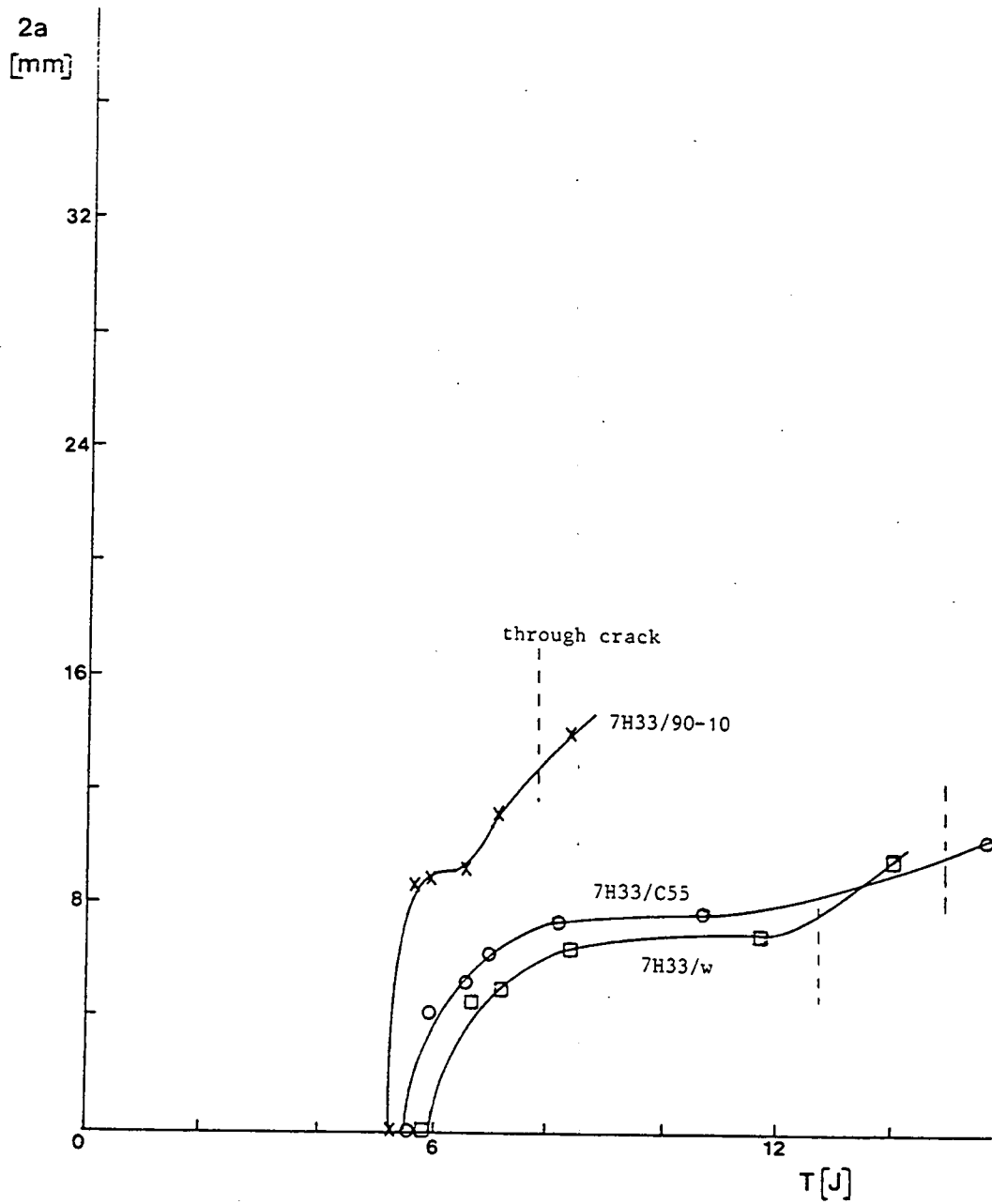
figure 7.52 The total crack length as function of the impact energy
for aramid ARALL.

        7H33/90-10:   prepreg with 90% of the fibres in one direction
                       and 10% in a perpendicular direction
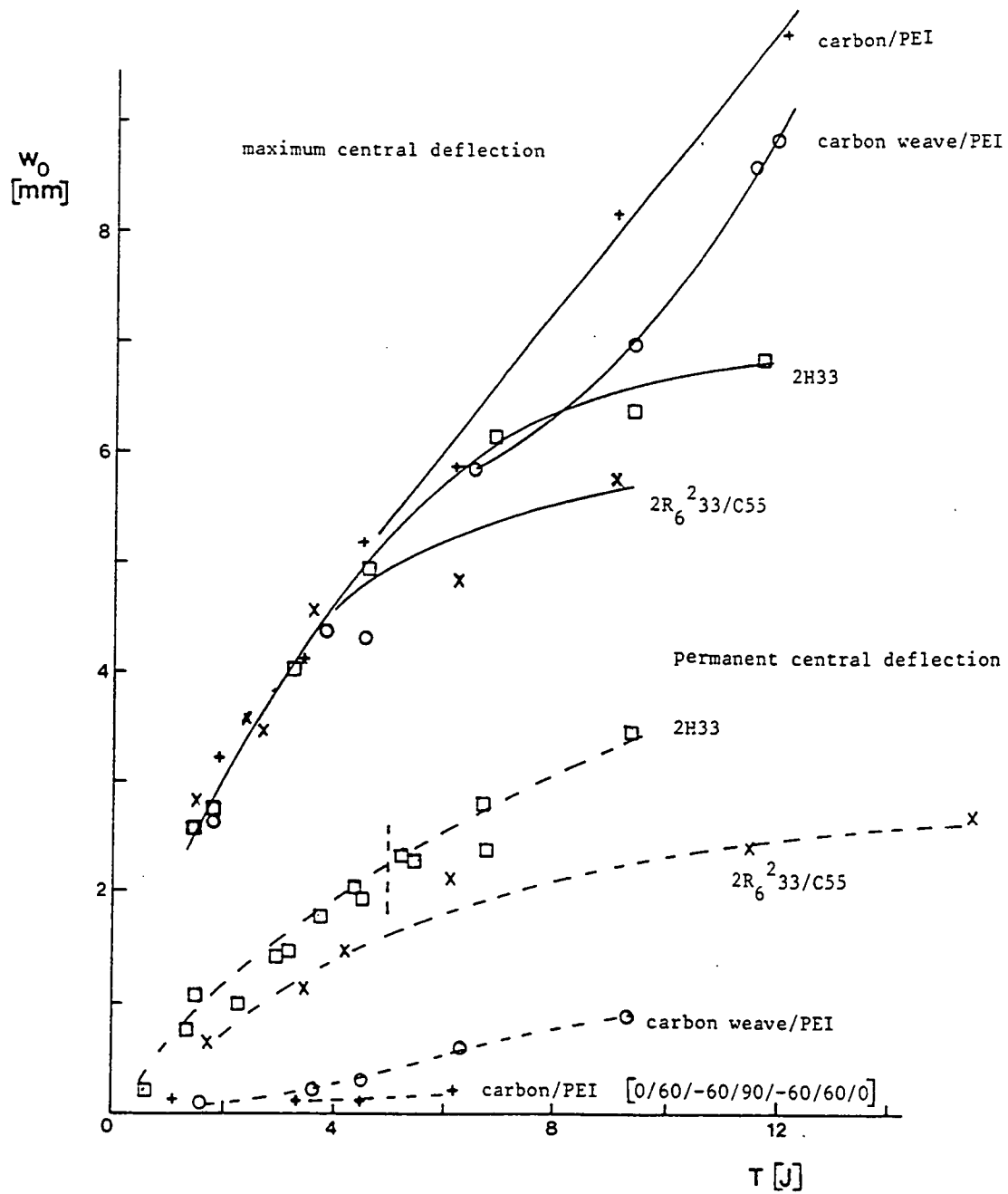   7H33/C55: cross-ply ARALL
        7H33/w: prepreg with a weave

figure 7.53 The maximum central deflection and the permanent central deflection as function of the impact energy for ARALL and thermoplastic composites.

2H33: aramid ARALL
2R$_6$32/C55: GLARE

267
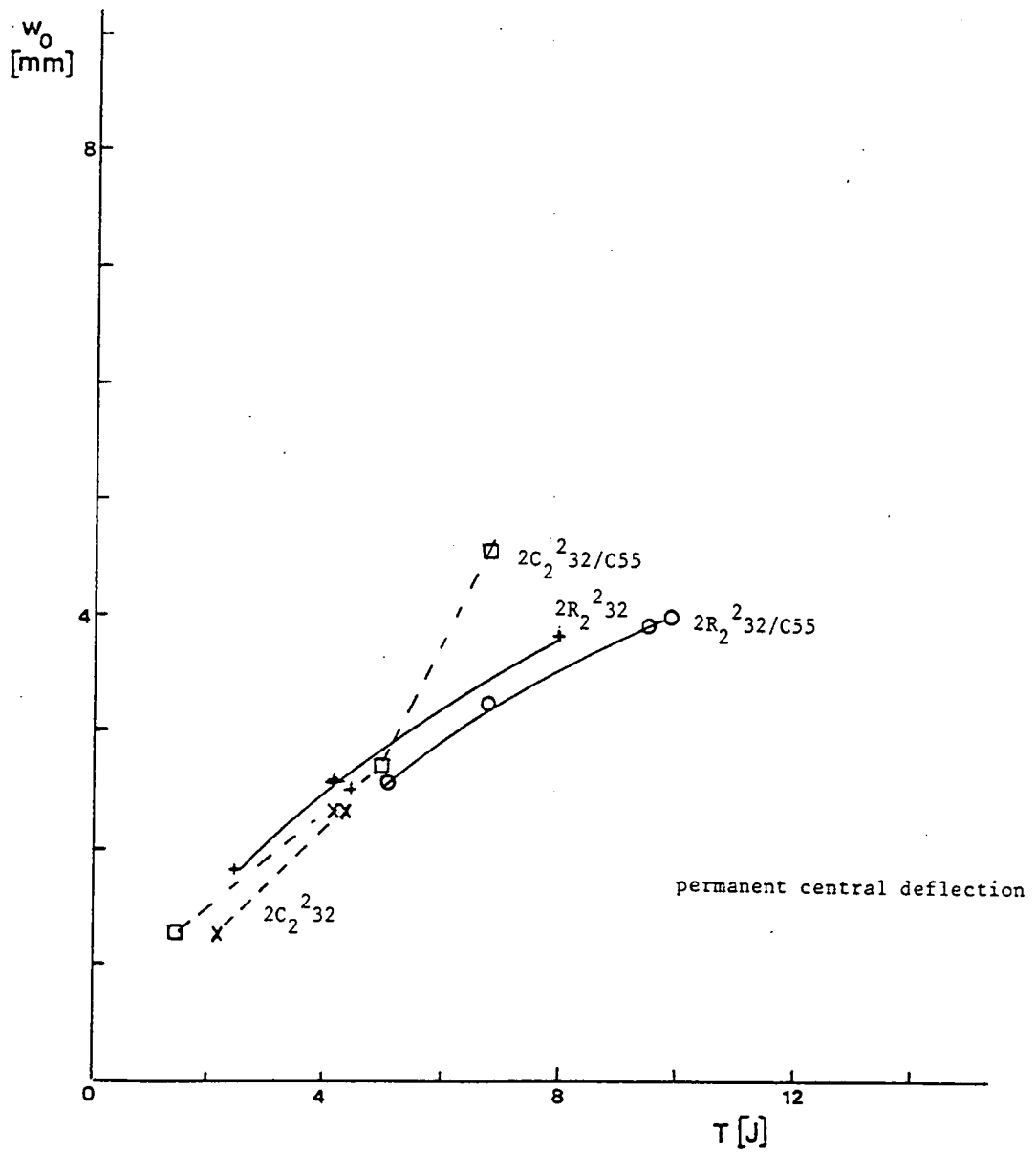
figure 7.54 The permanent central deflection as function of the impact energy for carbon ARALL and GLARE.

$2C_2{}^232$: unidirectional carbon ARALL

$2C_2{}^232/C55$: cross-ply carbon ARALL

$2R_2{}^232$: unidirectional GLARE

$2R_2{}^232/C55$: cross-ply GLARE
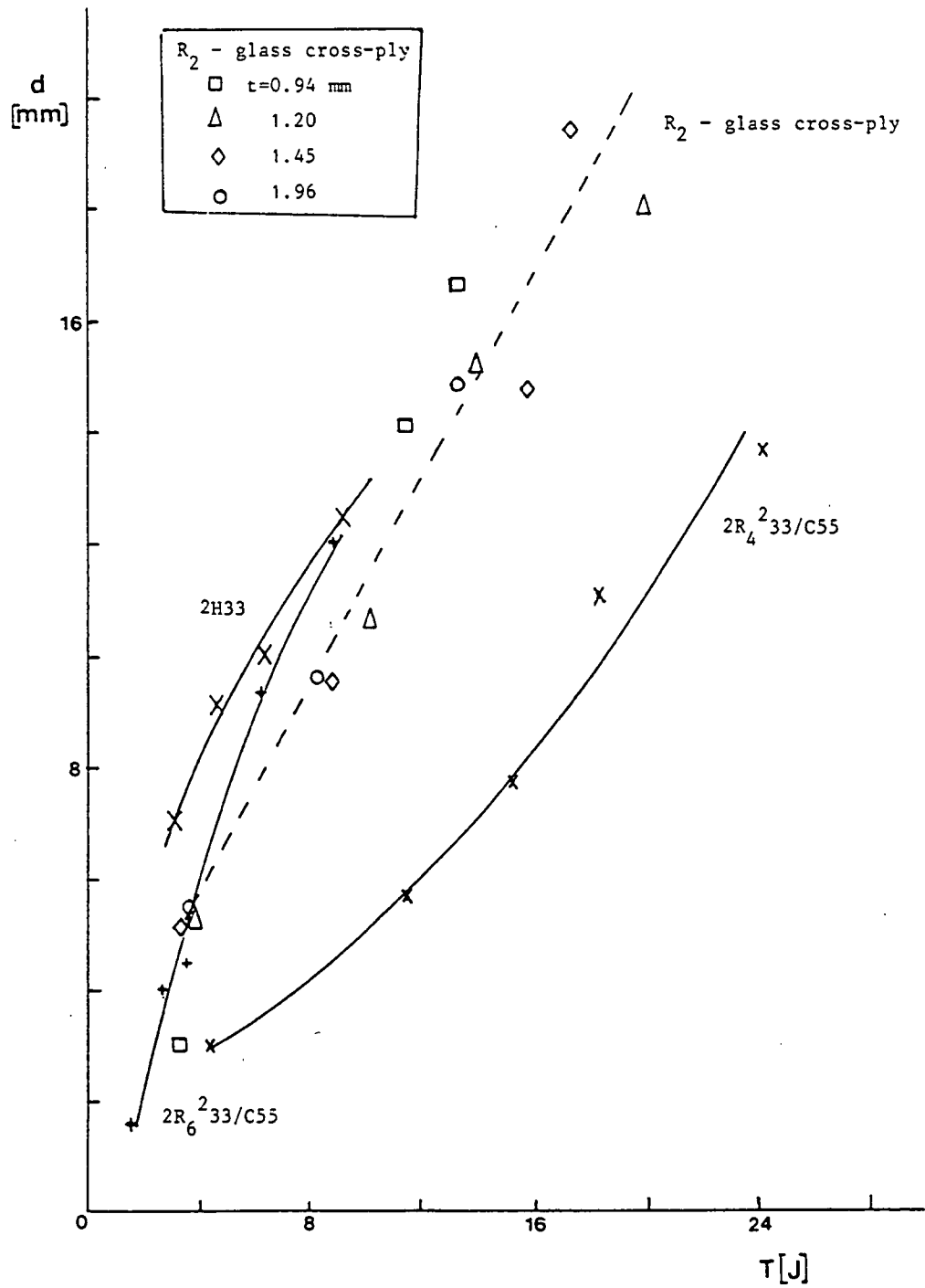
figure 7.55 The damage width as function of the impact energy for aramid ARALL, GLARE and cross-ply composites.

2H33: unidirectional aramid ARALL
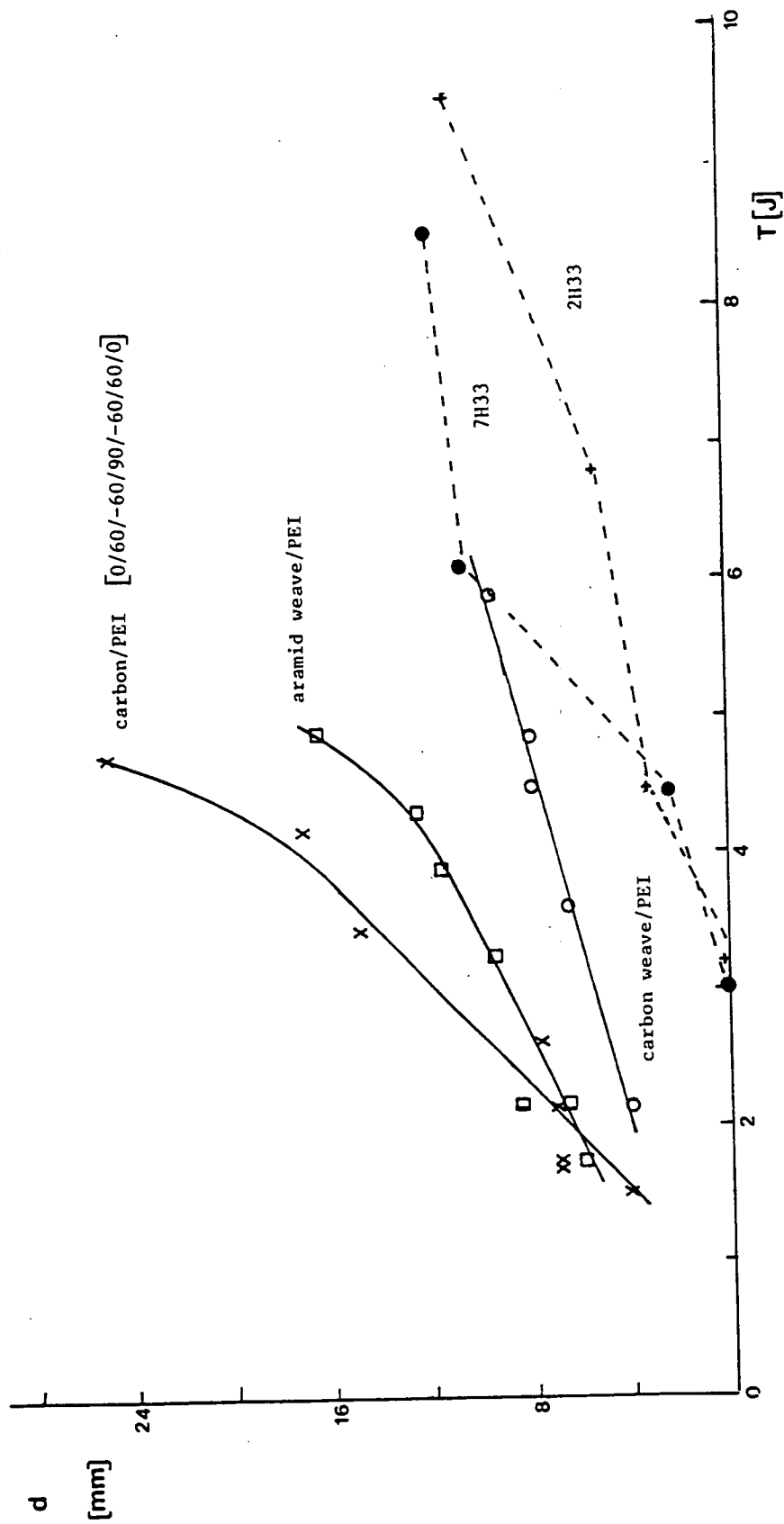$2R_6^2 33/C55$ and $2R_4^2 33/C55$: cross-ply GLARE

figure 7.56 The damage width as function of the impact energy for thermoplastic composites and aramid ARALL 2H33 and 7H33.
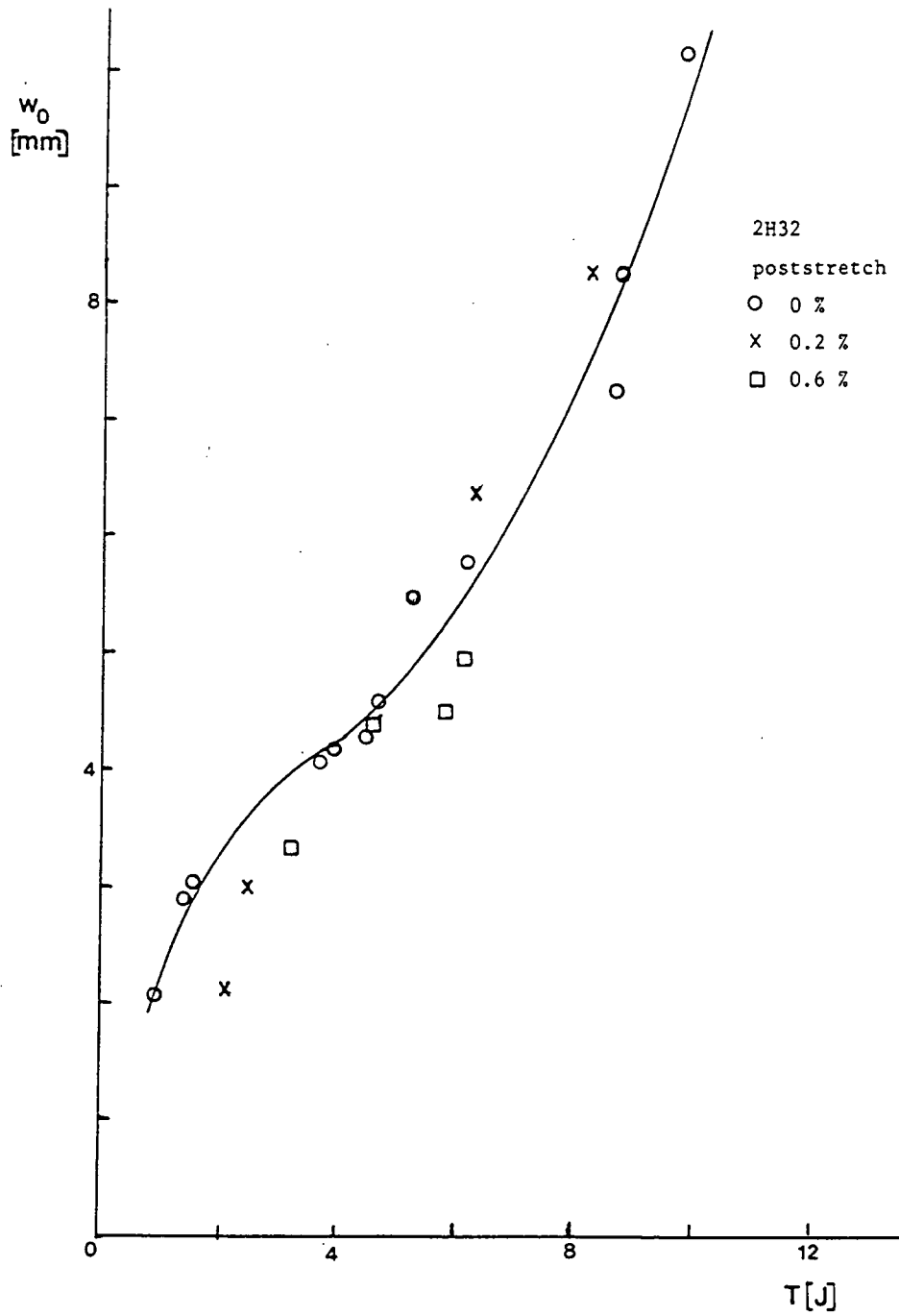
figure 7.57 The permanent central deflection after impact as function of the impact energy of aramid ARALL with different poststretch percentages.
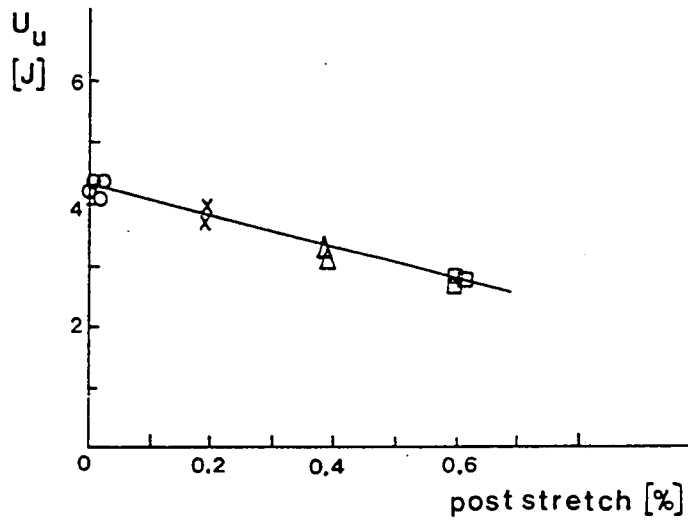
figure 7.58 The absorbed energy at ultimate load for aramid ARALL 2H32 as function of the poststretch percentage.
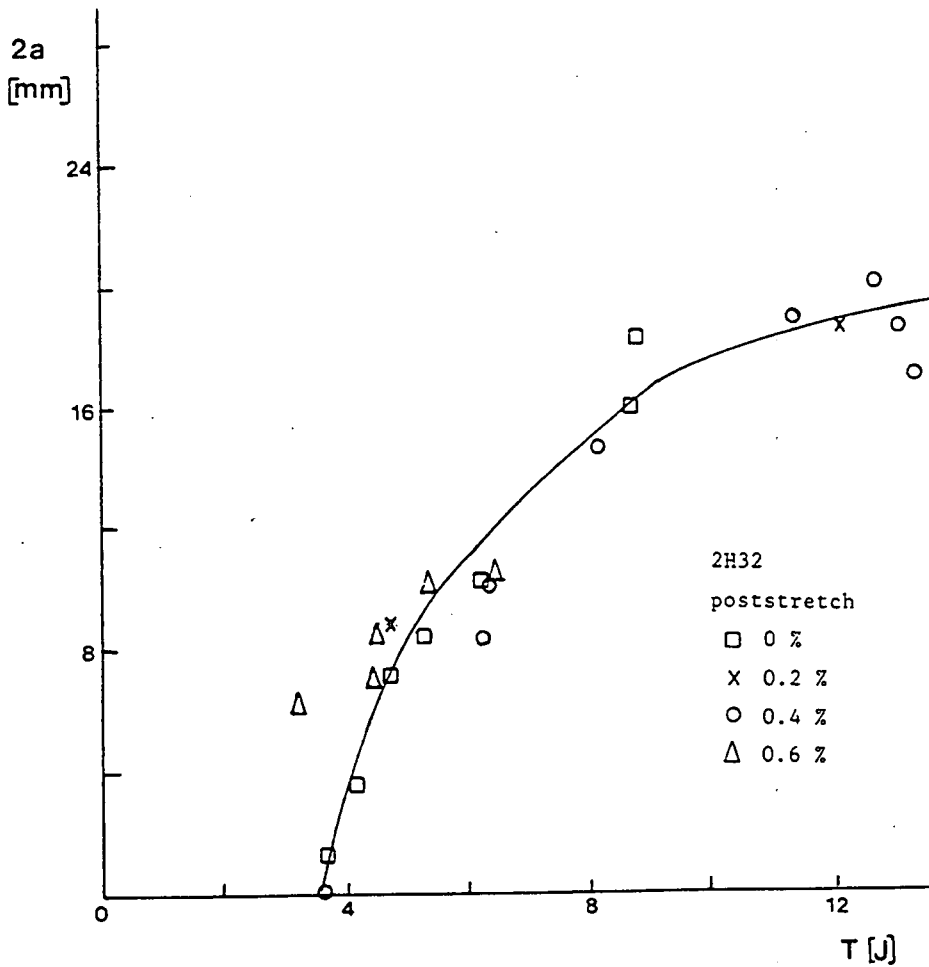

figure 7.59 The total crack length vs. the impact energy for aramid ARALL with varying poststretch percentage.
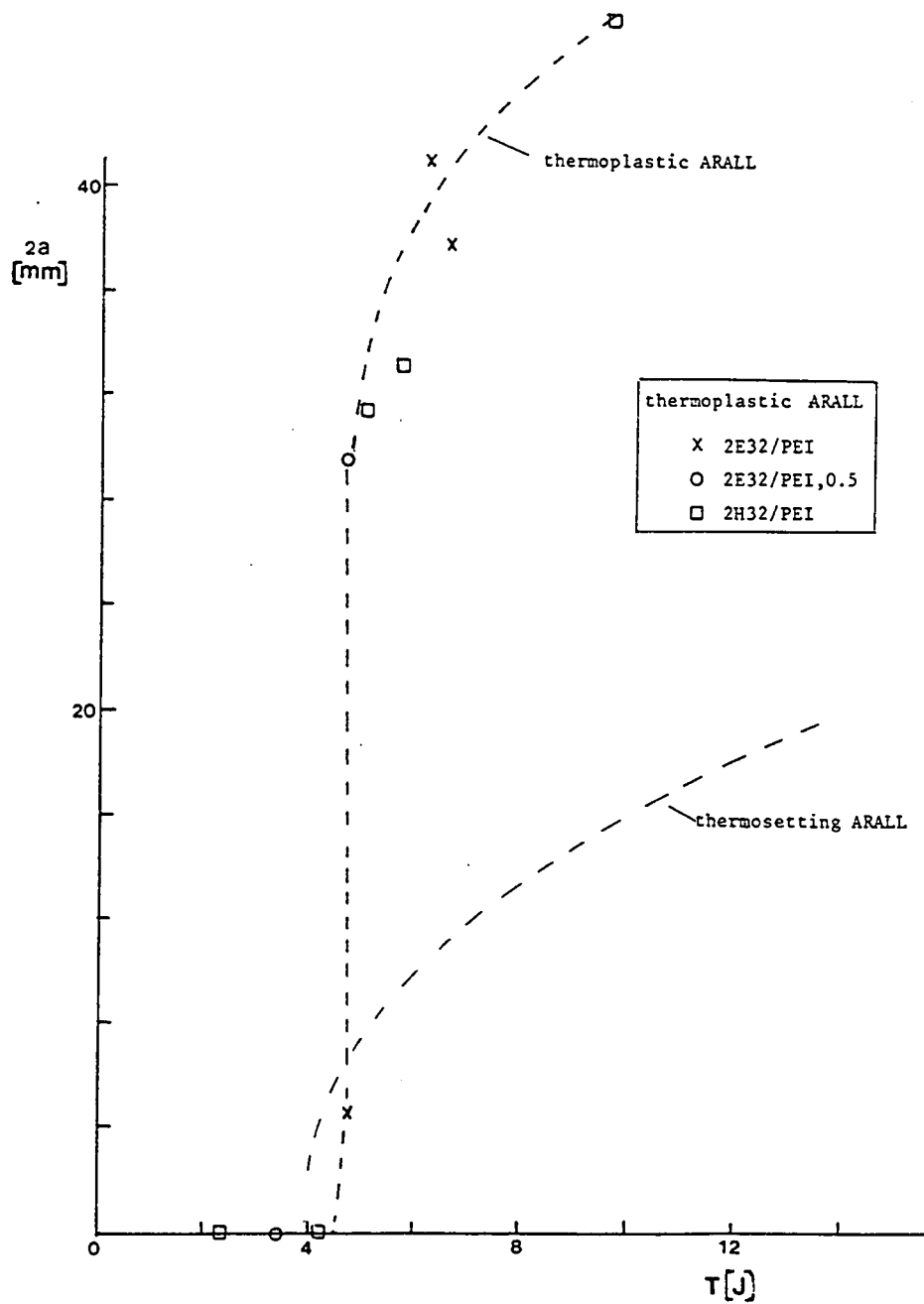
figure 7.60 The total crack length vs. the impact energy for thermoplastic ARALL types.

2E32/PEI: E-glass fibres, no poststretch
2E32/PEI.0.5: E-glass fibres, 0.5% poststretch
2H32/PEI: aramid fibres, no poststretch
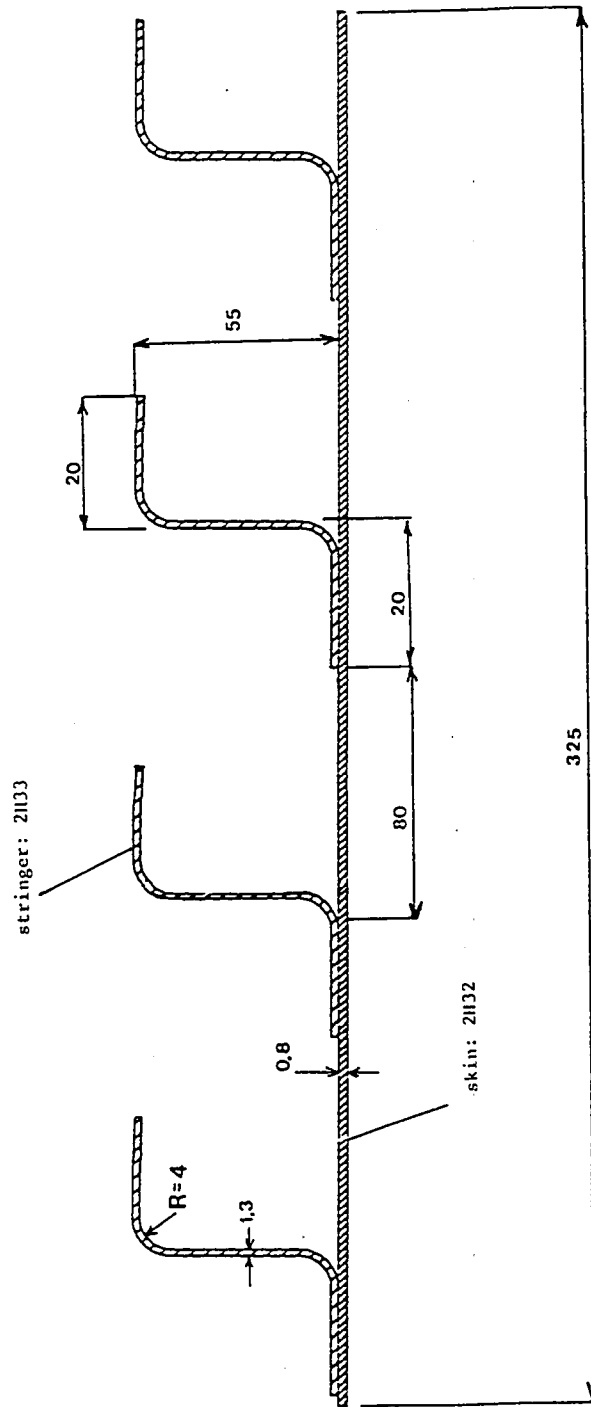
figure 7.61 Cross-section of the aramid ARALL panels.
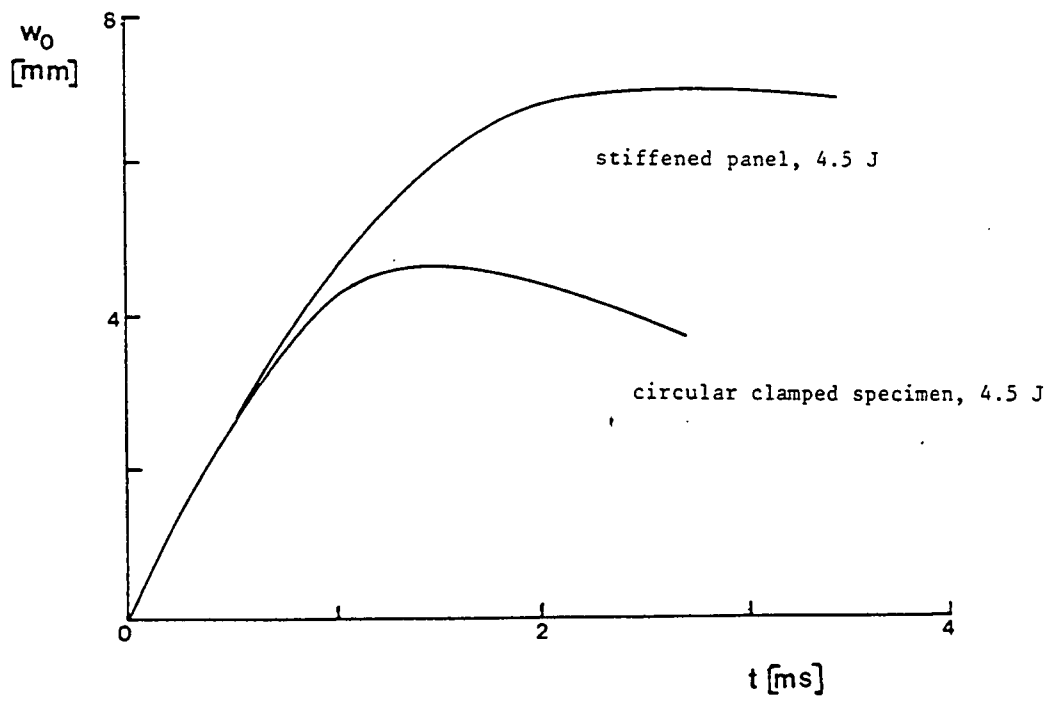
figure 7.62 The central deflection vs. time for a clamped specimen and a stiffened panel of aramid ARALL.
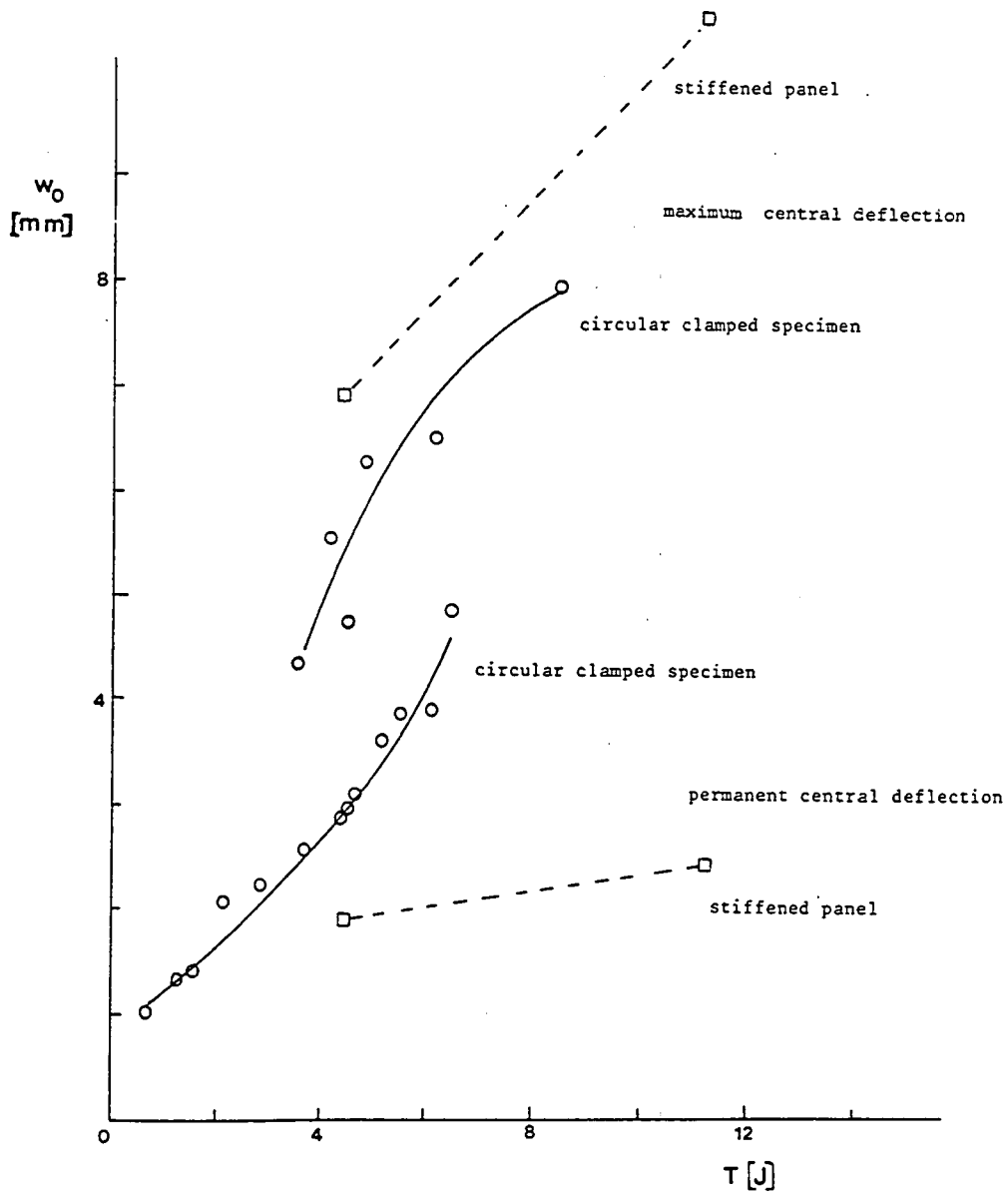
figure 7.63 The maximum central deflection and the permanent central deflection vs. the impact energy for clamped specimens and stiffened panels.
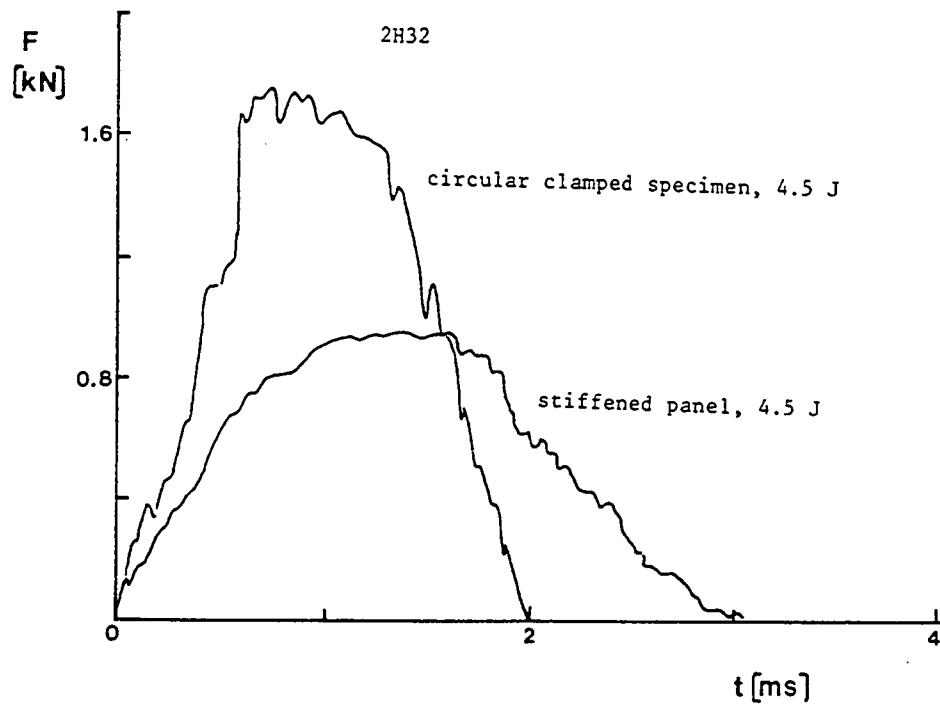
figure 7.64 Force- time curves of a clamped specimen and a stiffened panel.

figure 7.65 The permanent central deflection vs. the impact energy
for monolithic aluminium and aramid ARALL 2H33 for varying nose
radii of the impactor.

278

figure 7.66 The diameter of the punched hole vs. the impact energy in monolithic aluminium and aramid ARALL 2H33 with a conical tip impactor.

chapter 8 Impact tests on specimens under a tensile load

8.1 Introduction

The literature on impact on sheet specimens under load is relatively scarce. The aim of the literature found was not a better understanding of the imp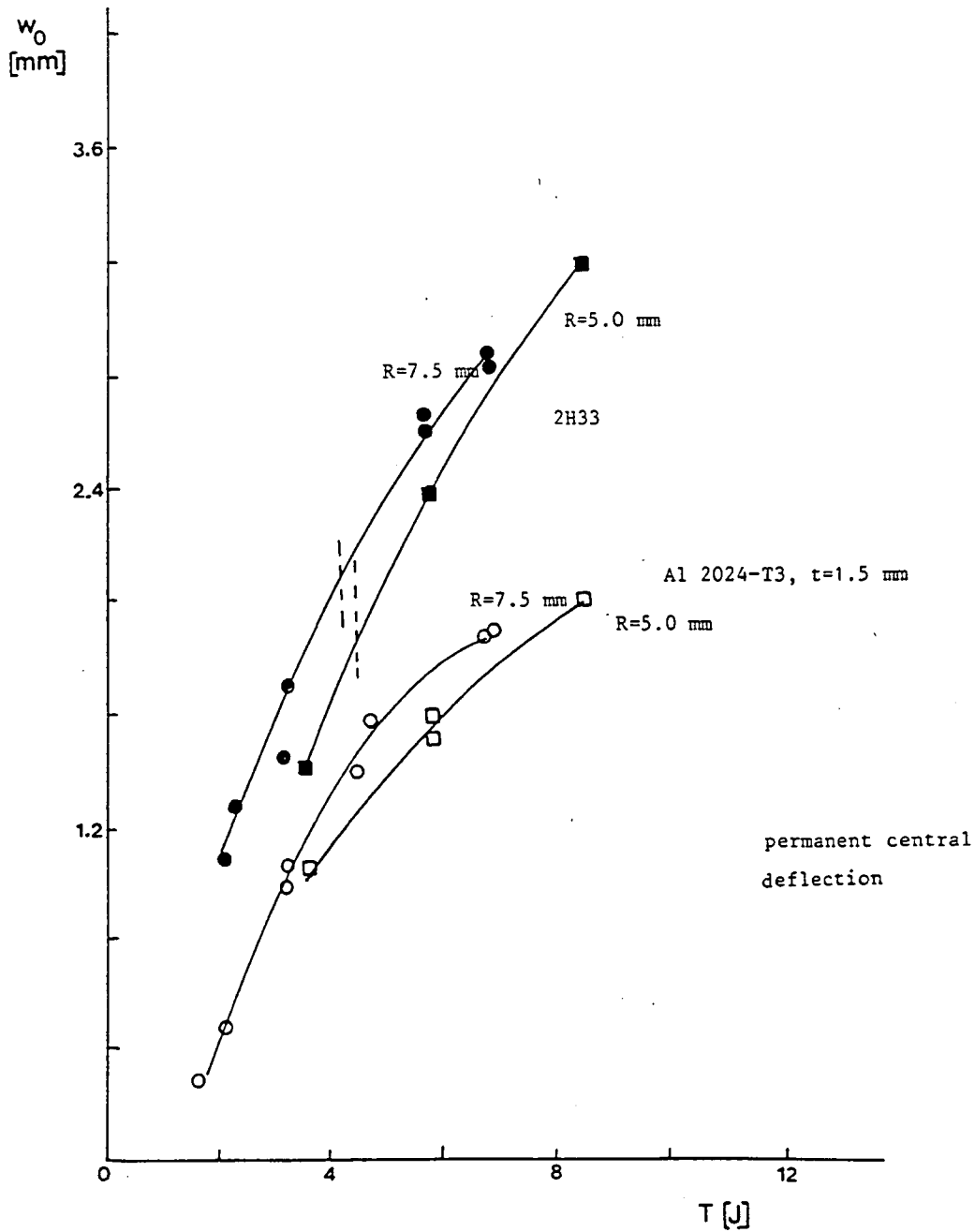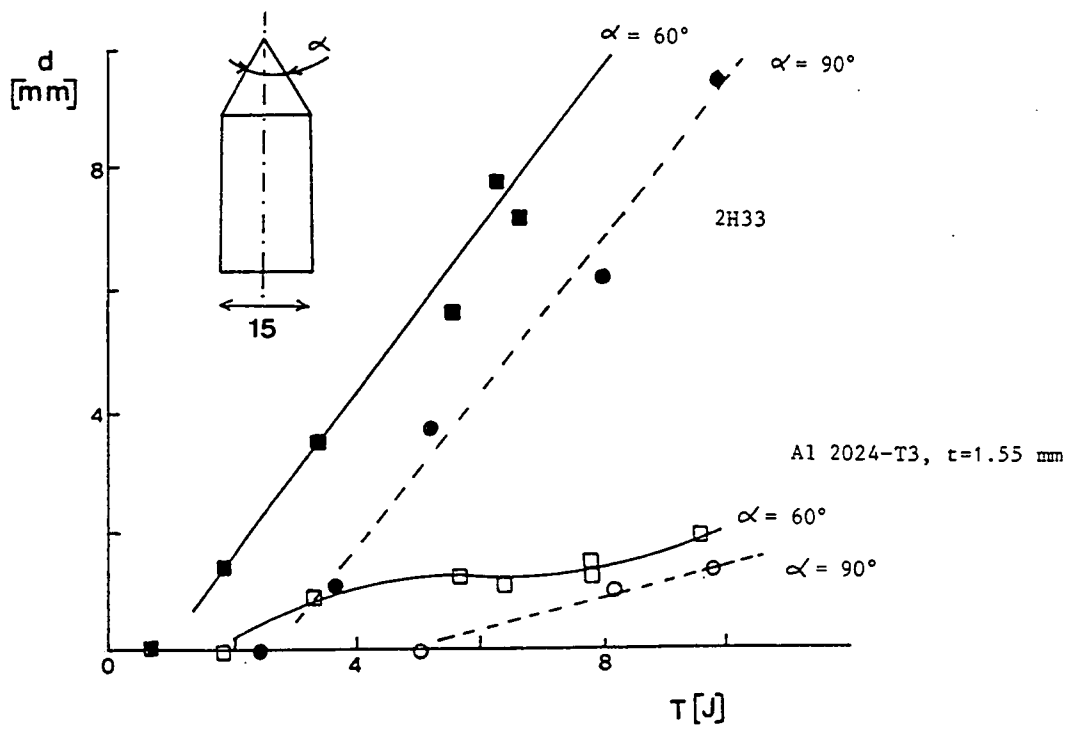act process, but the determination of the effect of a preload during impact on the residual strength. Literature on instrumented impact testing on loaded specimens could not be found. The measurement of the contact force during impact may help to understand more about the impact process.

Impact tests on specimens under load were mainly done on compression panels made of composite materials[2,3,4]. Compressive loading may cause local buckling of the delaminated zone. Results of tensile tests on panels, impacted by ballistic projectiles for military applications, were also found[6,7]. The tests were performed after impact on preloaded composite panels[7]. Small to significant negative effects of the preload on the damage size and residual strength were reported.

Sources of impact damage of aircraft structures were discussed in chapter 3. The following objects may strike an aircraft structure under initial loading:

1. runway debris. This source of damage may strike lower wing structural parts under compressive loading.

2. hail and bird strike. Especially the front section of the fuselage (around the cockpit) may be hit in flight, while the fuselage is under cabin pressure.

3. ice from propellers and engine debris. Probably this will be the most serious threat for the fuselage structure under loading.

4. ballistic projectiles. Terrorist actions in the aircraft cabin may have catastrophic results. For military aircraft, ballistic impacts may hit every structural part under initial loading. During the design of these aircraft this aspect has to be considered.

In this chapter instrumented impact tests are described on monolithic aluminium alloys and aramid ARALL laminates. A linear elastic model for

sheet material impacted under an initial load will be derived in chapter 12.

8.2 Test set-up and materials

Figure 8.1 shows the test set-up. The specimen dimensions were 300x160 mm^2, including the end-tabs for the grips of the 60 kN hydraulic testing machine. A specimen was loaded in the testing machine, and then clamped around a circular area with a diameter of 80 mm, see figure 8.1. Two plates clamped the specimen, The plates were firmly supported by braces attached to the hydraulic testing machine. This was done to assure well defined edge conditions of the tested area. The test area is identical to the test area of the specimens in chapter 7. The clamping plates were supported to prevent the lateral displacements of the specimen with the clamping plates.

The circular clamped region of the specimen was struck in its centre by a pendulum (see figure 5.1): a weight of 689 g guided by strings attached to the top of the hydraulic testing machine. The impactor had a hemispherical nose with a radius of 7.5 mm. A stable swing of the pendulum was assured. The pendulum was instrumented in the same way as the drop weight impact tester described in chapter 5: the contact force and the displacement were measured during impact and analyzed by computer.

The following materials were tested:
- 5 specimens of Al 2024-T3, t=1.03 mm
- 5 specimens of Al 7075-T6, t=1.03 mm
- 8 specimens of aramid ARALL 2H32, t=0.82 mm
- 3 specimens of aramid ARALL 7H32, t=0.82 mm

The specimens were tested in two ways:
1. 'Elastic' impact tests: very low impact energies, elastic deformation only. The specimens were tested at an impact energy of 0.13 J. These experiments were done for the verification of a model presented in chapter 12.
2. 'Plastic' impact tests: at higher energies, with plastic deformation. The impact energies are given in table 8.1.

The tensile stresses applied to the specimens before impact varied between S = 0 and S = 350 MPa, with a maximum value just below the yield stress of the material. After impact the crack length and the permanent deflection were measured.

8.3 Results and discussion

elastic impact tests

Figures 8.2, 8.3 and 8.4 give the results of the elastic impact tests on Al 2024-T3. Because the impact velocity showed some scatter for these tests with very low velocities (0.6 m/s), the maximum force and the maximum central deflection during impact are divided by the impact velocity. The validity of this procedure will be shown in chapter 12.

The maximum central deflection and the contact time during impact decrease for an increasing preload, while the maximum force increases. The increase of the preload is audible: the frequency of the radiated sound during impact increases. The variation of the impact results is relatively small for the large range of the initial stress.

plastic impact tests

Figures 8.5, 8.6 and 8.7 give some examples of measured force-time and force-displacement curves during impact (no filtering was applied). Figures 8.5 and 8.6 illustrate that the dependence of the force-time curve on the preload stress level is small for monolithic material. The force-deflection curves show that the specimen tends to respond somewhat more stiffly as a result of the initial stress, and the maximum force during impact is slightly higher.

The initial loading has more influence on the force-time and force-displacement curves of the aramid ARALL material, as illustrated by figure 8.7. This material shows cracking earlier in the deformation process for an increasing preload (see table 8.1). The stiffness of the specimen is increased by the initial loading.

Figures 8.8 and 8.9 show the measured maximum force and deflection during impact as a function of the preload. In figure 8.9 also the permanent central deflection is given for Al 7075-T6. The effect of the initial stress level on the results appears to be small, when the large variation of the initial loading is considered. In figure 8.8 the curves for 2H32 (6.12 J), 7H32 (6.12 J) and Al 2024-T3 (4.74 J) show the expected decrease of the maximum central deflection, but the decrease is very small. The ARALL 2H32 (9.4 J) material shows a rather strange shape of the maximum central deflection curve. This is due to extensive cracking in this material, with a complete failure of the specimen during impact at S = 300 MPa.

The permanent central deflection of Al 7075-T6 did not show a decreasing trend as a function of the preload as was expected, but a slightly increasing trend.

The contact time as a function of the initial stress is given in figure 8.10. Because of the fracture in ARALL 7H32 and 2H32 the contact time can increase for an increasing prestress, while the contact time for the Al 7075-T6 material remains approximately constant.

The absorbed energy at ultimate load of 2H32 and 7H32 is shown in figure 8.11. As figure 8.7 indicates, the central deflection at maximum load at failure (maximum force) decreases, while the maximum force remains approximately constant. Combined with the fact that the stiffness of the specimen increases, the absorbed energy at fracture does increase (for 2H32, S > 100 MPa) or decrease (for 7H32) at increasing preload.

The crack length as function of the initial stress is shown in figure 8.12. A significant rise of the crack length occurs at a relatively high prestress only: S > 150 MPa. This means that the effect will be small for operating stresses if S < 150 MPa.

The change of the shape of the damage is important. Cracks in unstressed material bend in fibre direction: a lip is formed in the material, and a hole is created. This will have a favourable influence on the stress concentration at the crack tip. The crack in prestressed material did not show this behaviour: the crack grows further in the direction perpendicular

to the fibres and the loading. This can be schematically illustrated by:

fibre
direction

crack in
unloaded material

crack in
preloaded material
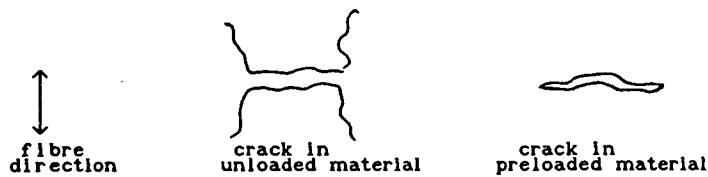
The stress concentration is not relieved, and this will have a negative influence on the residual strength.

The results of the residual strength tests on aramid ARALL 2H32 are shown in figure 8.13. A large reduction of the residual strength was found for impact damage obtained under a preload stress > 200 MPa.

8.4 Conclusions

1. The length of a crack caused by impact on aramid ARALL loaded in tension increases for an increasing preload tension stress S (figure 8.12). A significant increase of the crack length will occur only for a relatively high preload stress (S > 150 MPa).

2. The shape of the damage in aramid ARALL is changed by the preload. There is no longer a tendency for the crack to bend in fibre direction to form a lip and to create a hole. The crack remains in the direction perpendicular to the loading. This will have a negative influence on the stress concentration and residual strength.

3. If extensive cracking during impact of a preloaded specimen does not occur, a higher contact force during impact, and a smaller maximum central deflection are observed. The influence of the preload on the maximum contact force and the maximum central deflection was rather small.

references

1. Sankar, B.V.; Sun, C.T.; Low velocity impact damage in graphite-epoxy laminates subjected to tensile initial stresses, AIAA Journal Vol.24, No.3, 1986.

2. Hart, W.G.J. 't; Frijns, R.H.W.M.; Damage tolerance properties of new carbon composites, NLR Technical Publication TP 89032 L, 1989.

3. Hart, W.G.J. 't; Frijns, R.H.W.M.; Delamination growth in improved carbon composites under constant amplitude fatigue loading, NLR Technical Publication TP 89008 L, 1989.

4. Card, M.F.; Rhodes, M.D.; Effect of service environment on composite materials, AGARD 50th Meeting on the structures and materials panel specialists meeting, 1980.

5. Oplinger, D.W.; Slepetz, J.M.; Impact damage tolerance of Graphite/Epoxy sandwich panels, in: Foreign object impact damage to composites, ASTM STP 568, 1975.

6. Suarez, J.A. ; Whiteside, J.B.; Comparison of residual strength of composite and metal structures after ballistic damage,
   in: Foreign object impact damage to composites, ASTM STP 568, 1975.

7. Awerbuch, J.; Impact damage in composite materials, Composite materials workshop, Katholieke Universiteit, Leuven, 1984.

| material | initial stress | impact energy | max.during impact | | contact time | crack length | |
| | | | F_{max} | w_0 | | convex | concave |
	(MPa)	(J)	(kN)	(mm)	(ms)	(mm)	(mm)
2024-T3	0	4.74	1.87	5.32	3.03	0	0
	200	4.74	2.07	4.77	3.17	0	0
	350	4.74	1.84	4.69	2.77	0	0
	350	4.74	2.09	5.03	3.10	0	0
	350	6.80	1.78	5.96	3.03	0	0
7075-T6	0	7.32	2.80	6.52	2.53	0	0
	100	7.32	2.86	5.61	2.83	0	0
	200	7.32	3.08	4.20	2.57	0	0
	300	7.32	2.80	6.52	2.53	0	0
	300	7.32	2.64	4.51	-	0	0
2H32	0	6.12	2.21	-	-	7.9	0
	0	6.12	2.40	6.08	3.17	7.2	0
	100	6.12	2.37	5.54	4.36	7.7	0
	200	6.12	1.95	5.66	-	12.8	12.5
	300	6.12	1.95	5.50	4.69	20.9	19.1
	100	9.39	2.03	8.36	3.95	10.7	8.7
	200	9.39	2.26	12.5	3.90	12.8	12.5
	300	9.39	1.68	10.4	7.19	failure	
7H32	0	6.12	2.53	5.78	3.60	8.5	0
	150	6.12	2.33	5.42	2.93	9.7	0
	250	6.12	2.36	5.38	5.00	27.8	27.2

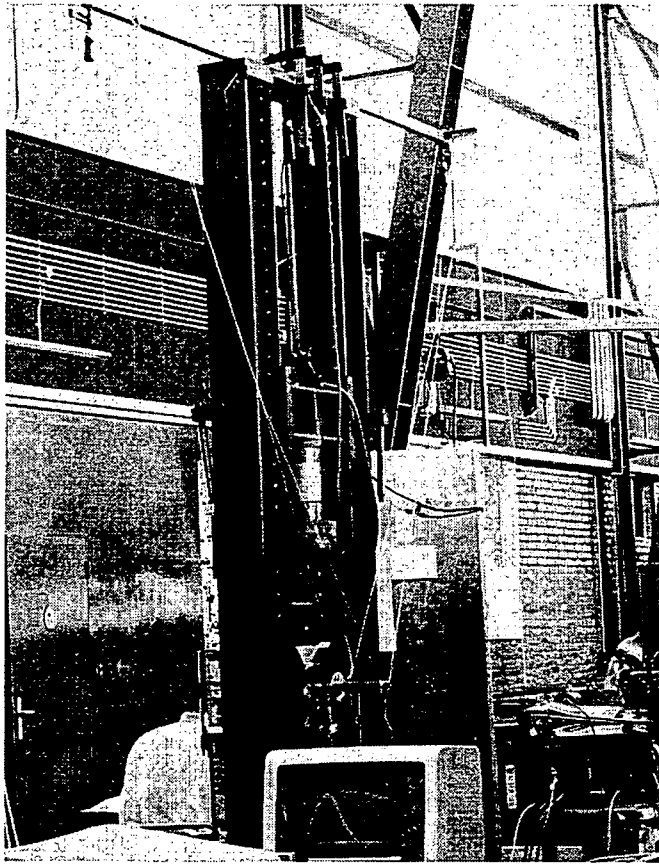table 8.1 Results of the plastic impact tests.
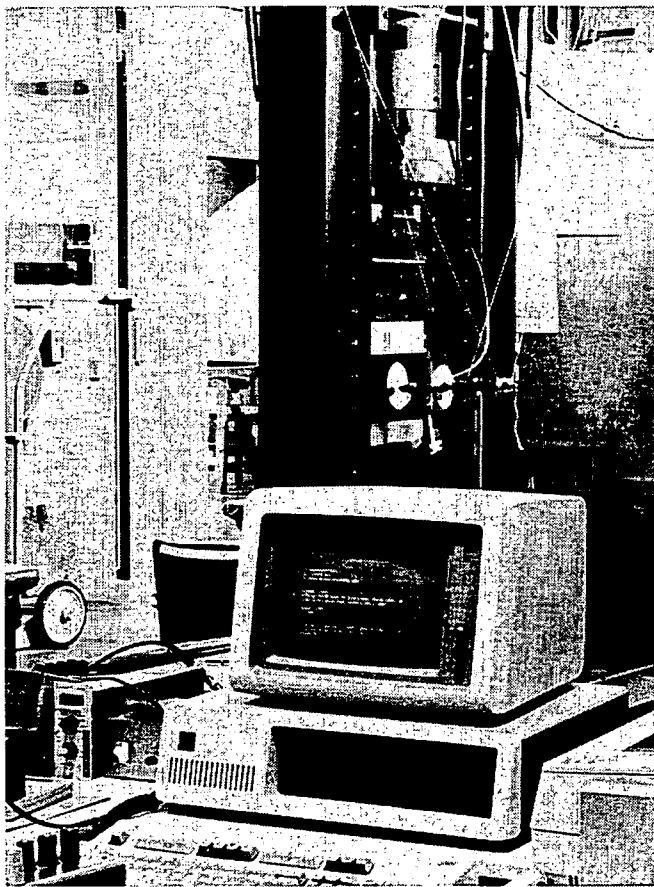
figure 8.1a The test
set-up for impact
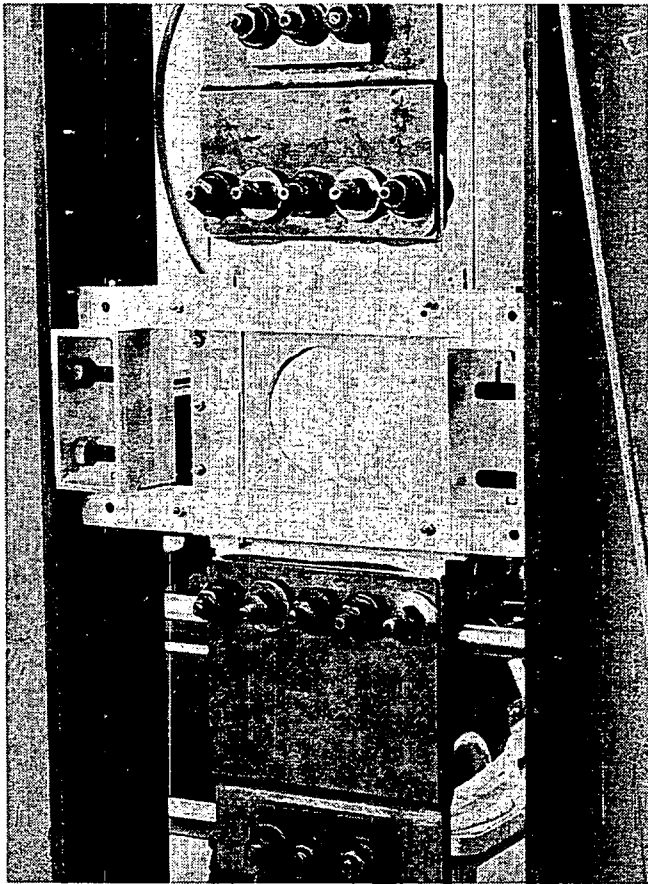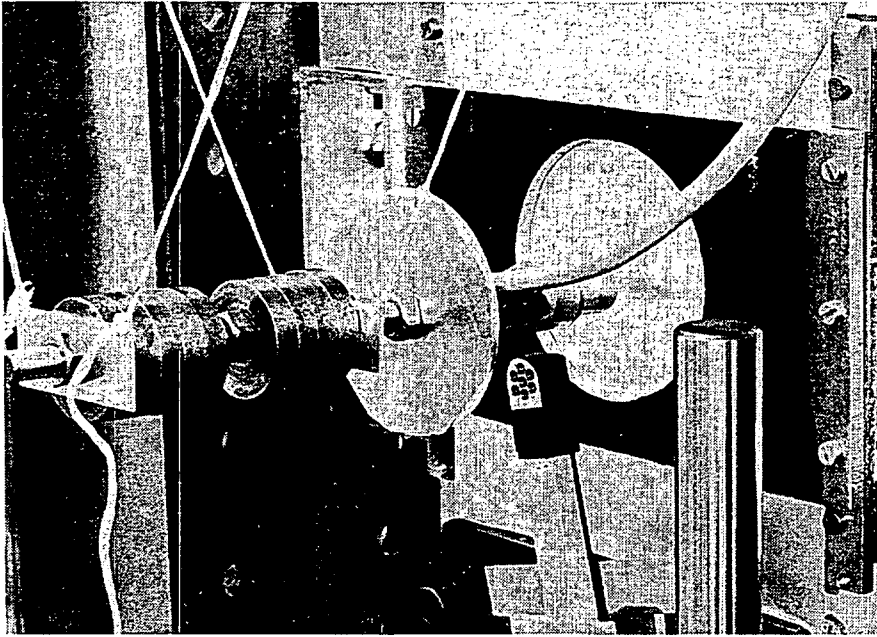on specimens
under a tensile stress.

figure 8.1b Detail of figure 8.1a.
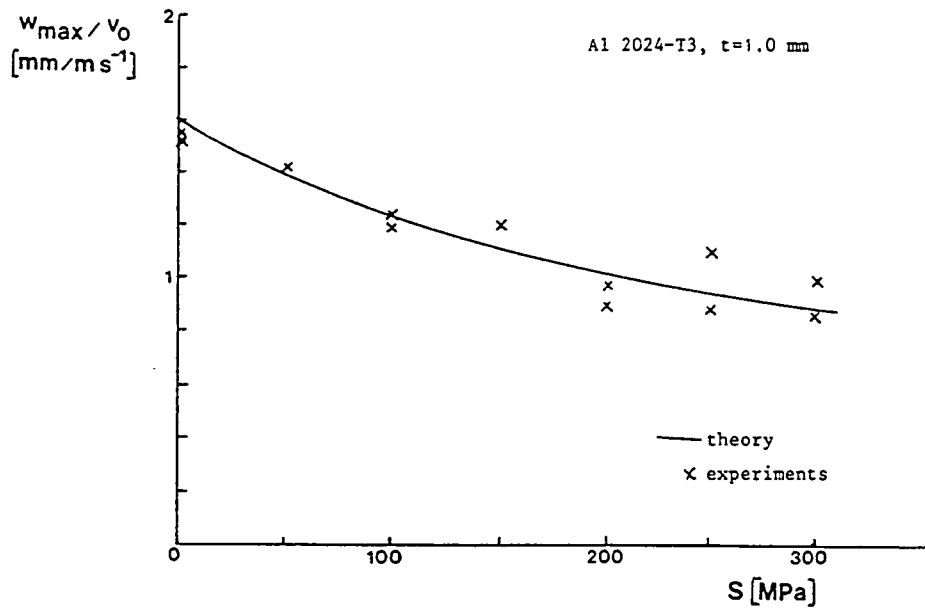
figure 8.2 The maximum central deflection divided by the impact velocity as function of the stress level during impact.
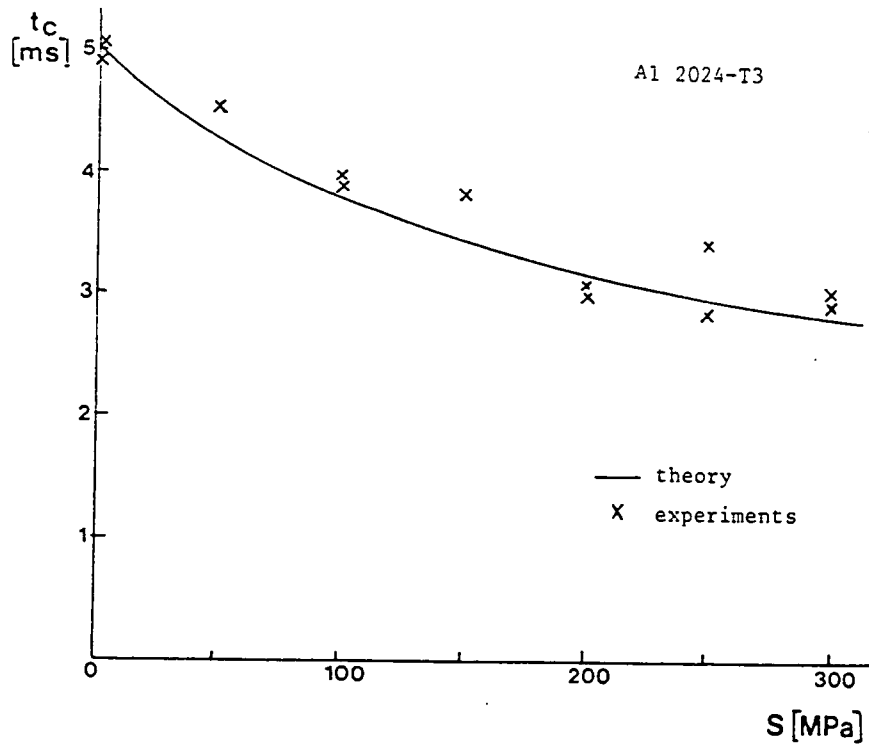
figure 8.3 The contact time as function of the stress level during impact.

figure 8.4 The maximum force during impact as function of the
stress level during impact.
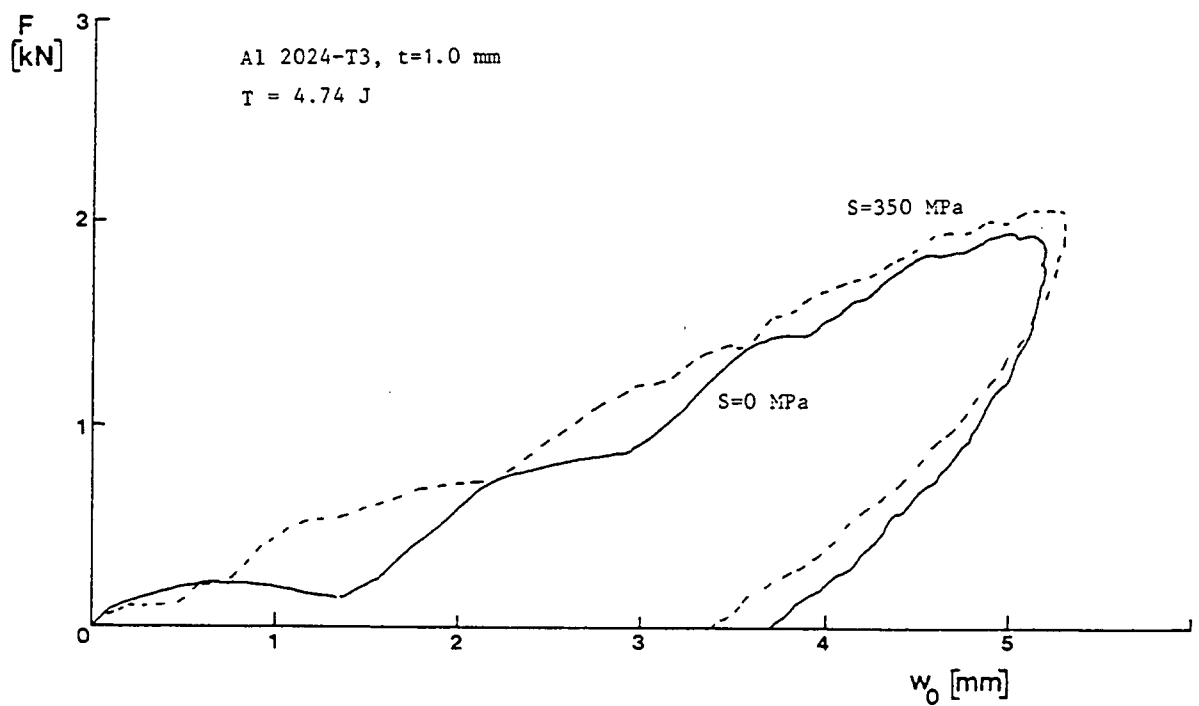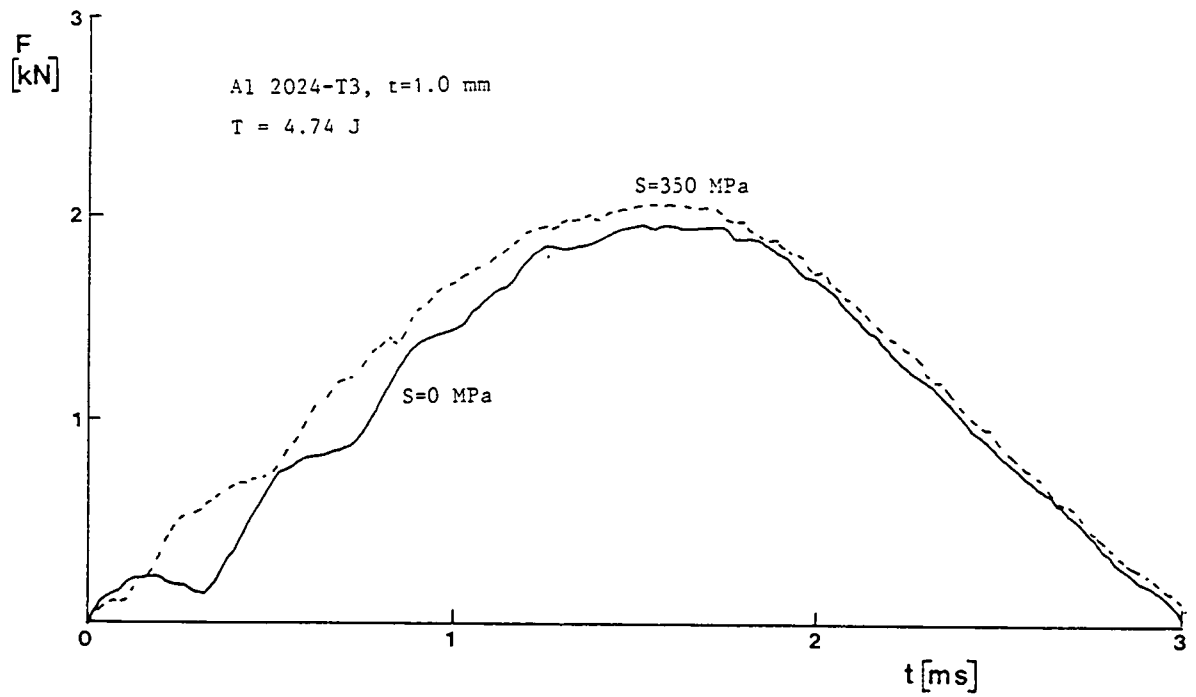
figure 8.5 Force-time and force-deflection curve for two values of the
stress level during impact.
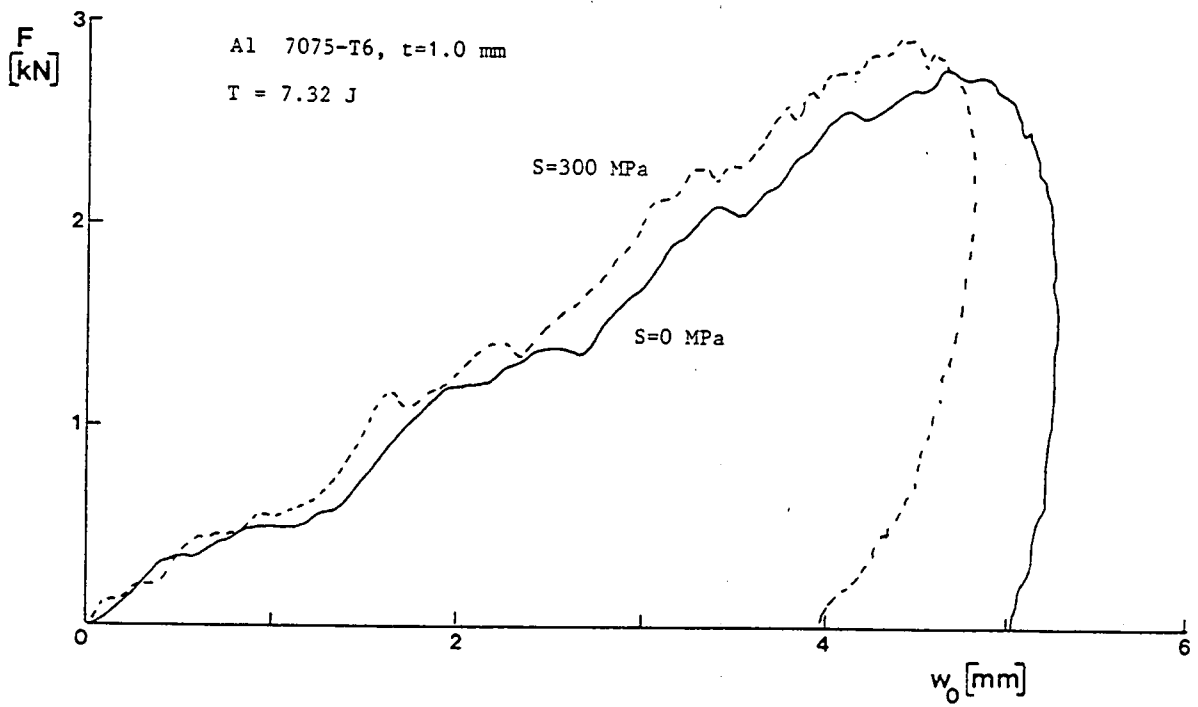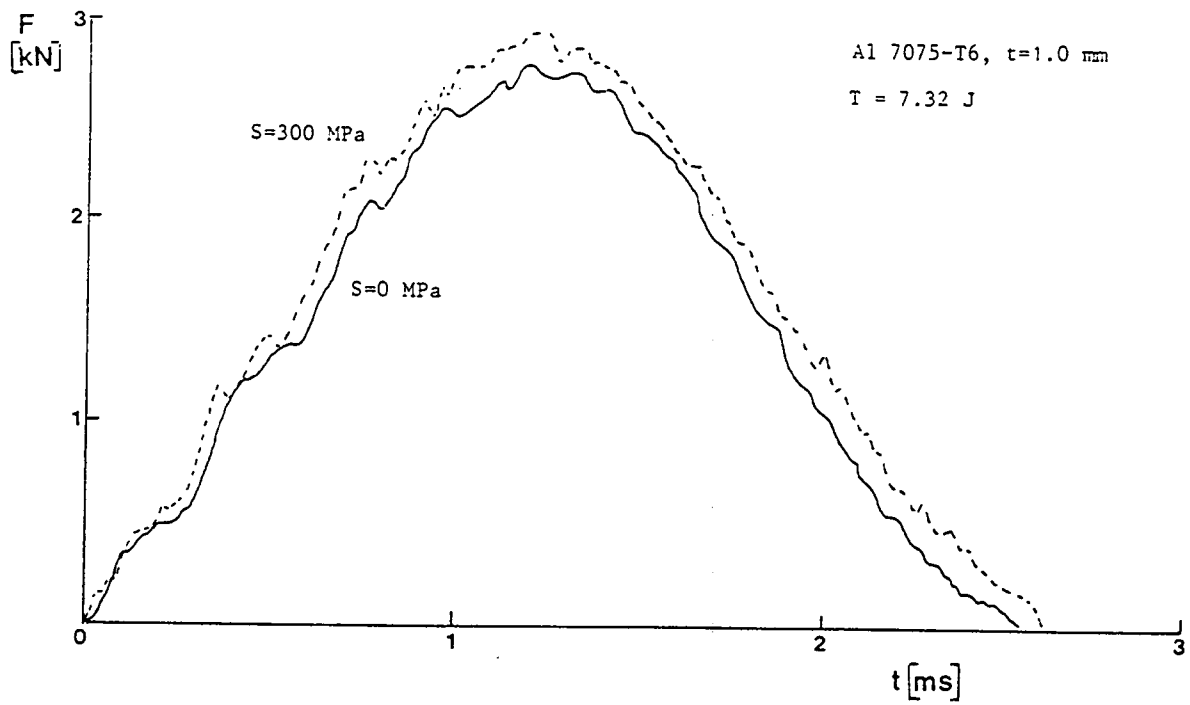
figure 8.6 Force-time and force-deflection curve for two values of the stress level during impact.

292
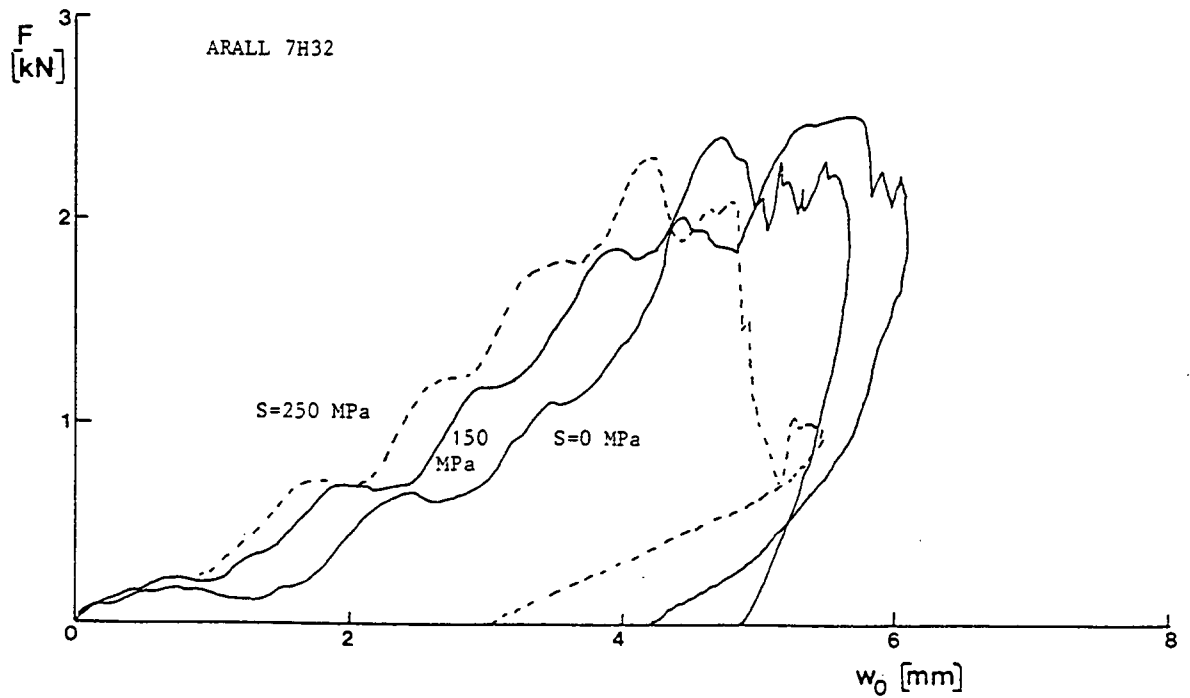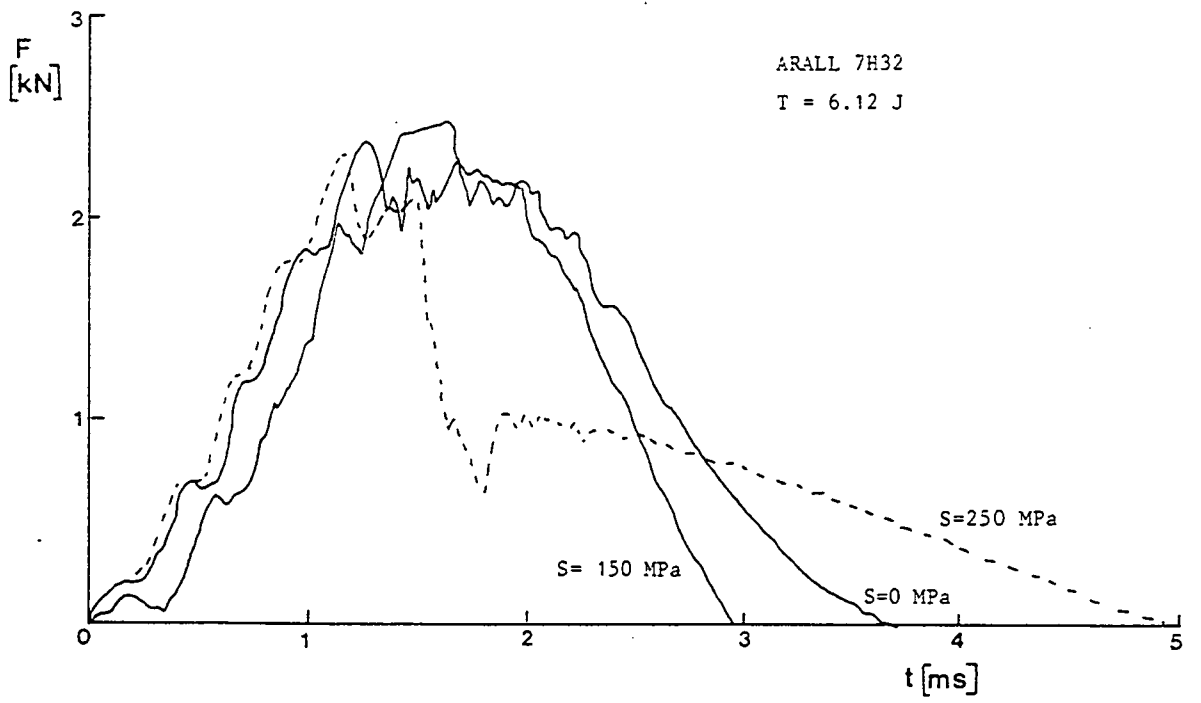
figure 8.7 Force-time and force-deflection curve for two values of
the stress level during impact.
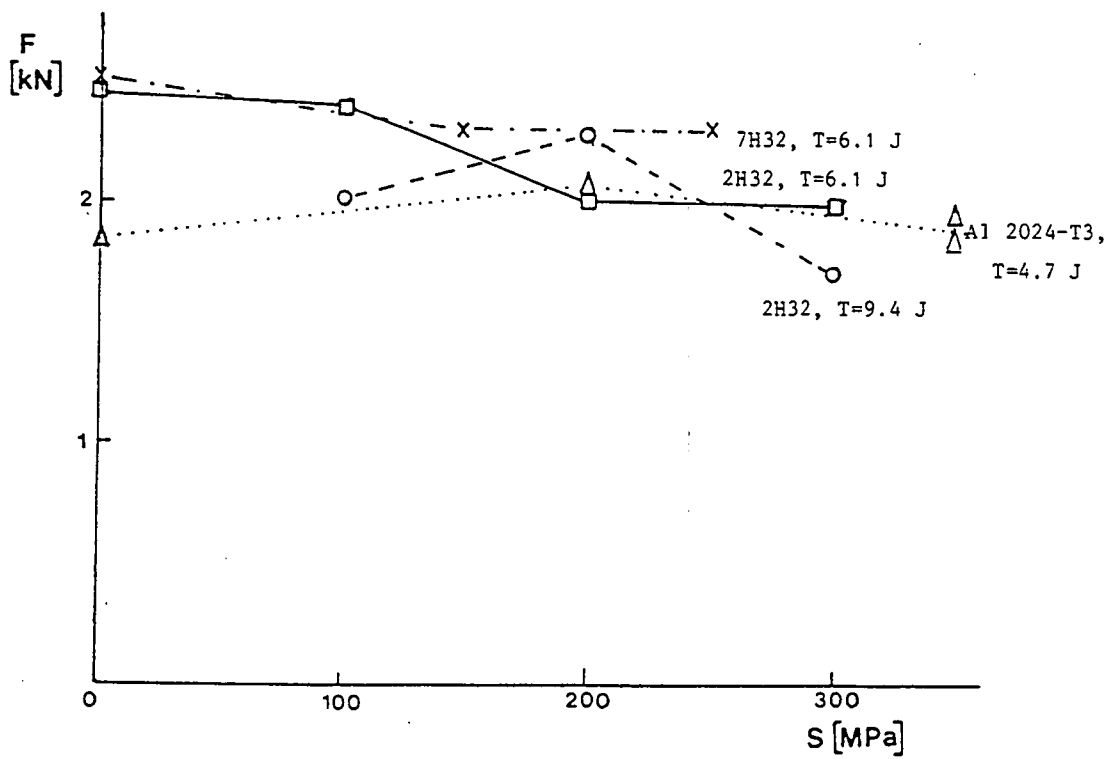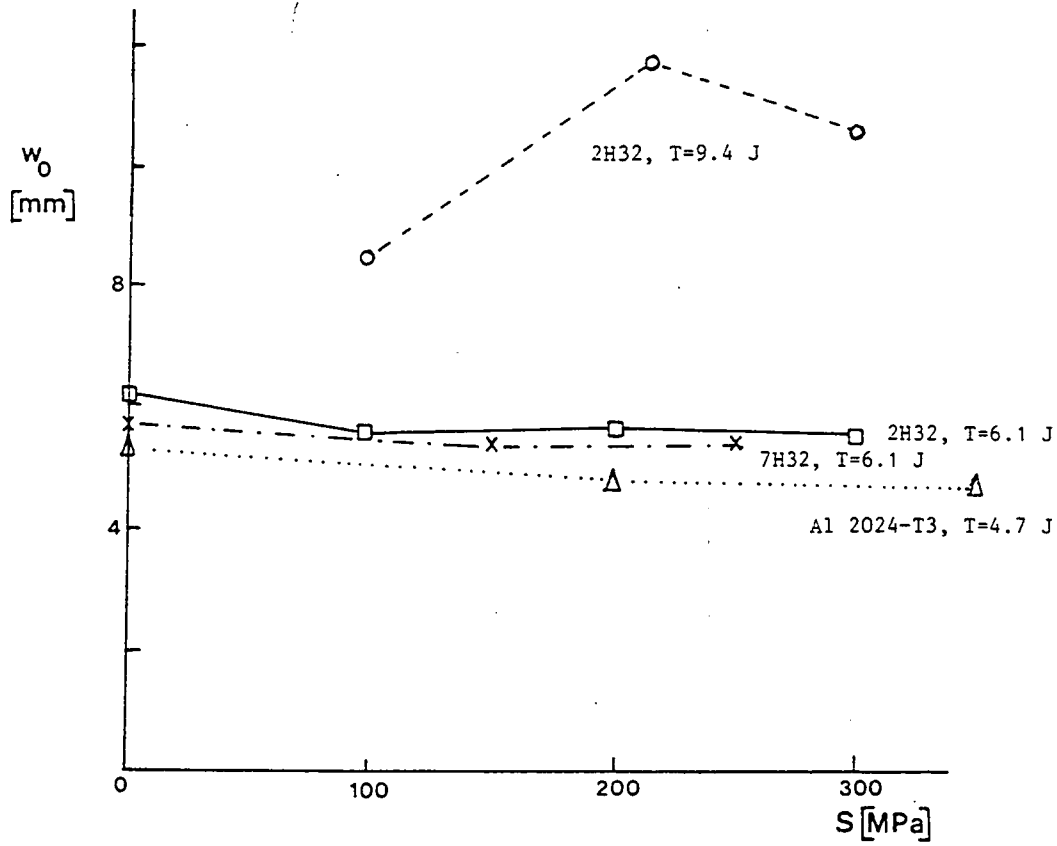
figure 8.8 Maximum central deflection and the maximum contact force during impact as function of the stress level during impact.
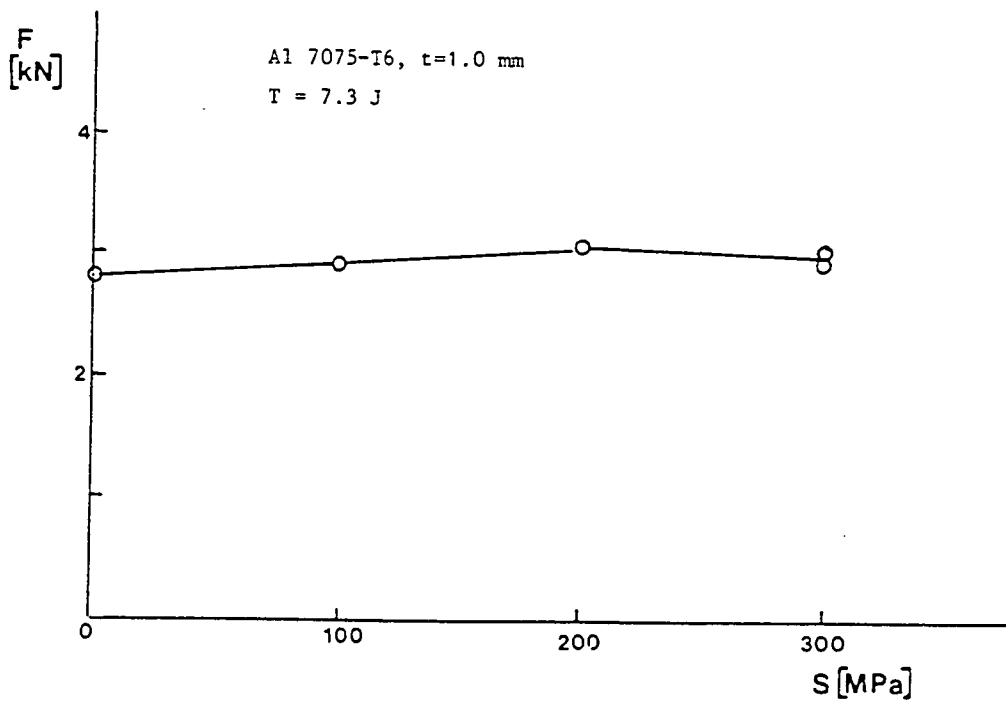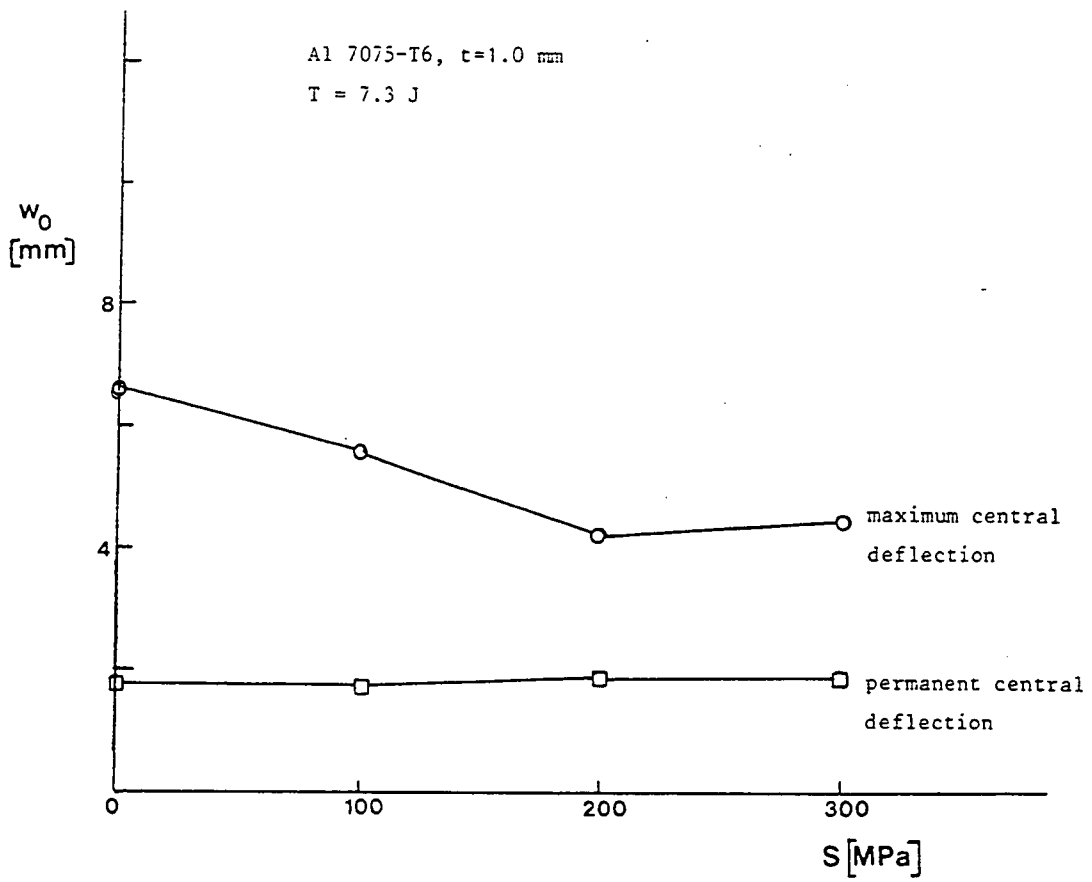
figure 8.9 The maximum central deflection and the maximum contact force during impact as function of the stress level during impact.
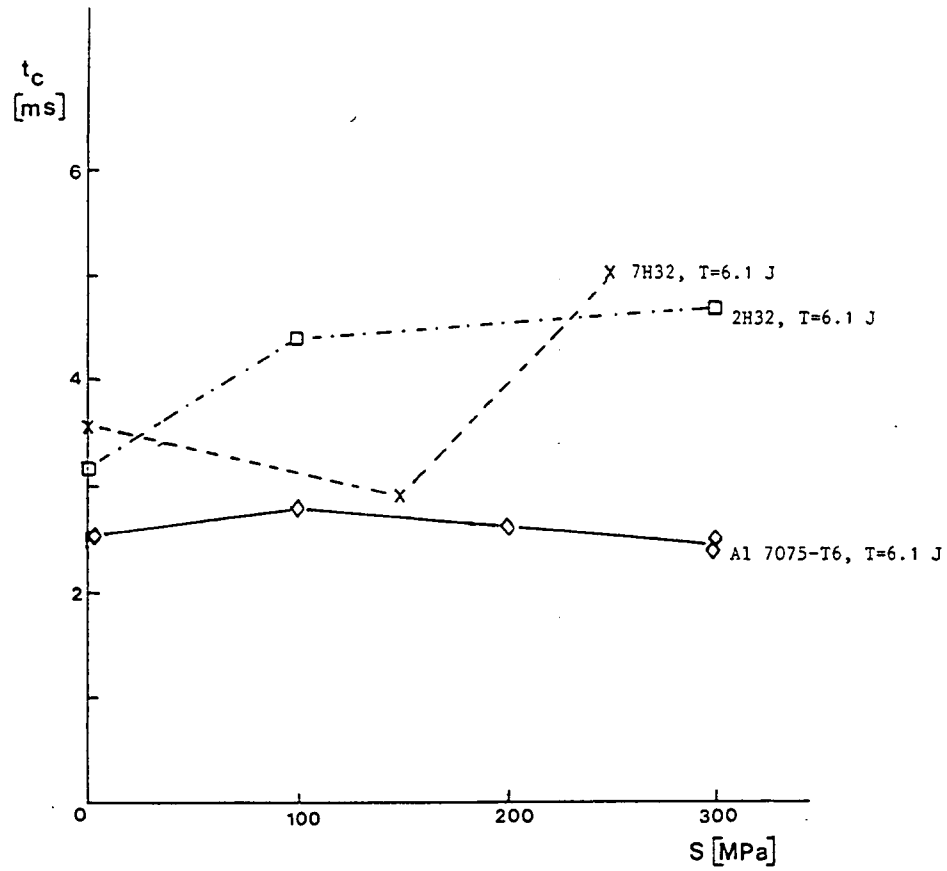
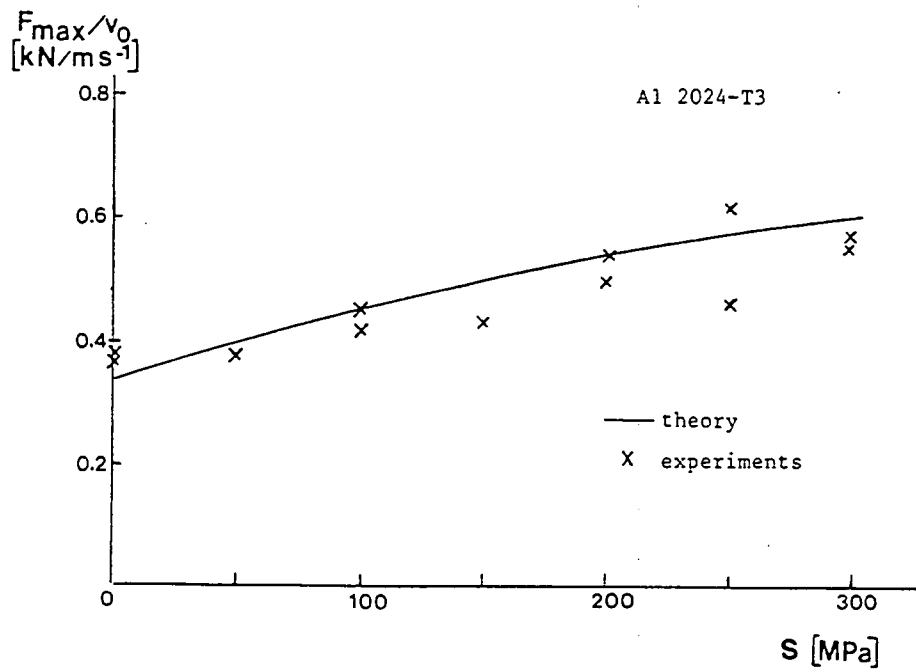**figure 8.10** The contact time as function of the stress level during impact.
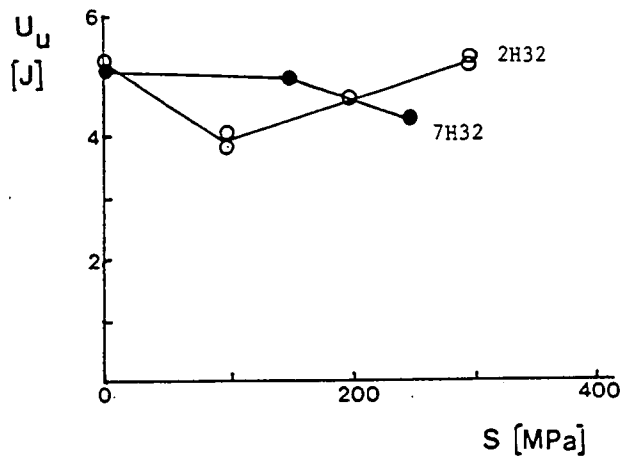
figure 8.11 The absorbed energy at ultimate force as function of the stress level during impact.
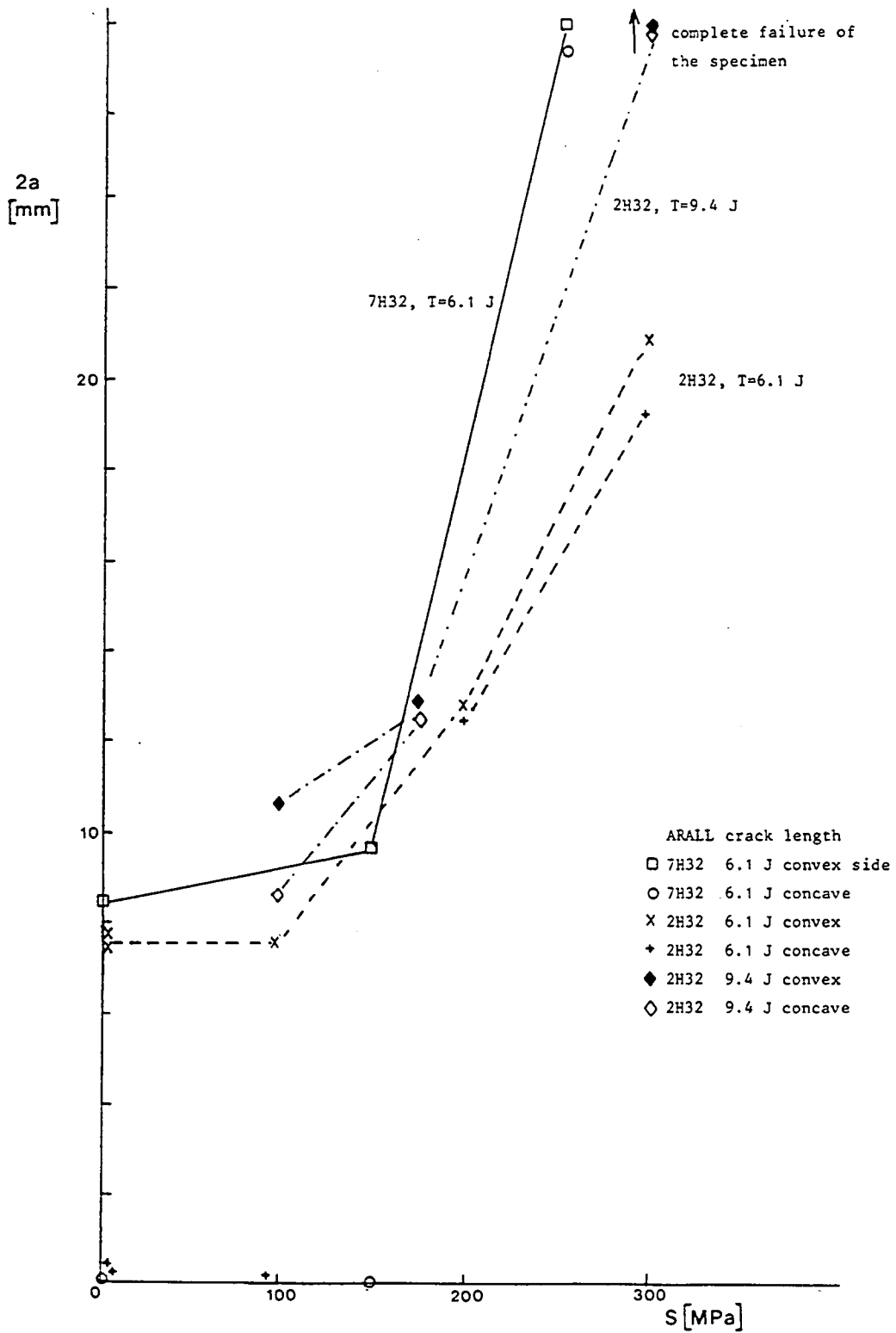
figure 8.12 The total crack length after impact as function of
the stress level during impact.
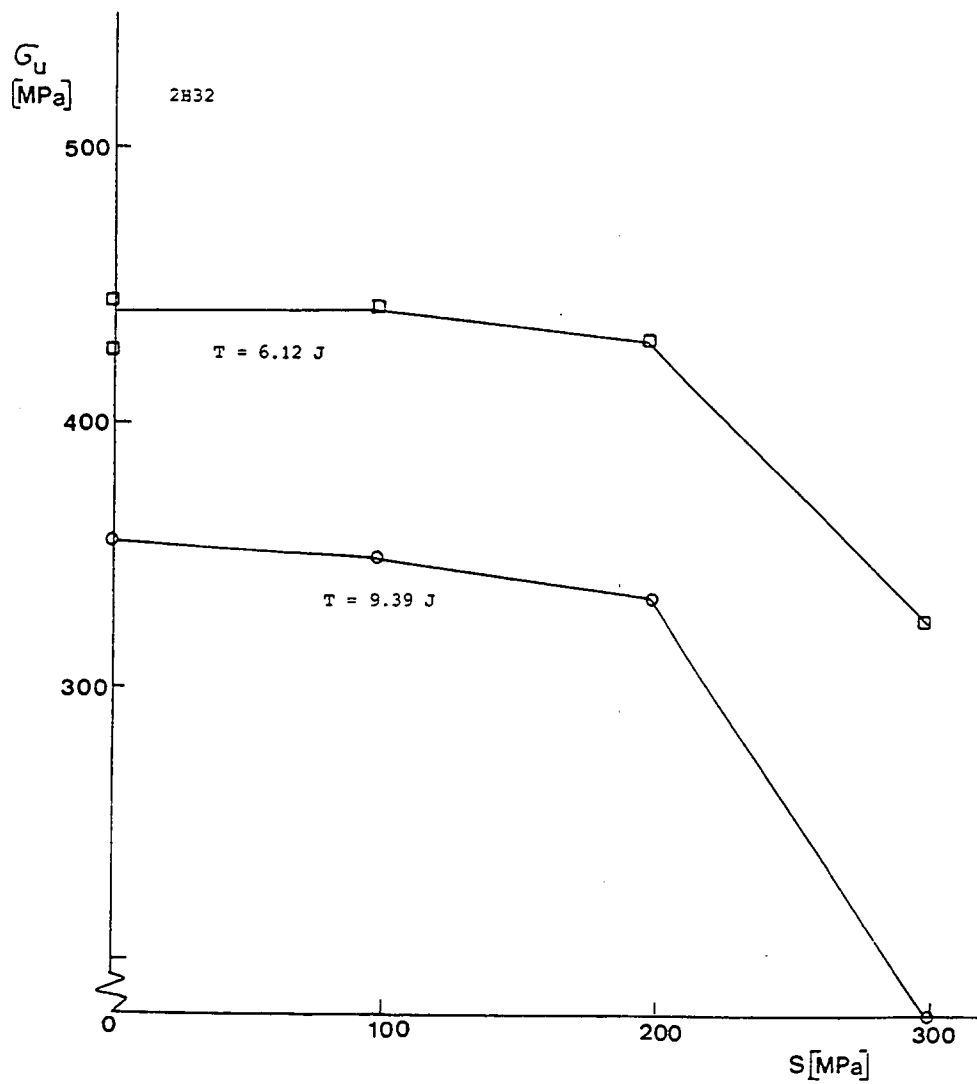
figure 8.13 The residual strength as function of the stress level during
impact for aramid ARALL 2H32.

PART III IMPACT MODELLING

chapter 9 Impact modelling: introduction and literature survey

9.1 Introduction

In this part of the thesis efforts are described to model the impact event, in order to understand more about the deformation process of a sheet specimen under transverse impact loading.
The analysis will apply to the low-velocity regime: the deformation of the impactor is small and the effect of the generation of heat will be neglected. Also stress wave effects will not be included.

Two basic types of models can be distinguished: finite element models (FEM) and analytical models. The analytical models can be divided in two categories: simple analytical models (equations which in principle can be solved with a pocket calculator) and complex analytical models (e.g. requiring numerical integration of differential equations).
Both FEM and analytical modelling are needed. The FEM approach needs both an analytical and an experimental background to assure reasonable results. The analytical models require more simplifying assumptions which can be checked by FEM calculations and experiments. The assumptions of FE models are generally more hidden than in an analytical model.

The references listed at the end of this chapter illustrate the large number of models that have been proposed. A closer study of the literature shows that the capability of the models is still relatively limited. An experimental basis of the models is generally lacking. Many curves are generated, but in general the influence of the material properties on the impact behaviour and the physical phenomena involved are not well understood.

The aim of impact modelling in general will be threefold:

1. A better understanding of the <u>physics of impact</u>. In this context some important questions are:
a. How is the stress and strain distributed in the plate?

300

What is the magnitude of the deformation energy for bending, membrane stretching and a local Hertzian indentation? What is the importance of geometric non-linearity due to large displacements? Is it allowed to ignore transverse shear effects (see section 9.4)?

b. Why does the material fail in tension at the backside beside the centre of impact and not in the centre of the plate?

c. The shape of the plate under loading is defined as the normalized deflection w/w_0 vs. one of the inplane coordinates. What is the shape of the deflected plate? Is this shape constant and equal to the linear elastic shape or will it change during loading?

d. What is the difference between quasi-static and dynamic loading? How important are the higher order vibrations of the specimen for the induced strains; and how large are strain rate effects?

e. What is the influence of the impactor radius and the dimensions and boundary conditions of the specimen on the impact response?

2. Modelling may help to explain experimental results of instrumented impact tests, and may guide the optimization process of new materials, like ARALL laminates.

3. Impact plays an important role in the design process of a composite structure. The optimization of a structure (e.g. choice of material and lay-up) may need an impact model.

The models needed for these three topics will become more complex from point 1 to point 3. The understanding of the impact process (point 1) can already be supported by relatively simple models. For the second topic (material comparison and optimization) at least some kind of fracture criterion is needed to predict the impact energy at which first fracture will occur. A maximum strain criterion will be the most simple approach, followed by a kind of critical stress function (e.g. Tsai-Hill-von Mises). Many criteria can be found in the literature.

For design purposes a model is needed with a fracture criterion, but also with a damage propagation description. A designer wants to optimize the

material and the structure with respect to the residual strength, which is dependent on the damage size and the character of the damage. A designer needs a model which can handle a plate with its actual boundary conditions (e.g. a panel with stiffeners) and not a model for clamped or simply supported specimens, sufficient for the second purpose (material testing and optimization). For the design analysis also some kind of initial preload on the plate must be considered.

It will be hard to describe damage propagation in detail (especially on a micro level). It must be done in terms of fibre failure, delamination, fibre pull-out etc., to describe the energy dissipation accurately. Plasticity has to be taken into account for metallic components. On the basis of the damage sizes and types, a model has to be derived to predict the residual strength of the material and the structure. Even if it would be possible to derive a damage initiation, propagation and residual strength model, another problem is to obtain the relevant material characteristics for the model.

The optimal impact model will be a model with the projectile and target properties as the input, and with the residual strength as the output. This 'ideal' model will be complex and it will be difficult to judge its correctness. The more complicated a model, the less suitable it will probably be for practical application.

A new element of the modelling in this thesis will be the inclusion of elastic and material non-linearities, in order to obtain a better description of the impact process. It should give indications on the influence of material properties. The models described in the literature are generally linear and elastic. They put much emphasis on the inclusion of transverse shear effects.

In the present chapter a survey of the models in the literature will be presented. The assumptions concerning the various physical aspects will be treated. The next chapter (chapter 10) will discuss a relation between the strains and the shape of the sheet under impact loading. Chapter 11 will show the results of high strain rate tensile and puncture tests, to give an

indication of strain rate effects. The formulation and the calculated results of the impact models will be given in chapter 12.

9.2 Geometry of the impact problem

Figure 9.1 shows the geometry of the impact problem to be considered here. The impactor strikes a circular or rectangular plate and exerts a dynamic pressure distribution on its surface. The impactor locally indents the specimen (reduces the specimen thickness at the impact point). This indentation α is equal to the displacement s of the impactor minus the central deflection w_0 of the plate (figure 9.2):

$$\alpha = s - w_0 \tag{9.1}$$

The plate shows a global deflection $w=w(r,\theta)$ (circular plate) or $w=w(x,y)$ (rectangular plate) of the midplane of the plate. A point on the midplane will also have horizontal displacements $u=u(r,\theta)$ and $v=v(r,\theta)$ (circular plate) or $u=u(x,y)$ and $v=v(x,y)$ (rectangular plate). The plate will have certain prescribed boundary conditions (clamped, simply supported, attached spring stiffness) at the edges, and possibly also at the backside of the plate (e.g. in the case of a honeycomb facing). The plate may be under an initial loading. The plate is anisotropic and built up from elastic orthotropic layers with an orientation ϕ relative to the global coordinate system and isotropic elasto-plastic metallic layers.

9.3 Contact law

The first particular aspect of the impact problem is the contact between projectile and plate. The method of modelling the contact problem will have a large influence on the output of the analysis. The deformation of the plate can be treated as a force acting on two (non-linear) springs in series: an indentation stiffness and a flexural and membrane stiffness of the plate. The indentation stiffness will in general be much higher than the combination of the combined flexural and membrane stiffness of the plate.

A contact law has to describe the load distribution for a certain contact

force, in order to link the impactor and the plate in the model. Basically there are three ways to describe this contact:

1. A rigid contact between projectile and target ($s = w_0$); the influence of the local indentation is neglected and contact during the whole deformation process is assumed. A rigid projectile can be modelled as a locally concentrated mass on the plate with an initial velocity. This type of contact is assumed in the simple mass-spring model of chapter 12.

2. The impact problem is modelled as a forced vibration of the plate (references 26 to 36): the excitation force is assumed to be known as a function of time, or the force-time curve is assumed to have a known shape (e.g. sinusoidal). This type of modelling is often applied, but its practical significance is rather limited because the force-time curve will generally be unknown.

3. A kind of Hertzian indentation law is used of the type:

$$F = k \, \alpha^{3/2} \qquad\qquad (9.2)$$

with F as the contact force, k as the indentation stiffness and α as the local indentation (see equation 9.1 and figure 9.2).

In the literature also a linearized contact force – indentation relation was found[72].

Hertz[2] derived his theory for the application to impact problems, while his derivation is valid only for static indentation. Equation 9.2 is used in impact models, in this case F and α in this equation are functions of time. Recently Tatara[73] showed that the formulation of Hertz can also be used for impact problems, as long as the indentation is small. Timoshenko[3] applied the Hertzian theory for the impact on beams, Karas[4] used it to describe the impact on plates.

The impression of a spherical body on a plate is generally described by relations which are valid for the static impression of a sphere in an elastic isotropic half-space[1]:

$$k = \frac{4}{3\pi} \sqrt{R} \quad \frac{1}{\delta_1 + \delta_2} \qquad (9.3)$$

$$\text{with} \quad \delta_1 = \frac{1 - \nu_1^2}{E_1 \pi} \qquad \text{for indentor and indented material}$$

with E as Young's modulus, ν as Poisson's ratio and R as the radius of the impactor.

Figure 9.2 shows shows the load distribution exerted by the indentor on the plate. The pressure distribution is assumed to be elliptical in shape (for elastic deformation) with a maximum pressure:

$$q_0 = \frac{3 F}{2 \pi c^2} \qquad (9.4)$$

F is the load on the indentor and c is the radius of the contact area. It can be derived that[11]:

$$c^3 = \frac{3}{4} \pi R (\delta_{indentor} + \delta_{target}) F \qquad (9.5)$$

For a steel indentor $\delta_{indentor}$ = 1.448 10^{-6} mm^2/N and for an aluminium plate δ_{target} = 4.023 10^{-6} mm^2/N. For a spherical impactor with a radius of 7.5 mm (the standard radius in this thesis) the maximum pressure will be:

$$q_0 = 226.65 \, F^{1/3} \quad \text{(with } q_0 \text{ in MPa, F in N)} \qquad (9.6)$$

This expression indicates that plastic deformation will occur at a relatively small contact force. The plastic deformation will flatten the pressure distribution on the plate. The contact stiffness will decrease. Apart from plasticity a second modification of the classical Hertzian theory will be needed to include the anisotropy of composite materials.

Tan and Sun[38] use a classical method to include plasticity, in their case to describe the plasticity of the matrix in composite plates. Equation (9.2) (with an experimental value of k which is different from the k value

for elastic deformation) is a good approximation for the loading path. The unloading path is described by (after Barnhart and Crook for metals, ref.1, p.92):

$$F = F_m \left(\frac{\alpha - \alpha_0}{\alpha_m - \alpha_0} \right)^q \tag{9.7}$$

with F_m as the contact force at the start of unloading, α_m as the indentation at F_m and α_0 as the permanent indentation. The constant q has to be determined by experiments. Sun et al. use experimentally determined values of k, α_0 and q as input parameters for their finite element impact model. They measure the indentation parameters during quasi-static loading, and assume no effect of the loading rate on the parameters.

Sun et al. give a modified version of equations (9.2) and (9.3) to describe the elastic indentation of an anisotropic plate. This equation is adopted by Springer et al.[46-49] for their impact model:

$$\delta_{composite} = \frac{1}{\pi E_{yy}} \tag{9.8}$$

with E_{yy} as the Young's modulus of the upper, loaded ply in the direction transverse to the fibres. In fact this expression has no analytical background; it is an 'educated guess' (according to Moon[15]). For a rigid projectile $(E_{indentor} \rightarrow \infty$) and with substitution of equation (9.8) the expression for the indentation stiffness can be calculated with[20,27,72]:

$$k = \frac{4}{3} \sqrt{R} \ E_{yy} \tag{9.9}$$

The loaded contact area of a plate built up from orthotropic layers is elliptical in shape, but in the models found in the literature this shape is approximated by a circle[4,7,21,39] or a rectangle[26,27]. The loading of the impactor on the plate is also approximated by a point loading: Sun et al.[37-41] , Springer[46], and references 20 and 22. The pressure distribution is generally approximated by a constant pressure over the

contact area (e.g. reference 72).

Greszczuk[16-18] pays much attention to the contact between projectile and plate. He studied the stress distribution in the plate due to the pressure distribution: the stresses due to flexural and membrane deformation of the plate are neglected. This is a reasonable assumption for thick plates, for which the local stress dominates. According to calculations done by Greszczuk[16] the surface pressure at fracture is dominated by indentation stresses for a ratio of the thickness and radius of the contact area larger than 2. If the ratio is smaller than 2 the stresses due to global deflection dominate.

Greszczuk presents complicated expressions for the indentation stiffness and the dimensions of the elliptical contact area, which are analytically derived for planar isotropic targets.

9.4 Transverse shear

The models presented in the literature generally include the deformation due to transverse shear of the plate. The simple analytical static models of Elber[7-9] and Stellbrink[10] reduce this type of deformation to its most simple form. For small deflections, and when shear stresses are constant over the thickness, the situation is as shown in figure 9.3. The contact force F is counterbalanced by shear stresses:

$$\tau(r) = \frac{F}{2 \pi r t} \tag{9.10}$$

with t as the plate thickness and r as the radial coordinate. The shear strain γ can be written as:

$$\gamma = \frac{\tau}{G} = \frac{F}{2 \pi r t G} \tag{9.11}$$

The central deflection $w_{0,s}$ due to the shear deformation only is obtained by integration of the shear strain, assuming that the contribution of the shear deformation for $r < c$ can be neglected (c is small)[7,10]:

$$w_{0,s}(r) = \int_r^a \gamma(r) \, dr = \frac{F}{2 \pi t G} \ln \left(\frac{a}{r} \right) \qquad \text{(for } r > c)$$

(9.12)

If the thickness of a plate is increased, the load F at a certain total deflection (due to shear, bending and flexure) will increase more than proportionally with the thickness. This means that for a relatively thick plate the shear deformation will become more important (see equation 9.10). For composite materials the shear stiffness may be small compared with the elongation stiffness of the material. This implies that the transverse shear deformation may become important for composite laminates. Whitney and Pagano[59] showed that the transverse shear deformation can effectively lower the stiffness and thus can not be neglected for square composite plates with side lengths A and thickness t if A/t < 20. According to Shivakumar et al.[19] shear can be neglected for A/t > 10.

The finite element model presented by Sun et al. and most of the complicated analytical models use the equations based on the work of Whitney and Pagano[59] for anisotropic plates. The approach of Whitney and Pagano is based on the theory for isotropic plates: the Reissner-Mindlin theory[58]. The Reissner-Mindlin theory corrects the classical theory of plates, which describes the equation of motion as the Lagrange's equation:

$$D \nabla^4 w + \rho \, t \, \frac{\delta^2 w}{\delta t^2} = q(x,y,t)$$

(9.13)

with:
$$\nabla^4 = \frac{\delta^4}{\delta x^4} + 2 \frac{\delta^4}{\delta x^2 \delta y^2} + \frac{\delta^4}{\delta y^4}$$

and D as the flexural stiffness, t as time, ρ as the density and q as the loading. For anisotropic plates a similar equation can be derived (Lekhnitskii[61]).

The classical plate theory (CPT) only takes into account pure bending. The

cross-sections of the plate are assumed to remain straight and perpendicular to the midplane of the plate. The CPT reduces the three dimensional plate problem to a two dimensional (plane) one, with only one displacement component (w).

The shear deformation of the plate makes the phenomenon three-dimensional. The Reissner-Mindlin theory reduces the problem again to a plane, two-dimensional one. This is done by the introduction of the planar rotations of the cross-sections of the plate as independent variables (independent of w): ψ_x and ψ_y.

Further a shear correction factor k is introduced to relate the resultant of the shear stresses over the thickness and the average shear strain:

$$k^2 = \frac{Q_x/t}{\Gamma_{xz} G}$$

$$\text{with:} \quad Q_x = \int_{-t/2}^{t/2} \tau_{xz} dz \quad \text{and} \quad \Gamma_{xz} = t^{-1} \int_{-t/2}^{t/2} \gamma_{xz} dz \qquad (9.14)$$

Hence,

$$Q_x = G' \, t \, \Gamma_{xz} \quad \text{with} \quad G' = k^2 G$$

In these equations Q is the shear stress resultant and Γ the average shear strain. The shear correction factor accounts for the non-uniformity of the shear strain distribution over the thickness[63].

For orthotropic plates, when the rotatory inertia and the stress resultants N (stretching) are neglected, the differential equations are reduced to (Reissner-Mindlin theory, after Qian and Swanson[72], corrected):

$$D_{11} \frac{\delta^2 \psi_x}{\delta x^2} + D_{66} \frac{\delta^2 \psi_y}{\delta y^2} + (D_{12} + D_{66}) \frac{\delta^2 \psi_y}{\delta x \delta y} - k \, A_{55} \left(\psi_x + \frac{\delta w}{\delta x} \right) = \frac{\rho t^3}{12} \frac{\delta^2 \psi_x}{\delta t^2}$$

309

$$D_{22} \frac{\delta^2 \psi_y}{\delta y^2} + D_{66} \frac{\delta^2 \psi_y}{\delta x^2} + (D_{12} + D_{66}) \frac{\delta^2 \psi_x}{\delta x \delta y} - k\,A_{44} \left(\psi_y + \frac{\delta w}{\delta y} \right) = \frac{\rho t^3}{12} \frac{\delta^2 \psi_y}{\delta t^2}$$

$$k\,A_{55} \left(\frac{\delta \psi_x}{\delta x} + \frac{\delta^2 w}{\delta x^2} \right) + k\,A_{44} \left(\frac{\delta \psi_y}{\delta y} + \frac{\delta^2 w}{\delta y^2} \right) + q(x,y,t) = \rho t \frac{\delta^2 w}{\delta t^2}$$

(9.15)

A_{ij} and D_{ij} are calculated from the elements c_{ij} of the stiffness matrix of the laminate:

$$D_{ij} = \int_{-t/2}^{t/2} Q_{ij}\, z^2\, dz \qquad Q_{i\alpha} = c_{i\alpha} - \frac{c_{i\alpha}}{c_{33}} c_{3\alpha} \qquad \begin{matrix} \alpha = 1,2,6 \\ i = 1,2,6 \end{matrix}$$

$$A_{ij} = \int_{-t/2}^{t/2} c_{ij}\, dz \qquad\qquad\qquad\qquad (9.16)$$

The shear correction factor k is introduced in these equations. The equations can be solved by the expansion of ψ_x, ψ_y, w and the loading function q(x,y,t) in Fourier series and substitution in equations 9.15. The Fourier series have to satisfy the boundary conditions of the plate. In practice this is only possible for simply-supported plates, other boundary conditions make the solution of the differential equations more complicated. The equations are used by Moon[15], Sun and Chattopadhyay[22], Ramkumar and Chen[26], Dobyns[28] and Reddy[51]. It is also possible to express the Reissner-Mindlin theory as energy equations which can be solved

310

by a Raleigh-Ritz analysis. In this way it is easier to predict the impact behaviour of plates with various boundary conditions. The Raleigh-Ritz approach is used by Qian and Swanson[72] and Cairns and Lagace[20].

A detailed treatise of the Reissner-Mindlin theory would be interesting but this would be beyond the scope of the present thesis. Looking at the assumptions of the theory, the following critical remarks can be made:

1. The shear correction parameter k remains a rather mysterious parameter in the impact models based on this theory. Generally values of 2/3 ($\cong$ 0.667, by Uflyand[58]), 5/6 ($\cong$ 0.833, ref. 20,63) or $\pi^2/12$ ($\cong$ 0.822, ref.15,22,26,28,31,35,36) are used, based on the shear correction factors proposed by Mindlin[58] and Whitney and Pagano[59]. But Mindlin and Whitney and Pagano state that the k value is dependent on the elastic properties of the material, e.g. Poisson's ratio. The k value is linearly dependent on Poisson's ratio for $0.874<k<0.955$ and $0<\nu<0.5$[75]. Qian and Swanson[72] do not even mention the value used in their calculations, while they do study the sensitivity of the theory for the magnitude of the time-step in their integration and the number of modes of the Fourier series. Also Reddy[30] does not explicitly mention his value of k. It is not clear how sensitive the models are for variations of k.

2. The necessity of the inclusion of transverse shear and the magnitude of the shear deformation is not made clear in the literature. Reddy[30] compares the classical plate theory and the shear deformation theory for span to thickness ratio's of A/t = 5, but this is not realistic (too small). It is also stated that the shear deformation especially will influence the situation around the impact point, where the shear stress will have its maximum (see equation 9.10), but no evidence was found on the influence of this shear deformation.

3. The Reissner-Mindlin approach is linear. It is therefore only valid for central deflections smaller than half the thickness of the plate (ref. 5). This means a serious limitation.

We may conclude that the application of the Reissner-Mindlin theory in the

311

form of Whitney and Pagano for anisotropic plates is widely accepted. The relevance of the theory and the validity of the shear correction factor is not very well described for impact models.

9.5 Non-linear elastic deformation

Nearly all the impact models presented in the literature are linear: a linear relation is assumed between the strains and the derivatives of the displacements u, v, and w (and possibly also of ψ, if transverse shear is included). This is only a reasonable assumption for small displacements. The non-linearity of the problem is generally limited to the local Hertzian deformation. For large displacements also the higher order non-linear terms have to be taken into account. The classical relations between the strains and the displacements for pure bending are:

$$\varepsilon_x = - z \frac{\delta^2 w}{\delta x^2}$$

$$\varepsilon_y = - z \frac{\delta^2 w}{\delta y^2}$$

$$\gamma_{xy} = - 2 z \frac{\delta^2 w}{\delta x \, \delta y}$$

(9.17)

These equations are valid only for small displacements, Timoshenko and Woinowsky-Krieger[5] assume that the linear theory will be accurate for the central deflection up to half the plate thickness. For larger deflections the deformation is no longer pure bending, but also membrane strains (stretching of the plate) have to be considered. The impact experiments of part II of the present thesis showed that large deflections may occur, even at low impact energies. Non-linear elastic deformation is treated in the simple analytical models of Elber[7], Stellbrink[10] and Haskell[11], and in the analytical models of Shivakumar et al.[19]. Reddy[51] introduced non-linear elastic deformation in his FE model, and Sun and Chin[44]

studied some special cases of static loading.

The simple analytical model of Elber[7] is isotropic in nature, although he uses it for anisotropic 'quasi-isotropic' laminates. He decomposes the stiffness of the plate into a membrane stiffness, a flexural stiffness and a shear stiffness. The total deflection of the plate is obtained by superposition of these deformation modes. The non-linearity is treated by the description of a membrane. The stretch of the membrane in the contact zone and outside this zone are approximated by geometrical analysis. In this way the load-deflection equation for pure membrane deformation can be written in the following form:

$$F = C \; \frac{E \; t \; w_0^3}{a^2} \qquad (9.18)$$

with a as the plate radius (see figure 9.1) and C as a constant during the loading. The deflection w_0 is proportional to $F^{1/3}$.

The approach of Stellbrink[10] is very simple. His isotropic model also consists of a superposition of the various stiffnesses to obtain the total stiffness of the plate. Whether the superposition is valid is not discussed by Stellbrink. The relation between the central deflection w_0 and the contact force is taken from Timoshenko and Woinowsky-Krieger (circular plates):

$$\frac{w_0}{t} + C_1 \left(\frac{w_0}{t} \right)^3 = C_2 \frac{F \; a^2}{E \; t^4} \qquad (9.19)$$

This is an approximate solution. C_1 and C_2 are dependent on the boundary conditions, and are given by Timoshenko and Woinowsky-Krieger (ref.5, p.416).

Shivakumar, Elber and Illg[19] present a model based on the von Kármán

equations for small strains and moderately large displacements (also described by Timoshenko and Woinowsky-Krieger):

$$\varepsilon_r = \frac{du}{dr} + \frac{1}{2} \left[\left(\frac{du}{dr} \right)^2 + \left(\frac{dw}{dr} \right)^2 \right] - z \frac{d^2w}{dr^2}$$

$$\varepsilon_\phi = \frac{u}{r} - \frac{z}{r} \frac{dw}{dr} \tag{9.20}$$

$$\varepsilon_{r\phi} = 0$$

The terms of the strains which are not dependent on z are the membrane terms, the other terms are related with the bending deformation. Shivakumar et al. use the displacement fields which are valid for small deflections (circular clamped plate, ref.5):

$$w = w_0 \left[1 - \left(\frac{r}{a} \right)^2 + 2 \left(\frac{r}{a} \right)^2 \ln \left(\frac{r}{a} \right) \right]$$

$$u = \frac{w_0^2}{a^3} r (a-r) \left(C_1 + C_2 \frac{r}{a} \right) \tag{9.21}$$

with w_0, C_1 and C_2 as unknowns. The solution is obtained by minimizing the potential energy with respect to C_1, C_2 and w_0. The model is restricted to a quasi-static loading, neglects the transverse shear deformation (thin plates) and assumes an axisymmetrical displacement field (equation 9.21).

The von Kármán equations are also used by Reddy[51] for his finite element formulation and Sun and Chin[38] for special cases of static loading.

Haskell[11] and Corran et al.[69] (both present models for metallic isotropic plates) simplify the von Kármán equations to the following form (rectangular plates):

$$\varepsilon_x = \frac{1}{2} \left(\frac{\delta w}{\delta x} \right)^2 - z \frac{\delta^2 w}{\delta x^2}$$

$$\varepsilon_y = \frac{1}{2} \left(\frac{\delta w}{\delta y} \right)^2 - z \frac{\delta^2 w}{\delta y^2} \tag{9.22}$$

$$\gamma_{xy} = \frac{\delta w}{\delta x} \frac{\delta w}{\delta y} - 2 z \frac{\delta^2 w}{\delta x \delta y}$$

Haskell neglects the strains due to the displacements u and v, without stating this explicitly and without proof. For a fixed plate u and v will be zero at the boundaries and due to symmetry also in the centre. The displacements u and v will be small compared with the deflection w. Haskell uses his model with a fixed form of the deflection field w, like Shivakumar et al.[19] (equation 9.21), for the analysis of a blast loading on a panel.

The membrane stretching terms in equation 9.22 can be derived when it is assumed that the radial displacement u is zero, as illustrated by figure 9.4:

$$\varepsilon_m = \sqrt{1 + \left[\frac{dw}{dx} \right]^2} - 1 \cong \frac{1}{2} \left[\frac{dw}{dx} \right]^2$$

$$\text{for} \quad \left[\frac{dw}{dx} \right]^2 \ll 1 \tag{9.23}$$

The contribution of the axial displacements to the strains was also ignored in the literature on the non linear vibration of beams and plates[77,78,80,82]. In these references the effects of the inplane displacements and the inplane inertia on the frequency ratio ω/ω_0 are calculated. The frequency ratio is the ratio of the non linear and the linear resonance frequency. Although the discussion on non-linear

vibrations is related to the impact problem, the situation is different. In the case of impact the plate is loaded by a load in the centre of the plate.

From a table given by Mei[81] it can be concluded that the influence of the inplane displacements and inertia on the frequency ratio is a reduction of some 10% (for a simply supported beam with immovable edges and a length to thickness ratio of 100). A difference in the order of 10% can also be derived from the results of Raju et al.[78] for simply supported circular plates. The accurateness of the assumption that the inplane displacements can be neglected for non linear vibrations is still in discussion[82]. The problem in the discussion is that the models are based on several physical assumptions and analytical methods (e.g. linearization). The calculations of Singh et al.[82] for example, are based on the assumption that the shape of the beam under non linear vibration will be sinusoidal like in the linear vibration case. The finite element results of other authors do also have this limitation.

A further simplification of the von Kármán equations is proposed by Calder and Goldsmith[67], for metallic, circular, isotropic plates. This approach is also used by Levy and Goldsmith[66]. The bending terms are neglected (thin sheets, large deflection), and the radial strain is written as:

$$\varepsilon_r = \frac{1}{2} \left(\frac{dw}{dr} \right)^2 \tag{9.24}$$

The transverse strain ε_ϕ is neglected. For very large deflections the membrane stresses are expected to dominate the deformation, therefore they take into account only these stresses. With this assumption the model for the impact on a metallic plate with elasto-plastic deformation becomes very simple. Calder and Goldsmith do not give direct experimental evidence for equation 9.24. Their approach is indirect: based on this equation they are able to give accurate predictions for the measured deflection of the plate during impact.

We may conclude that most of the models do not include non-linear effects

due to large deformations. We may expect that this will lead to serious limitations of the models. It is interesting to try to describe the non-linear elastic deformation for the dynamic loading of a plate. Analytically we can try to modify the elastic model presented by Shivakumar, Elber and Illg (based on the von Kármán equations). The modification has to include the following items:

1. Their model assumes a displacement field (valid for linear and elastic deformation, equations 9.21). However, it will be better to calculate this displacement field (output of the model).

2. Their model is quasi-static; to compare the model with experiments it has to include dynamic loading.

For anisotropic non linear elastic deformation we succeeded in deriving a dynamic model without assuming a fixed displacement field w(r) (section 12.6); for plastic deformation a static model is derived based on a measured displacement field.

In order to keep the model relatively simple, we will use the modified von Kármán equations after Haskell[11] and Corran et al.[69] who used their equation for metallic, isotropic plates. Impact models based on these equations are given in chapter 12. This means that the radial displacements will be neglected; this is in accordance with the literature found on non linear vibrations.

For the non linear plastic model in chapter 12 we will use a polynomial to describe the displacement field w(r). The strains will be calculated by taking the first and second derivatives (equation 9.22). The accuracy of this approach has to be supported by experiments: by measurement of the deflection field w(r,ϕ) or w(x,y), and by strain measurement. This will be done in chapter 10. The Levy-Goldsmith approach (equation 9.23) is expected to be too simple, the bending deformation will certainly by important, especially during the first part of the deflection.

9.6 Inertia effects

The dynamics of the impact problem consist of three parts:

1. the travelling of stress waves (section 9.8)

2. the strain rate dependence of the material properties (section 9.7)

3. inertia effects: the mass distribution in the impactor and plate will affect the process (the present section).

The inertia of the impactor is usually treated by considering its rigid body motion described by Newton's law. The inertia of the plate is more complicated: during deflection of the plate the displacements of the midplane will be u, v, and w (with corresponding accelerations) and the rotations ψ_x and ψ_y. Cairns and Lagace[20] therefore give the following expression for the kinetic energy of the plate (not taking into account u and v):

$$
T_{plate} = \int \int \frac{d}{dt} \begin{bmatrix} \psi_x \\ \psi_y \\ w \end{bmatrix}^T \begin{bmatrix} I & 0 & 0 \\ 0 & I & 0 \\ 0 & 0 & P \end{bmatrix} \frac{d}{dt} \begin{bmatrix} \psi_x \\ \psi_y \\ w \end{bmatrix} dx \, dy
$$

with: $P = \rho \, t$ and $I = \frac{1}{12} \rho \, t^3$ \hfill (9.25)

The rotatory inertia I of the plate is neglected in his model, which is common practice. Mindlin[58] already showed that the effect of the rotatory inertia will be small. In the case of a low velocity impact the mass of the impactor in general will be relatively large to reach realistic impact energies. When the mass of the impactor is large relative to the effective mass of the plate, the total inertia of the plate can be neglected.

Several models are static (e.g. Elber[7], Stellbrink[10], Shivakumar et al.[19] and Cairns and Lagace[21]), and obviously the inertia is absent in these models. Ramkumar and Chen[26] and Dobyns[28] use the Reissner-Mindlin theory (equation 9.15), and they neglect the rotatory inertia terms in these equations (substituting $\rho \, t^3 / 12 = 0$).

In the F.E. models of Sun et al. and Springer et al. the rotatory inertia is present.

A topic related to the inertia and mass effects is the influence of the gravitational forces. Strictly speaking the gravitational terms must enter the model if the impact velocity is vertical. In this case the potential energy of the impactor and the plate change during the vertical motion.

318

None of the models take into account this effect. It may be expected that the gravitational force is small relative to the contact force during impact.

9.7 Strain rate effects

Only some models (Kim[12] and Wierzbicki[32]) were found which incorporate a viscoelastic relation to account for strain rate effects. These models describe the behaviour of plastics. Models with a strain rate dependent behaviour for composite materials were not found. Generally the static properties of a material are used without discussion. The knowledge and experimental data on strain rate effects are too limited to describe the behaviour by mathematical relationships.

This aspect needs further study, some experimental results will be treated in chapter 11.

9.8 Stress wave propagation

The classical Lagrange's equation (equation 9.13) and the Reissner-Mindlin equations (equations 9.15) are differential equations, which in principle can describe the flexural stress wave propagation. Mindlin in fact derived his formulation to describe stress waves with a small wave length to plate thickness ratio. For small ratios the transverse shear effects become important. A three-dimensional theory is necessary for the complete behaviour of stress waves in the plate. Sun and Lai[23] and Moon[15] studied two-dimensional stress wave problems. Evans and Herne[33] presented a one-dimensional model to describe the stress wave travelling in the thickness direction of the laminate, with reflections at the boundaries between the laminae (these stress waves may lead to delamination: spallation). The stress wave effects will become important if the impact duration is smaller than 100 μs (Moon[15]). The reflection at the boundaries of the plate is not treated, neither by Sun and Lai nor by Moon, because an analysis which includes these effects will be very complex.

If an energy approach is used to solve the impact problem (Raleigh-Ritz analysis) it is not possible to describe the stress waves. In this case the

equations will be based on integrals over the whole plate. For this type of analysis fixed displacement functions can be used (e.g. equations 9.21), which are not able to describe the stress waves.

For the low-velocity impact phenomena treated in the present report, the impact duration will be long compared to the time required for the stress waves to reach the supports. In this case the stress wave phenomena (probably) will not be important.

9.9 Plasticity

Most of the low-velocity models are dealing with composite materials, assuming elastic deformation only. Analysis including plasticity is mainly done for ballistic purposes.
The prediction of the start of plastic deformation can be done by an elastic model, together with a yield criterion (e.g. von Mises). A plastically deformed dent can be regarded as the first 'damage' of an elasto-plastic material.

For further plastic analysis an expression for the effective stress and a measured strain hardening curve (effective stress-strain curve) are needed.
The Levy-Goldsmith model[66], based on the work of Calder and Goldsmith[67] is illustrative. The internal energy of a circular plate is written as:

$$U_{plate} = \int_V \left[\int \sigma_r \, d\varepsilon_r + \sigma_\theta \, d\varepsilon_\theta \right] dV \qquad (9.26)$$

The tangential strain consists of an elastic part (expressed by Hooke's law) and a plastic strain:

$$\varepsilon_\theta = \varepsilon_\theta^{el} + \varepsilon_\theta^{pl} = \frac{1}{E} \left(\sigma_\theta - \nu (\sigma_r + \sigma_z) \right) + \varepsilon_\theta^{pl} \qquad (9.27)$$

For plane stress ($\sigma_z = 0$), and if the tangential strain is neglected, (both

the elastic and the plastic part of the strain are assumed to be zero), this leads to:

$$\sigma_\theta = \nu \, \sigma_r \tag{9.28}$$

The von Mises effective stress is expressed by a linear strain hardening curve:

$$\sigma_e^{\,2} = \sigma_r^{\,2} - \sigma_r \, \sigma_\theta + \sigma_\theta^{\,2} = (\sigma_y + \alpha \, \varepsilon_r)^2 \tag{9.29}$$

With σ_y as the yield stress and α as the linear work hardening parameter. Substitution of equations (9.27) to (9.29) in (9.26) yields:

$$U_{plate} = \frac{2 \, \pi \, t}{\sqrt{1-\nu+\nu^2}} \int_0^a (\sigma_y \, \varepsilon_r + \frac{1}{2} \alpha \, \varepsilon_r^{\,2}) \, r \, dr \tag{9.30}$$

In fact this relation will be a lower bound for the internal energy, because the tangential strain will not be zero. Calder and Goldsmith use equation 9.24 to approximate the radial strain, and if a constant shape of the dent is assumed in the form of:

$$w(r) = w_0 \, f(r) \tag{9.31}$$

the internal energy U_{plate} can be calculated. Levy and Goldsmith use a simple relationship for the shape of the dent:

$$w(r) = w_0 \, e^{-cr} \tag{9.32}$$

with c as a constant which has to be measured. This relation does not exactly satisfy the boundary conditions of the plate, but Levy and Goldsmith claim an accurate approximation of the shape of the dent.
Finally they obtain the following relationship for the (plastic) internal energy of the plate:

$$U_{plate} = \frac{\pi\,t}{\sqrt{1-\nu+\nu^2}} \left[\frac{1}{64}\,\alpha\,c^2\,w_0^4 + \frac{1}{4}\,\sigma_y\,w_0^2 \right] \qquad (9.33)$$

The Levy-Goldsmith model is too simple, and a verification of the assumptions is not given. The unloading after plastic deformation can not be described by this model. A more realistic model based on the Levy-Goldsmith approach will be presented in chapter 12.

9.10 Fracture criterion

Finally a fracture criterion is needed to describe fracture initiation and propagation. This will be the most difficult and controversial part of the model, and at the same time a most important part. In the literature only Shivakumar et al.[19] and Wu and Springer[46] have included fracture initiation and propagation in their models. Elber[7] includes a fracture initiation criterion in his model.

The first fracture of a composite laminate can be:
1. matrix cracking: for brittle matrices this will be the first form of damage.
2. splitting (matrix cracking or debonding parallel to the fibres)
3. delamination
4. fibre failure: tensile (breakage) or compressive (crushing)

Especially the last two types of damage will influence the strength of the laminate. The damage types are interrelated: e.g. delamination may branch from matrix cracks.

The simplest fracture criterion will be:

somewhere in the matrix: $\tau > \tau_{max}$ then delamination

somewhere, in fibre direction:
$$\left. \begin{array}{c} \varepsilon > \varepsilon_{u,tension} \\ |\varepsilon| > |\varepsilon_{u,comp}| \end{array} \right\} \text{ then fibre failure}$$

Such an approach is used by Elber[7].

Shivakumar et al.[19] use a Tsai-Wu failure criterion and the following way to treat damage propagation. The load on the plate is increased by steps. The internal strain energy of the plate is obtained by summation of the internal energies of elements of the plate (integration). After each load step fracture is checked for each element using a fracture criterion. If a certain type of failure is indicated by the fracture criterion (fibre or matrix failure) for an element, a part of the stiffness of that element is removed from the model. In this way the stiffness of the plate is decreased by fracture and some of the energy is released. After the decrease of the stiffness the next load step is applied. It is not explicitly mentioned, but it is evident that this model does not describe the stress concentrations near the failed elements in the model.

Wu and Springer use a delamination model which is described in reference 46. They need the following parameters to predict the delaminated area:

- longitudinal tensile strength
- longitudinal compressive strength
- transverse tensile strength
- transverse compressive strength
- transverse shear strength
- interlaminar shear strength
- interlaminar critical stress intensity factor of mode I, K_{Ic}

The number of parameters illustrates the complexity of the fracture.

9.11 Conclusions

1. Most of the impact models for composite materials include transverse shear deformation, and are based on the Reissner-Mindlin theory of plates

(equations 9.15). The value of the shear correction factor is not clear, and the significance of the shear deformation for plates with realistic dimensions is not well understood. The models describe elastic and linear deformation, and are accurate for central deflections smaller than half the sheet thickness. Unfortunately, significantly larger deflections are of practical interest, and did occur in the present test series (part II of this thesis report).

2. Non linear elastic deformation can be included when the simplified von Kármán equations proposed by Haskell and Corran et al. are applied. In this case the radial in plane displacements of the midplane of the plate are neglected. This approach was also found in the literature.

3. The strain rate dependence of the material properties (stiffness matrix and strengths) is not included in the impact models, generally without discussion. This subject will be treated in chapter 11.

4. The fracture criterion will be a weak link of an impact model. The most straightforward method will be the use of an ultimate strain criterion for fibres and matrix. Shivakumar et al. describe an interesting step by step procedure for failure propagation the plate is divided in elements with stiffnesses depending on the amount of failure.

5. The stress wave effects do not have to be treated for low-velocity impact loading. The gravitational force is not included in the literature models. This force will generally be small compared with the contact force.

6. In general a Hertzian contact law is used to describe the contact between impactor and plate, or a prescribed load history is used. A third way to establish the contact is by a rigid contact during impact.

7. The rotatory inertia of the plate is usually neglected.

8. The models which include plasticity are usually applied for ballistic purposes. The Levy-Goldsmith theory may be used as a starting point for further analytical modelling.

references

classical

1. Goldsmith, W.; Impact, the theory and physical behaviour of colliding solids, Edward Arnold, London, 1960.

2. Hertz, H.; Ueber die Berührung fester elastischer Körper, Crelle Journal, Vol.92, p.156-171, 1882.

3. Timoshenko, St.; Zur Frage nach der Wirkung eines Stoßes auf einen Balken, Zeitschrift für Mathematik und Physik, Vol.62, p.198-209, 1913.

4. Karas, K.; Platten unter seitlichem Stoß, Ingenieur-Archiv, Vol.10, p.237-250, 1939.

5. Timoshenko, S.P.; Woinowsky-Krieger, S.; Theory of plates and shells, McGraw-Hill Book company, 1970

6. Lekhnitskii, S.G.; Anisotropic plates, Gordon and Breach science publishers, 1968.

simple analytical models

7. Bostaph, G.M.; Elber, W.; Static indentation tests on composite plates for impact susceptibility evaluation; in: Proceedings of the army symposium on solid mechanics, 1982 – critical mechanics problems in systems design,
1982.

8. Elber, W.; The effect of matrix properties on impact resistance, in: Tough composite materials, NASA CP 2334, 1983.

9. Elber, W.; Failure mechanics in low-velocity impacts on thin composite plates, NASA TP 2152, 1983.

10. Stellbrink, K.K.U.; Improved impact damage tolerance, in: Proceedings of the European Symposium on damage development and failure processes in composite materials, pp.152-161, 1987.

11. Haskell, D.F.; Damage tolerance of semimonocoque aircraft, in: Specialists meeting on impact damage tolerance of structures, AGARD CP

186, 1975.

12. Kim, J.W.; An analysis of the fracture initiation of falling type impact test for toughened rigid plastics, J.Mech.Solids, Vol.33, No.2, pp.141-152, 1985.

13. McQuillen, E.J.; Gause, L.W.; Low velocity transverse normal impact of graphite epoxy composite laminates, J.Composite materials, Vol.10, pp.79-91, 1976.

14. Sahraoui, S.; Gillaizeau, F.; Numerical simulation of the Charpy impact testing, Eng.Fracture Mechanics, Vol.33., No.6, pp.871-876, 1989.

complex analytical models

15. Moon, F.C.; Theoretical analysis of impact in composite plates, Princeton University, NASA CR 121110, 1973.

16. Greszcuk, L.B.; Response of isotropic and composite materials to particle impact, in: Foreign object damage to composites, ASTM STP 568, 1973.

17. Greszczuk, L.B. Damage in composite materials due to low velocity impact, in: Impact Dynamics, John Wiley & Sons, 1982.

18. Greszczuk, L.B.; Low velocity impact damage in composites, in: Impact dynamics of metals & composites, A continuing professional education course, Drexel University, 1989.

19. Shivakumar, K.N.; Elber, W.; Illg, W.; Prediction of low-velocity impact damage in thin circular laminates, AIAA Journal, Vol.23, No.3, pp.442-449, 1985.

20. Cairns, D.S.; Lagace, P.A.; Transient response of graphite/epoxy and Kevlar/epoxy laminates subjected to impact, AIAA/ASME/ASCE/AHS 29th structures, structural dynamics and materials conference, 1988.

21. Cairns, D.S.; Lagace, P.A.; Thick composite plates subjected to lateral loading, J.Applied Mechanics, Vol.54, pp.611-616, 1987.

22. Sun, C.T.; Chattopadhyay, S.; Dynamic response of anisotropic laminated plates under initial stress to impact of a mass, J.Applied

Mechanics, pp.693-698, 1975.

23. Sun, C.T.; Lai, R.Y.S.; Exact and approximate analysis of transient wave propagation in an anisotropic plate, AIAA Journal, Vol.12, No.10, pp.1415-1417, 1974.

24. Thangjitham, S.; Librescu, L.; Cederbaum, G.; Low velocity impact response of orthotropic plates using a higher order theory, AIAA, 1987.

25. Lee, Y.; Hamilton, J.F.; Sullivan, J.W.; The lumped parameter method for elastic impact problems, J.Applied Mechanics, Vol.50, pp.823-827, 1983.

forced vibration solutions (prescribed load history)

26. Ramkumar, R.L.; Chen, P.C.; Low-velocity impact response of laminated plates, AIAA Journal, Vol.21, No.10; pp.1448-1452, 1983.

27. Ramkumar, R.L.; Thakar, Y.R.; Dynamic response of curved laminated plates subjected to low velocity impact, J.Eng. Materials and Technology, Vol.109, pp.67-71, 1987.

28. Dobyns, A.L.; Analysis of simply-supported orthotropic plates subject to static and dynamic loads, AIAA Journal, Vol.19, No.5, pp.642-650, 1981.

29. Reismann, H.; Tendorf, Z.A.; Dynamics of initially stressed plates, J.Applied Mechanics, Vol.43, pp.304-308, 1976.

30. Reddy, J.N.; On the solutions to forced motions of rectangular composite plates, J.Applied Mechanics, Vol.49, pp.403-408, 1982.

31. Witt, M.; Sobczyk, K.; Dynamic response of laminated plates to random loading, Int.J. Solids Structures, Vol.16, pp.231-238, 1980.

32. Wierzbicki, T.; Impulsive loading of rigid viscoplastic plates, Int.J. Solids structures, Vol.3, pp.635-647, 1967.

33. Evans, K.E.; Herne, N.J. The prediction of damage due to high velocity impact in composite laminates, in: CAD in composite material technology, Proceedings of the international conference Southampton, 1988.

34. Qian, Y.; Swanson, S.R.; Experimental measurement of impact response in carbon/epoxy plates, in: proceedings of 30th structures,

structural dynamics and materials conference, Moblie, Alabama, U.S.A., 1989.

35. Whitney, J.M.; Sun, C.T.; Transient response of laminated composite plates subjected to transverse dynamic loading, J.Acoust.Soc.Am., Vol.61, No.1, pp.101-104, 1977.

36. Razi, H.; Lindsey, V.E.J.; Ananlysis of simply-supported orthotropic cylinder subjected to low velocity impact, AIAA, 1987.

finite element solutions

37. Sun, C.T.; An analytical method for evaluation of impact damage energy of laminated composites, in: Composite materials: testing and design, ASTM STP 617, 1977.

38. Tan, T.M.; Sun, C.T.; Use of statical indentation laws in the impact analysis of laminated composite plates, Transactions of the ASME, Vol.52, pp.6-12, 1985.

39. Sun, C.T.; Chen; J.K.; On the impact of initially stressed composite laminates, J.Composite Materials, Vol.19, pp.490-504, 1985.

40. Gu, Z.L.; Sun, C.T.; Prediction of impact damage region in SMC Composites, Composite structures, Vol.7, p.179-190, 1987.

41. Joshi, S.P.; Sun, C.T.; Impact-induced fracture initiation and detailed dynamic stress field in the vicinity of the impact, in: Proceedings of the American Society for composites, 2nd technical conference, University of Delaware, 1987.

42. Liou, W.J.; Sun, C.T.; Dynamic response of laminated composite plates using a three-dimensional hybrid-stress finite-element formulation, in: 58th Shock and vibration symposium, NASA CP 2488, 1987.

43. Sun, C.T.; Dowdy, A.B.; Impact damage and response in ARALL laminate, School of Aeronautics and Astronautics, Purdue University.

44. Sun, C.T.; Chin, H.; On large deflection effects in unsymmetric cross-ply composite laminates, J.Composite Materials, Vol.22, pp.1045-1059, 1988.

45. Sun, C.T.; Rechank, S.; Effect of adhesive layers on impact damage in composite laminates, in: Composite materials: testing and design (eighth conference), pp. 97-123, ASTM STP 972, 1988.

46. Wu, H.T.; Springer, G.S.; Impact induced stresses, strains and delaminations in composite plates, J.Composite Materials, Vol.22, pp.533-560, 1988.

47. Wu, H.T.; Springer, G.S.; Impact damage of composites, in: Damage tolerance of composites I.

48. Wu, H.T.; Impact damage of composites, PhD dissertation, Department of Aeronautics and Astronautics, Stanford University, 1986.

49. Peck, S.O.; Springer, G.S.; Foote, A.L.; Jeske, D.H.; Impact damage in thick laminated plates, in: Proceedings of the International conference on impact loading and dynamic behaviour of materials, Bremen 1988.

50. Tiu, W.P.; Gott, J.; Breckell, T.H.; Jones, L.; Residual static strength prediction of impacted composite laminates, in: Proceedings conference CAD in composite material technology, Proceedings of the international conference Southampton, 1988.

51. Reddy, J.N.; Impact on laminated composite plates: a review of recent computational developments, in: Computational aspects of penetration mechanics (ed. Brebbia, C.A.; Orszag, S.A.), Berlin, 1982.

phenomenological models

52. Cristescu, N,; Malvern, L.E.; Sierakowski, R.L.; Failure mechanisms in composite plates impacted by blunt-ended penetrators, in: Foreign object impact damage to composites, pp. 159-172, ASTM STP 568, 1973.

53. Takaeda, N.; Sierakowski,R.L.; Localized impact problems of composite laminates, The shock and vibration digest, Vol.12, No.8., pp. 3-10, 1980.

54. Clark, G.; Modelling of impact damage in composite laminates, Composites, Vol.20, No.3, pp.209-214, 1989.

55. Liu, D.; Impact-induced delamination- a view of bending stiffness mismatching, J.Composite Materials, Vol.22, pp.674-692, 1988.

56. Daniel, I.M.; Wooh, S.C.; Deformation and damage of composite plates under impact loading, in: Proceedings of int. symp. on composite materials and stuctures, pp. 630-637, Beijing, 1986.

57. Bowles, K.J.; The correlation of low-velocity impact resistance of graphite-fiber-reinforced composites with matrix properties, in: Composite materials: testing and design (eigth conference), ASTM STP

972, pp.124-142, 1988.

interlaminar shear deformation

58. Mindlin, R.D.; Influence of rotatory inertia and shear on flexural motions of isotropic, elastic plates, J.Applied Mechanics, Vol.18, pp. 31-38, 1951.

59. Whitney, J.M.; Pagano, N.J.; Shear deformation in heterogeneous anisotropic plates, J.Applied Mechanics, pp. 1031-1036, 1970.

60. Adams, D.F.; Miller, A.K.; The influence of transverse shear on the static flexure and Charpy impact response of hybrid composite materials, J.Materials Science, Vol.11, pp.1697-1710, 1976.

61. Huang, X.; Dong, W.; Effects of transverse shear on the nonlinear bending of rectangular plates laminated of bimodular composite materials, in: Proceedings of int. symp. on composite materials and structures, pp. 239-245, Beijing, 1986.

62. Liu, C.F.; Reddy, J.N.; On a third-order shear deformation theory for laminated composite shells, in: Proceedings of int. symp. on composite materials and structures, Beijing, pp.288-293, 1986.

63. Dawe, D.J.; Azizian, Z.G.; Potential energy approaches to the large deflection behaviour of shear deformable rectangular plates, in: Variational methods in engineering (ed. C.A. Brebbia), Springer Verlag, 1985.

metals, plasticity

64. Witmer, E.A.; Balmer, H.A.; Leech, J.W.; Pian, T.H.H.; Large dynamic deformations of beams, rings, plates and shells, AIAA journal, Vol.1, No.8, pp. 1848-1857, 1963.

65. Tanaka, K.; Kurokawa, T.; Dynamic deformation of thin plates and strips under impact loading, in: Proceedings 3rd conf. mech. properties at high rates of strain, Oxford, pp. 503-310, 1984.

66. Levy, N.; Goldsmith, W.; Normal impact and perforation of thin plates by hemispherically tipped projectiles (part I and II), Int.J.Impact Engng., Vol.2, No.3, pp.209-229, and No.4, pp.299-324, 1984.

67. Calder, C.A.; Goldsmith, W.; Plastic deformation and perforation of

thin plates resulting from projectile impact, Int.J.Solids Structures, Vol.7, pp.863-881, 1971.

68. Liss, J.; Goldsmith, W.; Kelly, J.M.; A phenomenological penetration model of plates, Int.J. Impact Engng., Vol.1, No.4, pp.321-341, 1983.

69. Corran, R.S.J.; Shadbolt, P.J.; Ruiz, C.; Impact loading on plates- an experimental investigation, Int.J. Impact Engng., Vol.1, No.1, pp.3-22, 1983.

70. Liss, J.; Goldsmith, W.; Plate perforation phenomena due to normal impact by blunt cylinders, Int.J. Impact Engng., Vol.2, No.1, pp.37-64, 1984.

71. Goldsmith, W.; Initiation of perforation in thin plates by projectiles, in: Metal forming and impact mechanics, Pergamon Press, 1985.

comparison of solution techniques for Reissner-Mindlin theory

72. Qian, Y.; Swanson, S.R.; A comparison of solution techniques for impact response of composite plates, Composite structures, Vol.14, pp.177-192, 1990.

contact law

73. Tatara, Y,; Extensive theory of force-approach relations of elastic spheres in compression and in impact, J.Engng.Materials and technology, Vol.111, pp.163-168, 1989.

74. Yang, S.H.; Sun, C.T.; Indentation law for composite laminates, NASA CR-165460, 1981.

general plate theory

75. Reismann, H.; Elastic plates, theory and application, John Wiley and sons, 1988.

large amplitude vibrations

76. Srinivasan, A.V.; Large amplitude-free oscillations of beams and plates, AIAA Journal, Vol.3, No.10, pp.1951-1953, 1965.

77. Venkateswara Rao, G.; Kanaka Raju, K.; Raju, I.S.; Finite element formulation for the large amplitude free vibrations of beams and orthotropic circular plates, Computers and Structures, Vol.6, pp.169-172, 1976.

78. Raju, I.S.; Venkateswara Rao, G.; Kanaka Raju, K.; Effect of longitudinal or inplane deformation and inertia on the large amplitude flexural vibrations of slender beams and thin plates, J.Sound and Vibration, Vol.49, No.3, pp.415-422, 1976.

79. Sathyamoorthy, M.; Nonlinear analysis of bemas, part I: a survey of recent advances, Shock and Vibration Digest, Vol.14, No.17, pp.19-35, 1982.

80. Kanaka Raju, K.; Venkateswara Rao, G.; A note on large amplitude vibrations, Computers and Structures, Vol.18, No.6, pp.1189-1191, 1984.

81. Mei, C.; Comments on 'Lagrange-type formulation for finite element analysis of non-liear beam vibrations, J.Sound and Vibration, Vol.94, No.3, pp.445-452, 1984.

82. Singh, G.; Sharma, A.K.; Venkateswara Rao, G.; Large amplitude free vibrations of beams, a discussion on various formulas and assumtions, J.Sound and Vibration, Vol.142, No.1, pp.77-85, 1990.
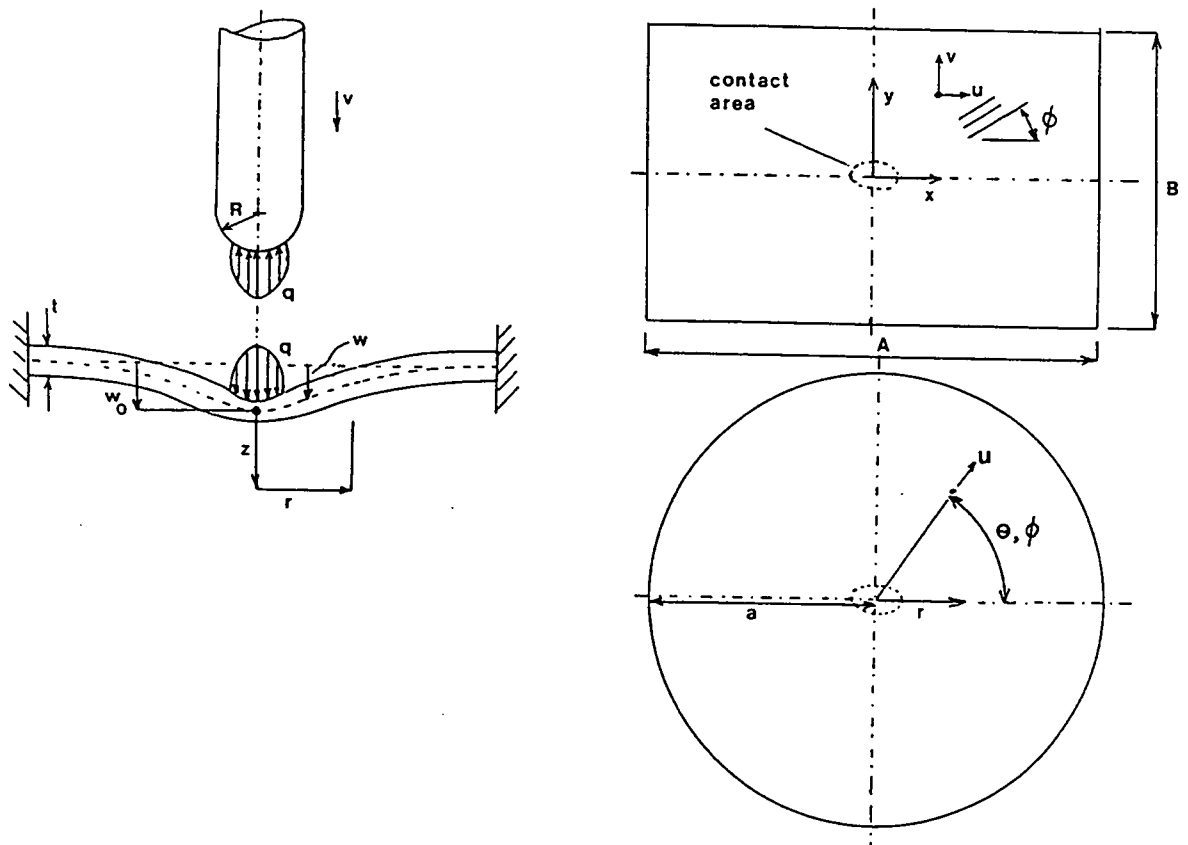
figure 9.1 The geometry of the impact problem, a rectangular and a
circular plate are considered.
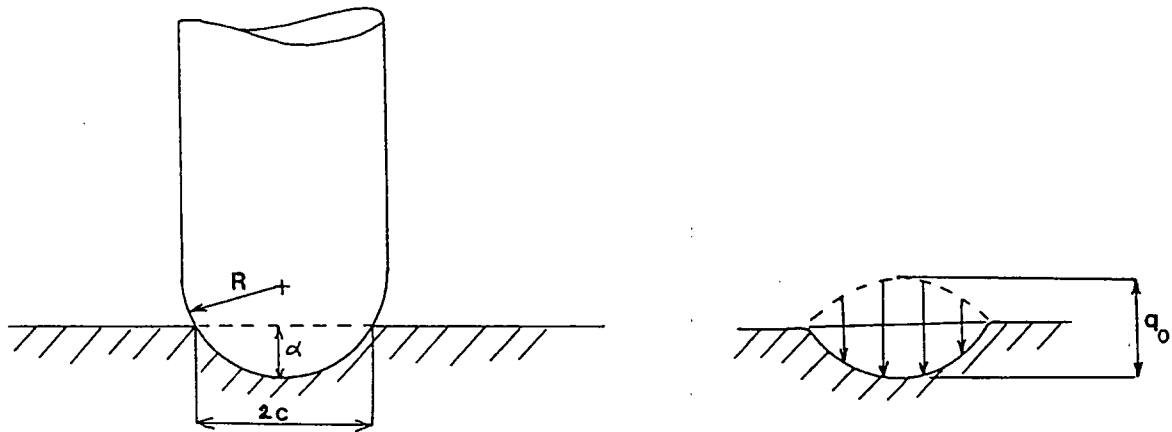
figure 9.2 The geometry of the indentation of the plate by the projectile.
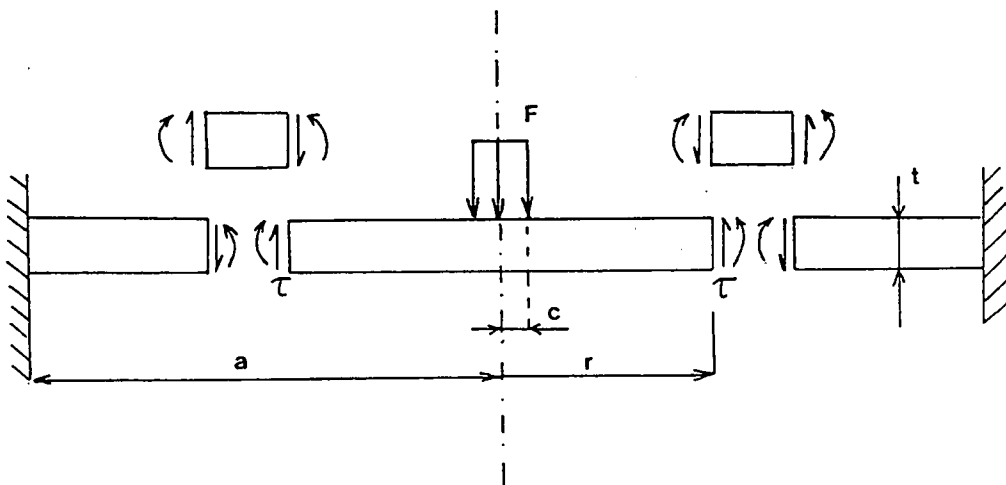
figure 9.3 Approximation of the transverse shear deformation.

$$\mathcal{E} = \sqrt{1 + \left[\frac{dw}{dr}\right]^2} - 1$$
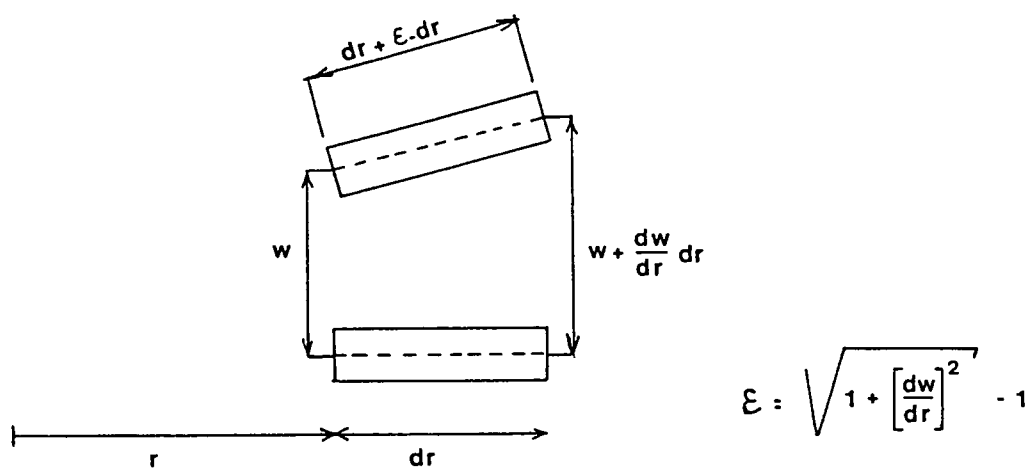
figure 9.4 Approximation of the membrane stretch $\mathcal{E}$.

chapter 10 The shape of the dent and the strain distribution

10.1 Introduction

The test results of part II of this thesis showed that non linear deformation will occur at realistic impact energies. In section 9.5 of the previous chapter a method was discussed to describe this non linear deformation: the simplified von Kármán equations as given by Haskell[1] and Corran et al.[3] (equations 9.22). The equations express the relation between the displacement field of the deformed dent w=w(x,y) (rectangular plate) or w=w(r,θ) (circular plate) and the strains. The dent is defined as the deformed shape of the impact specimens.

The simplified von Kármán equations will be used in an adjusted form. The displacement field w(r) is normalized. This normalized form is called the shape of the dent $\xi(\eta)$, and it is defined as:

$$\xi = \xi(\eta) \qquad \text{with} \qquad \xi = \frac{w}{w_0} \; , \quad \eta = \frac{r}{a} \tag{10.1}$$

For w, w_0, r and a: see figure 9.1.

The simplified von Kármán equations (see equation 9.22) for circular plates are rewritten as:

$$\varepsilon_r = \frac{w_0^2}{2a^2} \left[\frac{d\xi}{d\eta} \right]^2 - \frac{z \, w_0}{a^2} \frac{d^2\xi}{d\eta^2}$$

$$\varepsilon_\theta = - \frac{z \, w_0}{a^2 \, \eta} \left[\frac{d\xi}{d\eta} \right] \tag{10.2}$$

$$\gamma_{r\theta} = 0$$

For the definition of the z-coordinate: see figure 9.1. z = 0 in the midplane of the plate, the positive z-direction is in the direction of the loading.

The present chapter has the following aims:

1. To find empirical evidence that the simplified von Kármán can be used with sufficient accuracy.

2. In chapter 12 a non linear elastic impact model (NOLEIM) and a non linear elasto plastic impact model (EPIM) will be presented. For the elastic model no prescribed shape of the dent is necessary, because this shape will be calculated. The plastic model needs an empirical shape function to calculate the internal energy of the deformed plate. In this chapter it will be shown that the shape function $\xi = \xi(\eta)$ is approximately constant under increasing load, and an empirical function, which will be used for EPIM, will be presented.

3. Finite element calculations are done to show that the radial displacement (u) can be neglected relative to the out of plane displacement (w), and to compare the strain distribution calculated with the finite element model with the distribution calculated with the simplified von Kármán equations and the empirical shape function ξ.

4. The empirical shape function ξ for EPIM is determined for a tip radius of the indentor R = 7.5 mm. Force-deflection curves and strain-deflection curves were measured to see whether the tip radius will have a large influence on these curves.

It will be tried to fit the shape of the dent with the following function:

$$\xi(\eta) = \left(1 - \eta^2 \right)^2 \; f(\eta) \qquad\qquad (10.3)$$

with f(0) = 1.

It is the same function as used by Timoshenko and Woinowsky-Krieger[4], and it will be used in chapter 14 to describe the out of plane displacement of a buckled delamination (equation 14.15). The term $(1-\eta^2)^2$ in principle provides the function ξ with the correct shape; the function $f(\eta)$ is a fitting function, e.g. a polynomial with unknown coefficients.

10.2 Shape measurement

10.2.1 Test method

Specimens of ARALL and monolithic aluminium were clamped between two clamping plates with a circular hole with a diameter of 80 mm or 130 mm. Two thermoplastic composite specimens were tested with a square test area 100x100 mm^2 (test frame: see chapter 6). The specimens were statically loaded in the centre by an indentor with a tip radius of 7.5 mm.

The deflection field of the dent of the specimens was determined with the set-up shown in figure 10.1. The deflection field was measured with an LVDT (linear vertical displacement transducer) guided by a rail, both under load and after unloading (permanent dent). Two coordinates were plotted: r (in radial direction) and w (out of plane deflection).

Test results of the following materials will be presented (for each material two specimens were tested):

material	t(mm)	scanning direction	test area
Al 2024-T3	1.03	in rolling direction	dia. 80 mm
ARALL 2H32	0.83	in and perpendicular to fibre direction	ditto
ARALL 2H33	1.35	ditto	dia. 80 and 130 mm
GLARE $2R_6^2 33$/C55	1.41	in fibre direction of outer fibre layers	dia. 80 mm
thermoplastic carbon/PEI $[0/90]_{2s}$	1.65	ditto	square 100x100 mm

10.2.2 Results

1. Examples of measured contour plots during load and after unloading of the specimen are given in figure 10.2. The indentor shape becomes more pronounced in the deflection field for larger central deflections w_o (figure 10.2, 2H33). After unloading the permanent deflection field shows a

338

more localized deformation around the centre than in the loaded condition (figure 10.2, Al 2024-T3).

2. Figure 10.3, 10.4 and 10.5 show the normalized shape of the dent (ξ = w/w_0) for various materials under load for different values of the central deflection. The figures show that the shape of the dent remains approximately constant during increasing load, although a slight tendency for decreasing ξ values is visible (apart from ξ = 1 for η = 0, and ξ = 0 for η = 1).

3. The shape of ARALL under loading is not fully axisymmetrical, as illustrated by the shape curves in figure 10.6. During loading this effect is relatively small. After unloading the permanent dent clearly shows the anisotropy of the material, see the contour lines in figure 10.7 for aramid ARALL 2H32, after removal of the clamping plates.

4. The influence of the diameter of the clamped zone (a) of the plate on the mean shape during deformation under loading is not very large, see figure 10.4 (2H33), especially in the region around the centre.

10.2.3 The approximation of the shape function

The function

$$f(\eta) = \frac{\xi}{\left(1 - \eta^2 \right)^2} \qquad (10.4)$$

is plotted for Al 2024-T3, aramid ARALL 2H32 and GLARE $2R_6{}^2 33/C55$ in figures 10.8 and 10.9. The function proved to be approximately symmetrical around η = 0.5, to be 1 at η = 0 and η = 1, and to have a minimum of approximately 0.7 for η = 0.5.

Therefore it was tried to fit a parabola through the measured points, with

$$f(\eta) = 1 - 1.2 \, \eta + 1.2 \, \eta^2 \qquad (10.5)$$

As figures 10.8 and 10.9 show, this function fits the data points quite well, especially for η < 0.6. The function was substituted in the

expression for ξ (equation 10.3). The function $\xi(\eta)$ is compared with experimental results in figures 10.3 and 10.4. The fit of $\xi(\eta)$ is satisfactory.

The disadvantage of the choice of the second order polynomial (equation 10.5) to approximate $f(\eta)$ is that it is not an even function. The derivative of ξ is therefore not zero at $\eta = 0$, as is the case for the specimen under load. However, the strain outside the contact area probably will be described accurately enough.

10.3 Strain measurements

10.3.1 Test Method

The specimens were clamped between the same clamping plates as in the tests of the previous section. The specimens had a circular test area with a diameter of 80 mm. The indentor radius was 7.5 mm.

Aramid ARALL 2H32 (t = 0.83 mm) and Al 2024-T3 (t = 1 mm) were tested with the strain gage pattern indicated in figure 10.10. The gage length was 2 mm.

10.3.2 Results

1. The measured central strain is drawn in figure 10.11, together with the strain level based on the equation for pure bending around a radius with the neutral line in the centre of the plate:

$$\varepsilon = \frac{1}{1 + 2\,R/t} \qquad (10.6)$$

For R the indentor radius was substituted (7.5 mm). The strain for pure bending calculated with equation 10.6 does not correspond with the measured results.

2. The measured strains outside the centre of the specimens are shown in figures 10.12 and 10.13 for Al 2024-T3 (t = 1 mm) and in figures 10.14 and

340

10.15 for aramid ARALL 2H32. (Strain gage no.2 of the Al 2024-T3 specimen did not function properly, the strain measured by this gage is not presented.)

3. The simplified von Kármán equations were used (equation 10.2), substituting the ξ function of the previous section (equations 10.3 and 10.5). The strains were measured as function of the load F. The test results as described in chapter 7 were used to determine the corresponding central deflection w_0. The results are given in table 10.1.

The central deflections of table 10.1 were used to calculate the strains. The comparison between the calculated and the measured strains are made in figures 10.12 and 10.13 (Al 2024-T3) and figures 10.16 and 10.17 (ARALL 2H32).

The calculated tangential strains show a better correspondence with the measured strains than the calculated radial strains. This is because the expression of the radial strain contains a term with the second derivative and a term with square of the first derivative (equations 10.2). Significant differences between the measured and calculated strains occur. However, keeping in mind the simple expression for the strain, the strains are approximated quite well.

10.4 Finite element analysis

10.4.1 The model

Finite element calculations were performed for a circular clamped Al 2024-T3 plate with a thickness of 1 mm, loaded by a static lateral Hertzian pressure distribution around the centre. The finite element code SAMCEF was used. The geometrical non-linearities due to the large displacements and the material non-linearity due to plasticity were both taken into account.

Figure 10.18 shows the finite element model: an axisymmetrical plate with a radius of 40 mm and a thickness of 1 mm. At the clamping the rotation and displacements are zero. At the axis of rotational symmetry the horizontal displacement and the rotation are constrained. The model consists of 230 axisymmetric volume elements. The elements have four nodal points and are

of the first order (linear displacement field in an element).

The lateral loading of the plate is approximated by a Hertzian elliptical pressure distribution:

$$q = q_0 \sqrt{1 - \eta_{load}^2} \qquad \text{with} \quad \eta_{load} = \frac{r}{c} \qquad (10.7)$$

The total load is equal to:

$$F = \frac{2}{3} q_0 \pi c^2 \qquad (10.8)$$

The area of loading is constant: $c = 2$ mm. This assumption makes the calculated force-deflection curve of the model less accurate, because c should be a function of the applied load. However, for the verification of the relation between the displacement field and the strains this probably will be acceptable.

The real effective stress-strain curve is approximated by a bi-linear stress-strain curve. The effective stress-strain curve of the Al 2024-T3 (t=1 mm) material used in this study was determined by experiment (see figure 10.19). The bi-linear stress-strain curve used as input of the model is:

$$\bar{\sigma} = 72000 \, \bar{\varepsilon} \quad \text{(MPa)} \qquad \text{for:} \quad \bar{\sigma} < \sigma_y = 340 \text{ MPa}$$

$$(10.9)$$

$$\bar{\sigma} = 340 + 1371 \, (\bar{\varepsilon} - \varepsilon_{yield}) \text{ (MPa)} \qquad \text{after yield:} \quad \bar{\sigma} > \sigma_y$$

10.4.2 Results

The calculated and measured force-deflection curves are compared in figure 10.20. The results of the deflection and stresses at various points of the plate are presented in figure 10.21. The radial and tangential stress distributions are both shown in this figure. The plastic zone is indicated in black. It is clear that also at large deformations the stress distribution is not constant over the thickness of the plate. This implies that the plate will not only be stretched, but also bent. At $F = 1.75$ kN

342

the membrane deformation becomes more significant than at smaller loads, but also at this load the bending can not be neglected (as is done in the Levy-Goldsmith theory).

In figure 10.22 the out of plane deflection w and the radial displacement u in the midplane of the plate are given for F = 1.22kN. The results show that the radial in plane displacement u is much smaller than the out of plane displacement w: u(r) is on the order of 0.01 w(r). Also $\delta u/\delta r$ will be small compared with $\delta w/\delta r$. It is therefore reasonable to neglect the contribution of the in plane displacement to the strain and to use the simplified von Kármán equations for an approximation of the strains.

Figures 10.23 and 10.24 show the calculated radial and tangential strain distributions for F = 0.175 kN (w_0 = 0.636 mm) and F = 1.22 kN (w_0 = 2.93 mm) respectively. The results of the calculations, using the central deflections of the FEM results (w_0 = 0.636 and 2.93 mm), with the simplified von Kármán equations and the shape function ξ derived in section 10.2 are also presented in the figures.

Again, the tangential strain distributions correspond very well. The radial strain distribution shows a larger deviation.

The strain distributions illustrate that the strain gradient near the centre of the plate is very high. In the loaded area (η < 0.05) the strains become very high and probably these values are not reliable.

10.5 The influence of the indentor radius on the force-deflection and strain-deflection curves

10.5.1 Test method

The previous section related the strains with an assumed shape of the dent. The shape of the dent was determined for a tip radius of the indentor of R = 7.5 mm. In this section the influence is dicussed of the tip radius on the force-deflection curves and the strain outside the centre as function of the deflection.

Strain measurements were done with two strain gages (gage length 2 mm) in the positions as indicated in figure 10.25. The strain was plotted as function of the deflection w_0. The measurements were done with three tip

radii of the indentor (5, 7.5 and 12.5 mm). The clamped diameter of the plate was 80 mm. Al 2024-T3 (t = 1 mm), aramid ARALL 2H33 (t = 1.35 mm) and GLARE $2R_6^2 33/C55$ (t = 1.41 mm) were tested. The shapes of the dents were measured with the set-up of the section 10.2.

10.5.2 Results

1. The force-deflection curves for the different tip radii are given in figures 10.26 and 10.27. The force at first failure shows a stronger dependence on the radius of the indentor than the deflection at failure. The influence of the tip radius on the force-deflection curve until first failure is relatively small.

2. The central strain in fibre direction is presented in figures 10.28 and 10.29. The relatively high strains (compared with the strain at yield of 0.4%, while the Al-alloy failure strain is approximately 12%) at moderate deflections of 2 to 3 mm are remarkable.

3. The strain at 15 mm from the loaded centre is shown in figures 10.30 and 10.31. The strain is much smaller than in the centre of the specimen, and the influence of the tip radius remains small until first failure occurs.

4. Tables 10.2 and 10.3 show the measured shape of the dents of aramid ARALL 2H33 under load in fibre direction for R=5, 7.5 and 12.5 mm, at a central deflection of 3.0 and 4.0 mm respectively. In these tables also the shape according to equation 10.3 is given (the empirical shape function presented in section 10.2).

The tip radius has only a relatively small influence on the dent shape outside the centre for a specimen under loading.

10.6 Conclusions

1. The simplified von Kármán equations were compared with experimental and finite element results. They give a relatively good approximation for the calculations of the strains of a clamped specimen under central loading. They represent relations between the shape of the dent under loading and

the internal strains. The simplified von Kármán equations were also used by Corran et al.[3] and Haskell[1], but a verification was not yet available in the literature.

2. The shape of the dent for the ARALL, Al 2024-T3 and carbon/PEI specimens is approximately constant during deformation (see figure 10.3 to 10.5). The anisotropy of ARALL has a small influence on the shape of the dent during loading (figure 10.6). After unloading this influence is more pronounced (figure 10.7). A shape function was found which is able to fit the empirical results very well.

3. The bending deformation of the plate at large deflections can not be neglected, contrary to a suggestion in the literature[2].

4. The strain gradient near the loaded area ($\eta = r/a < 0.2$) is high.

5. The influence of the tip radius of the indentor on the force-deflection and strain (at r = 15 mm) vs. deflection curves and on the shape of the dent until fracture is relatively small.

references

1. Haskell, D.F.; Damage tolerance of semimonocoque aircraft, in: Specialists meeting on impact damage tolerance of structures, AGARD CP 186, 1975.

2. Levy, N.; Goldsmith, W.; Normal impact and perforation of thin plates by hemispherically tipped projectiles (part I and II), Int.J.Impact Engng. Vol.2, No.3, pp.209-229, and No.4, pp.229-324, 1984.

3. Corran, R.S.J.; Shadbolt, P.J.; Ruiz, C.; Impact loading on plates- an experimental investigation, Int.J. Impact Engng., Vol.1, No.1, pp.3-22, 1983.

4. Timoshenko, S.P.; Woinowsky-Krieger, S.; Theory of plates and shells, McGraw-Hill Book company, 1970.

	load F (kN)	central deflection w_0 (mm)
Al 2024-T3	0.23	1.00
	0.65	2.25
	1.15	3.05
	1.78	3.90
	2.56	4.65
	3.36	5.45
ARALL 2H32	0.48	2.05
	1.00	2.90
	1.44	3.75
	1.92	4.45

table 10.1 The load and the corresponding deflection of the specimens.

η	ξ ARALL 2H33 R=5 7.5 12.5 mm	ξ GLARE $2R_6^2$ 33/C55 R=7.5 mm	ξ Al 2024-T3 R=7.5 mm	ξ (eq.10.3)
0.042	0.952 0.967 0.985	0.950		0.948
0.125	0.810 0.842 0.841	0.815	0.852	0.842
0.250	0.651 0.700 0.674	0.664	0.656	0.681
0.375	0.524 0.583 0.530	0.547	0.525	0.531
0.500	0.381 0.467 0.394	0.413	0.393	0.394
0.625	0.365 0.350 0.258	0.279	0.279	0.267
0.750	0.238 0.233 0.129	0.161	0.164	0.148
0.875	0.111 0.133 0.030	0.060	0.049	0.047

table 10.2 The shape of the dent in a plane parallel to the fibre
direction of aramid ARALL, GLARE and Al 2024-T3, under load, for
various radii of the indentor (at w_0 = 3.0 mm).

η	ξ ARALL 2H33			ξ GLARE 2R$_6$^{2}33/C55	ξ Al 2024-T3	ξ
	R=5	7.5	12.5 mm	R=7.5 mm	R=7.5 mm	(eq.10.3)
0.042	0.946	0.971	0.976	0.970		0.948
0.125	0.811	0.835	0.841	0.811	0.808	0.842
0.250	0.649	0.682	0.671	0.657	0.628	0.681
0.375	0.514	0.553	0.524	0.504	0.487	0.531
0.500	0.392	0.435	0.390	0.391	0.372	0.394
0.625	0.270	0.329	0.256	0.279	0.256	0.267
0.750	0.149	0.212	0.122	0.149	0.141	0.148
0.875	0.054	0.100	0.012	0.043	0.046	0.047

table 10.3 The shape of the dent in a plane parallel to the fibre direction of aramid ARALL, GLARE and Al 2024-T3, under load, for various radii of the indentor (at w_0 = 4.0 mm).
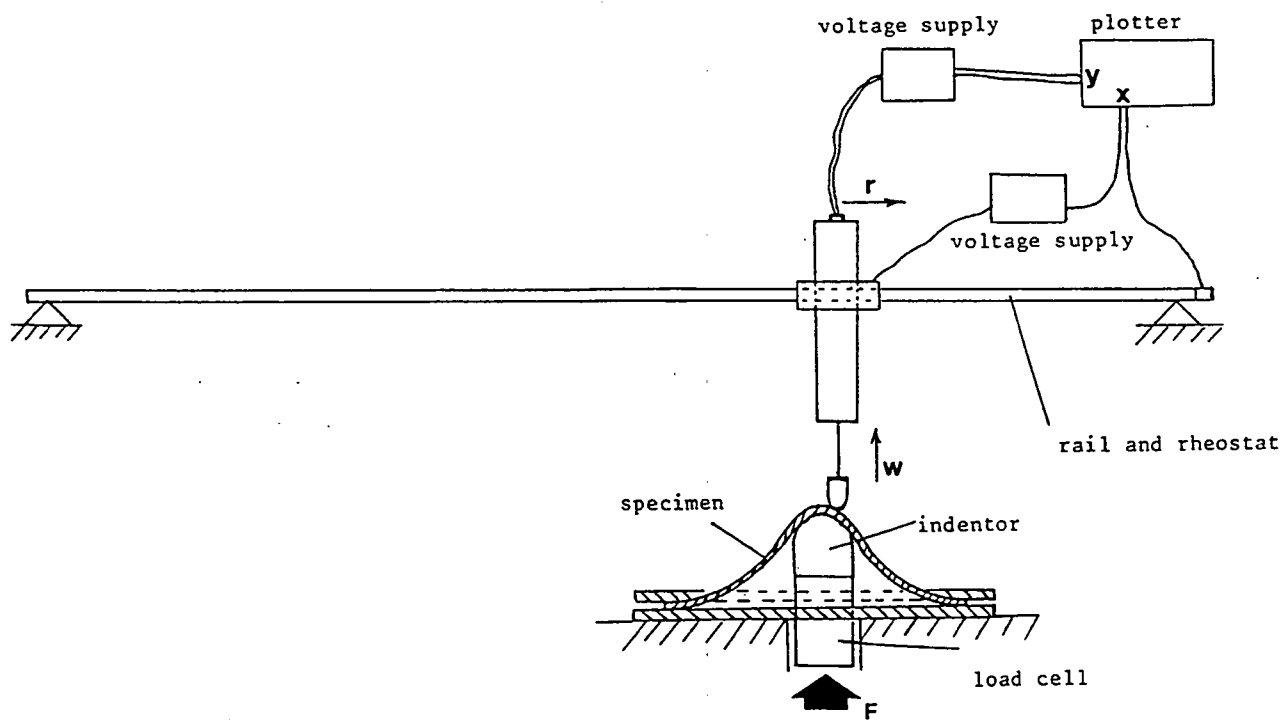
figure 10.1 Test set-up to measure the shape of the dent under loading, and after unloading.
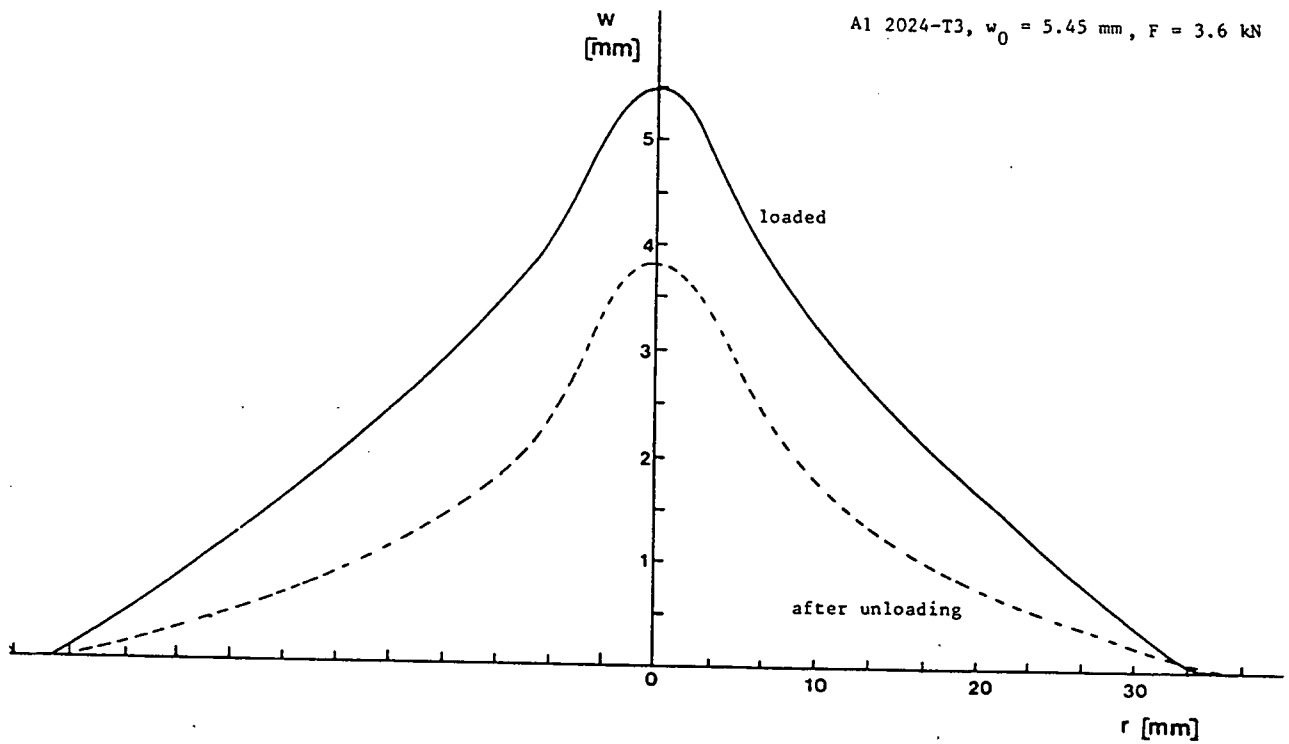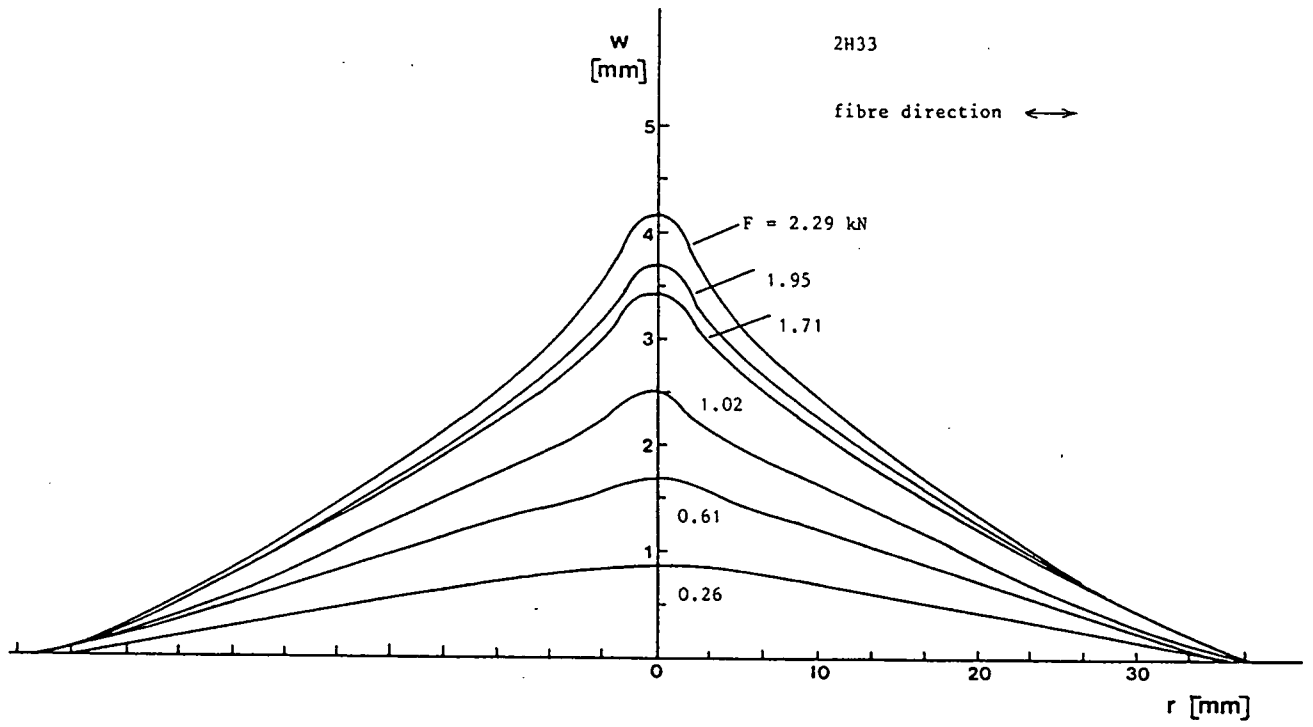
figure 10.2 Examples of measured deflection fields.
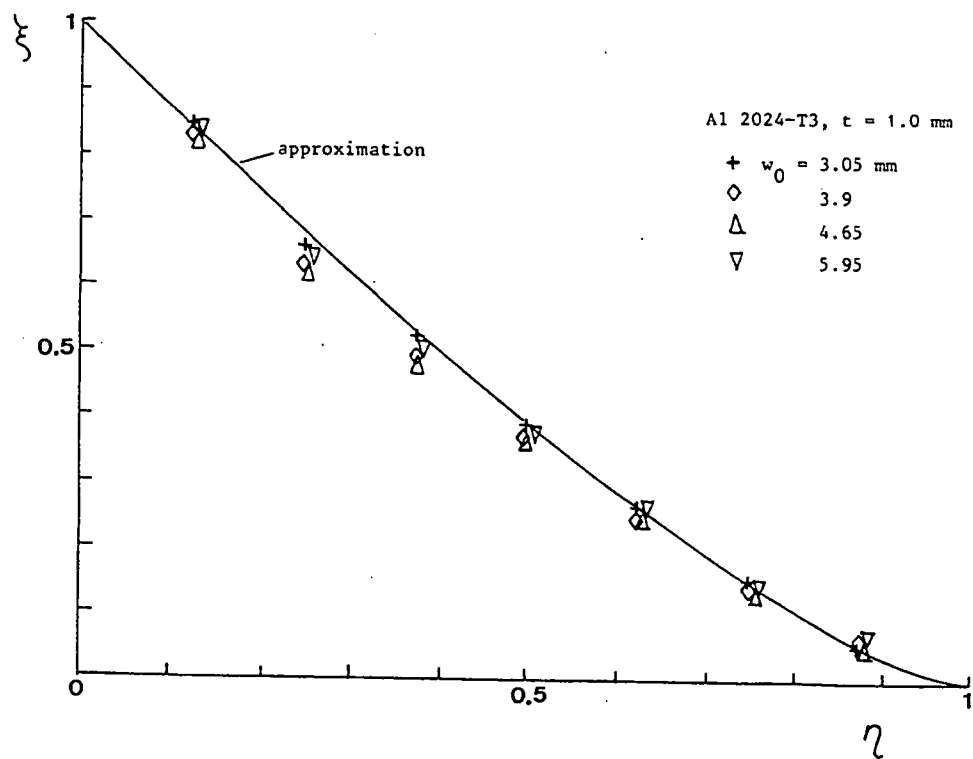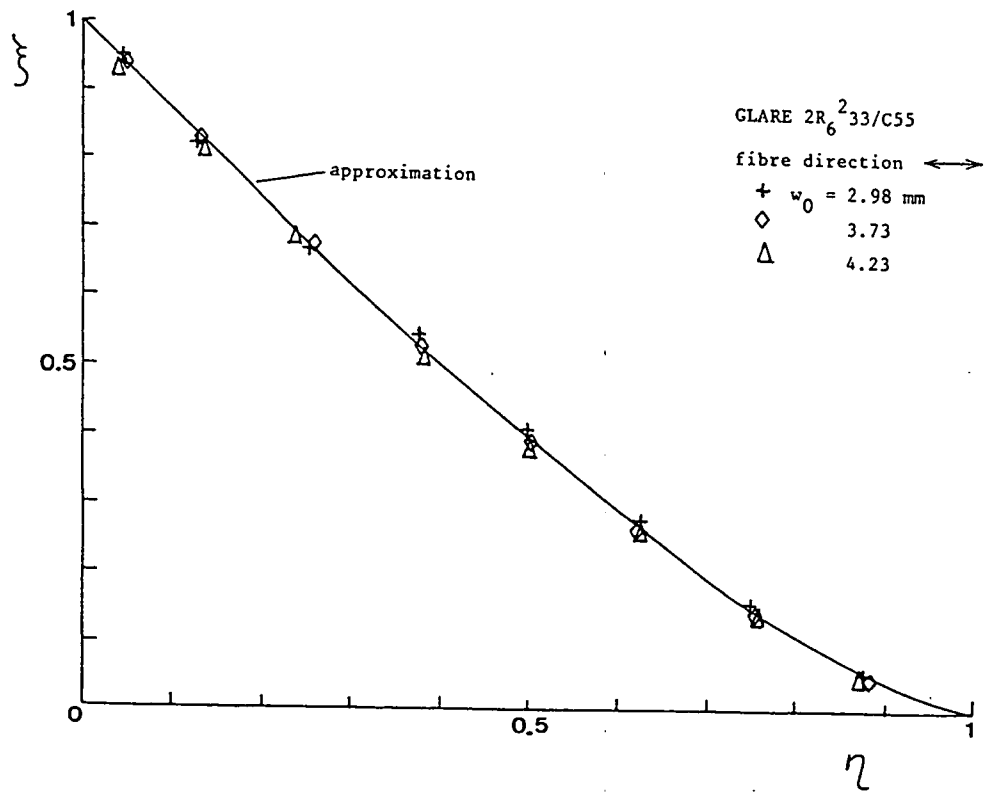
figure 10.3 The shape of the dents under loading of Al 2024-T3 and GLARE.
(circular specimens)
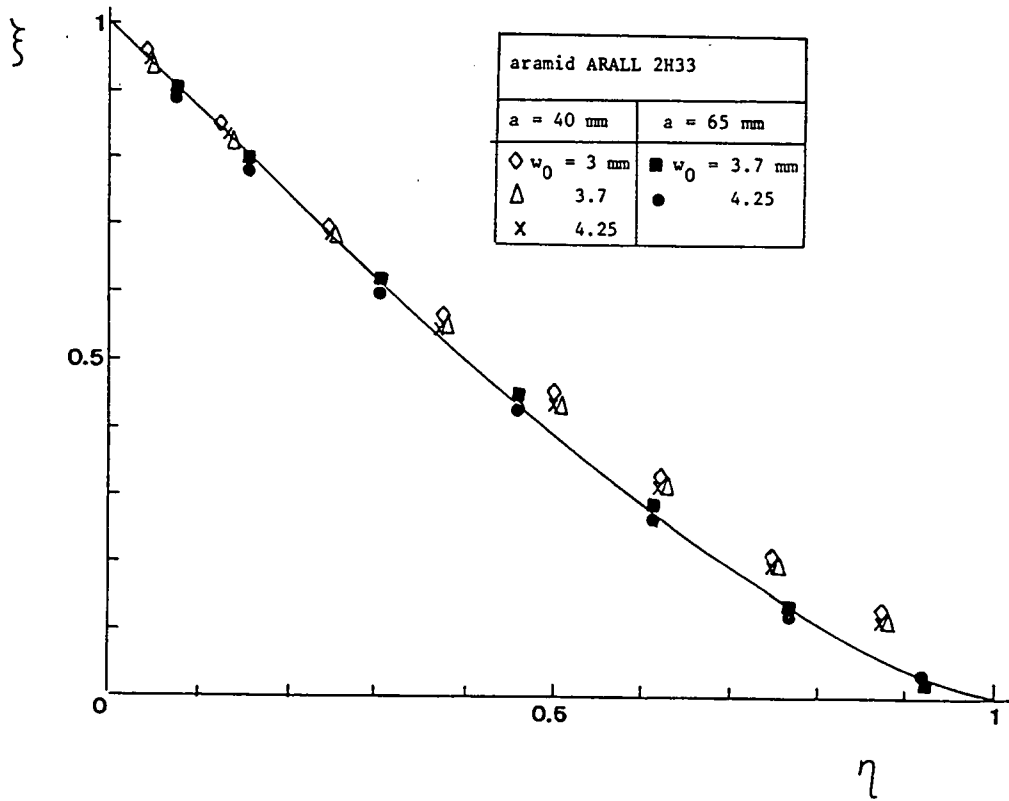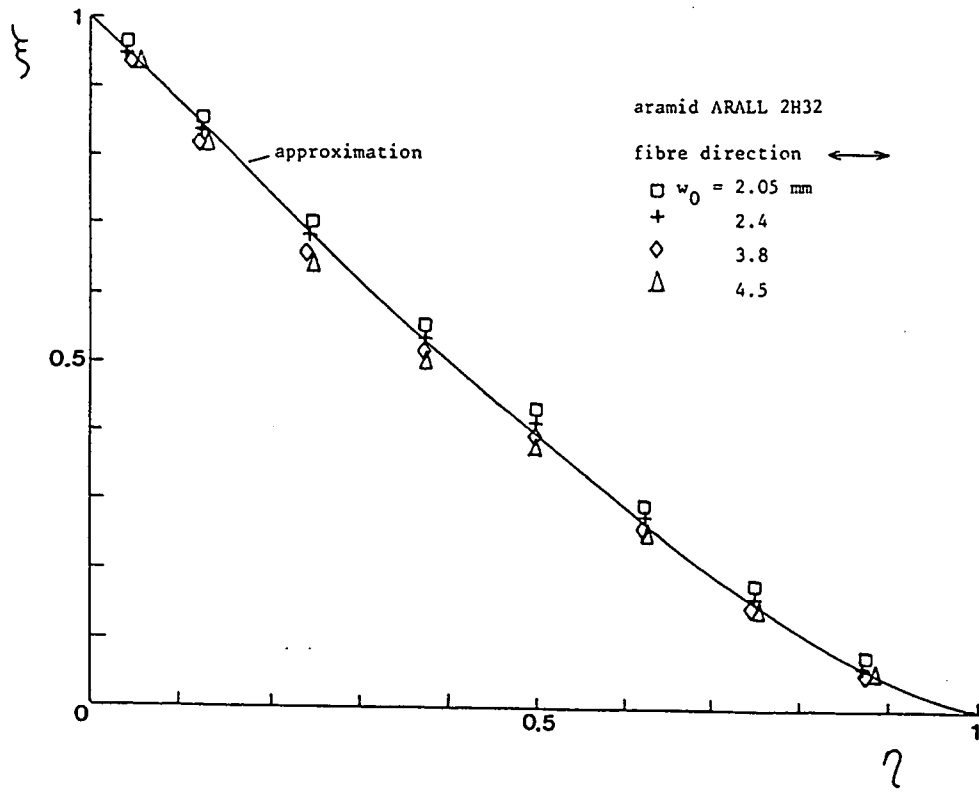
figure 10.4 Shapes of the dents under loading of ARALL 2H32 and 2H33. (circular specimens)
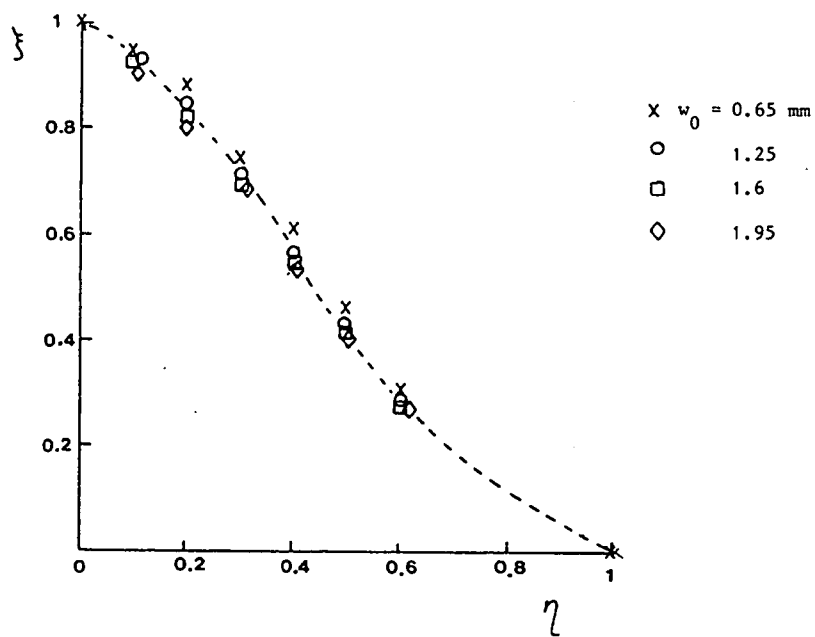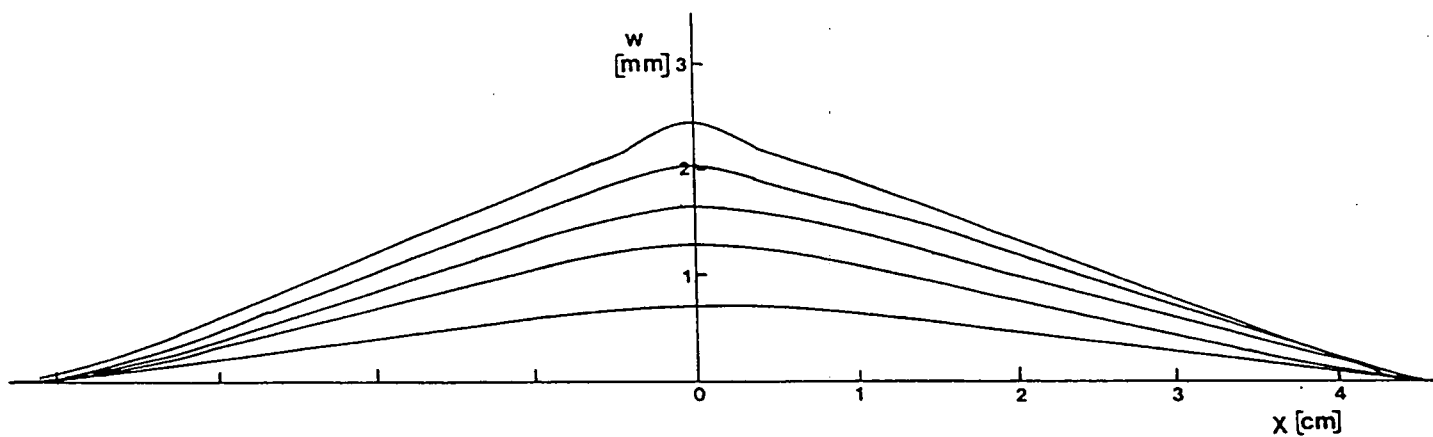
figure 10.5 Measured deflection field and shape of the deformation
under loading of a cross-ply carbon/PEI specimen with a square
100x100 mm^2 test area.
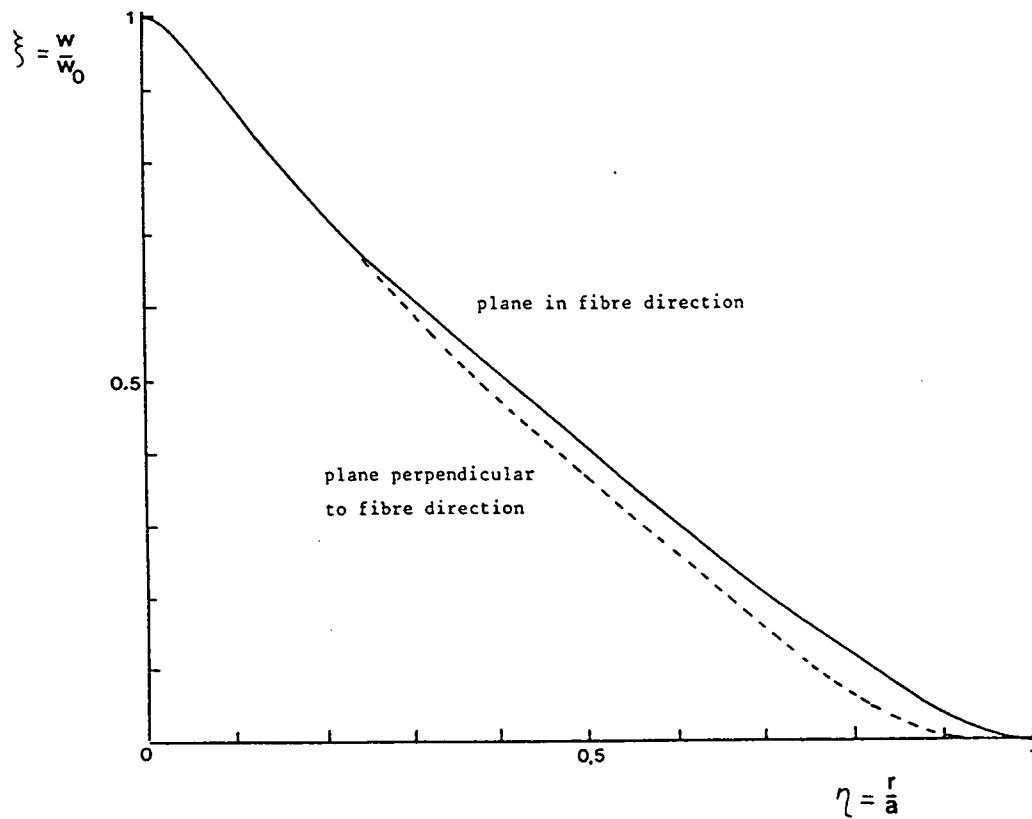
figure 10.6 The shape of the dent of aramid ARALL 2H32 in a plane in fibre direction and perpendicular to the fibre direction, under load.
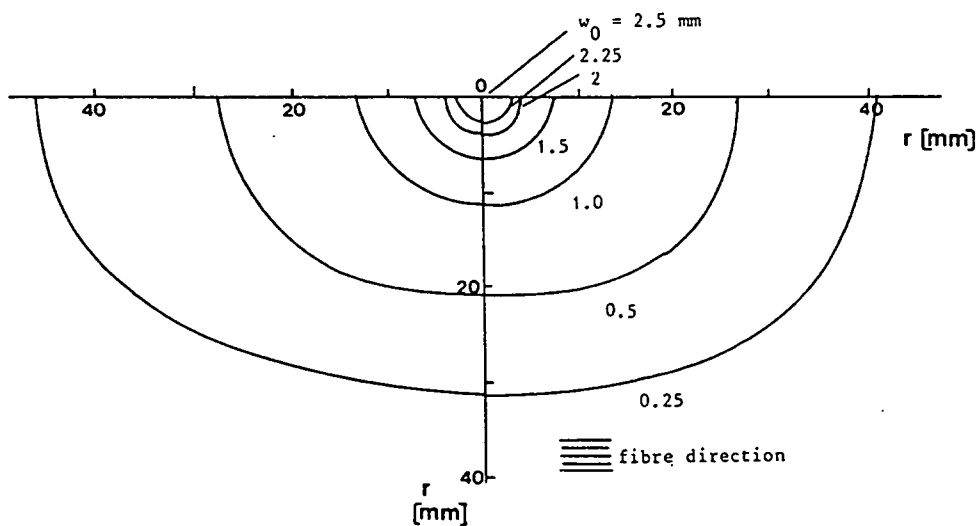
figure 10.7 The contour lines in aramid ARALL 2H32 after unloading, and removal of the clamping plates.
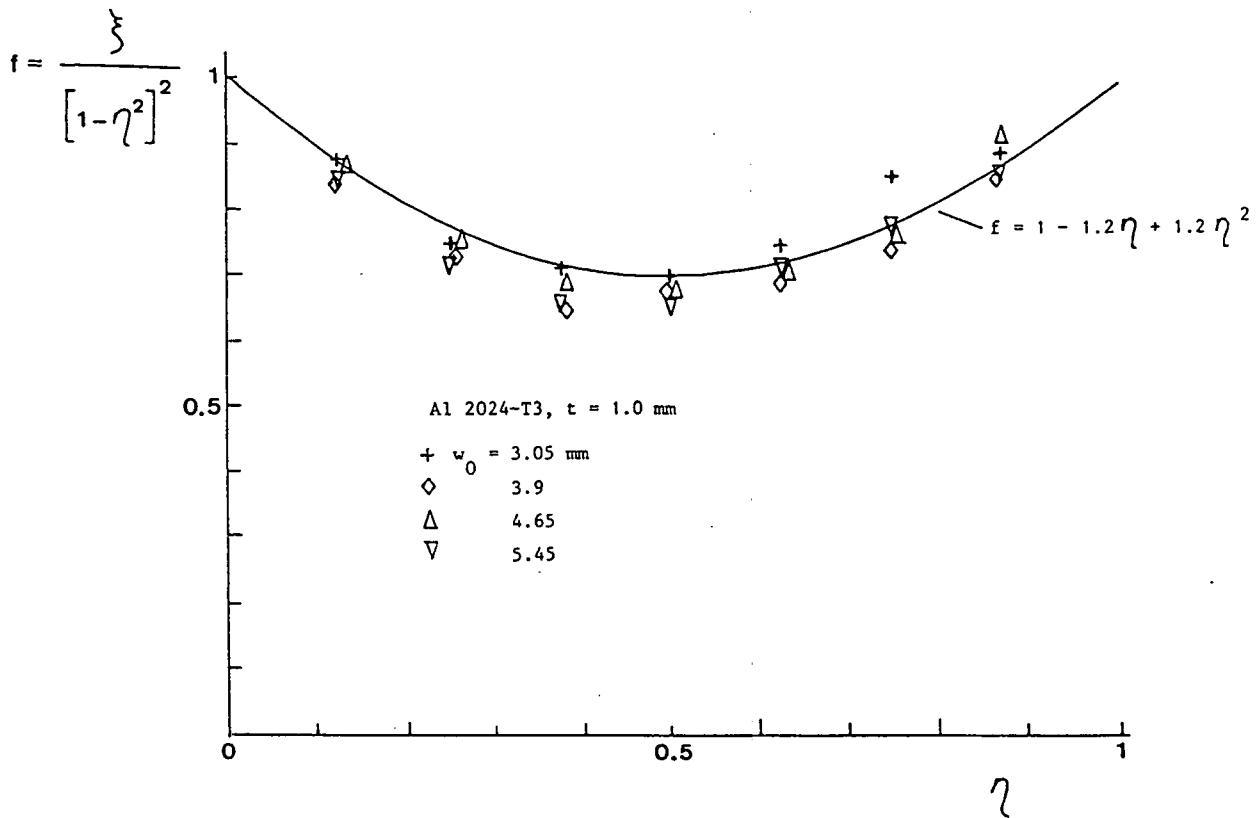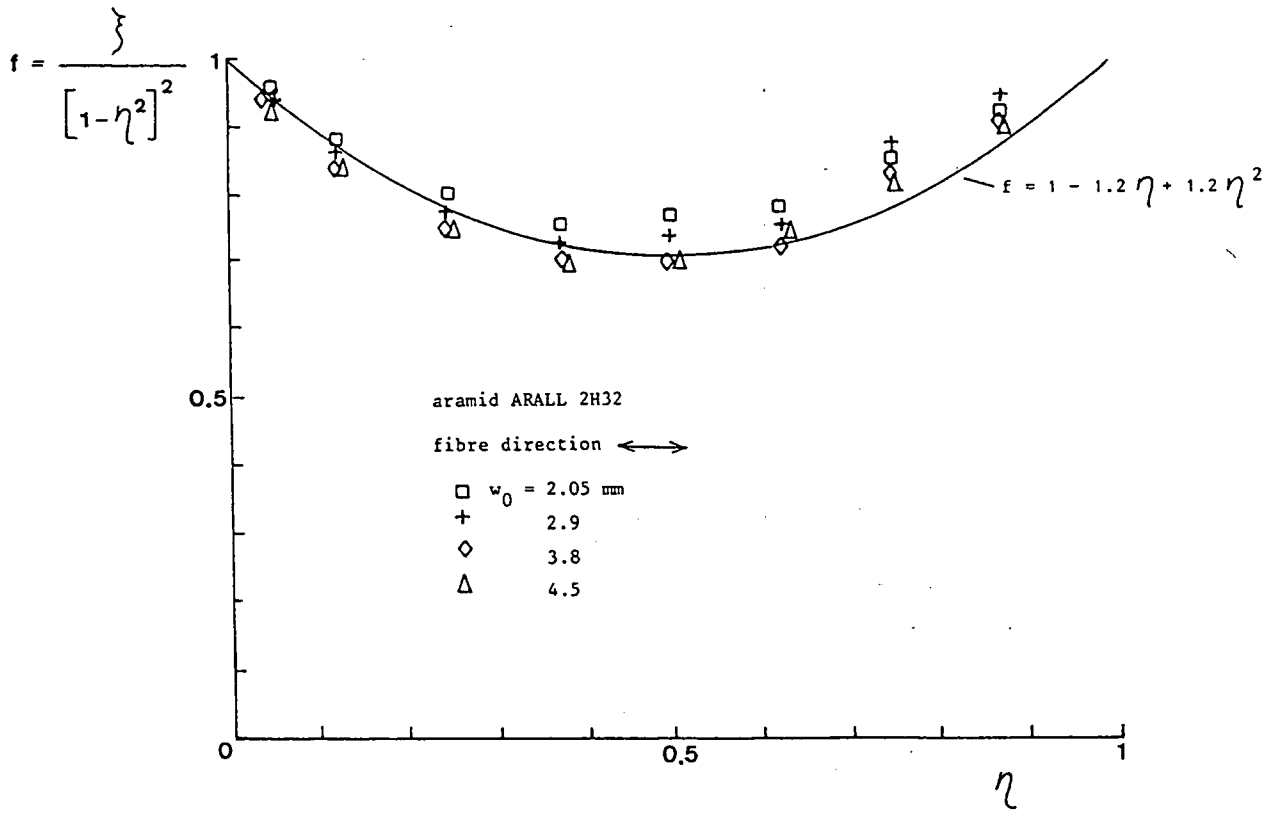
figure 10.8 The fitting function for the shape as function of the position in the plate η, for Al 2024-T3 and ARALL 2H32.

354
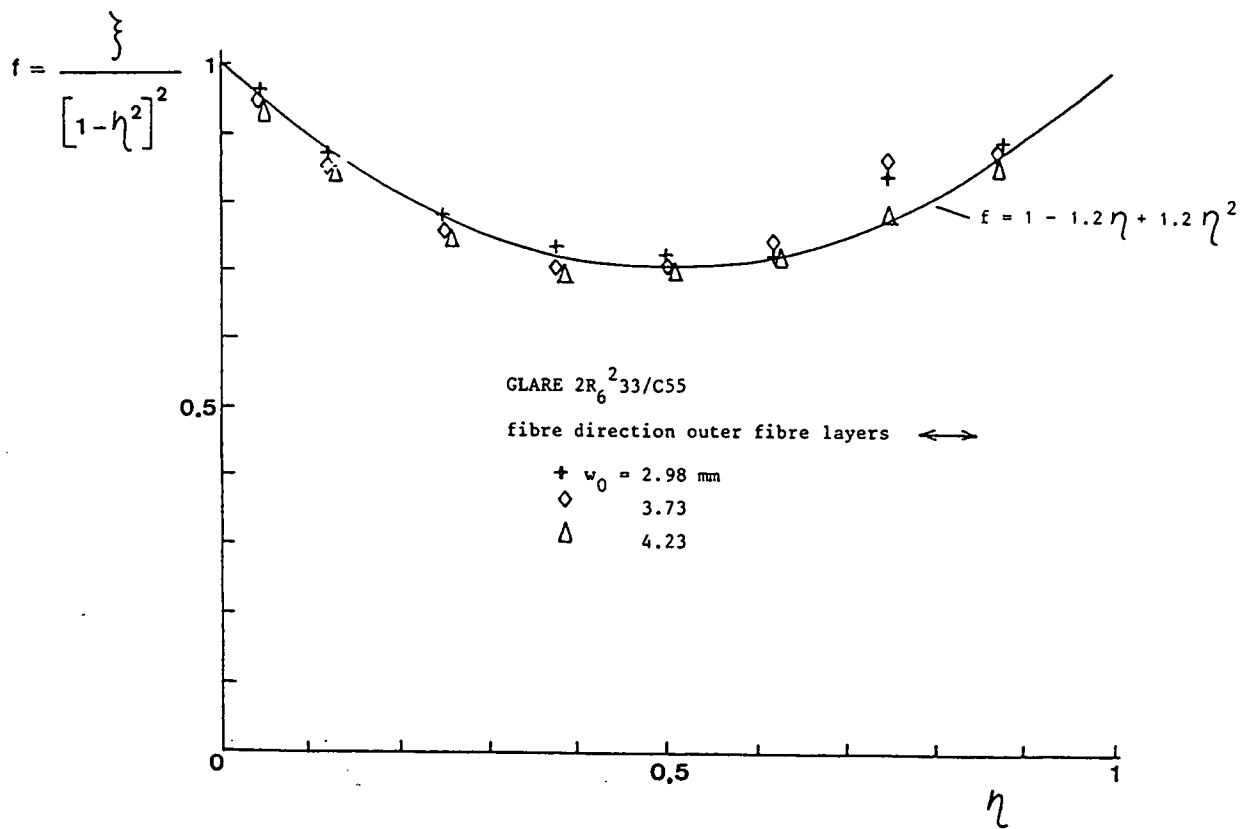
figure 10.9 The fitting function for the shape as function of the position in the plate η, for GLARE.

355

convex (not loaded) side

r = 20 mm

r = 10 mm

fibre direction

x only on the ARALL specimens

r = 10 mm

concave (loaded) side
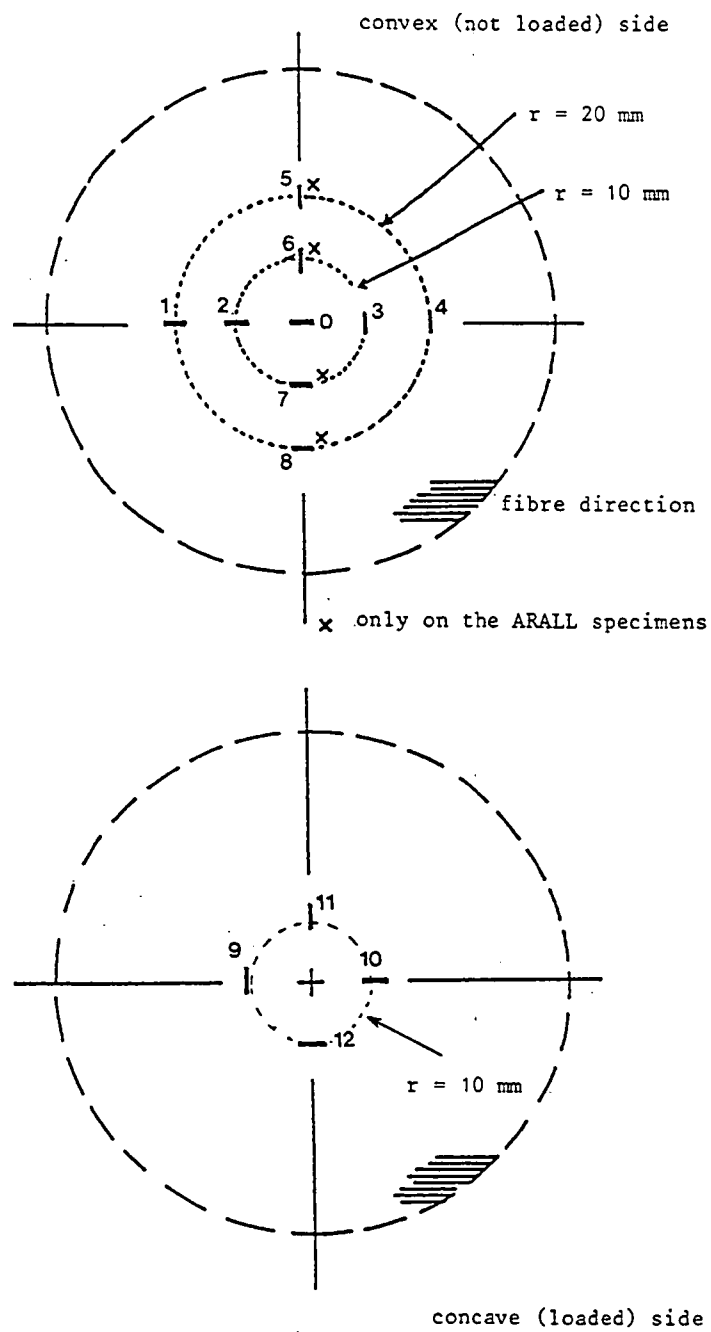
figure 10.10 The position of the strain gages on the specimens.

$$\mathcal{E} = \frac{1}{1 + 2\,R/t}$$

Al 2024-T3, t=1 mm

ARALL 2H32
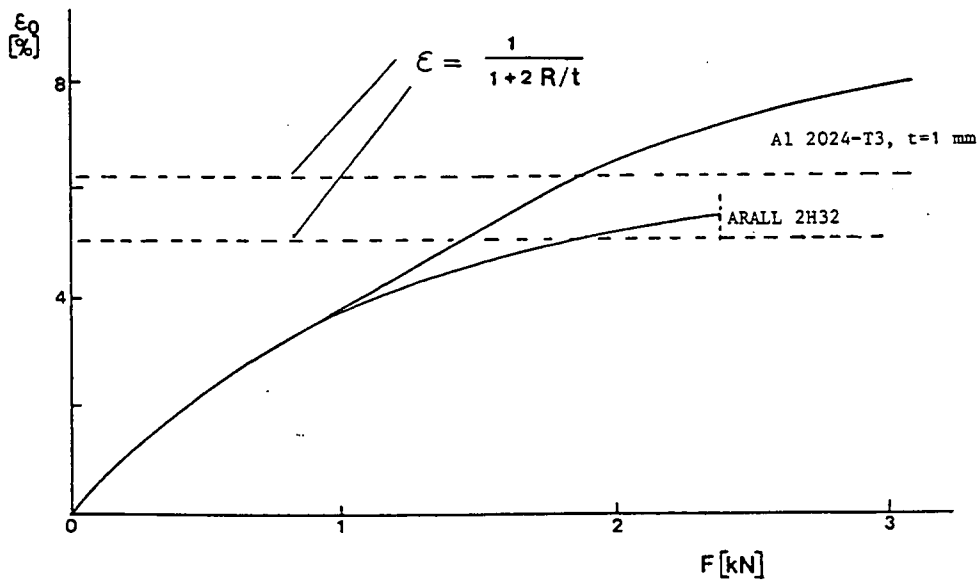
figure 10.11 Measured central strains.
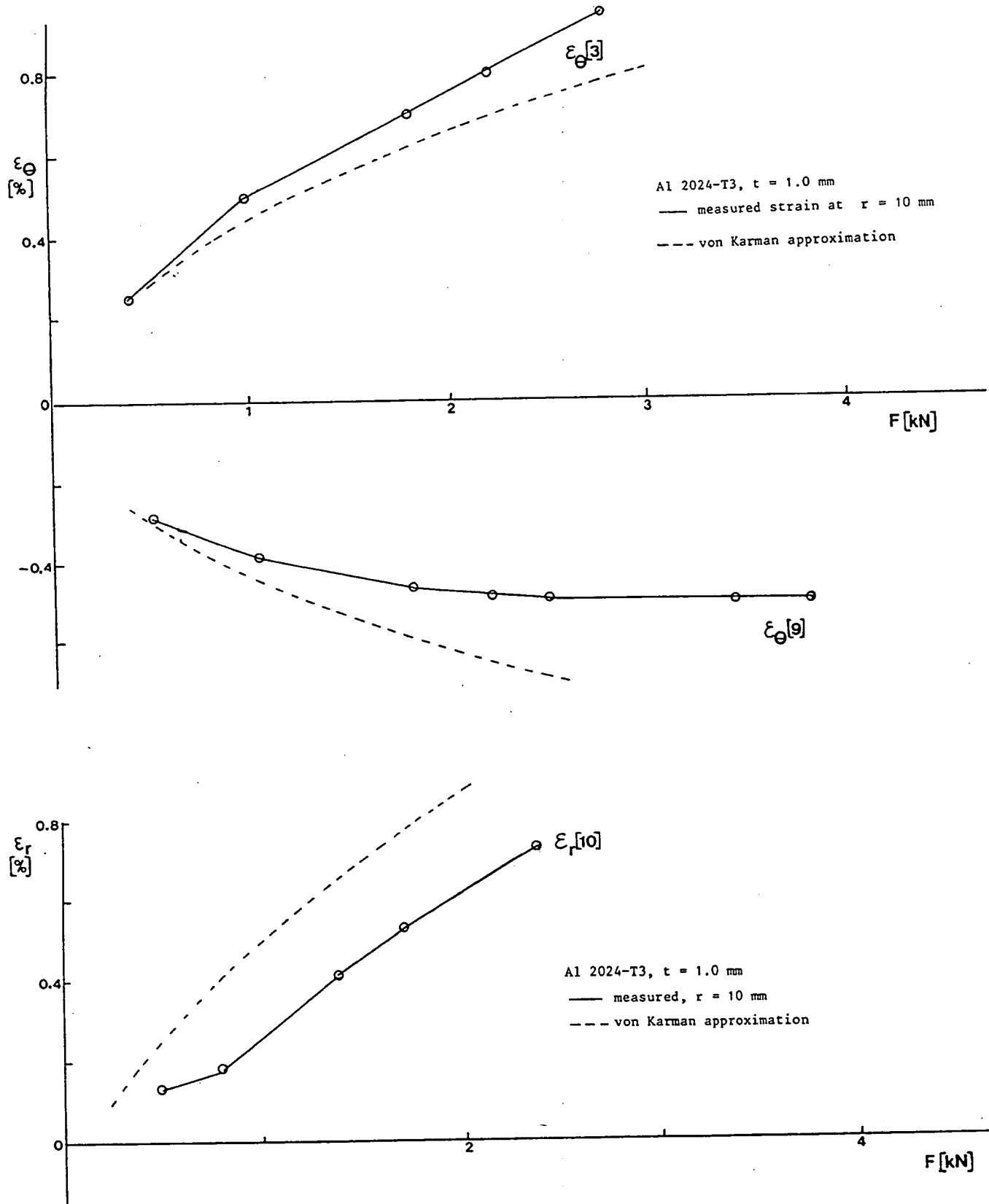
figure 10.12 Measured and calculated strains in Al 2024-T3, at r = 10 mm.
For the position of the strain gages, see figure 10.10.
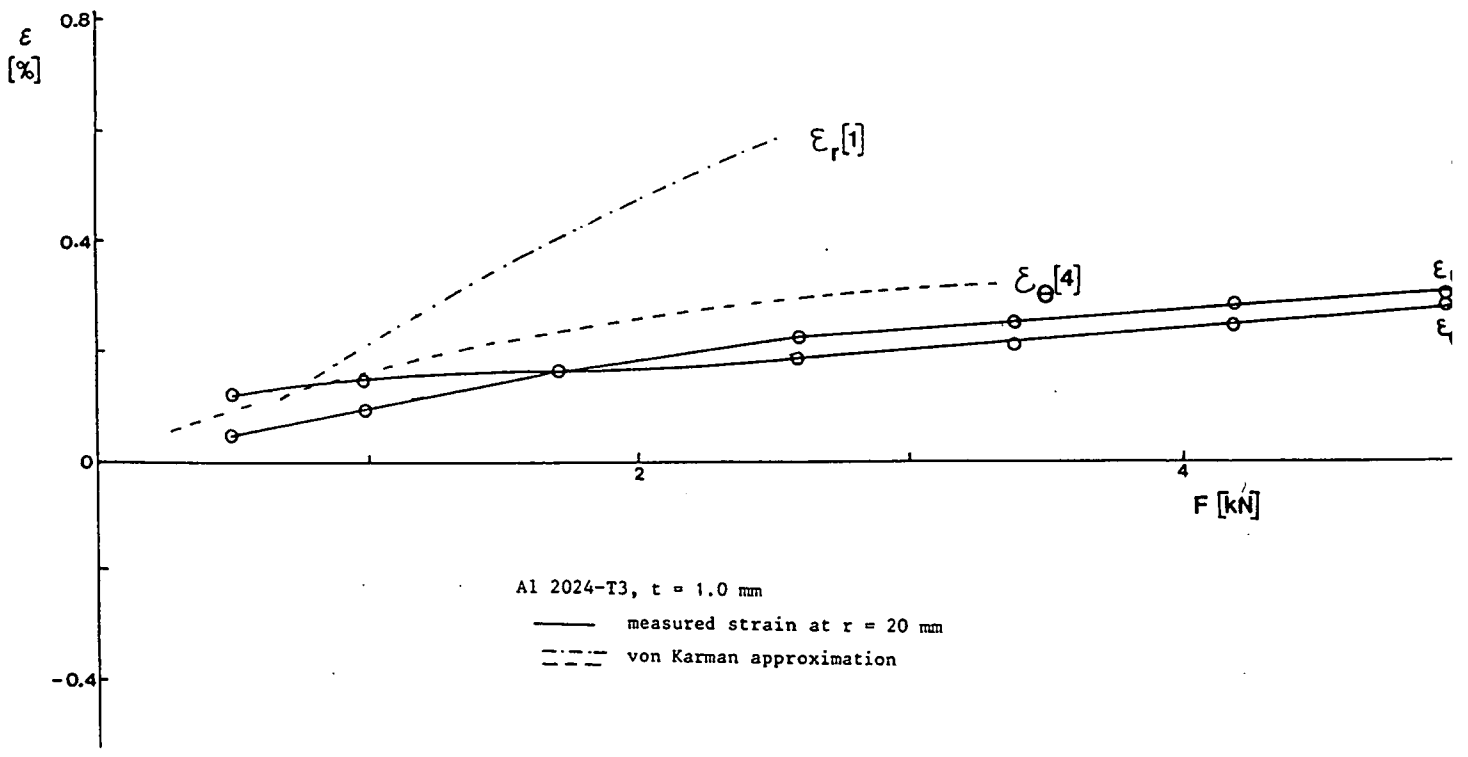
figure 10.13 Measured and calculated strains in Al 2024-T3, r = 20 mm.
For the position of the strain gages, see figure 10.10.

Top chart labels: ε [%], measured strains at r = 20 mm, aramid ARALL 2H32
Curves: // ε_r[1], ⊥ ε_r[5], // ε_Θ[8], ⊥ ε_Θ[4]
Axes: F [kN]

Bottom chart labels: ε_r [%], measured strains at r = 10 mm, aramid ARALL 2H32
Curves: // ε_r[10], ⊥ ε_r[11], // ε_r[2], ⊥ ε_r[6]
Axes: F [kN]
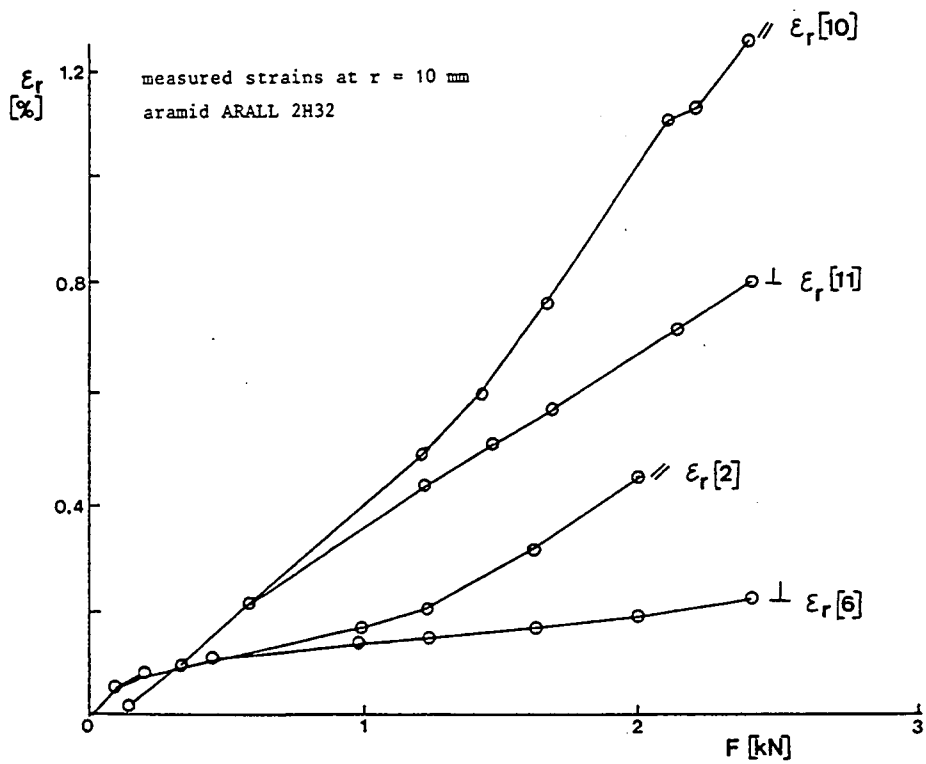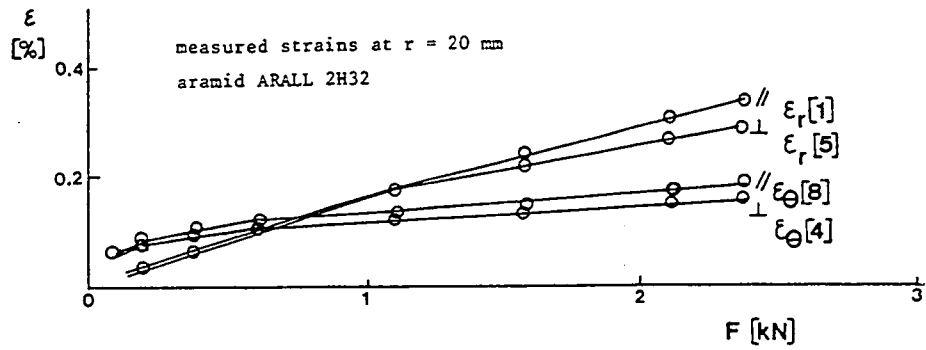
figure 10.14 Measured strains in aramid ARALL 2H32.
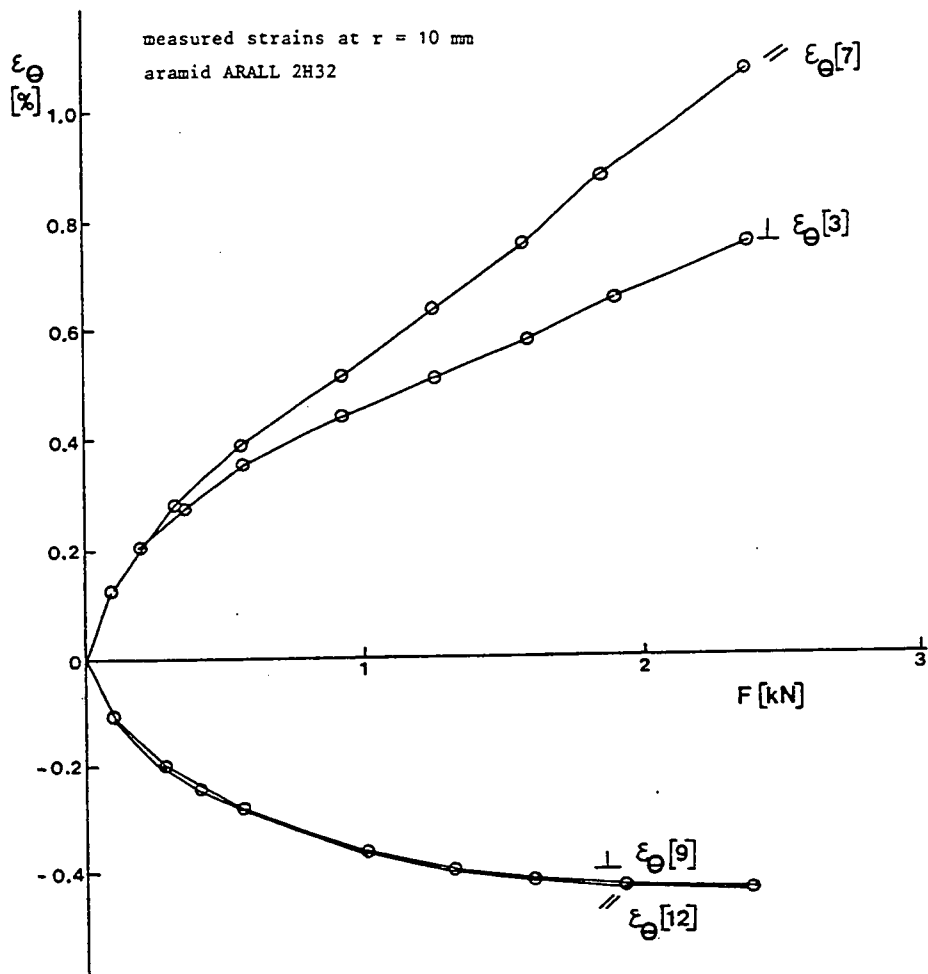
figure 10.15 Measured strains in aramid ARALL 2H32, r = 10 mm.
For the position of the strain gages, see figure 10.10.
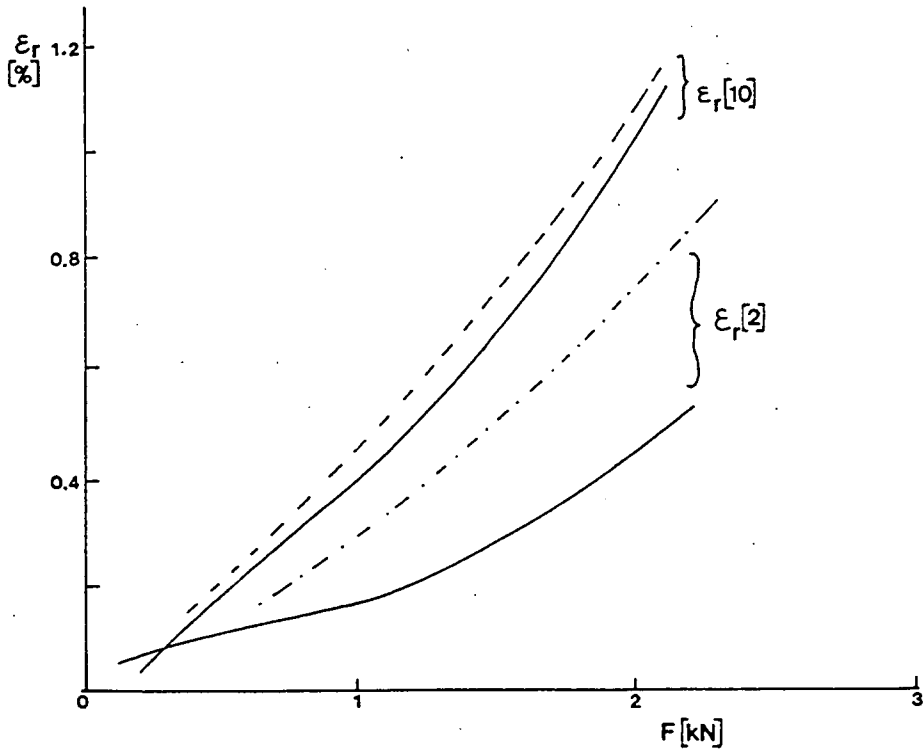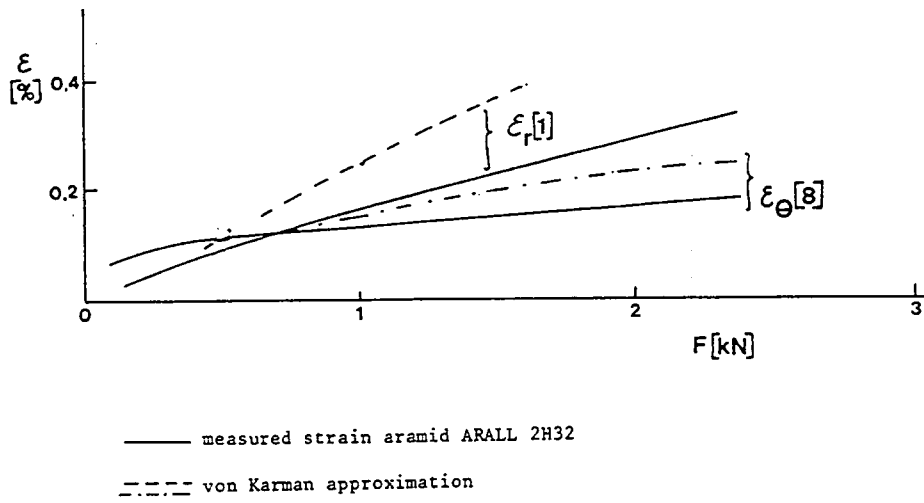
figure 10.16 Comparison between measured and calculated strains for
aramid ARALL 2H32.
For the position of the strain gages, see figure 10.10.
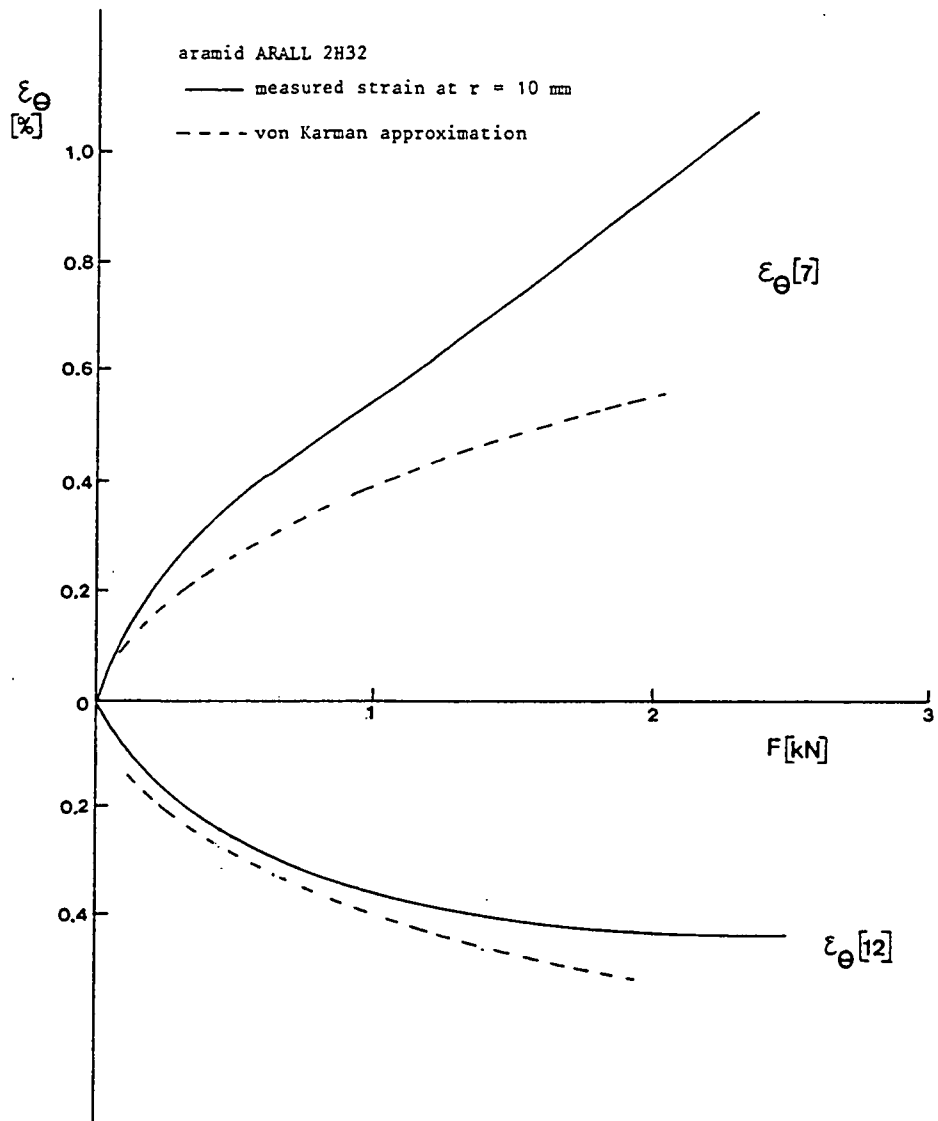
figure 10.17 Comparison between measured and calculated strains for aramid ARALL 2H32.
For the position of the strain gages, see figure 10.10.
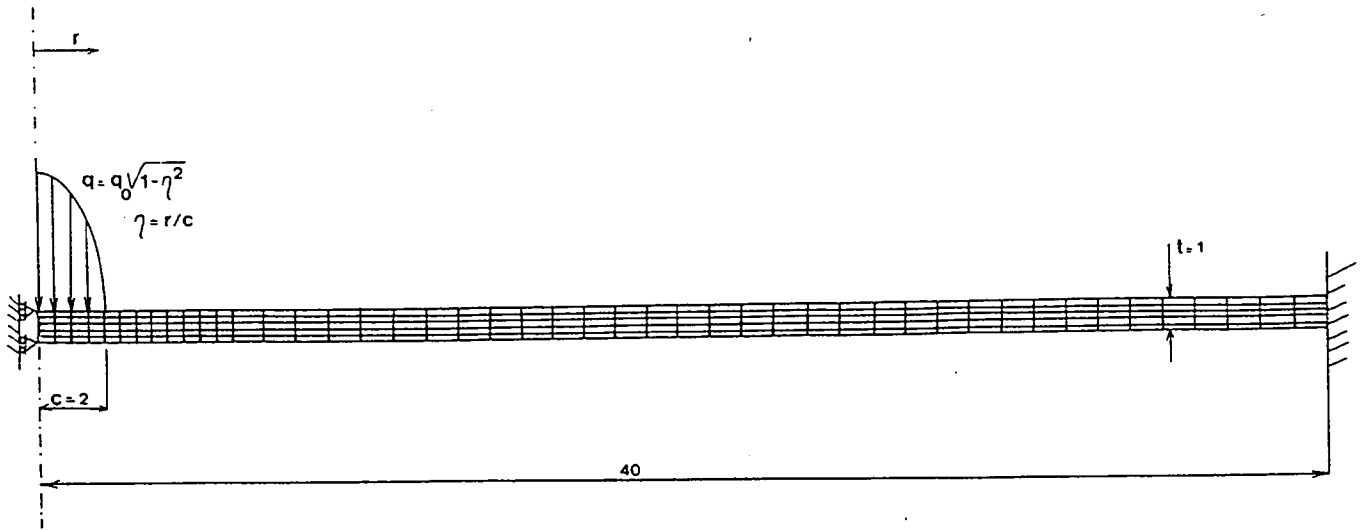
figure 10.18 The finite element model.
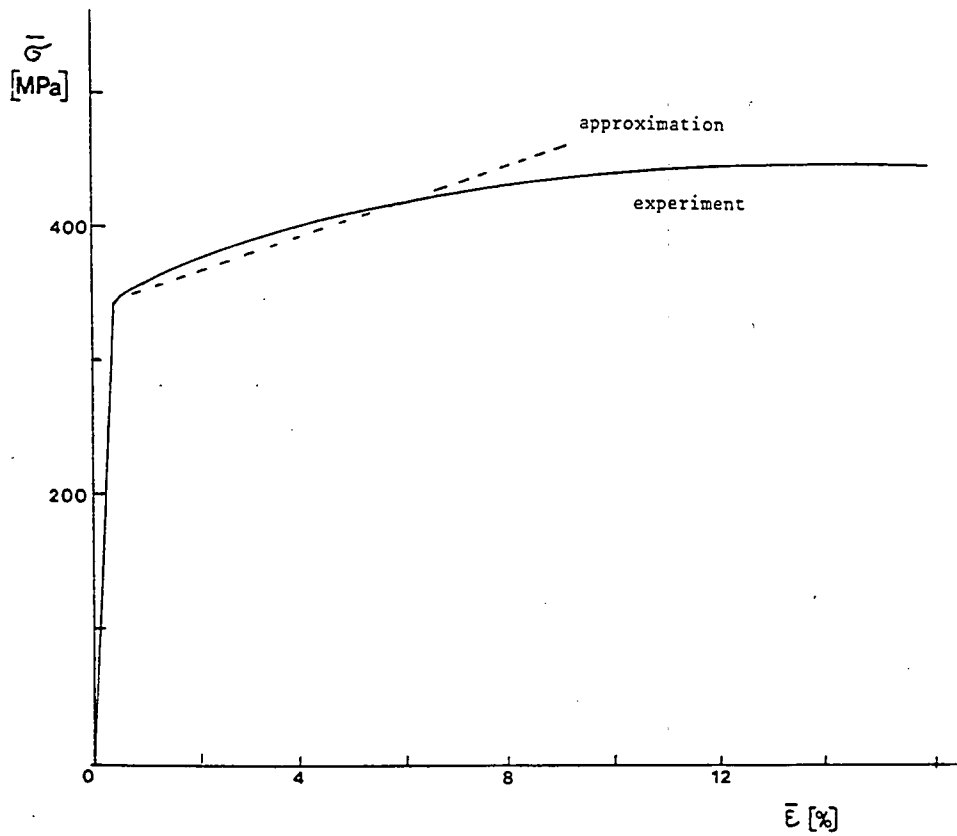
figure 10.19 The measured stress-strain curve for Al 2024-T3, and the approximation used for the finite element model.
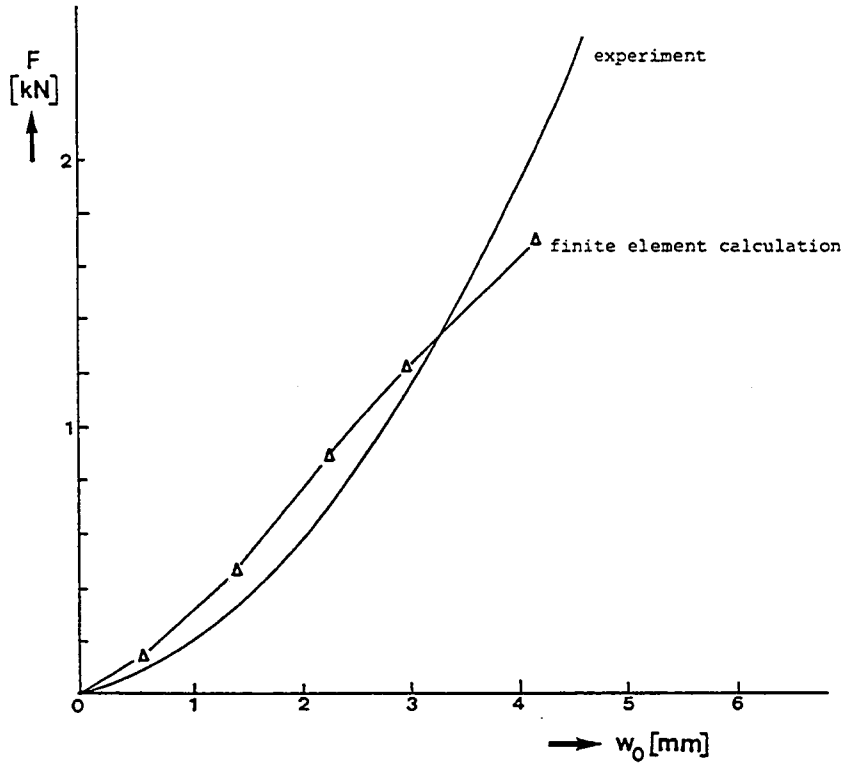
figure 10.20 Experimental and calculated force-deflection curves.
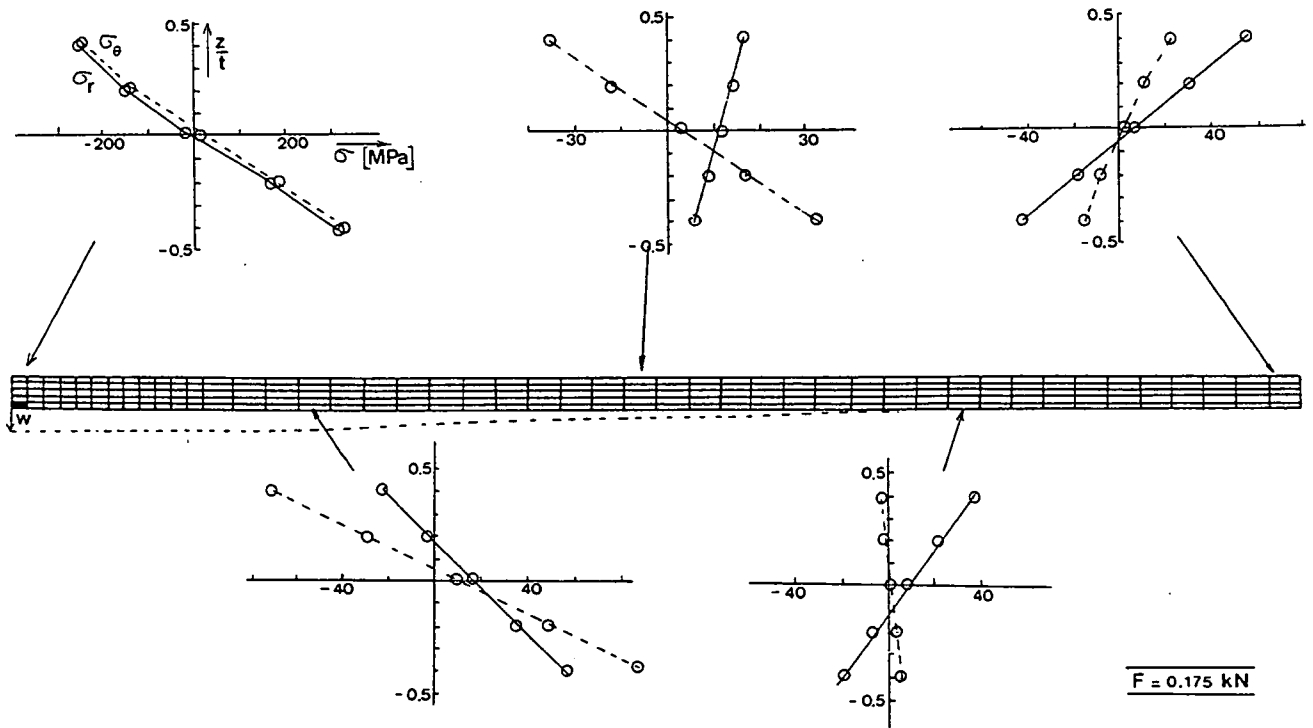
figure 10.21 Calculated stress distributions in the deflected sheet, F = 0.175 kN, plastic zone indicated in black.
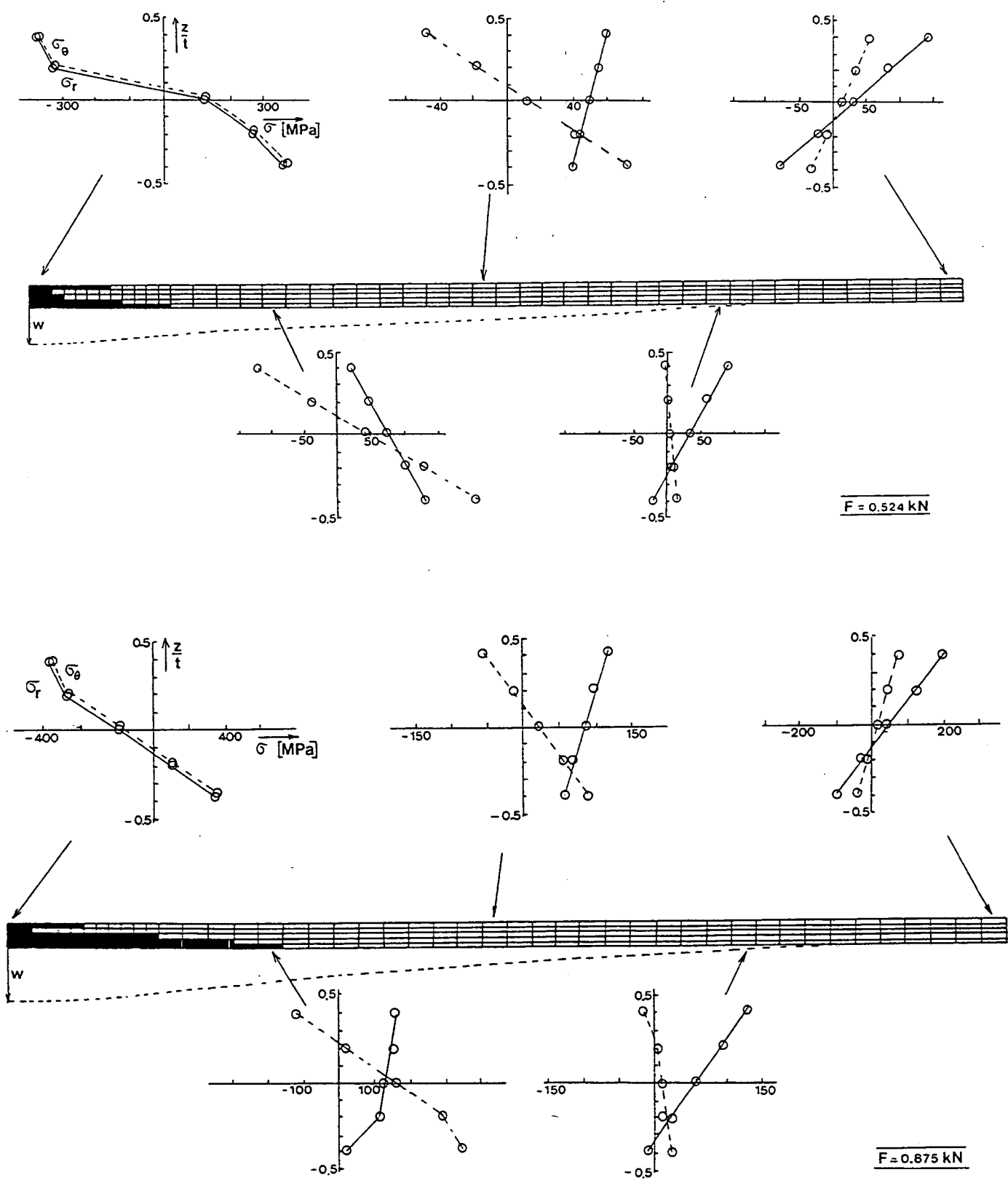
figure 10.21 (continued) Calculated stress distributions in a deflected sheet, F= 0.524 and 0.875 kN, plastic zone indicated in black.
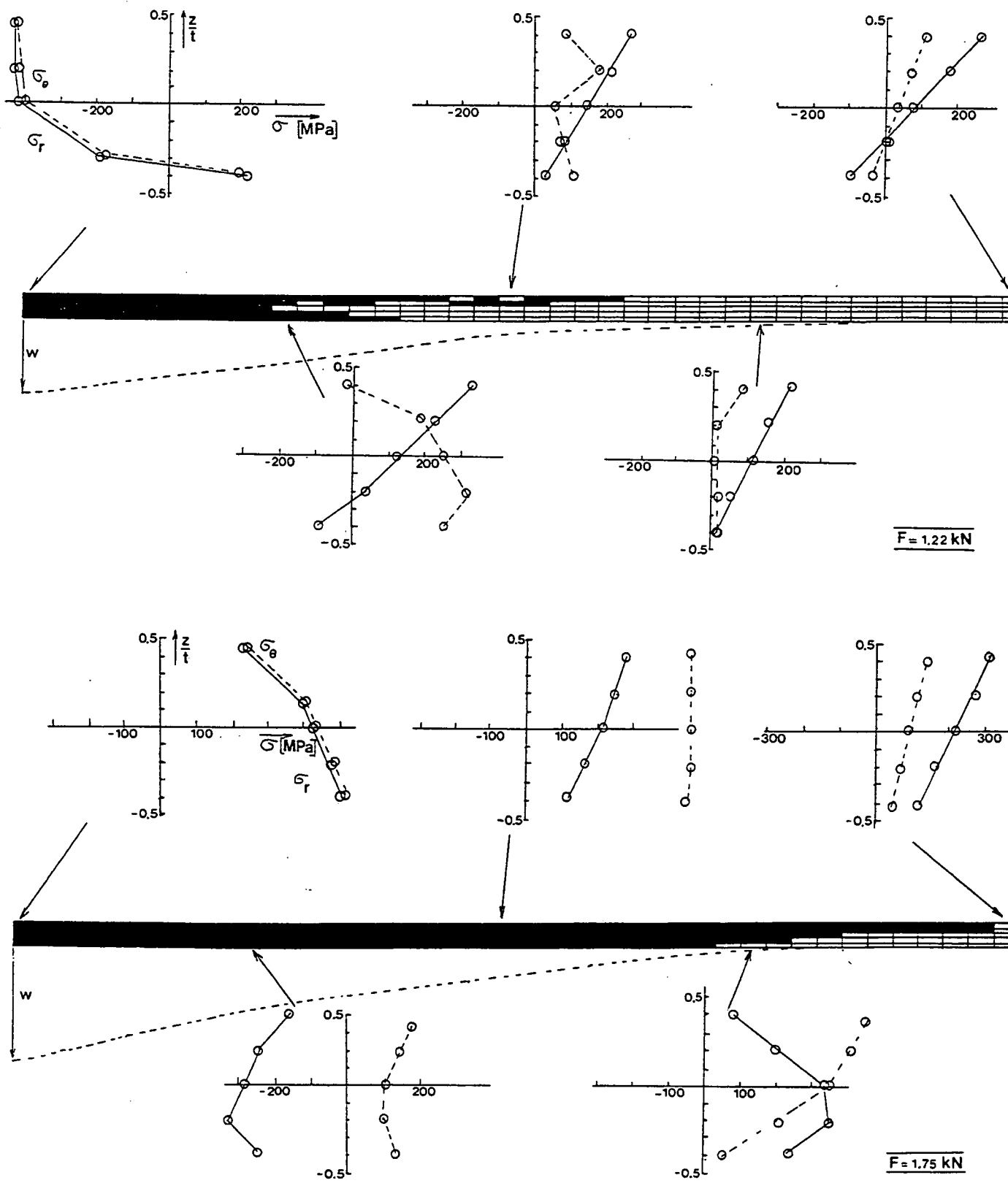
figure 10.21 (continued) Calculated stress distributions in a
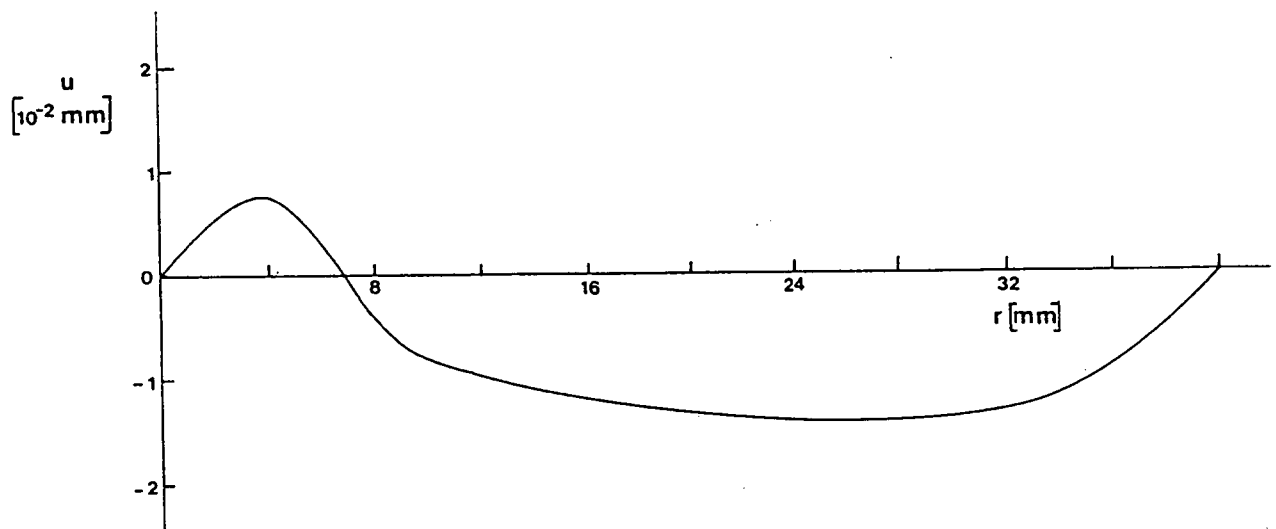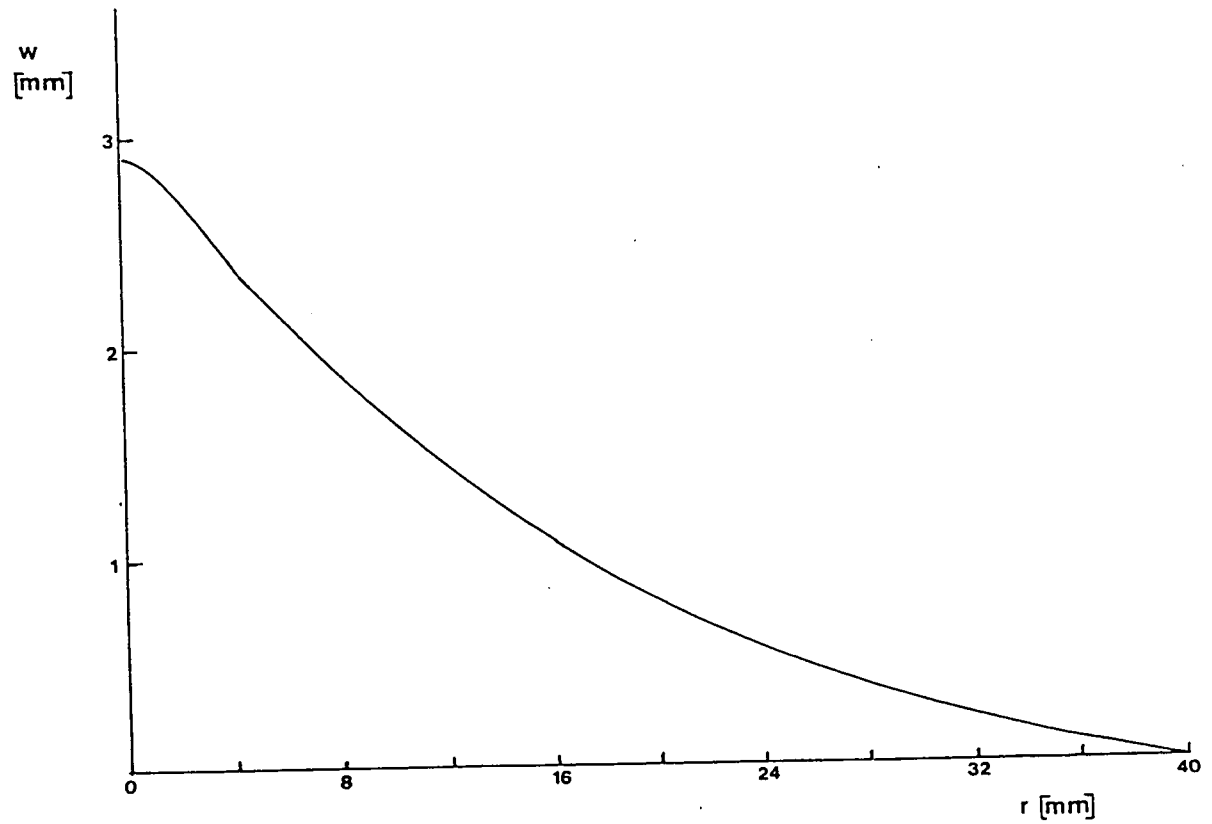deflected sheet, F= 1.22 and 1.75 kN, plastic zone indicated in
black.

figure 10.22 Calculated deflection field w and radial displacement u
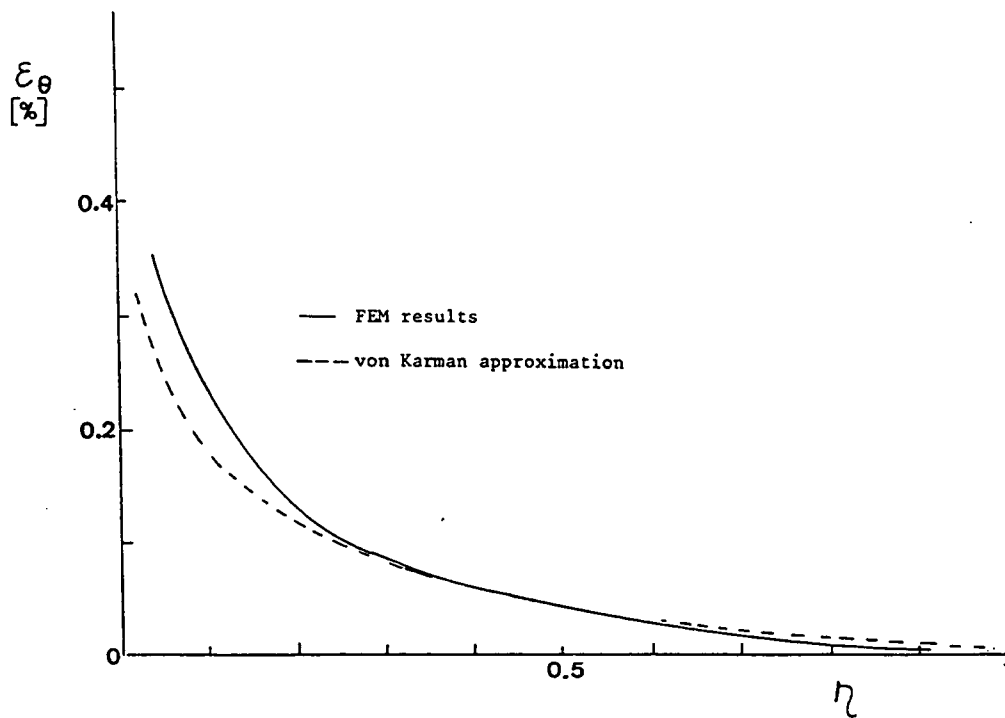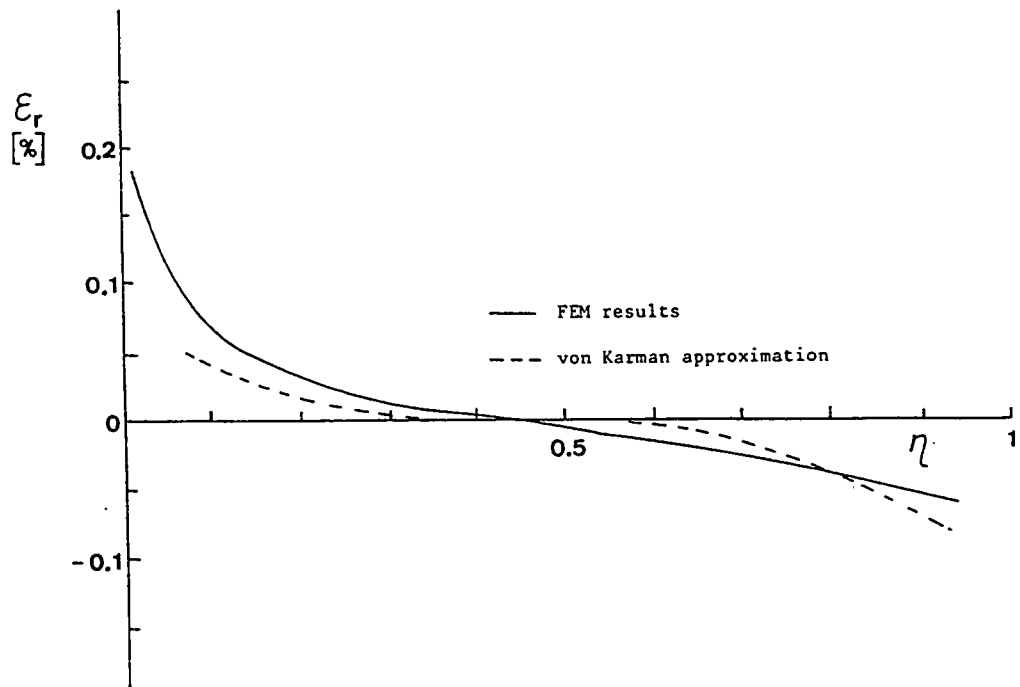of a deflected sheet, F = 1.22 kN.

figure 10.23 Strain distribution for F = 0.175 kN (w = 0.636 mm), compared
with strain distributions calculated with the simplified von Karman
equations.

figure 10.24 Strain distributions for F = 1.22 kN (w = 2.93 mm),
compared with strain distributions calculated with the
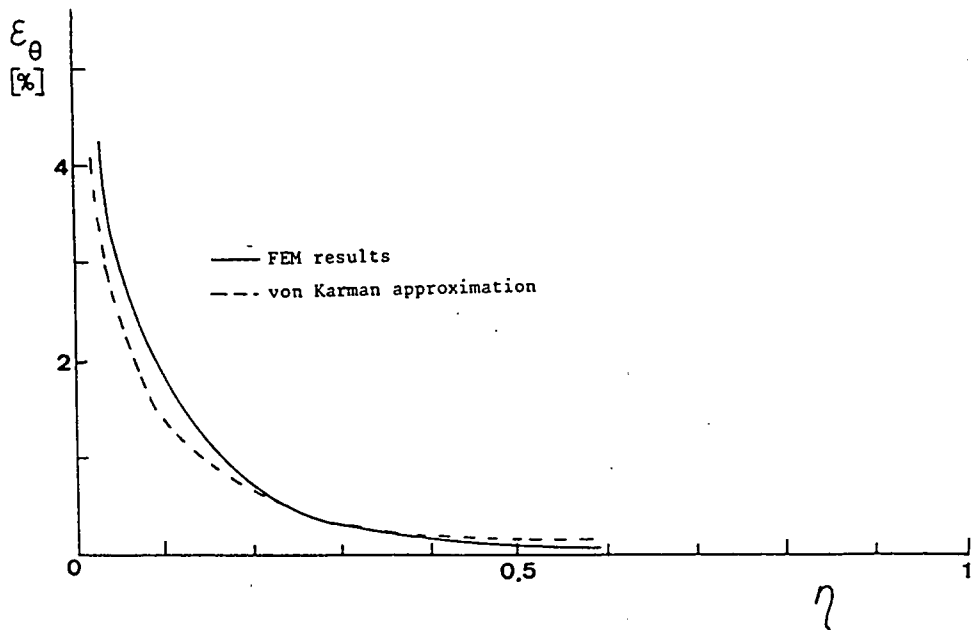simplified von Karman equations.

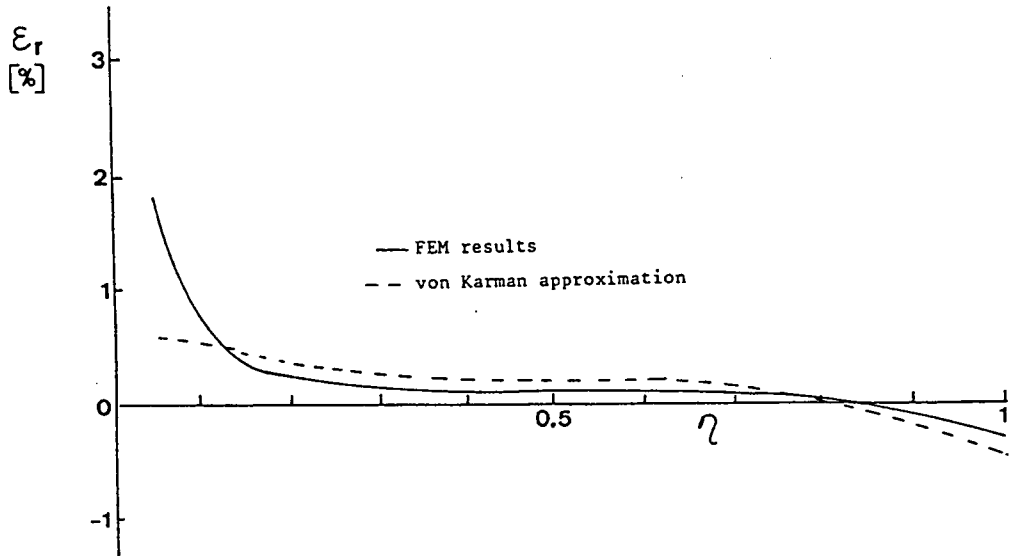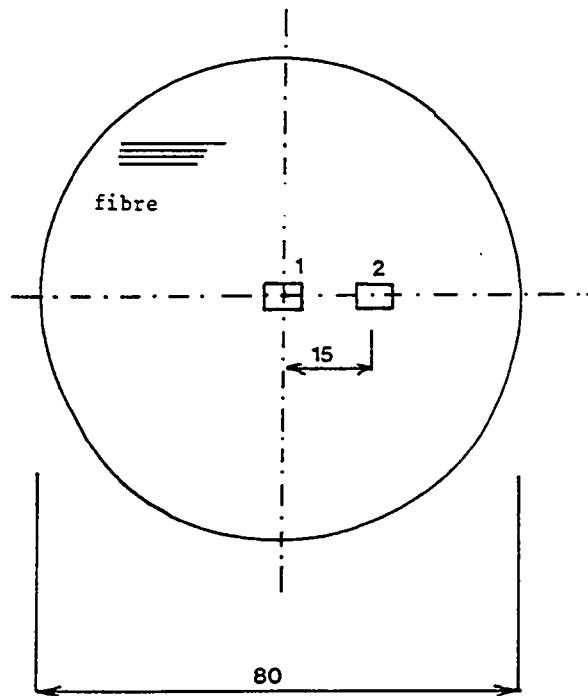**figure 10.25** Position of the strain gages.
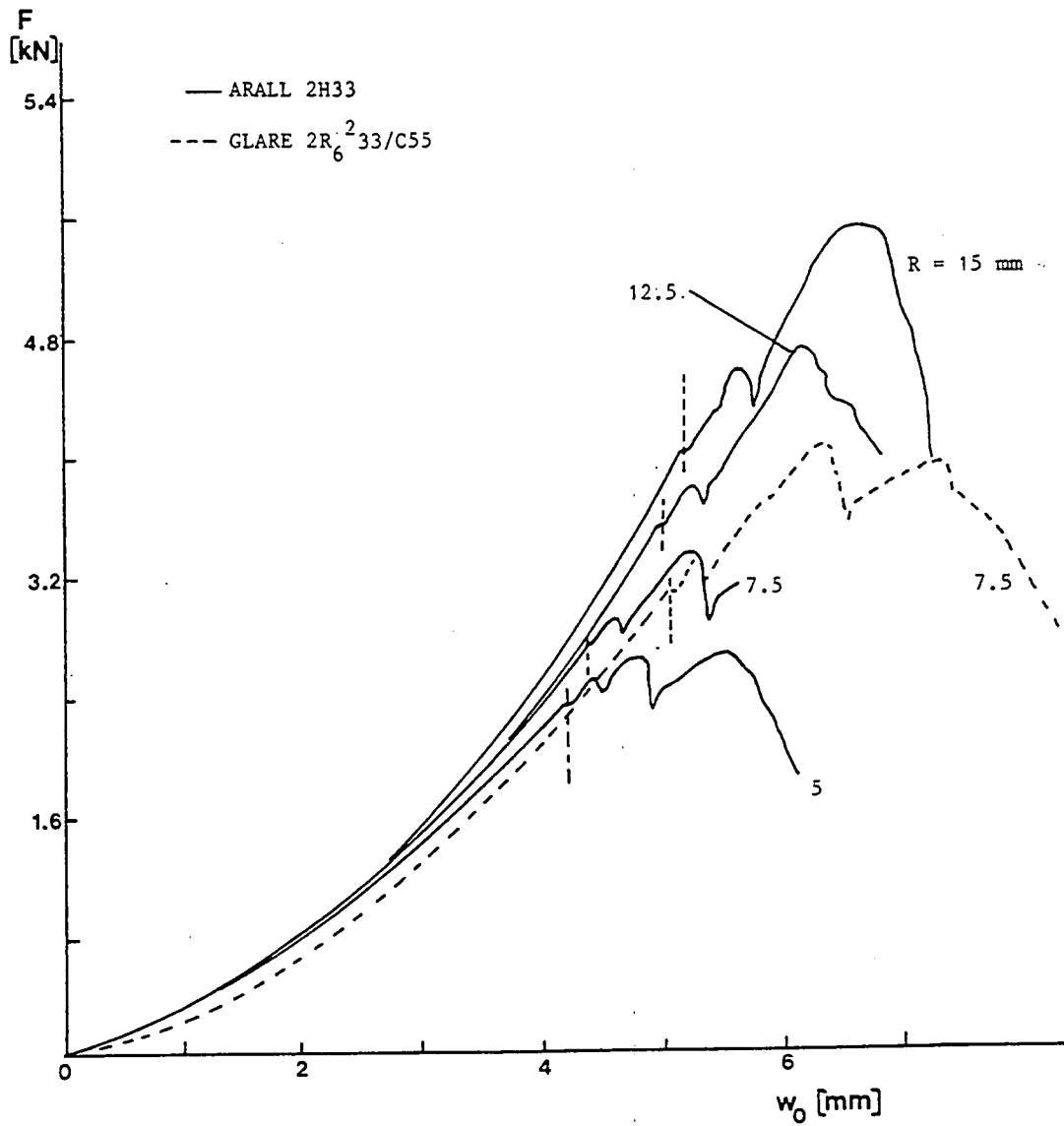
figure 10.26 Measured force-deflection curves for various radii of
the indentor for ARALL material.
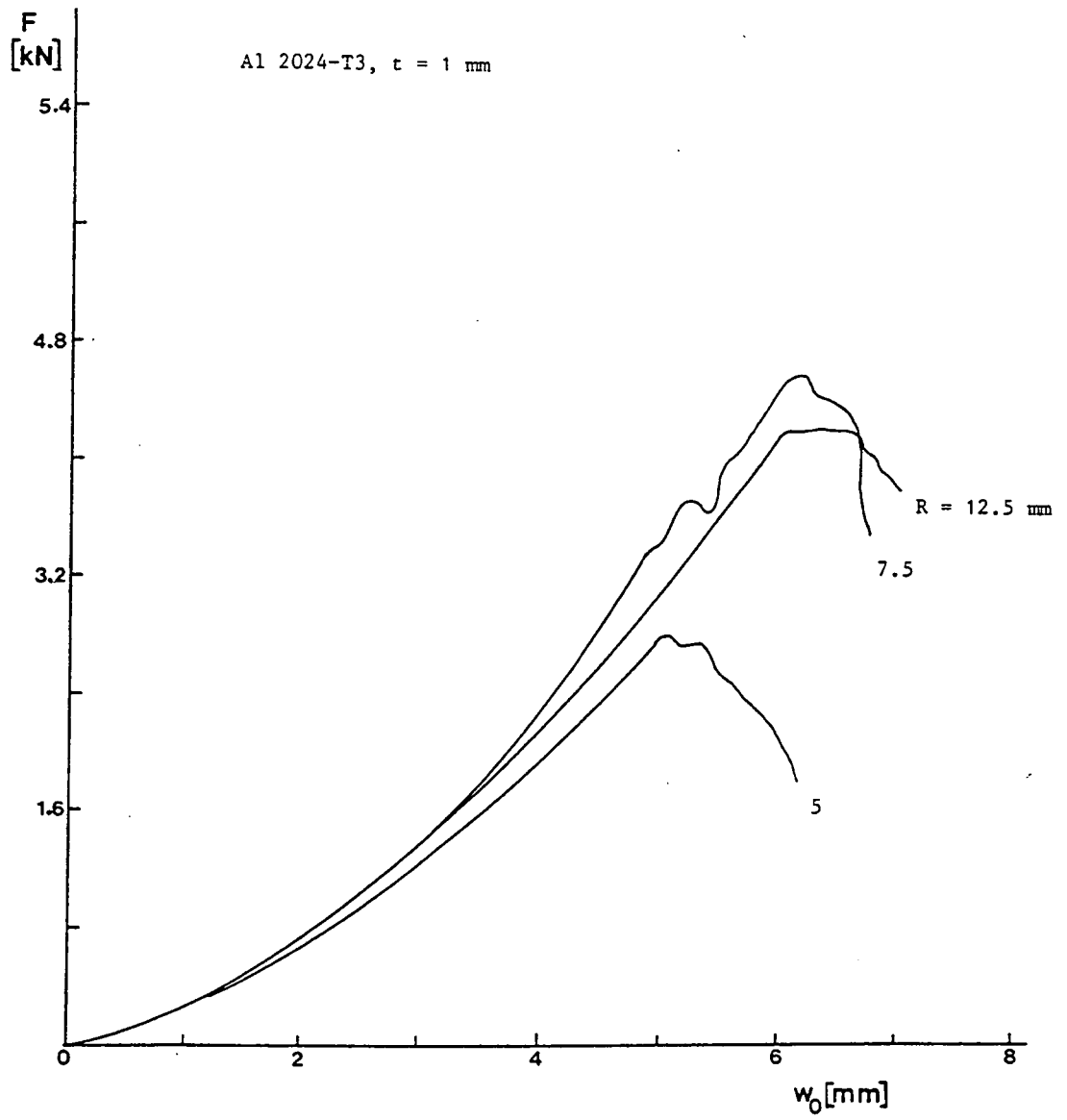
figure 10.27 Measured force-deflection curves for various radii of the indentor for Al 2024-T3.
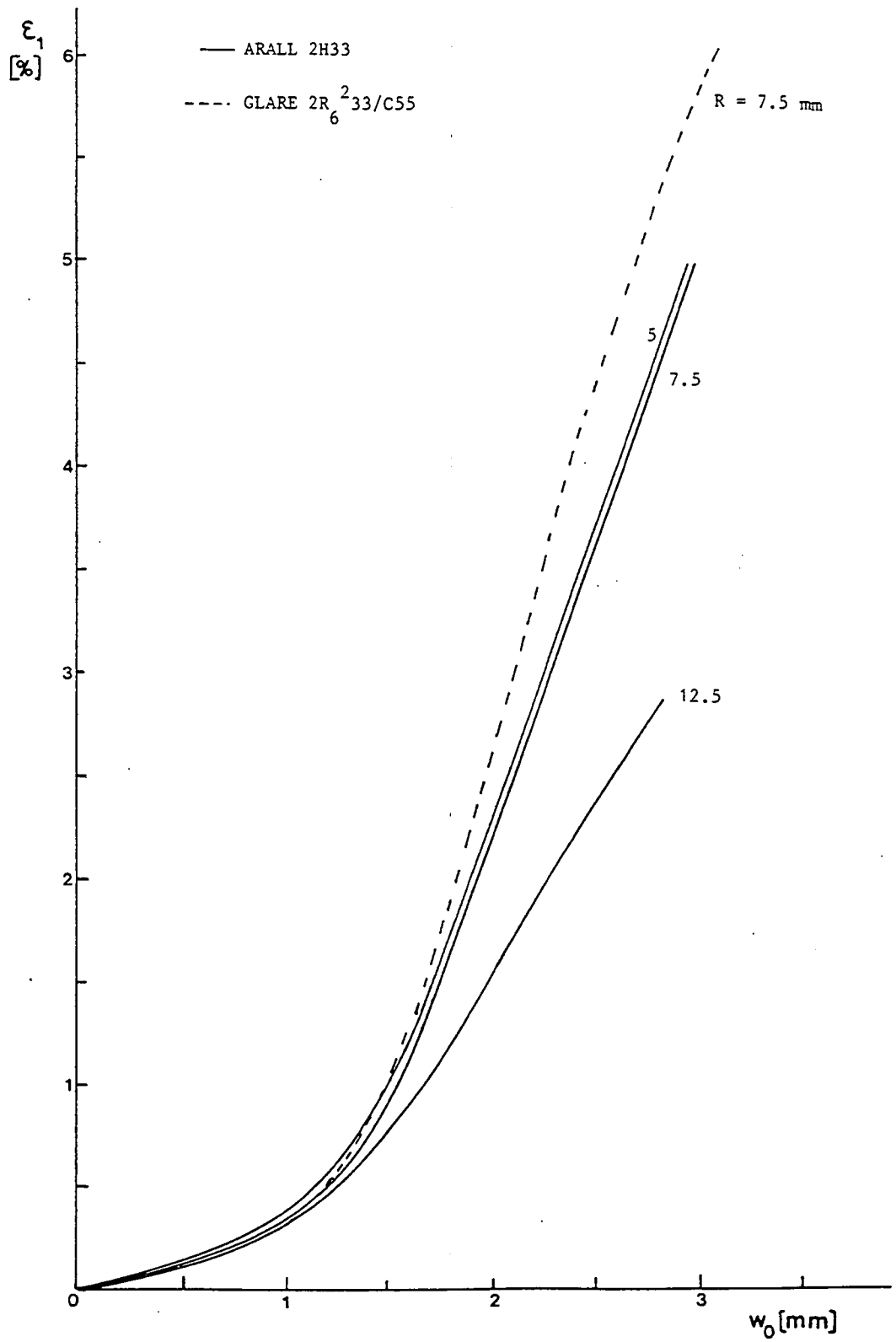
figure 10.28 Measured central strain for ARALL material as function
of the central deflection for various radii of the indentor.
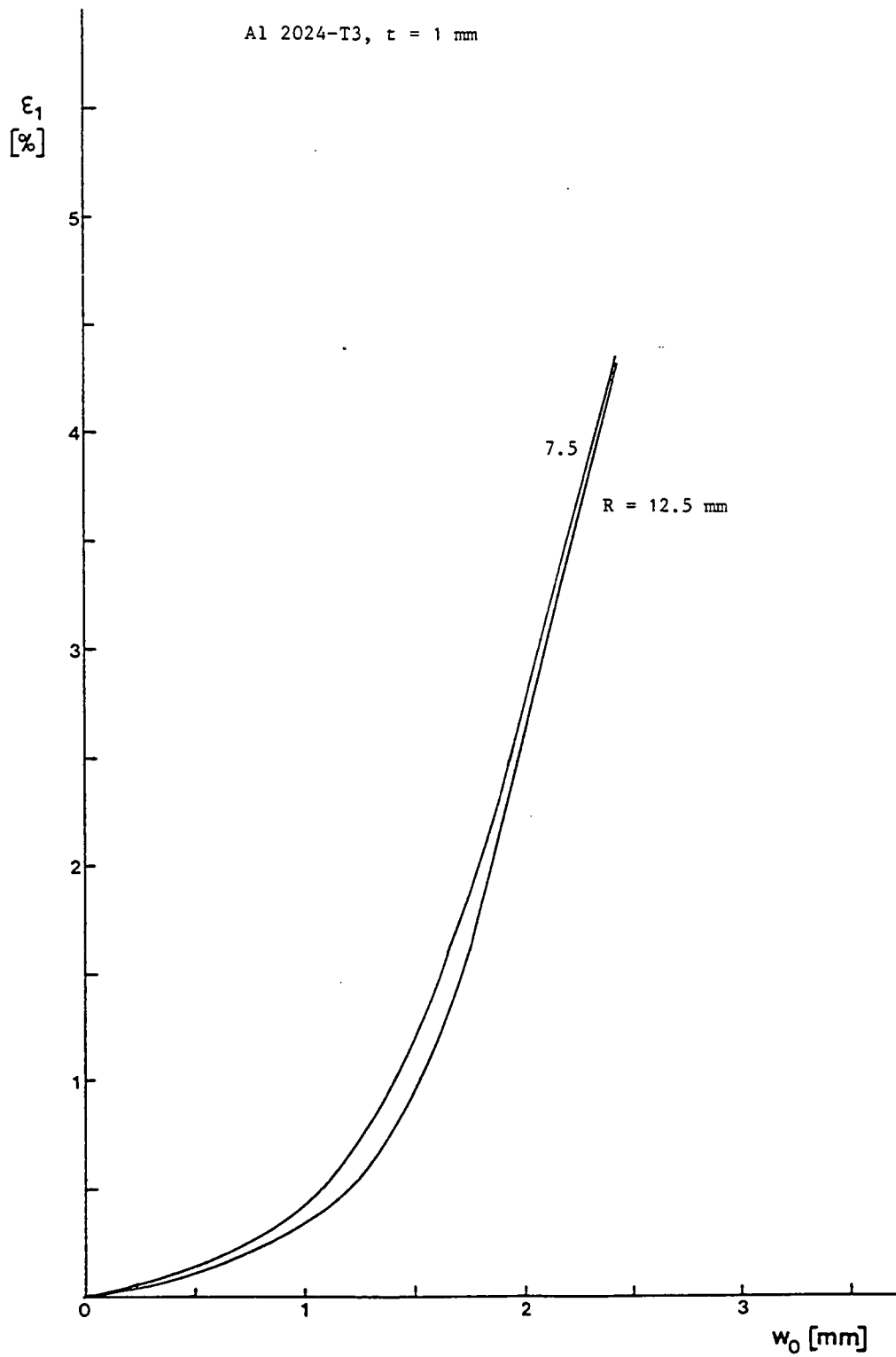
figure 10.29 Measured central strain as function of the central deflection for Al 2024-T3 for two radii of the indentor.
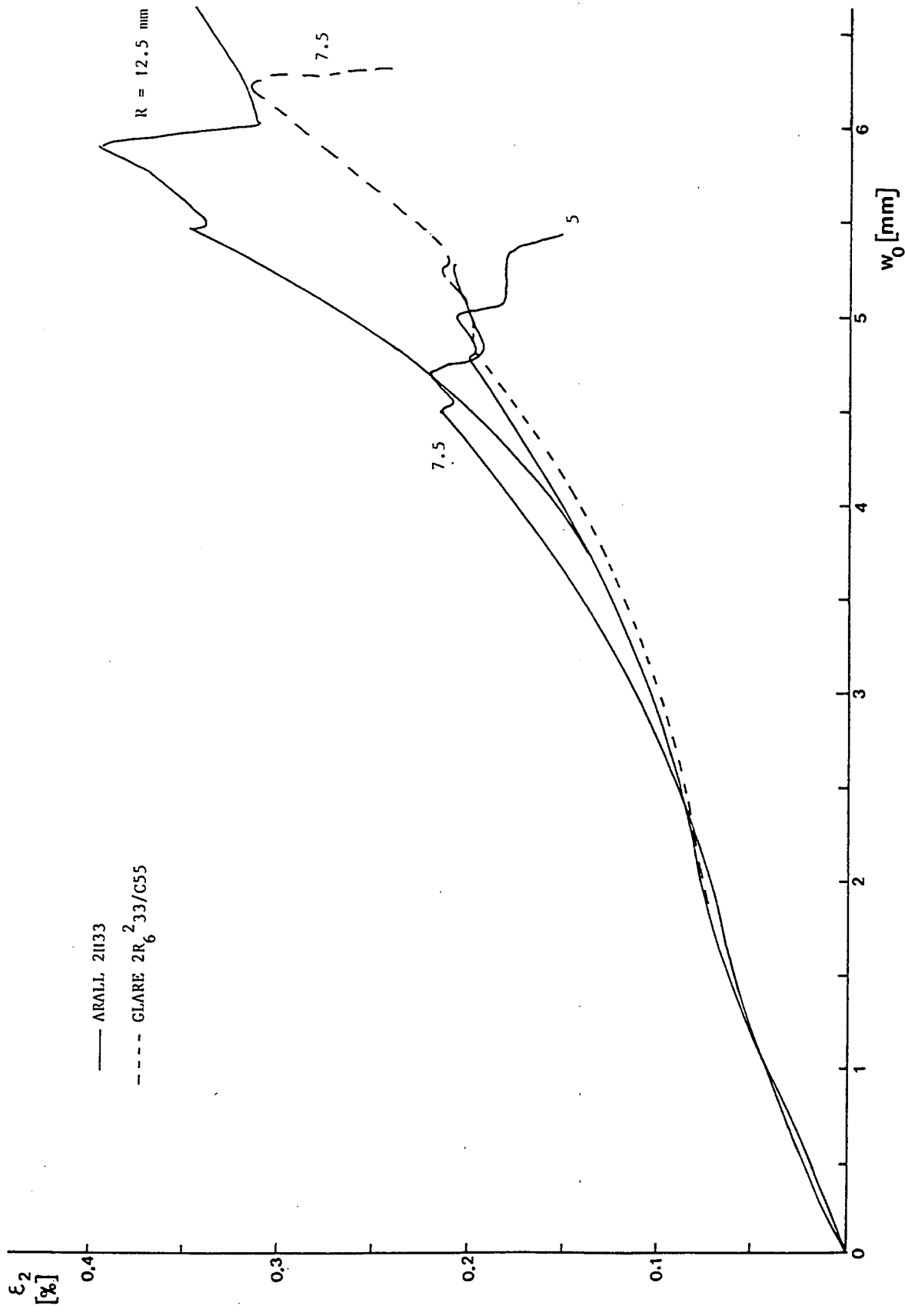
figure 10.30 Measured strain at r = 15 mm for ARALL material as function of the central deflection, for various radii of the indentor.

Al 2024-T3, t = 1 mm

figure 10.31 The measured strain at r = 15 mm for Al 2024-T3 material as function of the central deflection for two radii of the indentor.

chapter 11 Strain rate effects on the results of tensile and puncture tests

11.1 Introduction

The strain rate dependence of the material properties was already discussed in section 3.7. In the literature there is not much data available on the influence of the strain rate on the material properties of composite materials. T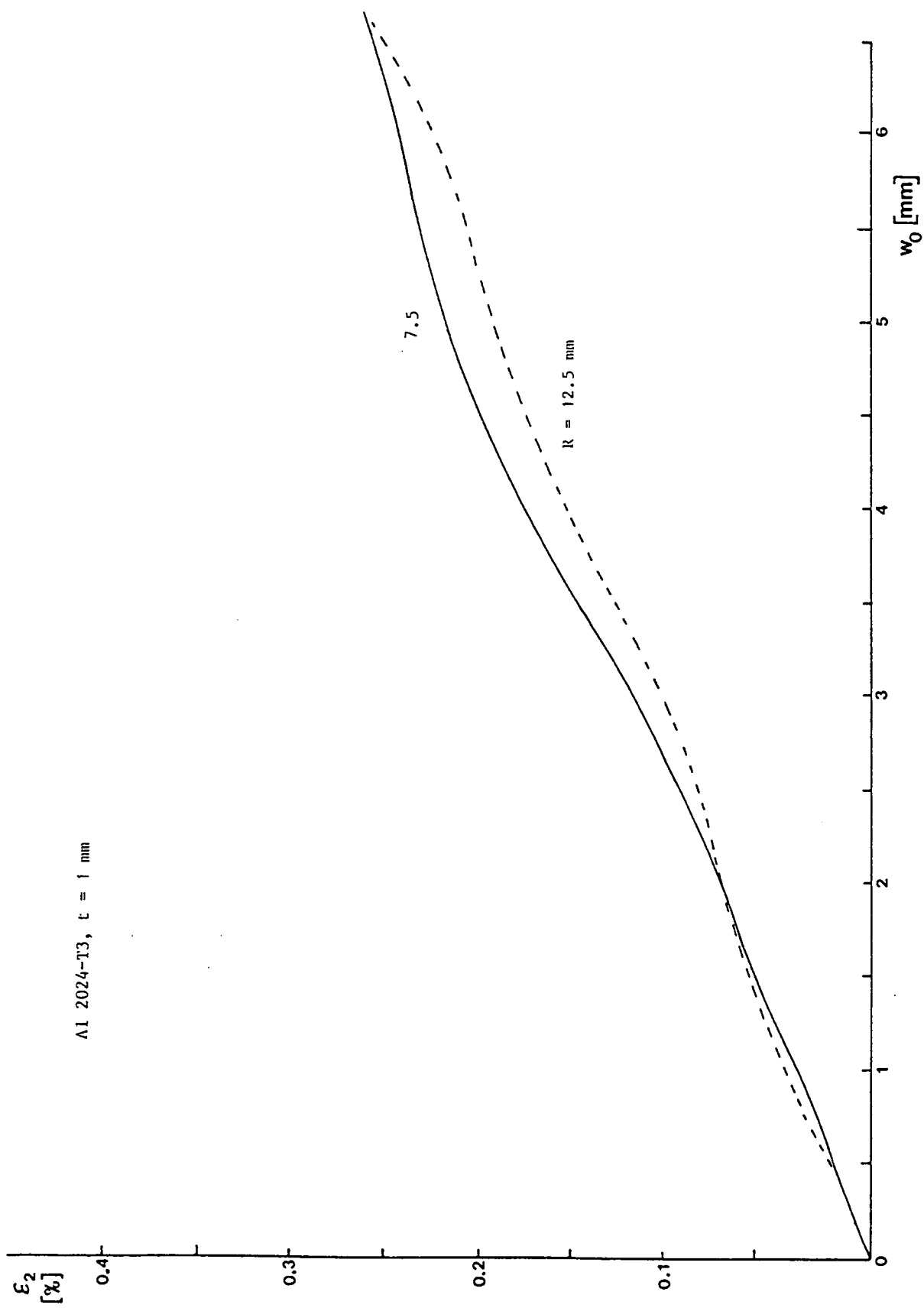his topic is generally not discussed in the papers concerning impact modelling. Quasi-static loading generally induces strain rates in the order of 10^{-4} s^{-1} in the material. However, the results of the strain measurements discussed in chapter 6 show that the strain rate induced by a drop weight impact tester will be in the order of 10^{2} s^{-1}, i.e. several orders of magnitude larger. High strain rate tensile tests with strain rates up to 70 s^{-1}, and puncture tests (perforation of a sheet specimen at a constant velocity, velocities up to 20 m/s) have been carried out. The tests were performed with a high speed hydraulic testing machine. In the present chapter the tests and the results are discussed.

11.2 Materials

The same materials were tested as used for the impact tests described in chapters 6 and 7. The ARALL codes used in this chapter has been explained in chapter 1 (introduction).

For the tensile tests:
- carbon/PEI, lay-up $[0_2/90_2]_s$, $[\pm45]_4$ and $[90]_8$. The lay-ups were chosen such that fibre dominant behaviour occurs for the first lay-up and matrix dominant behaviour for the last lay-up.
- monolithic aluminium Al 7075-T6, t = 1.55 mm.
- aramid ARALL 7H33, t = 1.35 mm
- R-glass GLARE $7R_2{}^2 33/C55$, t = 1.37 mm.

For the puncture tests:
- carbon/PEI, lay-up $[0_2/90_2]_{2s}$
- carbon/epoxy, lay-up $[0/60/-60/90/-60/60]_s$
- monolithic aluminium Al 2024-T3, t = 0.86 and 1.55 mm
   Al 7075-T6, t = 1.0 and 1.55 mm

Al 6061-T6. t = 1.5 mm

- aramid ARALL 2H33, t = 1.35 mm
- different grades of GLARE; the R-glass fibres RA 9041
  (designated as the R_4 prepreg, see chapter 7) and RC 10 (R_2
  prepreg) were tested. The lay-ups are given in table 11.2.

11.3 Test methods

The tensile and puncture tests were both performed with a high speed Schenk hydraulic testing machine of the Akzo Research Laboratory (ARLA) in Arnhem, see figure 11.1 (puncture test configuration) and figure 11.2 (tensile test configuration). This machine is capable of reaching crosshead speeds up to 20 m/s, The crosshead speed during the test is constant. The high speed testing machine with a piezo electrical load cell was not very accurate at low speeds (v < 1 m/s). Therefore the quasi-static tensile tests (crosshead speed of 2 mm/min) were performed with a 10 kN MTS hydraulic testing machine on the same type of tensile specimens.

The tensile specimens are shown in figures 11.3 and 11.4. A strain gage was mounted at the centre of the specimens to measure the strain (rate).
The puncture tests were performed on 60x60 mm^2 square specimens with a clamped circular test area with a diameter of 40 mm. The indentor has a hemispherical tip with a radius of 10 mm. The moving part of the machine is the clamping: the specimen is pushed against the indentor. The strain rate in the material induced by this test is not uniform in the specimen and not constant in time. The magnitude of the mean strain rate will be estimated in section 11.5 (point 6).

The output of the load cell and displacement of the cross head of the testing machine and the output of the strain gage on the tensile specimen were recorded by a computer and stored on a disk.

11.4 Experimental results

tensile tests

The results of the tensile tests are presented in table 11.1 and in figures

11.5 to 11.8. The results are the mean values of 3 tests.

The fracture surfaces (as examined with the naked eye) do not change much at higher strain rates , except for the $[90]_8$ carbon/PEI and GLARE materials. The $[90]_8$ carbon/PEI material failed at 1 point at a strain rate of 4.10^{-4} and 7 s^{-1} and at 3 to 4 points at a strain rate of 45 and 65 s^{-1}. At the higher strain rates the specimens broke in more than two pieces, probably due to stress wave effects. The GLARE material did not show much delamination after failure at quasi-static strain rates, but it delaminated from the fracture in the centre to the clamping during failure at the higher strain rates.

puncture tests

The results of the puncture tests are given in table 11.2, and in figures 11.9 to 11.13. The results are mean values of at least two tests; the scatter is less than 5%.

The force F_f, the central deflection $w_{0,f}$ and the failure energy U_f are the values at the first significant load drop, which indicates failure in the specimen. For most of the specimens this is the moment when the maximum force is reached, except for the materials GLARE $2R_4^3 32$, $2R_4^2 33/C55$, carbon/PEI and aramid ARALL 2H33. For these materials the force still rises after first failure.

Pictures of some typical specimens after failure are shown as figures 11.14 to 11.16. In the monolithic Al 2024-T3 and 7075-T6 specimens a plug is punched out of the sheet, the Al 6061-T6 shows a 'petaling' type of failure. The fracture modes did not change with the strain rate.

11.5 Discussion

tensile tests

1. At cross head speeds of 10 m/s and higher the load cell of the high speed hydraulic testing machine generally showed 13 kHz vibrations (see figures 11.5, 11.9, 11.10 and 11.11). The vibrations correspond with the resonant frequency of the load cell and may disturb the measured values.

The cross head speed was kept low enough to assure that this influence was small.

2. The monolithic and aramid ARALL materials showed an unexpected and relatively large decrease of Young's modulus (table 11.1). The modulus was determined by linear regression. The approximately 10% decrease of Young's modulus is probably due to inaccuracies of the measurements. The literature[6,7] shows that the strain rate affects the yield stress and the strength of the material, but a decrease of Young's modulus is unlikely.

The stiffness of the other materials and also the stiffness of the puncture specimens are less dependent on the strain rate.

3. The R-glass GLARE material showed a high strain rate dependence during the tensile tests. (σ_u = 666 MPa quasi-statically, and σ_u = 832 MPa at $\dot{\varepsilon}$ = 67 s^{-1}, a ratio of 1.25). Also the $[0_2/90_2]_s$ carbon/PEI material showed a large increase of the strength at a strain rate of 47 s^{-1}, but this observation is based on one test only. The monolithic material showed a minor decrease of the strength; thus the influence of the strain rate on the R-glass fibre is therefore even higher than on the GLARE material. The sensitivity of the glass fibre to the strain rate and the moderate influence of the strain rate on the material properties of the aluminum alloy was expected and was already discussed in section 3.7.

4. The strain rate has the largest influence on the tensile strength of the carbon/PEI $[90]_8$ material (see table 11.1 and figure 11.8).This is caused by the fact that the strength of the matrix material, which determines the transverse strength, is more affected by the strain rate than the strength of the fibre.

puncture tests

5. Figures 11.9, 11.10 and 11.11 show the influence of the cross head speed on the force-deflection curve. A higher speed leads to an increase of the strength. The curves rise to higher loads.

To include the strain rate effects of the material in an impact model, it appears that if sufficient to make the failure criterion strain rate dependent. The strain rate does not influence the deformation of the sheet,

because this deformation depends on the stiffness only, and not at the strain rate.

6. The mean strain rate during the puncture test can be estimated as follows. The aramid ARALL 2H33 material will fail when the failure strain of the aramid fibre (2 %) is reached. At a cross head speed of 1 m/s this happens at a central deflection of 3.66 mm, this corresponds with t = 3.66 ms after initial contact. The mean strain rate is in that case $\dot{\varepsilon}$ = 0.02/0.00366 = 5.5 s^{-1}. The strain rate is not constant during the test because the strain increases more than proportionally with the deflection. The estimated mean strain rate at 10 m/s is: $\dot{\varepsilon}$ = 0.02/0.000405 = 49 s^{-1}. The estimations indicate that the mean strain rate in the puncture test specimens is comparable to the high strain rates applied on the tensile specimens.

7. The monolithic material shows an unexpected increase of the failure energy during the puncture test when the cross headspeed is increased from 1 to 10 m/s (table 11.2 and figure 11.12). The GLARE material also shows a significantly higher failure energy for a larger crosshead speed. The influence of the cross head speed on the failure energy of aramid ARALL and the carbon composites is smaller. As already mentioned this improvement of the failure energy is due to a higher deflection and force at failure; the stiffness of the specimen will not be influenced (see figures 11.9, 11.10 and 11.11).

8. The monolithic aluminium alloy has the highest failure energy during the puncture tests, followed by GLARE, aramid ARALL and the carbon composites (figure 11.12 and 11.13). The cross-ply GLARE variants behave better than the unidirectional ones (figure 11.13).

9. The energy absorption after first failure is small for the monolithic aluminium alloy puncture specimens: the force drops quickly to zero after failure, see figure 11.10. For the carbon composites there is more energy needed to puncture through the specimen after first failure (figure 11.11). The ARALL laminates (figure 11.9) show a behaviour between that of monolithic aluminium alloy and carbon composite specimens.

11.6 Conclusions

1. A strain rate dependent behaviour of the materials is observed in the ultimate tensile strength and strain to failure. The influence on the stiffness of the specimens is small. As a consequence, the strain rate dependence of the material properties of an impact model, should be included in the failure criterion of the model. The strength of the material will increase.

2. R-glass GLARE showed a significant increase of the tensile strength at high strain rates. The largest effect on the strength was measured for carbon/PEI $[0/90]_s$. The influence of the strain rate on the strength of monolithic material and aramid ARALL is much smaller.

3. In the puncture tests the monolithic aluminium alloy specimens show a significant increase of the failure energy when the cross head speed is increased from 1 to 10 m/s. The increase of the failure energy of GLARE can be explained from the increase of the strength of the glass fibre at higher strain rates. The behaviour of the monolithic aluminium alloys was remarkable and could not be explained. This material showed the best behaviour during the puncture tests, followed by GLARE, aramid ARALL and the carbon composites. The cross-ply GLARE variants behaved better than the unidirectional types.

references

1. Lammerant, L.; Modellering van impakt van komposieten (in Dutch), Master Thesis KU Leuven/ TU Delft 1990.

2. Marom, G.; Harel, H.; Neumann, S.; Friedrich, K.; Schulte, K.; Wagner, H.D.; Fatigue behaviour and rate-dependent properties of aramid fibre/ carbon fibre hybrid composites, Composites, Vol.20, No.6; pp.537-544, 1989.

3. Daniel, I.M.; Yaniv, G.; Peimanidis, G.; Hygrothermal and strain rate effects on properties of graphite/epoxy composites, J.Eng.Materials and Technology, Vol.110, pp.169-173, 1988.

4. Chiem, C.Y.; Liu, Z.G.; The relationship between tensile strength and

shear strength in composite materials subjected to high strain rates, J.Eng.Materials and Technology, Vol.110, pp.110-194, 1988.

5. Daniel, I.M.; Liber, T.; Strain rate effects on mechanical properties of fiber composites, NASA report CR-135087, 1976.

6. Burstow, C.G.; Laird, M.P.B.; Lovell, M.C.; Rodgers, A.L.; Stewart, I.J.; The response of 7075-T73 aluminium alloy at high rates of strain, in: Chiem, C.Y. et al. (ed.); Impact loading and dynamic behaviour of materials, pp.557-564, 1987.

7. Harding, J.; Material behaviour at high rates of strain, in: Chiem, C.Y. et al. (ed.); Impact loading and dynamic behaviour of materials, pp.23-41, 1987.

material	code	t (mm)	$\dot{\varepsilon}$ (s^{-1})	σ_u (MPa)	ε_u (%)	E (GPa)
monolithic Al alloy	Al 7075-T6	1.55	4.10^{-4}	593		70
			3.5	546		64
			35	548		63
aramid ARALL	7H33	1.35	4.10^{-4}	823	2.50	64
			3.4	830	2.42	54
			40	830	2.28	57
			67	874	2.45	50
GLARE	7R$_2$^{2}33/C55	1.37	4.10^{-4}	666	3.40	56
			3.8	753	4.30	54
			38	803	4.80	57
			69	832	5.53	50
thermoplastic composites	carbon/PEI [0$_2$/90$_2$]$_s$	1.37	4.10^{-4}	786	1.23	63
			4.2	747	1.25	58
			47*	980	1.42	63
	carbon/PEI [±45]$_{2s}$	1.37	4.10^{-4}	261	17.0	13.6
			7	278	15.0	14.2
			47	287	15.5	14.7
	carbon/PEI [90]$_8$	1.37	4.10^{-4}	48	0.64	7.7
			7	64	0.86	8.0
			45	77	0.99	7.6
			65	80	1.14	7.1

table 11.1 Results of the high strain rate tensile tests.

(* only one specimen tested)

385

| material	t (mm)	1 m/S			10 m/S			20 m/S		
		F_f (kN)	$w_{o,f}$ (mm)	U_f (J)	F_f (kN)	$w_{o,f}$ (mm)	U_f (J)	F_f (kN)	$w_{o,f}$ (mm)	U_f (J)
Al 2024-T3	0.86	8.74	7.92	29.4	9.89	8.70	37.1			
	1.55	13.3	6.91	42.6	18.2	8.91	73.8			
Al 7075-T6	1.0	6.2	4.5	10.2	7.0	5.2	13.1			
	1.55	9.9	4.4	18.9	13.5	5.3	30.5			
Al 6061-T6	1.5	13.3	10.2	69.7	13.3	9.8	66.4			
2H33	1.35	4.34	3.66	7.1	4.44	4.05	7.3	4.69	4.24	10.0
$2R_4^3 32$	0.71	5.09	5.96	11.7	5.36	6.24	13.3			
$2R_4^3 32$	1.04	4.29	4.70	8.06	3.79	4.58	7.16			
$2R_4^3 32/C73$	1.06	8.90	6.67	22.8	9.29	6.89	24.0			
$2R_4 33$	1.14	7.28	5.85	16.5	7.76	6.10	19.2			
$2R_4^4 32/C55$	1.15	11.5	7.96	36.1	14.2	8.89	51.6			
$7R_2^2 33/C55$	1.37	7.04	4.22	12.1	8.96	4.96	18.6	9.67	4.88	19.2
$2R_4^2 33$	1.45	7.54	5.18	17.6	8.14	5.46	19.8			
$2R_4^2 33/C55$	1.45	10.2	5.60	23.0	12.5	6.44	33.9			
carbon/ep.	2.00	3.51	2.59	4.80	3.64	2.42	4.12	3.69	2.35	4.08
carbon/PEI	2.75	4.54	3.57	11.4	4.46	3.61	12.8			

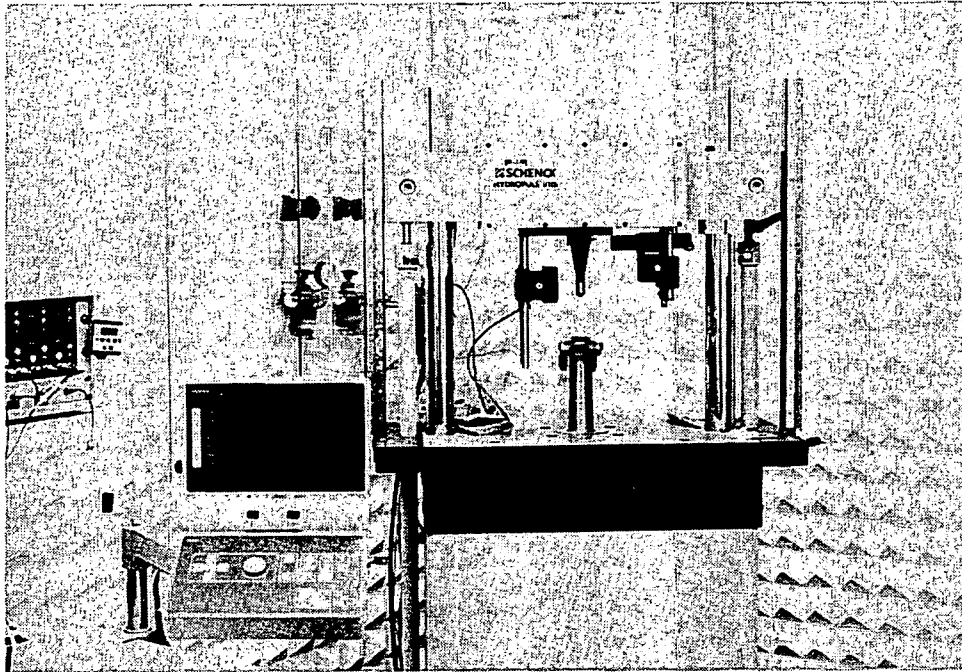table 11.2 Results of the high speed puncture tests.
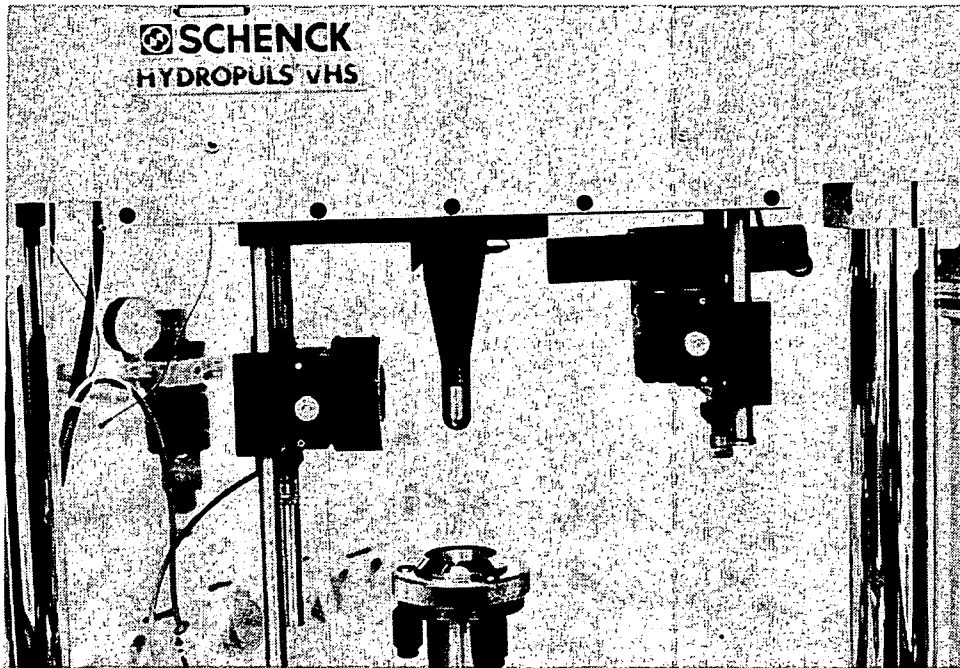
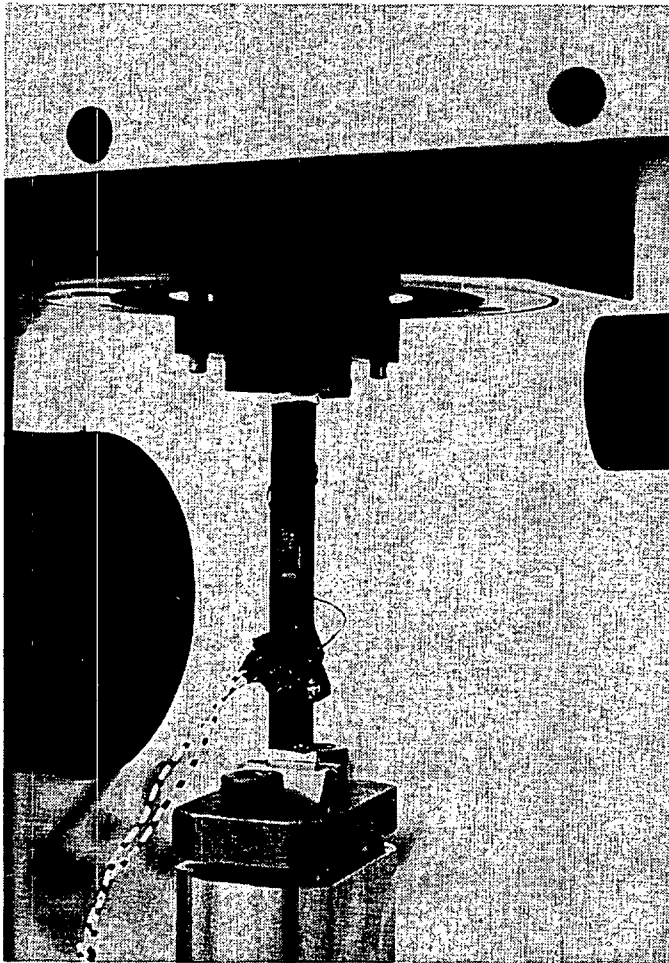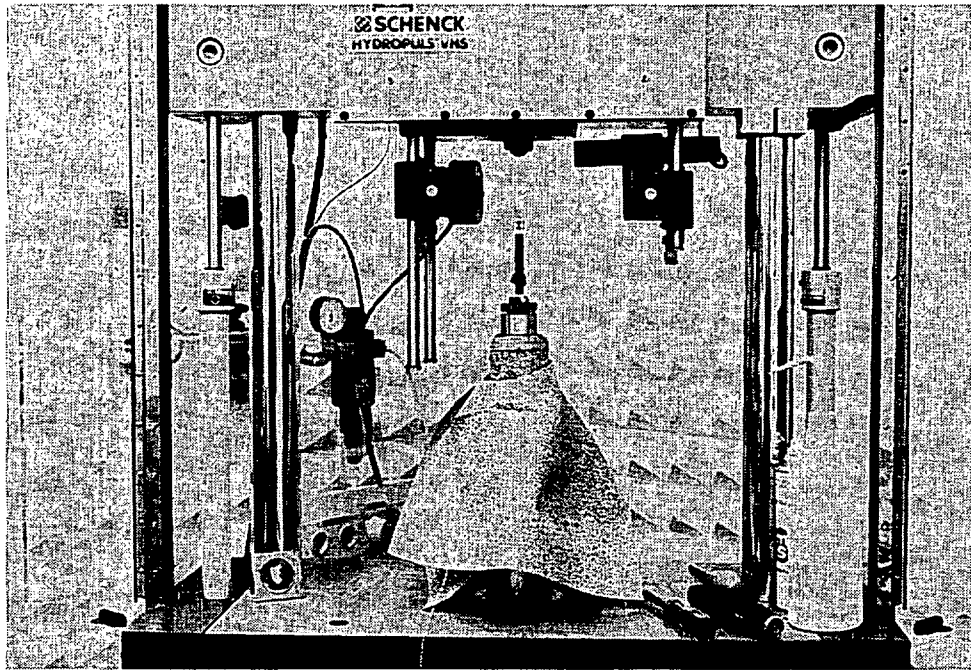figure 11.1 The high speed hydraulic testing machine, puncture test.

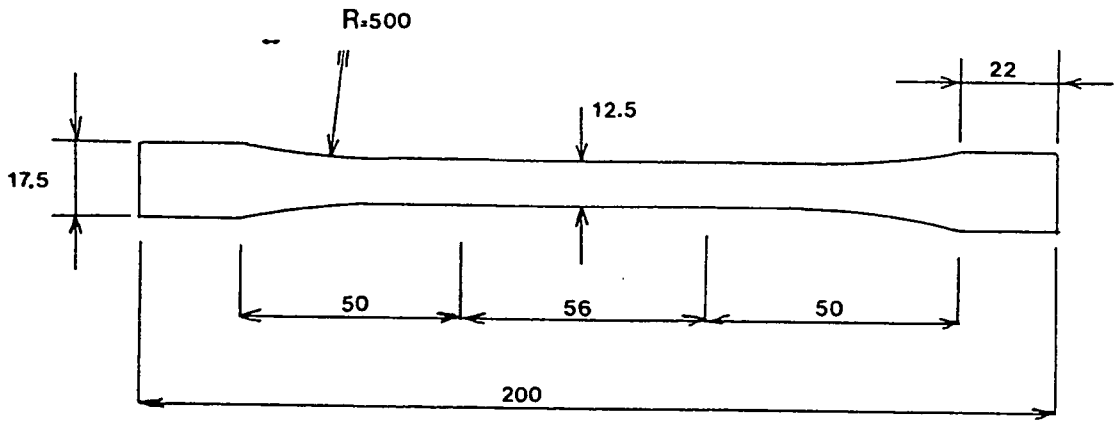figure 11.2 The high speed hydraulic testing machine, tensile test.

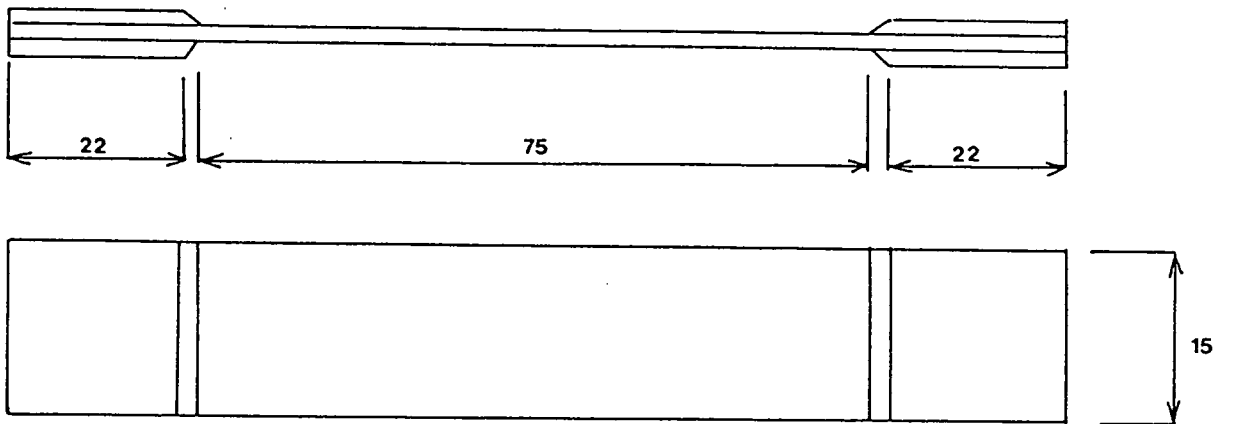figure 11.3 Tensile test specimen for monolithic aluminium and ARALL.

figure 11.4 Tensile test specimen for composite materials.

σ [MPa]

$\dot{\mathcal{E}} = 69 \ s^{-1}$

$\dot{\mathcal{E}} = 4.10^{-4} \ s^{-1}$

GLARE $7R_2{}^2 33/C55$

$\mathcal{E}$ [%]
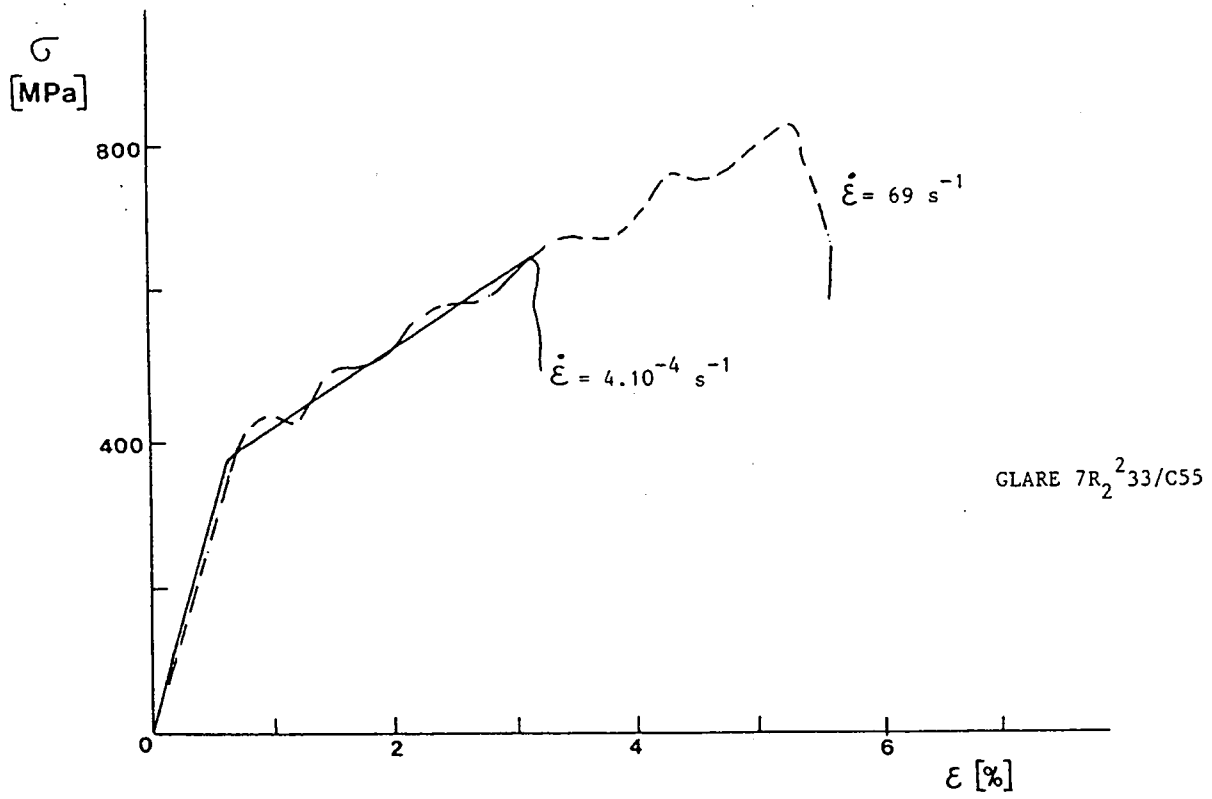
figure 11.5 Stress-curves during tensile test of GLARE $7R_2{}^2 33/C55$.

σ_u [MPa]

aramid ARALL 7H33

GLARE $7R_2{}^2 33/C55$

Al 7075-T6

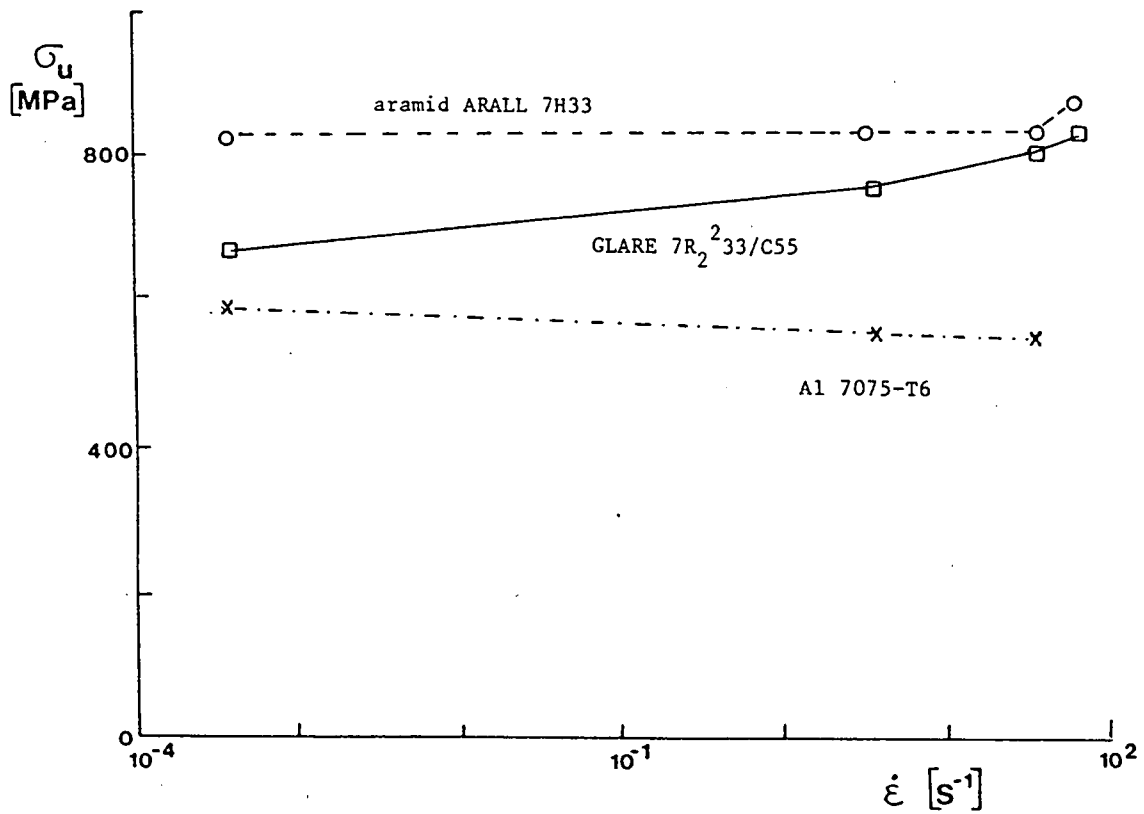$\dot{\mathcal{E}}$ [s^{-1}]

figure 11.6 The ultimate stress as function of the strain rate for monolithic material and ARALL.

390

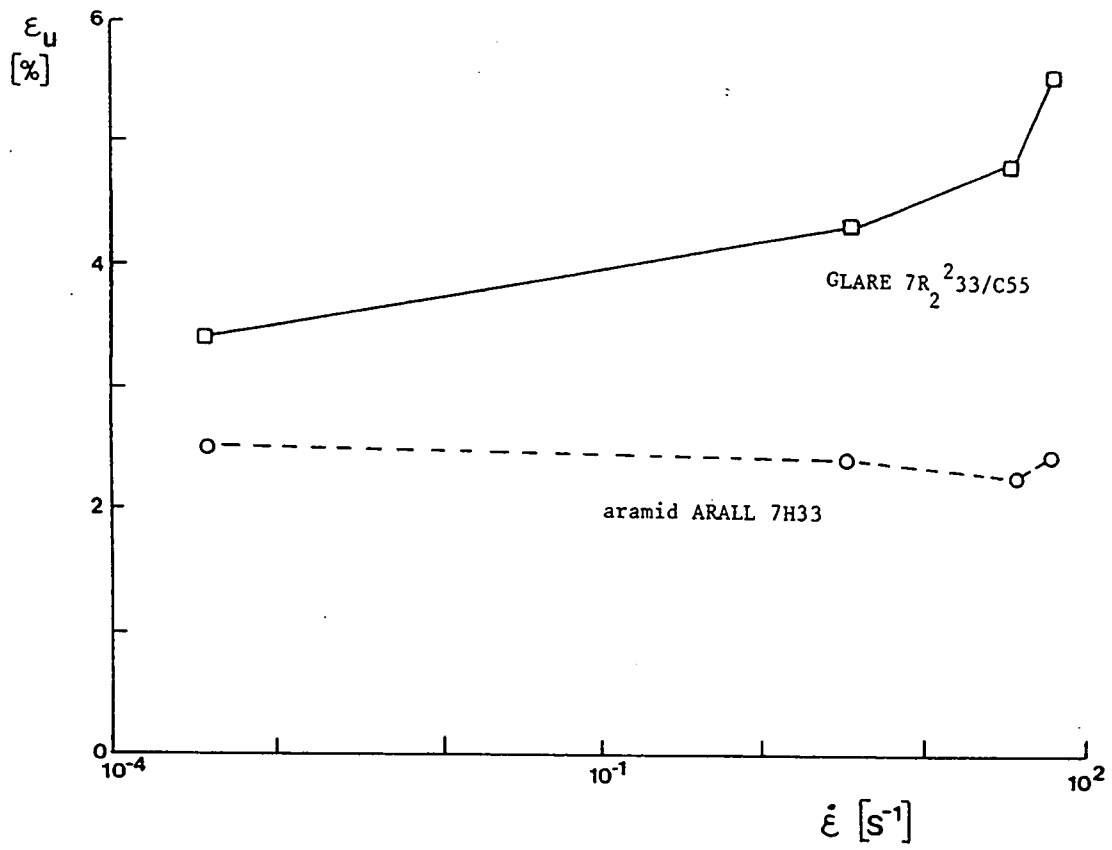figure 11.7 The strain at failure as function of the strain rate for ARALL laminates.

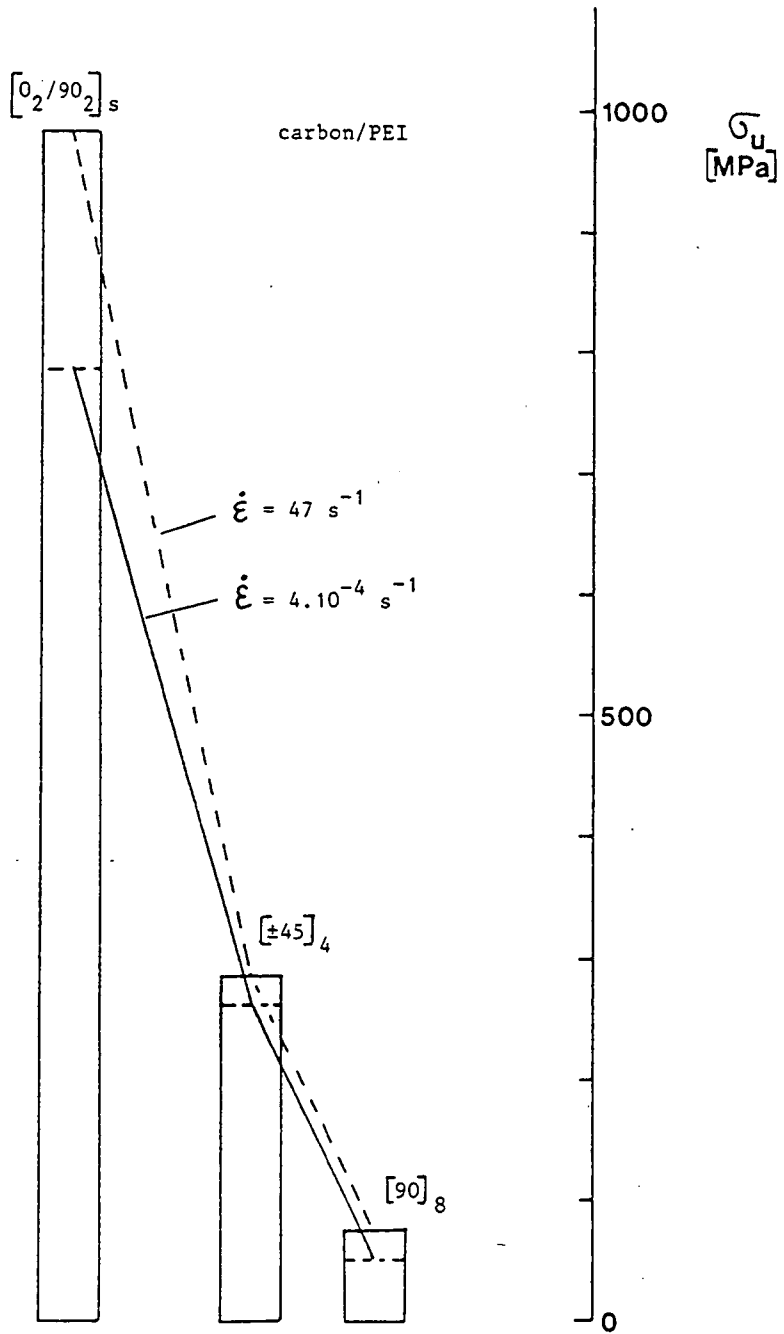figure 11.8 The failure stress at two strain rates for carbon/PEI
material.
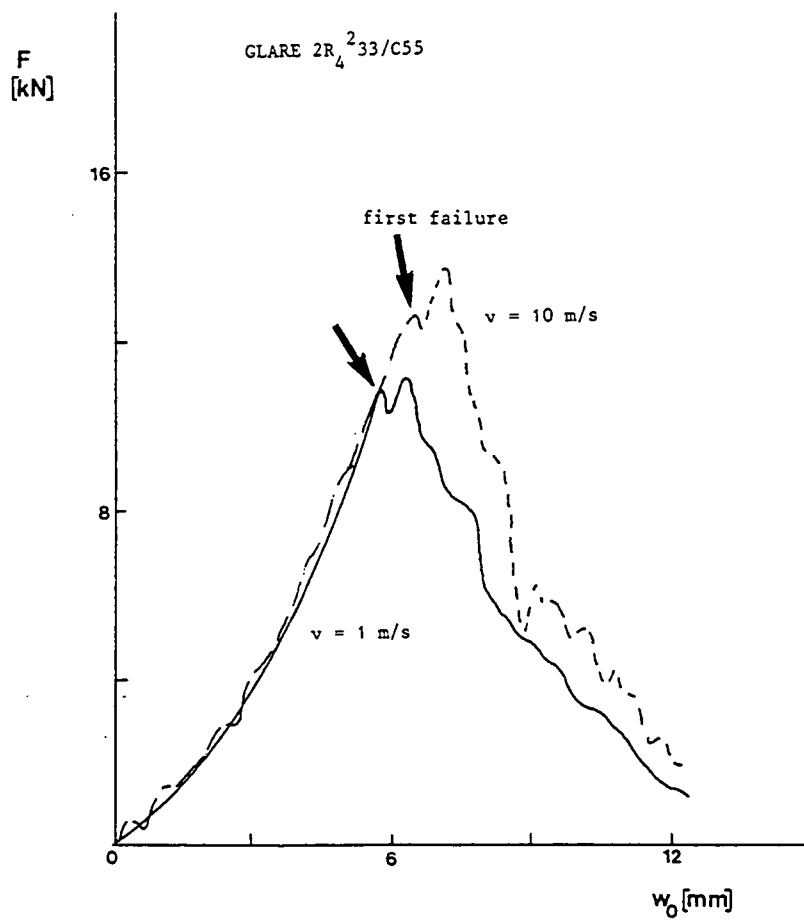
figure 11.9 Force-deflection curves during the puncture tests for GLARE $2R_4^2$ 33/C55 material, at two cross head speeds.
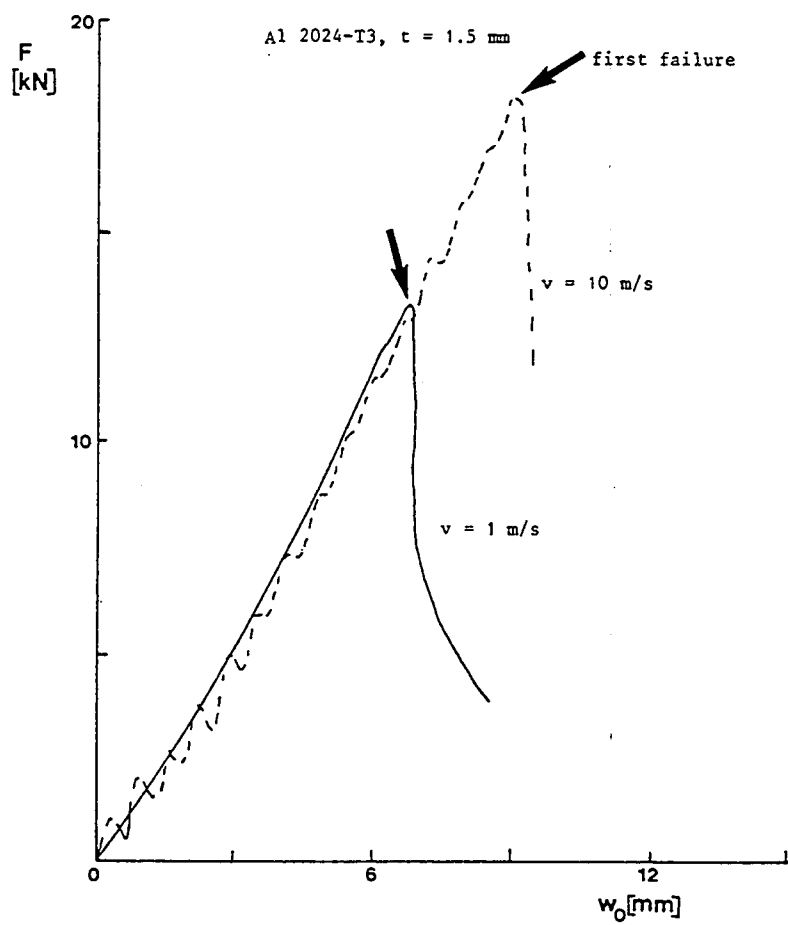
figure 11.10 Force-deflection curves during puncture tests of Al 2024-T3, t = 1.5 mm, at two cross head speeds.
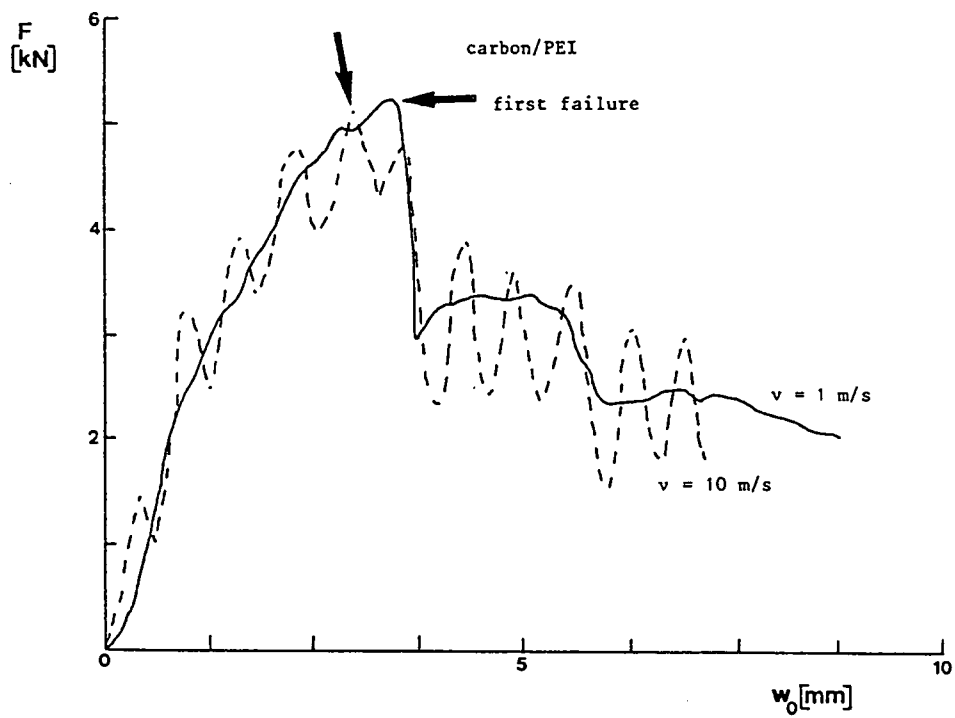
figure 11.11 Force-deflection curves during puncture tests of carbon/PEI material, at two cross head speeds.

Al 2024-T3, t=1.5 mm

v = 10 m/s

v = 1 m/s

Al 7075-T6, t=1.5 mm

$2R_4^{2}33/C55$

$7R_2^{2}33/C55$

$2R_4^{2}33$

7H33

carbon/PEI

carbon/epoxy

U_f
[J]

80

40

0
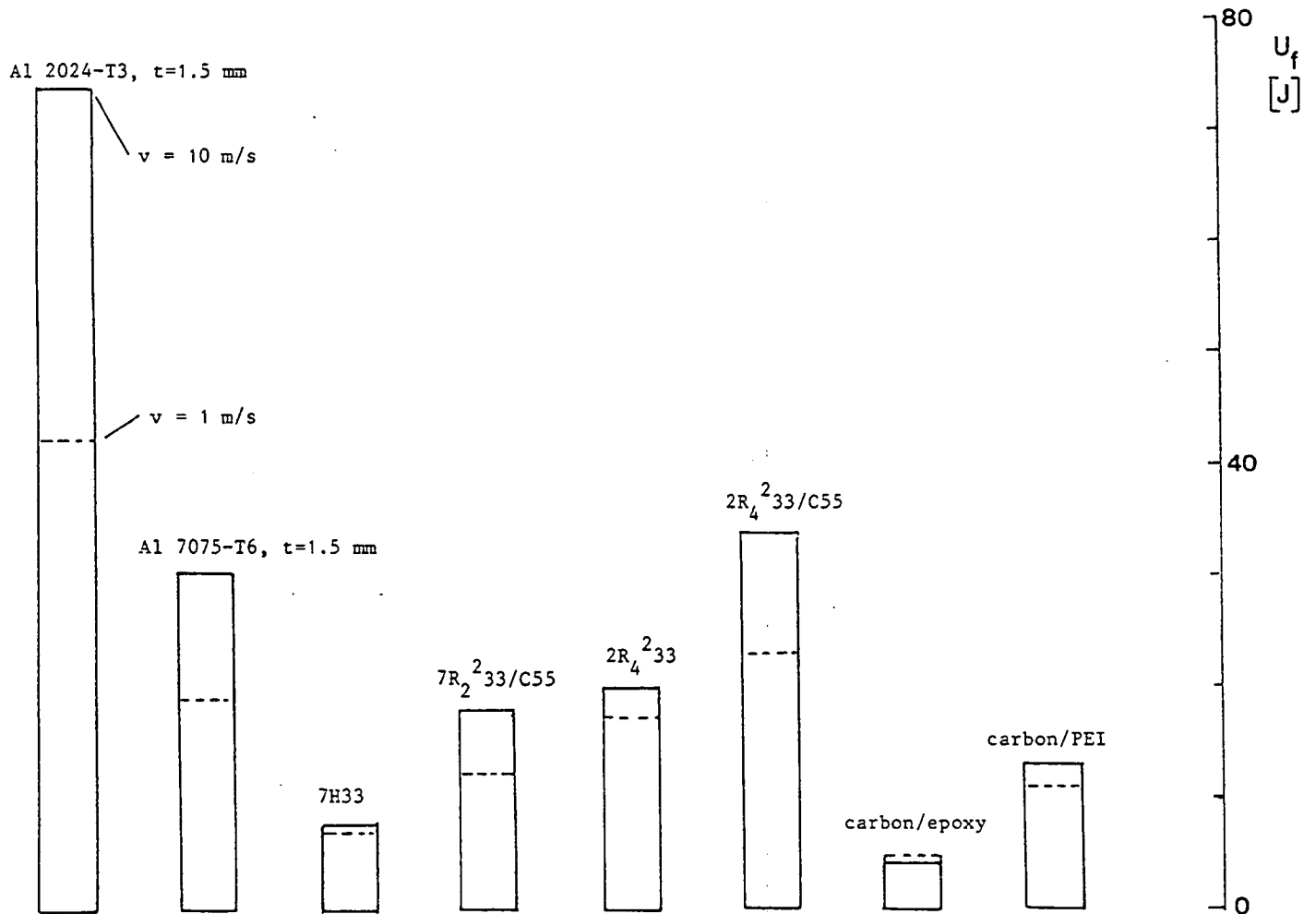
figure 11.12 The absorbed energy at first fracture during puncture
tests of various materials, at two cross head speeds.

U_f [J]

60

40

○ monolithic Al 2024-T3

□ e

□ crossed GLARE variant
◇ UD GLARE variant

□ c   □ f

20

◇ g   GLARE
d ◇

◇ a

◇ b

0   1   2

t [mm]

a. $2R_4 32$

b. $2R_4{}^3 32$

c. $2R_4{}^3 32/C73$

d. $2R_4 33$

e. $2R_4{}^2 32/C55$

f. $2R_4{}^2 33/C55$

g. $2R_4{}^2 33$

figure 11.13 Comparison of the absorbed energy at first fracture during puncture tests of monolithic material and GLARE, v = 10 m/s.

figure 11.14 Puncture specimen of Al 6061-T6.

figure 11.15 Puncture specimen of Al 2024-T3.

figure 11.16 Puncture specimen of GLARE $2R_4^2$33/C55.

chapter 12 Non linear impact modelling

12.1 Introduction

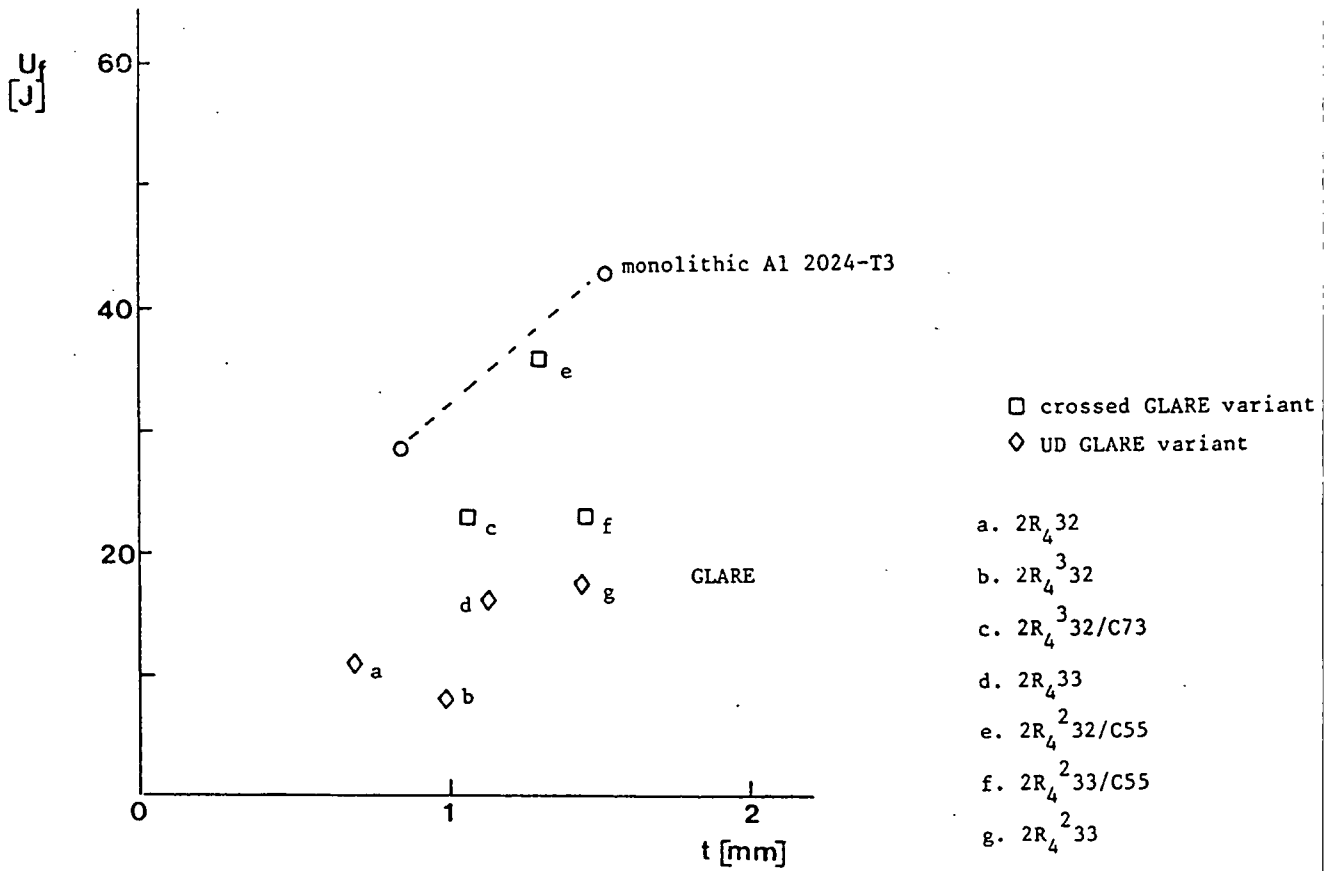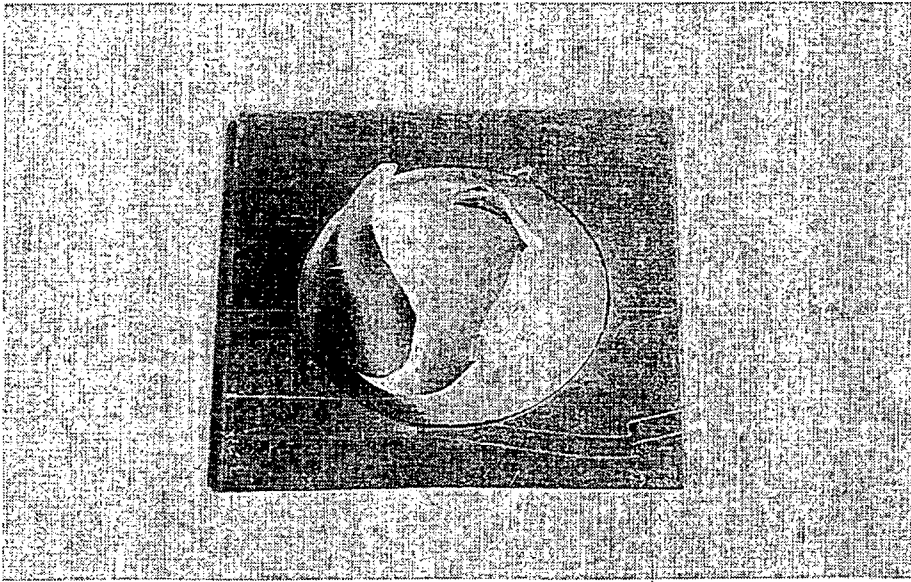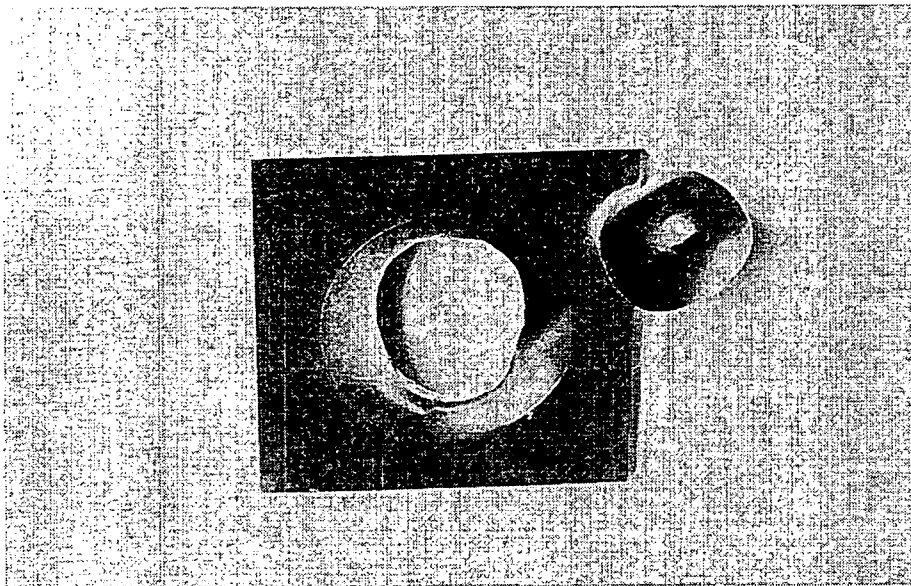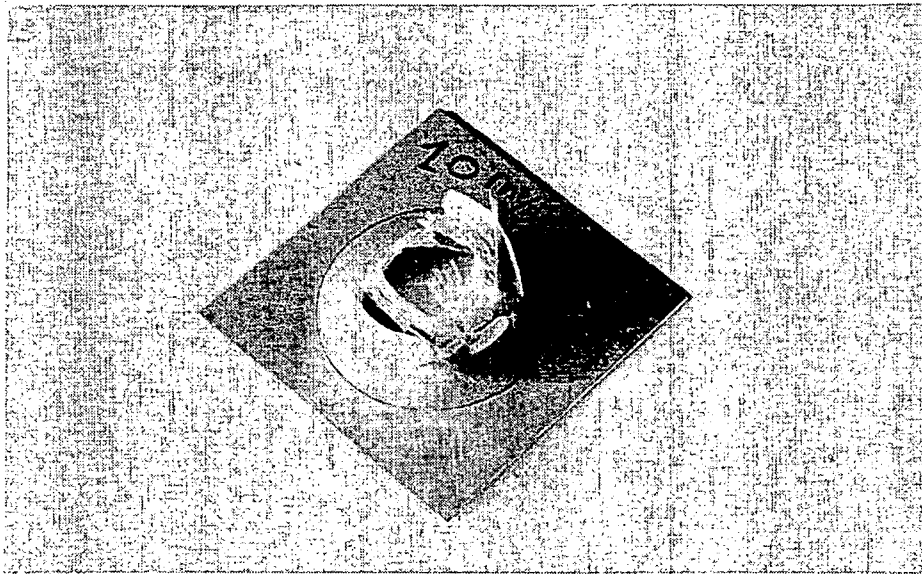In this chapter a non linear elastic and a non linear elasto-plastic impact model will be presented. Both models are analytical and will be derived on the basis of the simplified von Kármán equations as discussed in chapter 10. A kind of a 'building block approach' will be used. In section 12.2 a linear elastic model will be derived as a first step. The contact between impactor and plate in this section is established by assuming a rigid contact. Section 12.3 treats a Hertzian contact between impactor and plate. Section 12.4 deals with finite element calculations and starts with a linear elastic case. The results of these linear elastic calculations are compared with the results of section 12.2. Section 12.5 continues with non linear finite element calculations. The results of the non linear finite element model will be compared with the experimental results of chapter 6, and with the analytical results of the non linear model presented in section 12.6. The last section (section 12.7) deals with an elasto-plastic model.

12.2 Linear elastic analysis of impact on a clamped isotropic plate under initial tensile loading

12.2.1 The model

As pointed out by Goldsmith[1], the most simple way to model the impacted specimen (schematically shown in figure 12.1), is obtained by a mass-spring system as drawn in figure 12.2. The equations which describe this mass-spring model, were not found in the literature and will be derived in this section.

The clamped circular specimen is supposed to have a constant stiffness c and an equivalent mass m_{eq}. It is impacted by a mass m_p with an impact velocity v_o. The following three assumptions are made:

1. Contact between the impactor and the plate is maintained during impact. Tests have shown that this is a reasonable assumption. In some cases only during the initial phase of the impact contact may be lost. The initial

value of the velocity $v_0^{\bullet}$ at t=0 is derived from the conservation of momentum:

$$v_0^{\bullet} = \frac{m_p}{m_p + m_{eq}} \, v_0 \qquad (12.1)$$

2. The stiffness of the system is practically equal to the static stiffness of the plate. For low velocities and a relatively large impactor mass the effect of stress waves and higher order vibrations in the plate may be neglected, and the deformation will be quasi-static. The stiffness is then supposed to be independent of the deflection, i.e. it is constant. This is a reasonable assumption for deflections smaller than the plate thickness. The stiffness of the plate can be derived from Timoshenko and Woinowsky-Krieger[2]. The strain energy for pure bending of an isotropic circular plate (diameter 2a, thickness t, material stiffness E, Poisson's ratio ν) is:

$$U_{plate} = \frac{D}{2} \int_0^{2\pi} \int_0^a \left[\left[\frac{\delta^2 w}{\delta r^2} \right]^2 + \frac{1}{r^2} \left[\frac{\delta w}{\delta r} \right]^2 + \frac{2\nu}{r} \left[\frac{\delta w}{\delta r} \right] \frac{\delta^2 w}{\delta r^2} \right] r \, dr \, d\phi$$

with $\quad D = \dfrac{E \, t^3}{12 \, (1-\nu^2)} \qquad (12.2)$

For a point loading in the centre of a clamped circular plate the shape of the dent can be described by[2]:

$$w = w_0 \left[1 + \left(\frac{r}{a} \right)^2 \left(2 \ln \left(\frac{r}{a} \right) - 1 \right) \right] \qquad (12.3)$$

After integration of equation 12.2, with a substitution of equation 12.3, the internal strain energy of the plate can be expressed as:

$$U_{plate} = \frac{8 \pi D}{a^2} w_0^2 = \frac{1}{2} c \, w_0^2 \; \Rightarrow \; c = \frac{16 \pi D}{a^2} = \frac{4 \pi E t^3}{3(1-\nu^2)a^2}$$

$$(12.4)$$

with c as the spring stiffness of the plate. Spring stiffnesses of a circular and a square plate are presented in table 12.1 for two edge

conditions. The table shows that the boundary conditions of the plate have a large influence on its stiffness. The difference in stiffness between a circular and a square plate with the same dimensions is relatively small.

The deflection field of a circular plate (equation 12.3) can also be used to calculate the kinetic energy of the plate. If its rotatory inertia is neglected the kinetic energy can be expressed as:

$$T_{plate} = \int_0^a \int_0^{2\pi} \frac{1}{2} \dot{w}(r) \ \rho \ r \ t \ d\phi \ dr = \frac{7}{108} \pi \rho t a^2 \dot{w}_0^2$$

with the equivalent mass m_{eq} defined by: $T_{plate} = \frac{1}{2} m_{eq} \dot{w}_0^2$ the result is:

$$\Rightarrow m_{eq} = \frac{7}{54} \pi \rho t a^2 = \frac{7}{54} m_{plate} \cong 0.13 \ m_{plate} \qquad (12.5)$$

This means that the equivalent plate mass is only a small fraction of the total mass of the plate.

3. The kinetic energy of the impactor is fully transferred to kinetic energy of the impactor and the plate, and to internal strain energy of the plate. Higher order vibrations of the plate, the energy spent for local Hertzian indentation and the deformation of the clamping and impactor are neglected. Also the change of potential energy (the influence of gravity) is ignored. Higher order vibrations will have little effect for high impactor masses relative to the equivalent plate mass, as is the case in our tests.

With the above assumptions the impact problem can be reduced to its most simple form, described by:

$$m_{tot} \ddot{w}_0 + c \ w_0 = 0$$

with: $m_{tot} = m_{eq} + m_p$ \qquad (12.6)

The solution is:

$$w_{r=0} = v^*_{t=0} \sqrt{\frac{m_{tot}}{c}} \sin\left[\sqrt{\frac{c}{m_{tot}}}\, t\right]$$

$$v = v^*_{t=0} \cos\left[\sqrt{\frac{c}{m_{tot}}}\, t\right] \qquad\qquad (12.7)$$

$$F = v^*_{t=0}\, m_p \sqrt{\frac{c}{m_{tot}}} \sin\left[\sqrt{\frac{c}{m_{tot}}}\, t\right]$$

$$t_c = \pi \sqrt{\frac{m_{tot}}{c}}$$

The contact time t_c is the time at $F = 0$, after contact ($t_c > 0$).

The sine shape of the contact force-time and the deflection-time curves and the cosine shape of the velocity-time curve, as already described in chapters 6 and 7, return in these expressions. Another illustrative result is that the contact time t_c is independent of the impact velocity. The contact time only depends on the plate stiffness and the total mass.

According to this mass-spring model the residual velocity of the impactor after impact (at $t = t_c$) is:

$$v_r = -\frac{m_p}{m_{tot}}\, v_0 \qquad\qquad (12.8)$$

12.2.2 Comparison with experimental results

A comparison of this simple model with experimental results was not found in literature. However, here it is the first step to a more complex modelling. Therefore some impact tests were performed with the test set-up of figure 12.1. The acceleration of the cylindrical mass of 271 g was measured by an accelerometer mounted on the top of the impactor. The steel

impactor had a hemispherical tip with a radius of 7.5 mm. The impactor was guided by a piece of tube. The impactor was dropped from a height of 1, 2 and 3 cm on an Al 2024-T3 (t=1.03 mm) specimen with a clamped circular test area with a diameter of 80 and 130 mm respectively. The friction was neglected, the impact velocity was calculated from:

$$v_o = \sqrt{2 \, g \, h} \qquad\qquad (12.9)$$

The contact force was calculated from Newton's law (F = m_p a).
The linear model will be valid for deflections on the order of the plate thickness. For the drop heights of 1, 2 and 3 cm, the deflections (according to the mass-spring model) were 0.501, 0.708 and 0.867 mm respectively.

In figures 12.3 and 12.4 the measured force-time curve is compared with the mass-spring model for the plate with a circular clamped test area with a diameter of 80 mm and 130 mm respectively. The mean value of the measured contact force corresponds very accurately with the calculated value of the mass-spring model.

12.2.3 Extension of the model to a plate under initial stress

The above model model is the starting point of further modelling in this thesis. The first extension is the presence of an initial load N_x per unit of length in the x-direction of a circular plate. According to Timoshenko and Woinowsky-Krieger[2] the strain energy during bending of the plate will be increased with:

$$U_s = \frac{1}{2} \iint_{Area} N_x \left(\frac{\delta w}{\delta x} \right)^2 dx \, dy \qquad\qquad (12.10)$$

For the uniaxial initial stress S in the x direction, equation 12.3 can be used to calculate the derivative $\frac{\delta w}{\delta x}$. The internal strain energy due to the initial stress was calculated from equation 12.10:

$$U_s = \frac{1}{4} \pi S t w_0^2 \tag{12.11}$$

This energy is not dependent on the size of the clamped area of the plate. It means that the effective stiffness of the plate will be increased with:

$$\Delta c = \frac{1}{2} \pi S t \tag{12.12}$$

Equations (12.7) can still be used. The additional stiffness, due to the initial loading has to be taken into account by substitution of the total stiffness $c_{tot} = c + \Delta c$.

12.2.4 Comparison of the extended model with experimental results

The extended model was compared with the experimental results, obtained with the test set-up of chapter 8. The stiffness of the Al 2024-T3 (t= 1.0 mm) specimen is 212 N/mm. The additional stiffness Δc at an initial stress of 300 MPa is 471 N/mm, which is a significant stiffness increase. The equivalent mass of the specimen (calculated with equation 12.5) is 2 g. This mass is small relative to the impactor mass.

In figures 8.2 to 8.4 (in chapter 8) the extended mass-spring model is compared with the experimental results. The results of the model agree well with the measured values. The maximum force during impact increases and the maximum central deflection decreases with increasing initial load. The contact time becomes shorter.

12.3 Linear elastic analysis of the impact on a clamped isotropic plate using a Hertzian contact law

12.3.1 Governing equations

In the former section a permanent rigid contact between the impactor and the plate was assumed during impact. In this section the contact between projectile and plate is considered by using the Hertzian contact law in the form of equations 9.2 and 9.3. The plate is modelled by two springs in series: a non linear one with the Hertzian contact stiffness and a linear one with the bending stiffness of the plate. Equation 9.2 can be integrated

to obtain the indentation energy U_{ind}. The total strain energy of the plate then becomes:

$$U_{plate} = U_{bending} + U_{ind} = \frac{1}{2} c w_0^2 + \frac{2}{5} k (s-w_0)^{5/2}$$

(12.13)

with the bending stiffness of the plate c as given in section 12.1. $s-w_0$ is equal to the indentation in the plate (see figure 12.1), k is the indentation stiffness.

The kinetic energy of the plate is expressed by equation 12.5. The kinetic energy of the impactor is:

$$T_{impactor} = \frac{1}{2} m_p \dot{s}^2$$

(12.14)

The gravitational energy is included in the model, although the influence of the gravitational force generally will be small compared with the contact force. The change of the gravitational energy of the projectile is:

$$V_{impactor} = - m_p g s$$

(12.15)

The change of the gravitational energy of the plate is:

$$V_{plate} = - \int_0^a \int_0^{2\pi} \rho r g t w(r) d\theta dr$$

(12.16)

Substitution of the deflection field for a clamped plate (equation 12.3) yields:

$$V_{plate} = - \frac{1}{4} \pi \rho t g a^2 w_0$$

(12.17)

The governing equations can be obtained by expressing the conservation of energy:

$$T_{plate} + T_{impactor} + U_{plate} + V_p' + V_{plate} = \frac{1}{2} m_p v_0^2$$

<div align="right">(12.18)</div>

This energy equation can be solved using the equations of motion of Lagrange:

$$\frac{d}{dt} \left[\frac{\delta T}{\delta \dot{q}_1} \right] - \frac{\delta T}{\delta q_1} + \frac{\delta U}{\delta q_1} = 0$$

<div align="right">(12.19)</div>

with q_1 as the generalized coordinates (s and w_0), U as the total potential (elastic and gravitational) energy and T as the total kinetic energy of the system.

The equations of Lagrange lead to the following expressions:

$$-m_p \, g + k(s-w_0)^{3/2} + m_p \, \ddot{s} = 0$$

$$-\frac{1}{4} \pi \, \rho \, t \, a^2 \, g + k(s-w_0)^{3/2} + c \, w_0 + m_{eq} \, \ddot{w}_0 = 0$$

<div align="right">(12.20)</div>

s(t) and w_0(t) were solved by time integration of these equations. The velocities and accelerations in the equations were expressed by their finite difference equivalents:

$$\dot{q}(t) = \frac{1}{2\Delta t} \left[q(t+\Delta t) - q(t-\Delta t) \right]$$

<div align="right">(12.21)</div>

$$\ddot{q}(t) = \frac{1}{(\Delta t)^2} \left[q(t+\Delta t) + q(t-\Delta t) - 2 \, q(t) \right]$$

with Δt as the time increment.

The equations were implemented in a computer program (ELIM: ELastic Impact Model). The initial values of the displacements and velocities at t = 0 and

t = -Δt are:

t = -Δt $w_0 = 0$

$$s = -(v_0 - g \, \Delta t) \, \Delta t - \frac{1}{2} g \, (\Delta t)^2$$

t = 0 $w_0 = 0$

s = 0   (12.22)

If during the process $s(t) < w_0(t)$, the impactor loses contact with the plate. In the program this condition is tested. If it occurs the contact force will be set to zero by substitution of k = 0 in equation 12.20. The result is that the equations of motion of the plate and the impactor will be uncoupled. After loss of contact the plate will be in a free vibration. This means that the deflection field (equation 12.3) of a loaded plate no longer will be valid. The strain energy will probably be redistributed; this effect was not accounted for in the model.

12.3.2 Comparison with experimental results

The following input data were used for the calculations:

$E_{plate} = 72\,000$ MPa, $\nu_{plate} = 0.33$
$E_{impactor} = 200,000$ MPa, $\nu_{impactor} = 0.3$
R = 7.5 mm
$\rho_{plate} = 2.7$ kg/dm^3
t = 1.03 mm
$m_p = 271$ g
$v_0 = 0.443$ m/s (drop height = 1 cm)

The Hertzian indentation stiffness can be calculated from equation 9.3:

$k_{ref} = 215.7$ kN/mm$^{3/2}$

Calculations were done with k equal to 1, 0.1 and 0.01 times this reference k value, in order check the sensitivity of the model for the magnitude of

the k value. Different Δt values were used and a sufficiently small value was adopted.

Figure 12.5 shows the calculated results. The force-time curves of the present model generated by ELIM are compared with the results of the mass-spring model of the previous section. This figure shows that for a Hertzian stiffness of k_{ref} the force-time curve is completely dominated by the high frequency vibration due to the indentation stiffness. At the lower k values the contact force due to the deflection of the plate becomes more apparent. The mean contact force corresponds with the mass-spring model.

The deflection-time curve is less dependent on the k value. The curves practically coincide,; the same is true for the velocity-time curves. The maximum deflections are:

$$
\begin{array}{lll}
\text{mass-spring model} & w_{0,max} = & 0.501 \text{ mm} \\
\text{with Hertzian contact } k = k_{ref} & & 0.520 \\
\qquad\qquad k = 0.1\, k_{ref} & & 0.517 \\
\qquad\qquad k = 0.01\, k_{ref} & & 0.484 \\
\end{array}
$$

The model shows the importance of the indentation stiffness of an impact model. In general this stiffness will be large relative to the stiffness of the plate and may dominate the force-time curve. The velocity-time and deflection-time curves are less dependent on the indentation stiffness. The use of the k_{ref} value in the model leads in this case to large fluctuations of the contact force. After each force peak the contact between impactor and plate is lost. This does not correspond with the experimental results (see figure 12.3). Some possible explanations are:

1. The real indentations stiffness may be lower than the elastic Hertzian contact law predicts, e.g. because of plastic deformation.

2. The high frequency indentation vibration may be strongly damped.

3. The higher order vibrations of the plate may interfere with the Hertzian indentation, such that the very strong force fluctuations do not occur.

For an indentation stiffness of $0.1\, k_{ref}$ and $0.01\, k_{ref}$ the calculated force-time curves are more realistic. The high frequency vibration in the experimental curves (figure 12.3 and 12.4) are also found in the calculated

curves.

12.4 Linear elastic finite element calculations

12.4.1 The model

The finite element program MARC was used for the FEM calculations in this section. This program is especially suitable for non linear calculations. First linear elastic calculations were done with a simple model, in order to study the capability of MARC to handle impact problems. The results can be easily compared with experimental and analytical results of the previous sections. As shown before, the result of the simple analytical mass-spring model did correspond accurately with the experimental results, and can thus be used for comparison.

Figure 12.6 shows the FEM model: 16 thin-shell elements to model the plate, and 4 so called 'gap elements' to model the impactor. The model is axisymmetrical. The radius of the plate is 40 mm, its thickness is 1 mm. Young's modulus, Poisson's ratio and the density of aluminium were given to the shell elements (E = 72,000 MPa, ν = 0.33, ρ = 2.7 kg/dm^3). The thin-shell elements have two nodes and a linear displacement field. The elements are in the plane stress condition.

The impactor is modelled by gap elements, which can be open or closed, depending on the distance between the two outer nodes. The gap elements at one end are connected with nodes of the shell elements, and have one node in common at the other end (no.30 in figure 12.6). In this common node the mass is concentrated, and it is given the initial velocity (equal to the impact velocity). The critical distance at which the gap elements close is equal to the tip radius of the impactor, in this case 7.5 mm. The impactor is considered to be rigid. It is possible to give the gap elements a certain stiffness after closing, but this option was not used. It is also possible to include friction between the gap elements and the plate, but also this option was not adopted.

At the edge of the plate the rotation and displacements were set to zero; at the centre of the model the radial displacement and the rotation were

set to zero.

If a structure is loaded dynamically close to its resonant frequency, damping may be necessary to restrain the response of the plate[10]. At impact also the resonant frequency of the plate will be excited, and to avoid inaccuracies it may be necessary to include some damping in the model. Because the damping is a very uncertain quantity it is not worthwhile to have a very advanced damping model[10]. Rayleigh damping was assumed: a simplified way to model the damping matrix as a linear combination of the mass and stiffness matrix. Also a numerical damping term is introduced which is useful for damping out modes of the model which are excited during the transient numerical analysis, due to the value of the time step of integration.

The total damping matrix in MARC is given by[10]:

$$ C = \sum_{l=1}^{M} \left[\alpha_l \, M_l + (\beta_l + \gamma_l \, \frac{\Delta t}{\pi}) \, K_l \right] \tag{12.23} $$

with: M is the number of elements, M_l and K_l are the mass and stiffness matrix of an element, Δt is the time step, α_l and β_l are the damping coefficients associated with the mass and stiffness matrix respectively, and γ_l is the numerical damping coefficient.

The equations of motion are given by:

$$ M \, \ddot{\underline{u}} + C \, \dot{\underline{u}} + K \, \underline{u} = \underline{f} \tag{12.24} $$

with M as the mass matrix, K as the stiffness matrix and $\underline{f}$ as the loading vector.

The effect of the damping on the results is not large, as will be shown in the next section. The impact process (i.e. the deformation process during contact contains only half of a vibration cycle, and the energy dissipated in half a cycle is small. The damping has some effect in smoothing the peak forces in the force-time curve during impact. The damping coefficients used in the model were taken from the MARC manual: $\alpha = 0.5$, $\beta = 0$ and $\gamma = 1$.

411

The time integration was done with the Newmark β method. The impactor mass was 271 g, v_0 = 0.443, 0.626 and 0.767 m/s (corresponding with drop heights of 1, 2 and 3 cm respectively).

12.4.2 Results and conclusions

Figures 12.7 to 12.9 show the calculated curves for the force, velocity and displacement vs. time. The results are compared with the mass-spring model discussed in section 12.4.1, The latter model showed an excellent correspondence with experimental results. The calculated force-time curves show large fluctuations at the beginning of impact. This is also observed to some extent in the experimental results of section 12.2.2 (figure 12.4), and was also discussed in chapters 6 and 7: at initial contact the plate is pushed away by the impactor and the contact is lost.

The maximum force and maximum central deflection during impact calculated with the mass-spring model and the FE model are shown in table 12.2.

The residual velocities after impact (v_r) and the velocity restitution coefficient e_v were:

v_0 = 0.443 m/s v_r = 0.426 m/s $e_v = v_r/v_0$ = 0.962
     0.626   0.601   0.960
     0.767   0.735   0.958

A part of the kinetic energy of the impactor will be dissipated by damping during impact, another part will be stored as elastic energy in the plate (which is finally also dissipated by damping during the free vibrations of the plate).

We may conclude that the linear elastic MARC FEM calculations correspond quite well with both experimental and analytical results. The following section will extend this model to non linear deformations.

12.5 Non linear finite element calculations

12.5.1 The model

A square 100x100 mm^2 and a circular diameter 80 mm clamped plate is modelled, see figures 12.10 and 12.11. The models consist of 112 (square plate) and 104 (circular plate) shell elements and 28 gap elements. A quarter of the plate is modelled for reasons of symmetry. This quarter of the plate is impacted by a quarter of the total impactor mass. The impactor is considered to be rigid and modelled by the gap elements in the same way as described in the previous section. The 4 node bilinear shell elements are in the plane stress condition and transverse shear is not included. The elements consist of anisotropic layers.

The displacements at the boundaries are constrained. At the axis of symmetry the rotations around these axis, the rotations around an axis perpendicular to the plate and the displacement in the tangential direction are set to zero.

The FE mesh for a square plate is used to model monolithic Al 2024-T3 (t = 1.25 mm), aramid ARALL 2H33 (t = 1.35 mm) and quasi-isotropic carbon/PEI (t = 1.65 mm). The mesh for a circular plate is used to model impact on Al 2024-T3 (t = 1.0 mm). For monolithic Al 2024-T3 and the Al 2024-T3 layers in ARALL the true stress-strain curve of this material (figure 10.2) is approximated by a multi-linear curve which connects 8 points on the measured stress-strain curve (until ε = 13%).

The stiffness matrix which is used for the aramid prepreg of aramid ARALL is:

$$c_{11} = 63801 \text{ MPa}$$
$$c_{22} = 5021 \text{ MPa}$$
$$c_{12} = 1833 \text{ MPa}$$
$$c_{66} = 1462 \text{ MPa}$$

and the stiffness matrix of the carbon/PEI layers is given in table 6.1 of chapter 6. The lay-up of the quasi-isotropic carbon/PEI is [0/45/-45/90]$_s$, the ply thickness is 0.210 mm.

413

The Newmark β method is used to integrate the equations of motion. The impactor mass is 302 g for the square plates, and 411 g for the circular plates. These masses correspond with the impactor masses of the experiments.

12.5.2 Results and discussion

The calculations were performed with a Convex mini-supercomputer of the Delft University. Each impact calculation required approximately 30 minutes CPU time.

The application of damping as discussed in the previous section (α = 0.5, β = 0, and γ = 1) has only a small influence on the calculated deflection, see table 12.3. Damping causes a lower maximum force and a lower maximum central deflection during impact. The maximum elastic energy in the plate will be lower because of the damping. this corresponds with the smaller deflection. A smaller maximum force corresponds with the lower maximum deflection.

A comparison of experimental and calculated maximum force and central deflection during impact is given in table 12.4, and in figures 12.12 to 12.14 for the square model. The agreement between the calculated maximum force and the experimental values is somewhat disappointing, which is partly due to high peaks occurring in the calculated force-time curves. The calculated results for Al 2024-T3 and aramid ARALL 2H33 are better than those of carbon/PEI.

The difference between the experimental results and the FEM model can be explained as follows:
1. The boundary conditions of the FE model are exactly specified, whereas it was difficult to fully clamp the plates during the experiments. Difficulties in clamping a square plate were already discussed in chapter 6.
2. The elements of the stiffness matrix of the experimentally tested plates may differ from the measured values on unidirectional specimens. The resin flow of a unidirectional laminate during consolidation is different from that of a quasi-isotropic laminate: the fibres of a consolidated

414

unidirectional laminate are not exactly straight, and the fibre volume fraction may locally be somewhat lower (42% vs 45%).

3. The experimentally tested plates may show some damage (matrix cracking) during impact, this also changes the stiffness of the plate.

4. The plates of the press which consolidated the thermoplastic composites were not exactly parallel. This caused a minor variation of the thickness over the plates.

For a circular Al 2024-T3 (t = 1 mm) plate a comparison between calculated and measured force, velocity and displacement vs. time curves is presented in figure 12.15. The impact velocity is 3.02 m/s, the impactor mass is 411 g.

12.5.3 Conclusions

1. In general there is a fair correspondence between finite element calculations and experimental results.

2. The initial phase (t < 0.2 ms, large force fluctuations) in the force-time curve is also found in the finite element results.

12.6 A non linear elastic model for impact on a rectangular plate: NOLEIM

12.6.1 The model

In figure 9.1 of chapter 9 the geometry of the model is shown. We will consider a rectangular plate with sides A and B. The displacements in the midplane of the plate are u, v and w in the x, y and z direction respectively. The strains can be expressed by the von Kármán equations, if the transverse shear deformations are neglected (which is accurate for thin plates):

$$\varepsilon_x = \frac{\delta u}{\delta x} + \frac{1}{2}\left[\frac{\delta w}{\delta x}\right]^2 - z\left[\frac{\delta^2 w}{\delta x^2}\right]$$

$$\varepsilon_y = \frac{\delta v}{\delta y} + \frac{1}{2}\left[\frac{\delta w}{\delta y}\right]^2 - z\left[\frac{\delta^2 w}{\delta y^2}\right]$$

$$\gamma_{xy} = \frac{\delta u}{\delta y} + \frac{\delta v}{\delta x} + \frac{\delta w}{\delta x}\frac{\delta w}{\delta y} - 2z\frac{\delta^2 w}{\delta x \delta y} \qquad (12.25)$$

As shown in chapter 10, we may neglect the contributions of the displacements u and v, compared to the terms with the out of plane deflection w. This yields:

$$\varepsilon_x = \frac{1}{2}\left[\frac{\delta w}{\delta x}\right]^2 - z\left[\frac{\delta^2 w}{\delta x^2}\right]$$

$$\varepsilon_y = \frac{1}{2}\left[\frac{\delta w}{\delta y}\right]^2 - z\left[\frac{\delta^2 w}{\delta y^2}\right] \qquad (12.26)$$

$$\gamma_{xy} = \frac{\delta w}{\delta x}\frac{\delta w}{\delta y} - 2z\frac{\delta^2 w}{\delta x \delta y}$$

We assume a plane stress deformation in the plate. Then the internal strain energy can be written as:

$$U = \frac{1}{2}\iiint_V (\sigma_x \varepsilon_x + \sigma_y \varepsilon_y + \tau_{xy}\gamma_{xy})\ dx\ dy\ dz \qquad (12.27)$$

An orthotropic layer of the plate will have an angle ϕ relative to the coordinate system of the plate. The relations between the stresses and strains can be expressed as[11]:

$$\begin{bmatrix} \sigma_x \\ \sigma_y \\ \tau_{xy} \end{bmatrix} = \begin{bmatrix} c_{11} & c_{12} & c_{16} \\ c_{12} & c_{22} & c_{26} \\ c_{16} & c_{26} & c_{66} \end{bmatrix}_\phi \begin{bmatrix} \varepsilon_x \\ \varepsilon_y \\ \gamma_{xy} \end{bmatrix} \qquad (12.28)$$

with: $c_{11_\phi} = U_1 + U_2 \cos 2\phi + U_3 \cos 4\phi$

$c_{22_\phi} = U_1 - U_2 \cos 2\phi + U_3 \cos 4\phi$

$c_{12_\phi} = U_4 - U_3 \cos 4\phi$

$c_{66_\phi} = U_5 - U_3 \cos 4\phi$

$c_{16_\phi} = -0.5 \, U_2 \sin 2\phi - U_3 \sin 4\phi$

$c_{26_\phi} = -0.5 \, U_2 \sin 2\phi + U_3 \sin 4\phi$

and: $U_1 = (3 \, c_{11} + 3 \, c_{22} + 2 \, c_{12} + 4 \, c_{66}) \, / \, 8$

$U_2 = (c_{11} - c_{22}) \, / \, 2$

$U_3 = (c_{11} + c_{22} - 2 \, c_{12} - 4 \, c_{66}) \, / \, 8$

$U_4 = (c_{11} + c_{22} + 6 \, c_{12} - 4 \, c_{66}) \, / \, 8 = U_3 + c_{12}$

$U_5 = (c_{11} + c_{22} - 2 \, c_{12} + 4 \, c_{66}) \, / \, 8 = U_3 + c_{66}$

According to Lekhnitskii[12] the deflection field of a clamped plate can be written as the following Fourier series:

$$w(t) = \sum_{m}^{M} \sum_{n}^{N} w_{mn}(t) \left(1 - (-1)^m \cos \frac{m \, 2\pi \, x}{A} \right) \left(1 - (-1)^n \cos \frac{n \, 2\pi \, y}{B} \right)$$

(12.29)

This is a symmetrical deflection field relative to the x and y axis. If this deflection field is substituted in equations 12.26 and 12.27, together with the stress-strain relation (eq.12.28), the following terms of U are non zero:

$$U = \iint_{Area} \left[\frac{1}{8} A_{11} \left(\frac{\delta w}{\delta x} \right)^4 + \frac{1}{2} D_{11} \left(\frac{\delta^2 w}{\delta x^2} \right)^2 + \frac{1}{8} A_{22} \left(\frac{\delta w}{\delta y} \right)^4 \right.$$

$$+ \frac{1}{2} D_{22} \left(\frac{\delta^2 w}{\delta y^2} \right)^2 + \left(\frac{1}{2} A_{66} + \frac{1}{4} A_{12} \right) \left(\frac{\delta w}{\delta x} \right)^2 \left(\frac{\delta w}{\delta y} \right)^2$$

$$\left. - 2 \, B_{66} \left(\frac{\delta w}{\delta x} \right) \left(\frac{\delta w}{\delta y} \right) \left(\frac{\delta^2 w}{\delta x \delta y} \right) + 2 \, D_{66} \left(\frac{\delta^2 w}{\delta x \delta y} \right)^2 \right.$$

$$- \frac{1}{2} B_{12} \left(\frac{\delta w}{\delta x} \right)^2 \left(\frac{\delta^2 w}{\delta y^2} \right) - \frac{1}{2} B_{12} \left(\frac{\delta w}{\delta y} \right)^2 \left(\frac{\delta^2 w}{\delta x^2} \right)$$

$$+ D_{12} \left(\frac{\delta^2 w}{\delta x^2} \right) \left(\frac{\delta^2 w}{\delta y^2} \right) \quad \Bigg] \quad dx \; dy \tag{12.33}$$

with:
$$A_{ij} = \sum_{k=1}^{n} c_{ij}^{k} \left(z_k - z_{k-1} \right)$$

$$B_{ij} = \frac{1}{2} \sum_{k=1}^{n} c_{ij}^{k} \left(z_k^2 - z_{k-1}^2 \right)$$

$$D_{ij} = \frac{1}{3} \sum_{k=1}^{n} c_{ij}^{k} \left(z_k^3 - z_{k-1}^3 \right)$$

With c_{ij}^{k} as the element of the stiffness matrix of the kth layer.

For symmetrical laminates $B_{ij} = 0$, and the corresponding terms drop out of equation 12.33.

To obtain the equations of motion we will use the Lagrange equations 12.19, with w_{mn} as the generalized coordinates. Therefore we need the partial derivatives of the strain energy U with respect to the generalized coordinates w_{mn} (with $B_{ij} = 0$) :

$$\frac{\delta U}{\delta w_{mn}} = \iint\limits_{Area} \Bigg[\frac{1}{2} A_{11} \left(\frac{\delta w}{\delta x} \right)^3 \frac{\delta^2 w}{\delta w_{mn} \delta x} + \frac{1}{2} A_{22} \left(\frac{\delta w}{\delta y} \right)^3 \frac{\delta^2 w}{\delta w_{mn} \delta y}$$

$$+ \left(A_{66} + \frac{1}{2} A_{12} \right) \frac{\delta w}{\delta x} \left(\frac{\delta w}{\delta y} \right)^2 \frac{\delta^2 w}{\delta w_{mn} \delta x}$$

418

$$
+ \left(A_{66} + \frac{1}{2} A_{12} \right) \frac{\delta w}{\delta y} \left(\frac{\delta w}{\delta x} \right)^2 \frac{\delta^2 w}{\delta w_{mn} \delta y} \Bigg] dx \, dy
$$

$$
+ \iint\limits_{Area} \Bigg[D_{11} \frac{\delta^2 w}{\delta x^2} \frac{\delta^3 w}{\delta w_{mn} \delta x^2} + D_{22} \frac{\delta^2 w}{\delta y^2} \frac{\delta^3 w}{\delta w_{mn} \delta y^2}
$$

$$
+ 4 D_{66} \frac{\delta^2 w}{\delta x \delta y} \frac{\delta^3 w}{\delta w_{mn} \delta x \delta y}
$$

$$
+ D_{12} \frac{\delta^3 w}{\delta w_{mn} \delta x^2} \frac{\delta^2 w}{\delta y^2} + D_{12} \frac{\delta^3 w}{\delta w_{mn} \delta y^2} \frac{\delta^2 w}{\delta x^2} \Bigg] dx \, dy
$$

$$(12.34)$$

In the case of a symmetrical laminate we can decompose the internal strain in a non linear and a linear term. The first integral of equation 12.34 shows the non linear part (stretching), the second integral is associated with the linear part (bending).

The linear term of the partial derivative of the internal strain energy can be calculated by integration of equation 12.34:

$$
\left[\frac{\delta U}{\delta w_{ij}} \right]_{lin} = w_{ij} \Bigg[D_{11} \frac{12 \pi^4 B}{A^3} i^4 + D_{22} \frac{12 \pi^4 A}{B^3} j^4 + D_{66} \frac{16 \pi^4}{AB} i^2 j^2
$$

$$
D_{12} \frac{8 \pi^4}{AB} i^2 j^2 \Bigg]
$$

$$
+ \sum_{\substack{n \\ n \neq j}}^{N} w_{in} D_{11} \frac{8 \pi^4 B}{A^3} i^4 + \sum_{\substack{m \\ m \neq i}}^{M} w_{mj} D_{22} \frac{8 \pi^4 A}{B^3} j^4
$$

This yields that the vector of the partial derivatives can be expressed as

the product of a stiffness matrix K and a displacement matrix $\underline{w}$:

$$\Rightarrow \quad \left\{ \frac{\delta U}{dw_{ij}} \right\} = K \ \underline{w} \tag{12.35}$$

with K as the linear stiffness matrix and $\underline{w}$ as the generalized displacement vector. The elements of the vector

$$\left\{ \frac{\delta U}{dw_{ij}} \right\}$$

are the partial derivatives.

For a simply supported plate the displacement field is written as:

$$w(t) = \sum_{m}^{M} \sum_{n}^{N} w_{mn}(t) \ \sin \left[\frac{m \ \pi \ (x \ + \ 0.5A)}{A} \right] \sin \left[\frac{n \ \pi \ (y \ + \ 0.5B)}{B} \right] \tag{12.36}$$

In the case of a simply supported plate additional terms of the partial derivative of the strain has to be added to equation 12.34:

$$\Delta \ \frac{\delta U}{\delta w_{mn}} = \iint\limits_{Area} \left[2 \ D_{16} \ \frac{\delta^3 w}{\delta w_{mn} \delta x^2} \ \frac{\delta^2 w}{\delta x \delta y} \ + \ 2 \ D_{26} \ \frac{\delta^3 w}{\delta w_{mn} \delta y^2} \ \frac{\delta^2 w}{\delta x \delta y} \right.$$

$$\left. + \ 2 \ D_{16} \ \frac{\delta^3 w}{\delta w_{mn} \delta x \delta y} \ \frac{\delta^2 w}{\delta x^2} \ + \ 2 \ D_{26} \ \frac{\delta^3 w}{\delta w_{mn} \delta x \delta y} \ \frac{\delta^2 w}{\delta y^2} \right] dx \ dy \tag{12.37}$$

In this case the linear part of the partial derivative of the strain energy is:

$$\left[\frac{\delta U}{\delta w_{ij}} \right]_{lin} = w_{ij} \left[D_{11} \frac{\pi^4 B}{4 \ A^3} i^4 \ + D_{22} \frac{\pi^4 A}{4 \ B^3} j^4 \ + D_{66} \frac{\pi^4}{AB} i^2 j^2 \right.$$

$$\left. D_{12} \frac{\pi^4}{2AB} i^2 j^2 - D_{16} \frac{\pi^4}{A^2} i^3 j \ - D_{26} \frac{\pi^4}{B^2} ij^3 \right]$$

$$(12.38)$$

For both the clamped and the simply supported plate the total (linear and non linear) partial derivative of the strain energy U can be expressed by:

$$\left\{ \frac{\delta U}{\delta w_{ij}} \right\} \ = \ \underline{n} + K \ \underline{w}$$

$$(12.39)$$

with $\underline{n}$ as the vector which contains the non linear terms:

$$\left\{ n_{ij} \right\} = \iint\limits_{Area} \left[\frac{1}{2} A_{11} \left(\frac{\delta w}{\delta x} \right)^3 \frac{\delta^2 w}{\delta w_{mn} \delta x} \ + \ \frac{1}{2} A_{22} \left(\frac{\delta w}{\delta y} \right)^3 \frac{\delta^2 w}{\delta w_{mn} \delta y} \right.$$

$$+ \left(A_{66} + \frac{1}{2} A_{12} \right) \frac{\delta w}{\delta x} \left(\frac{\delta w}{\delta y} \right)^2 \frac{\delta^2 w}{\delta w_{mn} \delta x}$$

$$\left. + \left(A_{66} + \frac{1}{2} A_{12} \right) \frac{\delta w}{\delta y} \left(\frac{\delta w}{\delta x} \right)^2 \frac{\delta^2 w}{\delta w_{mn} \delta y} \right] dx \ dy$$

$$= \iint\limits_{Area} \left[k_1(x,y) \frac{\delta^2 w}{\delta w_{mn} \delta x} \ + k_2(x,y) \frac{\delta^2 w}{\delta w_{mn} \delta y} \right] dx \ dy$$

$$(12.40)$$

with for a clamped plate:

$$\frac{\delta^2 w}{\delta w_{mn} \delta x} = (-1)^m \frac{m\ 2\pi}{A} \sin\left(\frac{m\ 2\pi\ x}{A}\right) \left[1 - (-1)^n \cos\left(\frac{m\ 2\pi\ x}{A}\right)\right]$$

$$\frac{\delta^2 w}{\delta w_{mn} \delta y} = (-1)^n \frac{n\ 2\pi}{B} \sin\left(\frac{n\ 2\pi\ y}{B}\right) \left[1 - (-1)^m \cos\left(\frac{n\ 2\pi\ y}{B}\right)\right]$$

(12.41)

and for a simply supported plate:

$$\frac{\delta^2 w}{\delta w_{mn} \delta x} = \frac{m\ \pi}{A} \cos\left(\frac{m\ 2\pi\ (x+0.5A)}{A}\right) \sin\left(\frac{n\ 2\pi\ (y+0.5B)}{B}\right)$$

$$\frac{\delta^2 w}{\delta w_{mn} \delta y} = \frac{n\ \pi}{B} \cos\left(\frac{n\ 2\pi\ (y+0.5B)}{B}\right) \sin\left(\frac{m\ 2\pi\ (x+0.5A)}{A}\right)$$

(12.42)

The kinetic energy of the plate is (neglecting the rotatory inertia):

$$T_{plate} = \iiint\limits_{V} \frac{1}{2} \rho\ \dot{w}^2\ dx\ dy\ dz$$

(12.43)

If the deflection field of the simply supported and clamped plate are substituted, the following results are obtained for the derivative terms of the kinetic energy needed for the Lagrange's equations:

clamped plate:

$$\frac{\delta T_{plate}}{\delta \dot{w}_{ij}} = \sum_{m}^{M} \sum_{n}^{N} \alpha_{ij}\ \rho\ A\ B\ t\ \dot{w}_{mn}$$

(12.44)

422

with: $\alpha_{ij} = \dfrac{9}{4}$ for i = m and j = n

$\alpha_{ij} = \dfrac{3}{2}$ for i = m and j $\neq$ n

or i $\neq$ m and j = n

$\alpha_{ij} = 1$ for i $\neq$ m and j $\neq$ n

simply supported plate:

$$\frac{\delta T_{plate}}{\delta \dot{w}_{ij}} = \frac{1}{4} \, \rho \, A \, B \, t \, \dot{w}_{mn} \qquad \qquad (12.45)$$

The contact between projectile and plate is in two ways: (1) by a Hertzian contact law and (2) by assuming a permanent rigid contact between projectile and plate, and neglecting the Herzian indentation energy.

If a permanent contact is assumed the displacement of the impactor is equal to the central deflection of the plate. This yields for the kinetic energy of the impactor:

$$T_{proj} = \frac{1}{2} \, m_p \, \dot{w}_0^{\,2} \qquad \qquad (12.46)$$

For a clamped plate:

$$T_{proj} = \frac{1}{2} \, m_p \left(\sum_{m}^{M} \sum_{n}^{N} \left((1 - (-1)^m) \, (1 - (-1)^n) \, \dot{w}_{mn} \right) \right)^2$$

$$(12.47)$$

and:

$$\frac{\delta T_{proj}}{\delta \dot{w}_{ij}} = m_p \left(1-(-1)^i \right) \left(1-(-1)^j \right) \sum_{m}^{M} \sum_{n}^{N} \left(\left(1-(-1)^m \right) \left(1-(-1)^n \right) \dot{w}_{mn} \right)$$

(12.48)

For a simply supported plate:

$$T_{proj} = \frac{1}{2} m_p \left[\sum_{m}^{M} \sum_{n}^{N} \dot{w}_{mn} \sin\left(\frac{m\pi}{2} \right) \sin\left(\frac{n\pi}{2} \right) \right]^2$$

(12.49)

and:

$$\frac{\delta T_{proj}}{\delta \dot{w}_{ij}} = m_p \left[\sum_{m}^{M} \sum_{n}^{N} \dot{w}_{mn} \sin\left(\frac{m\pi}{2} \right) \sin\left(\frac{n\pi}{2} \right) \right] \sin\left(\frac{i\pi}{2} \right) \sin\left(\frac{j\pi}{2} \right)$$

(12.50)

The total kinetic energy term of the Lagrange's equations can be written in vector notation:

$$\left\{ \frac{\delta T_{tot}}{\delta \dot{w}_{ij}} \right\} = \left\{ \frac{\delta T_{plate}}{\delta \dot{w}_{ij}} \right\} + \left\{ \frac{\delta T_{proj}}{\delta \dot{w}_{ij}} \right\} = M \underline{\dot{w}}$$

(12.51)

with M as the total mass matrix of the system.

In the case of a permanent rigid contact between projectile and plate the Lagrange's equation are given by:

$$\frac{d}{dt} \left\{ \frac{T_{tot}}{\delta \dot{w}_{ij}} \right\} + \left\{ \frac{\delta U}{\delta w_{ij}} \right\} = M \underline{\ddot{w}} + K \underline{w} + \underline{n}(\underline{w}) = 0$$

(12.52)

424

In the case of a Hertzian contact[1]:

for a clamped plate:

$$\frac{d}{dt} \left\{ \frac{\delta T_{plate}}{\delta \dot{w}_{ij}} \right\} + \left\{ \frac{\delta U}{\delta w_{ij}} \right\} = F \ (\ 1 - (-1)^{m}) \ (\ 1 - (-1)^{n})$$

(12.53)

for a simply supported plate:

$$\frac{d}{dt} \left\{ \frac{\delta T_{plate}}{\delta \dot{w}_{ij}} \right\} + \left\{ \frac{\delta U}{\delta w_{ij}} \right\} = F \sin \left[\frac{1}{2} m \pi \right] \sin \left[\frac{1}{2} n \pi \right]$$

(12.54)

with F as the contact force:

$$F = k \ (s - w_0)^{3/2}$$

(12.55)

For Hertzian contact we have an extra independent generalized displacement s of the projectile, and the motion of the projectile is described by:

$$m_p \ g - F = m_p \ \ddot{s}$$

(12.56)

The equations of motion were integrated in time with the Newmark β method[13]:

$$\dot{q}(t+\Delta t) = \dot{q}(t) + \Delta t \left[(1-\gamma) \ \ddot{q}(t) + \gamma \ \ddot{q}(t+\Delta t) \right]$$

$$q(t+\Delta t) = q(t) + (\Delta t)\dot{q}(t) + (\Delta t)^2 \left[(0.5-\beta) \ \ddot{q}(t) + \beta\ddot{q}(t+\Delta t) \right]$$

(12.57)

Generally $\gamma = 0.5$ and $\beta = 0.25$ are chosen: a constant average acceleration during a time step and an unconditionally stable numerical scheme. The same

γ and β value were used in the present model.

This leads to the following equations:

$$\ddot{\underline{w}}_{t+\Delta t} = - \left[M + \frac{(\Delta t)^2}{4} K \right]^{-1} \left[\underline{n}_{t+\Delta t}(w) + F_{t+\Delta t} + K \left(\underline{w}_t + \Delta t \, \dot{\underline{w}}_t + \frac{(\Delta t)^2}{4} \ddot{\underline{w}}_t \right) \right]$$

$$\dot{\underline{w}}_{t+\Delta t} = \dot{\underline{w}}_t + \frac{\Delta t}{2} \left[\ddot{\underline{w}}_t + \ddot{\underline{w}}_{t+\Delta t} \right]$$

$$\underline{w}_{t+\Delta t} = \underline{w}_t + \frac{\Delta t}{2} \left[\dot{\underline{w}}_t + \dot{\underline{w}}_{t+\Delta t} \right] \tag{12.58}$$

With Δt as the time step, $F_{t+\Delta t}$ and $\underline{n}_{t+\Delta t}$ are obtained with a predictor-corrector method: an estimation is made of the displacement, velocity and acceleration vectors with equation 12.58 on the basis of F_t and $\underline{n}_t$. Corrected values of F and $\underline{n}$ are calculated with the estimated displacement, velocity and acceleration vector. These values are substituted as $F_{t+\Delta t}$ and $\underline{n}_{t+\Delta t}$ in equations 12.58. The calculation of the non linear term $\underline{n}$ is done with numerical integration of equation 12.40, with a Simpson integration over 15x15 points of the plate[15].

For a permanent contact the $F_{t+\Delta t}$ value of zero has to be substituted in equations 12.58. For Hertzian contact F_t is given by equation 12.55. In this case the displacement of the impactor is obtained by:

$$\ddot{s}_{t+\Delta t} = \frac{(\Delta t)^2}{m_p} \left[m_p \, g - F_{t+\Delta t} \right]$$

$$\dot{s}_{t+\Delta t} = s_t + \frac{\Delta t}{2} \left[\ddot{s}_t + \ddot{s}_{t+\Delta t} \right] \tag{12.59}$$

$$s_{t+\Delta t} = s_t + \frac{\Delta t}{2} \left[\dot{s}_t + \dot{s}_{t+\Delta t} \right]$$

426

12.6.2 Comparison of the linear part of the model with literature data

NOLEIM is a non linear model. The <u>linear</u> elastic part of our model was checked by a comparison with the results of linear elastic models available in the literature: Sun and Chen[3], Cairns and Lagace[5], Wu and Springer[4], and Qian and Swanson[7]. The present model was applied to five different cases in those references. The non linear part of the model was removed from equations 12.58 by setting $\underline{n}_{-t+\Delta t}$ to zero.

The first case is an impact calculation made by Sun and Chen (linear FEM), which is also used for a comparison by Wu, Cairns and Lagace, and by Qian and Swanson. This example impact event has a very low impact energy, which is characteristic for the linear impact results of the literature. The Hertzian indentation constant k is given by Sun and Chen (experimental result). Table 12.5 gives the plate geometry and the material properties for this case. The linear calculations with the present model were done with 10x10 modes (M=N=10) and a time step of Δt = 1 μs.

Figure 12.16a shows the force-time curves of different models. A multiple impact occurs, and the agreement of the present model with the literature results is very good. This is also true for the deflection-time curves (figure 12.16b).

The second case in table 12.5 was presented by Wu and Springer (linear FEM). In this case the impact velocity is somewhat higher than in the first case, but the impact energy is still low (0.94 J). The calculation with the present model was performed with 10x10 modes and a time step Δt = 0.4 μs. The Hertzian indentation stiffness was calculated with equation 9.3. Figures 12.17 (force-time curve and velocity-time curve) show that the agreement between the present model and the literature result is good.

The third and fourth impact event were taken from Cairns and Lagace (linear analytical, Reissner-Mindlin equations including transverse shear). The results are given in figures 12.18 and 12.19 respectively. Case 4 has a relatively high impact energy: 8 J. Also for this case the agreement is good.

The last case, case 5, is taken from Qian and Swanson (linear analytical, Reissner-Mindlin equations including transverse shear). They also present strain-time curves. The strain in the centre of the plate opposite to the point of impact in the ϕ = 0 direction was calculated with equation 12.26. For an accurate calculation of the strain more modes M and N have to be taken into account than for the force-time curves. The force-time and strain-time curves were calculated for two plates: one with a thickness h and one with a thickness 4h. 30x30 modes (NxM in equations 12.29 and 12.36) were taken into account. For this number of modes the force-time curves of both plates were accurately calculated, and also the strain-time curve of the thicker plate converged. For the strain-time curve of the plate with a thickness of h more modes are needed, but this was not possible due to the limited memory capacity of the computer (HP 9000). Figure 12.20 shows the force-time curves and the strain-time curves. The strain-time curve of NOLEIM corresponds quite well with the literature results for the thicker plate, more modes have to be taken into account to obtain accurate results for the thin plate.

12.6.3 Comparison of NOLEIM results with FEM and experimental results

The non linear model was compared with both finite element calculations and experimental results. The advantages of the FEM results of section 12.5 relative to the experimental results have already been discussed in section 12.5.2.

Non linear calculations were performed with NOLEIM with 5x5 modes and a time step of 1 μs.

Figure 12.21 compares the calculated and experimental force-time curve of a clamped 100x100 mm^2 Al 2024-T3 (t=1.26 mm) plate, impacted by an impactor mass of 594 g and an impact velocity of 0.767 m/S. Permanent contact between projectile and plate was assumed for this case. The agreement between experiment and theory is good.

Figure 12.22 and table 12.6 show the results for a clamped quasi-isotropic carbon 100x100 mm^2 plate with a [0/45/-45/90]$_s$ lay-up. The results are compared with the finite element and experimental results. The impactor mass is 302 g. Also in this case the impactor and the centre of the plate

were linked. The finite element results and the NOLEIM calculations agree relatively well. The lower contact force and the larger maximum central deflection of the experiments indicate that the plate has a smaller stiffness, probably due to a boundary condition which is not fully clamped.

Hertzian contact between projectile and plate and a condition of permanent rigid contact between them (displacement of impactor = central deflection of the plate) are compared in figure 12.23. The indentation stiffness was calculated with the Hertzian contact law (equation 9.3). The contact force with Hertzian contact shows much larger fluctuations. The higher order vibration of the plate with permanent contact is recognized in this curve.

12.7 Elasto-plastic model for impact on a circular plate: EPIM

12.7.1 The model

To incorporate plastic deformation in the model, additional simplifications have to be made. These are:

1. Unloading of plastically deformed material will make the model relatively complicated. Unloading may occur during impact because of vibration effects, and will occur when the maximum deflection is reached. Therefore the elasto-plastic impact model (EPIM) will consider quasi-static loading.

2. An axisymmetrical dent shape of the specimen under loading is assumed. For orthotropic material like ARALL this will be an approximation. The shape measurements of chapter 10 showed that this assumption will be relatively accurate.

3. The shape of the dent is assumed to be known and constant for the specimen under loading. The polynomial expression given in chapter 10 will be used for the dent shape.

4. The elasto-plastic material will be assumed to have a bilinear effective stress-strain curve. In this case the stress-strain curve can be described by the elastic Young's modulus E, the yield stress σ_y and the strain hardening coefficient α.

The strains will be calculated from an assumed axisymmetrical deformation field with the von Kármán equations (equations 12.26). After this the

stored internal energy of the plate will be calculated by integration.

The effective stresses and effective strains are assumed to be related by the effective stress-strain curve. The effective stress (von Mises stress) is defined by[8]:

$$\bar{\sigma}^2 = \frac{1}{2} \left[(\sigma_r - \sigma_\theta)^2 + (\sigma_\theta - \sigma_z)^2 + (\sigma_z - \sigma_r)^2 \right] \qquad (12.60)$$

The stress σ_z in thickness direction of the plate will be set to zero (plane stress).

The effective strain is[8]:

$$\bar{\varepsilon}^2 = \frac{4}{3} \left[\varepsilon_r^2 + \varepsilon_\theta^2 + \varepsilon_r \varepsilon_\theta \right] \qquad (12.61)$$

The stress-strain curve is shown schematically in figure 12.24. The strain energy dU of a volume element is the area under this curve:

$$dU = \frac{1}{2} E \bar{\varepsilon}^2 \qquad \text{for} \quad \bar{\varepsilon} < \frac{\sigma_y}{E} \qquad (12.62)$$

$$dU = \frac{1}{2} \alpha \bar{\varepsilon}^2 + \left[1 - \frac{1}{2} \frac{\alpha}{E} \right] \frac{\sigma_y}{\bar{\varepsilon}} - \frac{1}{2} \frac{\sigma_y^2}{E} \left[1 - \frac{\alpha}{E} \right] \qquad \text{for} \quad \bar{\varepsilon} > \frac{\sigma_y}{E}$$

The total strain energy in the elasto-plastic layers is obtained by:

$$U_p = \int\int_V dU \; 2 \pi \; r \; dr \; dz \qquad (12.63)$$

This integral is calculated by a numerical summation of the strain energy of small elements over the plate. For each element a mean radial and tangential strain is calculated with the simplified von Kármán equations with the known shape of the dent, at a certain value of the central deflection w_0. From these strain components the effective strain is calculated with equation 12.61. The contribution of the element to the total strain energy is obtained by substitution of this effective strain in

equation 12.62.

The shape of the dent is assumed to have the following form, taken from the results described in chapter 10:

$$\xi = \frac{w}{w_0} = \left(1 - \eta^2\right)^2 (1 - 1.2\,\eta + 1.2\,\eta^2) \tag{12.64}$$

Only the fibres are assumed to store the strain energy in the fibre/matrix layers. The strain in the fibre layer is given by:

$$\varepsilon_f(r,\theta) = \varepsilon_r(r)\,\cos^2\theta + \varepsilon_\theta(r)\,\sin^2\theta \tag{12.65}$$

And the strain energy is calculated by:

$$U_f = \int\!\!\int_V\!\!\int dU\; r\; d\theta\; dr\; dz = \int\!\!\int_V\!\!\int \frac{1}{2} E_f \left[\varepsilon_f(\theta)\right]^2 r\; d\theta\; dr\; dz =$$

$$\int\!\!\int_A \frac{1}{2}\,\pi\,E_f \left[\frac{3}{4}\,\varepsilon_r^2 + \varepsilon_r\varepsilon_\theta + \frac{3}{4}\,\varepsilon_\theta^2\right] r\; dr\; dz \tag{12.66}$$

with E_f as the stiffness of the fibre/matrix layer.
Also this integral is calculated by a summation of the strain contributions over small elements of the plate.

In the elasto-plastic impact model EPIM the internal strain energy is calculated as a summation over 25x25 elements as a function of the central deflection w_0. The corresponding contact force is determined by:

$$F = \frac{dU}{dw_0} \cong \frac{U(w_0 + \varepsilon) - U(w_0)}{\varepsilon} \tag{12.67}$$

with ε as a small quantity, in this case taken as 0.0001 w_0.

12.7.2 Comparison of the model with a literature model

Results of EPIM were compared with results of the model of Shivakumar et al.[15]. This model has already been discussed in section 9.5. They also include geometrical non linearity with the von Kármán equations, but they use the linear elastic deflection and radial displacement fields of equation 9.21. In the model the elastic energy of a deflected plate is calculated by the use of the total stiffness matrix of the plies, as is also done in NOLEIM (equation 12.28). In EPIM and NOLEIM the effect of the radial displacement is neglected, and in EPIM only the longitudinal stiffness of a fibre/matrix layer E_f is taken into account. To compare EPIM with the model of Shivakumar et al. the linear elastic deflection field (equations 9.21 and 12.3) was used instead of the polynomial in equation 12.64.

The carbon/epoxy plate of Shivakumar et al. has a thickness of 1.04 mm, the longitudinal stiffness of a ply is 131 GPa. The force-deflection curve was calculated for three different dimensions of the plate: a = 25.4, 38.1 and 50.8 mm. Figure 12.25 compares the literature model with the EPIM results. The failure boundary was calculated by Shivakumar et al. by a stress criterion: Tsai-Wu. They used a longitudinal tensile strength of 1500 MPa for the failure criterion. For the calculation of the failure boundary in EPIM a maximum strain criterion was used. The maximum strain was taken equal to the ratio of the longitudinal tensile strength and the stiffness in this direction ε_u = 1500/131,000 = 1.15 %. The results of Shivakumar et al. and EPIM agree well.

12.7.3 Comparison with experimental results

Results of quasi-static tests as described in chapter 7 were used to check the accuracy of the model. The input parameters of the metal and fibre/matrix layers are presented in tables 12.7 and 12.8. In figures 12.26 to 12.29 the model results are compared with experimental results. In figure 12.29 EPIM calculations are compared with the result of a puncture test of chapter 11. In general the stiffness of the plate is overestimated by the model (except for figure 12.29).

432

In figure 12.26 the total internal strain energy and the strain energy due to bending only are shown. The strain energy due to bending only is significantly smaller than the energy due to stretching of the plate, but it is not negligible.

12.8 Conclusions

1. Impact with very low impact energies and a large mass of the impactor relative to the effective mass of the plate can be accurately described by a simple mass-spring model.

2. This mass-spring model can be easily extended to account for an initial stress in the plate. The effect of an initial stress is an increase of the effective stiffness of the plate. The additional stiffness can be considerable.

3. In the mass-spring model the contact between the projectile and the plate is established by a rigid contact, by tying them together. A common way to describe this contact is by using a Hertzian contact law. This model describes the deformation of the plate as the deformation of two springs in series: a non linear indentation stiffness and a linear bending stiffness of the plate. When the elastic Hertzian contact law is applied for the indentation stiffness, the calculations for the impact on an aluminium plates leads to large contact force fluctuations and multiple impact. The deflection-time and velocity-time curves are less dependent on the indentation stiffness. The force fluctuations which were found in the experimental results appear in the results of the model, if the Hertzian contact law is applied.

4. A non-linear finite element analysis leads to results which are relatively accurate compared with experimental results.

5. The linear part of the non linear impact model NOLEIM was checked with literature data, which gives satisfactory agreement. The literature models all included transverse shear effects. It may be concluded that transverse shear is not an important phenomenon in the results presented in the literature.

6. The non linear calculations of NOLEIM corresponded very well with the non linear finite element calculations. The correspondence between NOLEIM results and experimental data is not in every case very good. This is probably due to the boundary conditions of the tested plates; they were not perfectly clamped.

7. The elasto-plastic impact model EPIM describes a quasi-static indentation. The model was compared with the model of Shivakumar et al.[15]. In EPIM only the longitudinal stiffness of a fibre layer is taken into account, whereas in the model of Shivakumar et al. the complete stiffness matrix is used. The model of Shivakumar also includes the radial displacement u in the model, whereas this displacement is neglected in EPIM. However, the results of the two models correspond very well.

8. EPIM overestimates the stiffness of the ARALL and monolithic aluminium sheet materials. The agreement is satisfactory. The calculated maximum strains in the fibre and metal layers at the fracture energy are realistic.

9. The non linear models presented in this chapter provide a way to describe the behaviour of plates with large deflections. The models are able to simulate the impact of objects with a more realistic impact energy as compared to models presented in the literature.

references

1. Goldsmith, W.; Impact, the theory and physical behaviour of colliding solids, London, 1960.

2. Timoshenko, S.P.; Woinowsky-Krieger, S.; Theory of plates and shells; McGraw-Hill Book Company, 1970.

3. Sun, C.T.; Chen, J.K.; On the impact of initially stressed composite laminates, J.Composite materials, Vol.19, pp.490-504, 1985.

4. Wu, H.T.; Springer, G.S.; Impact induced stresses, strains and delaminations in composite plates, J.Composite materials, Vol.22, pp.533-560, 1988.

5. Cairns, D.S.; Lagace, P.A.; Transient response of graphite/epoxy and Kevlar/epoxy laminates subjected to impact, AIAA/ASME/ASCE/AHS

29th structures, structural dynamics and materials conference, 1988.

6. Qian, Y.; Swanson, S.R.; Experimental measurement of impact response in carbon/epoxy plates, 30th AIAA/ASME/ASCE/AHS/ASC structural dynamics and materials conference, 1989.

7. Qian, Y.; Swanson, S.R.; A comparison of solution techniques for impact response of composite plates, Composite structures Vol.14, pp.177-192, 1990.

8. Mendelson; Plasticity, theory and application, New York, 1968.

9. Roark, R.J.; Young, W.C.; Formulas for stress and strain, fifth edition, McGraw-Hill International Book Company, 1975.

10. Schalkwijk, R. van; Konter, A.W.A.; Dynamic analysis with MARC, MARC Analysis Research Corporation - Europe, Zoetermeer, 1986.

11. Spies, G.J.; Composite materials (in Dutch), lecture notes, TU Delft, 1978.

12. Lekhnitskii, S.G.; Anisotropic plates, Gordon and Breach science publishers, 1968.

13. Zukas, J.A.; Nicholas, T.; Swift, H.; Greszcuk, L.B.; Curran, D.R.; Impact Dynamics, John Wiley & Sons, 1982.

14. Bathe, K.J.; Finite-elemente-methoden, Springer-Verlag, Berlin, 1986.

15. Shivakumar, K.N.; Elber, W.; Illg, W.; Prediction of low-velocity impact damage in thin circular laminates, AIAA Journal, Vol.23, No.3, pp.442-449, 1985.

boundary conditions	simply supported (1)	clamped (2)	(2)/(1) $\nu=0.3$
shape			
circular (1)	$\dfrac{4\pi \; E \; t^3}{3(3+\nu)(1-\nu)a^2}$	$\dfrac{4\pi \; E \; t^3}{3(1-\nu^2)a^2}$	2.54
square (2)	$\dfrac{7.893 \; E \; t^3}{A^2}$	$\dfrac{16.37 \; E \; t^3}{A^2}$	2.07
(1)/(2) $\nu=0.3, 2a=A$	0.9189	1.125	

table 12.1 Spring stiffness of circular and square plates, derived from ref.9.

v_0 (m/s)	analytical mass-spring		FEM analysis		comparison	
	F_{max} (N)	$w_{0,max}$ (mm)	F_{max} (N)	$w_{0,max}$ (mm)	$\dfrac{F_{max,anal}}{F_{max,FEM}}$	$\dfrac{w_{0,max,anal}}{w_{0,max,FEM}}$
0.443	106	0.501	110	0.485	0.96	1.03
0.626	150	0.708	172	0.670	0.87	1.05
0.767	183	0.867	218	0.806	0.84	1.07

table 12.2 Comparison of analytical mass-spring analysis and finite element calculations.

material	v_0 (m/s)	with damping			without damping			comparison	
		v_r (m/s)	F_{max} (kN)	$w_{0,max}$ (mm)	v_r (m/s)	F_{max} (kN)	$w_{0,max}$ (mm)	force ratio	defl. ratio
2024-T3	1.26	1.17	0.43	1.28	1.22	0.51	1.30	0.84	0.99
	7.68	4.23	4.04	5.40	4.48	4.49	5.61	0.90	0.96
2H33	2.33	1.90	0.93	1.97	1.95	1.12	2.00	0.83	0.99
carbon	0.94	0.93	0.36	0.91	0.93	0.36	0.93	1.00	0.98

table 12.3 The influence of damping on the maximum force and central deflection during impact and the velocity after impact.

material	experiments			FEM analysis		comparison	
	T (J)	F_{max} (kN)	$w_{0,max}$ (mm)	F_{max} (kN)	$w_{0,max}$ (mm)	force ratio	deflection ratio
2024-T3	0.24	0.56	1.79	0.51	1.30	0.91	0.73
	7.34	3.57	4.86	4.12	5.21	1.15	1.07
2H33	0.82	0.89	1.64	0.93	1.96	1.05	1.20
	5.86	2.76	5.20	2.82	4.42	1.02	0.85
carbon/	0.13	0.28	1.17	0.36	0.91	1.29	0.78
PEI	1.17	1.05	2.85	1.50	2.33	1.43	0.82

table 12.4 Comparison of experimental results and FEM calculations of impact on a square plate.

case	ref.	sheet		projectile
1/3	3,5,7	dim. (mm^2):200x200, simply supp.		m_p (g): 8.4
		lay-up:	$[90/0/90/0/90]_s$	v_0 (m/s): 3
		t_{ply} (mm):	0.269	2R (mm): 12.7
		c_{11} (GPa):	142.33	
		c_{22} (GPa):	9.798	
		c_{12} (GPa):	2.939	
		c_{66} (GPa):	5.53	
		k (kN/mm$^{3/2}$):	44.7	
		ρ (kg/m^3):	1536	
2	4	dim. (mm^2):76.4x76.4, clamped		m_p (g): 2.9
		lay-up:	$[0/-45/45/90]_{2s}$	v_0 (m/s): 25.4
		t_{ply} (mm):	0.1588	2R (mm):
		c_{11} (GPa):	146.33	
		c_{22} (GPa):	10.06	
		c_{12} (GPa):	3.018	
		c_{66} (GPa):	5.69	
		k (kN/mm$^{3/2}$):	equation 9.9	
		ρ (kg/m^3):	1536	
4	5	dim. (mm^2):190x70, clamped		m_p (g): 8.4
		lay-up:	$[45/-45/0]_{2s}$	v_0 (m/s): 44
		t_{ply} (mm):	0.1588	2R (mm): 12.7
		c_{11} (GPa):	142.8	
		c_{22} (GPa):	9.87	
		c_{12} (GPa):	2.961	
		c_{66} (GPa):	6.0	
		k (kN/mm$^{3/2}$):	equation 9.9	
		ρ (kg/m^3):	1540	

table 12.5 Cases to check the linear part of the impact model
with literature results.

5	7	dim.(mm^2):200x200, simply supp.	m$_p$ (g): 8.537
		lay-up: [0/90/0/90/0]$_s$	v$_0$ (m/s): 3.0
		t$_{ply}$ (mm): 0.269 and 1.076	2R (mm): 12.7
		c$_{11}$ (GPa): 142.33	
		c$_{22}$ (GPa): 9.798	
		c$_{12}$ (GPa): 2.939	
		c$_{66}$ (GPa): 5.53	
		k (kN/mm$^{3/2}$): 26.54	
		ρ (kg/m^3): 1536	

table 12.5 (continued) Cases to check the linear part of the impact model with literature results.

v$_0$ (m/S)	FEM		NOLEIM		experimental	
	F$_{max}$ (kN)	w$_0$ (mm)	F$_{max}$ (kN)	w$_0$ (mm)	F$_{max}$ (kN)	w$_0$ (mm)
0.94	0.36	0.93	0.32	0.91	0.28	1.17
2.79	1.50	2.33	1.38	2.25	1.05	2.85
4.50	2.94	3.32	2.78	3.18	–	–
6.01	4.09	4.06	4.37	3.85	2.88	5.21

table 12.6 Comparison between FEM, experimental and analytical NOLEIM results, impactor mass 302 g.

Al alloy	E (GPa)	σ_y (MPa)	α (MPa)
2024-T3	72	340	1370
7075-T6	72	570	640

table 12.7 Material properties used as input of EPIM.

439

fibre	prepreg code	E_f (GPa)
aramid	H	58.8
R-glass	R_2	51.6

table 12.8 Prepreg properties used as input of EPIM.

figure 12.1 Test set-up for linear elastic impact tests.

figure 12.2 Mass-spring model.

441
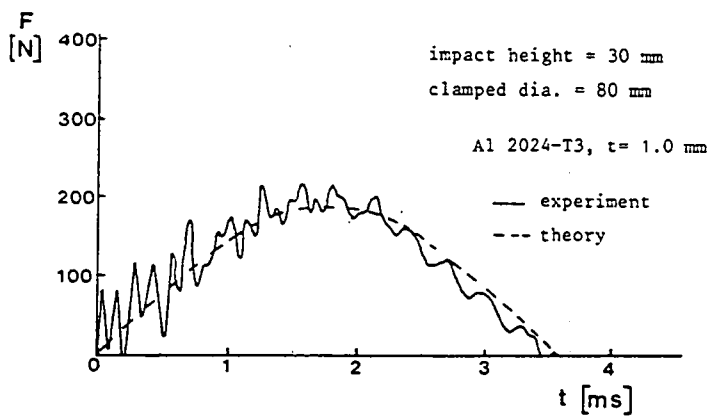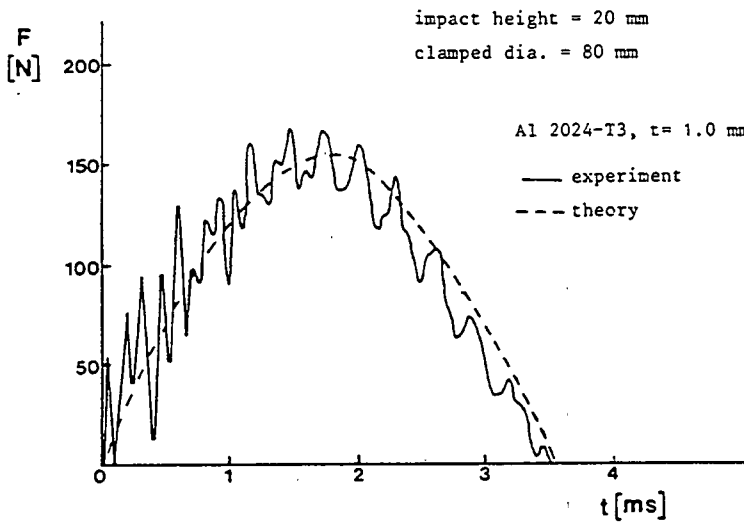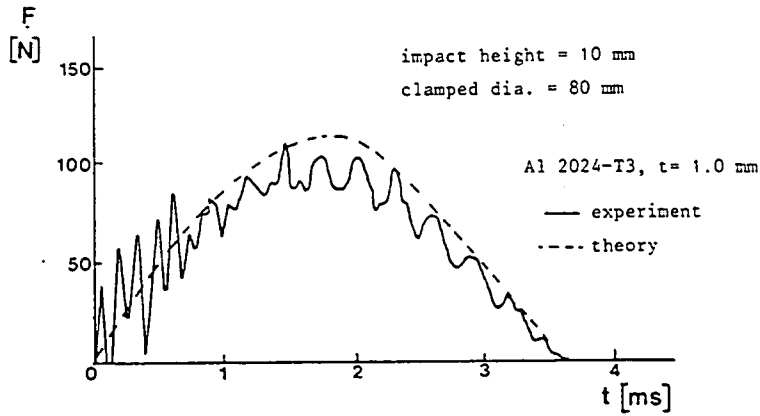
figure 12.3 Comparison of experimental results and the mass-spring-model, clamped diameter = 80 mm.
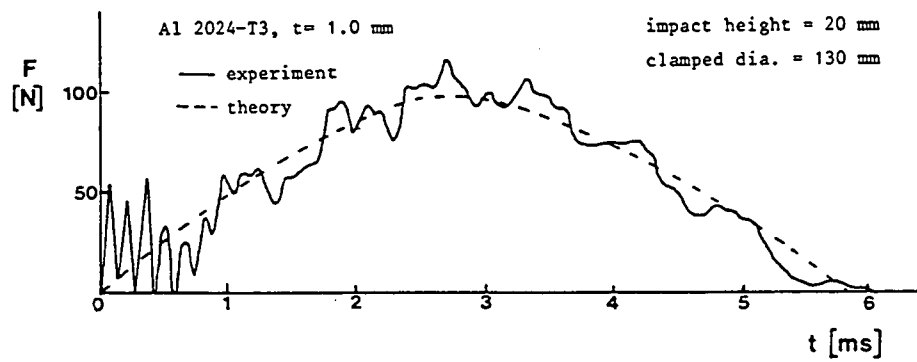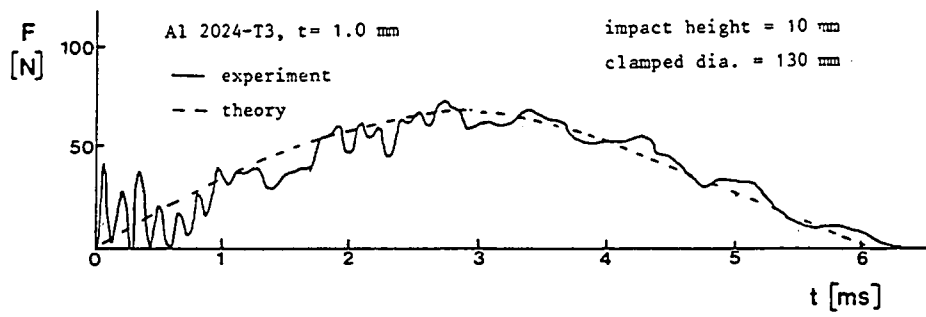
figure 12.4 Comparison of experimental results and the mass-spring
model, clamped diameter = 130 mm.
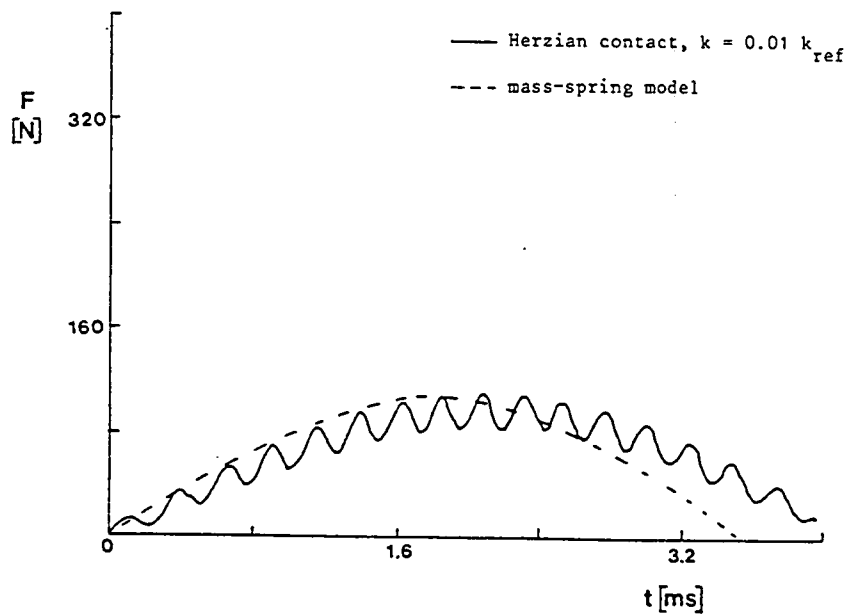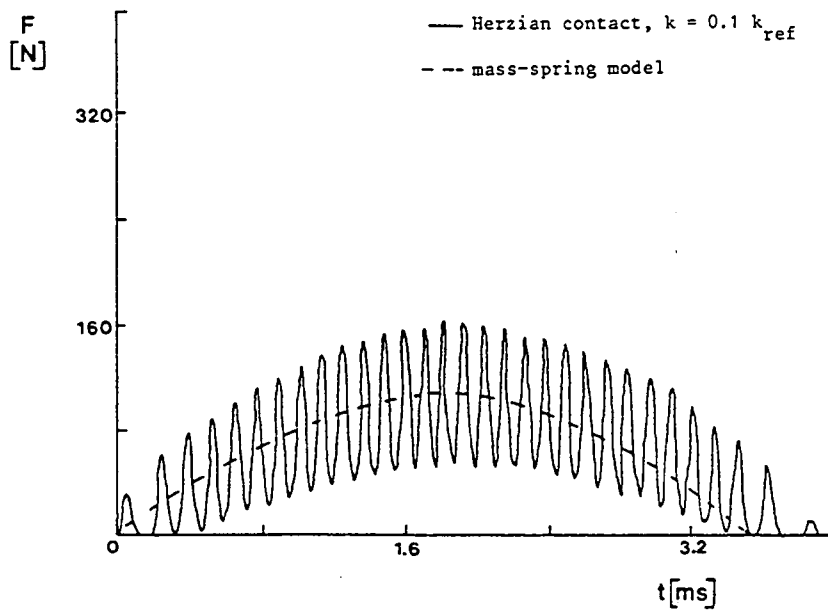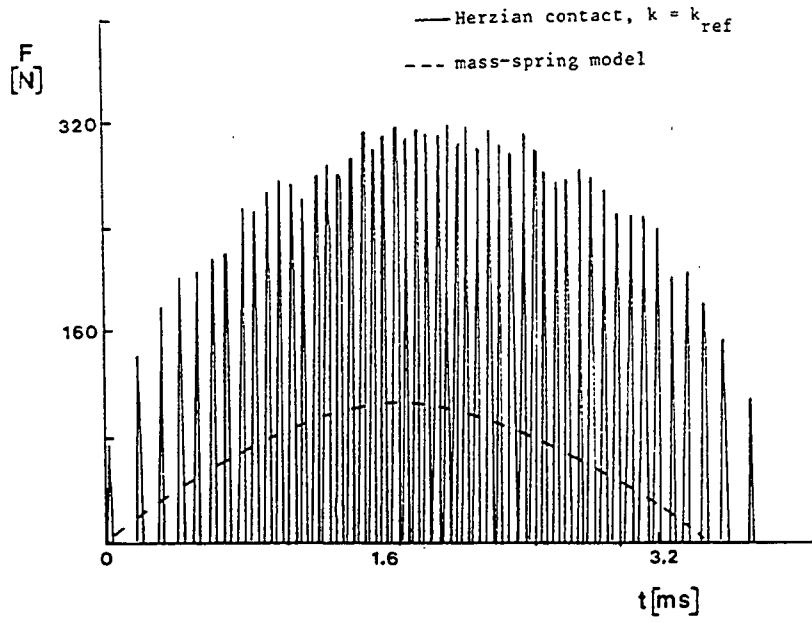
figure 12.5 Comparison of linear elastic impact model with Hertzian contact for varying indentation stiffness k and the mass-spring model.
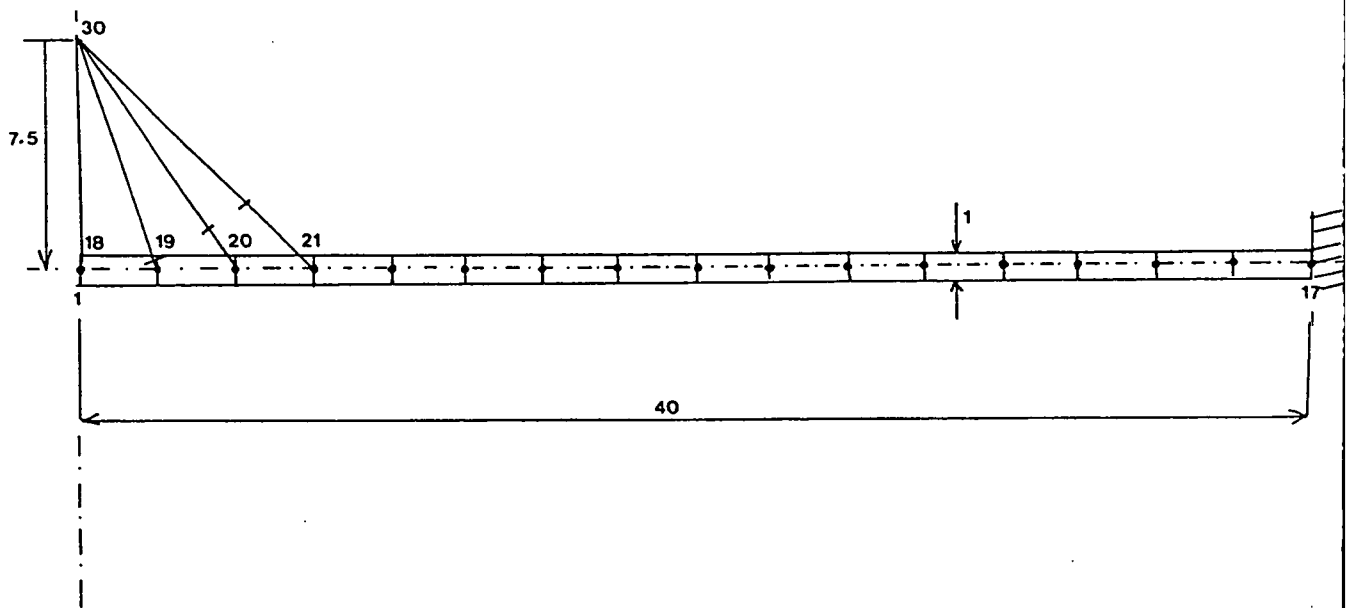
figure 12.6 Finite element model for linear elastic impact.
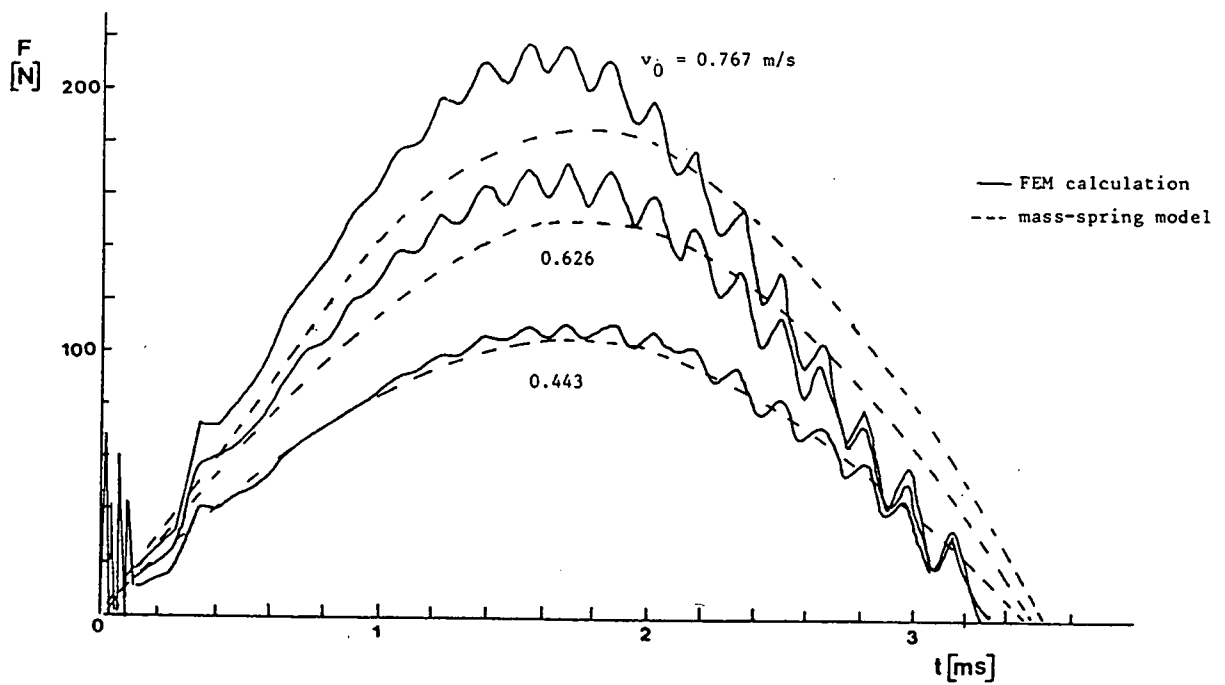
figure 12.7 Force-time curves, comparison of finite element results and the mass-spring model.
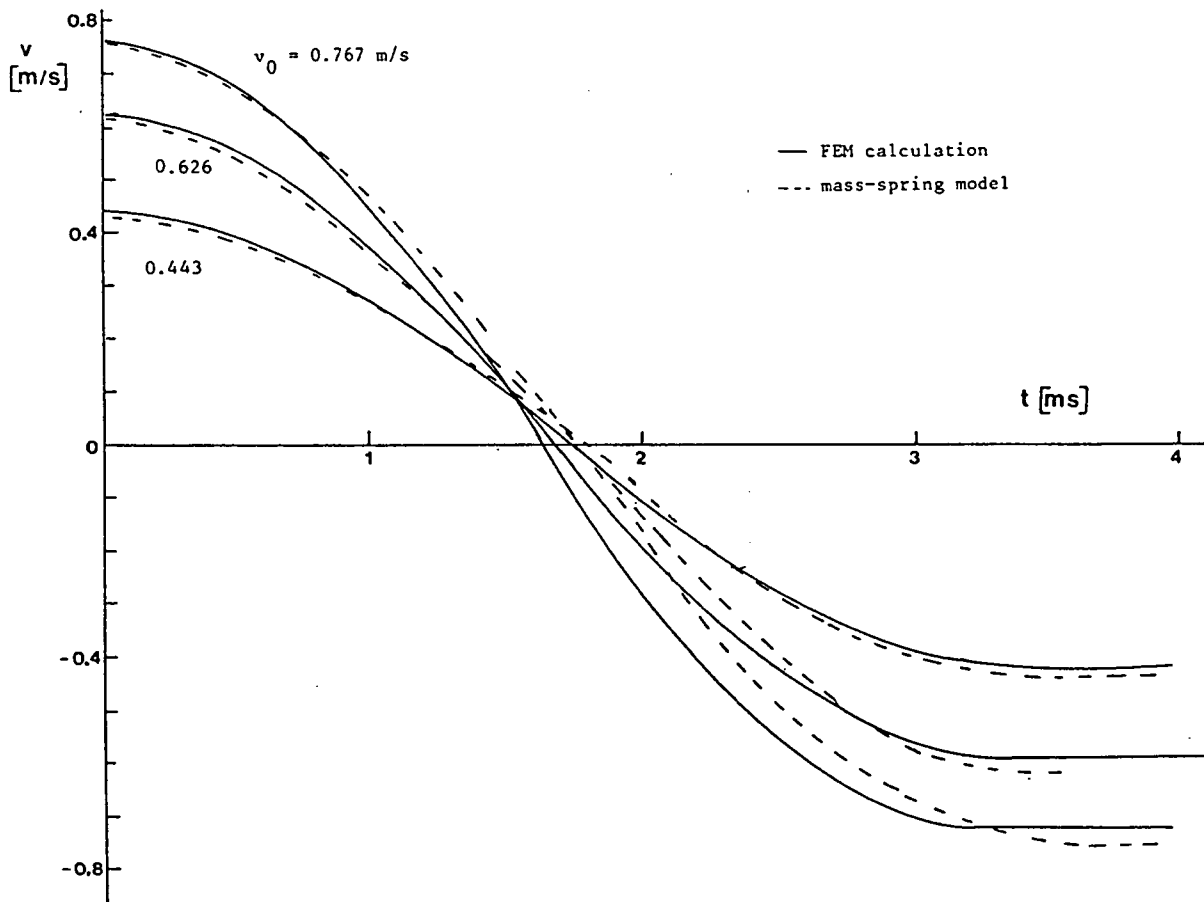
figure 12.8 Velocity-time curves, comparison of finite element
calculations and the mass-spring model.
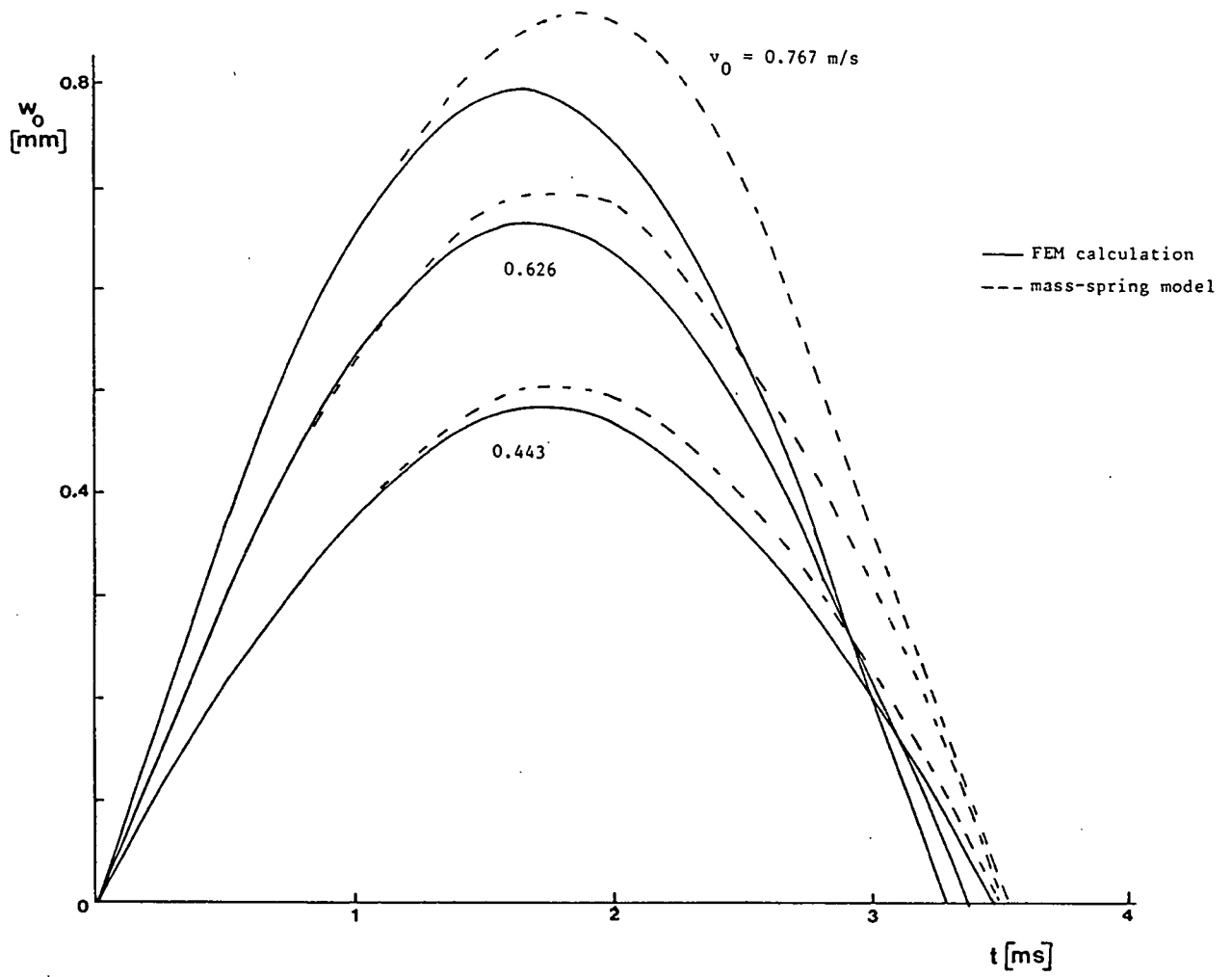
figure 12.9 Central deflection-time curves, comparison of finite
element calculations and the mass-spring model.

figure 12.10 Finite element model for square plates.

448
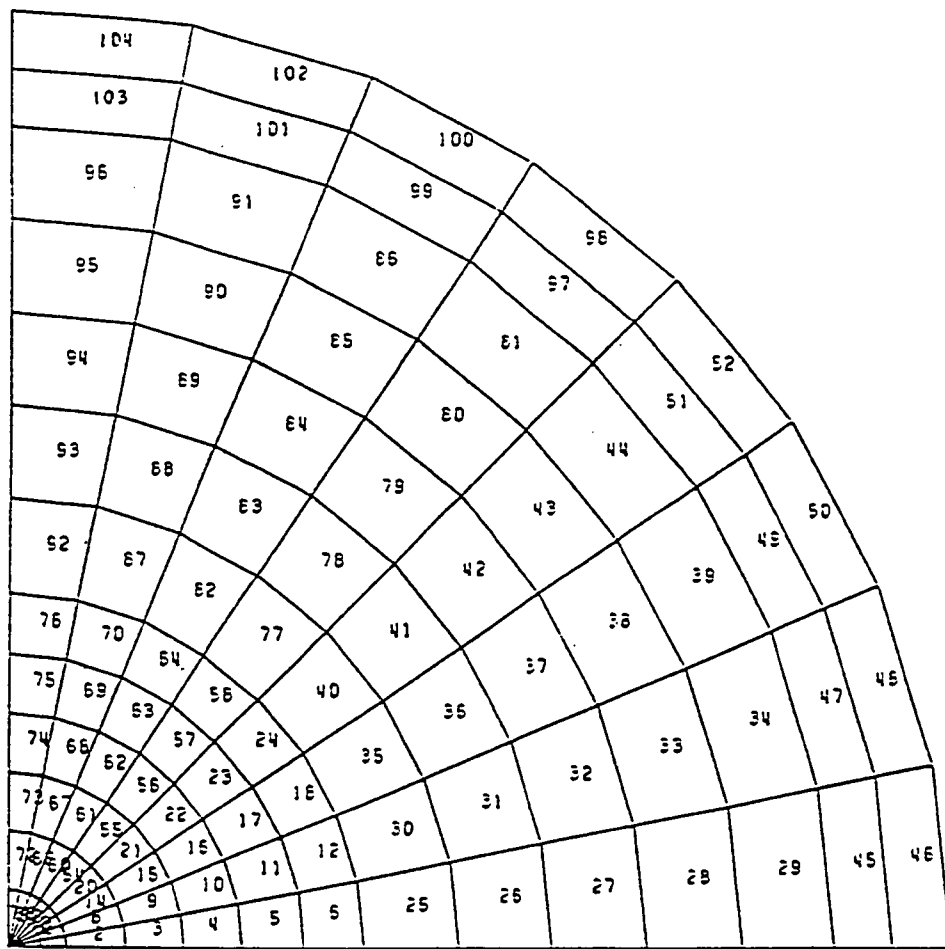
figure 12.11 Finite element model for circular plates.
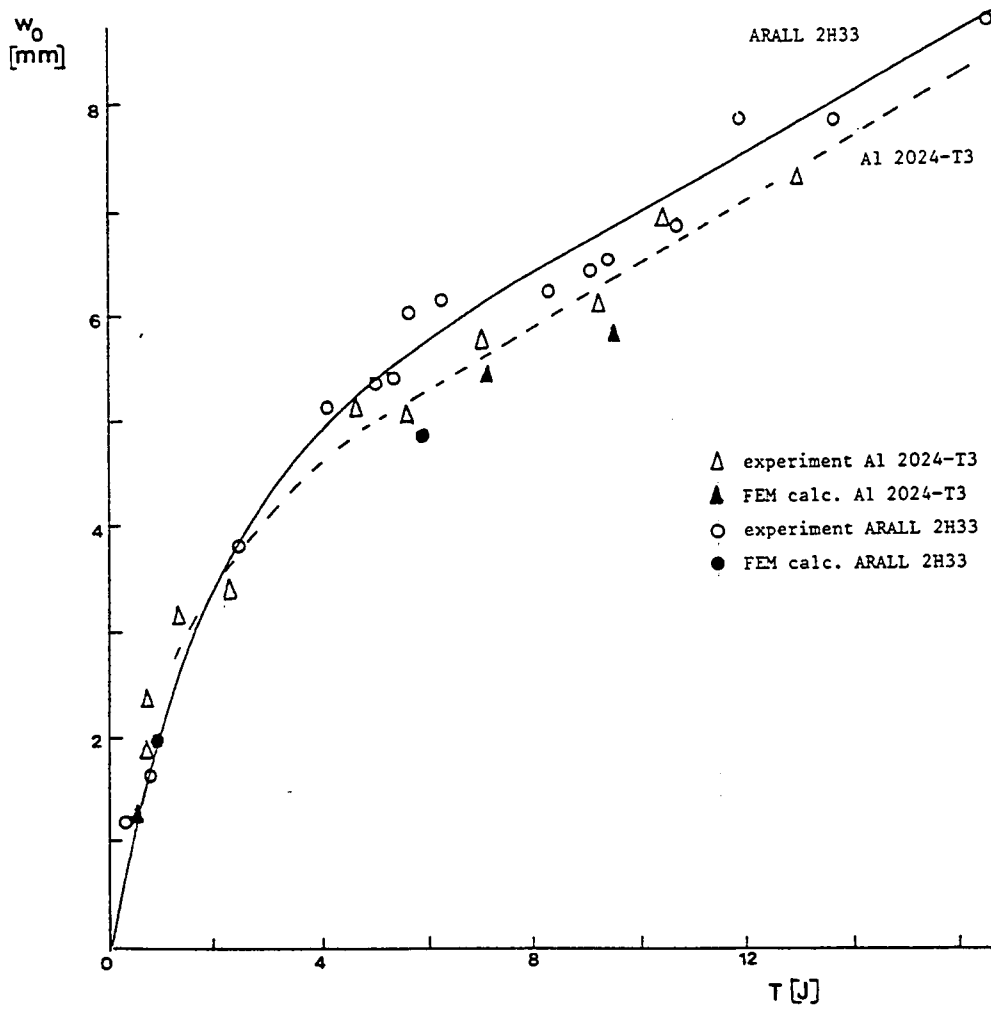
figure 12.12 Central deflection as function of the impact energy for monolithic Al 2024-T3 and aramid ARALL 2H33, comparison of finite element calculations and experimental results.
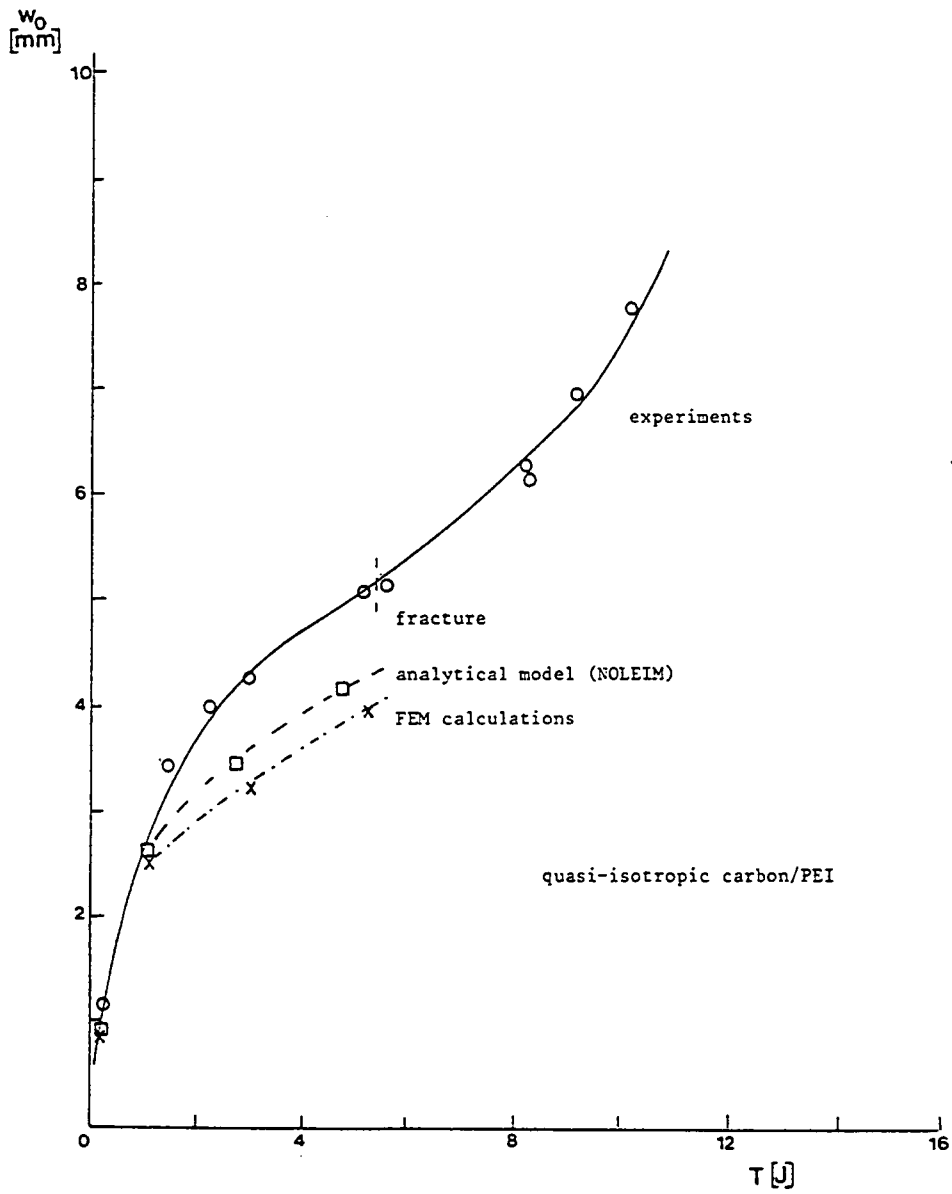
figure 12.13 Central deflection vs. impact energy for quasi-isotropic carbon/PEI, comparison of experimental results and FEM and analytical calculations.
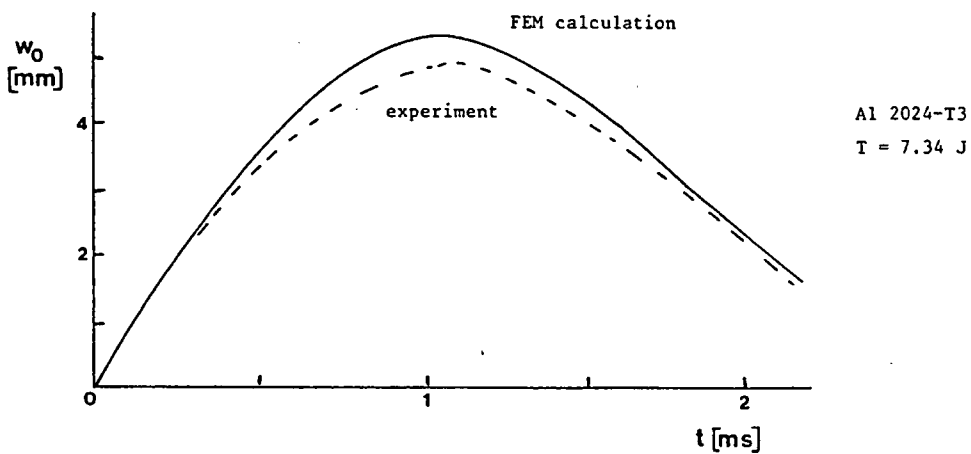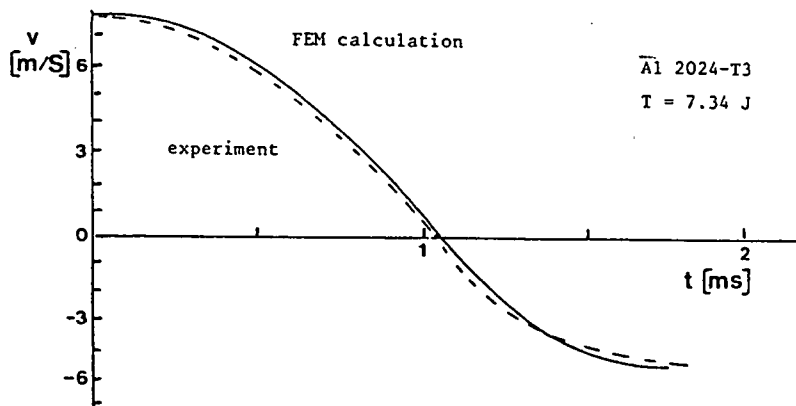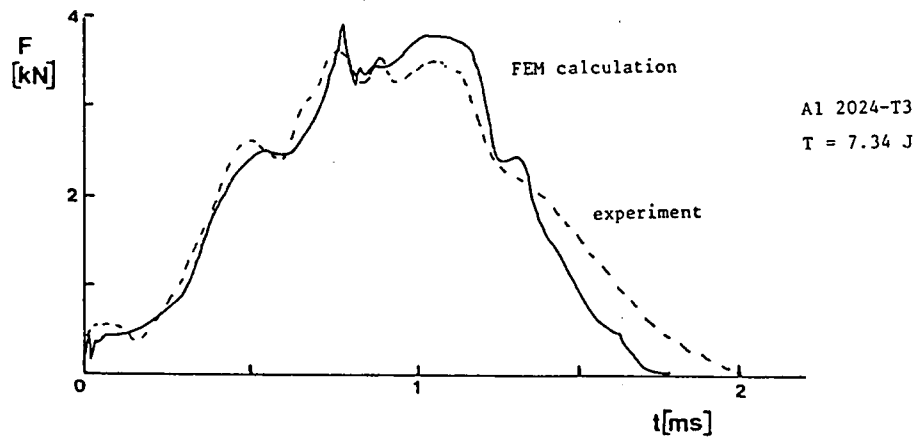
figure 12.14 Force-time, velocity-time and central deflection-time curves for Al 2024-T3, comparison of experimental and finite element results.

452
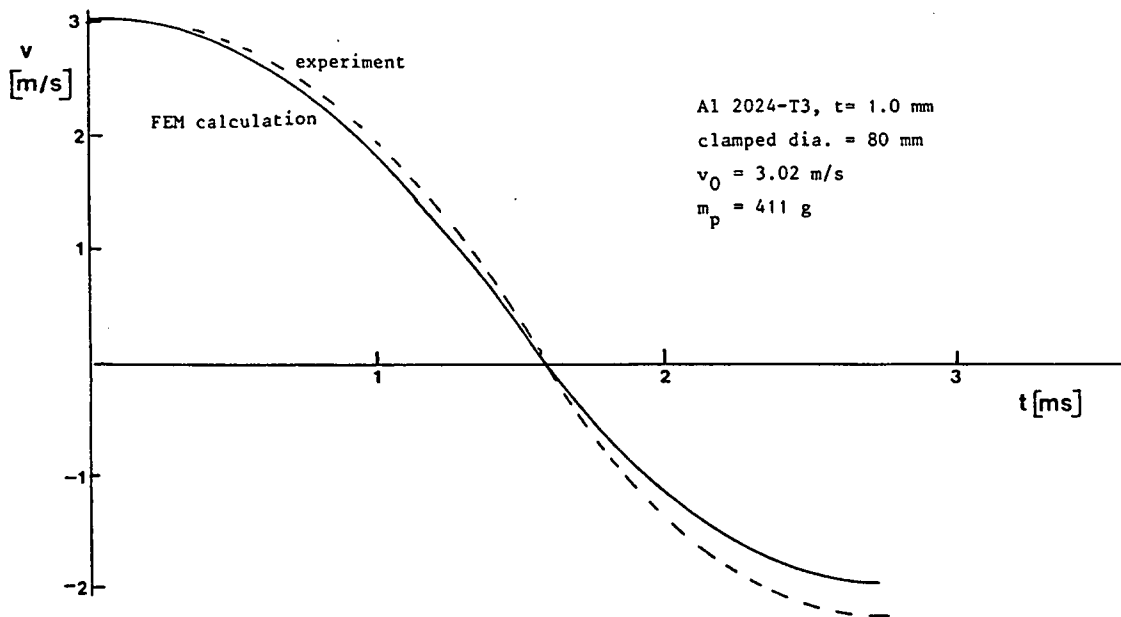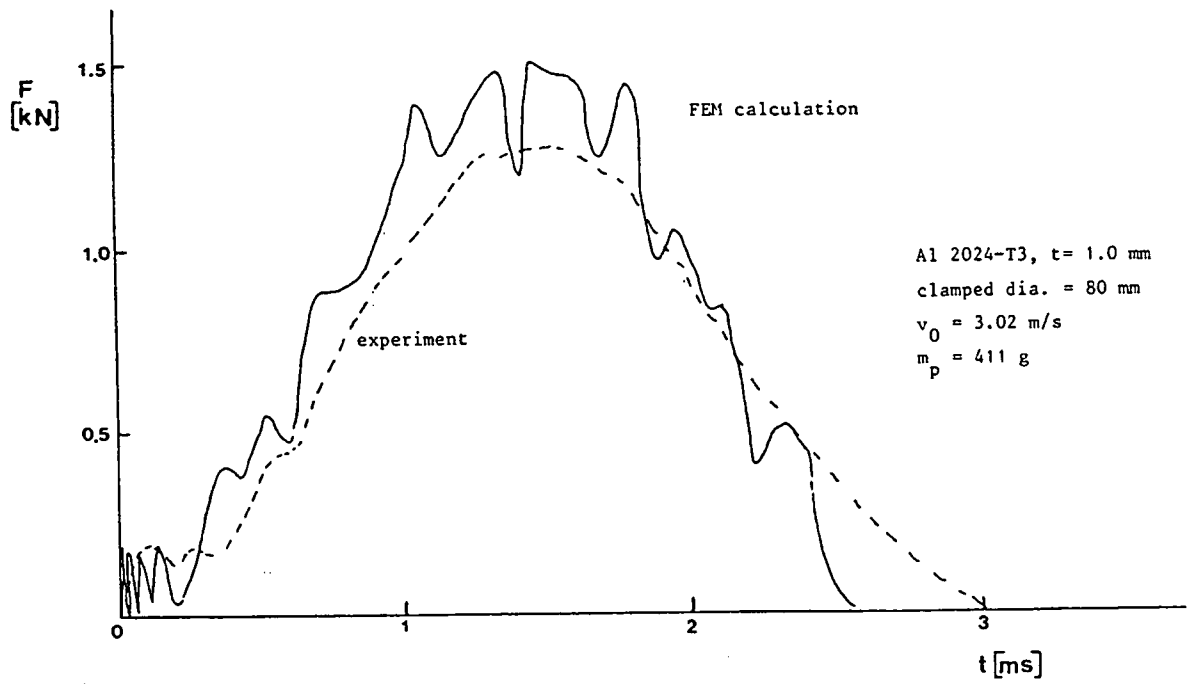
figure 12.15 Force-time and velocity-time curves for monolithic Al 2024-T3, comparison of experimental and finite element results.

experiment

FEM calculation

Al 2024-T3, t= 1.0 mm

clamped dia. = 80 mm

v_0 = 3.02 m/s

m_p = 411 g
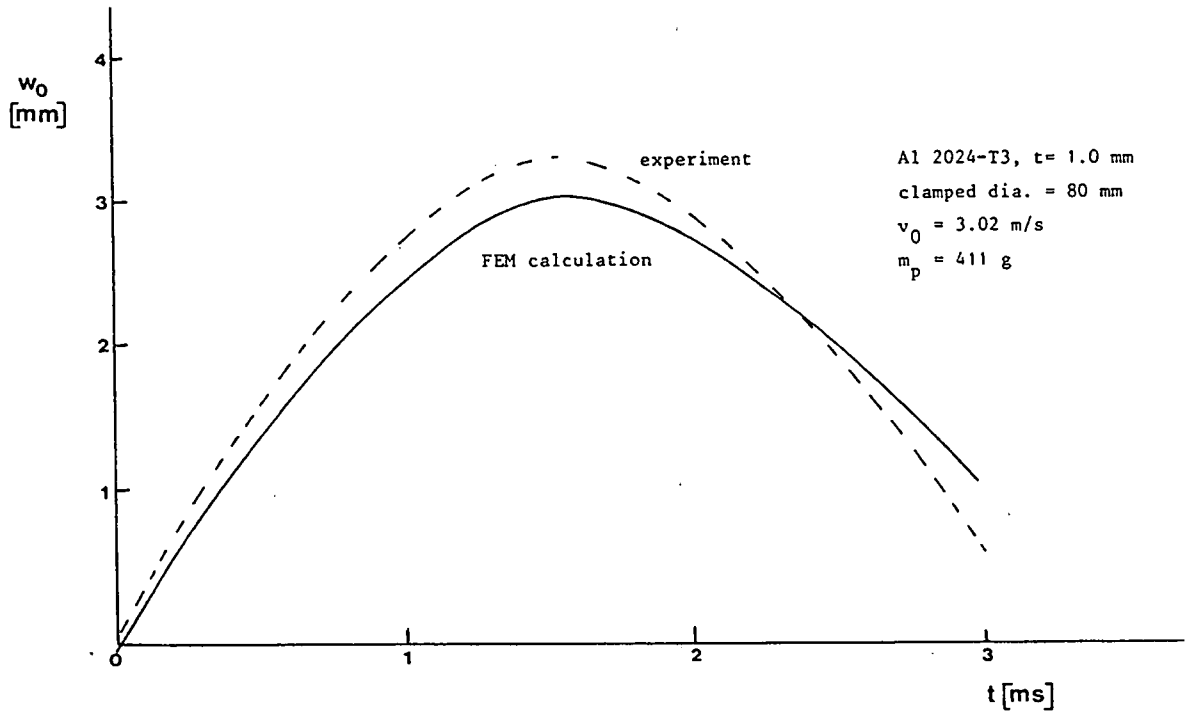
figure 12.15 (continued) Central deflection-time curve for monolithic Al 2024-T3, comparison of experimental and finite element results.

Cairns and Lagace

Sun and Chen

present model (NOLEIM)
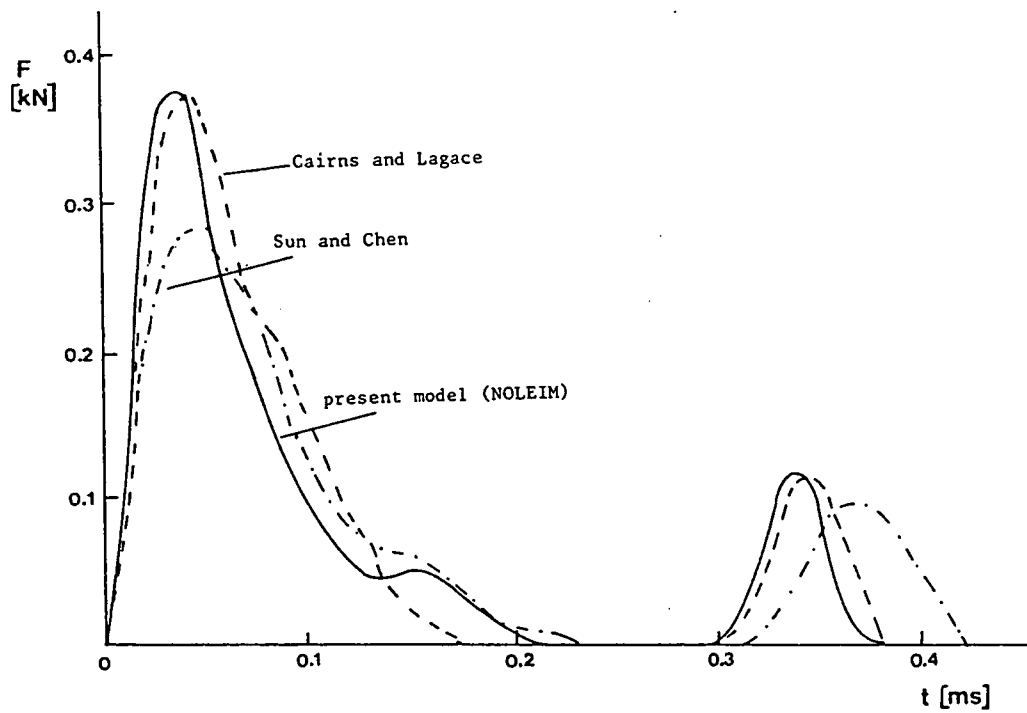
figure 12.16 Comparison of the linear part of the analytical model NOLEIM with results of model found in the literature (case 1).
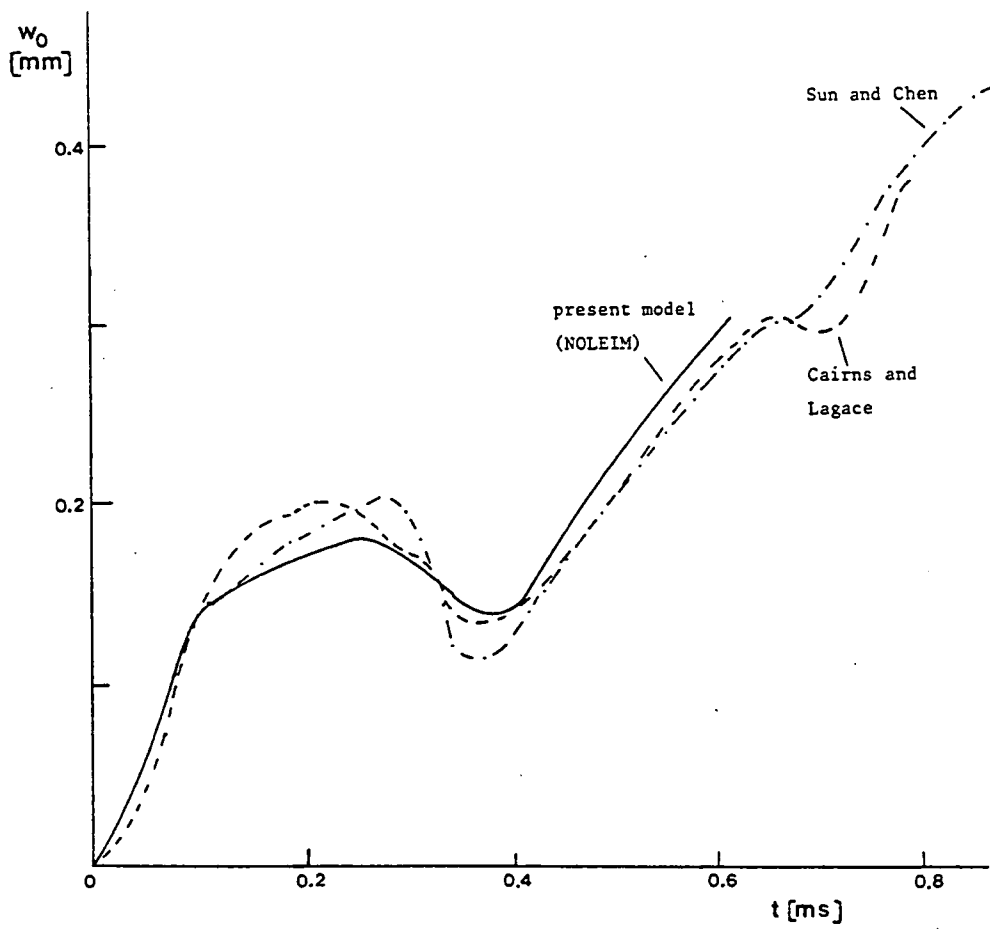
figure 12.16b Comparison of the linear part of the analytical model
NOLEIM with results found in the literature (case 1).
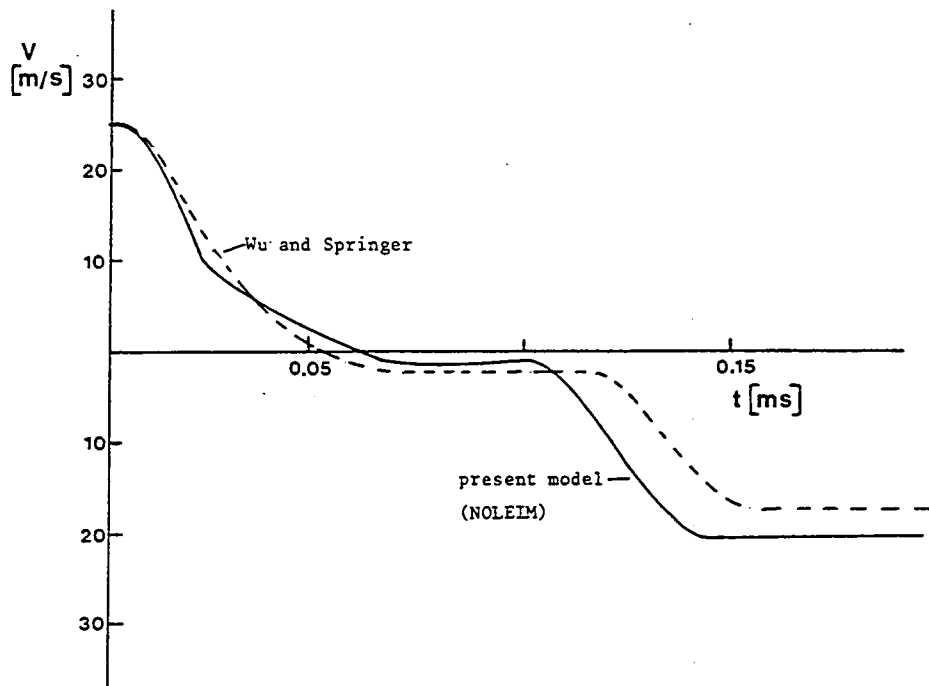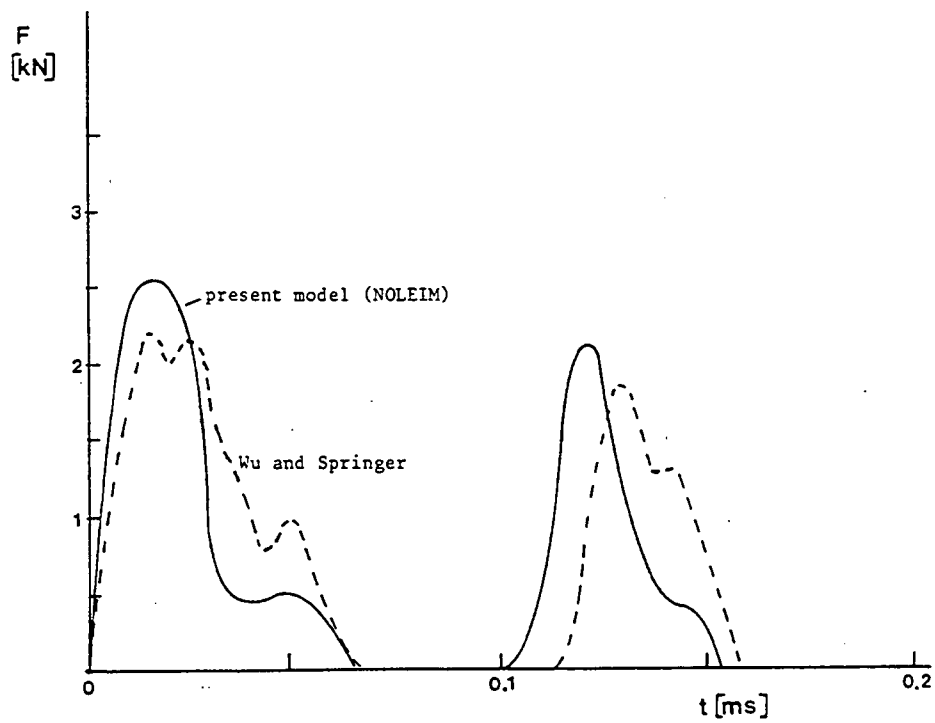
figure 12.17 Comparison of the linear part of the analytical model
NOLEIM with results a model found in the literature (case 2).
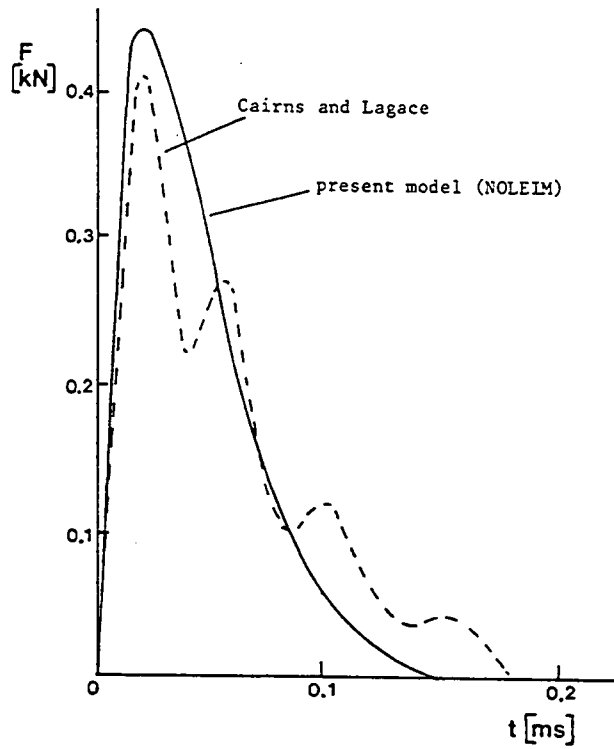
figure 12.18 Comparison of
the analytical model NOLEIM
with results of a model
found in the literature
(case 3).
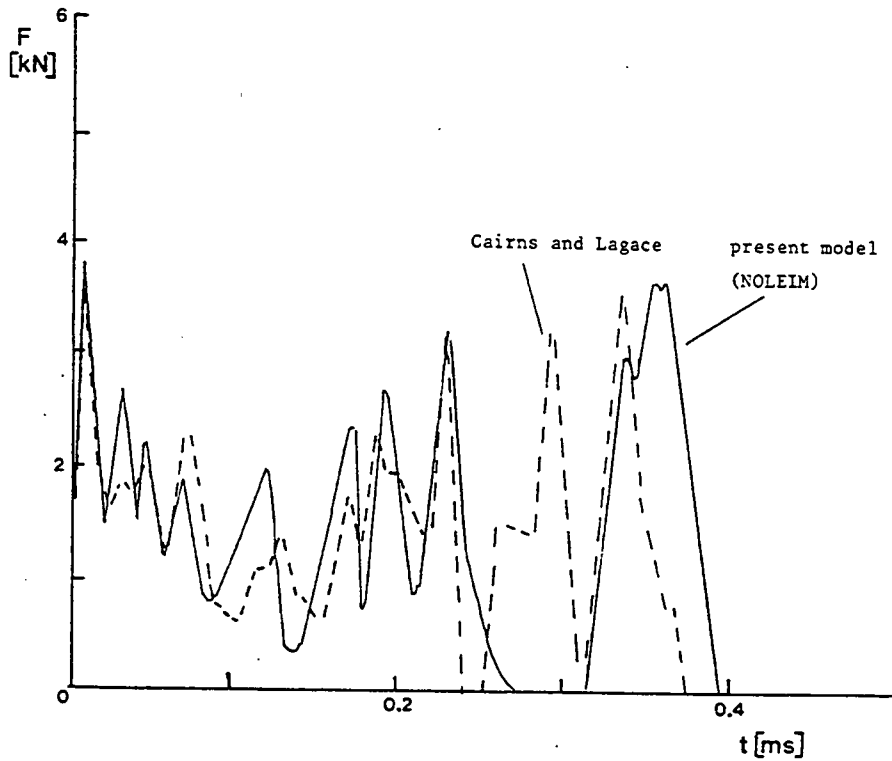
figure 12.19 Comparison of the analytical model NOLEIM with results
of a model found in the literature (case 4).
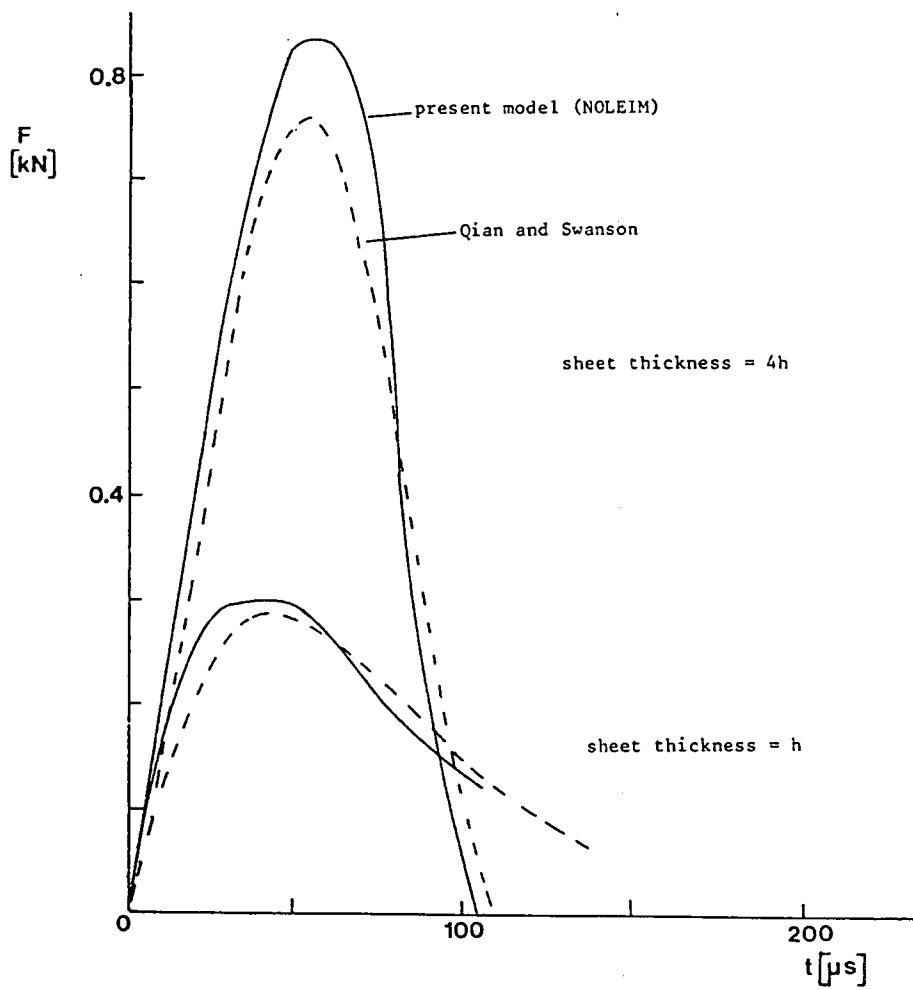
figure 12.20

Comparison of the analytical model NOLEIM with the results of a model found in the literature (case 5).
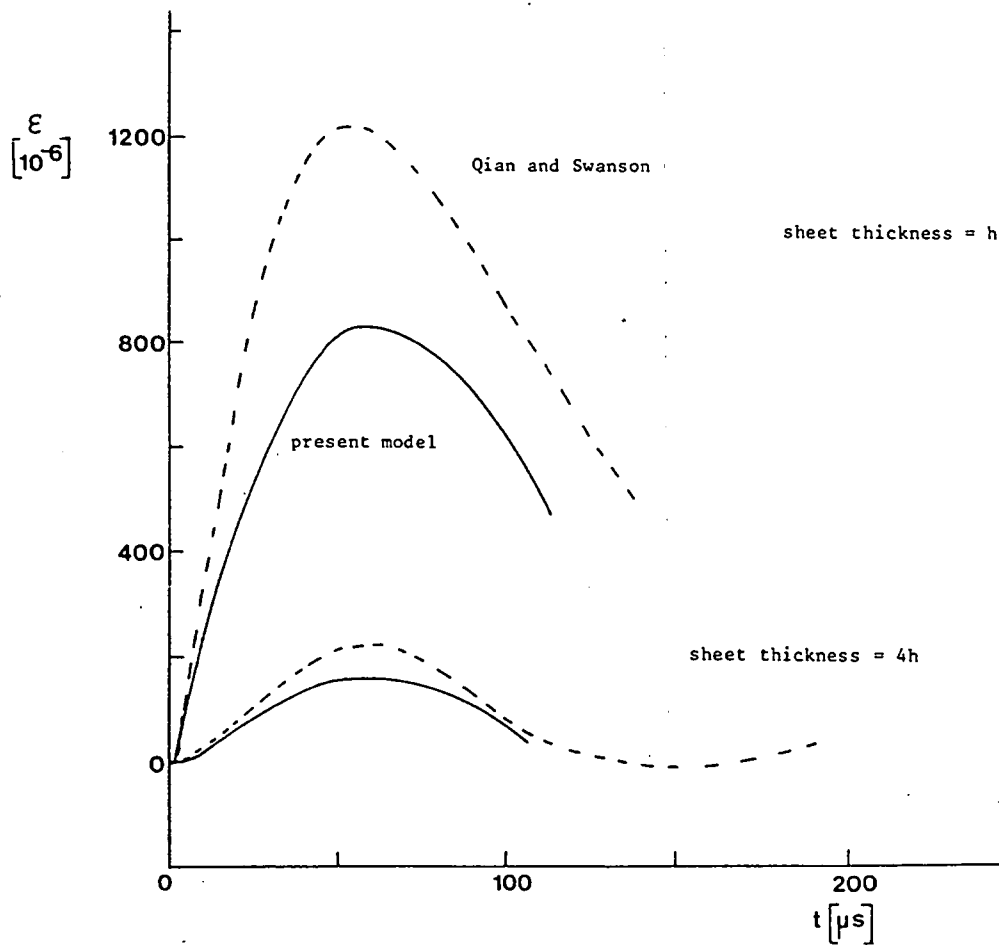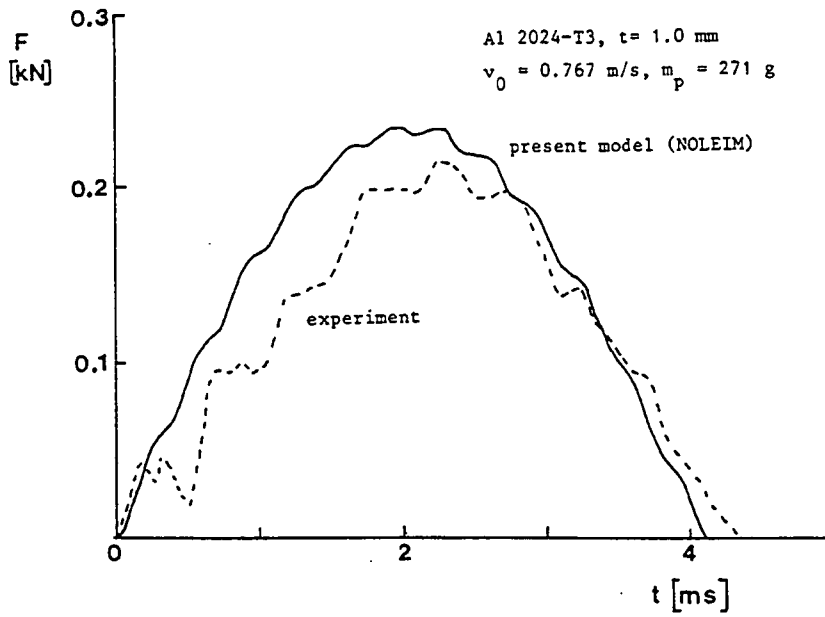
figure 12.21 Force-time curve for Al 2024-T3, comparison of experimental result and the analytical model NOLEIM.
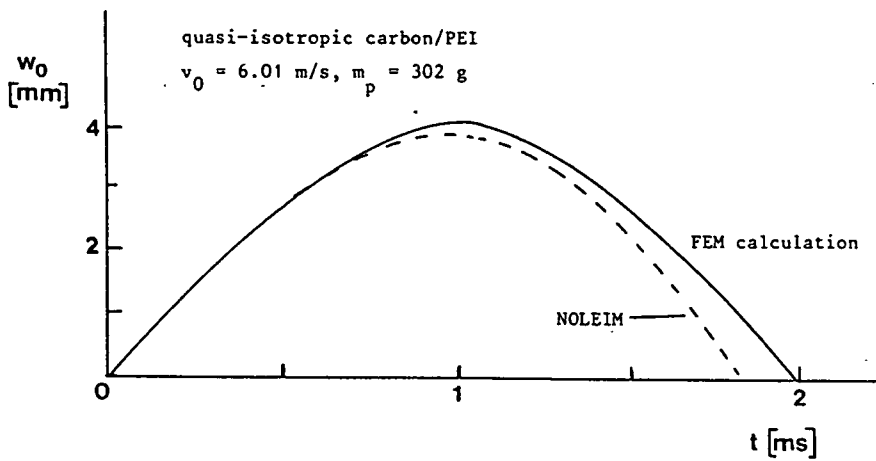
figure 12.22 Central deflection-time curve for quasi-isotropic carbon/PEI, comparison of the analytical model NOLEIM with experimental results.
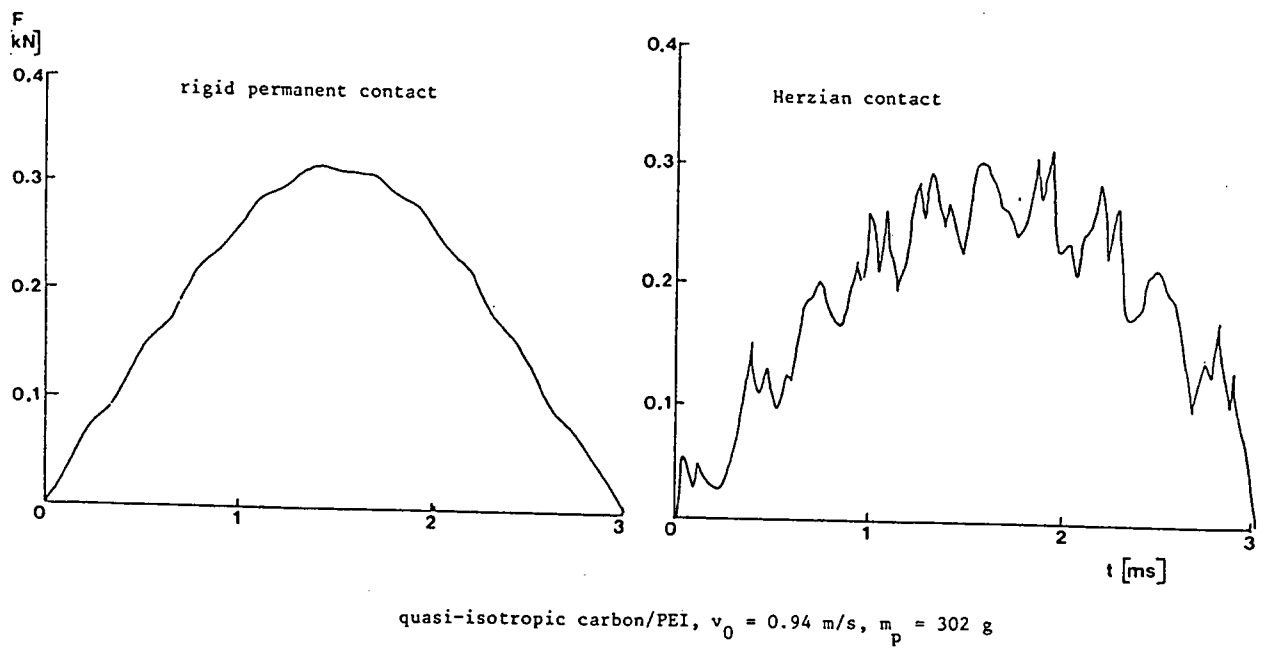
figure 12.23 Comparison of calculated force-time curves with NOLEIM for rigid permanent contact and Hertzian contact.
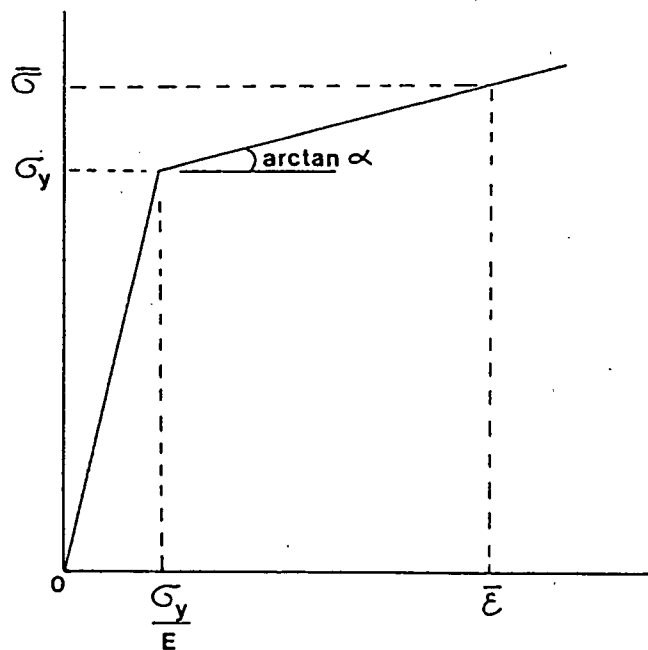
figure 12.24 Bi-linear stress-strain curve.
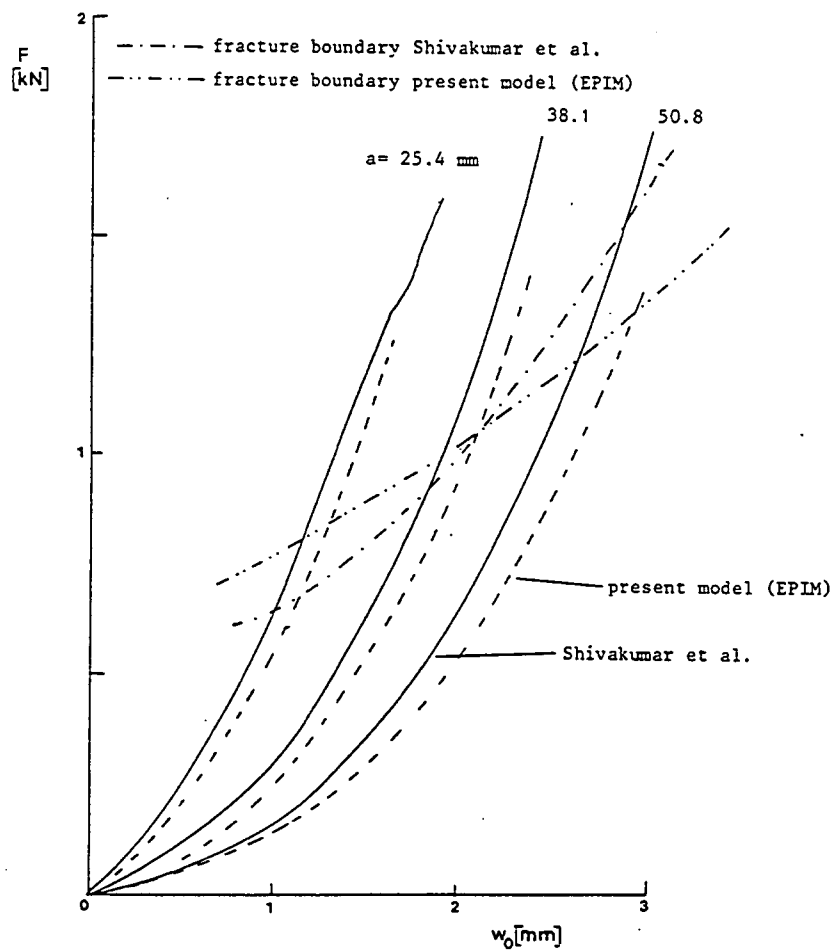
figure 12.25 Comparison of the analytical model EPIM with literature
results for quasi-isotropic carbon/epoxy, t=1.04 mm, for three
values of the diameter of the clamped area of the plate.
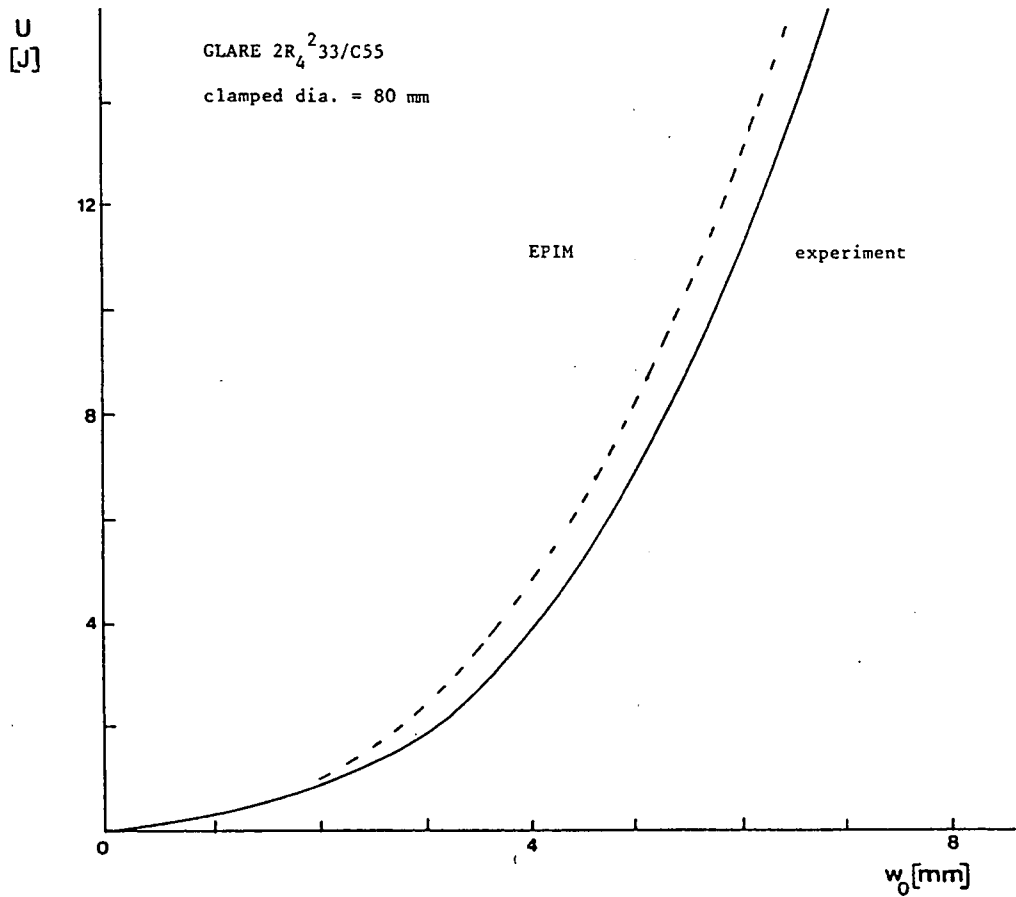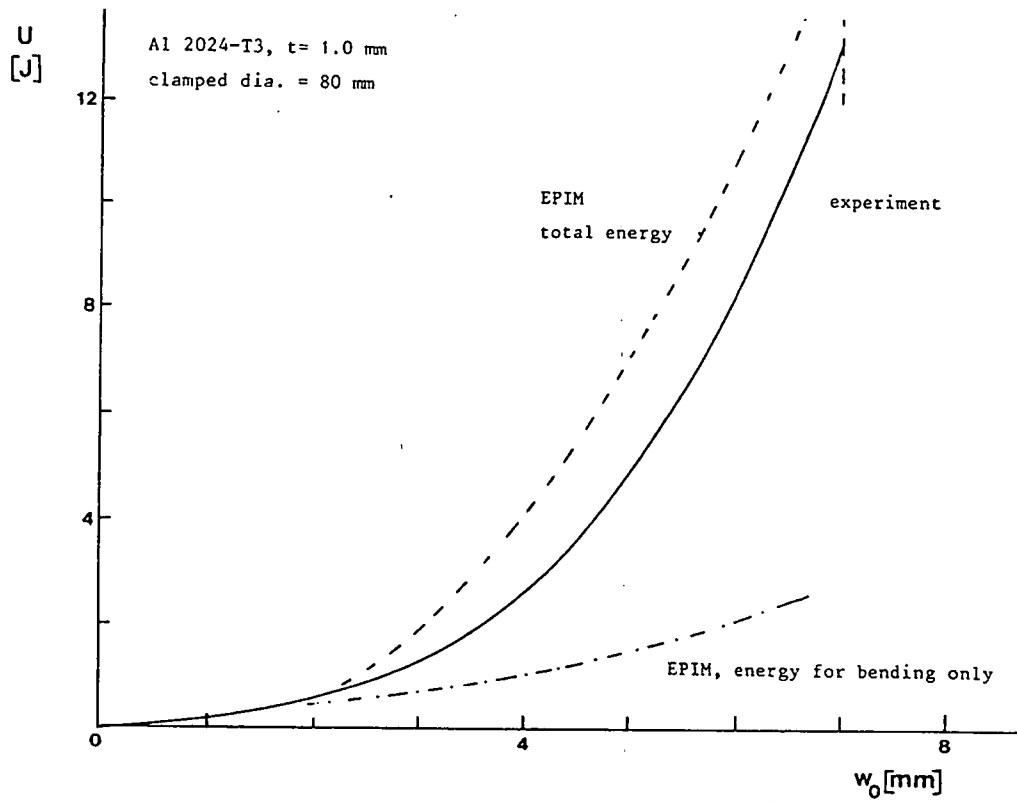
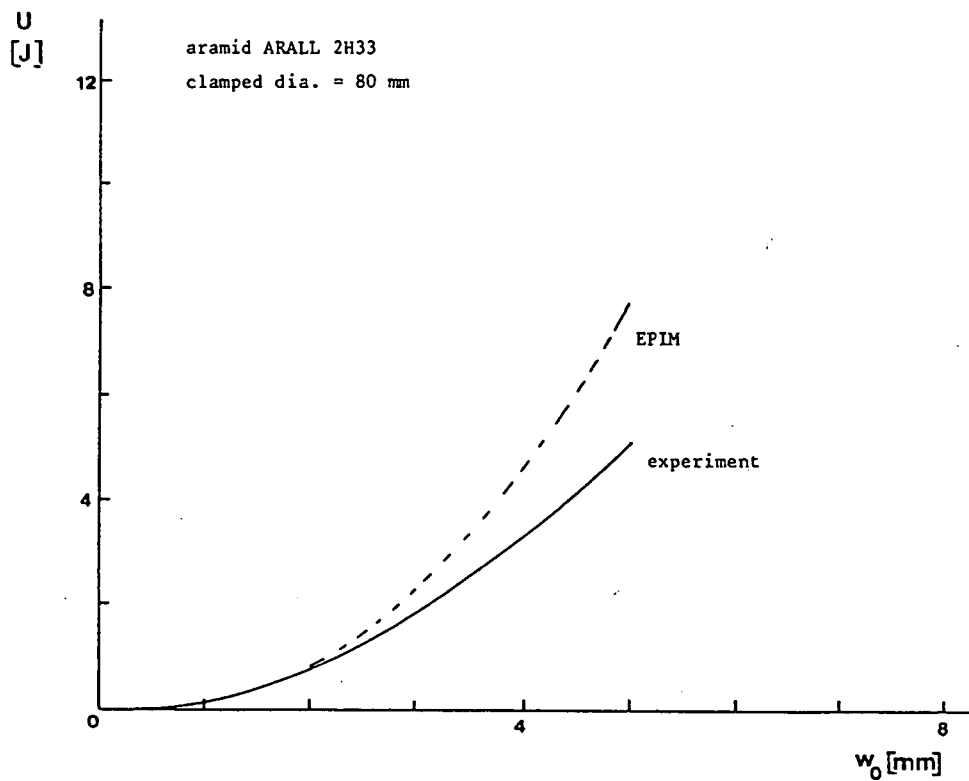figure 12.26 Calculated and experimental energy-deflection curves.

aramid ARALL 2H32
clamped dia. = 80 mm

EPIM

fracture

experiment

aramid ARALL 2H33
clamped dia. = 80 mm

EPIM
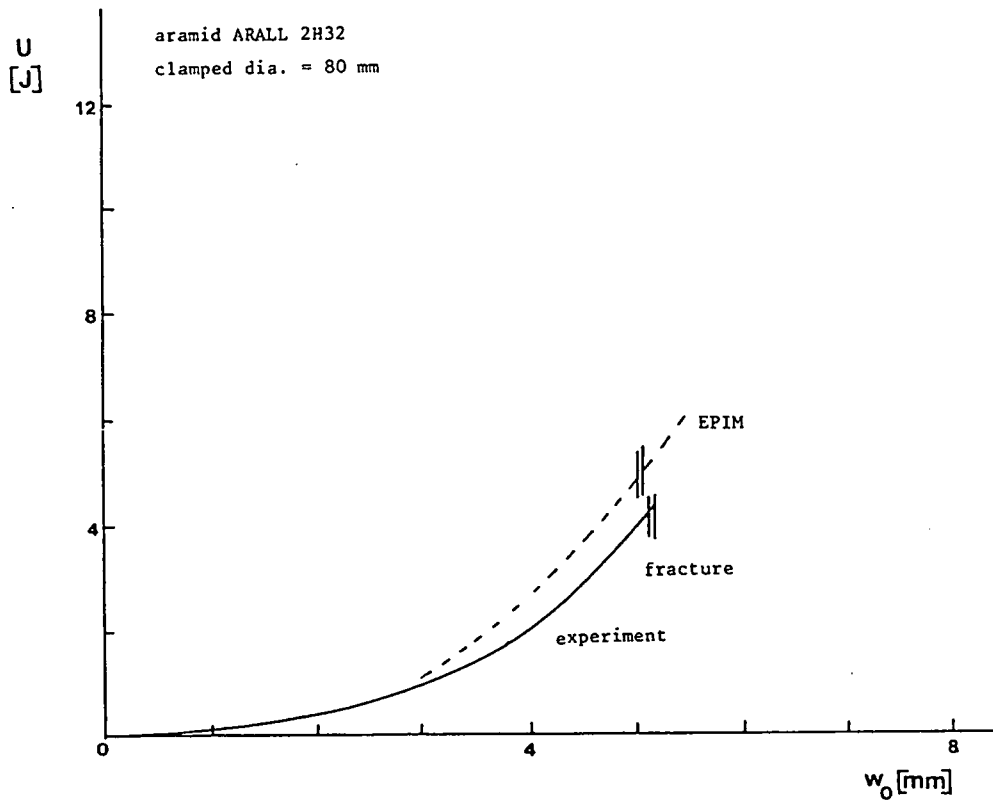
experiment

figure 12.27 Experimental and calculated energy-deflection curves.

463

U
[J]

Al 7075-T6, t=0.8 mm
clamped dia. = 80 mm

8

EPIM

4

fracture

experiment

0   2   4   6

w_0 [mm]

F
[kN]

GLARE $2R_4^2 32$

clamped dia. = 80 mm

EPIM   experiment

3

2

1

0   4   8

w_0 [mm]
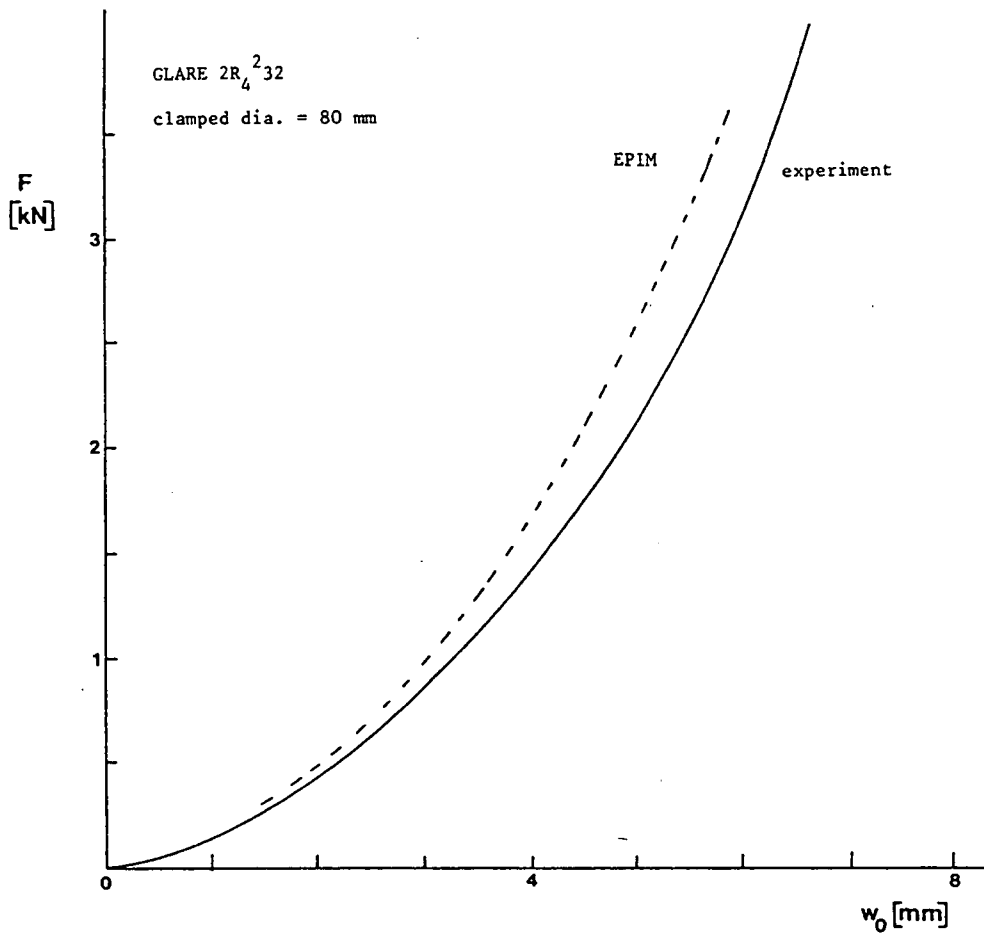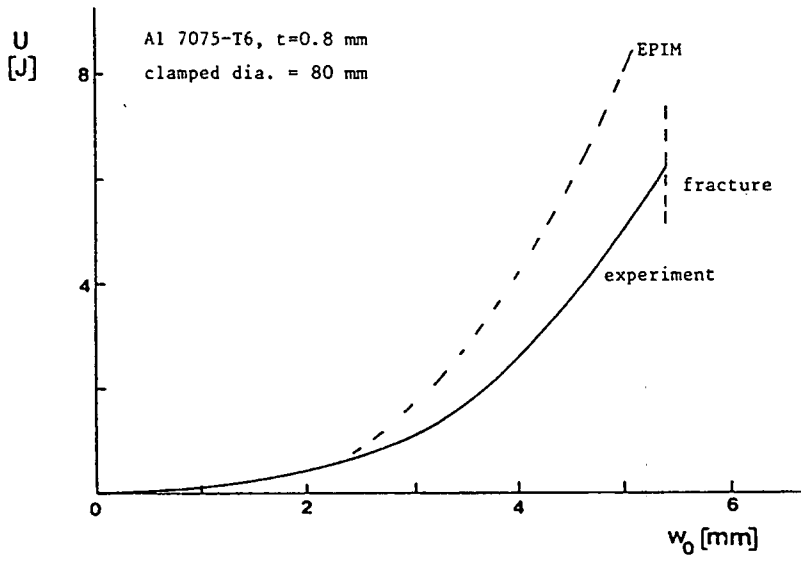
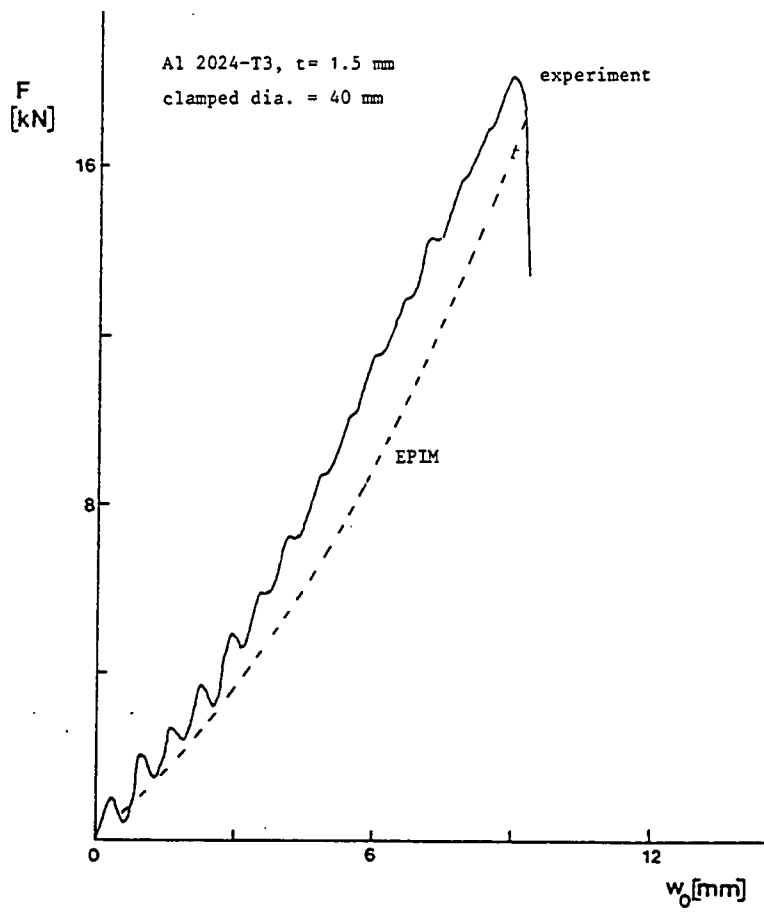figure 10.28 Experimental and calculated force-deflection and
energy deflection curves.

figure 12.29 Experimental and calculated force-deflection curves.

465

PART IV RESIDUAL STRENGTH AFTER IMPACT

chapter 13 Residual tensile strength and fatigue properties after impact damage

13.1 Introduction

The damage tolerance of a material is related to its residual strength in the presence of damage. In composite materials the tensile strength will be mainly affected by fibre failure, and less by delamination. In ARALL laminates also aluminium failure (cracks) and a plastically deformed dent may be present in the material. Residual strength tests on ARALL are usually performed on specimens with a saw cut. However, the dent left after impact may also cause a stress concentration and consequently a lower strength.

The aims of this chapter are:

1. To compare the residual tensile strength of ARALL laminates, monolithic aluminium alloys and thermoplastic composites.

2. To study the effect of the dent in ARALL laminates on the stress distribution in the material. Both residual strength and fatigue tests were carried out. For the residual strength of ARALL laminates a question is whether a saw cut can be a realistic simulation of impact damage.

13.2 Specimen types

Two specimen types were used in this study (see figure 13.1). Type A is a rectangular specimen and type B is a 'dog bone' specimen. The dog bone specimen has the advantage that the specimen will always fail at the damage location in the centre of the specimen. Specimen type B was used for some tests on monolithic aluminium alloy and aramid ARALL. Failure in the type A specimen will take place at the end tabs if the damage is too small. Then we only know that the influence of the stress concentration at the tabs is larger than the stress concentration due to the damage.

Unless otherwise stated, the impact tests were performed with an impactor with a tip radius of 7.5 mm. A circular area of the specimen was clamped (diameter of 80 mm). The impactor mass was 194 or 325 g.

13.3 Strain and displacement measurements

13.3.1 Introduction

The stress in a dent during a residual strength test on monolithic and ARALL material is a summation of the residual stress due to spring back after the impact loading and the bending of the dent under the loading of the sheet. Figure 13.2a shows the residual stress system after spring back, figure 13.2b gives an impression of the stress due to the bending of the dent introduced by the tension load. In both cases there is a tensile stress at the impacted (concave) side, and a compressive stress at the non impacted side of the dent. If the dent is not deep, the stress at the non impacted side due to the bending under loading may be positive.

The dent in the material will act as a zone of material with a lower effective stiffness, and a part of the stress will be transferred around the dent. In· this case the highest stress will not occur at the centre of the dent, but beside the dent.

The following effects of the damage due to impact will affect the residual strength and fatigue properties of ARALL laminates:

1. strain hardening of the aluminium due to the impact loading
2. residual stress system after deformation caused by impact loading, change of the initial residual stress system of the material
3. bending of the dent under loading
4. stress concentration beside the centre of the dent due to a lower effective stiffness of the dent
5. cracking of fibres and aluminium

It is clear that we have to deal with a complex situation.

13.3.2 Experiments

13.3.2.1 Specimens

The tests were carried out on specimens of type A (rectangular specimen). Materials tested were aramid ARALL 2H32, GLARE $2R_4{}^2 32$ and $2R_6 32$ and Al

2024-T3 (t=1.0 mm). The impact energies and permanent central deflections are shown in table 13.1. The impactor mass was 325 g. The specimens with an impact damage crack failed over that section. The other specimens with an impact dent but without a crack failed at the tab.

The out of plane deflection of the specimens at the centre at the convex side of the dent was measured by a displacement transducer. The nominal strain outside the dent and the strain at both sides of the centre of the dent were recorded. The gage length was 2 mm.

The strain gages were mounted on two $2R_4{}^2 32$ specimens according to the pattern in figure 13.8. The measured strains of these specimens were almost identical, therefore only the results of one of the specimens will be discussed here.

13.3.2.2 Results

The GLARE $2R_6 32$ material impacted at 11.2 J showed a remarkable failure behaviour. After impact the specimen had a crack of 22.3 mm in fibre direction (i.e. parallel to the loading direction), and a tiny crack at one tip of this crack perpendicular to the fibre direction. It failed during the residual strength test partly at the latter tip of the crack and for the other part through the centre of the dent, both parts perpendicular to the fibre direction (see figure 13.3a). A typical failure of aramid ARALL 2H32 is shown in figure 13.3b. It occurred through the centre of the dent, where a crack was already induced, perpendicular to the fibre direction.

Figure 13.4 shows the results of the displacement measurements. The dent in the material is bent backwards during the residual strength test, but this deformation remains relatively small compared with the original height of the dent (on the order of 20% of the original dent height). There is no significant difference between the various materials in the behaviour of their respective dents under load.

The results of the strain measurements are presented in figures 13.5 to 13.7. The strain at the impacted side remains negative during the whole or almost the whole test. The $2R_6 32$ and Al 2024-T3 specimens (in figures 13.6

and 13.7, respectively) did not have an impact damage crack. The 2H32 specimens (figure 13.5) had a crack at the non impacted (convex) side. The strain gage at this side was mounted at the crack tip, beside the centre of the dent. Initially, at low σ, the strain at the non impacted, convex side of the specimen is smaller than the nominal strain outside the dent. This is probably due to load transfer around the dent. The same observation applies to the Al 2024-T3 specimen (figure 13.7). In this specimen the strain at the concave side starts to increase significantly at general yield of the material (at $\varepsilon_y \cong 0.4$ %).

The strain concentration for the GLARE and the aramid ARALL specimens is in the order of 1.5 to 2 for large σ. The strain of the Al 2024-T3 could be recorded until the failure strain of the strain gages (6 %); for this material the strain concentration remained small. The 2H32 specimen (figure 13.5) failed at the failure strain of the aramid fibre (2.2 %), the $2R_6 32$ material (figure 13.6) failed at the failure strain of the R-glass fibre (5 %). The $2R_6 32$ specimen failed over the tabs, which means that the strain concentration at the tabs had more influence than the dent. The dented GLARE $2R_6 32$ material failed at 800 MPa, somewhat lower than than the tensile strength of the undamaged material.

Figure 13.8 shows the results of the strain measurements on GLARE $2R_4^2 32$. The figure indicates that the maximum strain is situated beside the dent ($\varepsilon_b > \varepsilon_a$). The strain at the centre of the dent at the impacted side ε_1 remains negative during the test. The strains at the same side of the sheet beside the dent (ε_2 and ε_3) remain positive. The strains above the dent (ε_c and ε_d) are smaller than the nominal strain outside the dent, due to the stress transfer around the dent.

13.4 Residual strength tests

13.4.1 Comparison of monolithic aluminium alloy with aramid ARALL

Specimen type B (dog bone) was used for the comparison between aramid ARALL and the monolithic aluminium alloy. Aramid ARALL 2H33 and Al 2024-T3 (t=1.55 mm) were impacted by a hemispherical tipped impactor with radii of 5 and 7.5 mm, with impact energies up to 10 J (impactor mass 194 g). Figure 13.9 shows the results. The monolithic material does not show cracking in

this regime, and the strength was not influenced by the presence of the dent. Aramid ARALL shows fibre failure (in combination with aluminium failure) at 4 J. The material shows no strength reduction up to this impact energy. The residual strength of aramid ARALL remains higher than the strength of monolithic material for impact energies smaller than 8 J. The strength reduction caused by the impactor with a tip radius of 5 mm seems to be higher than with the tip radius of 7.5 mm.

The impact of a sharp object will influence the strength of both monolithic and ARALL material. This was simulated by impactors with a conical nose with a tip angle of $\alpha = 60^o$ and $\alpha = 90^o$. The sharp impactors created a hole in the specimens. Figure 13.10 shows the results of the residual strength tests. In this case the strength reduction of ARALL is significantly higher than for the hemispherical nose shape. Figure 13.10 shows an increasing residual strength for aramid ARALL and $\alpha = 60^o$ if T > 4 J. It is probably due to the cleaner hole cut in the specimen at higher impact energies. The effect of the damage on the strength of aramid ARALL is larger than on the strength of the monolithic material. This is due to the relatively poor blunt notch behaviour of aramid ARALL.

13.4.2 Comparison between aramid ARALL and thermoplastic composites

13.4.2.1 Materials

The rectangular specimen type A was used. The impactor mass was 194 g. The following materials with a polyetherimide (PEI) thermoplastic matrix were tested:

fibre	matrix	lay-up	thickness (mm)
aramid weave	PEI	$[0-90/\pm45_2]_s$	1.50
carbon weave	PEI	[0-90/±45/0-90/±45/0-90]	1.50
carbon UD	PEI	[0/60/-60/90/-60/60/0]	1.46

The laminated carbon material (unidirectional laminae) was tested in two

directions: $\phi = 0^0$ and $\phi = 90^0$. This was done to check the difference between a laminate with 0^0 and 90^0 layer at the outside. As fibre cracking due to impact will start at the outside of the material, it can therefore be expected that the UD carbon/PEI material will be less damage tolerant for $\phi = 0^0$.

The comparison between aramid ARALL and thermoplastic composites can be done in several ways. Materials with an equal strength, an equal stiffness, an equal thickness or an equal surface density can be tested and compared. Here a comparison has been made for panels with an equal weight. The surface density ρ_s of the carbon/PEI specimens is 2.2 kg/m^2. The behaviour of this material was compared with aramid ARALL 2H32 (t = 0.86 mm) with a surface density of 2.1 kg/m^2.

13.4.2.2 Results

Figure 13.11 shows the results of the residual strength tests. The strength reduction of 2H32 is comparable to the test results of 2H33 described in section 13.4.1. Although the 2H32 material is thinner than the carbon/PEI composite material, the strength remains somewhat higher.

Figure 13.12 shows the relative strength reduction again as a function of the impact energy. The relative strength reduction of 2H32 is somewhat larger than for the laminated carbon/PEI materials. The laminates with carbon and aramid weaves show the best behaviour.

13.4.3 Comparison between ARALL and GLARE

The ARALL laminates with aramid fibres have a relatively poor blunt notch and residual strength behaviour[1]. The behaviour of GLARE material with R-glass fibres is much better. Furthermore, the results of chapter 7 showed that GLARE material is also considerably more damage resistant. Unidirectional GLARE material shows aluminium cracking in fibre direction, the strength in fibre direction is unaffected.

Tests were performed on GLARE $2R_2{}^232$ and $2R_2{}^232$/C55 material, with specimen type A (rectangular). The GLARE $2R_2{}^232$/C55 cross-ply material does not have a symmetrical lay-up. The specimens during impact were positioned with the

fibre direction at the impacted side in width direction of the specimen. The impactor mass was 325 g. The results in figure 13.13 are compared with test results on aramid ARALL 2H32 material. The unidirectional $2R_2{}^232$ material with an impact damage crack in fibre direction (i.e. parallel to the loading direction) failed at the tabs. However, the GLARE $2R_632$ specimens (see the results in in section 13.3.2) did not fail at the tabs but at a small crack perpendicular to the fibre direction. The occurrence of the small crack could not be explained.

The ARALL variant with R-glass fibres has a superior damage tolerance behaviour compared with aramid ARALL as shown by figure 13.13.

13.4.4 Comparison of the strength reduction by a hole, impact damage, and a saw cut

The purpose of the these tests was to observe the effect of the type of damage on the residual strength. The comparison includes a hole, impact damage and a saw cut.

Aramid ARALL 2H32 was tested with specimen type A (rectangular specimen). The impactor mass was 325 g. Impact tests were performed on the specimens, and the crack length in the aluminium layers at the outside of the material was determined. Holes were drilled and saw cuts were made in two other specimens with the same dimension as the maximum length of the impact damage at the non impacted, convex side.

Figure 13.14 shows the results. Until a through crack is created the residual strength with impact damage is close to the strength with an open hole with the same dimension. The strength becomes equal to the strength of the material with a saw cut when a through crack (fibres are cut) is caused by the impact loading. No additional effect of the dent on the strength was observed. The saw cut can be used as a worst case situation to simulate impact damage.

13.4.5 Comparison of strength of a specimen with a saw cut and a specimen with a dent due to impact and a saw cut

Residual strength tests were carried out on specimens with a saw cut and specimens with both a dent due to impact and a saw cut (made in the specimen after impact).

The tests were performed on GLARE 2R$_4^2$32 material (rectangular specimen type A). The impactor mass was 325 g. The impact energy was chosen below the energy needed to create a crack. A saw cut was then made over the centre of the dent, and of the same length as made in a flat specimen without a dent. The strength of the specimens can then be compared. The results are presented in table 13.2.

The specimens with dents with a depth of 4.0 and 8.1 mm and both with a saw cut of 5.5 mm, have approximately an equal strength. The specimens with a dent with saw cut lengths of 10.0 and 15.4 mm have approximately the same strength as the specimens with a saw cut and without a dent.

We may conclude that there is only a small effect of the dent on the residual strength. Probably this will be due to the fact the failure in the tensile tests is initiated in the fibre layers. These layers are close to the neutral line (small effect of the bending due to the dent). The non impacted specimens have the lower strength. This may be due to the load transfer around the dent (because the dented material will have a lower effective stiffness), which may cause a somewhat lower stress at the tip of the saw cut.

13.5 Fatigue tests

13.5.1 Specimens

The specimens were of type A (rectangular specimen). The impactor mass was 325 g. The materials, the impact energies and permanent central deflections are given in table 13.3. One specimen (2H32) had a small crack on the convex side after impact. For the other specimens the impact energy was kept low, such that no impact damage crack in the aluminium or fibre layers was present, in order to study the effect of the dent only.

To compare the impacted material with the non impacted material, a starter notch (small hole with two saw cuts) was applied. The starter notch had a

total length of 3 mm (tip to tip). The fatigue crack growth behaviour was compared with the behaviour of undamaged specimens with the same starter notch. Constant amplitude fatigue loading was applied at stress levels indicated in table 13.3.

13.5.2 Results

In all the dented specimens with a starter notch, fatigue crack growth occurred only on the impacted, concave side. At the other (convex) side a fatigue crack was not initiated by the starter notch. This can be explained by the strain measurements of section 13.3. At the convex side a compressive strain will be present in the material. Figure 13.15 shows both sides of the prepreg layer of $2R_2{}^2 33/C55$ after removal of the outer layers by chemical etching. At the concave side an elliptical delamination perpendicular to the fibre around the fatigue crack is visible. This delamination is caused by the fatigue loading. At the convex side an elliptical delamination in fibre direction caused by the impact loading is visible (as was also experienced during the tests described in part II of this report). At the convex side no fatigue crack is visible.

Figure 13.16 presents two crack growth curves for an impacted and a non impacted 2H32 specimen respectively. At the R=0 fatigue load the non impacted specimen showed fibre failure during crack growth, which explains the relatively fast crack growth of the material. This behaviour of aramid ARALL is typical for an R=0 fatigue load as described and explained by Roebroeks[1]. For the impacted 2H32 specimen no fibre failure could be observed after removal of the outer aluminium layers by chemical milling. The specimen initially showed a relatively fast crack growth for small crack lengths and a lower, stable constant crack growth rate for large crack lengths. A constant crack growth rate is characteristic for as cured ARALL laminates if the fibres remain intact.

The non impacted 7H32 specimen also showed fibre failure at 0-120 MPa for a>22 mm, see figure 13.17. The crack growth rate is also given in this figure. The difference in crack growth rate between impacted and non impacted material was larger for the $7R_6{}^2 32$, $2R_2{}^2 33/C55$, and Al 7075-T6 materials (see figures 13.19, 13.20 and 13.21). The crack growth rate of

the material with an impact dent was 1.5 to 2 times the crack growth rate of the non impacted material. However, the crack grows only at one side of the specimen. A comparison with the crack growth rate of the monolithic material shows that the ARALL laminates keep their superior fatigue behaviour, also if impact damage is present.

The impacted 7H32 material showed delamination growth in the dent around the starter notch, see figure 13.22. The non impacted 7H32 showed no fibre failure at a fatigue loading of 60-120 MPa. For this loading the crack length of the impacted material (at the concave side) remains longer than for the non impacted material. The crack growth rate for the impacted and non-impacted material is approximately equal (figure 13.8).

13.6 Conclusions

1. The bending of the dent under tensile loading causes a stress distribution in the material with a maximum stress beside the centre of the dent with a magnitude of 1.5 to 2 times the nominal stress outside the dent. The stress system is a combination of internal stresses due to spring back after impact loading, bending in the dent and load transfer around the dent.

2. The presence of a dent (without a crack) in impacted ARALL laminates has no influence on the residual strength. If the impact damage has caused a through crack it can be simulated with a saw cut. If the damage is a part through crack (aluminium layer at impacted side, concave side still intact) the strength will be between the strength of material with an open hole and a saw cut with the same dimension.

3. Fatigue crack growth in ARALL laminates with impact damage occurs only on the impacted, concave side. This is favourable for inspection.

4. It is remarkable that impact damage at low energies will first be visible on the non impacted, convex side of the structure, which is unfavourable for inspection.

5. The dent in impacted material prevents fibre failure in aramid ARALL at

R=0 fatigue loading. As a result the dented aramid ARALL material had a lower fatigue crack growth rate than non impacted material.

6. The fatigue crack growth rate of the crack at the concave side of impacted, dented GLARE material, was found to be approximately 1.5 to 2 times the crack growth rate of non impacted material. For as cured aramid ARALL the difference was much smaller or negligible, because the impacted aramid ARALL did not show fibre failure for an R=0 fatigue load.

7. The residual strength of GLARE material after impact is significantly higher than for aramid ARALL.

references

1. Roebroeks, G.H.J.J.; PhD thesis, Delft Technical University (to be published).

material	t (mm)	T (J)	total crack length (mm)	w_0 (mm)	$\sigma_{res,u}$ (MPa)	σ_u (MPa)
2024-T3	1.00	18.3	0	5.9	500*	
2H32	0.82	5.1	9.0	3.8	420	600
		9.6	9.6	4.7	400	
$2R_6 32$	0.95	5.8	0	3.8	800*	840
		11.2	22.3	5.8	550	
$2R_4^2 32$	0.95	11.0	0	6.0	**	

table 13.1 Specimens used for displacement and strain measurements.

   *   failed at the tabs
   ** strain gage measurements only

saw cut length (mm)	impacted specimen			non impacted specimen	ratio
	T (J)	w_0 (mm)	$\sigma_{u,i}$ (MPa)	$\sigma_{u,n}$ (MPa)	$\sigma_{u,n}/\sigma_{u,i}$
5.5	14.9	4.0	634		
5.5	26.8	8.1	629		
10.0	17.2	7.1	545	514	0.94
15.4	18.5	7.3	497	467	0.94

table 13.2 Influence of the presence and height of a   dent   on   the residual strength of GLARE $2R_4^2 32$.

material	t (mm)	T (J)	w_0 (mm)	total crack length after impact (mm)		fatigue loading (constant amplitude)
				convex	concave	(MPa)
Al 7075-T6	1.00	3.5	1.5	0	0	0-120
2H32	0.82	5.0	3.7	7.0	0	0-150
7H32	0.80	3.5	2.0	0	0	0-120 and 60-120
$7R_6{}^3 32$	0.95	3.5	2.5	0	0	0-120
$2R_2{}^2 33/C55$	1.45	3.5	2.0	0	0	0-120

table 13.3 Specimen data used for fatigue tests
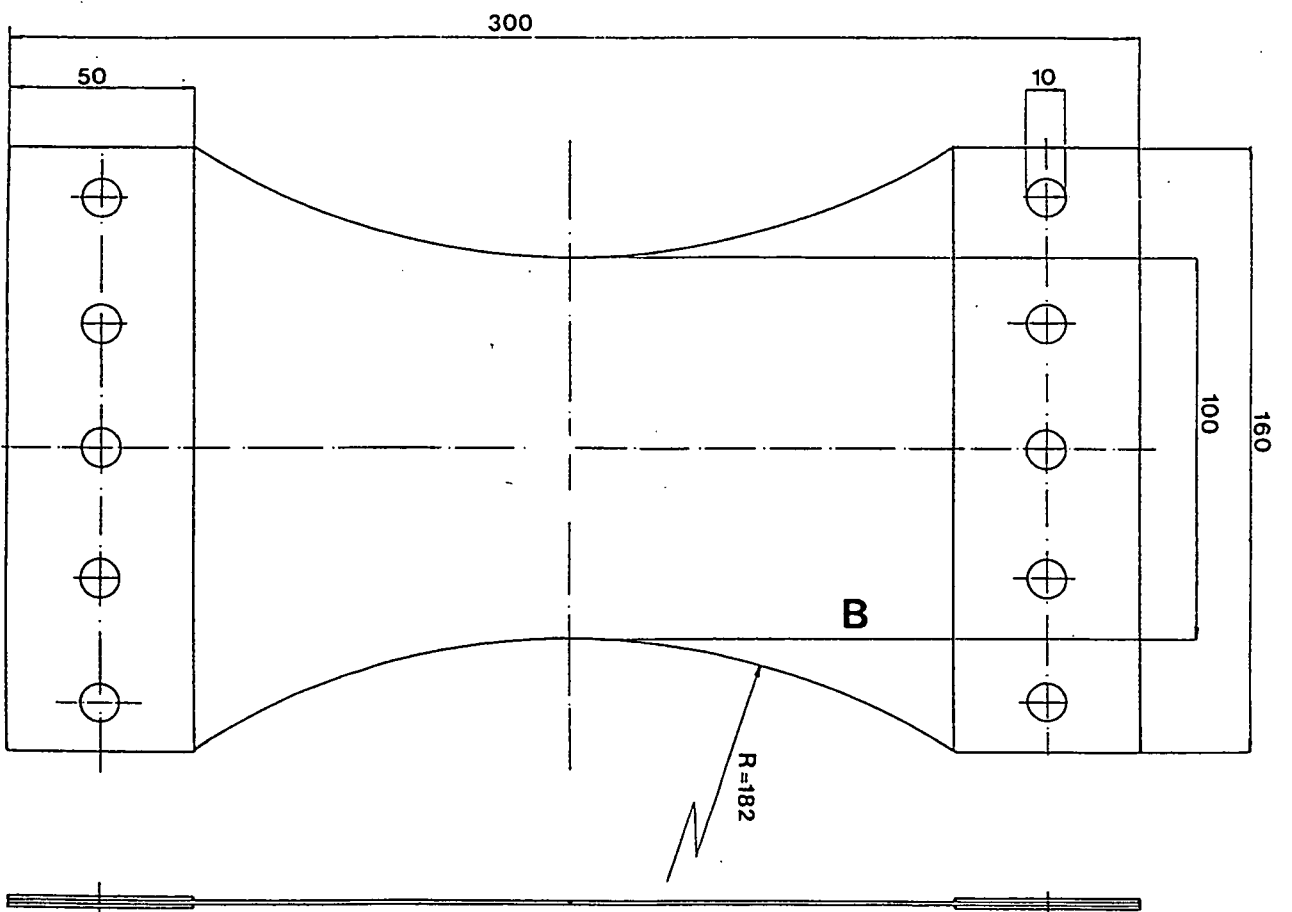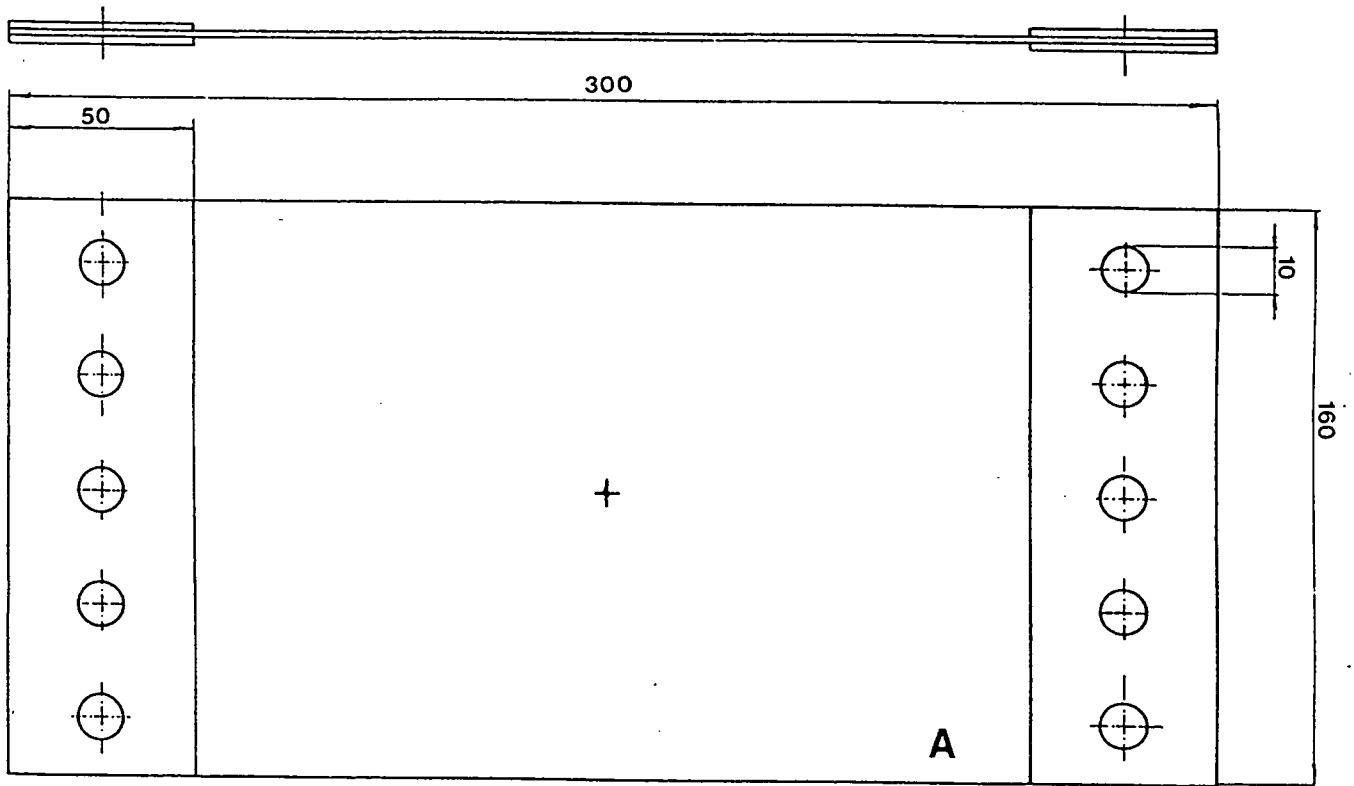
figure 13.1 The two specimen types: A. rectangular, B. dog bone
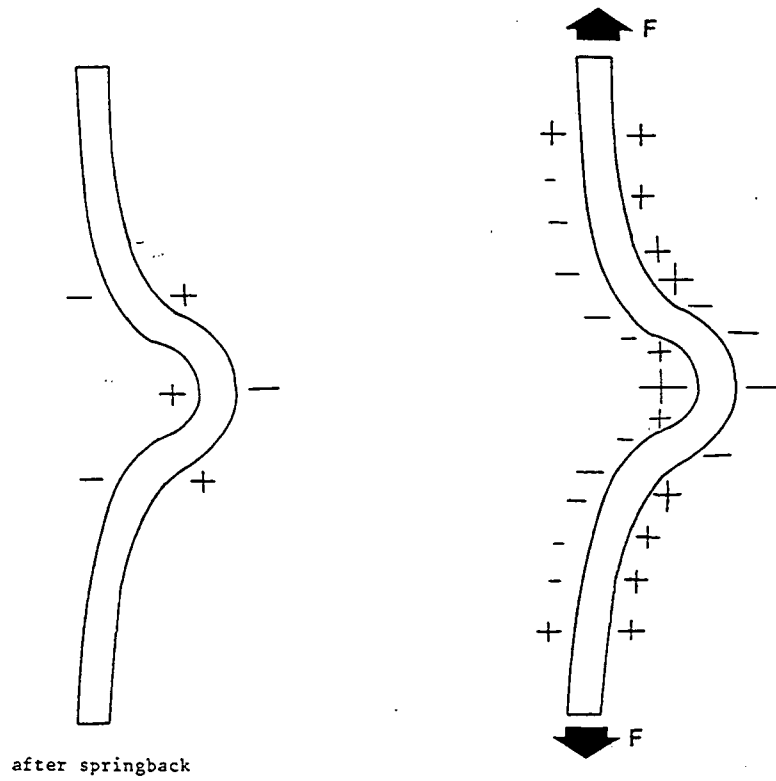
after springback

figure 13.2 Two sources of stresses in the dent: residual stresses
after spring back, and bending of the dent under loading.
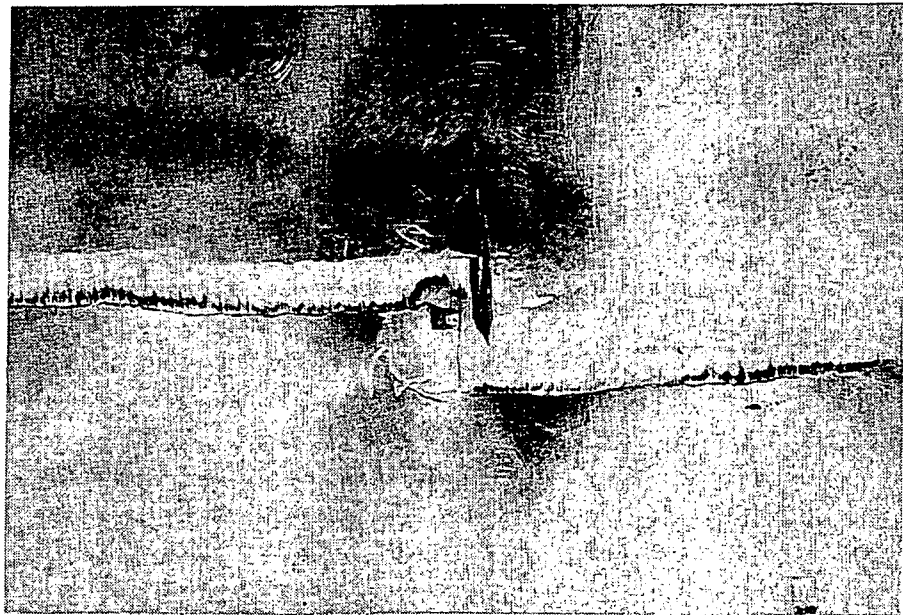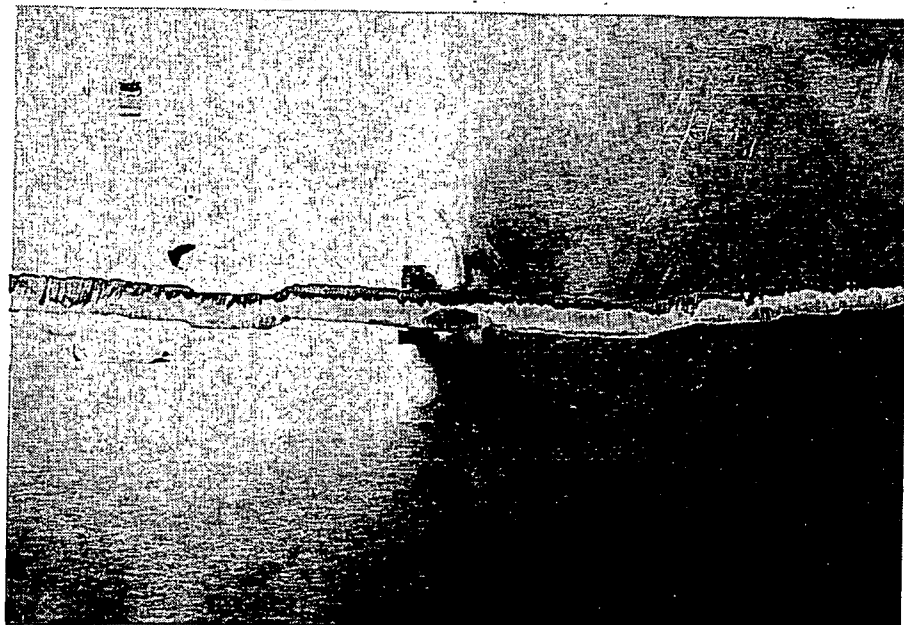
figure 13.3 Two fracture modes after the residual strength test:
a. unidirectional GLARE $2R_6 32$, vertical crack (22.3 mm) due to impact

b. unidirectional aramid ARALL 2H32, horizontal crack (9.6 mm) due to impact.

482
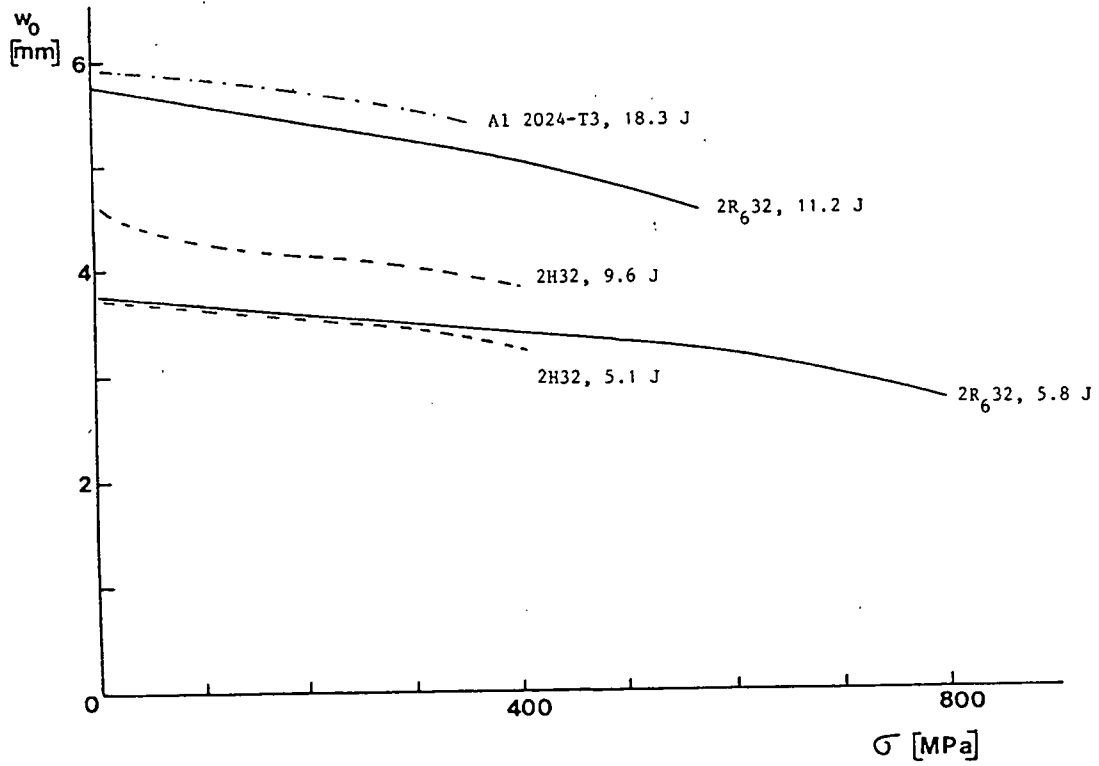
figure 13.4 The displacement of the centre of the dent under loading.
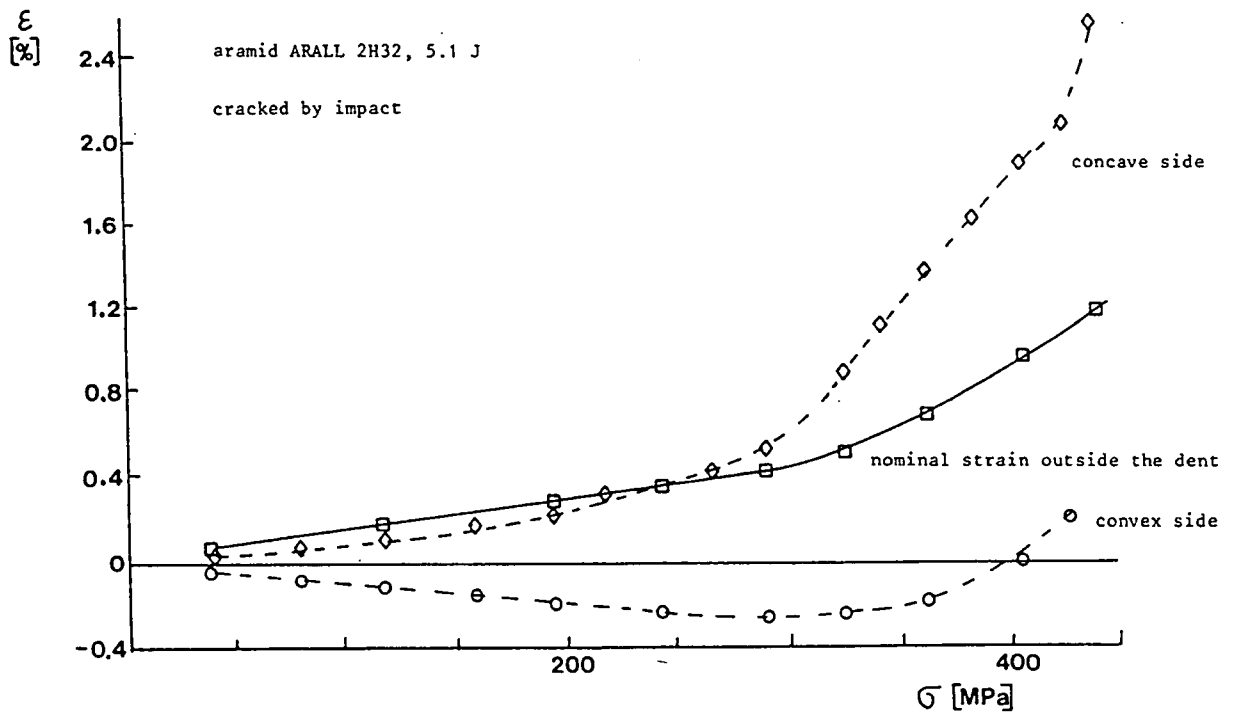
figure 13.5 The strains at both sides at the centre of the dent and the undisturbed strain as function of the loading stress for 2H32.
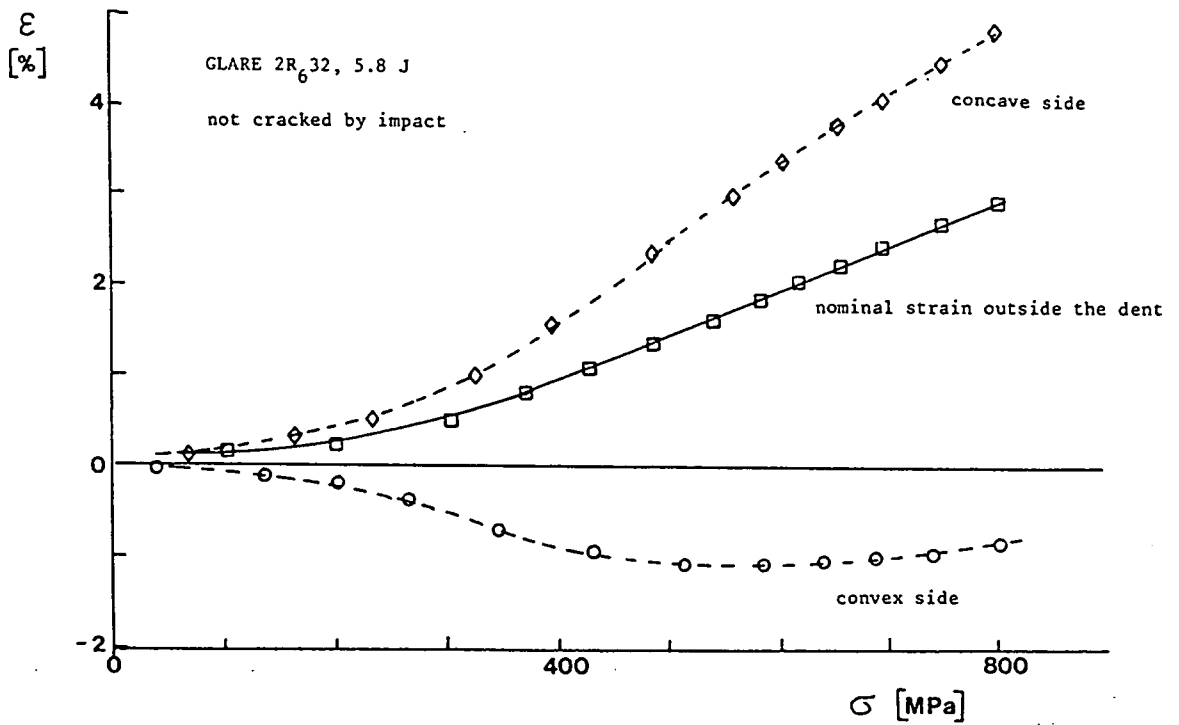
figure 13.6 The strains at both sides at the centre of the dent and the undisturbed strain as function of the loading stress for GLARE 2R$_6$32.
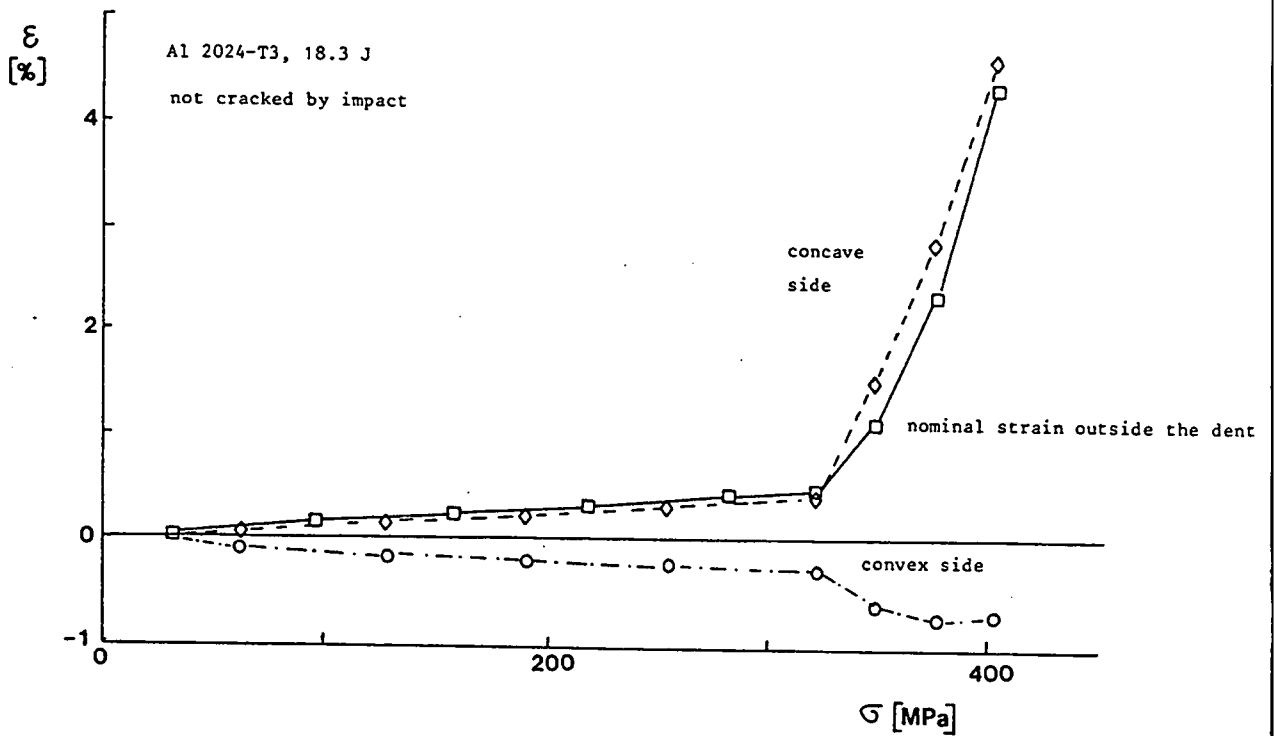
figure 13.7 The strains at both sides at the centre of the dent and the undisturbed strain as function of the loading stress for Al 2024-T3.
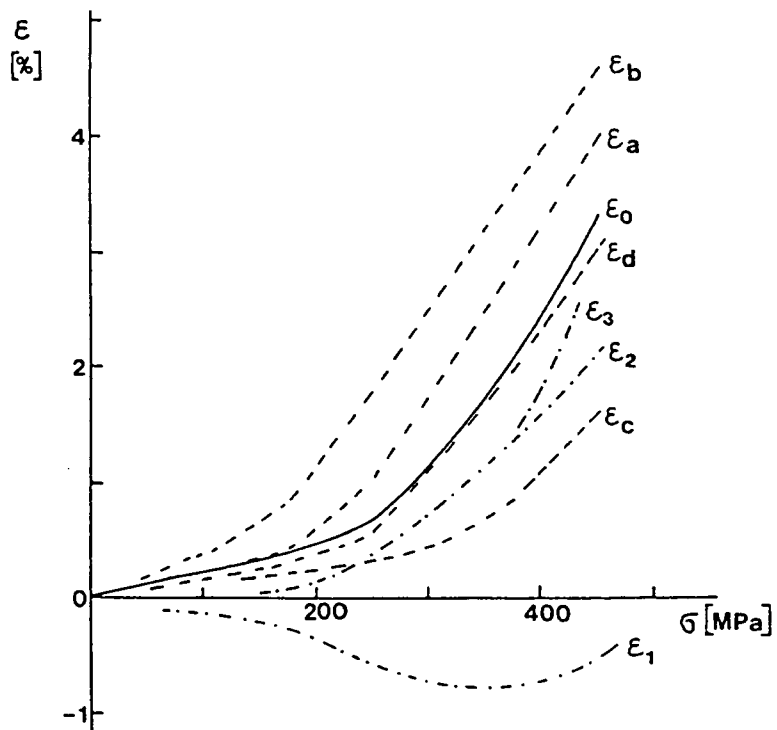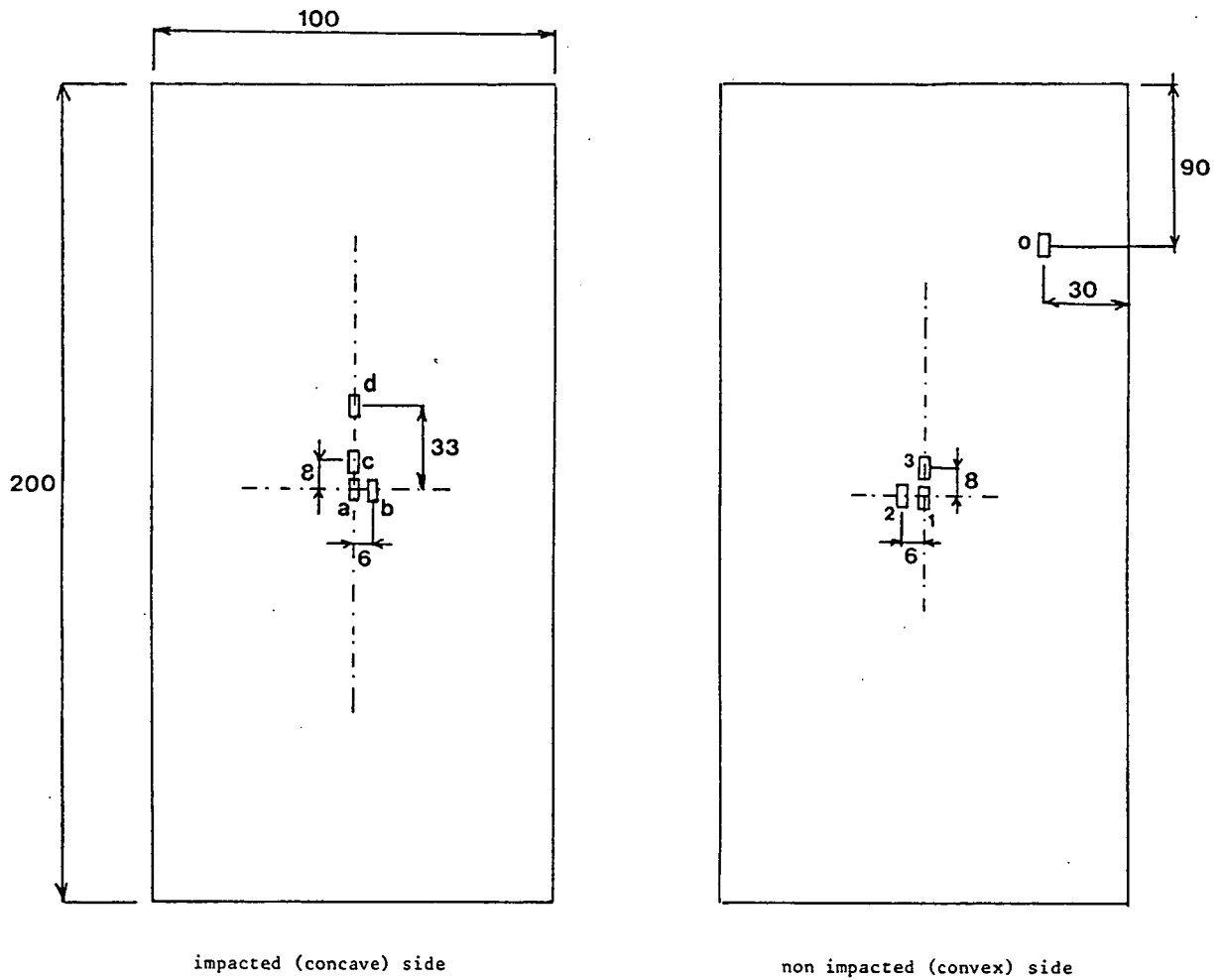
figure 13.8 The position of the strain gages and the measured
strains in GLARE $2R_4$ 32 as function of external stress applied
after impact.
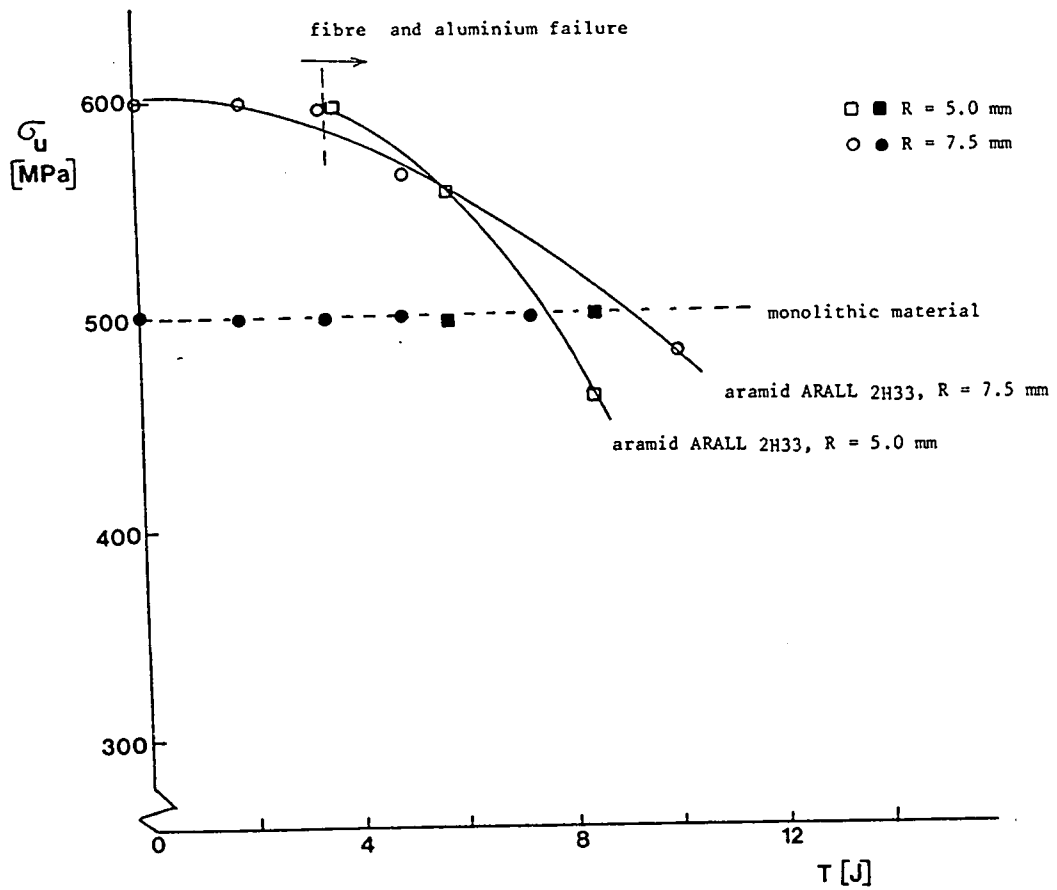
figure 13.9 The residual strength as function of the impact energy for ARALL and aluminium impacted by a hemispherical impactor.
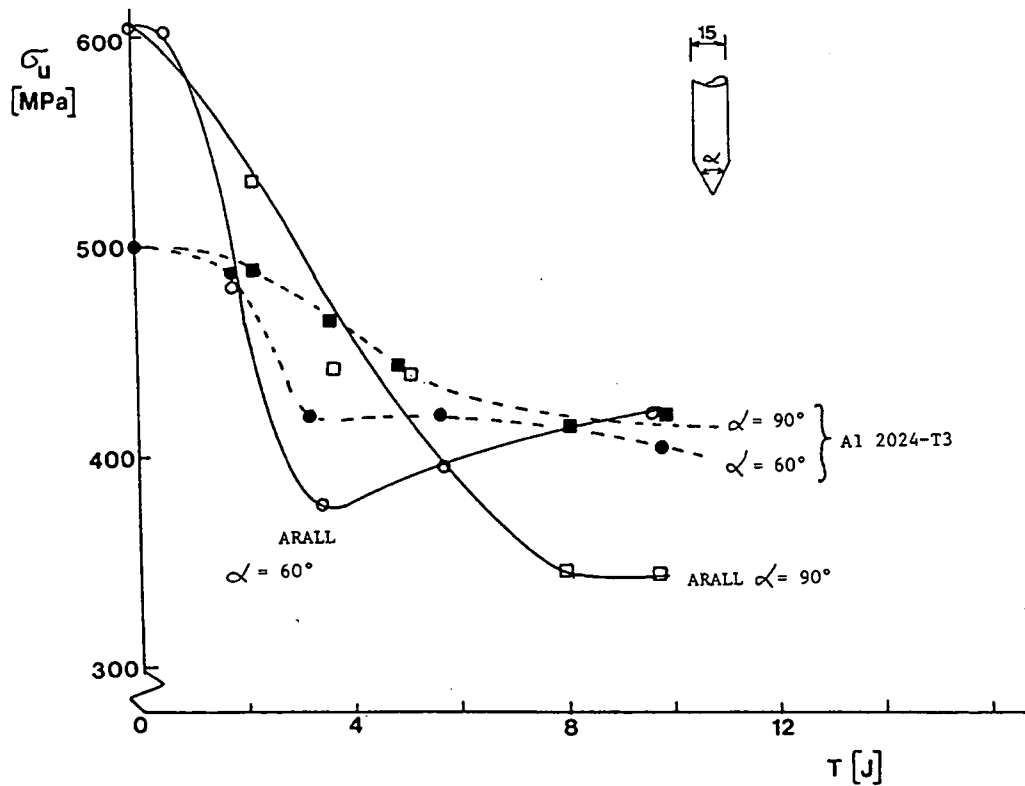
figure 13.10 The residual strength of aramid ARALL (2H32) and 2024-T3 as function of the impact energy, conical impactor with two tip angles α.
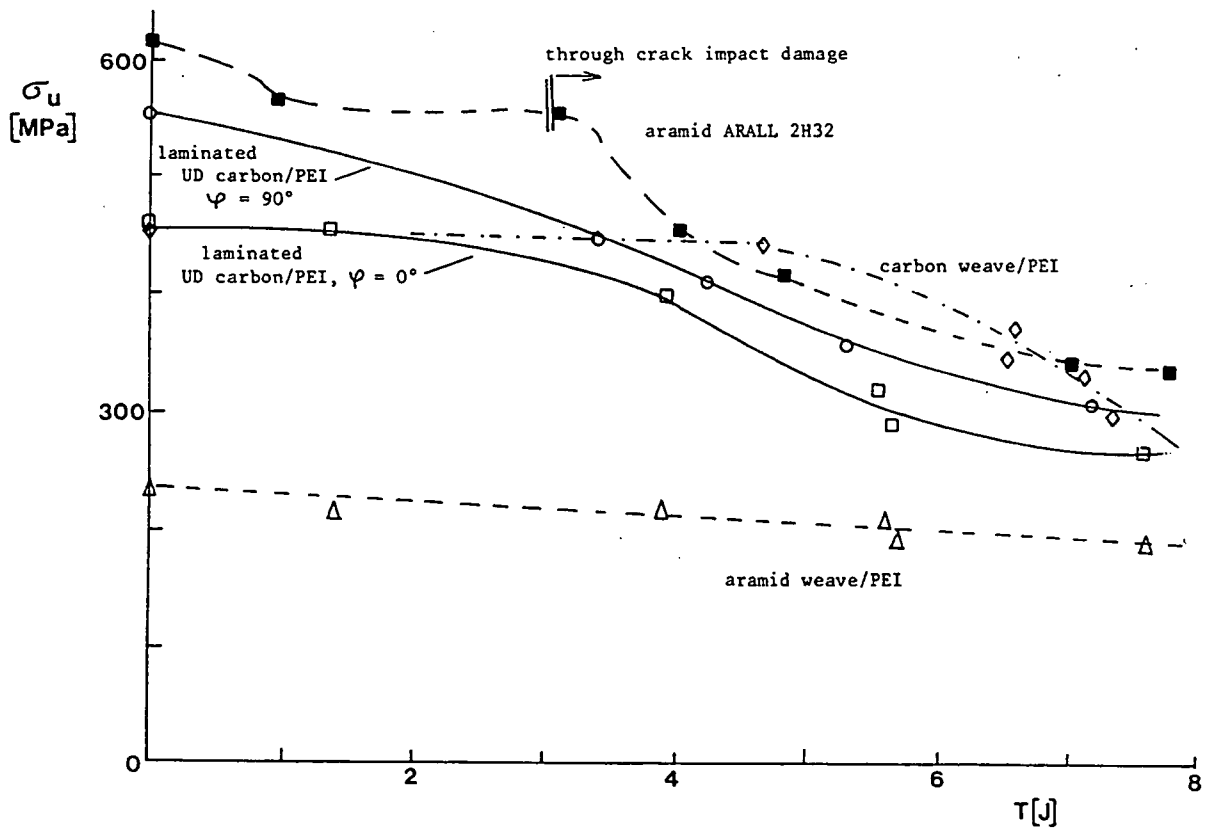
figure 13.11 The residual strength as function of the impact energy for aramid ARALL and thermoplastic composites.
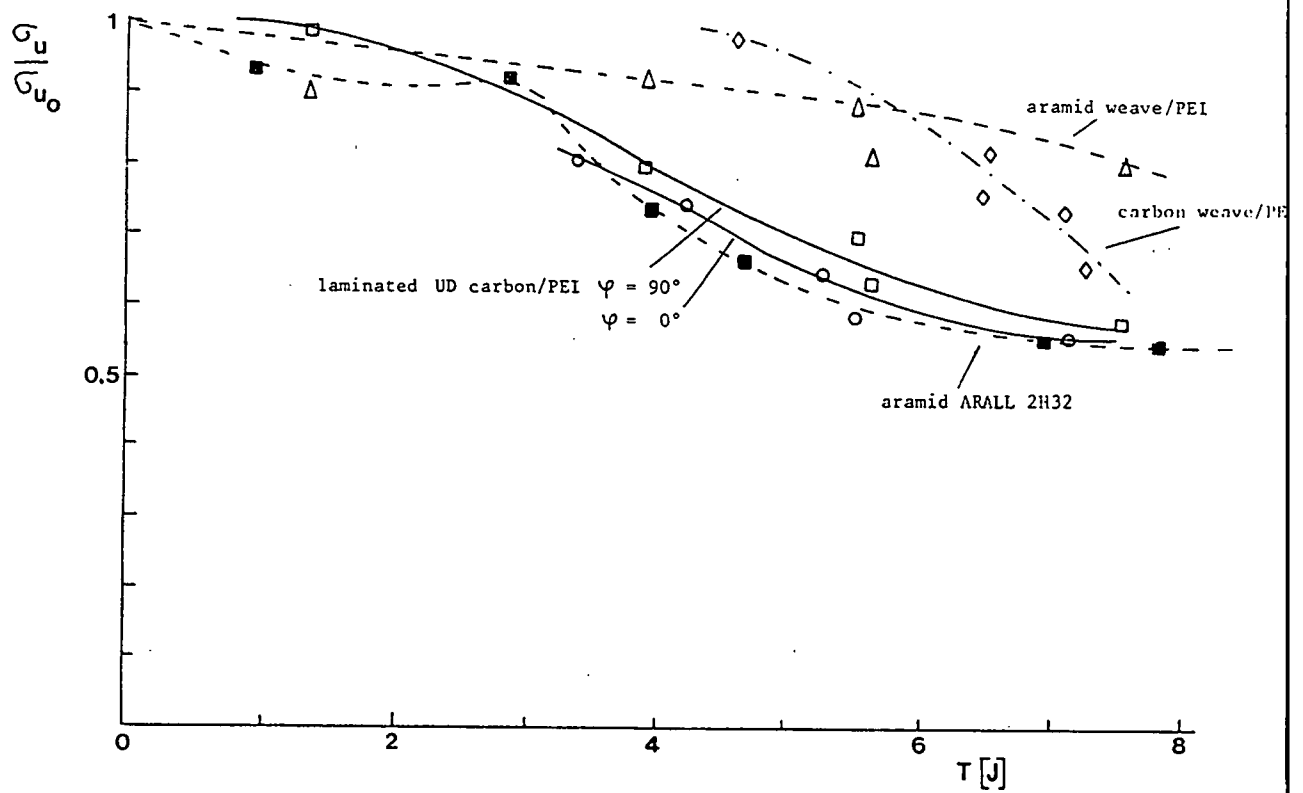
figure 13.12 The relative residual strength as function of the impact energy for aramid ARALL and thermoplastic composites.
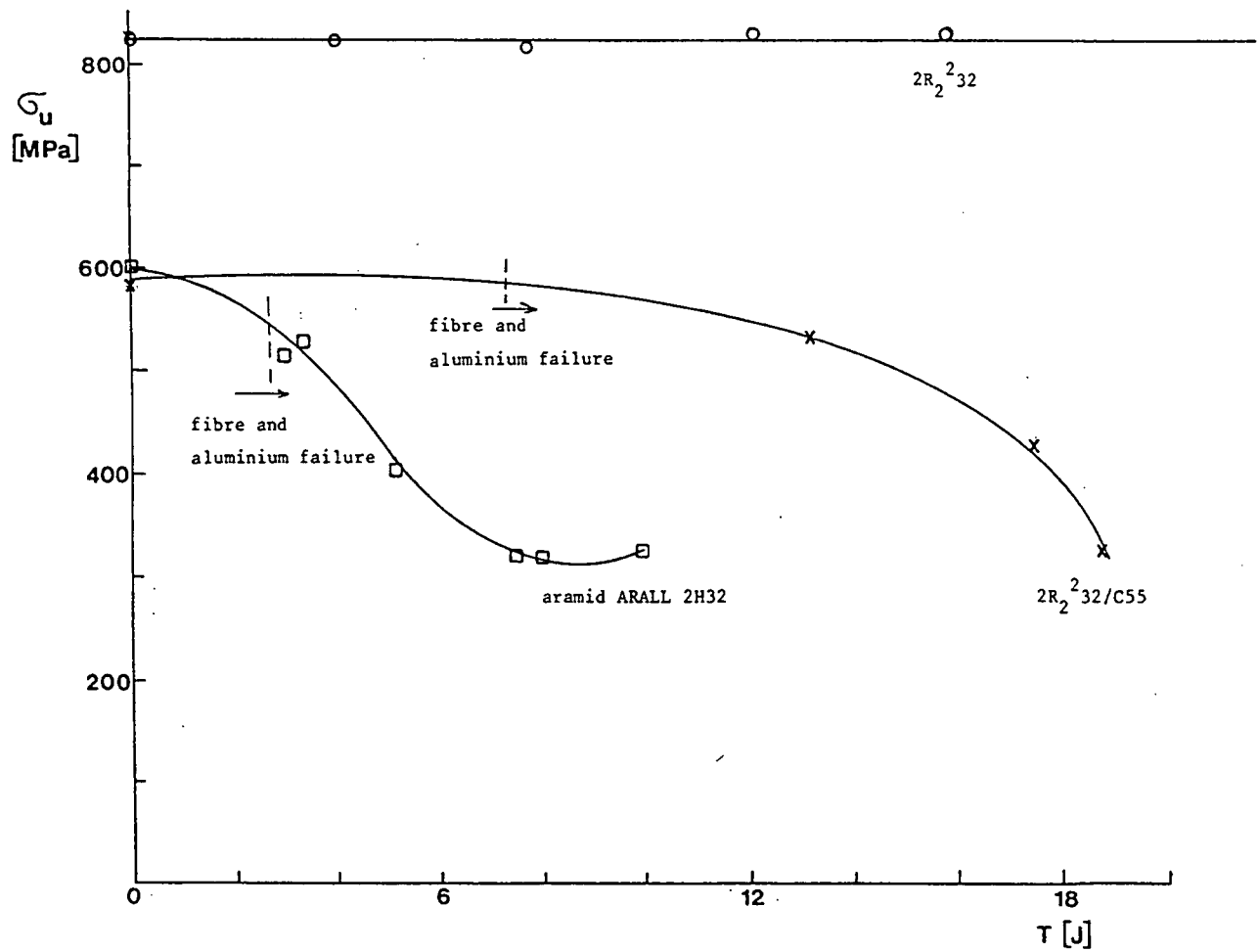
figure 13.13 The residual strength as function of the impact energy for aramid ARALL and GLARE.
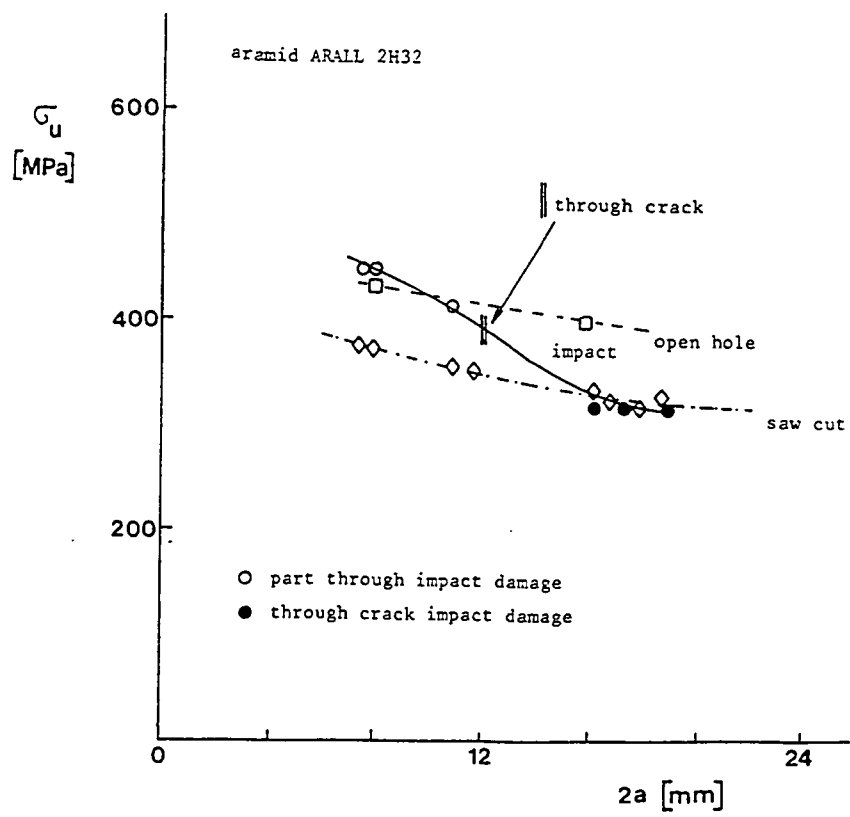
figure 13.14 The residual strength as function of the damage width and diameter for an open hole, impact damage and a saw cut.
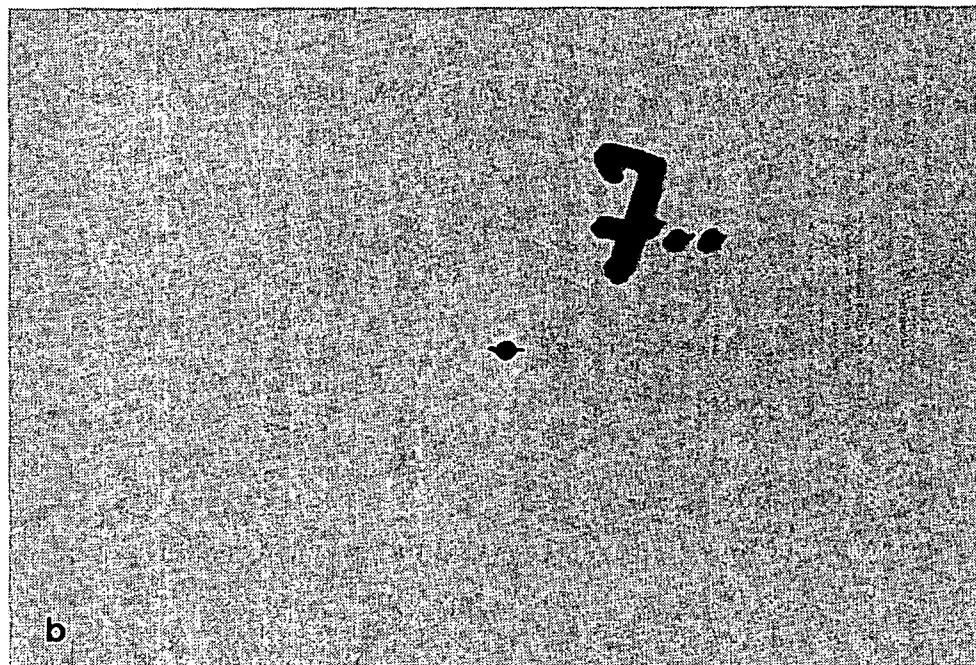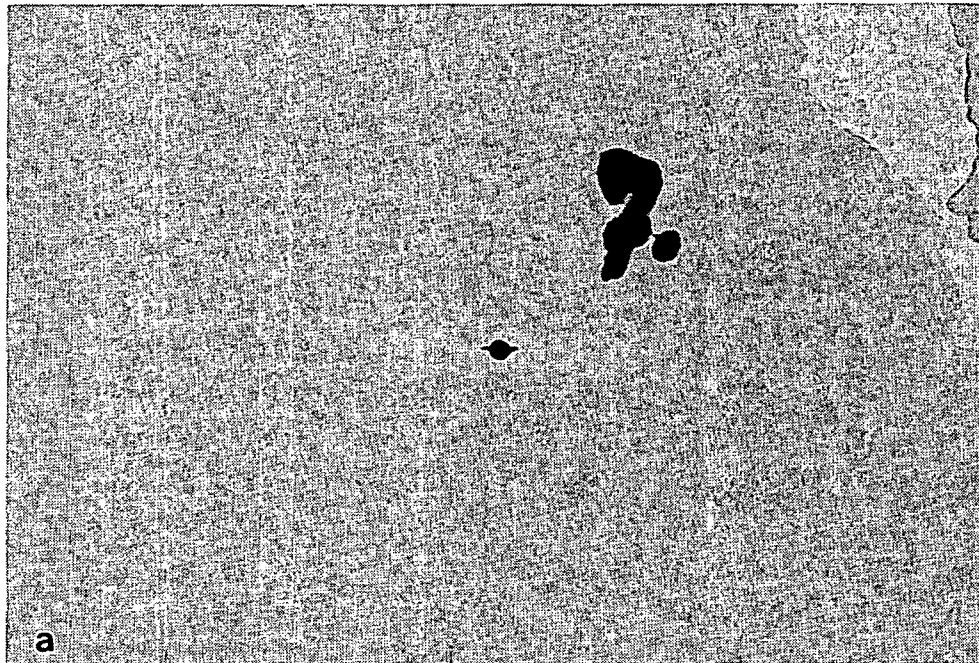
figure 13.15 The prepreg layer of dented GLARE $2R_2^2$ 33/C55 after the fatigue test: a. concave side
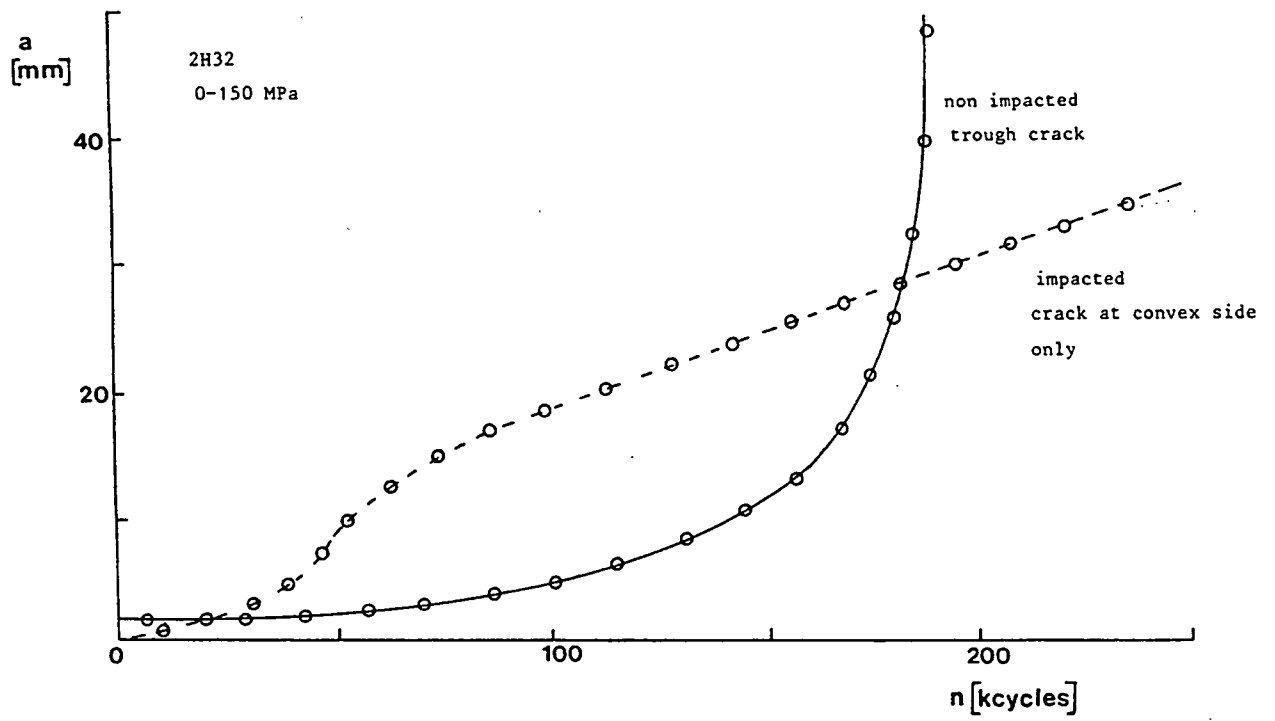
b. convex side.

figure 13.16 Semi crack length as function of the number of
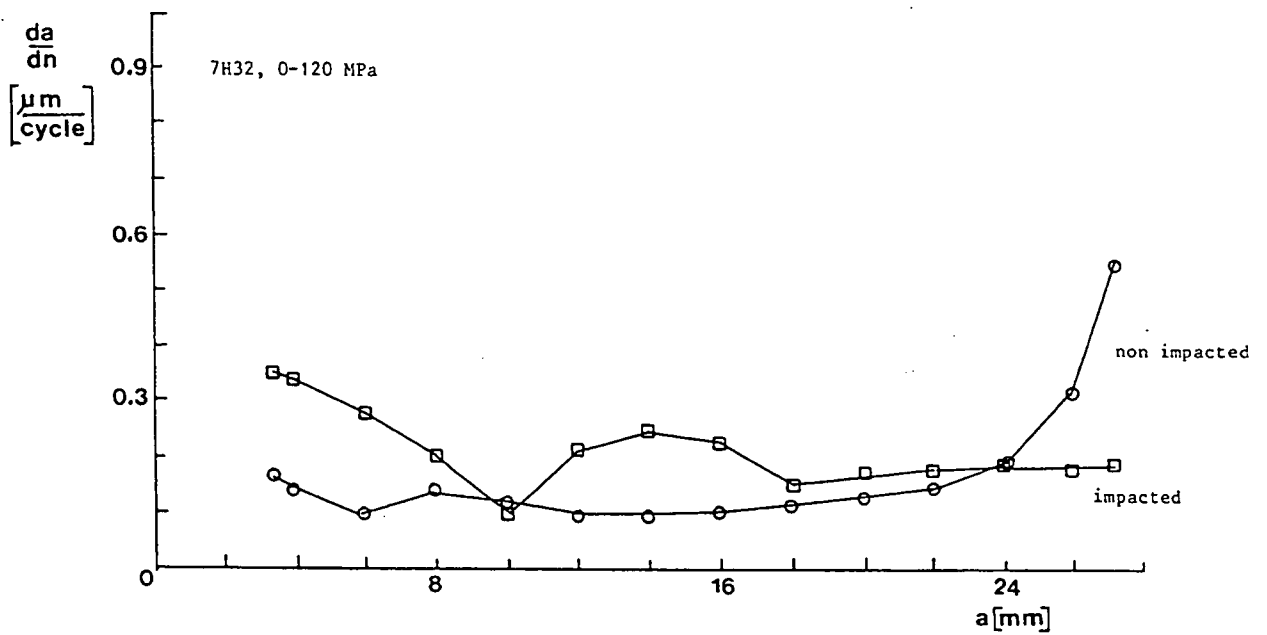cycles for impacted and non impacted aramid ARALL 2H32.
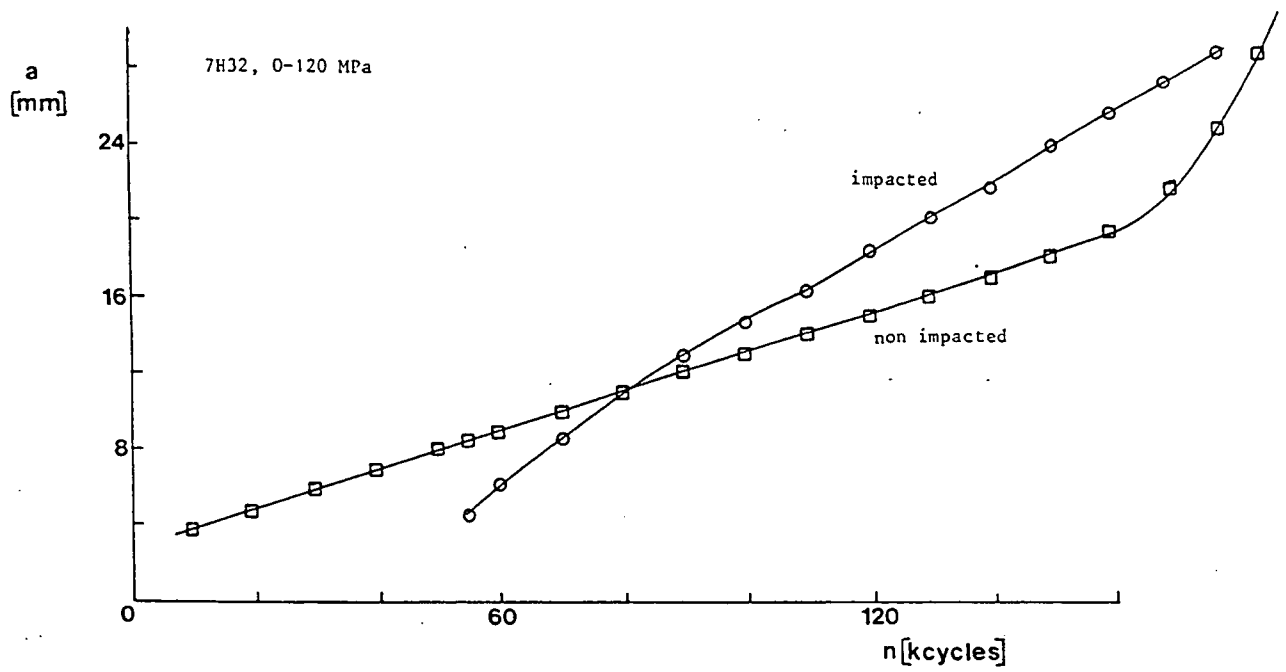
figure 13.17 Semi crack length and the crack growth rate as function of the number of cycles for aramid ARALL 7H32.
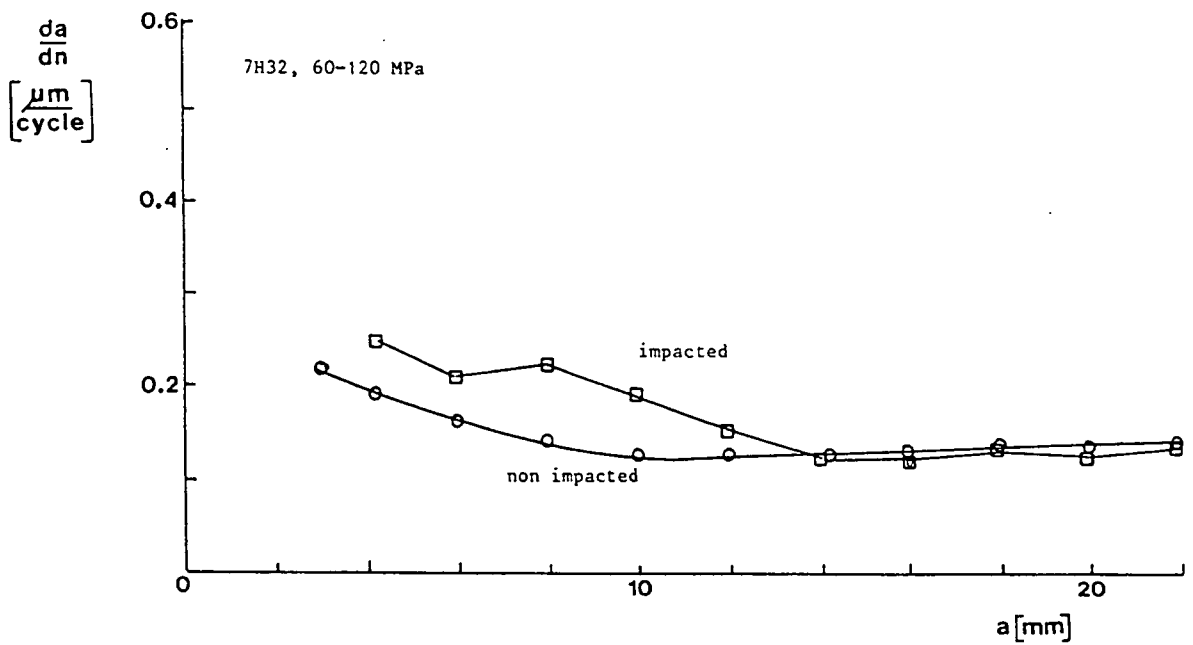
493

figure 13.18 Semi crack length and the crack growth rate as function of the number of cycles for aramid ARALL 7H32.

figure 13.19 Semi crack length and the crack growth rate as function of the number of cycles for GLARE $7R_6$32.
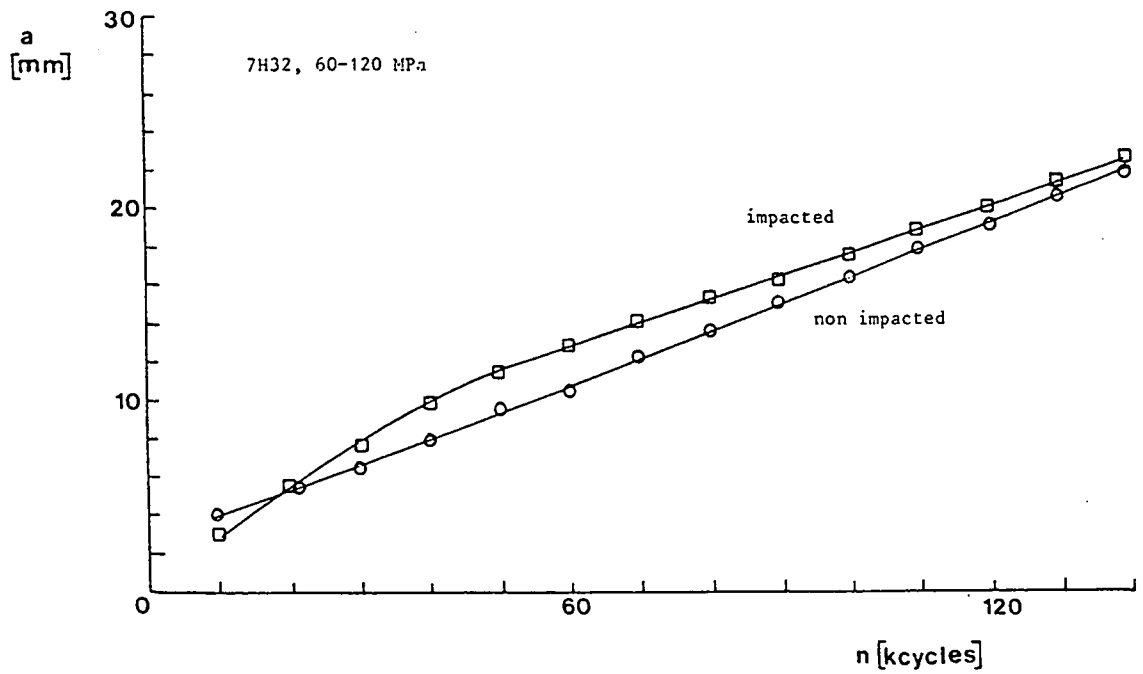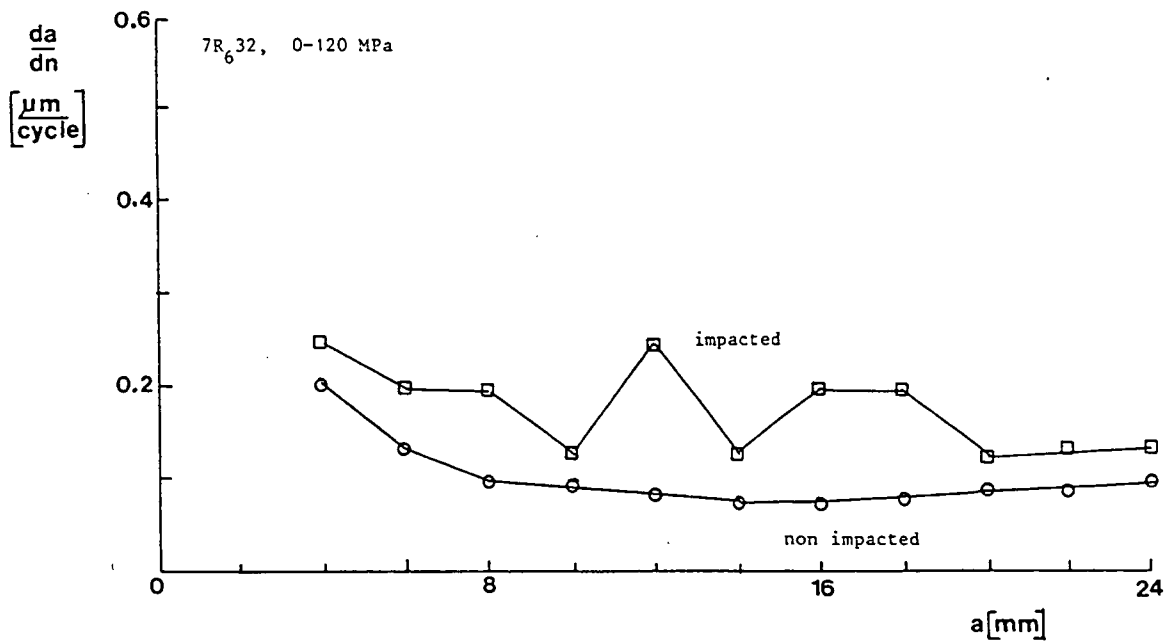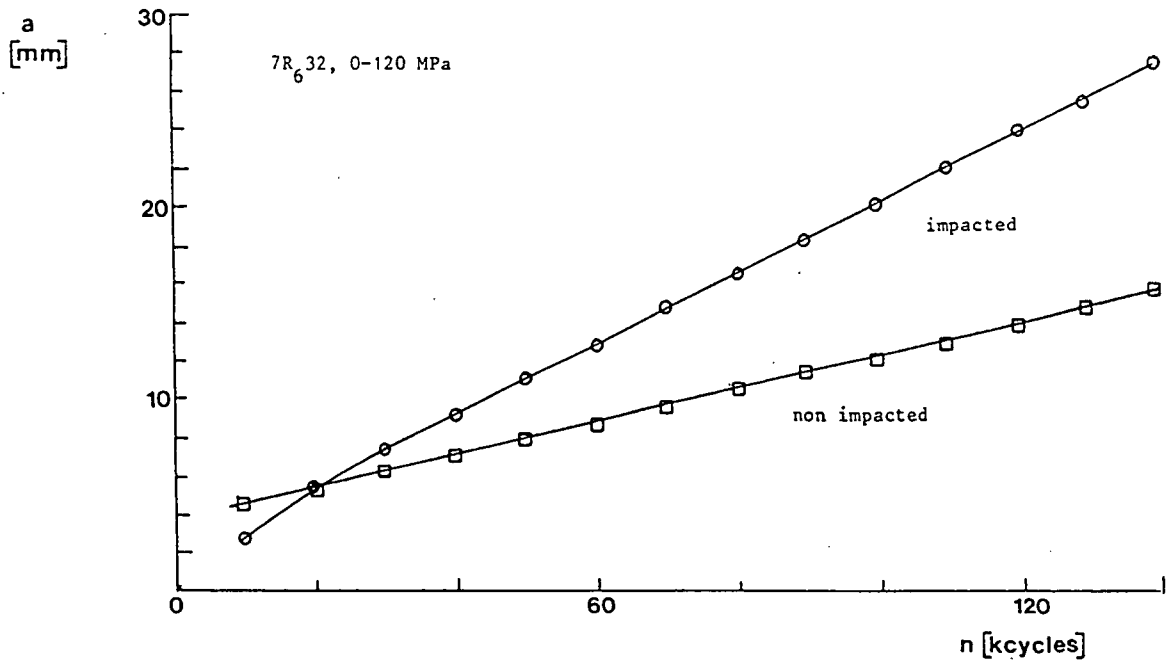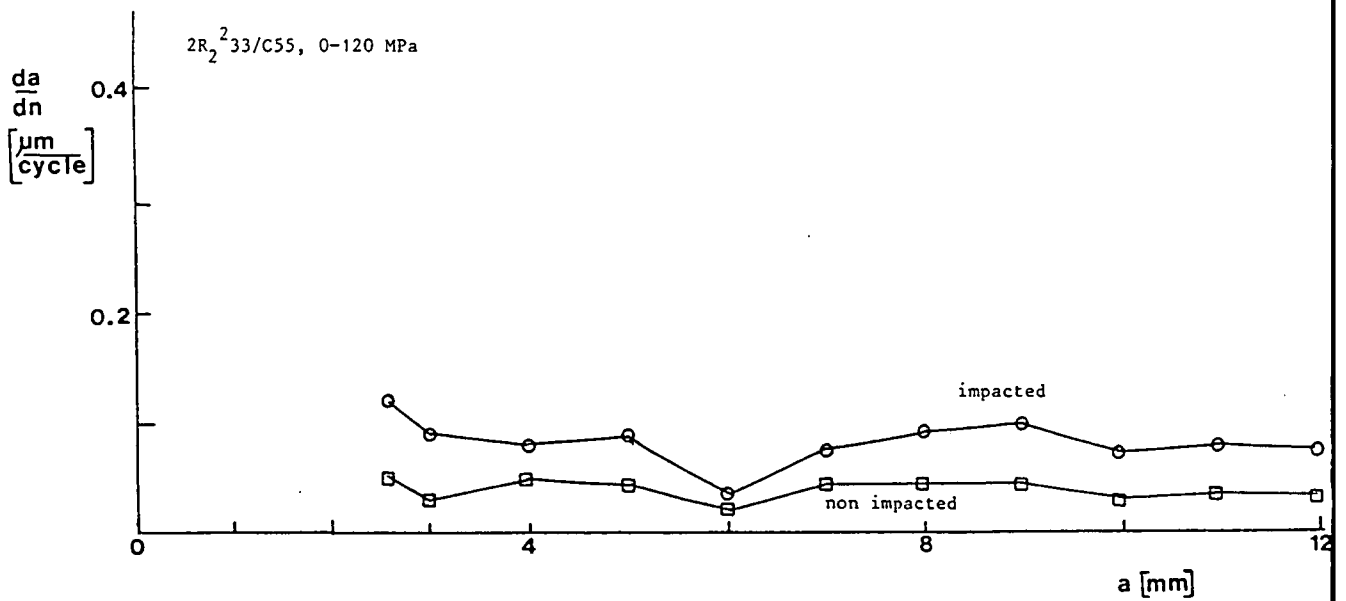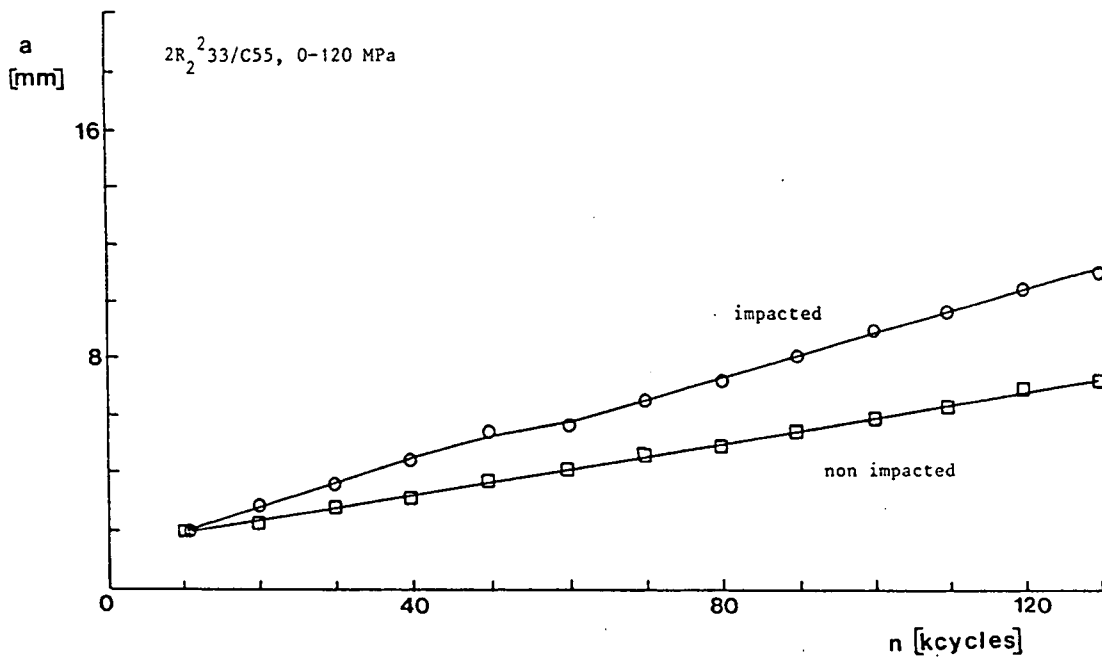
figure 13.20 Semi crack length and the crack growth rate as function of the number of cycles for GLARE 2R ^{2}33/C55.$_2$
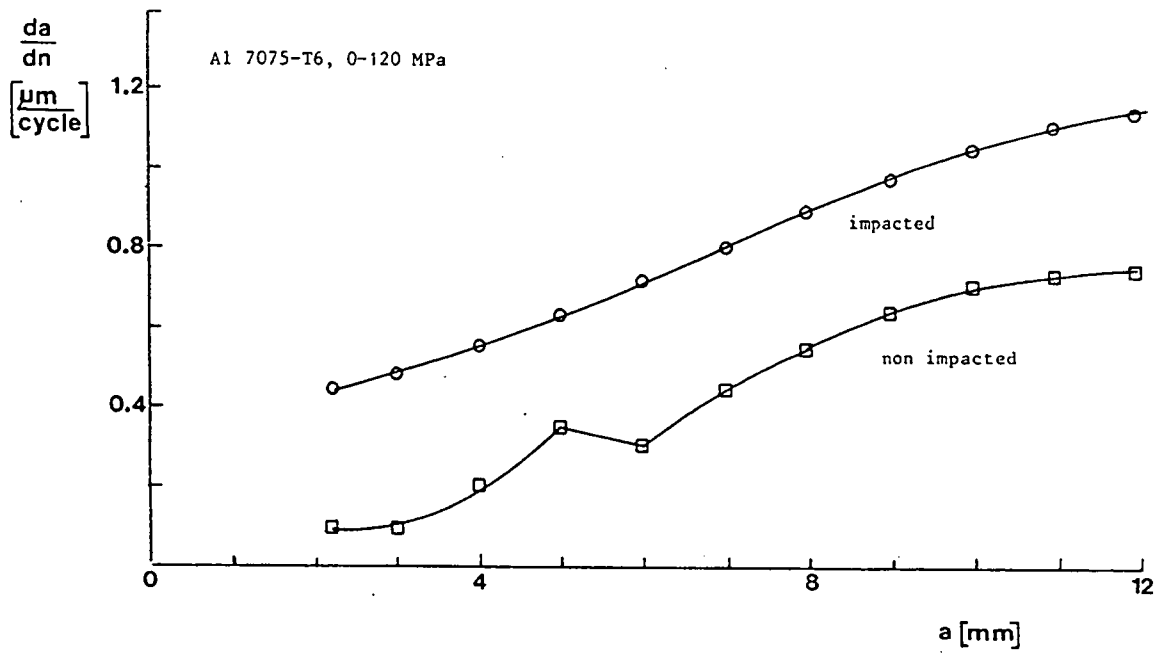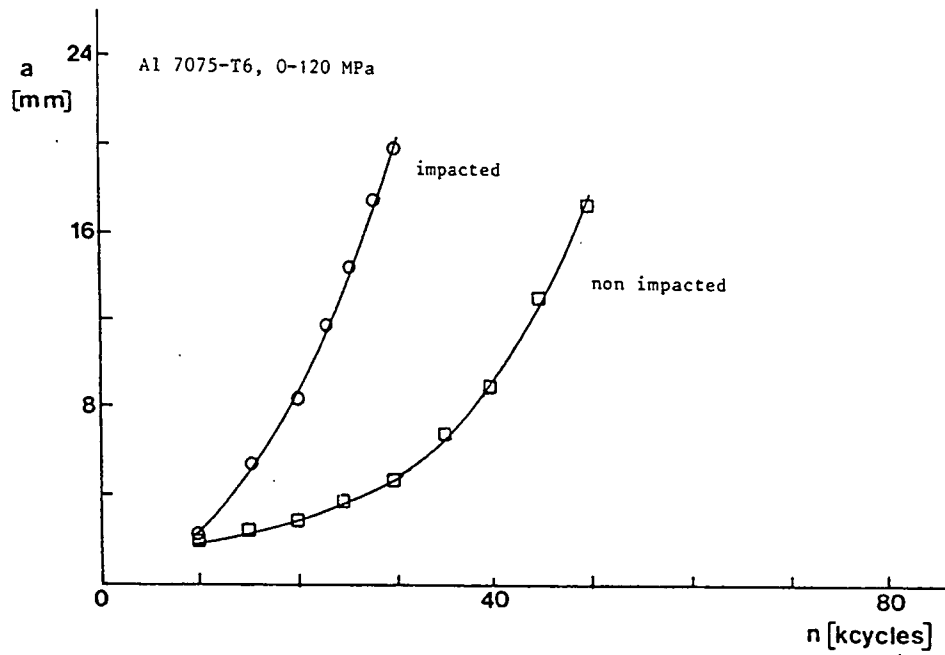
figure 13.21 Semi crack length and the crack growth rate as function of the number of cycles for Al 7075-T6.
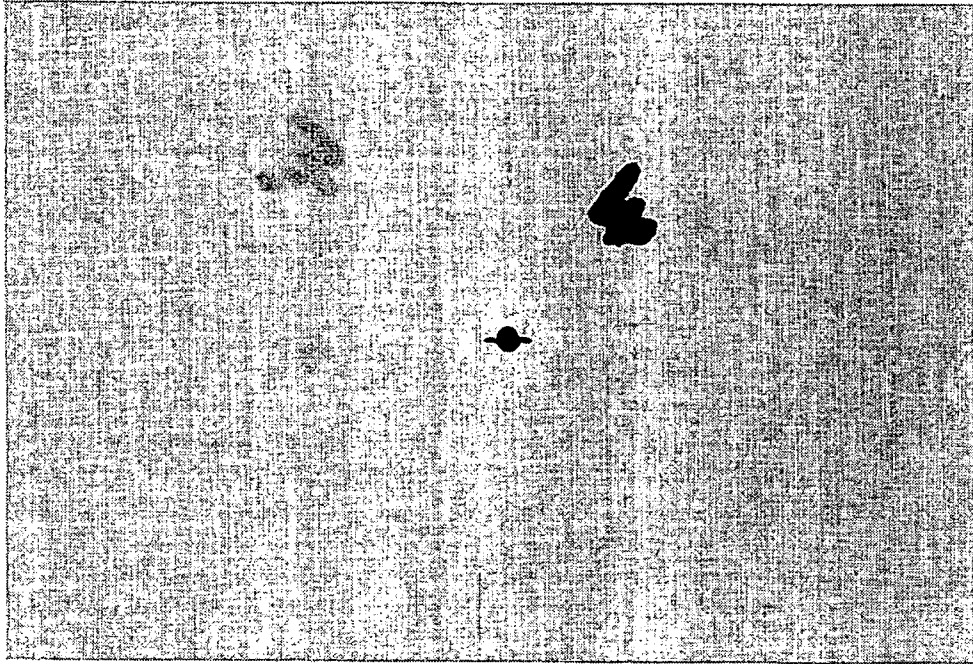
497

figure 13.22 Delaminated zone in aramid ARALL 7H32 due to fatigue loading.

chapter 14 Compressive strength: buckling of delaminations in aramid ARALL laminates

14.1 Introduction

The compressive strength of composite materials after impact has received much attention. The relatively thick laminates needed for heavily loaded (wing) panels are prone to a significant reduction of the compressive strength due to impact damage. The failure of such panels in compression can be initiated by various modes: global instability, shear crippling, fibre buckling, delamination buckling, etc. In the literature delamination buckling is a major topic, not least because it is a well defined problem for experiments and theoretical analysis. The critical buckling stress, the postbuckling behaviour, and the energy release rates of various types of delaminations have been studied both analytically and with finite element analysis. Experimental observations are rather scarce, and a connection with analytical work is seldom found. The reference list at the end of this chapter illustrates the extensive literature on delamination buckling, but it is beyond the scope of this study to give a full summary.

In this chapter we concentrate on the behaviour of ARALL laminates with aramid fibres. Because the aluminium alloy sheets of ARALL are very thin (0.2, 0.3 or 0.4 mm) local delamination in the prepreg layer may lead to buckling problems. This question was not yet studied for ARALL. Delaminations might be caused by impact damage or inadvertent manufacturing defects. To explore possible buckling effects, ARALL specimens were made with artificial delamination zones. The specimens were bonded to a thick backing plate of an aluminium alloy, in order to stabilize the specimen, and to obtain well defined buckling conditions, see figure 14.1. Buckling was then studied both under compressive and under bending loads. Figure 14.1 shows a schematic picture of the local buckling considered and the different types of delamination zones adopted. It is easily recognized that local buckling might lead to an increase of the delaminated area. It implies a mode I loading condition on the edge of the delamination (peeling). A growing delamination could also occur under cyclic loading.

In the present investigation several tests were carried out, also under

fatigue loads. Obviously the empirical results will have a more general meaning if they agree with theoretical predictions on the buckling strengths of the local buckling modes considered here. For that purpose equations were derived, based on the theory given by Whitcomb and Shivakumar[5]. The predictions are compared to the test results.

14.2. Experiments

14.2.1 Specimens

Three types of specimens were tested, see figures 14.2 to 14.6. The aluminium alloy of the thin sheets was Al 2024-T3. The material of the backing plate was Al 7075-T6, selected in view of its high yield stress. The artificial delamination zones were obtained by a local application of a release agent (a sort of wax) on the thin aluminium sheet. It locally prevents adhesion during the curing cycle, and as a consequence an artificial delamination is present between the thin aluminium layer and the prepreg.

Two variants (A and B in figure 14.2) were made for the large delamination specimen. Type A contains only one thin sheet, whereas type B carries a full ARALL sheet consisting of two Al- alloy sheets. As a result of the autoclave bonding cycle, specimens of type A have a low residual tensile stress in the thin sheet. Type B has seen two such cycles, the first one to produce the ARALL sheet. Before bonding this sheet to the backing plate it was poststretched to reverse the residual stress system to compression in the thin sheets and tension in the fibres. The residual stresses were calculated based on thermal expansion coefficients and stiffness[3]. The values are presented in table 14.1, which also gives the shape and size of the delamination zones.

Two small delamination specimens (figure 14.4) were produced to reduce the stability problems of the full specimen, to be able to reach a higher stress on the delamination. The dimensions were taken from Reiss et al.[9]. The disadvantage is that only small delaminations can be studied. Moreover, as a result of the much shorter length (65 mm as compared to 300 mm of the large specimen) the influence of the clamping of this specimen may still be

felt in the region of the delamination. According to calculation done by Reiss et al.[9] the influence of the clamping (lateral restraint) is still present at a distance of 1.33 times the width of the specimen from the clamping.

The 4-point bending loading avoids buckling of the specimen. The bending forces (F in figure 14.5) were applied by rollers (diameter 50 mm). With the available equipment static tests could be carried out, but a fatigue load could not be applied on the bending specimens. Circular, elliptical and square delamination zones were used.

14.2.2 Test Method

Large delamination specimen

Strain gages were mounted on the delamination area of the specimens (see figure 14.2) to determine the critical stress of the delamination. Due to buckling of the delamination the strain will suddenly change by a relatively large tensile increment (see figure 14.9). This is caused by the curvature and the corresponding bending moment in the buckled delamination.

The lateral displacements of some of the specimens and delaminations were measured by transducers (LVDT's). By this means also the amplitude or deflection of the buckled delamination could be determined. The lateral displacement of the whole specimen should be as small as possible to avoid a bending load on the specimen. Such a displacement can be caused by the initial curvature of the specimen and by imperfections of the clamping of the specimen.

Small delamination specimen

Strain gages were mounted on the specimens for the same reason as for the large specimens.

Four point bending delamination specimen

The deflection of this type of specimen was determined by an LVDT. Two

strain gages were mounted to detect buckling, see figure 14.5. One of the strain gages was mounted over the delamination, the other one beside the delamination. As long as both gages indicate the same strain no delamination buckling occurs. Buckling takes place when a deviation from the line $\varepsilon_1 = \varepsilon_2$ occurs (see figures 14.14 and 14.15).

14.2.3 Results of static tests

Large delamination specimens

In figures 14.7 and 14.8 pictures are shown of buckling of a strip delamination (rectangular delamination area over the whole width of the specimen) and an elliptical delamination respectively. Typical results of the strain gage measurements are given in figures 14.9 and 14.10. From such graphs the external buckling strain and thus the external buckling stress of the specimen can be determined. The results are given in table 14.1. In this case the strain measurements were preferred for the calculation of the buckling stress. The applied load on the specimen cannot be used to calculate the buckling stress because of the bending caused by imperfections of the specimen. The critical or buckling stress of the delamination is taken as the sum of the external stress on the specimen and the internal stress due the curing cycle and the post-stretching operation. Figure 14.11 gives typical results of the LVDT measurements on the lateral displacement of the specimen. The out of plane displacement of the delaminations are drawn in this figures and also in figure 14.12. The figures show that out of plane displacement occurred in the thin delaminated sheets at relatively low loads (lower than the critical buckling load). This can be caused by imperfections in the delaminated sheet of the delamination.

Small delamination specimens

The external buckling stress of the delamination was determined from the strain gage measurements. The results are given in table 14.1. The critical stress is determined in the same way as for the large delamination buckling specimens.

Four point bending delamination specimens

The deflection as function of the applied load for two types of specimens are given in figure 14.13. Elementary applied mechanics leads to the following equation for the deflection w of the centre of the four point bending specimen:

$$w = \frac{11 \ F \ l^3}{6 \ E \ I} \qquad \qquad (14.1)$$

with F as the applied load, l as the describing length (l = 200 mm in figure 14.5) and EI as the bending stiffness. This theoretical linear relationship is shown in figure 14.13. It agrees with the experimental result.

Typical strain gage measurements are given in the figures 14.14 and 14.15. The shape of the graphs will be discussed in section 14.4. The buckling strain is shown in these figures. The experimental buckling stresses are given in table 14.1. The critical stresses are determined as for the large buckling delamination specimen, as the sum of the internal and external stress.

14.2.4 Fatigue tests

Some of the large and the small delamination specimens were tested under fatigue loading. The load was a sine function between 0 and a maximum compressive load. The fatigue load, the frequency and the number of cycles are given in table 14.2. The fatigue load on two specimens (L1 and L3) was increased in steps, because no delamination growth was observed.

No delamination growth could be detected during the tests. The thin aluminium layers of the specimens were removed by chemical etching after the fatigue tests. No damage of the prepreg layers which might indicate delamination growth could be detected.

The small delamination buckling specimens showed crack initiation in the aluminium layers due to the large cyclic bending moment in the buckled

delamination.

14.3. Theory

14.3.1 Introduction

Figure 14.1 shows an elliptical delamination in an ARALL plate under compression. The edges of the rectangular ARALL plate are simply supported or clamped. When the compressive stress p is increased until a critical value is reached, either the whole plate or the delamination will buckle first. Whether the whole plate or the delamination buckles first will depend on the dimensions and clamping conditions of the specimen and the delamination dimensions.

If it is assumed that the plate, until instability, behaves like a plate without a delamination, the critical load of the plate can be calculated. The critical load of the delamination can also be determined, if it is approximated by the buckling load of a clamped, elliptical sheet under unidirectional compression.

In this chapter the buckling stress of the whole plate is compared with the buckling stress of an elliptical delamination. It is assumed that the delamination is present between the top layer and the rest of the laminate. So the delaminated (thin) sheet is isotropic aluminium with a thickness t = 0.3 mm.

14.3.2 Basic buckling equations

The textbook of Megson[1] gives the basic principles of buckling of beams and plates. The well known Euler equation for the critical load of perfect, slender columns is:

$$P_{cr} = \frac{n^2 \pi^2 E I}{l^2}$$

(14.2)

P_{cr} is the critical load, n is dependent on the boundary conditions (n = 2

504

for clamped ends, n = 1 for simply supported ends), EI is the bending stiffness and l is the length of the column.

For an isotropic rectangular plate with a rectangular cross section the critical stress σ_{cr} is[2]:

$$\sigma_{cr} = \frac{n^2 \pi^2 E}{12(1-\nu^2)} \left[\frac{t}{l} \right]^2 \qquad (14.3)$$

with t as the thickness of the plate.

Equation 14.3 gives the buckling stress of a rectangular strip delamination. This relation is depicted in figure 14.16 for t = 0.3 mm, n = 2, E = 72,000 MPa and ν = 0.33.

The critical stress of an isotropic rectangular plate with various edge conditions is given by[1]:

$$\sigma_{cr} = \frac{k \pi^2 E}{12(1-\nu^2)} \left[\frac{t}{B} \right]^2 \qquad (14.4)$$

where k depends on the edge conditions and the span/width ratio A/B. k is shown in figure 14.17. For a square plate (A/B = 1) with all edges clamped (k = 10.5) relation 14.4 is shown in figure 14.18.

14.3.3 Buckling of an ARALL plate

Lekhnitskii[2] presents the governing equation for bending of an anisotropic plate, for small deflections:

$$D_{11} \frac{\delta^4 w}{\delta w^4} + 2(D_{12} + 2D_{66}) \frac{\delta^4 w}{\delta w^2 \delta y^2} + D_{22} \frac{\delta^4 w}{\delta w^4} + P \frac{\delta^2 w}{\delta w^2} = 0 \qquad (14.5)$$

P is the force per unit width of the plate, D_{ij} is the flexural stiffness of the plate and $w(x,y)$ is the deflection field of the plate. The flexural stiffness is:

$$D_{ij} = \frac{1}{3} \sum_{k=1}^{n} c_{ij}^{k} \left[z_k^3 - z_{k-1}^3 \right] \tag{14.6}$$

with t and z as the thickness and the coordinate in thickness direction of the plate respectively, and:

$$\sigma_j = c_{ij} \varepsilon_i \tag{14.7}$$

For all edges simply supported the deflection field can be approximated by:

$$w = A_{mn} \sin \left[\frac{m\pi x}{A} \right] \sin \left[\frac{n\pi y}{B} \right] \tag{14.8}$$

with A and B as the length and the width of the plate respectively.

The buckling stress has a minimum for n=1, and equation 14.5 leads to:

$$p_{cr} t B^2 = \pi^2 \left[D_{11} \left[\frac{mB}{A} \right]^2 + 2(D_{12} + 2 D_{66}) + D_{22} \left[\frac{mA}{B} \right]^2 \right] \tag{14.9}$$

with m as the number of half waves of the buckled plate, and p_{cr} as the buckling stress.

For clamped unloaded edges and simply supported loaded edges the deflection field can be approximated by:

$$w = A_{mn} \left(1 - \cos \frac{2n\pi y}{B} \right) \sin \frac{m\pi x}{A} \tag{14.10}$$

and the critical stress can be approximated by:

$$p_{cr} t\ B^2 = \pi^2 \left[D_{11}\left[\frac{mB}{A}\right]^2 + \frac{8}{3}\ (D_{12}+ 2\ D_{66}) + \frac{16}{3}\ D_{22}\left[\frac{mA}{B}\right]^2 \right]$$ (14.11)

In equations 14.9 and 14.11 m is the value for which p_{cr} has a minimum.

With the theory of Lekhnitskii it is difficult to calculate the critical stress for clamped loaded edges However, as figure 14.17 shows (for isotropic material), the influence of the edge conditions of the loaded edges becomes very small for A/B > 2. In figure 14.17 the dotted lines (loaded edges clamped) and the full lines (loaded edges simply supported) converge. It is assumed that this is also true for anisotropic plates.

The elastic constants of the aramid and aluminium layers are given by Verbruggen[3]:

aramid: E_{xx} = 57692 MPa

E_{yy} = 5022 MPa

μ_{xy} = 0.368

μ_{yx} = 0.032

aluminium: E = 72000 MPa

ν = 0.33

With these constants the stiffness matrices of ARALL xH32 and xH34 and of the monolithic aluminium alloy can be calculated:

	monolithic	xH32	xH34
c_{11} (MPa)	80798	74783	72843
c_{22} (MPa)	80798	60484	53931
c_{12} (MPa)	26663	20011	17865
c_{66} (MPa)	27068	20180	17958

With these matrices the flexural stiffness is calculated and substituted into equations 14.9 and 14.11. The results are presented in figures 14.19 and 14.20. Apparently the critical stress for a certain value of B approaches a constant value for A/B > 2. The limit values of $p_{cr} B^2$ are (in 10^4 N):

	unloaded edges simply supported	unloaded edges clamped
xH32 total thickness 0.82 mm	14	26
monolithic t=0.82 mm	18	33
xH34 total thickness 1.86 mm	66	124
monolithic t=1.86 mm	92	168

The lower buckling strength of ARALL as compared to the monolithic Al-alloy is evident.

14.3.4 Buckling of an elliptical, isotropic delaminated sheet

The critical stress of a clamped, elliptical, isotropic plate under unidirectional compression was calculated with the energy method (Raleigh – Ritz analysis) as given by Shivakumar and Whitcomb[5]. The total potential energy of the plate has a stationary value in the neutral equilibrium of its buckled state.

The strain energy of a bent isotropic plate is given by Timoshenko[4]:

$$U = \frac{1}{2} D \int\int_{Area} \left[\left[\frac{\delta^2 w}{\delta x^2} \right]^2 + \left[\frac{\delta^2 w}{\delta y^2} \right]^2 + 2\nu \left[\frac{\delta^2 w}{\delta x} \frac{\delta^2 w}{\delta y^2} \right] + \right.$$

$$\left. + 2(1-\nu) \left[\frac{\delta^2 w}{\delta x \delta y} \right]^2 \right] \, dx \, dy \qquad (14.12)$$

with D as the flexural stiffness of an isotropic plate:

$$D = \frac{E t^3}{12(1-\nu^2)} \qquad (14.13)$$

The potential energy of the applied compressive force per unit of length of the edge N is:

$$V = - \frac{1}{2} \int\int_{Area} N \left[\frac{\delta w}{\delta x} \right]^2 dx \, dy \qquad (14.14)$$

A deflection field w(x,y) has to be assumed which satisfies the boundary conditions: zero deflection and zero slope at the edge of the ellipse. Shivakumar and Whitcomb[5] compared the following displacement field with results of finite element calculations:

$$w = \left[1 - \left[\frac{x}{a} \right]^2 - \left[\frac{y}{b} \right]^2 \right]^2 (c_0 + c_1 x^2 + c_2 y^2) \qquad (14.15)$$

where c_0, c_1 and c_2 are generalized displacements. This displacement field leads to accurate results for a delaminated sheet with a low anisotropy[5]. Substituting this deflection field in (14.12) and (14.14) yields:

$$U = \underline{c}^T D (K_1 + K_2 + 2K_3) \underline{c} \qquad (14.16)$$

$$V = - \underline{c}^T K_4 N \underline{c} \qquad (14.17)$$

with:

$$c = \begin{bmatrix} c_0 \\ c_1 \\ c_2 \end{bmatrix} \qquad (14.18)$$

509

$$K_1 = \frac{\pi b}{20a^3} \begin{bmatrix} 80 & 10 & 10 \\ 10 & 27 & 1 \\ 10 & 1 & 3 \end{bmatrix} \qquad (14.19)$$

$$K_2 = \frac{\pi a}{20b^3} \begin{bmatrix} 80 & 10 & 10 \\ 10 & 3 & 1 \\ 10 & 1 & 27 \end{bmatrix} \qquad (14.20)$$

$$K_3 = \frac{\pi}{60ab} \begin{bmatrix} 80 & 10 & 10 \\ 10 & 11 & 5 \\ 10 & 5 & 11 \end{bmatrix} \qquad (14.21)$$

$$K_4 = \frac{\pi b}{120a} \begin{bmatrix} 40 & 0 & 4 \\ 0 & 3 & 0 \\ 4 & 0 & 1 \end{bmatrix} \qquad (14.19)$$

The matrices K_1, K_2, K_3 and K_4 were calculated by integration of 14.12 and 14.14 over the elliptical plate.

The total potential energy is:

$$\Pi = U + V = \underline{c}^T K \underline{c} \qquad (14.23)$$

with:

$$K = D (K_1 + K_2 + 2K_3) - N K_4 \qquad (14.24)$$

The function Π has a stationary value when the critical load is reached[5], therefore:

$$\frac{\delta\Pi}{\delta c_0} = \frac{\delta\Pi}{\delta c_1} = \frac{\delta\Pi}{\delta c_2} = 0 \qquad (14.25)$$

this   yields:

$$D (K_1 + K_2 + 2K_3) - N_{cr} K_4 = 0 \qquad (14.26)$$

with:

$$\sigma_{cr} = \frac{N_{cr}}{t_{sub}} \qquad (14.27)$$

Therefore σ_{cr} is the lowest eigenvalue of the matrix:

$$\frac{D}{t_{sub}} K_4^{-1} \left[K_1 + K_2 + 2K_3 \right] \qquad (14.28)$$

The three eigenvalues of the matrix (14.28) were calculated as a function of a and b with the power method with hotelling deflation[6], with an accuracy of $\varepsilon < 0.0001$. Examples of calculated eigenvalues (in MPa) as function of a and b are given in table 14.3. The lowest positive eigenvalue corresponds with the critical stress of the delamination. The relations between the critical stress and the dimensions of the elliptical delamination are shown in figures 14.21 and 14.22. For a/b values > 1.5 the theory is not valid as will be discussed in the next section.

The delaminated thin sheet in ARALL will buckle when:

$$P_{cr} = \sigma_{cr} - \sigma_{int} \tag{14.29}$$

with: σ_{cr} as the lowest positive eigenvalue of matrix (14.28), the compressive buckling stress, and σ_{int} as the internal stress in the aluminium layers of ARALL (positive for tension).

With the computer program described in reference 8 the following internal stresses in the aluminium layers of ARALL were calculated:

ARALL code	(mm)	poststretch (%)	σ_{int} (MPa)
2H32	0.82	0	+30
2H34			+40
2H32,.4	1.86	0.4	-58
2H34,.4			-91

14.4 Discussion

1. The theoretical buckling stress of an elliptical delamination for large b (see figure 14.22), becomes equal to the critical stress of a strip delamination described by equation (14.3) as might be expected.

2. For a/b ≥ 1.5, one of the eigenvalues becomes negative (this is also the case for a/b = 0.5). This means that for a slender delamination (in loading direction) the plate may buckle under a tensile stress, when a/b ≥ 1.5. In this case the smallest positive eigenvalue (= critical compressive stress) and the smallest negative eigenvalue for a/b become relatively large. This can be explained as follows. For a/b ≥ 1.5 the plate wants to buckle with a number of half waves m > 1 (see figure 14.23). This is prevented by the assumed deflection field (because $c_0 \neq 0$). This means that, because a buckling mode with m > 1 is prevented, the calculated buckling stress will not be correct (too high) for a/b ≥ 1.5 . This is indicated in figure 14.21 ('theory not valid').

3. The strain gage measurements of the four point bending delamination

buckling specimens (figure 14.14 and 14.15) showed a small increase of the strain on the delamination after the initiation of buckling. This phenomenon is caused by the deflection of the specimen. Due to this deflection the delamination is initially compressed more when it buckles outwards. At higher deflections (higher ε_2) the ε_1 decreases because of the bending deformation in the buckled thin sheet.

4. The comparison of theoretical and experimental values of the critical stress for the strip delaminations is made in figure 14.16. For the circular delaminations this comparison is given in figure 14.24. The theoretical values for the elliptical delaminations are given in figure 14.22 and compared with experimental results in table 14.1. The critical stress was calculated as the sum of the external stress on the specimen and the internal stress due to the curing cycles and poststretching. The internal stresses calculated according to reference 3, are given in table 14.1. The theory can not predict the buckling stress of an elliptical delamination when the axis in loading direction is longer than in the transverse direction, as explained under point 2.

5. When figures 14.18 and 14.24 are compared it appears that the buckling stress of a clamped circular plate (a/b = 1) can be approximated by a clamped square plate with the same delamination width.

14.5 Conclusions

1. The theoretical model proved to give accurate results for the buckling stress of elliptical and rectangular delaminated thin sheets and strip delaminations.

2. The critical stress of a clamped circular plate (a/b = 1) can be approximated by the critical stress of a clamped square plate.

3. The critical stress of the full ARALL plate and the critical stress of a delaminated sheet are shown in figure 14.21 as function of B and b respectively (valid for A/B >2). From this figure it can be determined whether the delaminated thin sheet or the full plate will buckle first. The

513

internal stresses in ARALL have to be taken into account.

4. No delamination growth was detected due to buckling of the delaminated sheet under the circumstances of the tests, including static and cyclic loading.

5. The test showed that delamination growth due to delamination buckling is not a major concern for ARALL laminates. The buckling stress for delaminations smaller than 30x30 mm^2 is relatively high. Delamination growth was not detected for ARALL with aramid fibres. It may be expected that GLARE also will not exhibit delamination growth due to delamination buckling, because of the better adhesion between the R-glass fibres and the epoxy adhesive.

References

1. Megson, T.H.G.; Aircraft structures for engineering students; London 1972.

2. Lekhnitskii, S.G.; Anisotropic plates; New York, 1968.

3. Verbruggen, M.L.C.E.; Aramid Reinforced Aluminium Laminates: ARALL, Adhesion problems and environmental effects; TU Delft report LR 503; Delft, 1986.

4. Timoshenko, S. and Woinowsky-Krieger, S.; Theory of plates and shells; Singapore 1970.

5. Shivakumar, K.N. and Whitcomb, J.D.; Buckling of a sublaminate in a quasi-isotropic composite laminates, J.Composite Materials, Vol.19, pp.2-18, 1985.

6. Kan, J. van; Numerieke Analyse Cl; TU Delft college a105.

7. Ramkumar, R.L.; Compression fatigue behaviour of composites in the presence of delaminations; Damage in composite materials, ASTM STP 775, 1982.

8. Vlot, A.; Plasticity and formability aspects of ARALL; Master thesis TU Delft, 1986.

9 . Reiss, R.; Yao, T and Clark, R.K.; Effect of load introduction in compression testing of composite materials; in: Compression testing of homogeneous and composite materials, ASTM STP 808; 1983.

10. Yin, W.L.; The effects of laminated structure on delamination buckling

and growth, J.Composite Materials, Vol.22, pp.502-517, 1988.

11. Bruno, D.; Delamination buckling in composite laminates with interlaminar defects, Theoretical and applied fracture mechanics, Vol.9, pp.145-159, 1988.

12. Yin, W.L.; Cylindrical buckling of laminated and delaminated plates, AIAA/ASME/ASCE/AHS 27th Structures, structural dynamics and material conference, 1986.

13. Lagace, P.A.; Jensen, D.W.; Finch, D.C.; Buckling of unsymmetric composite laminates, Composite structures Vol.5, pp.101-123, 1986.

14. Bartels, G.; Delaminatie in gelaagd plaatmateriaal (in Dutch), National Aerospace laboratory NLR, memorandum SC-82-045 U, 1982.

15. Horban, B.; Palazotto, A.; The experimental buckling of cylindrical composite panels with eccentrically located circular delaminations, AIAA/ASME/ASCE/AHS, 27th Structures, structural dynamics and material conference, 1986.

16. Ramkumar, R.L.; Compression fatigue behaviour of composites in the presence of delaminations, in: Damage in composite materials, ASTM STP 775, pp.184-210, 1982.

17. Whitcomb, J.D.; Three-dimensional analysis of a postbuckled embedded delamination, J.Composite materials, Vol.23, pp.862-889, 1989.

18. Yin, W.L.; Wang, T.S.; The energy-release rate in the growth of a one-dimensional delamination, J.Applied mechanics, Vol.51, pp.939-941, 1984.

19. Yin, W.L.; Sallam, S.N.; Simitses, G.J.; Ultimate axial load capacity of a delaminated beam-plate, AIAA Journal, Vol.24, No.1, pp.123-128, 1986.

20. Whitcomb, J.D.; Shivakumar, K.N.; Strain energy release rate analysis of a laminate with postbuckled delamination, NASA Technical Memoradum 89091, 1987.

21. Garg, A.C.; Delamination- a damage mode in composite structures, Eng. Fracture Mechanics, Vol.29, No.5, pp.557-584, 1988.

22. Chai, H.; Babcock, C.D.; Two-dimensional modelling of compressive failure in delaminated laminates, J.Composite Materials, Vol.19, pp.67-97, 1985.

23. Simitses, G.J.; Sallam, S.; Yin, W.L.; Effect of delamination of axially loaded homogeneous laminated plates, Vol.23, No.9, pp.1437-1444, 1985.

24. Yin, W.L.; Energy balance and the speed of crack grwoth in a buckled strip delamination, AIAA, 1987.

25. Kapania, R.K.; Wolfe, D.R.; Delamination buckling and growth in axially loaded beam-plates, AIAA, 1987.

26. Whitcomb, J.D.; Strain-energy release rate analysis of cyclic delamination growth in compressively loaded laminates, in: Effects of defects in composite materials, ASTM STP 836, pp.175-193, 1984.

27. Bottega, W.J.; Maeval, A.; Delamination buckling and growth in laminates, J.Applied Mechanics, Vol.50, pp.184-189, 1983.

28. Whitcomb, J.D.; Finite element analysis of instability related delamination growth, J.Composite Materials, Vol.15, pp.403-426, 1981.

29. Siefert, G.; Palazotto, A.; The effect of a centrally located midplane delamination on the instability of composite panels, Experimental Mechanics, pp.330-336, December 1986.

30. Kardomateas, G.A.; Schmueser, D.W.; Effect of transverse shearing forces on buckling and postbuckling of delaminated composites under compressive loads, AIAA 1987.

31. Yin, W.L.; Axisymmetric buckling and growth of a circular delamination in a compressed laminate, Int.J.Solids Structures, Vol.21, No.5, pp.503-514, 1985.

32. Williams, J.F.; Stouffer, D.C.; Ilic, S.; Jones, R.; An analysis of delamination behaviour, Composite structures Vol.5, pp.203-216, 1986.

33. Chai, H.C.; Babcock, C.D.; Knauss, W.G.; One dimensional modelling of failure in laminated plates by delamination buckling, Int.J.Solids Structures, Vol.17, No.11, pp.1069-1083, 1981.

34. Sallam, S.; Simitses, G.J.; Delamination buckling and growth of flat cross-ply laminates, Vol.4, pp.361-381, 1985.

35. Chai, H.; Knauss, W.G.; Babcock, C.D.; Observation of damage growth in compressively loaded laminates, Experimental Mechanics, pp.329-337, September 1983.

36. Somers, M.; Weller, T.; Abramovich, H.; Buckling and postbuckling behaviour of sandwich structures in the presence of a delamination, Technion, Haifa Israel, TAE No.644, 1989.

37. Rothschilds, R.J.; Gillespie, J.W.; Carlson, L.A.; Instability-related delamination growth in thermoset and thermoplastic composites, in: Composite materials: testing and design (eight conference), ASTM STP 972, pp.161-179, 1988.

38. Whitcomb, J.D.; Shivakumar, K.N.; Strain-energy relase rate analysis of plates with postbuckled delaminations, J.Composite materials, Vol.23, pp.714-734, 1989.

39. Flanagan, G.; Two-dimensional delamination growth in composite laminates under compression loading, in: Composite materials: testing and design (eighth conference), ASTM STP 972, pp.180-190, 1988.

40. Kachanov, Delamination buckling of composite materials, Kluwer academic publishers, Dordrecht, 1988.

Type	Variant	No.	Delamination		Stresses (MPa)			
			Shape	Size	Internal	External	Critical	
				2a x 2b	Calc.	Exp.	Exp.	Theory
				fig.14.1				
Large	A	L1	strip	18x100	+5	-45	-40	-74
(fig.		L2				-50	-45	
14.2)	B	L3	ellips	35x25	-55	-77	-132	**
		L4	strip	24x100		*		
		L5	ellips	20x17		*		
Small		S1	strip	13x25	+3	-145	-142	-142
(fig.		S2	ellips	25x20		*		
14.4)								
4-point	B	F1	circle	25x25	≈0	-89	-89	-101
bending	B	F2	circle	30x30		-82	-82	-70
(fig.	B	F3	square	30x30		-63	-63	-70
14.5)	B	F4	ellips	25x15		-86	-86	**
	B	F5	ellips	60x30		-26	-26	-30
.	C	F6	circle	20x20	≈0	-130	-130	-158
	C	F7	circle	30x30		-86	-86	-70
	C	F8	square	20x20		-162	-162	-158
	C	F9	square	25x25		-119	-119	-101
	C	F10	square	30x30		-65	-65	-70
	C	F11	ellips	25x14		-151	-151	**
	C	F12	ellips	30x12		-86	-86	**
	C	F13	ellips	20x40		-97	-97	-80
	C	F14	ellips	25x50		-65	-65	-50

table 14.1 Delamination specimens, dimensions in mm, stresses in MPa

* used for fatigue tests only

** theoretical model not valid

519

specimen	step	min	maximum			kcycles	frequency (Hz)	delamination growth
			kN	MPa	σ/σ_{cr}			
L1	1	0	-50	-73	1.62	627	5	no
	2	0	-70	-103	2.28	351	5	no
	3	0	-100	-145	3.22	105	2	no
L3	1	0	-100	-94	1.22	139	2	no
	2	0	-110	-104	1.35	45	0.5	no
	3	0	-120	-113	1.46	5	0.5	no
	4	0	-130	-123	1.60	130	0.5	no
L4	1	0	-130	-123	2.46	177	0.5	no
L5	1	0	-100	-113	1.13	150	0.5	no
S1	1	0	-130	-149	1.02	19	0.5	no
S2	1	0	-130	-149	1.24	26	0.5	no

The "external loading" spans the step, min, and maximum columns; "maximum" spans kN, MPa, and σ/σ_{cr}.

table 14.2   Fatigue test program.

519

a/b	2b (mm)	eigenvalues (MPa)		
0.50	5	22218	18287	-16241
	10	5554	4572	-4060
	20	1389	1143	-1015
	30	617	508	-454
	40	347	286	-255
	50	222	183	-164
	60	154	127	-114
1.00	5	31553	7267	2533
	10	7888	1817	633
	20	1972	454	158
	30	876	202	70
	40	493	114	40
	50	316	73	25
	60	219	50	18
1.50	5	60368	6040	-3228
	10	15092	1510	-807
	20	3773	377	-202
	30	1677	168	-90
	40	943	94	-50
	50	604	60	-32
	60	419	42	-22
2.00	5	101714	7629	-7959
	10	25429	1907	-1990
	20	6357	477	-497
	30	2825	212	-221
	40	1589	119	-124
	50	1017	76	-79
	60	706	53	-55

table 14.3 Calculated eigenvalues of the buckling matrix as function of the geometry parameters of a clamped isotropic elliptical plate.
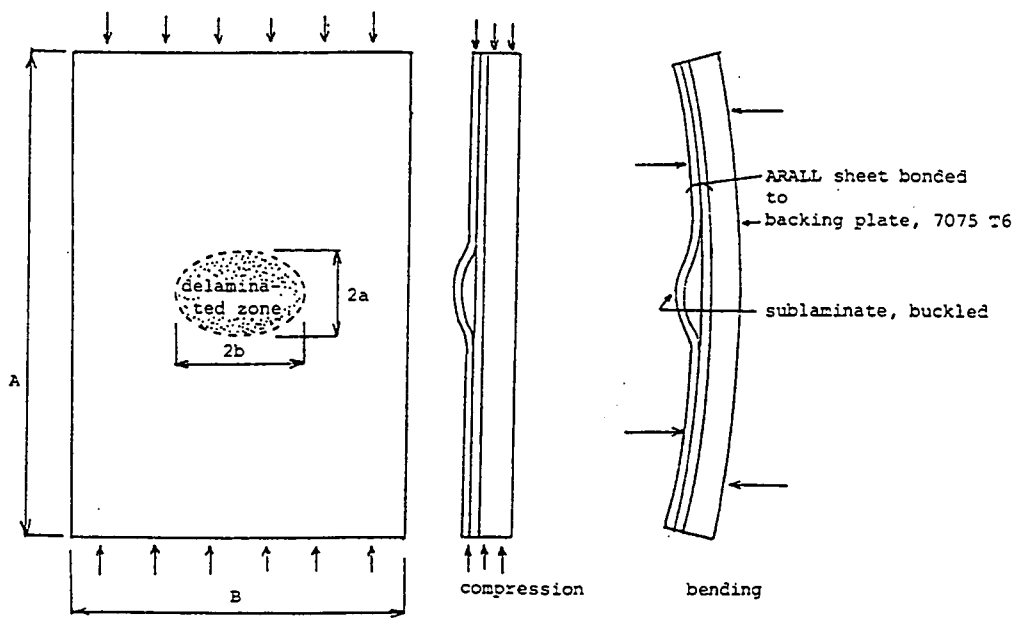
- 3 types of delaminated zones: 1. parallel zone over full width,
                                     strip delamination
                                  2. elliptical and circular
                                  3. square

- 2b = delamination width perpendicular to the loading direction
  2a = delamination length in loading direction

figure 14.1 ARALL sheet bonded to a backing plate, buckling of
delaminated zone.
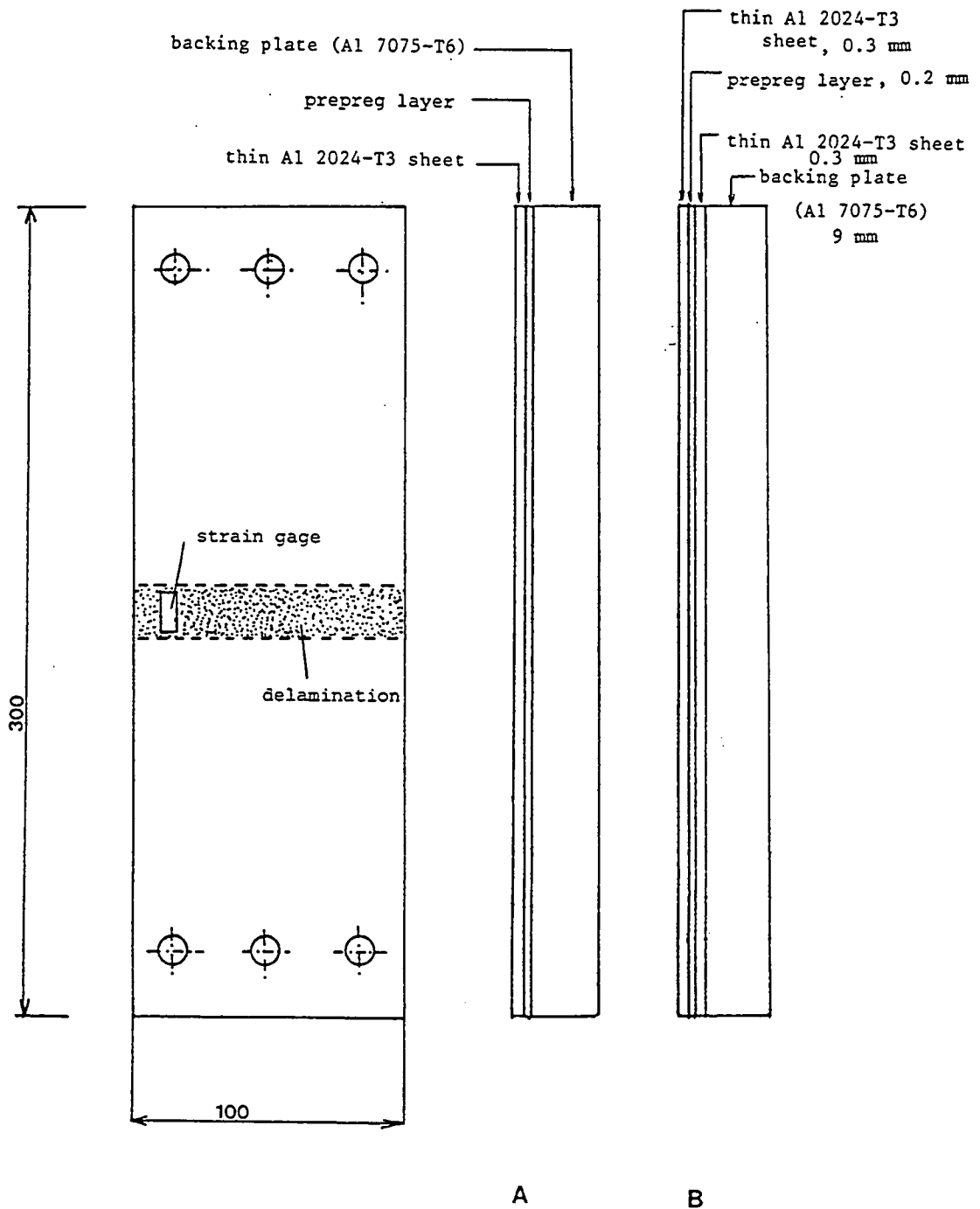
figure 14.2 Large delamination buckling specimen, dimensions in
mm delamination between outer thin sheet and prepreg layer (aramid
fibres)

A: non post-stretched specimen
B: post-stretched   specimen
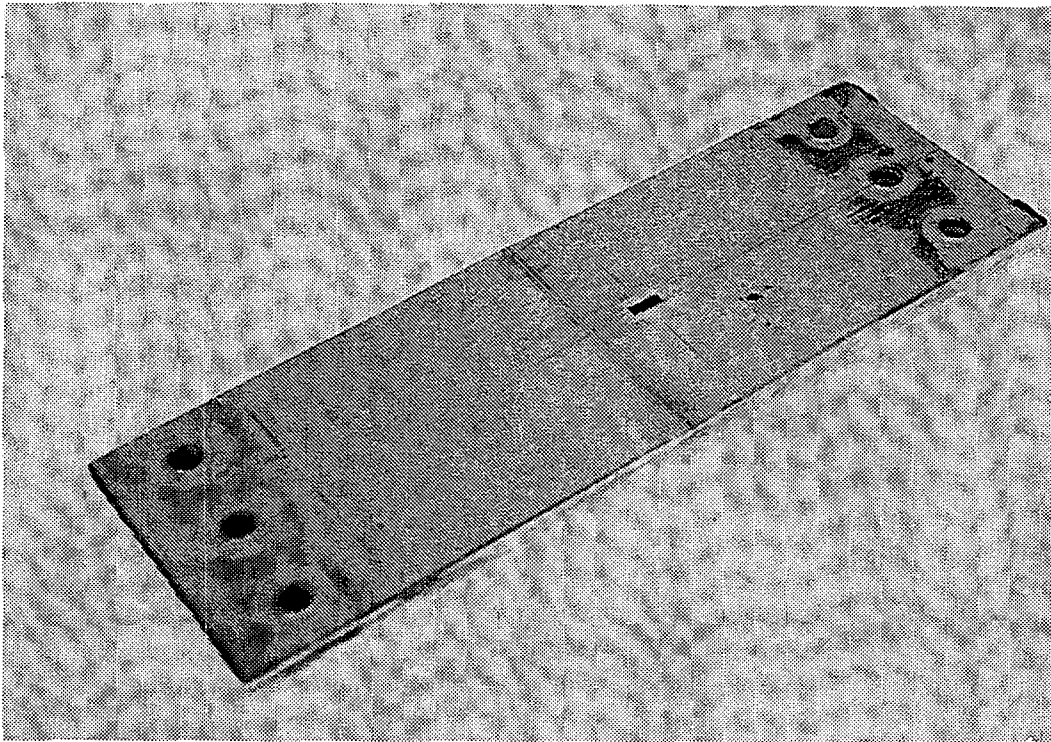
figure 14.3 Large delamination specimen.

25

250

clamped
area

strain
gage

delamina-
tion

thin Al 2024-T3 sheet, 0.3 mm

prepreg (aramid fibres) , 0.2 mm

Al 7075-T6 backing plate, 9 mm
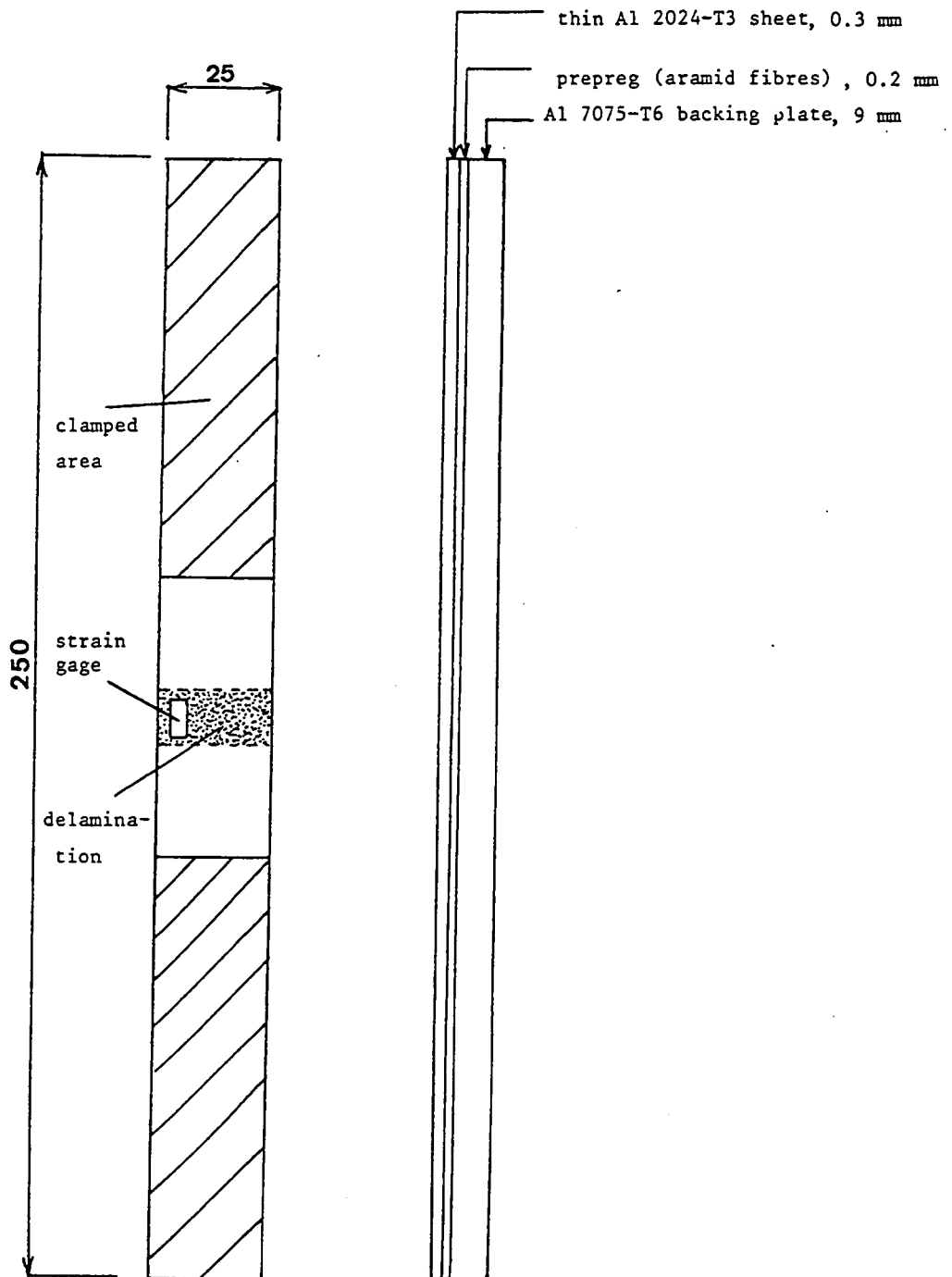
figure   14.4   Small   delamination   specimen,   dimensions   in   mm.
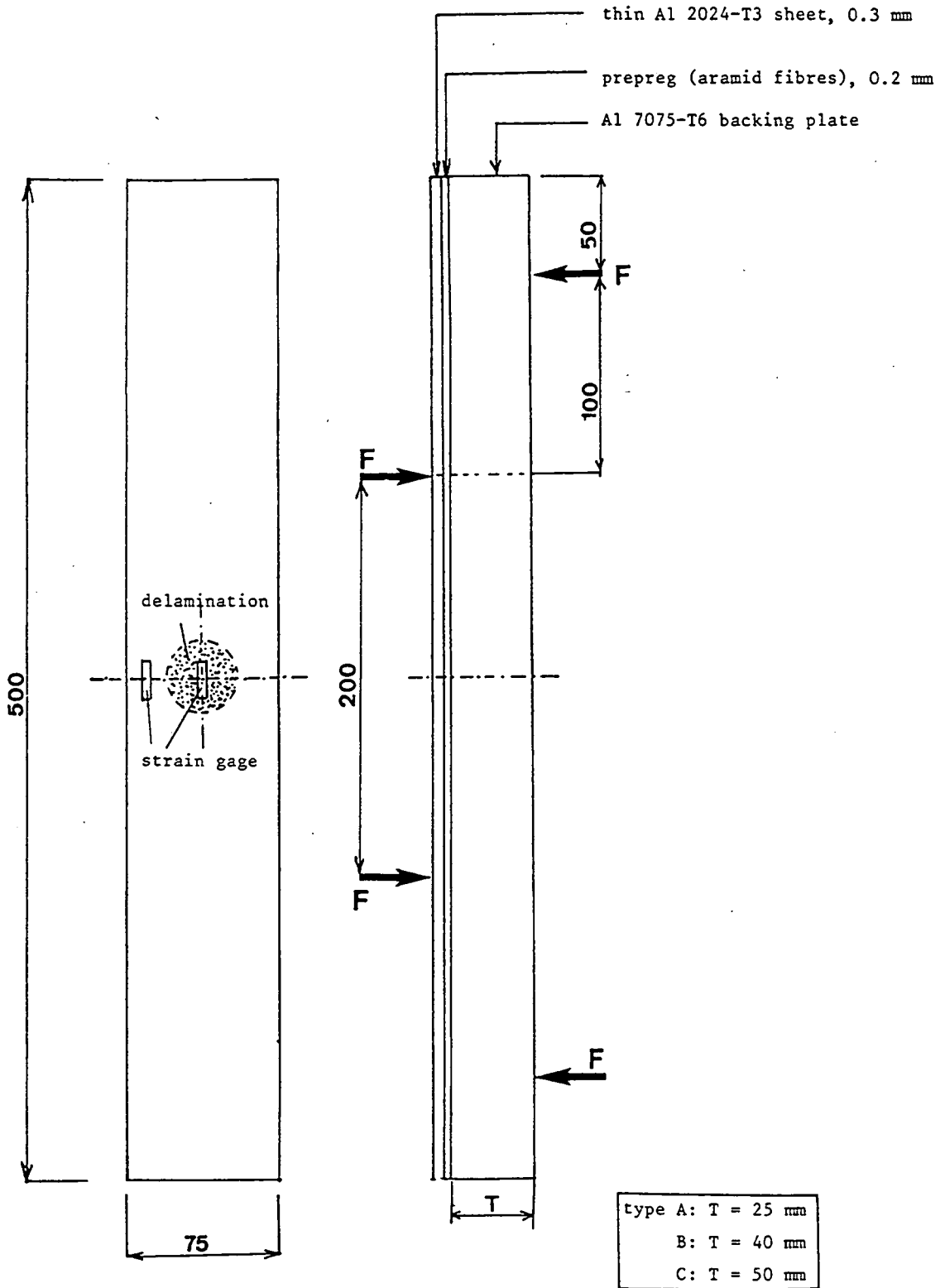
figure 14.5 Four point bending delamination specimen, dimensions in mm.
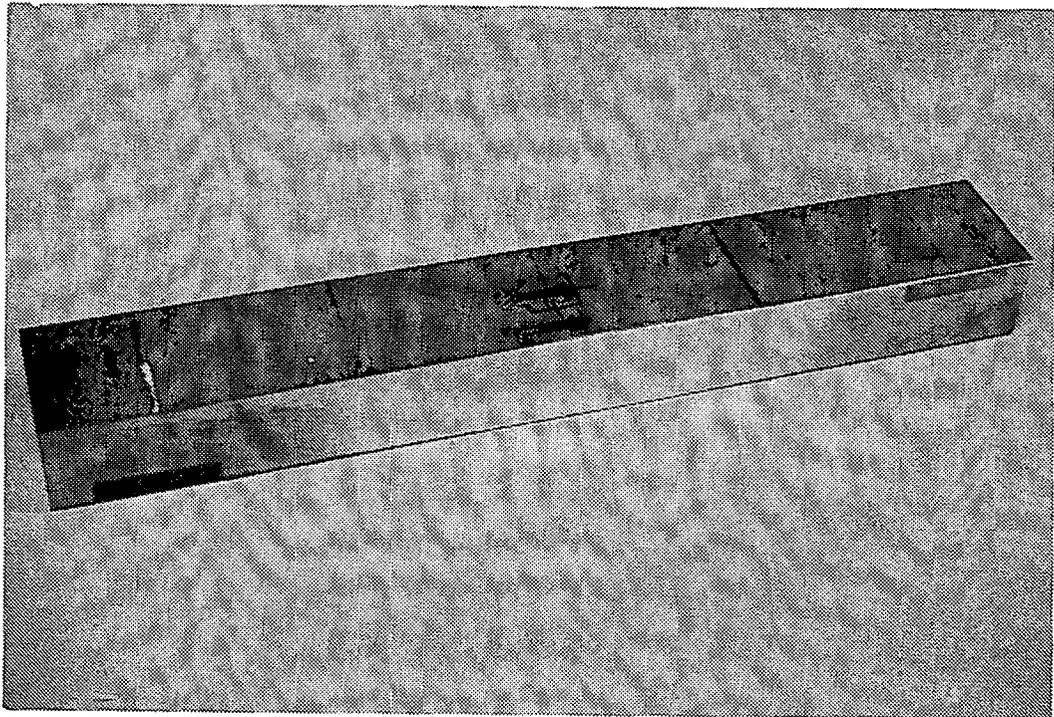
figure 14.6 Four point bending delamination specimen.
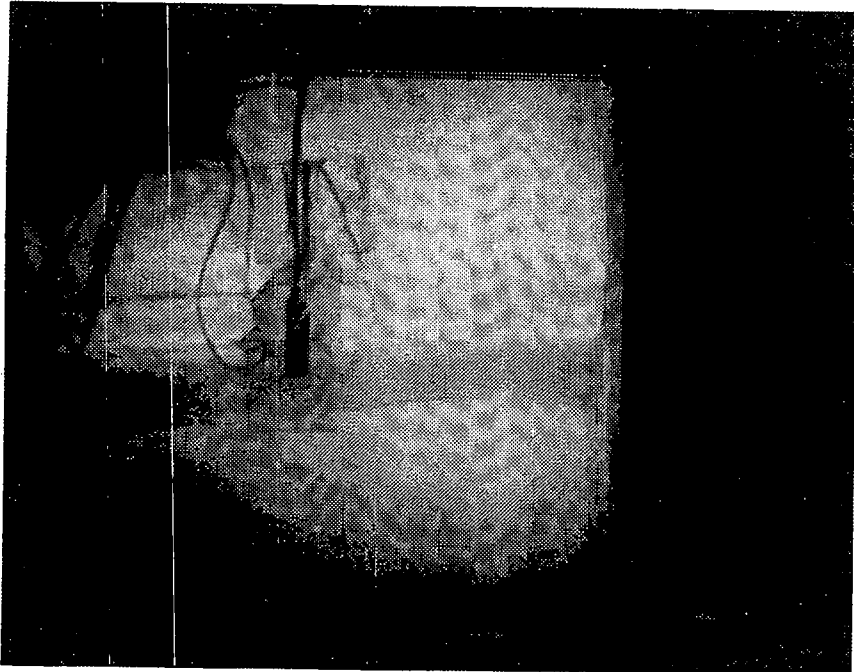
figure 14.7 Buckling of a strip delamination, specimen L1.
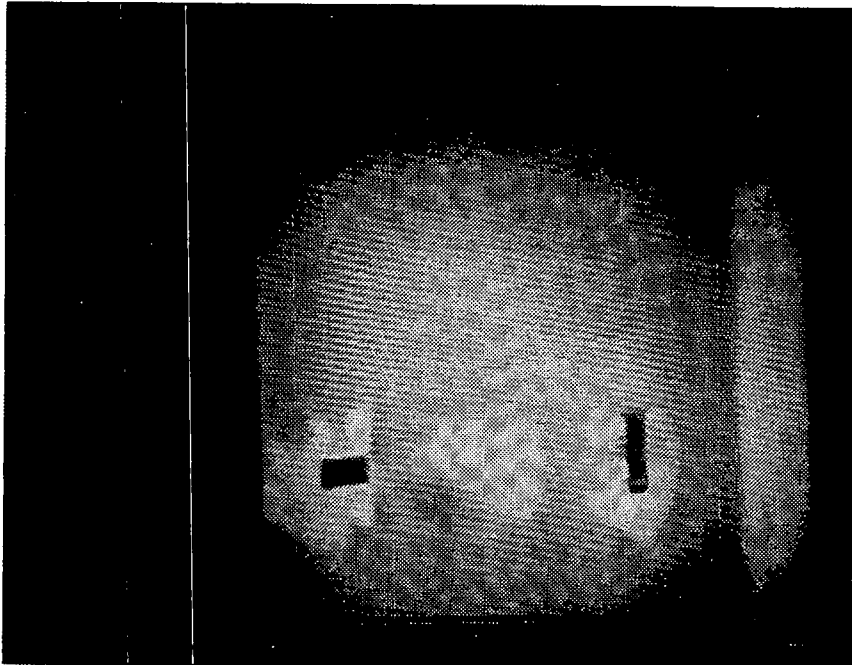
figure 14.8 Buckling of an elliptical delamination, specimen L3.

527
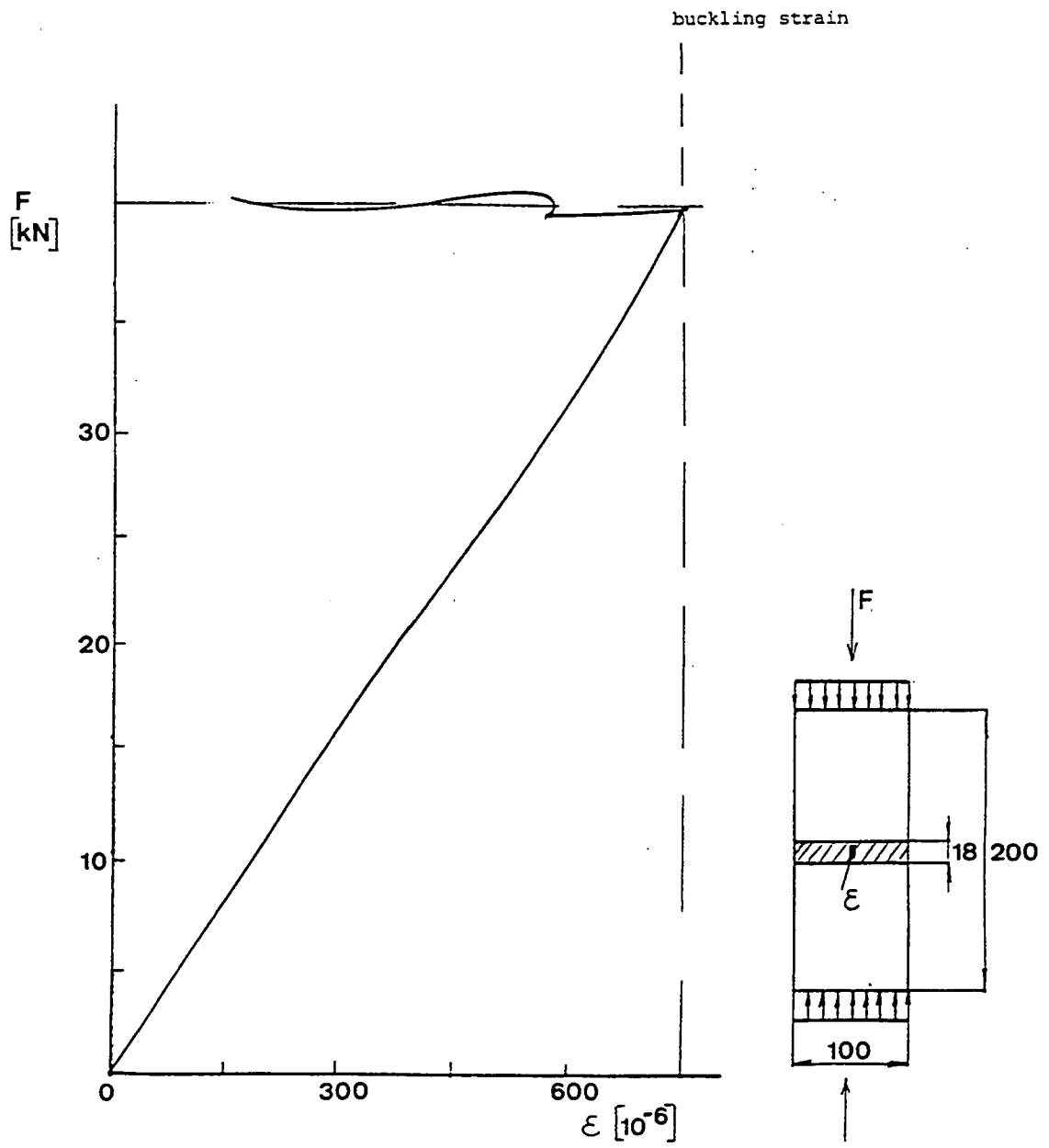
figure 14.9 The measured strain as function of the applied load on large delamination specimen L2.
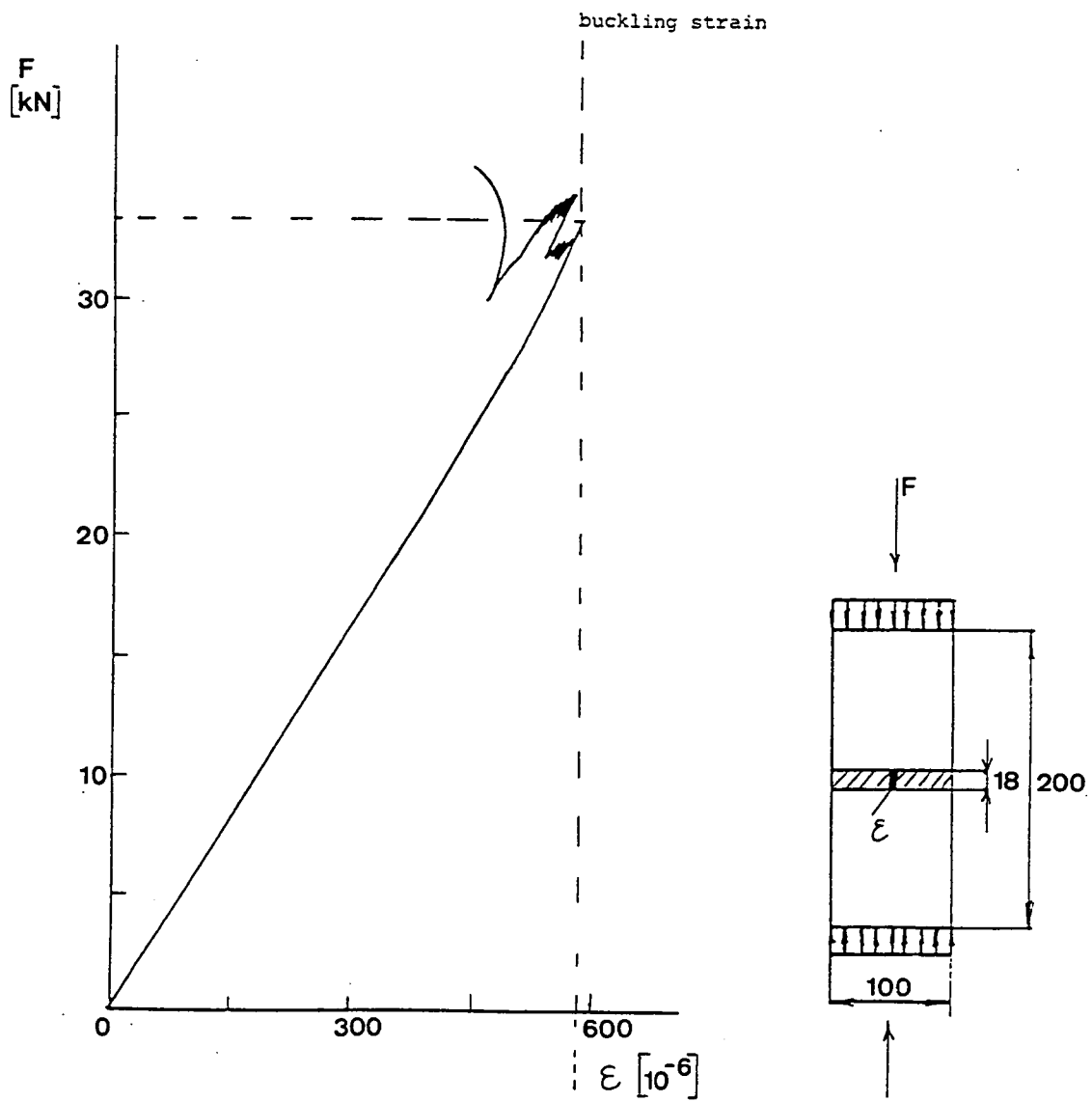
figure 14.10 The measured strain as function of the applied load for large delamination specimen L1.
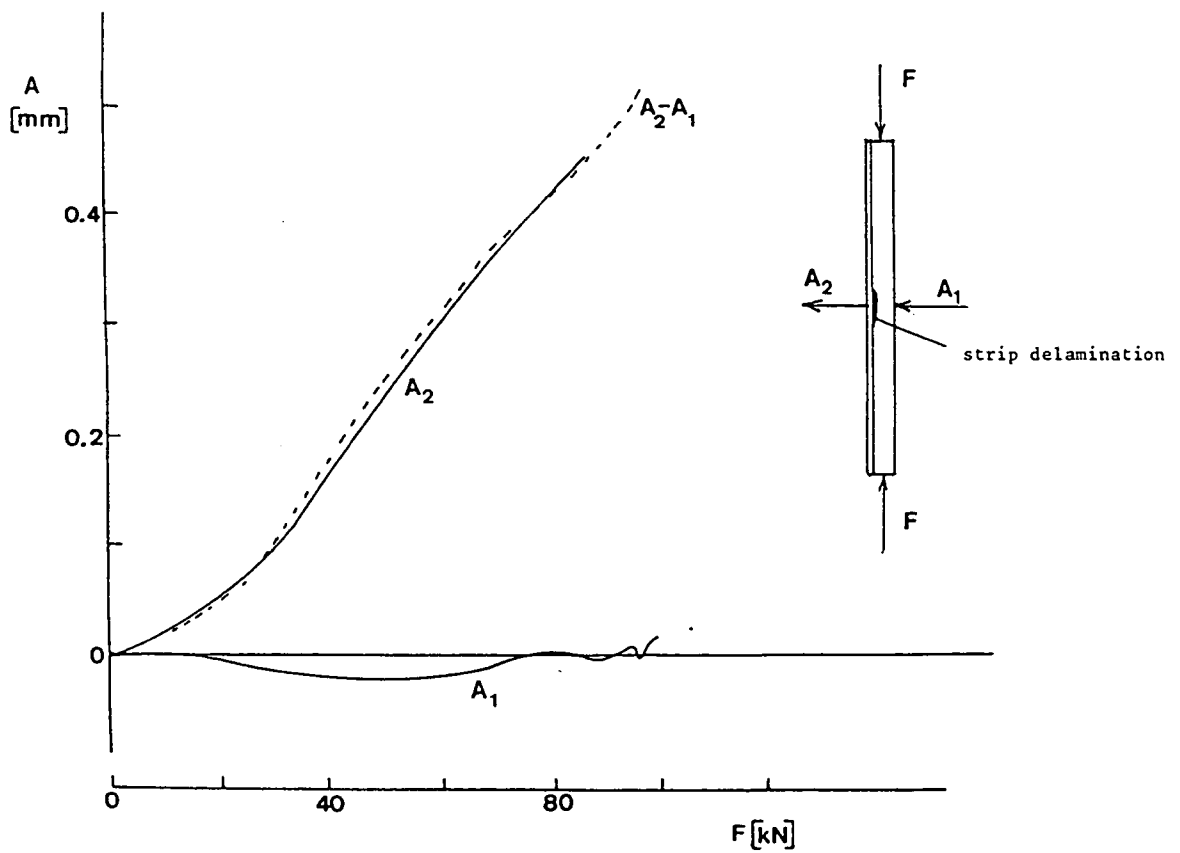
figure 14.11 The lateral displacement of the specimen and the delaminated sheet as function of the applied load for large delamination specimen L1.
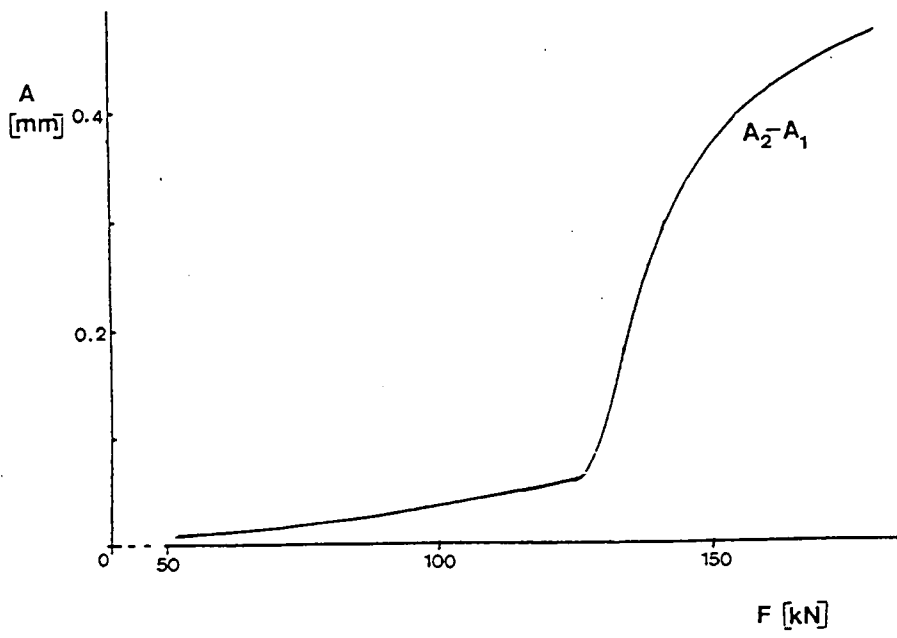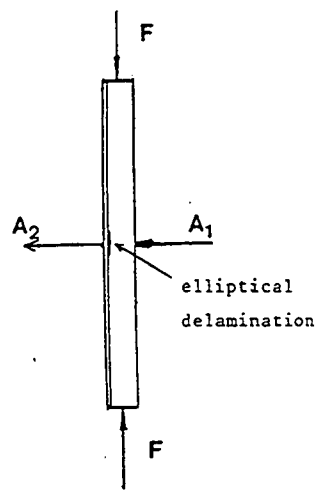
figure 14.12 The lateral displacement of the elliptical delaminated
sheet in large delamination specimen L3 as function of the applied,
external stress.
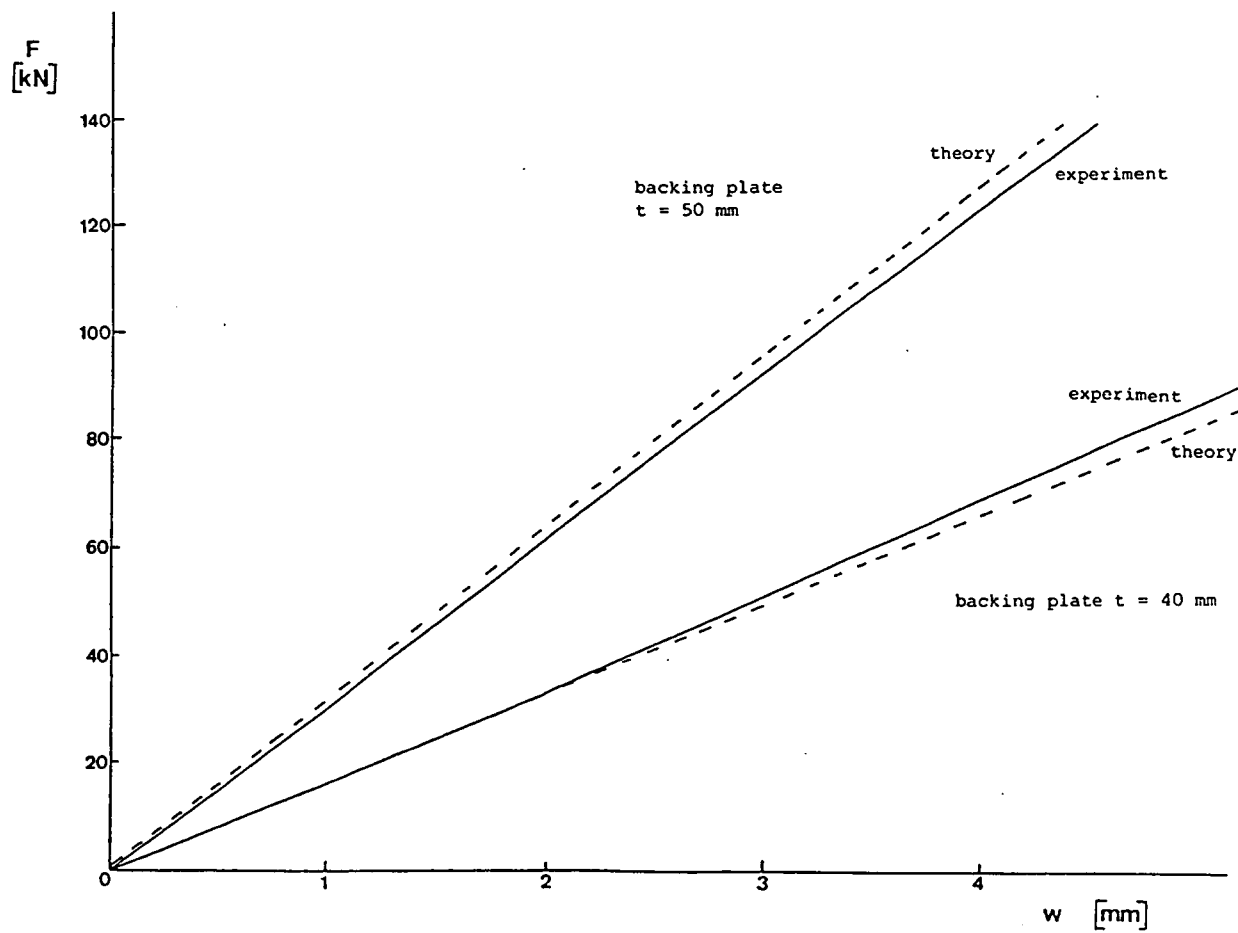
figure 14.13 The deflection as function of the applied load of the
four point bending delamination specimens.
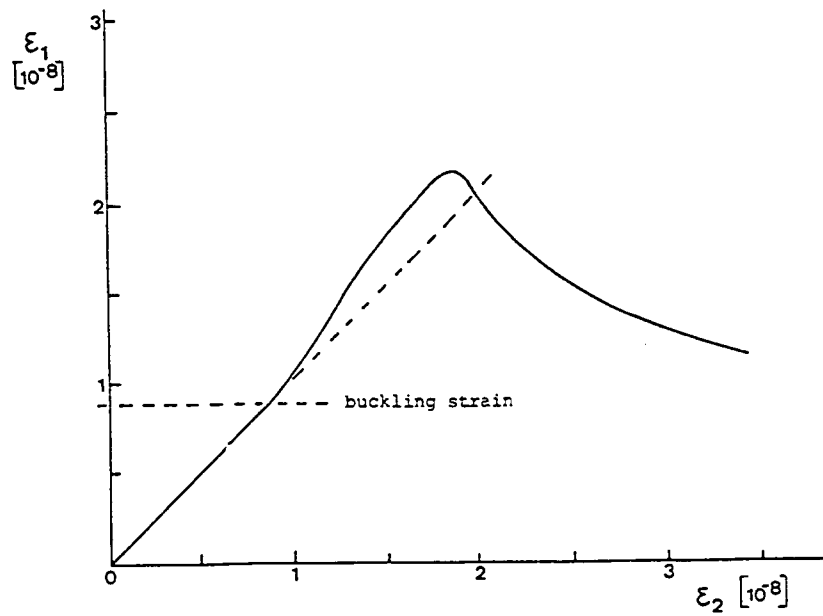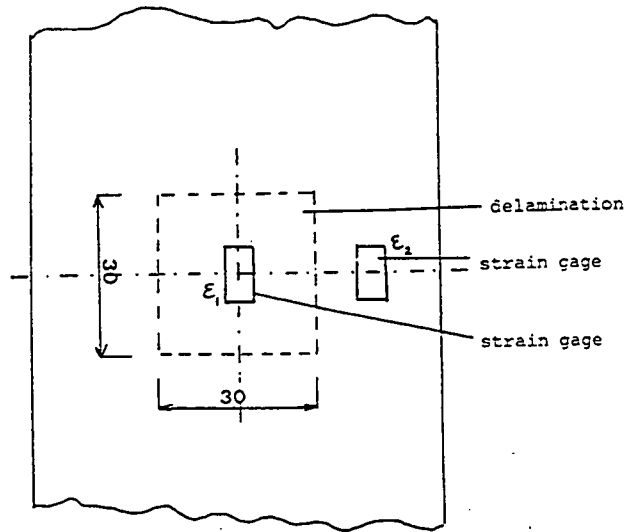
figure 14.14 Strain measurements on four point bending delamination specimen F10.
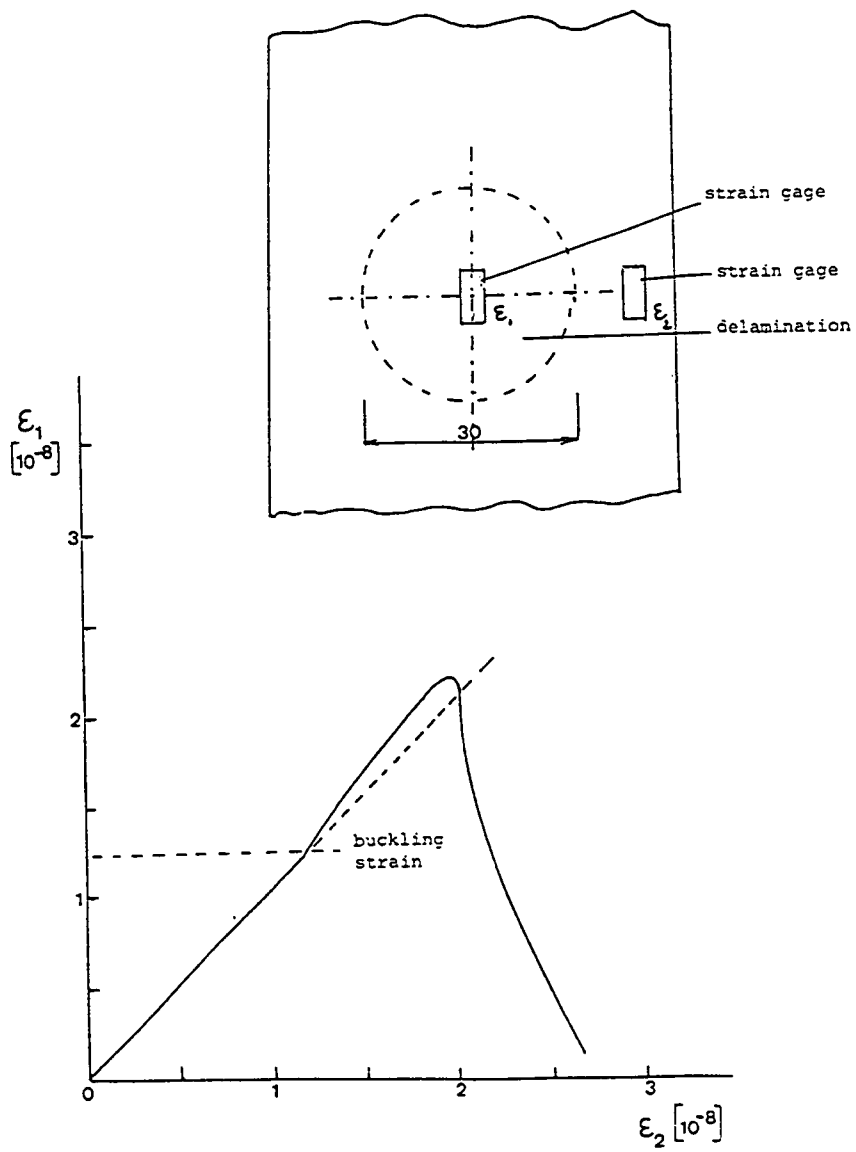
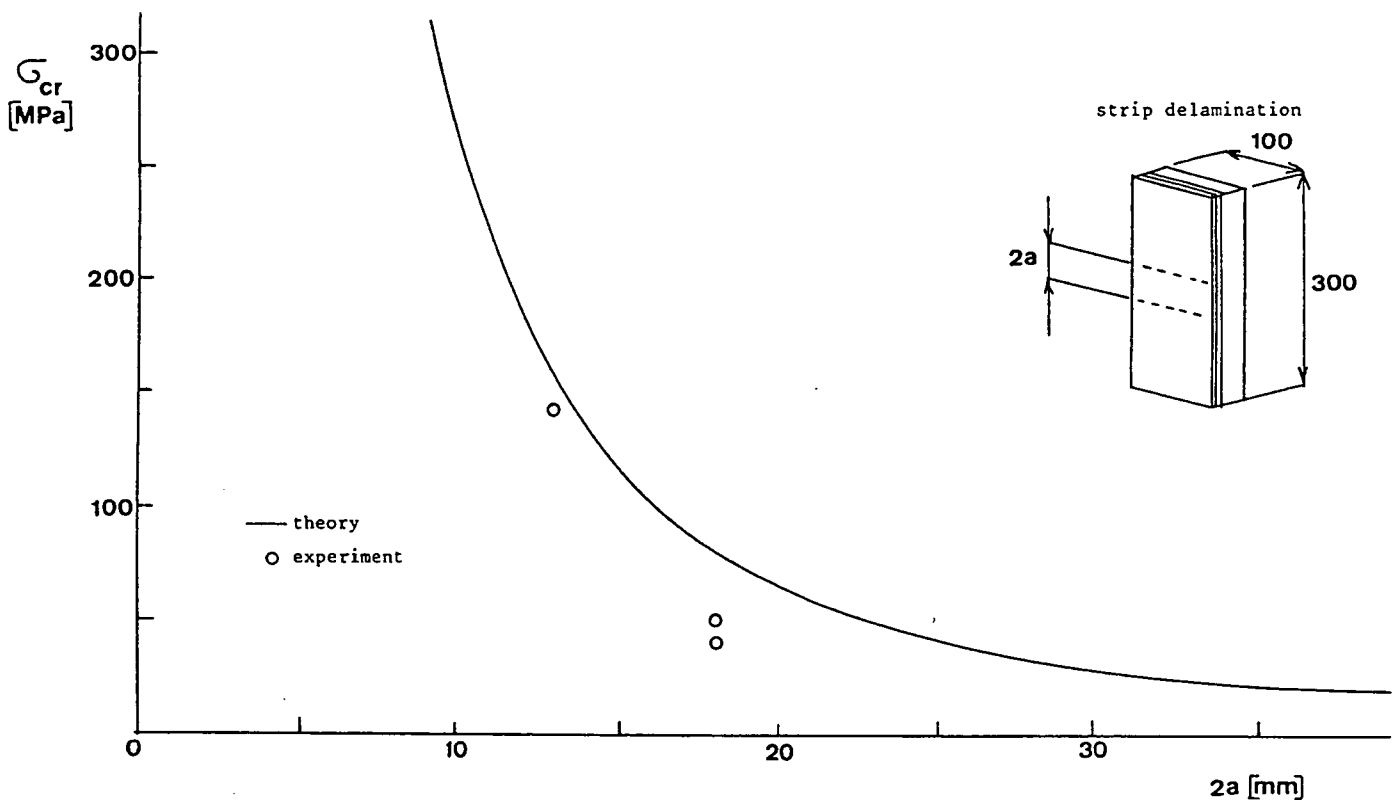figure 14.15 Strain measurements on four point bending delamination specimen F7.

figure 14.16 The buckling stress σ_{cr} as function of the length of an isotropic plate, loaded edges clamped, unloaded edges free (strip delamination).
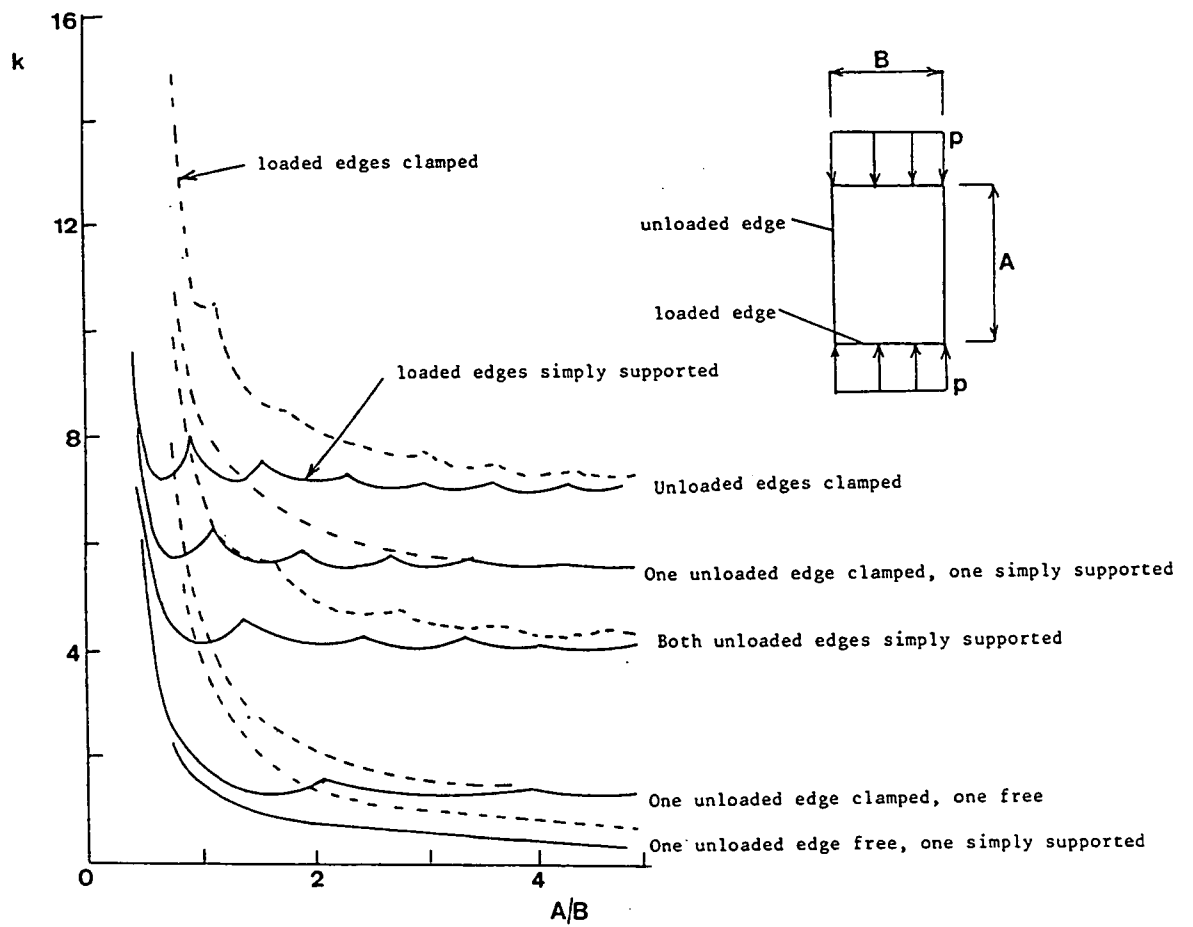
figure 14.17 The buckling coefficient k as function of the geometry
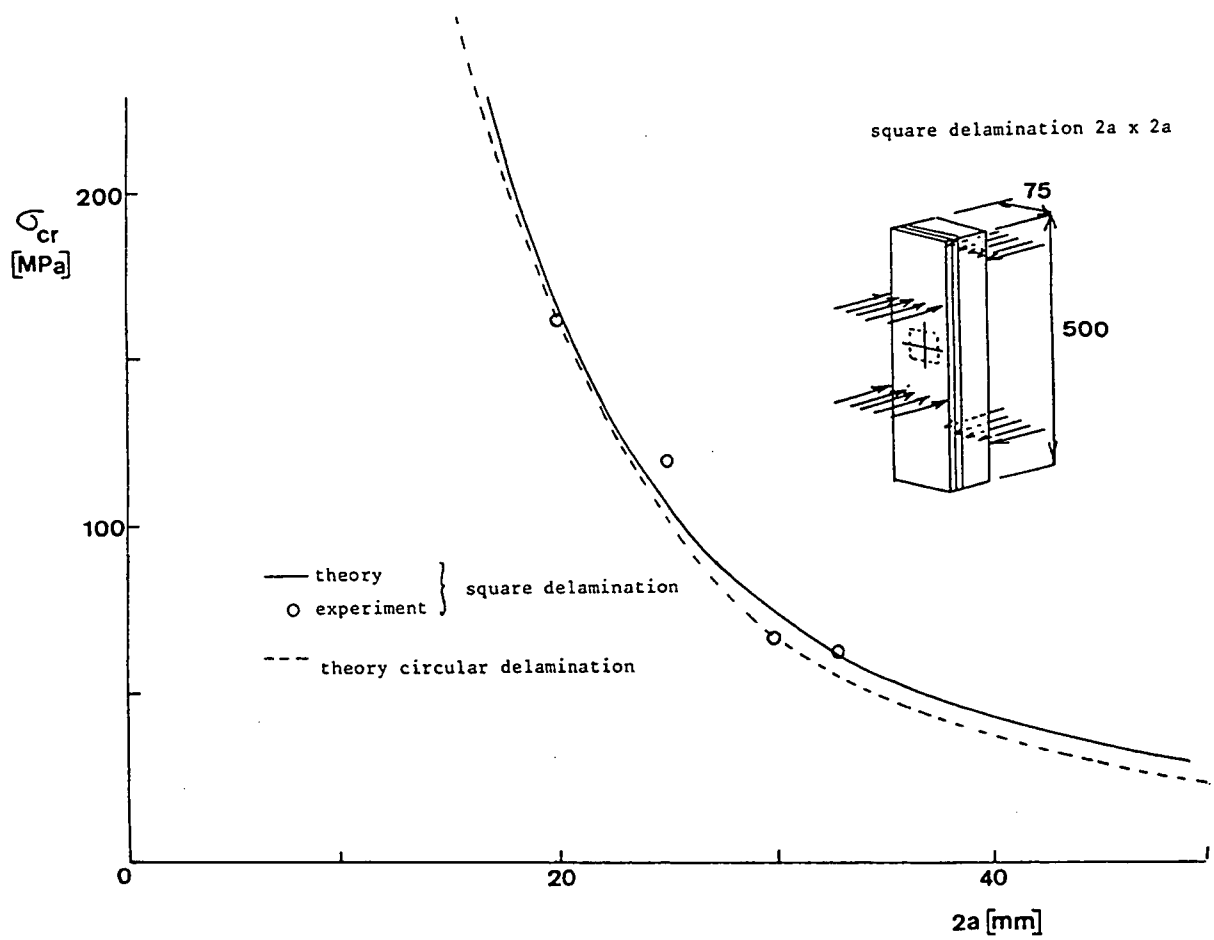parameter A/B, for various edge conditions (from ref. 1).

figure 14.18 The measured buckling stress σ_{cr} for a clamped square plate as function of the length of the sides 2a (delamination width), compared with the calculated critical stress of a clamped square plate.
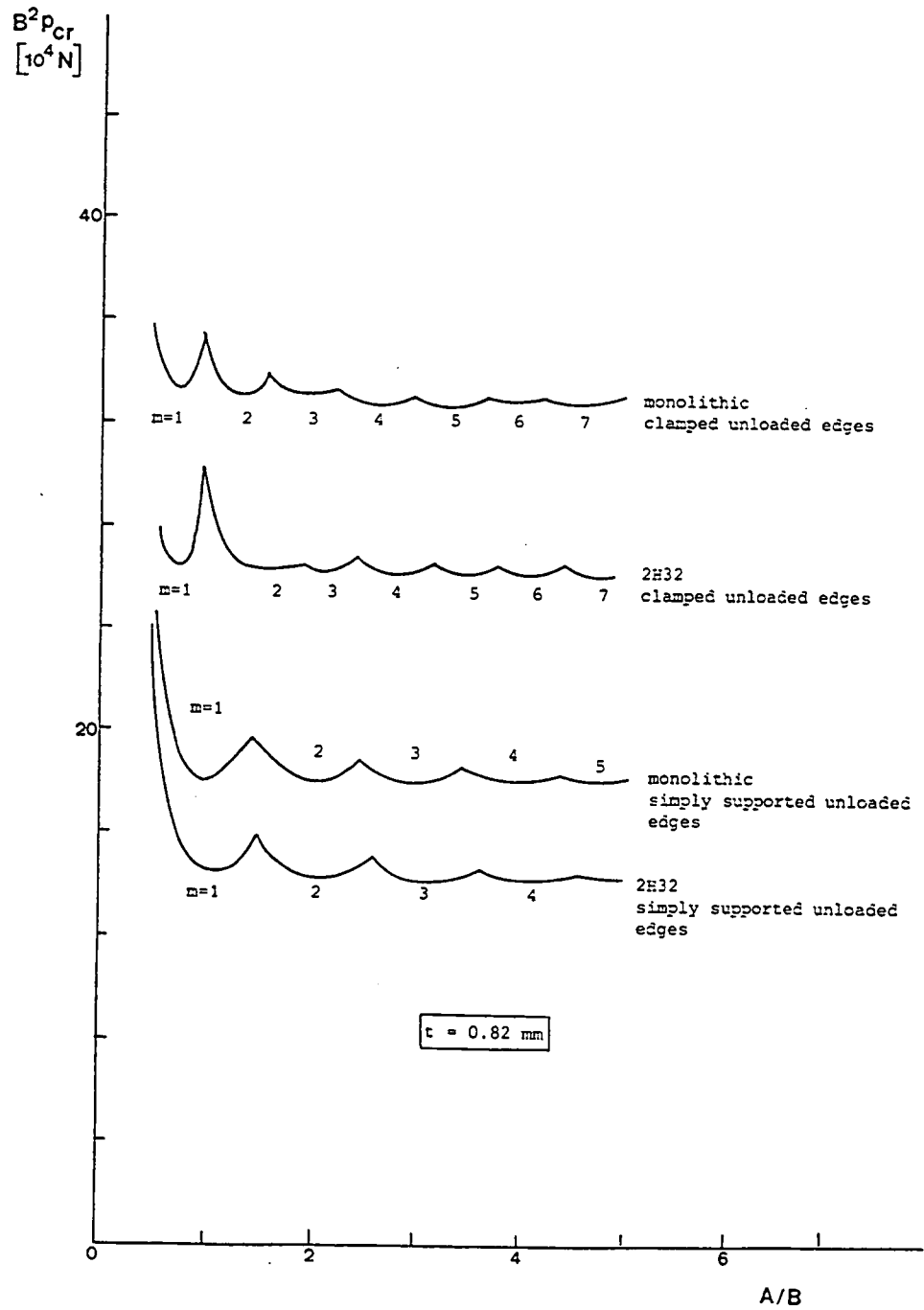
figure 14.19 The calculated critical stress p_{cr} as function of the geometry parameter A/B for ARALL and monolithic plates with various edge conditions.
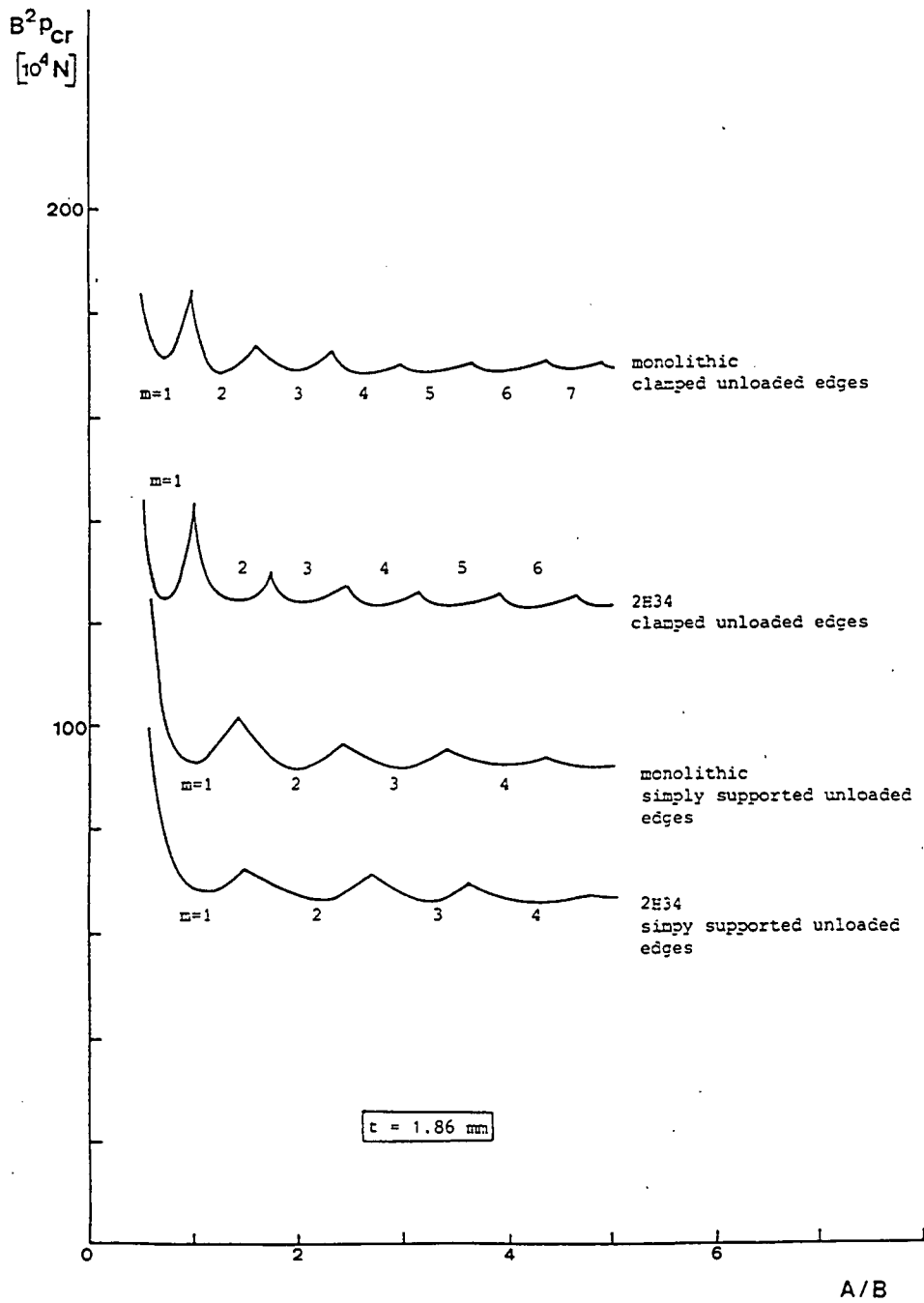
figure 14.20 The calculated critical stress p_{cr} as function of the geometry parameter A/B for ARALL and monolithic plates with various edge conditions.
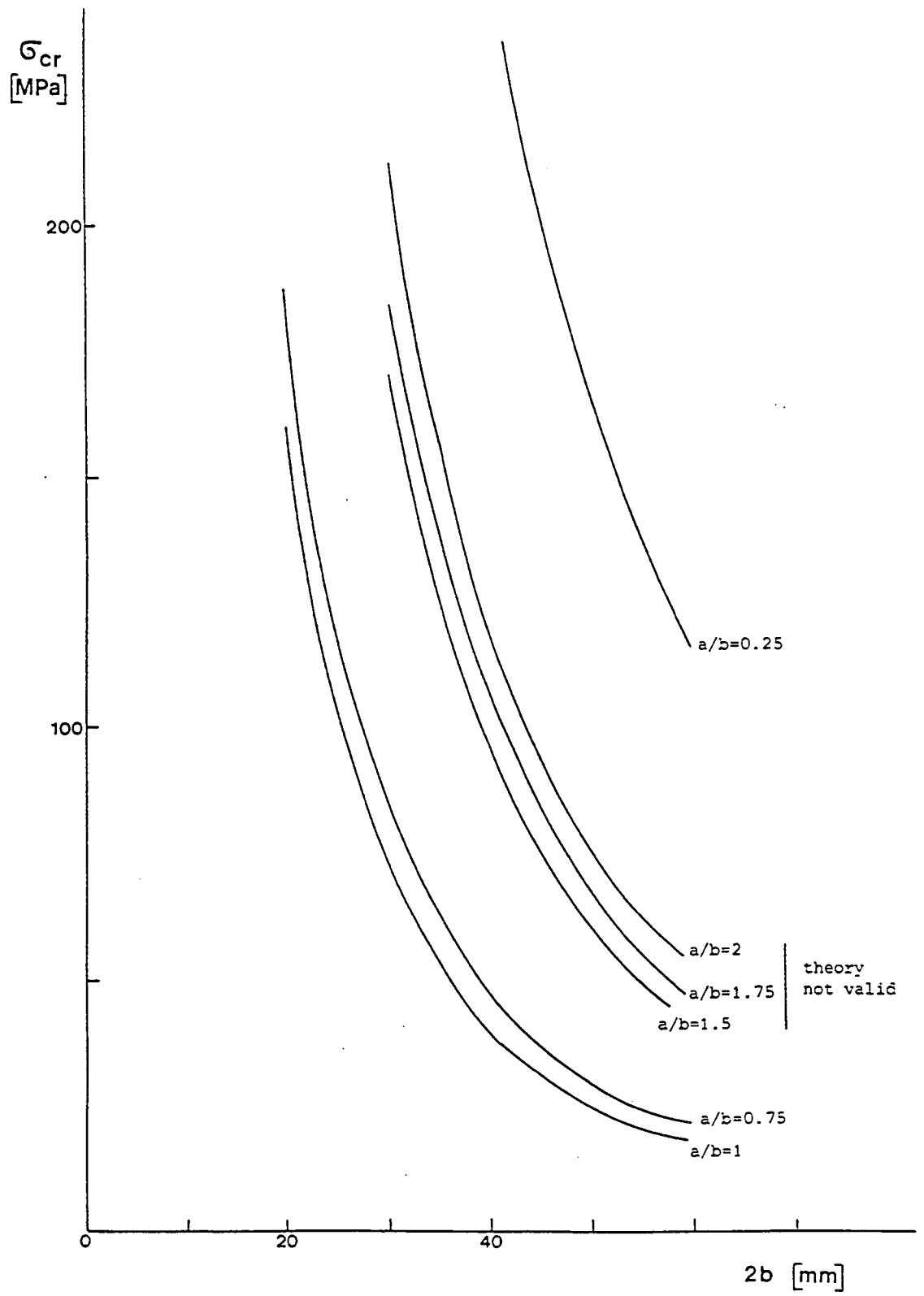
figure 14.21 The calculated critical stress σ_{cr} as function of the geometry parameters 2b and a/b for a clamped isotropic elliptical plate.
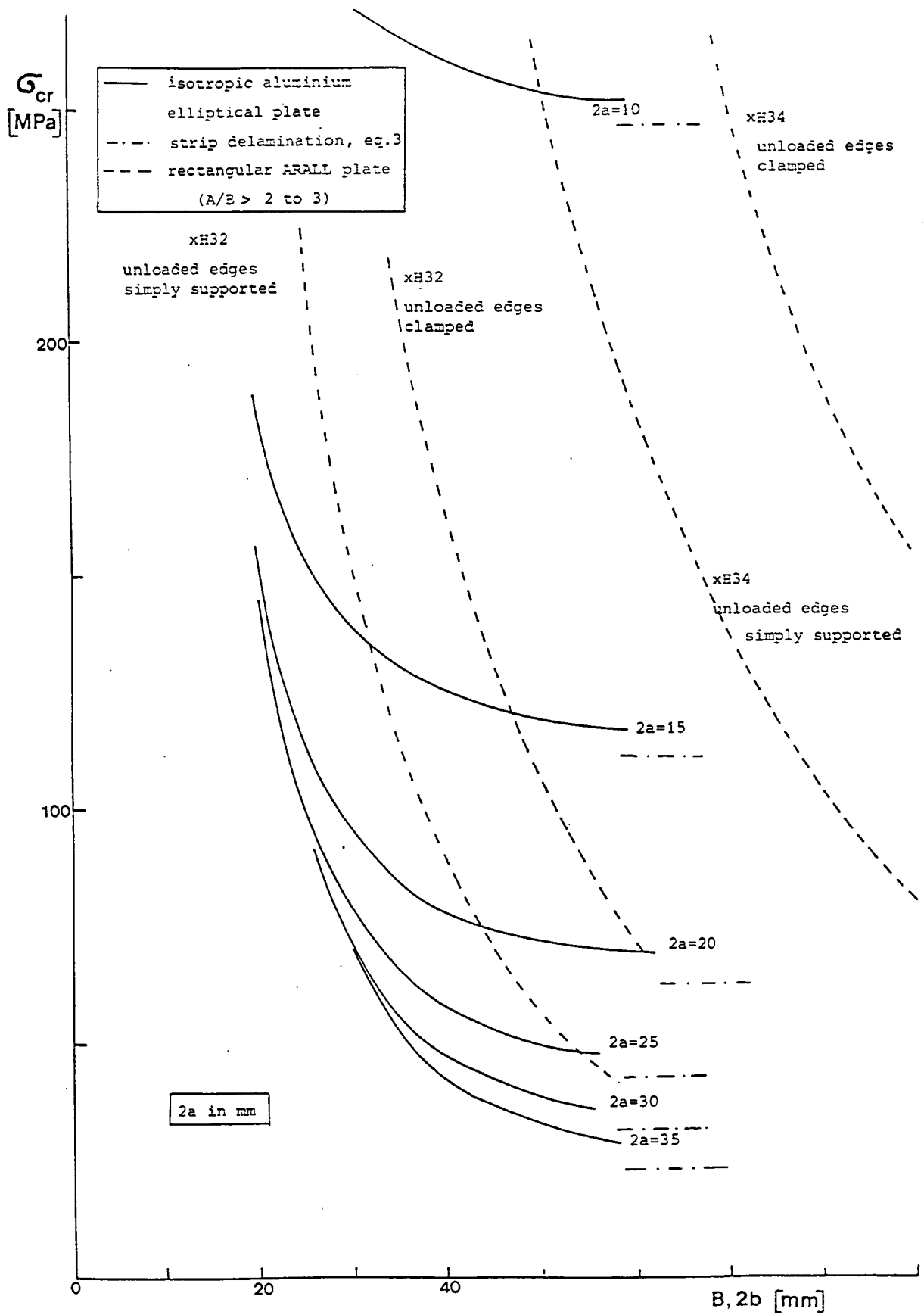
figure 14.22 The calculated critical stress σ_{cr} as function of the geometry parameters B and b of clamped isotropic elliptical laminated sheet and ARALL plates.
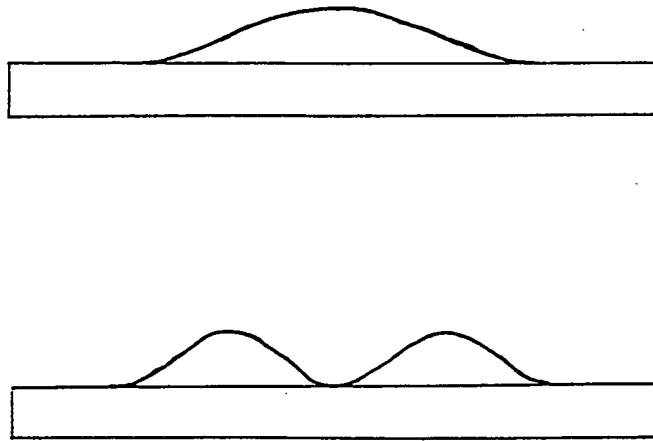
figure 14.23 Buckling modes with one half wave and two half waves in the delaminated sheet.
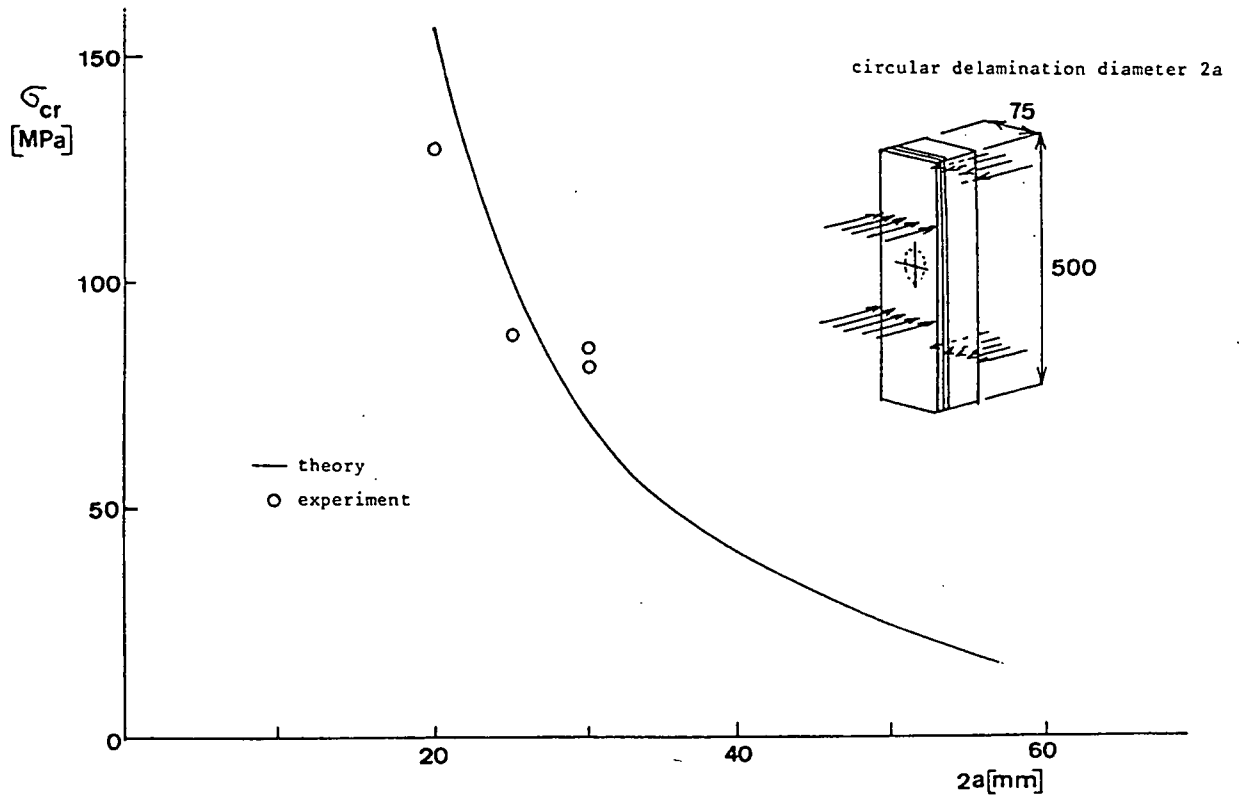

figure 14.24 Comparison of theoretical and experimental results of the buckling stress of circular delaminations.

chapter 15 Conclusions

15.1 Background and aims of this study

Most of the primary structures of modern civil aircraft are still made of conventional monolithic aluminium alloys. Two material types are promising candidates to replace aluminium: composite materials and ARALL laminates.

ARALL is a family of fibre reinforced aluminium laminates (see chapter 1). The variant with R-glass fibres is called 'GLARE', the one with aramid fibres is called 'aramid ARALL', and the variety reinforced by carbon fibres is called 'carbon ARALL' in this report.

The primary aim of the study was a comparison of the impact behaviour of aluminium alloys, composites and ARALL.

Because impact loading is a relatively new topic of materials science, a second aim of this study was to provide more understanding of the impact process by testing and analysis.

15.2 Impact and damage tolerance (chapter 2)

1. The importance of impact in the damage tolerance philosophy of composite materials and ARALL was discussed in chapter 2. Impact damage is the most important source of damage with respect to design and certification of composite and ARALL structures. The impact related material properties (damage resistance, damage tolerance, inspectability and repairability) pose a limitation to the widespread application of composite materials.

2. Generally impact is treated during certification of composite structures in the following way:
a. Coupon and panel tests are performed to determine the effect of the environment (primarily moisture) on the strength, and to determine 'safe' strain levels when impact damage is present in the material. This data is used to determine a design strain level.
b. A full scale static test is performed. The structure with 'barely' detectable impact damage has to be able to carry ultimate load (usually visual inspection is carried out at the impacted side of the structure, while the largest damage occurs at the non impacted side). Moreover the

structure has to be able to carry limit load at the expected maximum impact level. Environmental effects (moisture) also must be taken into account. This is accounted for by so called 'knock down factors' which are determined by the coupon tests.

It has to be realized that the 'barely' visible impact damage level, as well as the expected maximum impact damage, depends on the nose radius and the velocity regime of the impactor, as well as the position of the impact loading on the structure.

c. Full scale fatigue tests are carried out, with impact damage present in the structure. Generally it is demonstrated that the damage will not grow under realistic loading. Experimental scatter can be accounted for by a factor on the life and/or an enhancement factor on the load. An enhancement factor on the fatigue load is also applied to account for environmental effects.

3. The literature data available on ARALL indicate that impact will play an important role in the design and certification of aircraft structures of this material. The fatigue resistance and the resistance of this material to environmental degradation (corrosion and moisture absorption) are extremely good. The residual strength in the presence of a through crack caused by impact is the major design criterion.

15.3 Impact and aircraft structures (chapter 3)

The impact process and the sources of impact damage to aircraft structures were described (chapter 3). The physical phenomena which are observed during impact is very much dependent on the impact regime. A study of 688 repair reports of Boeing 747 fuselages showed that 13% of the repairs were due to impact damage. Also literature data on damage found for the Lufthansa fleet (tailplanes) showed that impact damage is a frequent event. The main cause of impact damage is low velocity impact damage due to maintenance and service cars. Damage resistance and inspectability are important for an economic use of aircraft structures.

15.4 Instrumented impact testing (chapter 5)

For the present study an instrumented drop weight impact tester was

designed and built (chapter 5). Signals, which can be measured during impact as a function of time, are coming from:

- a load cell in the impactor
- load cells under the clamping of the specimen
- a displacement transducer
- a strain gage mounted on the specimen

From these signals the force-time, the velocity-time, the displacement-time, the energy-time and the force-displacement curves are derived by numerical integration or differentiation.

Several problems associated with the instrumentation were analyzed:

- The elastic compliance of the impact system may have an effect on the measured data. It was shown that this effect is small.
- Dynamic calibration of the load cell is used in the literature, but was shown to be unnecessary.
- Various sources may cause vibration in the measured force signal.

Of these sources especially the vibrations of the impactor are unwanted. The vibrations were analyzed. The resonant frequency of the impactor was high enough (13.0 kHz) that it caused only little disturbance of the measured data. The data processing program has the option to filter out the vibrations of the data, but in general this is not necessary.

15.5 Results of damage resistance tests (chapters 4, and 7 to 8)

A literature survey on the results of impact tests on different materials showed that no standardized test method is used and that many test parameters are presented to rank materials (chapter 4). For the test series in the present study the energy needed for first failure, the damaged area and the permanent deflection of the specimen are used to describe the damage resistance. The residual strength and fatigue behaviour are a measure for damage tolerance.

Impact and static tests were done on specimens with a square, clamped test area (chapter 6, to compare the measured force-time, velocity-time and displacement-time curves with an impact model) and on specimens with a

clamped, circular tests area (chapter 7, ASTM standard).

15.5.1 Square test area: comparison of aramid ARALL/ monolithic Al alloys/ thermoplastic composites (chapter 6)

1. The impact test results on both square and circular specimens showed that aramid ARALL has low values of energy at first failure. The values are comparable with those of thermoplastic composites (aramid, glass and carbon in a Polyetherimide matrix). The energy at first failure is relatively low compared with monolithic aluminium. The fibre in aramid ARALL is critical; at fibre failure the aluminium layer on the convex (non impacted) side of the laminate also fails. At energies just higher than the first failure energy a part through crack is present, at higher energies also a crack in the layers at the concave (loaded) side is created.

2. The damage width of aramid ARALL is significantly smaller than for thermoplastic composites. At relatively low energies (in the order of 1 J, below the level of fibre failure) matrix cracking occurs: small cracks are visible as faded spots in the prepreg layer after removal of the outer aluminium layers by chemical milling. No significant delamination occurred, in contrast with the behaviour of the thermoplastic composites.
The permanent dent in aramid ARALL is significantly deeper than in the thermoplastic composites, which is favourable for visual inspection. Until fibre failure the dent depth of aramid ARALL is comparable with monolithic aluminium, after failure the dent in aramid ARALL is deeper.

15.5.2 Circular test area: static tests (chapter 7)

1. The energy at first failure is higher for GLARE material than for the corresponding cross-ply composite with the same glass fibre and epoxy matrix.

2. The energy at ultimate load is higher for the R-glass cross-ply composites than for ARALL laminates.

3. With GLARE material first failure energies can be obtained, which are

comparable to those of monolithic aluminium alloys. In general the cross-ply ARALL laminates have a higher energy at first fracture than the unidirectional variants. This also true for aramid ARALL.

4. The GLARE materials shows two possible failure modes: aluminium critical and fibre critical failures. For the unidirectional laminates a aluminium critical failure occurs: the crack runs in the fibre direction. For cross-ply variants a fibre critical failure may occur: the crack runs perpendicular to the fibre direction of the outer fibre layer. Aramid and carbon ARALL variants always have a fibre critical behaviour.

5. Al 7075-T6 has a significant lower energy at first failure than Al 2024-T3. The same is true for the corresponding ARALL types if the failure mode is aluminium critical (GLARE, not for aramid ARALL and carbon ARALL).

15.5.3 Circular test area: impact tests (chapter 7)

1. The failure modes of the various materials and the ranking of the materials in the impact tests is the same as for similar static tests.

2. The energy restitution coefficient of ARALL until first failure is equal to or slightly higher than for monolithic aluminium. The coefficient is relatively constant ($\approx$ 0.5) as function of the impact energy. Until first failure the energy restitution coefficient of the composites is high (> 0.9), because there is no plastic deformation involved.

3. For the same impact energy ARALL shows a larger central deflection than the monolithic aluminium alloys. Also the permanent deflection is somewhat higher. For both materials the maximum central deflection during impact is generally in the order of 2x the permanent dent height. Al 7075-T6 material has a smaller permanent deflection than Al 2024-T3 material, but has a significantly lower first failure energy.

4. Cross-ply ARALL variants and ARALL material with a weave have a (somewhat) higher energy at first failure, and afterwards a smaller crack length in the aluminium layers at higher impact energies.

547

5. The damage zone of the prepreg of GLARE is smaller than of aramid ARALL and thermoplastic composites.

6. Poststretching of ARALL material, which is favourable for fatigue, lowers the energy absorption capability. Poststretching of thermoplastic ARALL changed the failure mode from aluminium critical to a fibre critical behaviour.

7. Stiffened panels have a significantly higher energy at first failure than coupon specimens. The deflection of the panel during impact is larger; the energy is spread over a larger area.

15.5.4 Static vs. dynamic loading (chapters 6 and 7)

1. The dynamic force-deflection curve corresponds very well with the static force-deflection curve (chapters 6 and 11). Also the (maximum) deflection - (impact) energy curves were equal for the static and the dynamic cases.

2. Aramid ARALL tends to fail at slightly lower energies under impact loading than under static loading (chapters 6 and 7). The same is true for unidirectional GLARE (aluminium critical). Cross-ply GLARE fails dynamically at a significantly higher impact energy. This is caused by the strong strain rate dependent behaviour of the R-glass fibre (chapter 11).

15.5.5 Impact tests: experimental observations (chapters 6 and 7)

1. The first phase during impact showed a characteristic inertia effect. During initial contact (the first 0.2 ms) between impactor and plate the force remains relatively low, and contact may even be lost (F = 0). This phase can also be found in the strain-time curve. The plate is pushed away by the impactor.

2. Measured strain-time curves reveal higher order vibrations of the specimen during impact. Vibrations with the same frequency are also present in the force-time curve.

15.5.6 Impact on specimens under load (chapter 8)

1. A tensile load on a specimen during impact causes a higher effective stiffness of the specimen and consequently a smaller contact time, a higher maximum contact force and a smaller maximum deflection during elastic impact, but the effects are relatively small. Linear elastic impact can accurately be described by a model which is derived in this report (chapter 12). An extra stiffness term must be added to the stiffness of the material.

2. A tensile load in fibre direction causes a different shape of the crack after impact (chapter 8). The crack no longer tends to turn from the direction perpendicular to the fibre to fibre direction, but keeps its direction perpendicular to the fibre. Consequently the stress intensity is not relieved.

3. A tensile load during impact has a significant effect on the crack length and the residual strength of ARALL after impact if the tensile load corresponds to a relatively high stress level (S > 150 MPa).

15.6 Impact modelling (chapters 9 to 12)

1. The following phenomena play an important role in impact models:
a. The contact between impactor and plate and the Hertzian indentation of the plate. Usually this contact is described by a Hertzian contact law, modified for composite (anisotropic) materials by Sun et al. The relation between contact force and indentation is non linear.
b. Transverse shear of the plate. Generally a Reissner-Mindlin theory is applied, using a shear correction factor k. This shear correction factor accounts for the non-uniformity of the shear strain distribution over the thickness. Generally a k value of 0.822 is applied. The k value is dependent on the Poisson ratio of the material.
c. Non-linear elastic deformation at high deflections of the plate. At large deflections not only bending but also stretching of the plate will occur, making the deformation non-linear. The impact models found in the literature are generally linear, but at deflections at realistic impact energies the non-linearity has to be considered.

This behaviour can be described by the von Kármán equations. Also simplified von Kármán equations are used in the literature, neglecting the contribution of the in-plane displacements to the strain.

d. Inertia of the plate. The inertia of the plate consists of two parts: rotatory inertia and translational inertia, Generally the rotatory inertia is neglected.

e. Strain rate effects and damping. Generally these effects are not taken into account in the models.

f. Stress wave propagation. These effects are only important when the contact time is small relative to the time required by the bending waves to reach the edges of the plate.

g. Plasticity is only described by models for high velocity, ballistic impact.

h. A fracture criterion is a very important part of the model which describes the onset and the propagation of damage. Because of the many failure modes of composite materials a fracture criterion is complex and several material properties are involved.

2. The deflection field of the material under static loading was measured (chapter 10). The normalized deflection field ξ (= w/w_0) as a function of η (= r/a) is approximately independent of the deflection for large deflections and similar for monolithic aluminium and ARALL.

3. The influence of the anisotropy of ARALL on the shape of the dent during loading is small. Although this shape is clearly not axisymmetrical after unloading.

4. An empirical function for the shape of the dent was found. This shape was used to calculate the radial and tangential strains of the plate under loading. The strains calculated with the simplified von Kármán equations agreed with measured strains with a reasonable accuracy.

5. Very low velocity elastic impact of an impactor with a relatively large mass relative to the mass of the plate can be analytically described by a simple mass-spring model. An initial tensile load on the plate means an increase of the stiffness in the model.

6. A non linear elastic impact model (NOLEIM) was derived based on the simplified von Kárman equations. The linear part of this model correspond very well with literature models. NOLEIM was able to calculate force-time, velocity-time and displacement-time functions, which correspond well with experimental and finite element calculations. When a fracture criterion is added to the model in the future, it can also be used to predict damaged zones.

7. The empirical shape of the dent of ARALL and monolithic aluminium was used for a static elasto plastic impact model (EPIM). The results of this model agrees very well with an elastic impact model which incorporates the in-plane displacements by using the non modified von Kárman equations (Shivakumar et al.). The results of EPIM (deflection-energy curves) correspond with experimental results.

15.7 Damage tolerance: residual tensile strength and fatigue tests (chapter 13)

1. A saw cut is a realistic simulation for impact damage with a through crack. The plastically deformed dent does not have an effect on the tensile strength.

2. Fatigue crack growth after impact damage only occurs on the impacted, concave side, while a crack due to impact damage at low energies first will be created at the non-impacted, convex side of the dent.
Fatigue crack growth at the non-impacted, convex side of the dent does not occur because of the bending in the dent, which causes compression at the convex side and tension at the concave side of the dent.
The crack growth rate of the crack at the convex side of the dent is 1.5 to 2 times the crack growth rate of non impacted material.

3. The residual strength after impact damage of GLARE is significantly higher than for aramid ARALL.

15.8 Damage tolerance: delamination buckling (chapter 14)

1. The critical (buckling) stress of an elliptical delamination is

accurately described by a Raleigh-Ritz analysis. In general, the critical stress will be relatively high. The critical stress is influenced by the internal stress system of ARALL.

2. No delamination growth of aramid ARALL was found due to delamination buckling under static or fatigue loading.

Samenvatting

Een vliegtuig ondervindt tijdens zijn leven regelmatig stootbelastingen ('impacts'). Deze impact-belastingen kunnen worden veroorzaakt door vallend gereedschap, opspattende stenen van de startbaan, botsingen met karretjes tijdens het beladen op het vliegveld, hagelstenen, vogelaanvaringen, etc.

De weerstand van een materiaal tegen schade ten gevolge van stootbelastingen (schade resistentie) is belangrijk voor het ontwerp en de certificatie van vliegtuigen. Het is gewenst dat het materiaal en de constructie schade-tolerant zijn, en dus een hoge rest-sterkte en goede vermoeiingseigenschappen hebben bij de aanwezigheid van schade.

De primaire delen van civiele vliegtuigconstructies worden in het algemeen nog steeds vervaardigd uit traditionele aluminium-legeringen, vaak in de vorm van plaatwerk-constructies. Tijdens de studie zijn de impact eigenschappen (schade-resistentie an schade-tolerantie) onderzocht van het nieuwe vliegtuigmateriaal 'ARALL'. De eigenschappen van dit materiaal zijn vergeleken met het gedrag van aluminium legeringen en het gedrag van een ander type nieuwe materialen, de zgn. vezelversterkte kunststoffen (composieten).

Het impact-gedrag van materialen is een tamelijk nieuw vakgebied binnen de materiaalkunde. Wat gebeurt er precies tijdens de botsing van een object tegen een plaat-constructie? Hoe kunnen de optredende krachten, verplaatsingen, snelheden en rekken het best gemeten worden? Hoe kan er aan deze botsing gerekend worden? Op deze vragen wordt in deze studie getracht een voorlopig antwoord te geven. Het doel was om inzicht te krijgen in het impact-proces, zodat duidelijker wordt wat de invloed is van de verschillende materiaaleigenschappen op de schade die tijdens dit proces ontstaat.

Gebleken is dat de schade resistentie van ARALL materiaal met sterke R-glas vezels niet veel onderdoet voor die van aluminium legeringen. Daarentegen hebben composiet-materialen en ARALL varianten met koolstof en aramide vezels een veel slechtere schade-resistentie.

De rest-sterkte (schade-tolerantie) van ARALL met aramide is vergelijkbaar met die van thermoplastische composiet-materialen, en is daarom laag. De schade-tolerantie van ARALL met R-glas vezels is superieur ten opzichte van die van ARALL met aramide.

In de literatuur werden alleen reken-modellen gevonden die op lineair-elastische wijze de botsing kunnen beschrijven tussen een vallend voorwerp en een dunne plaat. Met deze modellen kan het gedrag van ARALL, dat plastisch vervormt, niet worden beschreven. Bovendien is uit het onderzoek gebleken dat ook de vervorming van elastische materialen (zoals de composiet-materialen) een sterk niet-lineair karakter heeft. Een niet-lineair elastisch impact computer-model (NOLEIM genaamd) werd ontwikkeld. Dit model bleek in staat met een redelijke nauwkeurigheid het impact-proces te beschrijven. Ook werd een niet-lineair plastisch model opgesteld waar het gedrag van ARALL mee beschreven kan worden.

Curriculum Vitae

Ad Vlot werd op 1 november 1962 in Zwijndrecht geboren. Na het Atheneum examen begon hij in 1981 met de studie luchtvaart- en ruimtevaarttechniek aan de Technische Universiteit Delft. Tijdens zijn stage en zijn afstudeerfase werkte hij bij Fokker (Papendrecht) en onderzocht daar de vervormbaarheid en de bewerkbaarheid van het nieuwe vliegtuigmateriaal 'ARALL', in het kader van het 'ARALL F27 onderhuid-paneel project'. Het doctoraalexamen werd afgelegd in 1986 (cum laude). Enige bestuurlijke ervaring werd tijdens de studie opgedaan als ab-actis van de Vereniging voor Gereformeerde Studenten te Delft (VGSD).

Hij vervolgde zijn studie in de vorm van een promotieonderzoek aan de Faculteit der Luchtvaart- en Ruimtevaarttechniek van de TU Delft binnen de 'ARALL-groep' van de vakgroep Fabricage, vormgeving en materialen (b2). Het onderzoek werd verricht onder leiding van prof.dr.ir. J. Schijve en ir. L.B. Vogelesang en werd gefinancierd door de Stichting voor de Technische Wetenschappen (STW).

Na de afronding van zijn promotieonderzoek werd hij Universitair Docent binnen de vakgroep b2.

De auteur is getrouwd en heeft twee dochters. Hij probeert tevens naast zijn werk tijd te vinden voor een filosofische studie met als onderwerp: 'techniek en geloof'.

index